

Demonstration of cooling by the Muon Ionization Cooling Experiment

<https://doi.org/10.1038/s41586-020-1958-9>

MICE collaboration*

Received: 22 July 2019

Accepted: 13 December 2019

Published online: 5 February 2020

Open access

The use of accelerated beams of electrons, protons or ions has furthered the development of nearly every scientific discipline. However, high-energy muon beams of equivalent quality have not yet been delivered. Muon beams can be created through the decay of pions produced by the interaction of a proton beam with a target. Such ‘tertiary’ beams have much lower brightness than those created by accelerating electrons, protons or ions. High-brightness muon beams comparable to those produced by state-of-the-art electron, proton and ion accelerators could facilitate the study of lepton–antilepton collisions at extremely high energies and provide well characterized neutrino beams^{1–6}. Such muon beams could be realized using ionization cooling, which has been proposed to increase muon-beam brightness^{7,8}. Here we report the realization of ionization cooling, which was confirmed by the observation of an increased number of low-amplitude muons after passage of the muon beam through an absorber, as well as an increase in the corresponding phase-space density. The simulated performance of the ionization cooling system is consistent with the measured data, validating designs of the ionization cooling channel in which the cooling process is repeated to produce a substantial cooling effect^{9–11}. The results presented here are an important step towards achieving the muon-beam quality required to search for phenomena at energy scales beyond the reach of the Large Hadron Collider at a facility of equivalent or reduced footprint⁶.

High-quality muon beams

Fundamental insights into the structure of matter and the nature of its elementary constituents have been obtained using beams of charged particles. The use of time-varying electromagnetic fields to produce sustained acceleration was pioneered in the 1930s^{12–14}. Since then, high-energy and high-brightness particle accelerators have delivered electron, proton and ion beams for applications ranging from the search for new phenomena in the interactions of quarks and leptons to the study of nuclear physics, materials science and biology.

Muon beams can be created using a proton beam striking a target to produce a secondary beam comprising many particle species including pions, kaons and muons. The pions and kaons decay to produce additional muons, which are captured by electromagnetic beamline elements to produce a tertiary muon beam. Capture must be realized on a timescale compatible with the muon lifetime at rest, 2.2 μ s. Without acceleration, the energy and intensity of the muon beam is limited by the energy and intensity of the primary proton beam and the efficiency with which muons are captured.

Accelerated high-brightness muon beams have been proposed as a source of neutrinos at neutrino factories and for the delivery of multi-TeV lepton–antilepton collisions at muon colliders^{1–6}. Muons have attractive properties for the delivery of high-energy collisions. The muon is a fundamental particle with mass 207 times that of the electron. This high mass results in suppression of synchrotron radiation, potentially enabling collisions between beams of muons and

antimuons at energies far in excess of those that can be achieved in an electron–positron collider, such as the proposed International Linear Collider¹⁵, the Compact Linear Collider¹⁶, the Circular Electron–Positron Collider¹⁷ and the electron–positron option of the Future Circular Collider¹⁸. The virtual absence of synchrotron radiation makes it possible to build a substantially smaller facility with the same or greater physics reach.

The energy available in collisions between the constituent gluons and quarks in proton–proton collisions is considerably less than the energy of the proton beam because the colliding quarks and gluons each carry only a fraction of the proton’s momentum. Muons carry the full energy of the beam, making muon colliders attractive for the study of particle physics beyond the energy reach of facilities such as the Large Hadron Collider¹⁹.

Most of the proposals for accelerated muon beams exploit the proton-driven muon-beam production scheme outlined above and use beam cooling to increase the brightness of the tertiary muon beam before acceleration and storage to ensure sufficient luminosity or beam current. Four cooling techniques are in use at particle accelerators: synchrotron radiation cooling²⁰, laser cooling²¹, stochastic cooling²² and electron cooling²³. In each case, the time required to cool the beam is long compared to the muon lifetime. Frictional cooling of muons, in which muons are electrostatically accelerated through an energy-absorbing medium at energies significantly below 1 MeV, has been demonstrated but with low efficiency^{24–26}.

*A list of participants and their affiliations appears at the end of the paper.

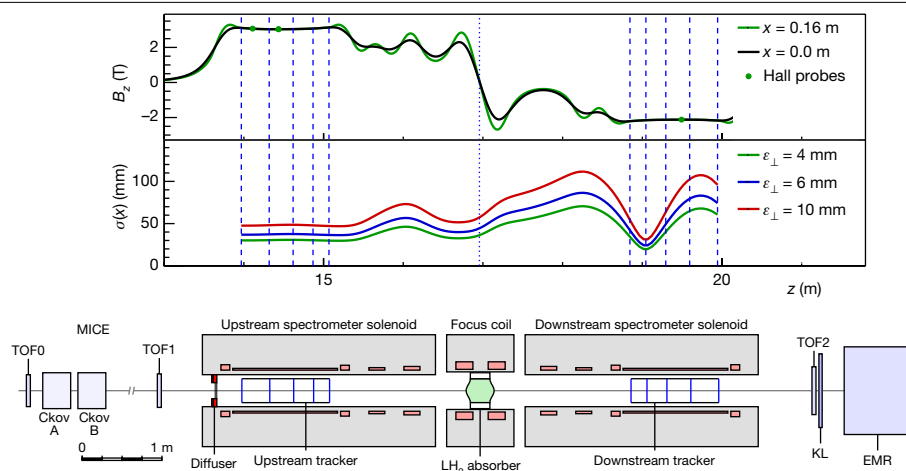


Fig. 1 | The MICE apparatus, the calculated magnetic field and the nominal horizontal width of the beam. The modelled field, B_z , is shown on the beam axis (black line) and at 160 mm from the axis (green line) in the horizontal plane. The readings of Hall probes situated at 160 mm from the beam axis are also shown. Vertical lines indicate the positions of the tracker stations (dashed

lines) and the absorber (dotted line). The nominal r.m.s. beam width, $\sigma(x)$, is calculated assuming a nominal input beam and using linear beam transport equations. See text for the description of the MICE apparatus. TOF0, TOF1 and TOF2 are time-of-flight detector stations; KL is a lead-scintillator pre-shower detector; EMR is the Electron–Muon Ranger.

The technique demonstrated in this study, ionization cooling^{7,8}, is based on a suitably prepared beam passing through an appropriate material (the absorber) and losing momentum through ionization. Radio-frequency cavities restore momentum only along the beam direction. Passing the muon beam through a repeating lattice of material and accelerators causes the ionization cooling effect to build up in a time much shorter than the muon lifetime^{9–11}. Acceleration of a muon beam in a radio-frequency accelerator has recently been demonstrated²⁷, and reduced beam heating, damped by the ionization cooling effect, has been observed²⁸. Ionization cooling has not been demonstrated so far. Experimental validation of the technique is important for the development of muon accelerators. The international Muon Ionization Cooling Experiment (MICE; <http://mice.iit.edu>) was designed to demonstrate transverse ionization cooling, the realization of which is presented here.

The brightness of a particle beam can be characterized by the number of particles in the beam and the volume occupied by the beam in position–momentum phase space. The phase-space volume occupied by the beam and the phase-space density of the beam are conserved quantities in a conventional accelerator without cooling. The phase space considered here is the position and momentum transverse to the direction of travel of the beam, $\mathbf{u} = (x, p_x, y, p_y)$, where x and y are coordinates perpendicular to the beam line, and p_x and p_y are the corresponding components of the momentum. The z axis is the nominal beam axis.

The normalized root-mean-square (r.m.s.) emittance is conventionally used as an indicator of the phase-space volume occupied by the beam²⁹, but this quantity is not conserved when scraping or optical aberrations affect the edge of the beam. The distribution of amplitudes^{30,31} is used here to study effects in the core of the beam. The amplitude of a particle is the distance of the particle from the beam centroid in normalized phase space, and is a conserved quantity in a conventional accelerator without cooling. The phase-space density of the beam is also directly studied using a k -nearest-neighbour technique³².

MICE cooling apparatus

The MICE collaboration has built a tightly focusing solenoid lattice, absorbers and instrumentation to demonstrate the ionization cooling of muons. A schematic of the apparatus is shown in Fig. 1.

A transfer line^{33–35} brought a beam, composed mostly of muons, from a target³⁶ in the ISIS synchrotron³⁷ to the cooling apparatus. The central momentum of the muons could be tuned between $140 \text{ MeV } c^{-1}$ and $240 \text{ MeV } c^{-1}$ (c , speed of light in vacuum). A variable-thickness brass and tungsten diffuser allowed the emittance of the incident beam to be varied between 4 mm and 10 mm.

The tight focusing (low β function) and large acceptance required by the cooling section was achieved using 12 superconducting solenoids. The solenoids were contained in three warm-bore modules cooled by closed-cycle cryocoolers. The upstream and downstream modules (spectrometer solenoids) were identical, each containing three coils to provide a uniform field region of up to 4 T within the 400-mm-diameter warm bore for momentum measurement, as well as two ‘matching’ coils to match the beam to the central pair of closely spaced ‘focus’ coils, which focus the beam onto the absorber. The focus coils were designed to enable peak on-axis fields of up to 3.5 T within one module with a 500-mm-diameter warm bore containing the absorbers.

For the experiment reported here the focus coils were operated in ‘flip’ mode with a field reversal at the centre. Because the magnetic lattice was tightly coupled, the cold mass-suspension systems of the modules were designed to withstand longitudinal cold-to-warm forces of several hundred kN, which could arise during an unbalanced quench of the system. At maximum field, the inter-coil force on the focus coil cold mass was of the order of 2 MN. The total energy stored in the magnetic system was of the order of 5 MJ and the system was protected by both active and passive quench-protection systems. The normal charging and discharging time of the solenoids was several hours. The entire magnetic channel was partially enclosed by a 150-mm-thick soft-iron return yoke for external magnetic shielding. The magnetic fields in the tracking volumes were monitored during operation using calibrated Hall probes.

One of the matching coils in the downstream spectrometer solenoid was not operable owing to a failure of a superconducting lead. Although this necessitated a compromise in the lattice optics and acceptance, the flexibility of the magnetic lattice was exploited to ensure a clear cooling measurement.

The amplitude acceptance of approximately 30 mm, above which particles scrape, was large compared to that of a typical accelerator. Even so, considerable scraping was expected and observed for the highest-emittance beams. Ionization cooling cells with even larger acceptances, producing less scraping, have been designed^{9–11}.

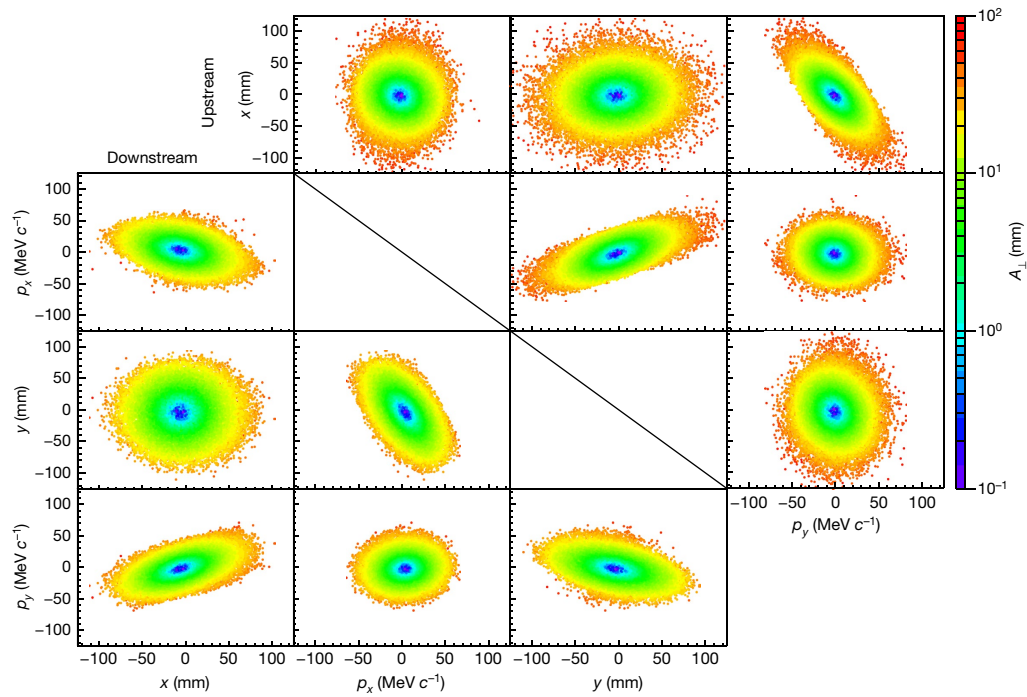


Fig. 2 | Beam distribution in phase space for the 6–140 Full LH2 setting of MICE. Measured beam distribution in the upstream tracker (above the diagonal) and in the downstream tracker (below the diagonal). The measured coordinates of the particles are coloured according to the amplitude A_{\perp} of the particle.

The magnetic lattice of MICE, shown in Fig. 1, was tuned so that the focus of the beam was near the absorber, resulting in a small beam width and large angular divergence. The tight focusing, corresponding to a nominal transverse β function of around 430 mm at the centre of the absorber, yielded an optimal cooling performance.

Materials with low atomic number, such as lithium and hydrogen, have a long radiation length relative to the rate of energy loss, and consequently better cooling performance, making them ideal absorber materials. Therefore, cooling by both liquid-hydrogen and lithium hydride absorbers was studied.

The liquid hydrogen was contained within a 22-l vessel³⁸ in the warm bore of the focus coil. Hydrogen was liquefied by a cryocooler and piped through the focus coil module into the absorber body. When filled, the absorber presented 349.6 ± 0.2 mm of liquid hydrogen along the beam axis with a density of 0.07053 ± 0.00008 g cm⁻³ (all uncertainties represent the standard error). The liquid hydrogen was contained between a pair of aluminium windows covered by multi-layer insulation. A second pair of windows provided a secondary barrier to protect against failure of the primary containment windows. These windows were designed to be as thin as possible so that any scattering in them would not cause substantial heating. The total thickness of all four windows on the beam axis was 0.79 ± 0.01 mm.

The lithium hydride absorber was a disk of thickness 65.37 ± 0.02 mm with a density of 0.6957 ± 0.0006 g cm⁻³. The isotopic composition of the lithium used to produce the absorber was 95% ⁶Li and 5% ⁷Li. The cylinder had a thin coating of parylene to prevent ingress of water or oxygen. Configurations with the empty liquid-hydrogen containment vessel and with no absorber were also studied.

MICE beam instrumentation

Detectors placed upstream and downstream of the apparatus measured the momentum, position and species of each particle entering and leaving the cooling channel in order to reconstruct the full four-dimensional phase space, including the angular momentum introduced by the solenoids. Particles were recorded by the apparatus

one at a time, which enabled high-precision instrumentation to be used and particles other than muons to be excluded from the analysis. Each ensemble of muons was accumulated over a number of hours. This is acceptable because space-charge effects are not expected at a neutrino factory and in a muon collider they become important only at very low longitudinal emittance³⁹. Data-taking periods for each absorber were separated by a period of weeks owing to operational practicalities. The phase-space distribution of the resulting ensemble was reconstructed using the upstream and downstream detectors. The emittance reconstruction in the upstream detector system is described in ref. ⁴⁰.

Upstream of the cooling apparatus, two time-of-flight (TOF) detectors⁴¹ measured the particle velocity. A complementary velocity measurement was made upstream by the threshold Cherenkov counters Ckov A and Ckov B⁴². Scintillating fibre trackers, positioned in the uniform-field region of each of the two spectrometer solenoids, measured the particle position and momentum upstream and downstream of the absorber^{43,44}. Downstream, an additional TOF detector⁴⁵, a mixed lead-scintillator pre-shower detector and a totally active scintillator calorimeter, the Electron–Muon Ranger^{46,47}, identified electrons produced by muon decay and allowed cross-validation of the measurements made by the upstream detectors and the trackers.

Each tracker consisted of five planar scintillating-fibre stations. Each station comprised three views; each view was composed of two layers of 350- μ m-diameter scintillating fibres positioned at an angle of 120° with respect to the other views. The fibres were read out by cryogenic visible-light photon counters⁴⁸. The position of a particle crossing the tracker was inferred from the coincidence of signals from the fibres, and the momentum was calculated by fitting a helical trajectory to the signal positions, with appropriate consideration for energy loss and scattering in the fibres.

Each TOF detector was constructed from two orthogonal planes of scintillator slabs. Photomultiplier tubes at each end of every TOF detector slab were used to determine the time at which a muon passed through the apparatus with a 60-ps resolution⁴¹. The momentum resolution of particles with a small helix radius in the tracker was improved

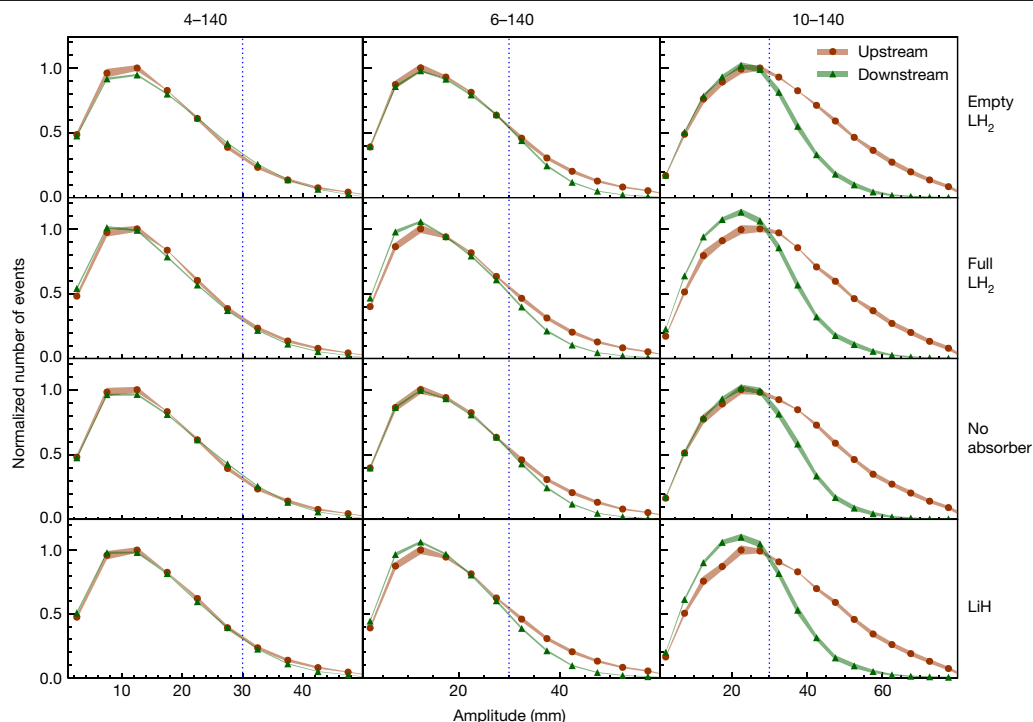


Fig. 3 | Muon amplitudes measured by MICE. The measured upstream distributions are shown by red circles while the downstream distributions are shown by green triangles. Both upstream and downstream distributions are normalized to the bin with the most entries in the upstream distribution (see text). Coloured bands show the estimated standard error, which is dominated

by systematic uncertainties. Vertical lines indicate the approximate channel acceptance above which scraping occurs. The number of events in each sample is listed in Extended Data Table 2. Data for each experimental configuration were accumulated in a single discrete period.

by combining the TOF measurement of velocity with the measurement of momentum in the tracker.

A detailed Monte Carlo simulation of the experiment was performed to study the resolution and efficiency of the instrumentation and to determine the expected performance of the cooling apparatus^{49,50}. The simulation was found to give a good description of the data⁴⁰.

Demonstration of cooling

The data presented here were taken using beams with a nominal momentum of $140 \text{ MeV } c^{-1}$ and a nominal normalized r.m.s. emittance in the upstream tracking volume of 4 mm, 6 mm and 10 mm; these settings are denoted as ‘4–140’, ‘6–140’ and ‘10–140’, respectively. Beams with a higher emittance have more muons at high amplitudes and occupy a larger region in phase space. For each beam setting, two samples were considered for the analysis. The ‘upstream sample’ contained particles identified as muons by the upstream TOF detectors and tracker, for which the muon trajectory reconstructed in the upstream tracker was fully contained in the fiducial volume and for which the reconstructed momentum fell within the range $135 \text{ MeV } c^{-1}$ to $145 \text{ MeV } c^{-1}$ (which is considerably higher than the momentum resolution of the tracker, $2 \text{ MeV } c^{-1}$). The ‘downstream sample’ was the subset of the upstream sample for which the reconstructed muons were fully contained in the fiducial volume of the downstream tracker. Each of the samples had between 30,000 and 170,000 events. Examples of the phase-space distributions of the particles in the two samples are shown in Fig. 2. The strong correlations between y and p_x and between x and p_y are due to the angular momentum introduced by the solenoidal field. The shorter tails along the semi-minor axis compared to the semi-major axis in these projections arise from scraping in the diffuser.

The distributions of amplitudes in the upstream and downstream samples for each of the 4–140, 6–140 and 10–140 datasets are shown in Fig. 3. The nominal acceptance of the magnetic channel is also

indicated. A correction has been made to account for the migration of events between amplitude bins due to the detector resolution and to account for inefficiency in the downstream detector system (see Methods). Distributions are shown for the measurements with an empty liquid-hydrogen vessel (‘Empty LH_2 ’), with a filled liquid-hydrogen vessel (‘Full LH_2 ’), with no absorber (‘No absorber’) and with the lithium hydride absorber (‘LiH’). The distributions were normalized to allow a comparison of the shape of the distribution between different absorbers. Each pair of upstream and downstream amplitude distributions is scaled by $1/N_{\text{max}}^u$, where N_{max}^u is the number of events in the most populated bin in the upstream sample.

The behaviour of the beam at low amplitude is the key result of this study. For the ‘No absorber’ and ‘Empty LH_2 ’ configurations, the number of events with low amplitude in the downstream sample is similar to that observed in the upstream sample. For the 6–140 and 10–140 configurations for both the ‘Full LH_2 ’ and the ‘LiH’ samples, the number of events with low amplitude is considerably larger in the downstream sample than in the upstream sample. This indicates an increase in the number of particles in the beam core when an absorber is installed, which is expected if ionization cooling takes place. This effect can occur only because energy loss is a non-conservative process.

A reduction in the number of muons at high amplitude is also observed, especially for the 10–140 setting. Whereas part of this effect arises owing to migration of muons into the beam core, a substantial number of high-amplitude particles outside the beam acceptance intersected the beam pipe or fell outside the fiducial volume of the downstream tracker. The beam pipe was made of materials with higher atomic number than those of the absorber materials, so interactions in the beam pipe tended to be dominated by multiple Coulomb scattering, leading to beam loss.

A χ^2 test was performed to determine the confidence with which the null hypothesis that for the same input beam setting, the amplitude distributions in the downstream samples of the ‘Full LH_2 ’ and ‘Empty LH_2 ’

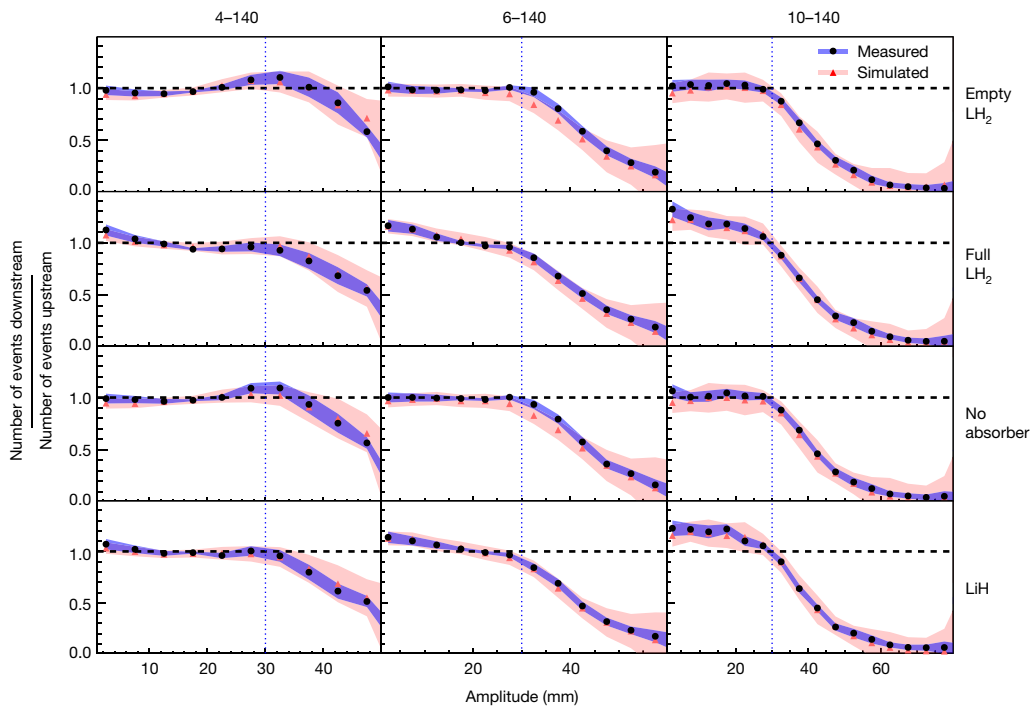


Fig. 4 | Downstream-to-upstream ratio of number of events in MICE. A ratio greater than unity in the beam core, which is evidence of ionization cooling, is observed in the data obtained with the 6–140 and 10–140 beams with both the full LH_2 absorber and the LiH absorber. The effect predicted from the simulation is shown in red and that measured is shown in black. The

corresponding shading shows the estimated standard error, which is dominated by systematic uncertainty. Vertical lines indicate the channel acceptance above which scraping occurs. The number of events in each sample is listed in Extended Data Table 2. Data for each experimental configuration were accumulated in a single discrete period.

configurations are compatible, and the amplitude distributions in the downstream samples of the ‘ LiH ’ and ‘No absorber’ configurations are compatible. The test was performed on the uncorrected distributions using only statistical uncertainties. Systematic effects are the same for the pairs of distributions tested, and cancel. Assuming that this null hypothesis is correct, the probability of observing the effect seen in the data is considerably lower than 10^{-5} for each beam setting and for each ‘Full LH_2 ’–‘Empty LH_2 ’ and ‘ LiH ’–‘No absorber’ pair; therefore, the null hypothesis was rejected.

The fractional increase in the number of particles with low amplitude is most pronounced for the 10–140 beams. High-amplitude beams have high transverse emittance, ε_{\perp} , and a larger transverse momentum relative to the stochastic increase in transverse momentum due to scattering, so they undergo more cooling. For the magnet settings and beams studied here, heating due to multiple Coulomb scattering becomes dominant over ionization cooling at an emittance of around 4 mm. As a result, only modest cooling is observed for the 4–140 setting in both the ‘Full LH_2 ’ and ‘ LiH ’ configurations.

The ratios of the downstream to the upstream amplitude distributions are shown in Fig. 4. In the ‘No absorber’ and ‘Empty absorber’ configurations, the ratios are consistent with 1 for amplitudes of less than 30 mm, confirming the conservation of amplitude in this region, irrespective of the incident beam. Above 30 mm the ratios drop below unity, indicating that at high amplitude there are fewer muons downstream than upstream, as outlined above. The presence of the absorber windows does not strongly affect the amplitude distribution. For the 6–140 and 10–140 datasets, the addition of liquid-hydrogen or lithium hydride absorber material causes the ratios to rise above unity for the low-amplitude particles that correspond to the beam core. This indicates an increase in the number of particles in the beam core and demonstrates ionization cooling.

The density in phase space is an invariant of a symplectic system; therefore, an increase in phase-space density is also an unequivocal

demonstration of cooling. Figure 5 shows the normalized density of the upstream and downstream samples, $\rho_i(\mathbf{u}_i)/\rho_0$, as a function of α , the fraction of the upstream sample that has a density greater than or equal to ρ_i . This is known as the quantile distribution. To enable comparison between different beam configurations, the densities for each configuration have been normalized to the peak density in the upstream tracker, ρ_0 . To enable comparison between the upstream and downstream distributions, the fraction of the sample is always relative to the total number of events in the upstream sample. The transmission is the fraction of the beam for which the density in the downstream tracker reaches zero. For the ‘No absorber’ and ‘Empty LH_2 ’ cases, the downstream density in the highest-density regions is indistinguishable from the upstream density. A small amount of scraping is observed for the 4–140 and 6–140 beams. More substantial scraping is observed for the 10–140 beam. In all cases, for ‘Full LH_2 ’ and ‘ LiH ’ the phase-space density increases, and the increase is greater for higher-emittance beams. These observations demonstrate the ionization cooling of the beam when an absorber is installed. In the presence of an absorber, beams with larger nominal emittance show a greater increase in density than those with a lower nominal emittance.

Conclusions

Ionization cooling has been unequivocally demonstrated. We have built and operated a section of a solenoidal cooling channel and demonstrated the ionization cooling of muons using both liquid hydrogen and lithium hydride absorbers. The effect has been observed through the measurement of both an increase in the number of small-amplitude particles (Figs. 3, 4) and an increase in the phase-space density of the beam (Fig. 5). The results are well described by simulations (Fig. 4). This demonstration of ionization cooling is an important advance in the development of high-brightness muon beams. The seminal results presented in this paper encourage further development of high-brightness

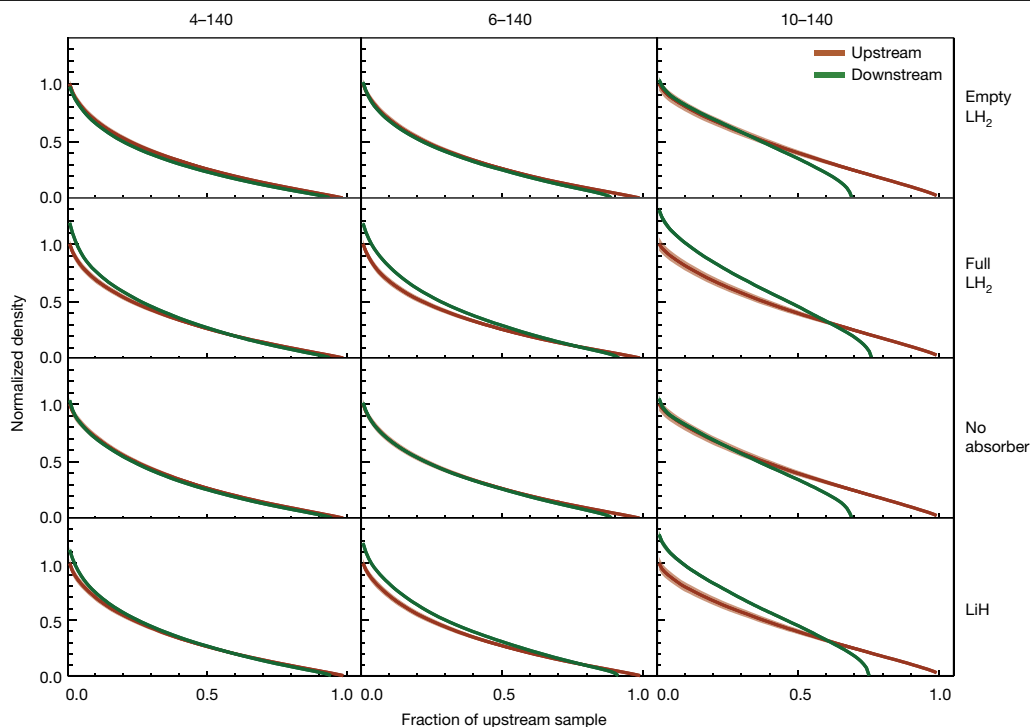


Fig. 5 | Normalized quantile distribution of the beam density in MICE.

Upstream and downstream quantiles are indicated by orange and green lines, respectively, as a function of the fraction of the upstream sample. For each configuration, the density is normalized to the highest-density region in the

upstream sample. The estimated standard error is indicated by the thickness of the coloured bands and is dominated by systematic uncertainty. The number of events in each sample is listed in Extended Data Table 2. Data for each experimental configuration were accumulated in a single discrete period.

muon beams as a tool for the investigation of the fundamental properties of matter.

Online content

Any methods, additional references, Nature Research reporting summaries, source data, extended data, supplementary information, acknowledgements, peer review information; details of author contributions and competing interests; and statements of data and code availability are available at <https://doi.org/10.1038/s41586-020-1958-9>.

- Neuffer, D. V. & Palmer, R. B. A high-energy high-luminosity $\mu^+\mu^-$ collider. *AIP Conf. Proc.* **356**, 344–358 (1996).
- Geer, S. Neutrino beams from muon storage rings: characteristics and physics potential. *Phys. Rev. D* **57**, 6989–6997 (1998).
- Alsharo'a, M. M. et al. Recent progress in neutrino factory and muon collider research within the Muon Collaboration. *Phys. Rev. Accel. Beams* **6**, 081001 (2003).
- Palmer, R. B. Muon colliders. *Rev. Accel. Sci. Tech.* **7**, 137–159 (2014).
- Boscolo, M. et al. Low emittance muon accelerator studies with production from positrons on target. *Phys. Rev. Accel. Beams* **21**, 061005 (2018).
- Neuffer, D. & Shiltsev, V. On the feasibility of a pulsed 14 TeV c.m.e. muon collider in the LHC tunnel. *J. Instrum.* **13**, T10003 (2018).
- Skrinsky, A. N. & Parkhomchuk, V. V. Cooling methods for beams of charged particles. *Sov. J. Part. Nucl.* **12**, 223–247 (1981).
- Neuffer, D. Principles and applications of muon cooling. *Part. Accel.* **14**, 75–90 (1983).
- Rogers, C. T. et al. Muon front end for the neutrino factory. *Phys. Rev. Accel. Beams* **16**, 040104 (2013).
- Stratakis, D. & Palmer, R. B. Rectilinear six-dimensional ionization cooling channel for a muon collider: a theoretical and numerical study. *Phys. Rev. Accel. Beams* **18**, 031003 (2015).
- Neuffer, D. et al. Final cooling for a high-energy high-luminosity lepton collider. *J. Instrum.* **12**, T07003 (2017).
- Lawrence, E. O. & Livingston, M. S. The production of high speed protons without the use of high voltages. *Phys. Rev.* **38**, 834 (1931).
- Lewis, G. N., Livingston, M. S. & Lawrence, E. O. The emission of alpha-particles from various targets bombarded by deuterons of high speed. *Phys. Rev.* **44**, 55–56 (1933).
- R. Wideröe. Das Betatron. *Z. Angew. Phys.* **5**, 187–200 (1953).
- Behnke, T. et al. *The International Linear Collider Technical Design Report – Volume 1: Executive Summary* (ILC, 2013).
- Burrows, P. N. et al. (eds) *The Compact Linear Collider (CLIC): 2018 Summary Report* (CERN, 2018).
- CEPC Study Group. *CEPC Conceptual Design Report: Volume 1 – Accelerator*. (IHEP, 2018).
- Abada, A. et al. FCC-ee: the lepton collider. *Eur. Phys. J. Spec. Top.* **228**, 261–623 (2019).
- Myers, S. The Large Hadron Collider 2008–2013. *Int. J. Mod. Phys. A* **28**, 1330035 (2013).
- Lee, S. Y. *Accelerator Physics* 3rd edn (World Scientific, 2012).
- Schröder, S. et al. First laser cooling of relativistic ions in a storage ring. *Phys. Rev. Lett.* **64**, 2901–2904 (1990).
- Möhl, D., Petrucci, G., Thorndahl, L., & van der Meer, S. Physics and technique of stochastic cooling. *Phys. Rep.* **58**, 73–119 (1980).
- Parkhomchuk, V. V. & Skrinsky, A. N. Electron cooling: 35 years of development. *Phys. Uspekhi* **43**, 433–452 (2000).
- Mühlbauer, M. et al. Frictional cooling: experimental results. *Hyperfine Interact.* **119**, 305–310 (1999).
- Abramowicz, H. et al. A muon collider scheme based on frictional cooling. *Nucl. Instrum. Methods Phys. Res. A* **546**, 356–375 (2005).
- Taqqi, D. Compression and extraction of stopped muons. *Phys. Rev. Lett.* **97**, 194801 (2006).
- Bae, S. et al. First muon acceleration using a radio frequency accelerator. *Phys. Rev. Accel. Beams* **21**, 050101 (2018).
- Mori, Y. et al. Neutron source with emittance recovery internal target. In *Proc. of the 23rd Particle Accelerator Conference (JACoW, 2009)*; <http://accelconf.web.cern.ch/AccelConf/PAC2009/papers/th4gac04.pdf>.
- Penn, G. & Wurtele, J. S. Beam envelope equations for cooling of muons in solenoid fields. *Phys. Rev. Lett.* **85**, 764–767 (2000).
- Holzer, E. B. Figure of merit for muon cooling – an algorithm for particle counting in coupled phase planes. *Nucl. Instrum. Methods Phys. Res. A* **532**, 270–274 (2004).
- Rogers, C. *Beam Dynamics in an Ionisation Cooling Channel*. PhD thesis, Imperial College London (2008).
- Drielsma, F. *Measurement of the Increase in Phase Space Density of a Muon Beam through Ionization Cooling*. PhD thesis, Univ. Geneva (2018).
- Bogomilov, M. et al. The MICE muon beam on ISIS and the beam-line instrumentation of the Muon Ionization Cooling Experiment. *J. Instrum.* **7**, P05009 (2012).
- Adams, D. et al. Characterisation of the muon beams for the Muon Ionisation Cooling Experiment. *Eur. Phys. J. C* **73**, 2582 (2013).
- Bogomilov, M. et al. Pion contamination in the MICE muon beam. *J. Instrum.* **11**, P03001 (2016).
- Booth, C. N. et al. The design and performance of an improved target for MICE. *J. Instrum.* **11**, P05006 (2016).
- Thomason, J. W. G. The ISIS Spallation Neutron and Muon Source – the first thirty-three years. *Nucl. Instrum. Methods Phys. Res. A* **917**, 61–67 (2019).
- Bayliss, V. et al. The liquid-hydrogen absorber for MICE. *J. Instrum.* **13**, T09008 (2018).
- Stratakis, D., Palmer, R. B. & Grote, D. P. Influence of space-charge fields on the cooling process of muon beams. *Phys. Rev. Accel. Beams* **18**, 044201 (2015).

40. Blackmore, V. et al. First particle-by-particle measurement of emittance in the Muon Ionization Cooling Experiment. *Eur. Phys. J. C* **79**, 257 (2019).
41. Bertoni, R. et al. The design and commissioning of the MICE upstream time-of-flight system. *Nucl. Instrum. Methods Phys. Res. A* **615**, 14–26 (2010).
42. Cremaldi, L. et al. A Cherenkov radiation detector with high density aerogels. *IEEE Trans. Nucl. Sci.* **56**, 1475–1478 (2009).
43. Ellis, M. et al. The design, construction and performance of the MICE scintillating fibre trackers. *Nucl. Instrum. Methods Phys. Res. A* **659**, 136–153 (2011).
44. Dobbs, A. et al. The reconstruction software for the MICE scintillating fibre trackers. *J. Instrum.* **11**, T12001 (2016).
45. Bertoni, R. et al. *The Construction of the MICE TOF2 Detector*. MICE Technical Note 254 (2010); <http://mice.iit.edu/micenotes/public/pdf/MICE0286/MICE0286.pdf>.
46. Adams, D. et al. Electron–Muon Ranger: performance in the MICE Muon Beam. *J. Instrum.* **10**, P12012 (2015).
47. Asfandiyarov, R. et al. The design and construction of the MICE Electron–Muon Ranger. *J. Instrum.* **11**, T10007 (2016).
48. Petroff, M. D. & Stapelbroek, M. G. Photon-counting solid-state photomultiplier. *IEEE Trans. Nucl. Sci.* **36**, 158–162 (1989).
49. Agostinelli, S. et al. GEANT4: a simulation toolkit. *Nucl. Instrum. Methods Phys. Res. A* **506**, 250–303 (2003).
50. Asfandiyarov, R. et al. MAUS: the MICE Analysis User Software. *J. Instrum.* **14**, T04005 (2019).

Publisher's note Springer Nature remains neutral with regard to jurisdictional claims in published maps and institutional affiliations.



Open Access This article is licensed under a Creative Commons Attribution 4.0 International License, which permits use, sharing, adaptation, distribution and reproduction in any medium or format, as long as you give appropriate credit to the original author(s) and the source, provide a link to the Creative Commons license, and indicate if changes were made. The images or other third party material in this article are included in the article's Creative Commons license, unless indicated otherwise in a credit line to the material. If material is not included in the article's Creative Commons license and your intended use is not permitted by statutory regulation or exceeds the permitted use, you will need to obtain permission directly from the copyright holder. To view a copy of this license, visit <http://creativecommons.org/licenses/by/4.0/>.

© The Author(s) 2020

MICE collaboration

M. Bogomilov¹, R. Tsenov¹, G. Vankova-Kirilova¹, Y. P. Song², J. Y. Tang², Z. H. Li³, R. Bertoni⁴, M. Bonesini⁴, F. Chignoli⁴, R. Mazza⁴, V. Palladino⁵, A. de Bari⁶, D. Orestano⁷, L. Tortora⁷, Y. Kuno⁸, H. Sakamoto^{8,34}, A. Sato⁸, S. Ishimoto⁹, M. Chung¹⁰, C. K. Sung¹⁰, F. Filthaut^{11,12}, D. Jokovic¹³, D. Maletic¹³, M. Savic¹³, N. Jovancevic¹⁴, J. Nikolov¹⁴, M. Vretenar¹⁵, S. Ramberger¹⁵, R. Asfandiyarov¹⁶, A. Blondel¹⁶, F. Drielsma¹⁶, Y. Karadzhev¹⁶, S. Boyd¹⁷, J. R. Greis¹⁷, T. Lord¹⁷, C. Pidcott^{17,35}, I. Taylor^{17,36}, G. Charnley¹⁸, N. Collomb¹⁸, K. Dumbell¹⁸, A. Gallagher¹⁸, A. Grant¹⁸, S. Griffiths¹⁸, T. Hartnett¹⁸, B. Martlew¹⁸, A. Moss¹⁸, A. Muir¹⁸, I. Mullacraane¹⁸, A. Oates¹⁸, P. Owens¹⁸, G. Stokes¹⁸, P. Warburton¹⁸, C. White¹⁸, D. Adams¹⁹, V. Bayliss¹⁹, J. Boehm¹⁹, T. W. Bradshaw¹⁹, C. Brown^{19,20}, M. Courthold¹⁹, J. Govans¹⁹, M. Hills¹⁹, J.-B. Lagrange¹⁹, C. Macwaters¹⁹, A. Nichols¹⁹, R. Preece¹⁹, S. Ricciardi¹⁹, C. Rogers^{19*}, T. Stanley¹⁹,

J. Tarrant¹⁹, M. Tucker¹⁹, S. Watson^{19,37}, A. Wilson¹⁹, R. Bayes^{21,38}, J. C. Nugent²¹, F. J. P. Soler²¹, G. T. Chatzitheodoridis^{21,22,23}, A. J. Dick^{22,23}, K. Ronald^{22,23}, C. G. Whyte^{22,23}, A. R. Young^{22,23}, R. Gamet²⁴, P. Cooke²⁴, V. J. Blackmore²⁵, D. Colling²⁵, A. Dobbs^{25,39}, P. Dornan²⁵, P. Franchini²⁵, C. Hunt^{25,40}, P. B. Jurj²⁵, A. Kurup²⁵, K. Long²⁵, J. Martyniak²⁵, S. Middleton^{25,41}, J. Pasternak²⁵, M. A. Uchida^{25,42}, J. H. Cobb²⁶, C. N. Booth²⁷, P. Hodgson²⁷, J. Langlands²⁷, E. Overton^{27,43}, V. Pec²⁷, P. J. Smith²⁷, S. Wilbur²⁷, M. Ellis^{20,44}, R. B. S. Gardener²⁰, P. Kyberd²⁰, J. J. Nebrensky²⁰, A. DeMello²⁸, S. Gourlay²⁸, A. Lambert²⁸, D. Li²⁸, T. Luo²⁸, S. Prestemon²⁸, S. Virostek²⁸, M. Palmer²⁹, H. Witte²⁹, D. Adey^{30,45}, A. D. Bross³⁰, D. Bowring³⁰, A. Liu^{30,46}, D. Neuffer³⁰, M. Popovic³⁰, P. Rubinov³⁰, B. Freemire^{31,46}, P. Hanlet^{31,47}, D. M. Kaplan³¹, T. A. Mohaya^{31,47}, D. Rajaram³¹, P. Snopok³¹, Y. Torun³¹, L. M. Cremaldi³², D. A. Sanders³², D. J. Summers³², L. R. Coney^{33,48}, G. G. Hanson³³ & C. Heidt³³

¹Department of Atomic Physics, St Kliment Ohridski University of Sofia, Sofia, Bulgaria.

²Institute of High Energy Physics, Chinese Academy of Sciences, Beijing, China.

³Sichuan University, Chengdu, China.

⁴Sezione INFN Milano Bicocca, Dipartimento di Fisica G. Occhialini, Milan, Italy.

⁵Sezione INFN Napoli and Dipartimento di Fisica, Università Federico II, Complesso Universitario di Monte S. Angelo, Naples, Italy.

⁶Sezione INFN Pavia and Dipartimento di Fisica, Pavia, Italy.

⁷INFN Sezione di Roma Tre and Dipartimento di Matematica e Fisica, Università Roma Tre, Rome, Italy.

⁸Osaka University, Graduate School of Science, Department of Physics, Toyonaka, Japan.

⁹High Energy Accelerator Research Organization (KEK), Institute of Particle and Nuclear Studies, Tsukuba, Japan.

¹⁰UNIST, Ulsan, South Korea.

¹¹Nikhef, Amsterdam, The Netherlands.

¹²Radboud University, Nijmegen, The Netherlands.

¹³Institute of Physics, University of Belgrade, Belgrade, Serbia.

¹⁴Faculty of Sciences, University of Novi Sad, Novi Sad, Serbia.

¹⁵CERN, Geneva, Switzerland.

¹⁶DPNC, Section de Physique, Université de Genève, Geneva, Switzerland.

¹⁷Department of Physics, University of Warwick, Coventry, UK.

¹⁸STFC Daresbury Laboratory, Daresbury, Cheshire, UK.

¹⁹STFC Rutherford Appleton Laboratory, Harwell Oxford, Didcot, UK.

²⁰Brunel University, Uxbridge, UK.

²¹School of Physics and Astronomy, The University of Glasgow, Glasgow, UK.

²²SUPA and Department of Physics, University of Strathclyde, Glasgow, UK.

²³Cockcroft Institute, Daresbury Laboratory, Daresbury, UK.

²⁴Department of Physics, University of Liverpool, Liverpool, UK.

²⁵Department of Physics, Blackett Laboratory, Imperial College London, London, UK.

²⁶Department of Physics, University of Oxford, Oxford, UK.

²⁷Department of Physics and Astronomy, University of Sheffield, Sheffield, UK.

²⁸Lawrence Berkeley National Laboratory, Berkeley, CA, USA.

²⁹Brookhaven National Laboratory, Upton, NY, USA.

³⁰Fermilab, Batavia, IL, USA.

³¹Illinois Institute of Technology, Chicago, IL, USA.

³²University of Mississippi, Oxford, MS, USA.

³³University of California, Riverside, CA, USA.

³⁴Present address: RIKEN 2-1 Horosawa, Wako, Japan.

³⁵Present address: Department of Physics and Astronomy, University of Sheffield, Sheffield, UK.

³⁶Present address: Defence Science and Technology Laboratory, Salisbury, UK.

³⁷Present address: ATC, Royal Observatory Edinburgh, Edinburgh, UK.

³⁸Present address: Laurentian University, Sudbury, Ontario, Canada.

³⁹Present address: OPERA Simulation Software, Kidlington, UK.

⁴⁰Present address: CERN, Geneva, Switzerland.

⁴¹Present address: School of Physics and Astronomy, University of Manchester, Manchester, UK.

⁴²Present address: Cavendish Laboratory, Cambridge, UK.

⁴³Present address: Arm, Sheffield, UK.

⁴⁴Present address: Westpac Group, Sydney, New South Wales, Australia.

⁴⁵Present address: Institute of High Energy Physics, Chinese Academy of Sciences, Beijing, China.

⁴⁶Present address: Euclid Techlabs, Bolingbrook, IL, USA.

⁴⁷Present address: Fermilab, Batavia, IL, USA.

⁴⁸Present address: European Spallation Source ERIC, Lund, Sweden.

*e-mail: chris.rogers@stfc.ac.uk

Characterization of beam brightness

In particle accelerators, the average beam brightness \bar{B} is defined as the beam current, I , passing through a transverse phase-space volume \mathcal{V}_4 (ref. ³¹)

$$\bar{B} = \frac{I}{\mathcal{V}_4} \quad (1)$$

The normalized r.m.s. emittance is often used as an indicator of the phase-space volume occupied by the beam and is given by²⁹

$$\varepsilon_{\perp} = \frac{\sqrt[4]{|V|}}{m_{\mu}c} \quad (2)$$

where m_{μ} is the muon mass and $|V|$ is the determinant of the covariance matrix of the beam in the transverse phase space $\mathbf{u} = (x, p_x, y, p_y)$. The covariance matrix has elements $v_{ij} = \langle u_i u_j \rangle - \langle u_i \rangle \langle u_j \rangle$. The distribution of individual particle amplitudes also describes the volume of the beam in phase space.

The amplitude is defined by³⁰

$$A_{\perp} = \varepsilon_{\perp} R^2(\mathbf{u}, \langle \mathbf{u} \rangle) \quad (3)$$

where $R^2(\mathbf{u}, \mathbf{v})$ is the square of the distance between two points, \mathbf{u} and \mathbf{v} , in the phase space, normalized to the covariance matrix:

$$R^2(\mathbf{u}, \mathbf{v}) = (\mathbf{u} - \mathbf{v})^T V^{-1} (\mathbf{u} - \mathbf{v}) \quad (4)$$

The normalized r.m.s. emittance is proportional to the mean of the particle amplitude distribution. In the approximation that particles travel near the beam axis, and in the absence of cooling, the particle amplitudes and the normalized r.m.s. emittance are conserved quantities. If the beam is well described by a multivariate Gaussian distribution, then R^2 is distributed according to a χ^2 distribution with four degrees of freedom, so the amplitudes are distributed according to

$$f(A_{\perp}) = \frac{A_{\perp}}{4\varepsilon_{\perp}^2} \exp\left(\frac{-A_{\perp}}{2\varepsilon_{\perp}}\right) \quad (5)$$

The rate of change of the normalized transverse emittance as the beam passes through an absorber is given approximately by^{8,29,31}

$$\frac{d\varepsilon_{\perp}}{dz} \approx -\frac{\varepsilon_{\perp}}{\beta^2 E_{\mu}} \left| \frac{dE_{\mu}}{dz} \right| + \frac{\beta_{\perp} (13.6 \text{ MeV } c^{-1})^2}{2\beta^3 E_{\mu} m_{\mu} X_0} \quad (6)$$

where βc is the muon velocity, E_{μ} is the muon energy, $|dE_{\mu}/dz|$ is the mean energy loss per unit path length, X_0 is the radiation length of the absorber and β_{\perp} is the transverse betatron function at the absorber²⁹. The first term of this equation describes ‘cooling’ by ionization energy loss and the second term describes ‘heating’ by multiple Coulomb scattering. Equation (6) implies that there is an equilibrium emittance for which the emittance change is zero.

If the beam is well described by a multivariate Gaussian distribution both before and after cooling, then the downstream and upstream amplitude distributions $f^d(A_{\perp})$ and $f^u(A_{\perp})$ are related to the downstream and upstream emittances ε_{\perp}^d and ε_{\perp}^u by

$$\frac{f^d(A_{\perp})}{f^u(A_{\perp})} = \left(\frac{\varepsilon_{\perp}^u}{\varepsilon_{\perp}^d} \right)^2 \exp\left[-\frac{A_{\perp}}{2} \left(\frac{1}{\varepsilon_{\perp}^d} - \frac{1}{\varepsilon_{\perp}^u} \right) \right] \quad (7)$$

In the experiment described in this paper, many particles do not travel near the beam axis. These particles experience effects from

optical aberrations, as well as geometrical effects such as scraping, in which high-amplitude particles outside the experiment’s aperture are removed from the beam. Scraping reduces the emittance of the ensemble and selectively removes those particles that scatter more than the rest of the ensemble. Optical aberrations and scraping introduce a bias in the change in r.m.s. emittance that occurs because of ionization cooling. In this work the distribution of amplitudes is studied. To expose the behaviour in the beam core, independently of aberrations affecting the beam tail, V and ε_{\perp} are recalculated for each amplitude bin, including particles that are in lower-amplitude bins and excluding particles that are in higher-amplitude bins. This results in a distribution that, in the core of the beam, is independent of scraping effects and spherical aberrations.

The change in phase-space density provides a direct measurement of the cooling effect. The k -nearest-neighbour algorithm provides a robust non-parametric estimator of the phase-space density of the muon ensemble^{32,34,52}. The separation of pairs of muons is characterized by the normalized squared distance, $R_{ij}^2(\mathbf{u}_i, \mathbf{u}_j)$, between muons with positions \mathbf{u}_i and \mathbf{u}_j . A volume \mathcal{V}_{ik} is associated with each particle, which corresponds to the hypersphere that is centred on \mathbf{u}_i and intersects the k th nearest particle (that is, the particle that has the k th smallest R_{ij}). The density, ρ_i , associated with the i th particle is estimated by

$$\rho_i(\mathbf{u}_i) = \frac{k}{n} \frac{1}{|V|^{1/2} \mathcal{V}_{ik}} = \frac{2k}{n\pi^2} \frac{1}{|V|^{1/2} R_{ik}^4} \quad (8)$$

where n is the number of particles in the ensemble. An optimal value for k is used, $k = n^{4/(4+d)} = \sqrt{n}$, with phase-space dimension $d = 4$ (ref. ³²).

Data taking and reconstruction

Data were buffered in the front-end electronics and read out after each target actuation. Data storage was triggered by a coincidence of signals in the photomultiplier tubes (PMTs) serving a single scintillator slab in the upstream TOF station closest to the cooling channel (TOF1). The data recorded in response to a particular trigger are referred to as a ‘particle event’.

Each TOF station was composed of a number of scintillator slabs that were read out using a pair of PMTs, one mounted at each end of each slab. The reconstruction of the data began with the search for coincidences in the signals from the two PMTs serving any one slab in a TOF plane. Such coincidences are referred to as ‘slab hits’. ‘Space points’ were then formed from the intersection of slab hits in the x and y projections of each TOF station separately. The position and time at which a particle giving rise to the space point crossed the TOF station were then calculated using the slab position and the times measured in each of the PMTs. The relative timing of the two upstream TOF stations (TOF0 and TOF1) was calibrated relative to the measured time taken for electrons to pass between the two TOF detectors, on the assumption that they travelled at the speed of light.

Signals in the tracker readout were collected to reconstruct the helical trajectories (‘tracks’) of charged particles in the upstream and downstream trackers (TKU and TKD, respectively). Multiple Coulomb scattering introduced significant uncertainties in the reconstruction of the helical trajectory of tracks with a bending radius of less than 5 mm. For this class of track, the momentum was deduced by combining the tracker measurement with the measurements from nearby detectors. The track-fitting quality was characterized by the χ^2 per degree of freedom

$$\chi_{\text{df}}^2 = \frac{1}{n} \sum_i \frac{\delta x_i^2}{\sigma_i^2} \quad (9)$$

where δx_i is the distance between the fitted track and the measured signal in the i th tracker plane, σ_i is the resolution of the position measurement in the tracker planes and n is the number of planes that had

a signal used in the track reconstruction. Further details of the reconstruction and simulation may be found in ref. ⁵⁰.

Beam selection

Measurements made in the instrumentation upstream of the absorber were used to select the input beam. The input beam (the upstream sample) was composed of events that satisfied the following criteria:

- Exactly one space point was found in TOF0 and TOF1 and exactly one track in TKU.
- The track in TKU had $\chi_{df}^2 < 8$ and was contained within the 150-mm fiducial radius over the full length of TKU.
- The track in TKU had a reconstructed momentum in the range 135–145 MeV c^{-1} , corresponding to the momentum acceptance of the cooling cell.
- The time-of-flight between TOF0 and TOF1 was consistent with that of a muon, given the momentum measured in TKU.
- The radius at which the track in TKU passed through the diffuser was smaller than the diffuser aperture.

The beam emerging from the cooling cell (the downstream sample) was characterized using the subset of the upstream sample that satisfied the following criteria:

- Exactly one track was found in TKD.
- The track in TKD had $\chi_{df}^2 < 8$ and was contained within the 150-mm fiducial radius of TKD over the full length of the tracker.

The same sample-selection criteria were used to select events from the simulation of the experiment, which included a reconstruction of the electronics signals expected for the simulated particles.

Calculation of amplitudes

The amplitude distributions obtained from the upstream and downstream samples were corrected for the effects of the detector efficiency and resolution and for the migration of events between amplitude bins. The corrected number of events in a bin, N_i^{corr} , was calculated from the raw number of events, N_j^{raw} , using

$$N_i^{\text{corr}} = E_i \sum_j S_{ij} N_j^{\text{raw}} \quad (10)$$

where E_i is the efficiency correction factor and S_{ij} accounts for the detector resolution and event migration. E_i and S_{ij} were estimated from the simulation of the experiment. The uncorrected and corrected amplitude distributions for a particular configuration are shown in Extended Data Fig. 1. The correction is small relative to the ionization cooling effect, which is clear even in the uncorrected distributions.

It can be seen from equation (7) that in the limit of small amplitudes, and in the approximation that the beam is normally distributed in the phase-space variables, the ratio of the number of muons is equal to the ratio of the square of the emittances,

$$\lim_{A_{\perp} \rightarrow 0} \frac{f^d(A_{\perp})}{f^u(A_{\perp})} = \left(\frac{\varepsilon_{\perp}^u}{\varepsilon_{\perp}^d} \right)^2 \quad (11)$$

The ratio of f^d to f^u in the lowest-amplitude bin of Fig. 3, which is an approximation to this ratio, is listed in Extended Data Table 1.

Data availability

The unprocessed and reconstructed data that support the findings of this study are publicly available on the GridPP computing Grid at <https://doi.org/10.17633/rd.brunel.3179644> (MICE unprocessed data) and <https://doi.org/10.17633/rd.brunel.5955850> (MICE reconstructed data). Source data for Figs. 3–5 and Extended Data Fig. 1 are provided with the paper.

Publications using MICE data must contain the following statement: “We gratefully acknowledge the MICE collaboration for allowing us access to their data. Third-party results are not endorsed by the MICE collaboration.”

Code availability

The MAUS software⁵⁰ that was used to reconstruct and analyse the MICE data is available at <https://doi.org/10.17633/rd.brunel.8337542>. The analysis presented here used MAUS version 3.3.2.

51. Reiser, M. in *Theory and Design of Charged Particle Beams* 51–103 (John Wiley & Sons, 2008).
52. Mack, Y. P. & Rosenblatt, M. Multivariate k-nearest neighbor density estimates. *J. Multiv. Anal.* **9**, 1–15 (1979).

Acknowledgements The work described here was made possible by grants from the Science and Technology Facilities Council (UK), the Department of Energy and the National Science Foundation (USA), the Istituto Nazionale di Fisica Nucleare (Italy), the European Union under the European Union’s Framework Programme 7 (AIDA project, grant agreement number 262025; TIARA project, grant agreement number 261905; and EuCARD), the Japan Society for the Promotion of Science, the National Research Foundation of Korea (number NRF-2016R1A5A1013277), the Ministry of Education, Science and Technological Development of the Republic of Serbia, the Institute of High Energy Physics/Chinese Academy of Sciences fund for collaboration between the People’s Republic of China and the USA, and the Swiss National Science Foundation in the framework of the SCOPES programme. We gratefully acknowledge all sources of support. We are grateful for the support given to us by the staff of the STFC Rutherford Appleton and Daresbury laboratories. We acknowledge the use of Grid computing resources deployed and operated by GridPP in the UK, <http://www.gridpp.ac.uk/>.

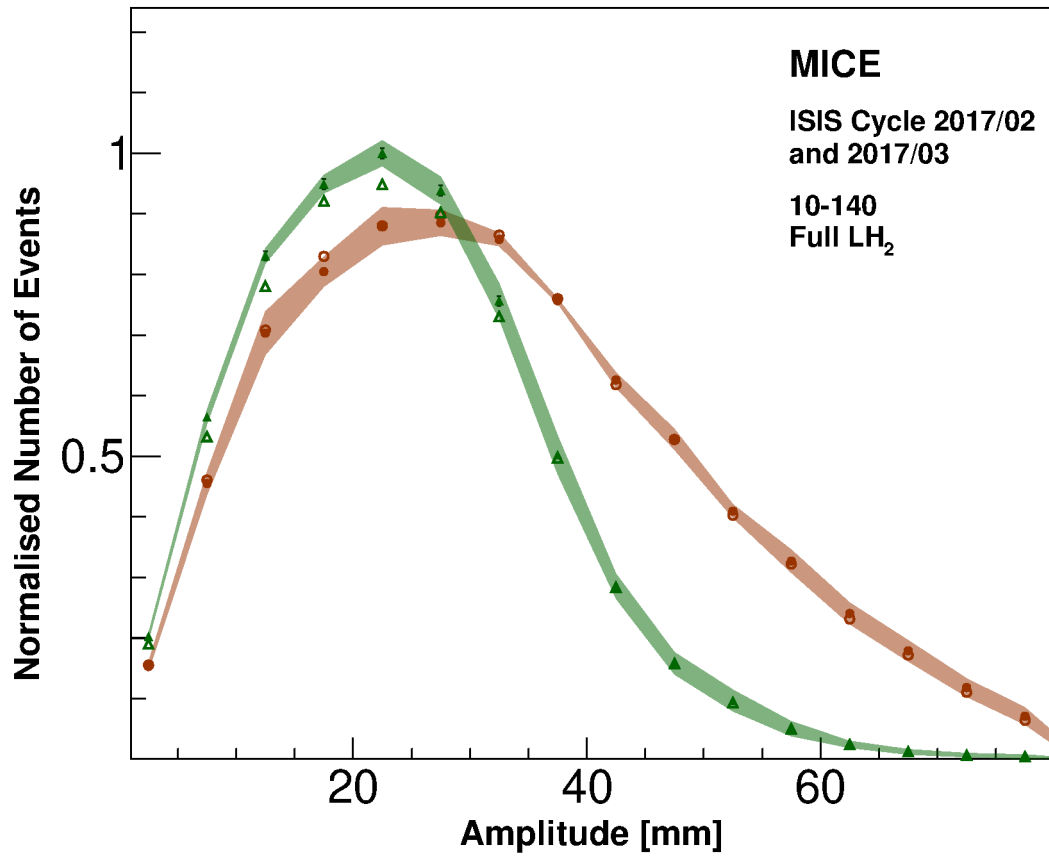
Author contributions All authors contributed considerably to the design or construction of the apparatus or to the data taking or analysis described here.

Competing interests The authors declare no competing interests.

Additional information

Correspondence and requests for materials should be addressed to C.R.

Reprints and permissions information is available at <http://www.nature.com/reprints>.



Extended Data Fig. 1 | Corrected and uncorrected amplitude distributions for the 10–140 ‘LH2 full’ configuration. The uncorrected data are shown by open points and the corrected data by filled points. Orange circles correspond

to the upstream distribution and green triangles to the downstream distribution. Shading represents the estimated total standard error. Error bars show the statistical error and for most points are smaller than the markers.

Extended Data Table 1 | Ratio of number of muons downstream to number of muons upstream having an amplitude of less than 5 mm

	4-140	6-140	10-140
LH2 empty	$0.98 \pm 0.005 \pm 0.05$	$1.01 \pm 0.006 \pm 0.05$	$1.02 \pm 0.02 \pm 0.05$
LH2 full	$1.12 \pm 0.009 \pm 0.05$	$1.16 \pm 0.009 \pm 0.05$	$1.32 \pm 0.02 \pm 0.07$
None	$0.99 \pm 0.006 \pm 0.05$	$1.00 \pm 0.005 \pm 0.05$	$1.06 \pm 0.02 \pm 0.06$
LiH	$1.07 \pm 0.008 \pm 0.05$	$1.14 \pm 0.01 \pm 0.05$	$1.23 \pm 0.03 \pm 0.07$

Uncertainties denote standard error; statistical uncertainty is followed by the total uncertainty.

Article

Extended Data Table 2 | Number of events in the samples shown in Fig. 3–5

	4-140		6-140		10-140	
	Upstream	Downstream	Upstream	Downstream	Upstream	Downstream
LH2 empty	163508	153813	158520	140981	123067	85082
LH2 full	71823	67640	117383	107329	82371	62660
None	91804	86877	172606	153809	54195	37436
LiH	87514	82682	98443	89875	43423	32715

Transverse emittance reduction in muon beams by ionization cooling

Received: 12 October 2023

The MICE Collaboration*

Accepted: 15 May 2024

Published online: 17 July 2024

 Check for updates

Accelerated muon beams have been considered for the next-generation studies of high-energy lepton–antilepton collisions and neutrino oscillations. However, high-brightness muon beams have not yet been produced. The main challenge for muon acceleration and storage stems from the large phase-space volume occupied by the beam, derived from the production mechanism of muons through the decay of pions. The phase-space volume of the muon beam can be decreased through ionization cooling. Here we show that ionization cooling leads to a reduction in the transverse emittance of muon beams that traverse lithium hydride or liquid hydrogen absorbers in the Muon Ionization Cooling Experiment. Our results represent a substantial advance towards the realization of muon-based facilities that could operate at the energy and intensity frontiers.

Muon accelerators are considered to be potential enablers of fundamental particle physics studies at the energy and intensity frontiers. Such machines have great potential to provide multi-TeV lepton–antilepton collisions at a muon collider^{1–3} or act as sources of intense neutrino beams with well-characterized fluxes and energy spectra at a neutrino factory^{4–6}.

The benefit of using muons in circular storage rings arises from their fundamental nature and their mass, which is 207 times that of electrons. As elementary particles, colliding muons offer the entire centre-of-mass energy to the production of short-distance reactions. This is an advantage over proton–proton colliders, such as the Large Hadron Collider⁷, where each colliding proton constituent carries only a fraction of the proton energy. Compared with the electron, the larger muon mass leads to a dramatic reduction in synchrotron radiation losses, which scale as $1/m^4$. In addition, the spread in the effective centre-of-mass energy induced by beamstrahlung⁸, the emission of radiation resulting from the interaction of a charged particle beam with the electric field produced by an incoming beam, is substantially lower for muons. Thus, a muon collider could achieve multi-TeV and precise centre-of-mass energies with a considerably smaller facility than an electron–positron collider such as the proposed electron–positron variant of the Future Circular Collider⁹, the Circular Electron Positron Collider¹⁰, the International Linear Collider¹¹ or the Compact Linear Collider¹².

The primary challenges in building a muon collider facility stem from the difficulty of producing intense muon bunches with a small

phase-space volume, as well as the short muon lifetime (2.2 μ s at rest). A proton-driver scheme is currently the most attractive option due to its potential to generate intense muon beams. An alternative, positron-driven muon source has been proposed and is under conceptual study¹³. In the proton-driver scheme, an intense proton beam impinges on a target to produce a secondary beam primarily composed of pions and kaons. The pions and kaons decay into muons to create a tertiary muon beam. The resulting muon beam occupies a large phase-space volume, which must be reduced (cooled) to allow efficient acceleration and sufficient flux and luminosity. The muon capture, cooling and acceleration must be executed on a timescale comparable with the muon lifetime.

Traditional cooling techniques such as stochastic cooling¹⁴, electron cooling¹⁵ or synchrotron radiation cooling¹⁶ are impractical as the amount of time required to adequately cool the beam greatly exceeds the muon lifetime. Alternative muon cooling techniques are currently under development. A scheme developed at the Paul Scherrer Institute, whereby a surface muon beam is moderated to $\mathcal{O}(\text{eV})$ kinetic energies in cryogenic helium gas and has its beam spot decreased using strong electric and magnetic fields, has demonstrated promising phase-space compression¹⁷. Another demonstrated technology is the production of ultracold muons through resonant laser ionization of muonium atoms¹⁸. This technique for cooling positive muons has been proposed for an $e^- \mu^+$ collider¹⁹.

This paper describes the measurement of ionization cooling, the proposed technique by which the phase-space volume of the muon

*A list of authors and their affiliations appears at the end of the paper. ✉e-mail: paul.jurj13@imperial.ac.uk

beam can be sufficiently compressed before substantial decay losses occur^{20,21}. Ionization cooling occurs when a muon beam passes through a material, known as the absorber, and loses both transverse and longitudinal momenta by ionizing atoms. The longitudinal momentum can be restored using radio-frequency accelerating cavities. The process can be repeated to achieve sufficient cooling within a suitable time frame²².

The Muon Ionization Cooling Experiment (MICE; <http://mice.iit.edu>) was designed to provide the first demonstration of ionization cooling by measuring a reduction in the transverse emittance of the muon beam after the beam has passed through an absorber. A first analysis conducted by the MICE collaboration has demonstrated an unambiguous cooling signal by observing an increase in the phase-space density in the core of the beam on passage through an absorber²³. Here we present the quantification of the ionization cooling signal by measuring the change in the beam's normalized transverse emittance, which is a central figure of merit in accelerator physics. A beam-sampling procedure is employed to improve the measurement of the cooling performance by selecting muon subsamples with optimal beam optics properties in the experimental apparatus. This beam sampling enables the probing of the cooling signal in beams with lower input emittances than those studied in the first MICE analysis²³ and facilitates a comparison between the measurement and theoretical model of ionization cooling.

Ionization cooling

The normalized root-mean-square (r.m.s.) emittance is a measure of the volume occupied by the beam in phase space. It is a commonly used quantity in accelerator physics that describes the spatial and dynamical extent of the beam, and it is a constant of motion under linear beam optics. This work focuses on the four-dimensional phase space transverse to the beam propagation axis. The MICE coordinate system is defined such that the beam travels along the z axis, and the state vector of a particle in the transverse phase space is given by $\mathbf{u} = (x, p_x, y, p_y)$. Here x and y are the position coordinates and p_x and p_y are the momentum coordinates. The normalized transverse r.m.s. emittance is defined as²⁴

$$\varepsilon_{\perp} = \frac{1}{m_{\mu}c} |\Sigma_{\perp}|^{\frac{1}{4}}, \quad (1)$$

where m_{μ} is the muon mass and $|\Sigma_{\perp}|$ is the determinant of the beam covariance matrix. The covariance matrix elements are calculated as $\Sigma_{\perp,ij} = \langle u_i u_j \rangle - \langle u_i \rangle \langle u_j \rangle$.

The impact of ionization cooling on a beam crossing an absorber is best described through the rate of change of the normalized transverse r.m.s. emittance, which is approximately equal to^{21,25,26}

$$\frac{d\varepsilon_{\perp}}{dz} \simeq -\frac{\varepsilon_{\perp}}{\beta^2 E_{\mu}} \left| \frac{dE_{\mu}}{dz} \right| + \frac{\beta_{\perp} (13.6 \text{ MeV}c^{-1})^2}{2\beta^3 E_{\mu} m_{\mu} X_0}, \quad (2)$$

where βc is the muon velocity, E_{μ} is the muon energy, $|dE_{\mu}/dz|$ is the average rate of energy loss per unit path length, X_0 is the radiation length of the absorber material and β_{\perp} is the beam transverse betatron function at the absorber defined as $\beta_{\perp} = \frac{(x^2 + y^2)}{2m_{\mu}c\varepsilon_{\perp}} \langle p_z \rangle$. The emittance reduction (cooling) due to ionization energy loss is expressed through the first term. The second term represents emittance growth (heating) due to multiple Coulomb scattering by the atomic nuclei, which increases the angular spread of the beam. MICE recently measured scattering in lithium hydride (LiH) and observed good agreement with the GEANT4 model²⁷.

The cooling is influenced by both beam properties and absorber material. Heating is weaker for beams with lower transverse betatron function at the absorber. This can be achieved by using superconducting solenoids that provide strong symmetrical focusing in the

transverse plane. The absorber material affects both terms in the equation, and optimal cooling can be realized by using materials with a low atomic number for which the product $X_0 |dE_{\mu}/dz|$ is maximized. The performance of a cooling cell can be characterized through equilibrium emittance, which is obtained by setting $d\varepsilon_{\perp}/dz = 0$ and is given by

$$\varepsilon_{\perp}^{\text{eqm}} \simeq \frac{\beta_{\perp} (13.6 \text{ MeV}c^{-1})^2}{2\beta m_{\mu} X_0} \left| \frac{dE_{\mu}}{dz} \right|^{-1}. \quad (3)$$

Beams having emittances below equilibrium are heated, whereas those having emittances above are cooled.

Experimental apparatus

The main component of the experiment was the MICE channel, a magnetic lattice of 12 strong-focusing superconducting coils symmetrically placed upstream and downstream of the absorber module. The schematic of the MICE channel and instrumentation is shown in Fig. 1.

Muons were produced by protons from the ISIS synchrotron²⁸ impinging on a titanium target²⁹ and were delivered to the cooling channel via a transfer line^{30,31}. Tuning the fields of two bending magnets in the transfer line enabled the selection of a beam with average momentum in the range of 140–240 MeV c^{-1} . A variable-thickness brass and tungsten diffuser mounted at the entrance of the channel allowed the generation of beams with input emittance in the range of 3–10 mm.

The superconducting coils were grouped in three modules: two identical spectrometer solenoids situated upstream and downstream of the focus-coil module that housed the absorber. Each spectrometer solenoid contained three coils that provided a uniform magnetic field of up to 4 T in the tracking region, and two coils used to match the beam into or out of the focus-coil module. The focus-coil module contained a pair of coils designed to tightly focus the beam at the absorber. The large angular divergence (small β_{\perp}) of the focused beam reduced the emittance growth caused by multiple scattering in the absorber and increased the cooling performance. The two focus coils could be operated with identical or opposing magnetic polarities. For this study, the focus coils and the spectrometer solenoids were powered with opposite-polarity currents, thereby producing a field that flipped polarity at the centre of the absorber. This magnetic-field configuration was used to prevent the growth of the beam canonical angular momentum. The field within the tracking regions was monitored using calibrated Hall probes. A soft-iron partial return yoke was installed around the magnetic lattice to contain the field.

Due to a magnet power lead failure during the commissioning phase, one of the matching coils in the downstream spectrometer solenoid was rendered inoperable. The built-in flexibility of the magnetic lattice allowed a compromise between the cooling performance and transmission that ensured the realization of an unambiguous ionization cooling signal.

As discussed above, absorber materials with low atomic numbers are preferred for ionization cooling lattices. Lithium hydride and liquid hydrogen (LH₂) were the materials of choice in MICE. The LiH absorber was a disc with a thickness of 65.37 ± 0.02 mm and a density of 0.6957 ± 0.0006 g cm^{-3} (all uncertainties represent the standard error)²³. The lithium used to produce the absorber had an isotopic composition of 95.52% ⁶Li and 4.48% ⁷Li.

The liquid hydrogen was contained within a 22-litre aluminium vessel: a 300-mm-diameter cylinder with a pair of dome-shaped containment windows at its ends³². An additional pair of aluminium windows were mounted for safety purposes. The on-axis thickness of the LH₂ volume was 349.6 ± 0.2 mm. The density of LH₂ was measured to be 0.07053 ± 0.00008 g cm^{-3} at 20.51 K (ref. 33). The cumulative on-axis thickness of the aluminium windows was 0.79 ± 0.01 mm.

A comprehensive set of detectors were used to measure the particle species, position and momentum upstream and downstream of

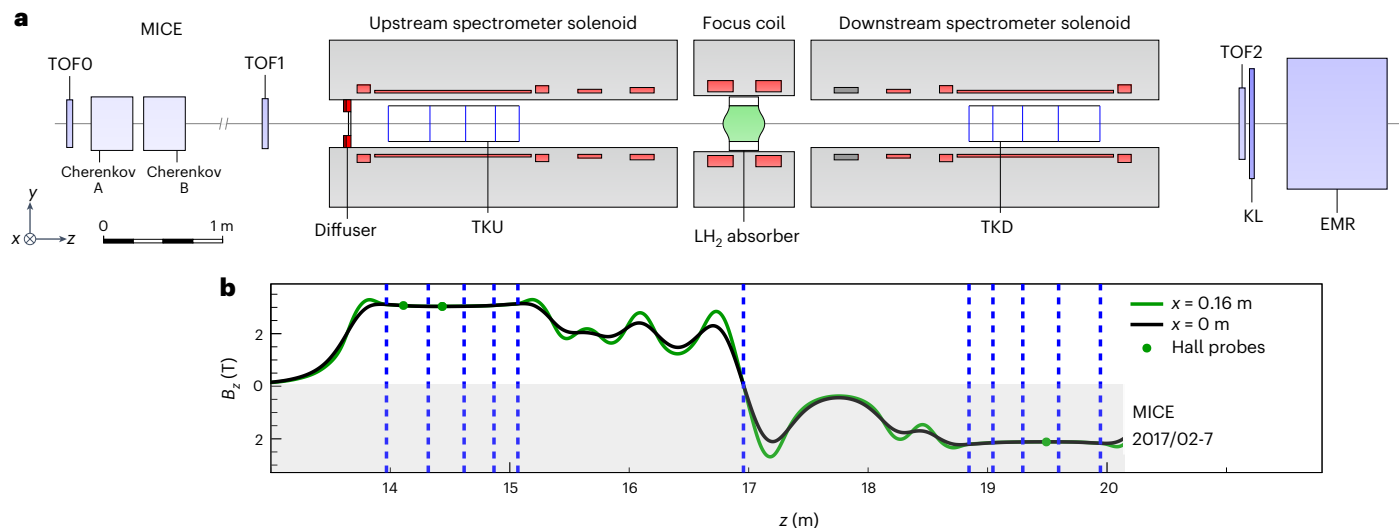


Fig. 1 | Schematic layout of the MICE experimental setup and the modelled magnetic field. a, Powered magnet coils are shown in red, absorber in green and detectors are individually labelled (see the main text for descriptions). TOFO, TOF1 and TOF2 are TOF hodoscopes; KL is a lead–scintillator pre-shower calorimeter; EMR is the electron–muon ranger. **b**, Modelled longitudinal

magnetic field B_z is shown along the length of the MICE channel on axis (black line) and at 160 mm from the beam axis (green line) in the horizontal plane. The measurements of Hall probes situated at 160 mm from the axis are also shown (green circles). The vertical dashed lines indicate the positions of the tracker stations and the absorber.

the absorber^{33,34}. The rate of muons delivered to the experiment was sufficiently low to allow the individual measurement of each incident particle. The data collected in cycles of several hours were aggregated offline and the phase space occupied by the beam before and after the absorber was reconstructed.

Upstream of the cooling channel, a velocity measurement provided by a pair of time-of-flight (TOF) detectors³⁵ was used for electron and pion rejection. A pair of threshold Cherenkov counters³⁶ were used to validate the TOF measurement. Downstream, a further TOF detector (TOF2)³⁷, a pre-shower sampling calorimeter and a fully active tracking calorimeter, namely, the electron–muon ranger^{38,39}, were employed to identify electrons from muon decays that occurred within the channel as well as to validate the particle measurement and identification by the upstream instrumentation. Particle position and momentum measurements upstream and downstream of the absorber were provided by two identical scintillating fibre trackers⁴⁰ immersed in the uniform magnetic fields of the spectrometer solenoids.

Each tracker (named TKU and TKD for upstream and downstream, respectively) consisted of five detector stations with a circular active area of 150 mm radius. Each station comprised three planes of 350- μm -diameter scintillating fibres, each rotated 120° with respect to its neighbour. In each station, the particle position was inferred from a coincidence of fibre signals. The particle momentum was reconstructed by fitting a helical trajectory to the reconstructed positions and accounting for multiple scattering and energy loss in the five stations⁴¹. For particles with a helix radius comparable with the spatial kick induced by multiple scattering, the momentum resolution was improved by combining the tracker momentum measurement with the velocity measurement provided by the upstream TOF detectors. The measurements recorded by the tracker reference planes, at the stations closest to the absorber, were used to estimate the beam emittance.

Observation of emittance reduction

The data studied here were collected using beams that passed through a lithium hydride or liquid hydrogen absorber. Scenarios with no absorber present or the empty LH_2 vessel were also studied for comparison. For each absorber setting, three beam-line configurations were used to deliver muon beams with nominal emittances of 4, 6 and

10 mm and a central momentum of approximately $140 \text{ MeV } c^{-1}$ in the upstream tracker. For each beam-line/absorber configuration, the final sample contained particles that were identified as muons by the upstream TOF detectors and tracker and had one valid reconstructed trajectory in each tracker. The kinematic, fiducial and quality selection criteria for the reconstructed tracks are listed in Methods. A Monte Carlo simulation of the whole experiment was used to estimate the expected cooling performance and to study the performance of the individual detectors⁴².

The beam matching into the channel slightly differed from the design beam optics due to inadequate focusing in the final section of the transfer line. This mismatch resulted in an oscillatory behaviour of the transverse betatron function in the TKU region and an increased, sub-optimal β_{\perp} at the absorber, which degraded the cooling performance. An algorithm based on rejection sampling was developed to select beams with a constant betatron function in the TKU, in agreement with the design beam optics. The selection was performed on the beam ensemble measured in the TKU and was enabled by the unique MICE capability to measure the muon beams particle by particle. An example comparison between the betatron function of an unmatched parent beam and that of a matched subsample is shown in Fig. 2. The β_{\perp} value of the subsample is approximately constant in the TKU, and consequently, its value at the absorber centre is ~28% smaller than the corresponding value of the parent beam.

The sampling algorithm enabled the selection of subsamples with specific emittances. This feature was exploited to study the dependence of the cooling effect on input emittance. For each absorber setting, each of the three parent beams were split into two distinct samples and six statistically independent beams with matched betatron functions ($\beta_{\perp} = 311 \text{ mm}$, $d\beta_{\perp}/dz = 0$) and emittances of 1.5, 2.5, 3.5, 4.5, 5.5 and 6.5 mm at the TKU were sampled. The numbers of muons in each sample are listed in Extended Data Table 1. The two-dimensional projections of the phase space of the sampled beams on the transverse position and momentum planes are shown in Extended Data Figs. 1 and 2, respectively.

Figure 3 shows the emittance change induced by the lithium hydride and liquid hydrogen absorbers, as well as the corresponding empty cases, for each emittance subsample. The measurement uncertainty (Fig. 3, coloured bands) is dominated by systematic

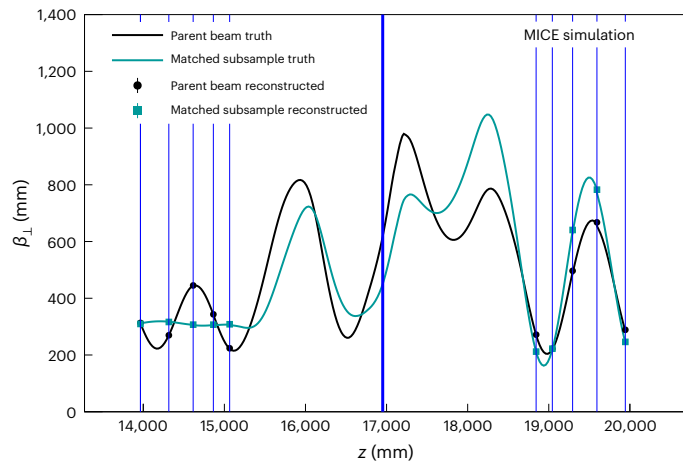


Fig. 2 | Simulated MICE muon beam betatron function. Evolution of the simulated transverse betatron function β_{\perp} through the cooling channel containing the full LH₂ vessel for the parent beam (black) and matched subsample (dark cyan). The corresponding lines represent the simulation truth, whereas the circles and squares at the tracker stations (vertical blue lines) represent the reconstructed simulation. The thick vertical blue line marks the central position of the absorber. The error bars show the statistical standard error and are smaller than the markers for all the points.

uncertainties, which are listed in Extended Data Table 3 and described in detail in Methods. A correction was made to account for detector effects and for the inclusion only of events that reached the TKD. Good agreement between data and simulation is observed in all the configurations. The reconstructed data agree well with the model prediction. The model includes the heating effect in aluminium windows (Methods). The properties of the absorber and window materials used for the model calculation are listed in Extended Data Table 2.

The empty absorber cases show no cooling effects. In the empty channel case (No absorber), slight heating occurs due to optical aberrations and scattering in the aluminium windows of the two spectrometer solenoids. Additional heating caused by scattering in the windows of the LH₂ vessel is observed in the Empty LH₂ case. The LiH and Full LH₂ absorbers demonstrate emittance reduction for beams with emittances larger than ~2.5 mm. This is a clear signal of ionization cooling, a direct consequence of the presence of absorber material in the path of the beam.

For beams with 140 MeV c^{-1} momentum and $\beta_{\perp} = 450$ mm at the absorber centre, the theoretical equilibrium emittances of the MICE LiH and LH₂ absorbers, including the contributions from the corresponding set of aluminium windows, are ~2.5 mm in both cases. By performing a linear fit to the measured cooling trends (Fig. 3), the effective equilibrium emittances of the absorber modules are estimated to be 2.6 ± 0.4 mm for LiH and 2.4 ± 0.4 mm for LH₂. The parameters of the linear fits to the four emittance change trends are shown in Table 1. Our null hypothesis was that for each set of six input-beam settings, the slopes of the emittance change trends in the presence and absence of an absorber are compatible. A Student's t -test found that the probabilities of observing the effects measured here are lower than 10^{-5} for both the LiH–No absorber and Full LH₂–Empty LH₂ pairs; hence, the null hypotheses were rejected.

There is no significant improvement in cooling in this measurement when using liquid hydrogen compared with lithium hydride. Scattering in the absorber windows degraded the performance of LH₂ and rendered it similar to that of LiH. MICE was based on an early stage cooling-channel concept, requiring a large-bore absorber to accommodate the beam. In lower-emittance cooling systems with smaller-bore beam pipes, the relative window thickness may be reduced, leading to a better performance of hydrogen absorbers.

Towards a muon collider

The measurement reported here demonstrates the viability of this beam cooling technique as a means of producing low-emittance muon beams for a muon collider or a neutrino factory. The muon collider targets a transverse emittance of $\mathcal{O}(10^{-2}$ mm) and a longitudinal emittance of $\mathcal{O}(10^2$ mm). To achieve these targets, substantial longitudinal and transverse emittance reduction is required, which must be demonstrated. The muon beam must traverse multiple cooling cells that produce magnetic fields stronger than those achieved by MICE and which contain high-gradient radio-frequency cavities to restore the beam longitudinal momentum²². Design studies for a muon cooling demonstrator facility are currently in progress^{43–45}.

Our measurement is an important development towards the muon cooling demonstrator, a key intermediary step in the pursuit of a muon collider. The demonstration of ionization cooling by the MICE collaboration constitutes a substantial and encouraging breakthrough in the

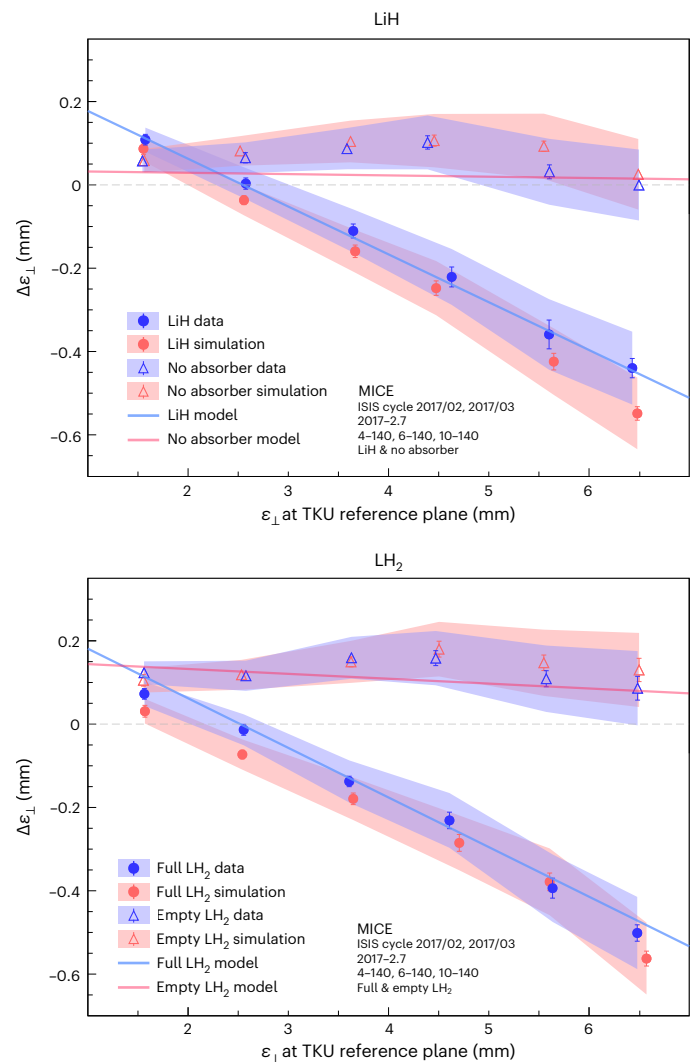


Fig. 3 | Transverse emittance change measured by MICE. Emittance change between the TKU and TKD reference planes, $\Delta\epsilon_{\perp}$, as a function of emittance at TKU for 140 MeV c^{-1} beams crossing the LiH (top) and LH₂ (bottom) MICE absorbers. Results for the empty cases, namely, No absorber and Empty LH₂, are also shown. The measured effect is shown in blue, whereas the simulation is shown in red. The corresponding semitransparent bands represent the estimated total standard error. The error bars indicate the statistical error and for some of the points, they are smaller than the markers. The solid lines represent the approximate theoretical model defined by equation (10) (Methods) for the absorber (light blue) and empty (light pink) cases. The dashed grey horizontal lines indicate a scenario where no emittance change occurs.

Table 1 | Best-fit parameters of the measured emittance change trends

Absorber configuration	Intercept (mm)	Slope
No absorber	0.102±0.007	-0.011±0.012
LiH	0.297±0.006	-0.115±0.013
Empty LH ₂	0.150±0.005	-0.006±0.013
Full LH ₂	0.279±0.007	-0.118±0.013

Parameters of the linear fits performed on the measured emittance change trends corresponding to the four absorber configurations. Uncertainties represent the total standard error.

research and development efforts to deliver high-brightness muon beams suitable for high-intensity muon-based facilities.

Online content

Any methods, additional references, Nature Portfolio reporting summaries, source data, extended data, supplementary information, acknowledgements, peer review information; details of author contributions and competing interests; and statements of data and code availability are available at <https://doi.org/10.1038/s41567-024-02547-4>.

References

- Neuffer, D. V. & Palmer, R. B. Progress toward a high-energy, high-luminosity $\mu^+\mu^-$ collider. *AIP Conf. Proc.* **356**, 344–358 (1996).
- Ankenbrandt, C. M. et al. Status of muon collider research and development and future plans. *Phys. Rev. ST Accel. Beams* **2**, 081001 (1999).
- Palmer, R. Muon colliders. *Rev. Accel. Sci. Tech.* **7**, 137–159 (2014).
- Geer, S. Neutrino beams from muon storage rings: characteristics and physics potential. *Phys. Rev. D* **57**, 6989–6997 (1998).
- De Rújula, A., Gavela, M. & Hernández, P. Neutrino oscillation physics with a neutrino factory. *Nucl. Phys. B* **547**, 21–38 (1999).
- Bogomilov, M. et al. Neutrino factory. *Phys. Rev. ST Accel. Beams* **17**, 121002 (2014).
- Evans, L. The Large Hadron Collider. *New J. Phys.* **9**, 335 (2007).
- Noble, R. J. Beamstrahlung from colliding electron-positron beams with negligible disruption. *Nucl. Instrum. Methods Phys. Res. A* **256**, 427–433 (1987).
- Abada, A. et al. FCC-ee: the lepton collider. *Eur. Phys. J. Spec. Top.* **228**, 261–623 (2019).
- CEPC Study Group et al. CEPC conceptual design report: volume 1—accelerator. Preprint at <https://arxiv.org/abs/1809.00285> (2018).
- Behnke, T. et al. The International Linear Collider technical design report—volume 1: executive summary. Preprint at <https://arxiv.org/abs/1306.6327> (2013).
- Charles, T. K. et al. The Compact Linear Collider (CLIC)—2018 summary report. Preprint at <https://arxiv.org/abs/1812.06018> (2018).
- Antonelli, M., Boscolo, M., Di Nardo, R. & Raimondi, P. Novel proposal for a low emittance muon beam using positron beam on target. *Nucl. Instrum. Methods Phys. Res. A* **807**, 101–107 (2016).
- Möhl, D., Petrucci, G., Thorndahl, L. & Van Der Meer, S. Physics and technique of stochastic cooling. *Phys. Rep.* **58**, 73–102 (1980).
- Parkhomchuk, V. V. & Skrinskii, A. N. Electron cooling: 35 years of development. *Phys. Uspekhi* **43**, 433–452 (2000).
- Kolomenski, A. A. & Lebedev, A. N. The effect of radiation on the motion of relativistic electrons in a synchrotron. In *CERN Symposium on High Energy Accelerators and Pion Physics* 447–455 (CERN, 1956).
- Antognini, A. et al. Demonstration of muon-beam transverse phase-space compression. *Phys. Rev. Lett.* **125**, 164802 (2020).
- Bakule, P. et al. Slow muon experiment by laser resonant ionization method at RIKEN-RAL muon facility. *Spectrochim. Acta Part B* **58**, 1019–1030 (2003).
- Hamada, Y., Kitano, R., Matsudo, R., Takaura, H. & Yoshida, M. μ TRISTAN. *Prog. Theor. Exp. Phys.* **2022**, 053B02 (2022).
- Skrinskii, A. N. & Parkhomchuk, V. V. Methods of cooling beams of charged particles. *Sov. J. Part. Nucl.* **12**, 223–247 (1981).
- Neuffer, D. Principles and applications of muon cooling. *Part. Accel.* **14**, 75–90 (1983).
- Stratakis, D. & Palmer, R. B. Rectilinear six-dimensional ionization cooling channel for a muon collider: a theoretical and numerical study. *Phys. Rev. ST Accel. Beams* **18**, 031003 (2015).
- Bogomilov, M. et al. Demonstration of cooling by the muon ionization cooling experiment. *Nature* **578**, 53–59 (2020).
- Wiedemann, H. *Particle Accelerator Physics* 4th edn (Springer Nature, 2015).
- Penn, G. & Wurtele, J. S. Beam envelope equations for cooling of muons in solenoid fields. *Phys. Rev. Lett.* **85**, 764–767 (2000).
- Jurj, P. B. *Normalised Transverse Emittance Reduction via Ionisation Cooling in MICE ‘Flip Mode’*. PhD thesis, Imperial College London (2022).
- Bogomilov, M. et al. Multiple Coulomb scattering of muons in lithium hydride. *Phys. Rev. D* **106**, 092003 (2022).
- Thomason, J. The ISIS Spallation Neutron and Muon Source—the first thirty-three years. *Nucl. Instrum. Methods Phys. Res. A* **917**, 61–67 (2019).
- Booth, C. N. et al. The design, construction and performance of the MICE target. *J. Instrum.* **8**, P03006 (2013).
- Bogomilov, M. et al. The MICE muon beam on ISIS and the beam-line instrumentation of the Muon Ionization Cooling Experiment. *J. Instrum.* **7**, P05009 (2012).
- Adams, D. et al. Pion contamination in the MICE muon beam. *J. Instrum.* **11**, P03001 (2016).
- Bayliss, V. et al. The liquid-hydrogen absorber for MICE. *J. Instrum.* **13**, T09008 (2018).
- Bogomilov, M. et al. Performance of the MICE diagnostic system. *J. Instrum.* **16**, P08046 (2021).
- Bogomilov, M. et al. The MICE particle identification system. *Nucl. Phys. B* **215**, 316–318 (2011).
- Bertoni, R. et al. The design and commissioning of the MICE upstream time-of-flight system. *Nucl. Instrum. Methods Phys. Res. A* **615**, 14–26 (2010).
- Cremaldi, L., Sanders, D. A., Sonnek, P., Summers, D. J. & Reidy, J. A Cherenkov radiation detector with high density aerogels. *IEEE Trans. Nucl. Sci.* **56**, 1475–1478 (2009).
- Bertoni, R. et al. *The Construction of the MICE TOF2 Detector* Tech. Report No. MICE-NOTE-DET-286 (MICE Collaboration, 2010).
- Asfandiyarov, R. et al. A totally active scintillator calorimeter for the Muon Ionization Cooling Experiment (MICE). Design and construction. *Nucl. Instrum. Methods Phys. Res. A* **732**, 451–456 (2013).
- Adams, D. et al. Electron-muon ranger: performance in the MICE muon beam. *J. Instrum.* **10**, P12012 (2015).
- Ellis, M. et al. The design, construction and performance of the MICE scintillating fibre trackers. *Nucl. Instrum. Methods Phys. Res. A* **659**, 136–153 (2011).
- Dobbs, A. et al. The reconstruction software for the MICE scintillating fibre trackers. *J. Instrum.* **11**, T12001 (2016).
- Asfandiyarov, R. et al. MAUS: the MICE analysis user software. *J. Instrum.* **14**, T04005 (2019).
- Rogers, C. A demonstrator for muon ionisation cooling. *Phys. Sci. Forum* **8**, 37 (2023).
- Accettura, C. et al. Towards a muon collider. *Eur. Phys. J. C* **83**, 864 (2023).
- The International Muon Collider Collaboration; <https://muoncollider.web.cern.ch>

Publisher's note Springer Nature remains neutral with regard to jurisdictional claims in published maps and institutional affiliations.

Open Access This article is licensed under a Creative Commons Attribution 4.0 International License, which permits use, sharing, adaptation, distribution and reproduction in any medium or format, as long as you give appropriate credit to the original author(s) and the source, provide a link to the Creative Commons licence, and indicate if changes were made. The images or other third party material in this

article are included in the article's Creative Commons licence, unless indicated otherwise in a credit line to the material. If material is not included in the article's Creative Commons licence and your intended use is not permitted by statutory regulation or exceeds the permitted use, you will need to obtain permission directly from the copyright holder. To view a copy of this licence, visit <http://creativecommons.org/licenses/by/4.0/>.

© The Author(s) 2024, corrected publication 2024

The MICE Collaboration

M. Bogomilov¹, R. Tsenov¹, G. Vankova-Kirilova¹, Y. P. Song², J. Y. Tang², Z. H. Li³, R. Bertoni⁴, M. Bonesini⁴, F. Chignoli⁴, R. Mazza⁴, A. de Bari⁵, D. Orestano⁶, L. Tortora⁶, Y. Kuno⁷, H. Sakamoto^{7,33}, A. Sato⁷, S. Ishimoto⁸, M. Chung⁹, C. K. Sung⁹, F. Filthaut^{10,11}, M. Fedorov¹¹, D. Jokovic¹², D. Maletic¹², M. Savic¹², N. Jovancevic¹³, J. Nikolov¹³, M. Vretenar¹⁴, S. Ramberger¹⁴, R. Asfandiyarov¹⁵, A. Blondel¹⁵, F. Drielsma^{15,34}, Y. Karadzhov¹⁵, S. Boyd¹⁶, J. R. Greis^{16,35}, T. Lord^{16,36}, C. Pidcott^{16,37}, I. Taylor^{16,38}, G. Charnley¹⁷, N. Collomb¹⁷, K. Dumbell¹⁷, A. Gallagher¹⁷, A. Grant¹⁷, S. Griffiths¹⁷, T. Hartnett¹⁷, B. Martlew¹⁷, A. Moss¹⁷, A. Muir¹⁷, I. Mullacrane¹⁷, A. Oates¹⁷, P. Owens¹⁷, G. Stokes¹⁷, P. Warburton¹⁷, C. White¹⁷, D. Adams¹⁸, V. Bayliss¹⁸, J. Boehm¹⁸, T. W. Bradshaw¹⁸, C. Brown^{18,26}, M. Courthold¹⁸, J. Govans¹⁸, T. Hayler¹⁸, M. Hills¹⁸, J. B. Lagrange¹⁸, C. Macwaters¹⁸, A. Nichols¹⁸, R. Preece¹⁸, S. Ricciardi¹⁸, C. Rogers¹⁸, T. Stanley¹⁸, J. Tarrant¹⁸, M. Tucker¹⁸, S. Watson^{18,39}, A. Wilson¹⁸, R. Bayes^{19,40}, J. C. Nugent¹⁹, F. J. P. Soler¹⁹, G. T. Chatzitheodoridis^{19,20,21}, A. J. Dick^{20,21}, K. Ronald^{20,21}, C. G. Whyte^{20,21}, A. R. Young^{20,21}, R. Gamet²², P. Cooke²², V. J. Blackmore²³, D. Colling²³, A. Dobbs^{23,41}, P. Dornan²³, P. Franchini^{23,42}, C. Hunt²³, P. B. Jurj²³✉, A. Kurup²³, K. Long²³, J. Martyniak²³, S. Middleton^{23,43}, J. Pasternak²³, M. A. Uchida^{23,44}, J. H. Cobb²⁴, C. N. Booth²⁵, P. Hodgson²⁵, J. Langlands²⁵, E. Overton^{25,45}, V. Pec²⁵, P. J. Smith²⁵, S. Wilbur²⁵, M. Ellis^{26,46}, R. B. S. Gardener²⁶, P. Kyberd²⁶, J. J. Nebrensky^{26,47}, A. DeMello²⁷, S. Gourlay²⁷, A. Lambert²⁷, D. Li²⁷, T. Luo²⁷, S. Prestemon²⁷, S. Virostek²⁷, M. Palmer²⁸, H. Witte²⁸, D. Adey^{29,48}, A. D. Bross²⁹, D. Bowring²⁹, A. Liu^{29,49}, D. Neuffer²⁹, M. Popovic²⁹, P. Rubinov²⁹, B. Freemire^{30,49}, P. Hanlet^{30,50}, D. M. Kaplan³⁰, T. A. Mohayal^{30,51}, D. Rajaram^{30,52}, P. Snopok³⁰, Y. Torun³⁰, L. M. Cremaldi³¹, D. A. Sanders³¹, L. R. Coney^{32,53}, G. G. Hanson³² & C. Heidt^{32,54}

¹Department of Atomic Physics, St Kliment Ohridski University of Sofia, Sofia, Bulgaria. ²Institute of High Energy Physics, Chinese Academy of Sciences, Beijing, China. ³Sichuan University, Chengdu, China. ⁴Sezione INFN Milano Bicocca, Dipartimento di Fisica G. Occhialini, Milano, Italy. ⁵Sezione INFN Pavia and Dipartimento di Fisica, Università di Pavia, Pavia, Italy. ⁶INFN Sezione di Roma Tre and Dipartimento di Matematica e Fisica, Università Roma Tre, Roma, Italy. ⁷Department of Physics, Graduate School of Science, Osaka University, Toyonaka, Japan. ⁸High Energy Accelerator Research Organization (KEK), Institute of Particle and Nuclear Studies, Tsukuba, Japan. ⁹Pohang University of Science & Technology, Pohang, Korea. ¹⁰Nikhef, Amsterdam, The Netherlands. ¹¹Radboud University, Nijmegen, The Netherlands. ¹²Institute of Physics, University of Belgrade, Belgrade, Serbia. ¹³Faculty of Sciences, University of Novi Sad, Novi Sad, Serbia. ¹⁴CERN, Geneva, Switzerland. ¹⁵DNPC, Section de Physique, Université de Genève, Geneva, Switzerland. ¹⁶Department of Physics, University of Warwick, Coventry, UK. ¹⁷STFC Daresbury Laboratory, Daresbury, UK. ¹⁸STFC Rutherford Appleton Laboratory, Harwell Oxford, Didcot, UK. ¹⁹School of Physics and Astronomy, University of Glasgow, Glasgow, UK. ²⁰SUPA and the Department of Physics, University of Strathclyde, Glasgow, UK. ²¹Cockcroft Institute, Daresbury Laboratory, Daresbury, UK. ²²Department of Physics, University of Liverpool, Liverpool, UK. ²³Department of Physics, Blackett Laboratory, Imperial College London, London, UK. ²⁴Department of Physics, University of Oxford, Oxford, UK. ²⁵Department of Physics and Astronomy, University of Sheffield, Sheffield, UK. ²⁶College of Engineering, Design and Physical Sciences, Brunel University, Uxbridge, UK. ²⁷Lawrence Berkeley National Laboratory, Berkeley, CA, USA. ²⁸Brookhaven National Laboratory, Upton, NY, USA. ²⁹Fermilab, Batavia, IL, USA. ³⁰Illinois Institute of Technology, Chicago, IL, USA. ³¹University of Mississippi, Oxford, MS, USA. ³²University of California, Riverside, CA, USA. ³³Present address: RIKEN 2-1 Horosawa, Wako, Japan. ³⁴Present address: SLAC National Accelerator Laboratory, Menlo Park, CA, USA. ³⁵Present address: TNG Technology Consulting, Unterföhring, Germany. ³⁶Present address: Dimensional Fund Advisors, London, UK. ³⁷Present address: Department of Physics and Astronomy, University of Sheffield, Sheffield, UK. ³⁸Present address: Defence Science and Technology Laboratory, Salisbury, UK. ³⁹Present address: ATC, Royal Observatory Edinburgh, Edinburgh, UK. ⁴⁰Present address: Laurentian University, Sudbury, Ontario, Canada. ⁴¹Present address: OPERA Simulation Software, Kidlington, UK. ⁴²Present address: Department of Physics, Royal Holloway, University of London, Egham, UK. ⁴³Present address: The Division of Physics, Mathematics and Astronomy, Caltech, Pasadena, CA, USA. ⁴⁴Present address: Rutherford Building, Cavendish Laboratory, University of Cambridge, Cambridge, UK. ⁴⁵Present address: Arm, Sheffield, UK. ⁴⁶Present address: Macquarie Group, Sydney, New South Wales, Australia. ⁴⁷Present address: United Kingdom Atomic Energy Authority (UKAEA), Culham Science Centre, Abingdon, UK. ⁴⁸Present address: Institute of High Energy Physics, Chinese Academy of Sciences, Beijing, China. ⁴⁹Present address: Euclid Techlabs, Bolingbrook, IL, USA. ⁵⁰Present address: Fermilab, Batavia, IL, USA. ⁵¹Present address: Department of Physics, Indiana University Bloomington, Bloomington, IN, USA. ⁵²Present address: KLA, Ann Arbor, MI, USA. ⁵³Present address: European Spallation Source ERIC, Lund, Sweden. ⁵⁴Present address: Swish Analytics, Oakland, CA, USA.

✉ e-mail: paul.jurj13@imperial.ac.uk

Methods

Event reconstruction

Each TOF hodoscope was composed of two planes of scintillator slabs oriented along the x and y directions. Photomultiplier tubes (PMTs) at both ends of each slab were used to collect and amplify the signal produced by a charged particle traversing the slab. A coincidence of signals from the PMTs of a slab was recorded as a slab hit. A pair of orthogonal slab hits formed a space point. The information collected by the four corresponding PMTs was used to reconstruct the position and the time at which the particle passed through the detector. A detailed description of the TOF time calibration is provided elsewhere⁴⁶. The MICE data acquisition system readout was triggered by a coincidence of signals from the PMTs of a single slab of the TOF1 detector. All the data collected by the detector system after each TOF1 trigger were aggregated, forming a particle event.

For each tracker, signals from the scintillating fibres in the five stations were combined to reconstruct the helical trajectories of the traversing charged particles. The quality of each fitted track was indicated by the χ^2 per degree of freedom as

$$\chi_{\text{dof}}^2 = \frac{1}{n-5} \sum_{i=1}^n \frac{\delta x_i^2}{\sigma_i^2}, \quad (4)$$

where n is the number of tracker planes that contributed to the reconstruction, δx_i is the distance between the measured position in the i th tracker plane and the fitted track and σ_i is the position measurement resolution in the tracker planes. A more detailed description of the reconstruction procedure and its performance can be found in other MICE work^{33,41}.

Sample selection

The measurements taken by the detector system were used to select the final sample. The following selection criteria ensured that a pure muon beam, with a narrow momentum spread, and fully transmitted through the channel, was selected for analysis:

- One reconstructed space point found in TOF0 and TOF1, and one reconstructed track found in TKU and TKD
- Time-of-flight between TOF0 and TOF1 consistent with that of a muon
- Momentum measured in TKU consistent with that of a muon, given the TOF0–TOF1 time-of-flight
- In each tracker, a reconstructed track contained within the cylindrical fiducial volume defined by a radius of 150 mm and with $\chi_{\text{dof}}^2 < 8$
- Momentum measured in TKU in the 135–145 MeV c^{-1} range
- Momentum measured in TKD in the 120–170 MeV c^{-1} range for the empty absorber configurations and 90–170 MeV c^{-1} range for the LiH and LH₂ absorbers
- At the diffuser, a track radial excursion contained within the diffuser aperture radius by at least 10 mm

The same set of selection criteria was applied to the simulated beams.

Beam sampling

The sampling procedure developed to obtain beams matched to the upstream tracker is based on a rejection sampling algorithm^{47,48}. It was designed to carve out a beam subsample that followed a four-dimensional Gaussian distribution described by a specific (target) covariance matrix from an input-beam ensemble (parent).

The custom algorithm required an estimate of the probability density function underlying the beam ensemble. Since the MICE beams were only approximately Gaussian and approximately cylindrically symmetric, the kernel density estimation technique was used to evaluate the parent-beam density in a non-parametric fashion^{49,50}. In the kernel density estimation, each data point is assigned a smooth weight

function, also known as the kernel, and the contributions from all the data points in the dataset are summed. The multivariate kernel density estimator at an arbitrary point \mathbf{u} in d -dimensional space is given by

$$\hat{f}(\mathbf{u}) = \frac{1}{nh^d} \sum_{i=1}^n K\left(\frac{\mathbf{u} - \mathbf{u}_i}{h}\right), \quad (5)$$

where K is the kernel, n is the sample size, h is the width of the kernel and \mathbf{u}_i represents the coordinate of the i th data point in the sample. In this analysis, Gaussian kernels of the following form were used:

$$K\left(\frac{\mathbf{u} - \mathbf{u}_i}{h}\right) = \frac{1}{\sqrt{(2\pi)^d |\boldsymbol{\Sigma}_\perp|}} \exp\left[-\frac{1}{2} \frac{(\mathbf{u} - \mathbf{u}_i)^\top \boldsymbol{\Sigma}_\perp^{-1} (\mathbf{u} - \mathbf{u}_i)}{h^2}\right], \quad (6)$$

where $\boldsymbol{\Sigma}_\perp$ is the covariance matrix of the dataset. The width of the kernel is chosen to minimize the mean integrated squared error, which measures the accuracy of the estimator⁵¹. Scott's rule of thumb was followed in this work, where the kernel width was determined from the sample size n and the number of dimensions d through $h = n^{-1/(d+4)}$ (ref. 50).

The kernel density estimation form described in equations (5) and (6) was used to estimate the transverse phase-space density of the initial, unmatched beams, with the estimated underlying density denoted by Parent(\mathbf{u}). The target distribution Target(\mathbf{u}) is a four-dimensional Gaussian defined by a covariance matrix parameterized through the transverse emittance (ε_\perp), transverse beta-tron function (β_\perp), mean longitudinal momentum and mean kinetic angular momentum²⁵.

The sampling was performed on the beam ensemble measured at the TKU station closest to the absorber. For each particle in the parent beam, with four-dimensional phase-space vector \mathbf{u}_i , the sampling algorithm worked as follows:

1. Compute the selection probability as

$$P_{\text{select}}(\mathbf{u}_i) = c \times \frac{\text{Target}(\mathbf{u}_i)}{\text{Parent}(\mathbf{u}_i)}, \quad (7)$$

where the normalization constant c ensures that the selection probability $P_{\text{select}}(\mathbf{u}_i) \leq 1$;

2. Generate a number ξ_i from the uniform distribution $\mathcal{U}([0, 1])$;
3. If $P_{\text{select}}(\mathbf{u}_i) > \xi_i$, then accept the particle. Otherwise, reject it.

The normalization constant c was calculated before the sampling iteration presented in steps 1–3 above. It required an iteration through the parent ensemble (of size n) and it was calculated as

$$c = \min_{i \in \{1, \dots, n\}} \frac{\text{Parent}(\mathbf{u}_i)}{\text{Target}(\mathbf{u}_i)}. \quad (8)$$

The target parameters of interest were ε_\perp , β_\perp and $\alpha_\perp = -\frac{1}{2} d\beta_\perp/dz$. For beams with central momentum of 140 MeV c^{-1} and a solenoidal magnetic field of 3 T, the matching conditions in the TKU were ($\beta_\perp, \alpha_\perp$) = (311 mm, 0). The target mean kinetic angular momentum was kept at the value measured in the parent beam for which the sampling efficiency was at a maximum.

Emittance change calculation and model

The emittance change measured by the pair of MICE scintillating fibre trackers is defined as

$$\Delta\varepsilon_\perp = \varepsilon_\perp^d - \varepsilon_\perp^u, \quad (9)$$

where ε_\perp^d is the emittance measured in the downstream tracker and ε_\perp^u is the emittance measured in the upstream tracker. In each tracker, the measurement is performed at the station closest to the absorber.

Starting from the cooling equation shown in equation (2), the emittance change induced by an absorber material of thickness z can be expressed as a function of the input emittance ε_{\perp}^u as follows:

$$\Delta\varepsilon_{\perp}(\varepsilon_{\perp}^u) \approx (\varepsilon_{\perp}^{\text{eqm}} - \varepsilon_{\perp}^u) \left[1 - \exp\left(-\frac{|dE_{\mu}/dz|}{\beta^2 E_{\mu}} z\right) \right], \quad (10)$$

where $\varepsilon_{\perp}^{\text{eqm}}$ is the equilibrium emittance and the mean energy loss rate $|dE_{\mu}/dz|$ is described by the Bethe–Bloch formula⁵².

The expected emittance change depends on the type and amount of material that the beam traverses between the two measurement locations. Aside from the absorber material under study and absorber-module windows, the beam crossed an additional pair of aluminium windows, one downstream of TKU and the other upstream of TKD. All the windows were made from Al 6061-T651 alloy. Equation (10) was used to estimate the theoretical cooling performance, including the effect of aluminium windows. The properties of the absorber and window materials required for the calculation are shown in Extended Data Table 2. For each absorber configuration, the beam properties required for the model (β , β_{\perp} , E_{μ}) were obtained from the simulation of the 3.5 mm beam.

Systematic uncertainties

The emittance change measurement assumes a specific arrangement of detector and magnetic fields. As this arrangement is known with limited accuracy, it is a source of systematic uncertainty in the $\Delta\varepsilon_{\perp}$ measurement. To assess this uncertainty, the experimental geometry was parameterized and these parameters were varied one by one in the simulation of the experiment. For each parameter considered, the resulting shift in the simulated emittance change was assigned as its associated systematic uncertainty. The following contributions to the systematic uncertainty were considered in this analysis.

Uncertainties in the tracker alignment affect the reconstructed beam phase space. A tracker displacement along an axis perpendicular to the beam line by ± 3 mm and a tracker rotation about an axis perpendicular to the beam line by ± 3 mrad were investigated. These variations are conservative estimates determined from the MICE tracker alignment surveys. The cylindrical symmetry of the tracker measurement was validated by performing translations and rotations along and about different axes perpendicular to the beam line.

A significant systematic uncertainty arises due to the limited knowledge of the magnetic-field strength in the tracking region, which directly impacts the momentum measurement. The three coils that produced the magnetic field in the tracking region were labelled as End 1, Centre and End 2, with the End 1 coil closest to the absorber. The effect associated with the uncertainty in the magnetic field was studied by varying the Centre coil current by $\pm 1\%$ and the currents in the End coils by $\pm 5\%$. A conservative approach was taken when investigating the End coils, as the effect of the soft-iron partial return yoke was not included in the magnetic-field model used for track reconstruction.

The amount of energy loss and multiple scattering in each tracker station depends on the materials used. A variation of $\pm 50\%$ in the density of the glue used to fix the scintillating fibres was investigated. This alteration was used to account for uncertainty in the amount of silica beads added to the glue mixture.

All the sources of uncertainty presented so far were studied in both spectrometer solenoids. Additionally, as the TOF01 time measurement was used to assist the momentum reconstruction of muons with low transverse momentum, a variation corresponding to the 60 ps uncertainty on the TOF measurement was studied. The uncertainties associated with the individual parameter alterations are shown in Extended Data Table 3, for beams with input emittances in the [1.5, 2.5...6.5] mm range. For each input emittance, the total systematic uncertainty was obtained by adding all the individual contributions in quadrature.

Data availability

The unprocessed and reconstructed data that support the findings of this study are publicly available on the GridPP computing grid^{53,54}. Source data are provided with this paper. Publications using MICE data must contain the following statement: ‘We gratefully acknowledge the MICE collaboration for allowing us access to their data. Third-party results are not endorsed by the MICE collaboration.’

Code availability

The MAUS software that was used to reconstruct and analyse the MICE data is available at ref. 55. The analysis presented here used MAUS version 3.3.2.

References

46. Karadzhov, Y., Bonesini, M., Graulich, J. S. & Tzenov, R. *TOF Detectors Time Calibration* Tech. Report No. 251 (2009).
47. von Neumann, J. Various techniques used in connection with random digits. *J. Res. Natl Bureau Stand. Appl. Math. Series* **12**, 36–38 (1951).
48. Wells, M. T., Casella, G. & Robert, C. P. Generalized accept-reject sampling schemes. *Lect. Notes Monogr. Series* **45**, 342–348 (2004).
49. Silverman, B. W. *Density Estimation for Statistics and Data Analysis* 1st edn (Routledge, 1998).
50. Scott, D. W. *Multivariate Density Estimation: Theory, Practice, and Visualization* (John Wiley & Sons, 2015).
51. Marron, J. S. & Wand, M. P. Exact mean integrated squared error. *Ann. Stat.* **20**, 712–736 (1992).
52. Leroy, C. & Rancoita, P. G. *Principles of Radiation Interaction in Matter and Detection* (World Scientific, 2011).
53. Bogomilov, M. et al. MICE raw data. *figshare* <https://doi.org/10.17633/rd.brunel.3179644.v1> (2016).
54. Bogomilov, M. et al. MICE reconstructed data. *figshare* <https://doi.org/10.17633/rd.brunel.5955850.v1> (2018).
55. Bogomilov, M. et al. Source code of MAUS—the MICE analysis user software. *figshare* <https://doi.org/10.17633/rd.brunel.8337542.v2> (2019).
56. Zyla, P. A. et al. Review of particle physics. *Progr. Theor. Exp. Phys.* **2020**, 083C01 (2020).

Acknowledgements

The work described here was made possible by grants from the Science and Technology Facilities Council (UK); the Department of Energy and the National Science Foundation (USA); the Istituto Nazionale di Fisica Nucleare (Italy); the European Union under the European Union’s Framework Programme 7 (AIDA project, grant agreement no. 262025; TIARA project, grant agreement no. 261905; and EuCARD); the Japan Society for the Promotion of Science; the National Research Foundation of Korea (no. NRF2016R1A5A1013277); the Ministry of Education, Science and Technological Development of the Republic of Serbia; the Institute of High Energy Physics/Chinese Academy of Sciences fund for collaboration between the People’s Republic of China and the USA; and the Swiss National Science Foundation in the framework of the SCOPES programme. We gratefully acknowledge all sources of support. We are grateful for the support given to us by the staff of the STFC Rutherford Appleton and Daresbury laboratories. We acknowledge the use of the grid computing resources deployed and operated by GridPP in the UK (<https://www.gridpp.ac.uk/>). This publication is dedicated to the memory of V. Palladino and D. Summers who passed away while the data analysis from which the results presented here was being developed.

Author contributions

All authors contributed considerably to the design or construction of the apparatus or to the data taking or analysis described in this Article.

Competing interests

The authors declare no competing interests.

Additional information

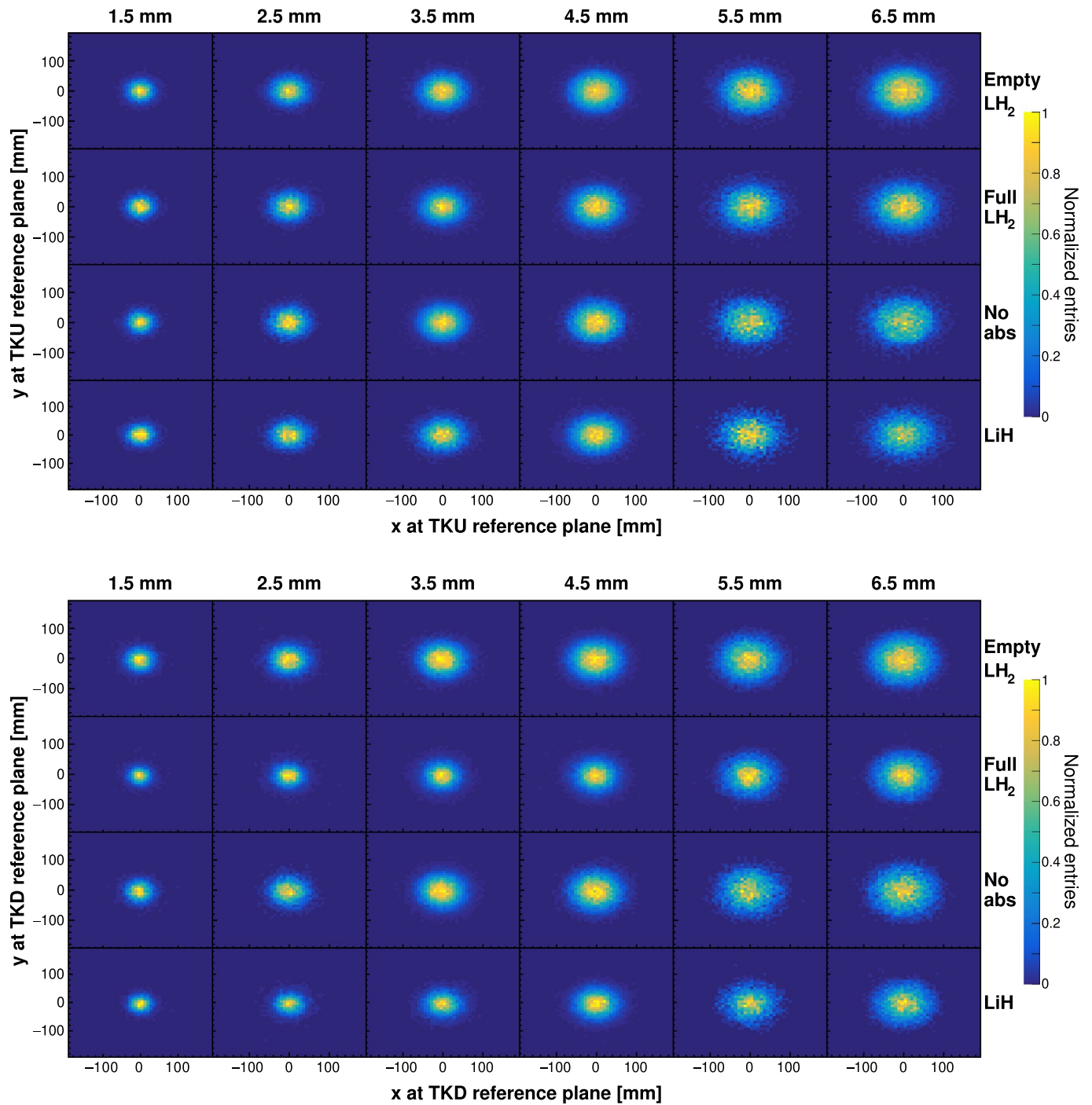
Extended data is available for this paper at <https://doi.org/10.1038/s41567-024-02547-4>.

Supplementary information The online version contains supplementary material available at <https://doi.org/10.1038/s41567-024-02547-4>.

Correspondence and requests for materials should be addressed to P. B. Jurj.

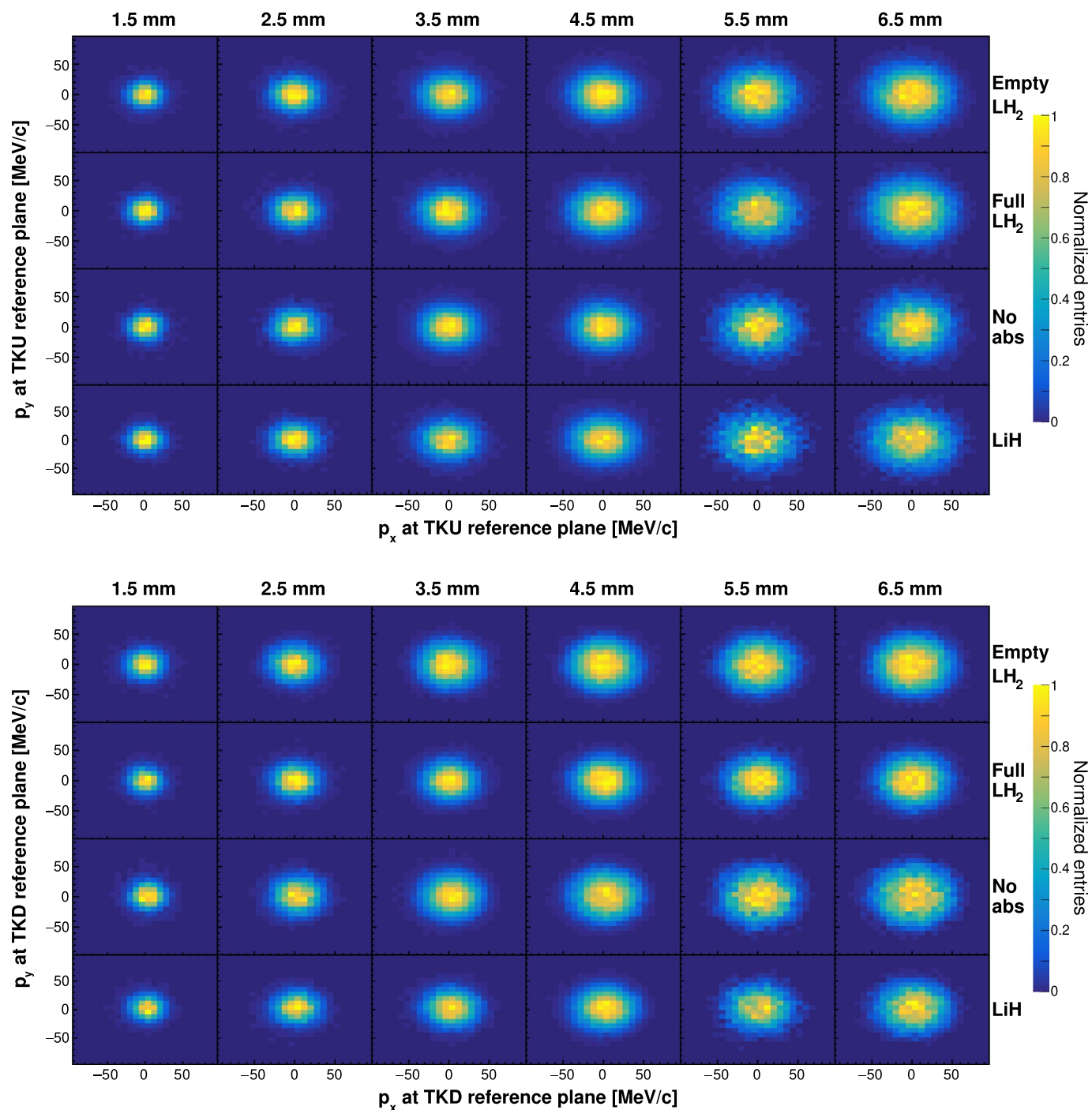
Peer review information *Nature Physics* thanks Seweryn Kowalski and Masashi Otani for their contribution to the peer review of this work.

Reprints and permissions information is available at www.nature.com/reprints.



Extended Data Fig. 1 | Beam transverse profiles in the (top) upstream and (bottom) downstream trackers (TKU and TKD). Measured transverse beam profiles for each absorber configuration (rows) and input emittance (columns). In each histogram, the number of events in each bin is normalized to the number

of events contained by the bin with most entries. The beams that pass through an absorber present a smaller transverse size in the downstream tracker than the beams that traverse an empty absorber module. This effect is caused by a change in focusing due to energy loss.



Extended Data Fig. 2 | Beam transverse momentum in the (top) upstream and (bottom) downstream trackers (TKU and TKD). Measured x and y components of the beam transverse momentum, p_x and p_y , for each absorber configuration (rows) and input emittance (columns). In each histogram, the number of events

in each bin is normalized to the number of events contained by the bin with most entries. The beams that pass through an absorber present a smaller transverse momentum in the downstream tracker than the beams that traverse an empty absorber module.

Extended Data Table 1 | The sample size of the MICE matched beams

Absorber	Input ε_{\perp} [mm]	1.5	2.5	3.5	4.5	5.5	6.5
	Empty LH ₂		8141	10162	19525	29896	13196
Full LH ₂		5199	8541	16757	20836	9063	15326
No absorber		4496	4792	32836	17659	5324	8573
LiH		4549	4372	9150	21071	3927	7618

The number of muons in each final sample is listed for each absorber configuration and target input transverse emittance ε_{\perp} .

Extended Data Table 2 | Material properties of the MICE absorbers and aluminium alloy windows

Property	Material		
	MICE LiH	Liquid H ₂	Al 6061-T651
Density, ρ [g/cm ³]	0.6957	0.07053	2.727
$\langle Z/A \rangle$	0.56716	0.99212	0.48145
I [eV]	36.5	21.8	166
X_0 [cm]	102.04	866	8.68

Z and A are the atomic and mass numbers of the material, respectively, I is the mean excitation energy of the atoms in the material, and X_0 is the radiation length of the material⁵⁶.

Extended Data Table 3 | Systematic uncertainties affecting the measurement of emittance change $\Delta\epsilon_{\perp}$

Input ϵ_{\perp} [mm]	Systematic uncertainty [mm]					
	1.5	2.5	3.5	4.5	5.5	6.5
Parameter alteration						
TKU translation	0.003	0.002	0.001	0.005	0.003	0.002
TKU rotation	0.003	0.003	0.002	0.005	< 0.001	0.003
TKU glue density	0.003	0.001	0.003	0.003	0.004	0.002
Upstream End 1 coil current	0.009	0.011	0.016	0.018	0.024	0.023
Upstream Centre coil current	0.018	0.021	0.028	0.034	0.042	0.050
Upstream End 2 coil current	0.007	0.006	0.006	0.005	0.010	0.015
TKD translation	0.003	0.003	0.001	0.001	0.004	< 0.001
TKD rotation	0.001	0.002	0.001	0.005	< 0.001	0.001
TKD glue density	0.005	< 0.001	0.001	0.004	0.003	0.002
Downstream End 1 coil current	0.003	0.010	0.014	0.018	0.024	0.027
Downstream Centre coil current	0.013	0.021	0.032	0.044	0.053	0.054
Downstream End 2 coil current	0.001	0.005	0.009	0.007	0.008	0.012
TOF01 time	0.001	< 0.001	0.004	0.006	0.007	0.007
Total systematic uncertainty	0.026	0.035	0.048	0.063	0.077	0.084

The systematic uncertainties associated with parameter alterations in the upstream tracker (TKU), downstream tracker (TKD), upstream and downstream coils, and time-of-flight measurement (TOF01) are listed for each input transverse emittance ϵ_{\perp} .

Space Weather



RESEARCH ARTICLE

10.1029/2020SW002712

Key Points:

- Correction of meteorological effects on muon component of secondary cosmic rays significantly extends the usability of muon monitors
- A new method for modeling of meteorological effects utilizing multivariate analysis and machine learning techniques is presented
- Correction efficiency of the best performing algorithm is greater than for other commonly used methods

Correspondence to:


M. Savić,
msavic@ipb.ac.rs

Citation:

Savić, M., Maletić, D., Dragić, A., Veselinović, N., Joković, D., Banjanac, R., et al. (2021). Modeling meteorological effects on cosmic ray muons utilizing multivariate analysis. *Space Weather*, 19, e2020SW002712. <https://doi.org/10.1029/2020SW002712>

Received 30 DEC 2020
 Accepted 13 JUL 2021

Modeling Meteorological Effects on Cosmic Ray Muons Utilizing Multivariate Analysis

M. Savić¹ , D. Maletić¹, A. Dragić¹, N. Veselinović¹, D. Joković¹, R. Banjanac¹, V. Udovičić¹, and D. Knežević¹

¹Institute of Physics Belgrade, University of Belgrade, Belgrade, Serbia

Abstract Correction of meteorological effects on muon component of secondary cosmic rays significantly extends the usability of muon monitors. We propose a new data driven empirical method for correction of meteorological effects on muon component of secondary cosmic rays, based on multivariate analysis. Several multivariate algorithms implemented in Toolkit for Multivariate Data Analysis with ROOT framework are trained and then applied to correct muon count rate for barometric and temperature effects. The effect of corrections on periodic and aperiodic cosmic ray variations is analyzed and compared with integral correction method, as well as with neutron monitor data. The best results are achieved by the application of linear discriminant method, which increases sensitivity of our muon detector to cosmic ray variations beyond other commonly used methods.

Plain Language Summary Primary cosmic rays are energetic particles that arrive at Earth from space. On their journey toward Earth they are affected by the solar wind (a stream of charged particles emanating from the sun), which has information about various solar processes embedded in it. In top layers of the atmosphere primary cosmic rays interact with nuclei of air molecules and produce large number of secondary particles that propagate toward Earth's surface. These secondary particles preserve information about variations of primary cosmic rays, which allows for the study of solar processes using Earth based detectors. One type of secondary particles that can be detected on the ground are muons. However, muons are affected by the conditions in the atmosphere, which can disturb the information about variations of primary cosmic rays. That is why it is important to model these atmospheric effects on cosmic ray muons as well as possible so they can be corrected for. In this study, we present a new method for modeling and correction of atmospheric effects on cosmic ray muons, that is based on multivariate analysis utilizing machine learning algorithms. This method increases sensitivity of our muon detector to cosmic ray variations beyond other commonly used methods.

1. Introduction

Meteorological effects on muon component of secondary cosmic rays have been known and studied for almost a century. A number of meteorological parameters contribute to variation of muon flux in the atmosphere, but two are the most significant: atmospheric pressure and atmospheric temperature.

Aperiodic fluctuations of intensity, discovered in the very early cosmic ray measurements, were eventually attributed to the variation of atmospheric pressure by Myssowsky & Tuwim (1926) (associated effect dubbed *barometric*), while *temperature effect* has been discovered more than a decade later and has two components: *negative* (first quantitatively described by Blackett, 1938) and *positive* (suggested by Forró, 1947). Barometric effect represents variation of muon flux due to variation of the mass of the absorber (air column) above the detector. Negative temperature effect is a consequence of dependence of effective height of muon generation level on the atmospheric temperature, resulting in longer muon path and increased probability of decay with higher temperature. Positive temperature effect has to do with positive correlation between atmospheric temperature and air density, decreasing the probability of nuclear interactions and increasing the probability of decay of muon-generating pions with the increase of temperature.

In order to study variations of primary cosmic rays (CR) using Earth based muon detectors, it is of the utmost importance to describe these meteorological effects as precisely as possible so they can be corrected for. A precise correction for meteorological effects significantly increases sensitivity of muon detectors to CR variations, making them a more usable counterpart to neutron monitors (the other widely used type of

© 2021. The Authors.

This is an open access article under the terms of the [Creative Commons Attribution-NonCommercial-NoDerivs License](https://creativecommons.org/licenses/by-nc-nd/4.0/), which permits use and distribution in any medium, provided the original work is properly cited, the use is non-commercial and no modifications or adaptations are made.

ground based cosmic ray detectors), as muon detectors are normally responsive to higher energy primary cosmic rays. Additionally, muon monitors have a unique application in diagnostics of the atmosphere, allowing for prediction of atmospheric temperatures provided a good model of meteorological effects is available (Belov et al., 1987; Kohno et al., 1981).

Several empirical and theoretical models of meteorological effects have been proposed over the years, based on which corrections can be performed. Even though full set of meteorological effects is larger, in this analysis we will concentrate on the correction of temperature and barometric effect only, so results can be more easily compared to other methods.

Some of the most commonly used methods for temperature correction are: method of effective level of generation, introduced by Duperier (1949), integral method, developed by Feinberg (1946), Dorman (1954), and others (Maeda & Wada, 1954; Wada, 1962), method of mass-averaged temperature developed by Dvornikov et al. (1976), and method of effective temperature (mostly applicable to underground detectors) (Barrett et al., 1952).

Each of these methods have their own advantages, but in this study, we have decided to use the integral method as a reference against which to compare the results of our analysis. Main reason being is that it is derived from the theory of meteorological effects, which involves the most detailed analysis, as well as it being the least approximative. According to this approach, relative variation of muon count rate due to the temperature effect can be expressed as:

$$\left(\frac{\delta I}{I}\right)_{temp} = \int_0^{h_0} \alpha(h) \cdot \delta T(h) \cdot dh, \quad (1)$$

where α is temperature coefficient density function, δT is temperature variation and h_0 is atmospheric depth of the observation level expressed in g/cm^2 . Temperature coefficient density function is calculated theoretically, while temperature variation is calculated relative to some reference temperature for the period, usually mean temperature. In practical application, integration in Equation 1 is substituted with a sum, taking into account some finite number of isobaric levels.

Analysis of barometric effect is also included in the theory of meteorological effects, but barometric coefficient is rarely calculated theoretically. Most commonly it is determined using linear regression, assuming linear dependence between atmospheric pressure and muon flux:

$$\left(\frac{\delta I}{I}\right)_{pres} = \beta \cdot \delta P, \quad (2)$$

where β is barometric coefficient, and δP represents atmospheric pressure variation.

Each of the mentioned methods is at least in some part approximative, so the idea behind this work is to introduce a new empirical method for correction of meteorological effects that would be data driven, assuming as little as possible upfront. Other advantages of such approach are that it does not depend on the design of the detector, location of the site or topology of the surrounding terrain (as these would ideally be factored in by the model), and that it can be applied in near-real time. Additionally, proposed method can be used in the analysis and potential correction of temperature effect of neutron component of cosmic rays, as part of detected neutrons can originate from cosmic ray muons captured in the nuclei of the shielding of a neutron monitor detector (Dorman, 2004). Finally, in principle it can easily be generalized to take wider set of meteorological parameters into account.

As the presented problem is multidimensional, involving a relatively large number of correlated variables, we have decided to employ multivariate analysis, relying on machine learning techniques. In some recent work (Morozova et al., 2017; Savic et al., 2019) decorrelation of atmospheric variables and numerical modeling has been successfully applied to the study of interaction of cosmic rays with Earth's atmosphere, so utilizing adaptive and flexible machine learning methods could possibly yield further improvement, potentially revealing additional dependencies and taking higher order effects into account. This approach involves application of a number of multivariate algorithms, more or less rooted in statistical machine learning, to our problem and comparing their consistency and effectiveness with selected reference results.

Large part of variations observed in continuous cosmic ray measurements can be attributed to different space weather phenomena, due to modulation of primary cosmic rays in the heliosphere. In terms of temporal properties, they can be classified as periodic or aperiodic. We will test how newly introduced methods for correction of meteorological effects affect the sensitivity for detection of both periodic as well as aperiodic variations of muon flux of nonterrestrial origin, and how it ultimately compares to the sensitivity of neutron monitors.

2. Data

For the analysis of meteorological effects both muon flux and meteorological data are needed. Muon flux was measured experimentally in the Low Background Laboratory at the Institute of Physics Belgrade, while meteorological data is a combination of modeled atmospheric temperature profiles, and atmospheric pressure and ground level temperature measured locally.

2.1. CR Muon Data

Low Background Laboratory (LBL) is located on the grounds of the Institute of Physics Belgrade. Geographical coordinates for the laboratory are $44^{\circ}51'N$ and $20^{\circ}23'E$, with elevation of 75 m and geomagnetic cutoff rigidity of 5.3 GV. Detector system is comprised of a $100 \times 100 \times 5$ cm plastic scintillator with accompanying read-out electronics. Median energy for the detector system is (59 ± 2) GeV (Veselinović et al., 2017), with muon flux of $(1.37 \pm 0.06) \times 10^{-2}$ per cm^2 s. Electron contamination determined for a previously used experimental setup was $\sim 24\%$ (Dragić et al., 2008), and is assumed to be comparable for the current one (Joković, 2011). More detailed description of the laboratory and the experimental setup can be found elsewhere (Dragić et al., 2011). Native muon count rate data has time resolution of 5 min, but hour sums are also frequently used in analysis.

Continuous cosmic ray muon flux measurements have been ongoing in LBL since 2002, current setup being utilized since 2009. Data are available to public via an online interface on the Belgrade Cosmic Ray Station internet site (Low Background Laboratory for Nuclear Physics, 2020).

As with any long-term measurement, some shorter interruptions and inconsistencies are unavoidable, hence when choosing the interval to be used for the analysis we decided to use a one-year period from June 1, 2010 to May 31, 2011, where measurements had the most continuity and consistency. Additionally, using a one-year period should remove any potential bias, primarily due to annual temperature variation.

2.2. Meteorological Data

Meteorological parameters needed for the analysis come from two sources: Atmospheric temperature profile data are produced by an atmospheric numerical model, while atmospheric pressure and ground temperature data come from local measurements.

Meteorological balloon soundings above Belgrade done by Republic Hydro-meteorological Service of Serbia (RHMZ, 2020) are not frequent enough for the purposes of this analysis, so modeled data for atmospheric temperature profile are used instead. Several numerical atmospheric models can provide such data. In this work, we have chosen Global Forecast System (GFS) produced by National Centers for Environmental Prediction (GFS, 2020), which has been found to be in best agreement with balloon soundings done above Belgrade. Comparison was done where soundings data were available, as described in our previous study (Savić et al., 2019). GFS provides a large number of modeled atmospheric parameters among which are atmospheric temperatures for different isobaric levels. Modeled data sets are being produced four times per day (at hours 00:00, 06:00, 12:00, and 18:00). In addition, analysis data are also available, reprocessed *post festum* and taking into account real data measured by world network of meteorological services. In this analysis, we have been using such reprocessed atmospheric temperatures for the following isobaric levels: 10, 20, 30, 50, 70, 100, 150, 200, 250, 300, 350, 400, 450, 500, 550, 600, 650, 700, 750, 800, 850, 900, 925, and 975 mb. Data are available with spatial resolution of 0.5° of geographical longitude/latitude, so coordinates closest to the laboratory coordinates were chosen. Data were then interpolated with cubic spline, similar as in Berkova et al. (2012), and sampled in finer time resolution needed for the analysis.

Atmospheric pressure and ground temperature data are compiled from different meteorological stations in and around Belgrade, and then interpolated as described in more detail elsewhere (Savic et al., 2016). Finally, unique time series of combined modeled and measured meteorological data, with finest time resolution of 5 min, is assembled to be used in the analysis.

3. Methodology

The use of machine learning has seen an unprecedented expansion in the last decade. The main strength of such approach being that it does not assume any a priori model, but is data driven and thus able to potentially discover hidden dependencies. This is especially true when applied to large data sets with many correlated variables. In this study, we want to establish whether such approach would yield any improvements when applied to the problem of meteorological effect on cosmic ray muons.

To test this, we have decided to use toolkit for multivariate analysis (TMVA) package which provides a ROOT-integrated environment for application of multivariate classification and regression techniques (Hoecker et al., 2007). The package has been developed for the use in high-energy physics and contains implementation of a number of supervised learning algorithms, which utilize training and testing procedures on a sample data set to determine the mapping function. Mapping function maps the input parameters to output target value, trying to model the actual functional dependence (“target” function) as accurately as possible. The structure of the mapping function is algorithm specific, and can be a single global function or a set of local models. Trained algorithm is then applied to the full data set and provides either a signal/background separation (in case of classification) or prediction of target value (in case of regression).

For us, the later application is especially interesting. The idea is to train the mapping function, using meteorological parameters as input variables, and muon count rate as the regression target, and use trained function to produce the predicted target output for a larger data set. In principle, implementation of this procedure is specific for different analysis frameworks. TMVA provides template code for the training and application of multivariate methods, where optimal parameters obtained in the training/testing phase are stored in “weight” files to be used in the application phase. Thusly predicted muon count rate would ideally contain only variations related to meteorological effects, while the residual difference between modeled and measured muon count rate would contain variations of non-meteorological origin. We would apply this procedure for a number of algorithms implemented in TMVA, compare their performance and efficiency based on several criteria, and finally suggest the methods best suited for the modeling, and ultimately the correction, of meteorological effects.

Corrected muon count rate would be calculated according to the following equation:

$$N_{\mu}^{(corr)} = \Delta N_{\mu} + \langle N_{\mu} \rangle, \quad (3)$$

where

$$\Delta N_{\mu} = N_{\mu}^{(mod)} - N_{\mu} \quad (4)$$

is the difference between the modeled and measured muon count rate.

Not all machine learning methods are equally suited for all types of problems and selection of the optimal method for a particular application is rarely straightforward. The efficiency of different algorithms depends on a number of factors: Whether they are used for classification or regression, is correlation between parameters linear or nonlinear, what is the general complexity of the problem and required level of optimization, and so on. One can only assume the efficiency of any given algorithm upfront but there is no clear general rule which one will perform best in a particular situation. Often, several algorithms with specific strengths and weaknesses can be applied to the same problem and only through analysis of the final result the optimal one can be determined. For this reason, in our analysis we have decided to indiscriminately include the largest number of algorithm classes available in TMVA, and only after extensive parallel testing narrow the selection down to the optimal one.

We will briefly describe different classes of multivariate methods available in TMVA, as well as list specific algorithms that were chosen as representative for each class. First class are methods based on probability

density estimation (PDE) techniques, where actual probability density function is estimated based on the available data. Here we have selected to test two specific multidimensional implementations, somewhat similar in nature: PDE range-search (PDE-RS) and k-nearest neighbor (KNN) algorithms. Examples of use of this approach for multivariate regression are scarce, but the success with which PDERS was applied in classification problems in high-energy physics (Carli & Koblitz, 2003) motivated its use here. Second class are methods based on function discriminant analysis. These methods are widely used for dimensionality reduction and classification. Here, we selected the linear discriminant (LD) algorithm which shares some similarities in the approach with principal component analysis (PCA), in that it maps a space of potentially correlated input variables onto a smaller space of uncorrelated variables, but in addition to PCA it also maximizes the separation between output classes, making it a natural choice for application to our problem. Algorithms that employ higher order functions were also tested, but as could be expected performed more poorly. Application of artificial neural networks (ANN) to multivariate regression problems has seen expansion in recent years, where ANN methods often perform better than more straightforward regression techniques, especially if some degree of nonlinearity is present. Even though the dependence of cosmic ray muon flux on atmospheric temperatures is linear, we felt it is certainly worth investigating how ANN methods would perform when applied to this problem, and if any additional hidden dependence would be revealed. We have chosen to apply the MLP, as it is the fastest and most flexible available ANN algorithm in TMVA. Finally, method of boosted regression trees (BDT) employs a larger number (*forest*) of binary decision trees, which split the phase space of input variables based on a yes/no decision to a series of sequential cuts applied, so to predict a specific value of the output variable. They have been very successfully applied to classification problems in high-energy physics (Lalchand, 2020), but can also be used for multivariate regression with the similar rationale as for the ANN. We have selected two representative algorithms for testing: boosted decision tree (BDT) and gradient boosted decision tree (BDTG).

In this analysis, the procedure is applied to correction of barometric and temperature effect but it is easy to see how it can be extended to include more atmospheric variables, especially as such data is readily available from atmospheric numerical models.

3.1. Training Procedure

For the training/testing data subset we have selected data for the 10 geomagnetically quietest days of each month (list provided by GFZ German Research Center for Geosciences, GFZ Potsdam, 2020), as we expect variations due to meteorological effects to be more pronounced here. This subset was then further split into training and testing data set, where 70% of randomly selected data was used for training while remaining 30% was used for testing. Data time resolution used was 5 min as it gave us a larger statistics for training.

There is a number of settings that can be manipulated for each of the multivariate algorithms used. They vary from some basic parameters, to selection of different subalgorithms or various options that can be turned on or off. For each algorithm, we have selected the optimal set of parameters. The criterium for optimal performance was minimizing the average quadratic deviation of the modeled output versus the target value. Also, where allowed by the algorithm, input variables were decorrelated prior to further processing.

Table 1 shows the values of average quadratic deviation for the modeled output (modeled muon count rate) versus the target value (measured muon count rate) for different algorithms. First two columns refer to the training data subset while second two columns refer to the testing data subset. First and third column represent average quadratic deviation defined as $(\sum(f_{MVA} - f_{target})^2)^{1/2}$ (where f_{MVA} and f_{target} represent modeled and measured count rates, respectively), while second and fourth columns represent truncated average quadratic deviation which takes into account 90% of data with least deviation. As previously mentioned, the criterium for selection of optimal parameters for every algorithm is the minimal value of average quadratic deviation for the test data subset.

3.2. Algorithm Performance Analysis

All presented multivariate algorithms have no built in knowledge about the studied effect, so in addition to quantitative test mentioned in the section above, we introduce some qualitative analysis designed to estimate the integrity of modeled data. Prime concern here would be to test whether the suggested procedure

Table 1
Average Quadratic Deviation for Selected Multivariate Methods

Method	Training		Testing	
	Average deviation (counts/5 min)	Truncated deviation (counts/5 min)	Average deviation (counts/5 min)	Truncated average (counts/5 min)
PDERS	234	185	258	201
KNN	224	177	233	185
LD	286	225	284	223
MLP	228	180	234	186
BDT	219	182	237	188
BDTG	223	174	236	187

Abbreviations: BDT, boosted decision tree; BDTG, gradient boosted decision tree; KNN, k-nearest neighbor; LD, linear discriminant.

for the correction of barometric and temperature effect (PT correction) removes these meteorological effects only, while leaving all other features nonperturbed. To this end, we will analyze several distributions of modeled data, compare them with raw and reference PT corrected data (obtained using the integral method) and look for possible anomalous features.

First, we will look into structure of distributions of difference between modeled and measured muon count rate as a function of measured count. We want to make comparison between these distributions in the training phase (for the test data subset) and after the trained algorithm was applied to the full data set. We would expect these distributions to be consistent, and appearance of some new structures or strong trends would point to some perturbation in the application phase. We have selected two examples to illustrate the difference in consistency of application of trained algorithms—BDTG and PDERS, their distributions shown in Figure 1.

We can see that distributions for BDTG algorithm for test data subset (Figure 1a) and full data set (Figure 1b) are fairly similar, and any structures and trends in the test distributions are mostly well replicated in the full data set distributions (different statistics taken into account). This is the case for most applied algorithms except for PDERS, where some dependence of the count rate, negligible for the test data distribution (Figure 1c), exists for the full data set distribution (Figure 1d).

Another, more important feature, is that for some algorithms distributions we analyzed in the previous paragraph are not smooth, but rather display some structures. To get further insight into these structures, for all featured methods we plotted distributions of modeled muon count rate along with the distribution of raw count rate on the same graph, as shown in Figure 2.

In order to better understand shapes of distributions and any structures observed in plots in Figure 2, it would be helpful to compare them to equivalent plots for muon count rates corrected for pressure and temperature effects using a well-established reference method. However, before we take a look at these distributions, we will first briefly describe procedures used to obtain reference PT correction.

Temperature and barometric effect are typically corrected for independently, where one of several methods mentioned in Section 1 is used for temperature correction, and barometric coefficient for pressure correction is determined empirically. Integral method for correction of temperature effect is widely accepted as the most accurate one. It is based on the theory of meteorological effects and takes complete atmospheric temperature profile and relevant processes into account. Most thorough description of the theory of meteorological effects is given by Dorman (2004), where temperature coefficient density function $\alpha(h)$ in Equation 1 is given in its integral form. In order to be applied, this function is then calculated through integration, substituting parameters specific to the location of the experiment. Temperature coefficient density functions for the location of Low Background Laboratory for Nuclear Physics were calculated using Monte Carlo integration technique. In order to determine barometric coefficient, temperature corrected muon data were plotted as a function of atmospheric pressure (using entries for 10 geomagnetically quietest days

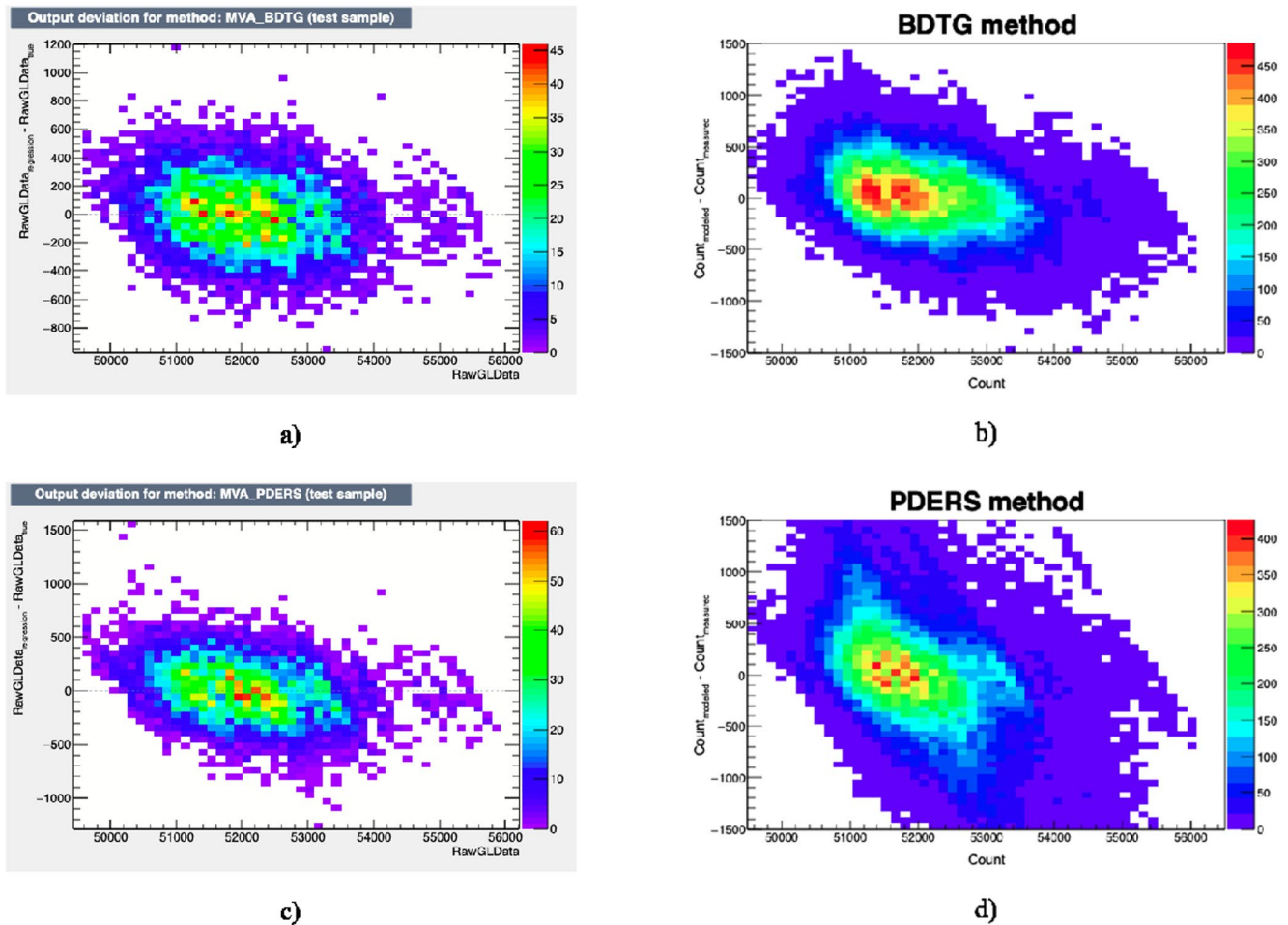


Figure 1. Distribution of difference between modeled (regression) and measured (true) muon count rate as a function of measured muon count rate for: (a) gradient Boosted decision tree (BDTG)—test data set, (b) BDTG—full data set, (c) PDERS—test data set, and (d) PDERS—full data set.

of each month only), coefficient determined via linear regression separately for each calendar year. Both procedures are presented in greater detail in our previous work (Savic et al., 2016).

Distributions equivalent to ones shown in Figures 1 and 2 were plotted for reference pressure and temperature corrected data, as shown in Figure 3. The analog for the modeled muon count rate is calculated from the variation due to pressure and temperature effects calculated based on the integral method. It is worth pointing out that distributions for reference PT corrected data are noticeably less smooth, which can be mostly attributed to lower statistics used as only hour summed data was available for this correction.

Based on these plots, we can conclude that we should not expect a significant deviation between raw and corrected data and that corresponding distributions should not have any characteristic structures. Most plots in Figure 2 are consistent with this expectation, however, some structures can be observed in KNN plots, and to a degree in BDT plots, while distribution plotted for PDERS algorithm does not have these structures but appears to somewhat deviate from raw data distribution.

Another insight into performance and consistency of different multivariate algorithms when applied to the modeling of meteorological parameters can be gathered by the way of spectral analysis of PT corrected data. Pressure and temperature corrected muon count rate was determined for all selected algorithms using modeled data, as described in Section 3. Since some gaps exist in our muon data, Lomb-Scargle algorithm was used to obtain the power spectra, as it is less sensitive to uneven data sampling (Press et al., 2007). Figure 4 shows power spectra for raw and muon count rates corrected for pressure and temperature effects using integral and two illustrative examples of multivariate methods. Full spectrum as well as selected interval

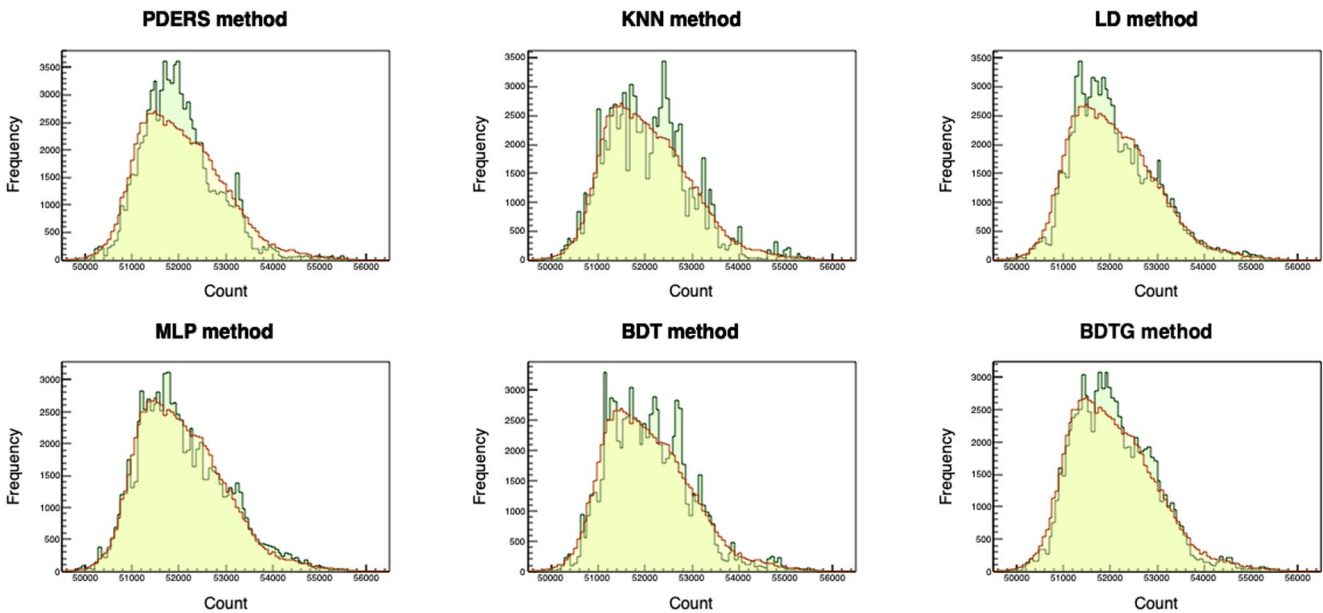


Figure 2. Comparison between distributions of raw (yellow) and muon count rate modeled by selected multivariate methods (green).

of frequencies around the periodicity of one day are shown, red dashed line indicating significance level of 0.01.

If integral method is again used as a reference, we can see that thus obtained PT correction does not remove daily variation, but rather makes it more pronounced. This should not come as a surprise, as only smaller part of the diurnal variation can be attributed to meteorological effects (Quenby & Thambyahpillai, 1960), while larger part is of nonmeteorological origin. Hence, removing variation due to atmospheric pressure would make daily variation more prominent. LD, and to a degree BDT/BDTG methods, have an effect on daily variation similar to the integral method, but for BDT method (bottom right in Figure 4) we observe emergence of some frequencies with significant power that cannot be associated with any known periodicity of cosmic rays, and probably have artificial origin. Such features are even more pronounced for the remaining multivariate algorithms, where in addition an over-reduction of power frequency corresponding to diurnal variation to can be observed. Over-reduction of daily variation coupled with introduction of artificial variations with significant powers points to possible inadequateness or overtraining of some of the multivariate methods.

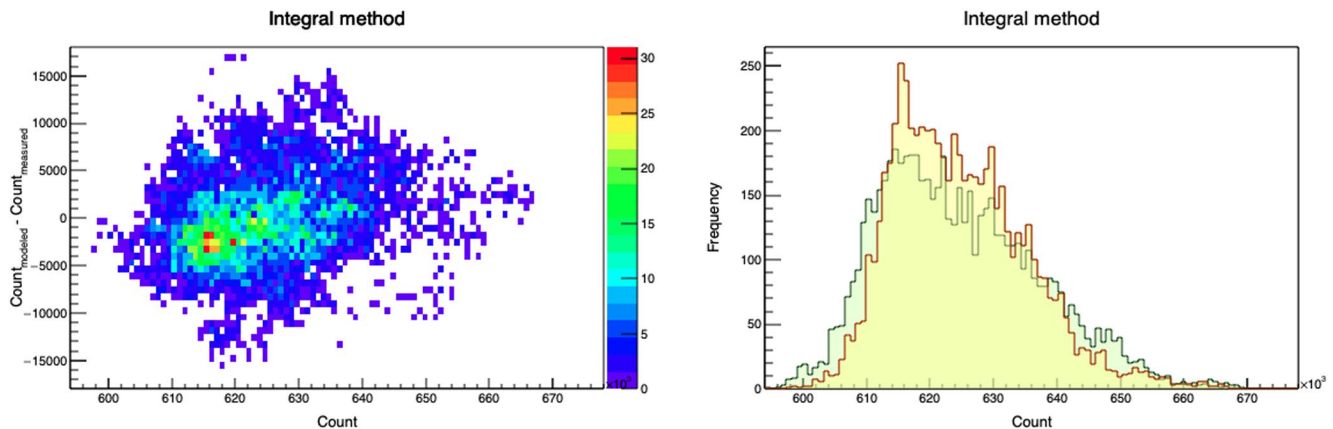


Figure 3. Distribution of difference between muon count rate calculated from the variation due to pressure and temperature effect using integral method and measured muon count rate as a function of measured muon count rate (left), and comparison between distributions of raw (yellow) and calculated muon count rate (green) shown on the right.

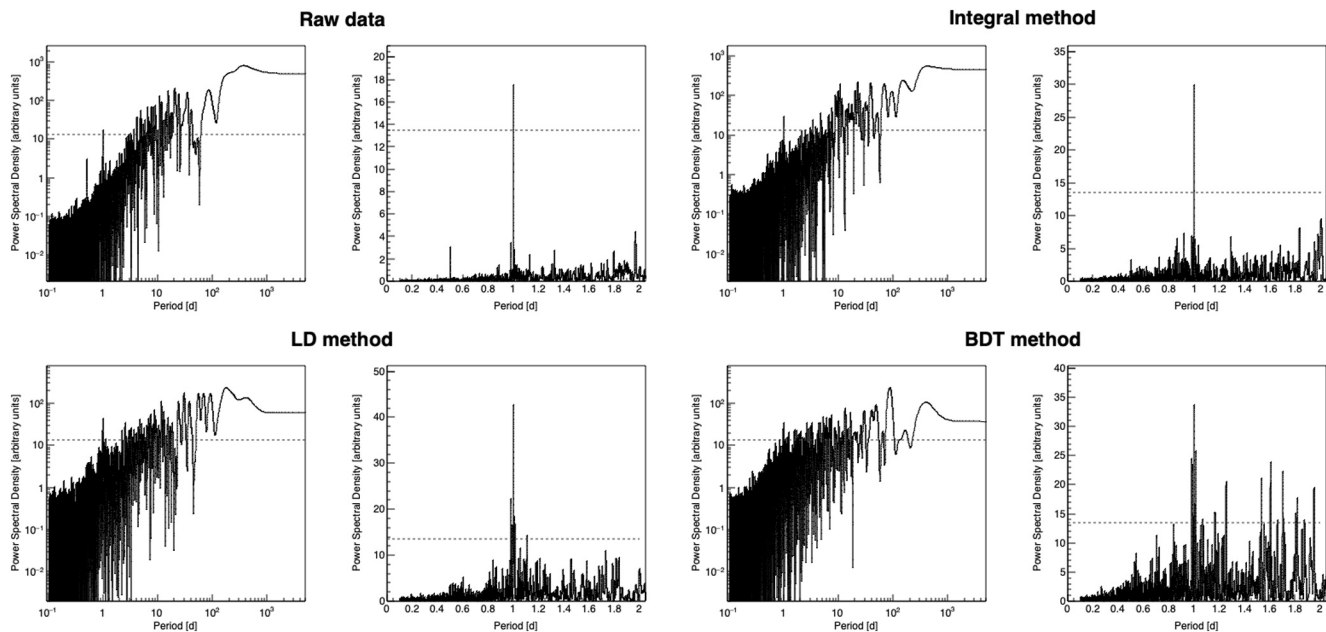


Figure 4. Power spectra for raw data (top left), PT corrected data using integral method (top right), and PT corrected data using selected multivariate methods (second row). For each method, both full spectrum and a range of frequencies around periodicity of one day are shown. Significance level of 0.01 is indicated by the red dashed line.

The effect on annual variation is difficult to determine based on the spectral analysis as period of only one year is analyzed, but we will introduce some quantitative tests in the next section that will help us with this estimate.

4. Results

We will use two criteria to estimate the efficiency of newly introduced methods for PT corrections. One will rely on the effectiveness with which the multivariate algorithms remove the annual variation and reduce variance, while the other will be based on the effect the correction has on detection sensitivity for aperiodic events, such as Forbush decreases (Forbush, 1937). In both cases, we will compare the results with the ones obtained by the integral method.

4.1. Effects of PT Correction on Periodic CR Variations

Significant part of the annual variation of cosmic ray muon flux can be attributed to the variation of atmospheric temperature (Hess, 1940). As mentioned before, the effectiveness with which this effect is corrected for will affect the detector sensitivity to variations of primary cosmic rays of non-atmospheric origin.

We will examine time series for pressure and temperature corrected data and compare them with raw and pressure corrected time series, especially taking note of how PT correction affects the annual variation. In order to estimate this effect, we fit the time series (except for raw data) with sine function with a period of one year. The amplitude of pressure corrected data determined from such fit will be used as an estimate of the annual muon flux variation, and serve as a reference against which to compare the effect of PT correction by different methods. In Figure 5 time series for raw, pressure corrected and pressure and temperature corrected data are shown. For the sake of simplicity, not all time series for data PT corrected using multivariate algorithms are shown, but rather only characteristic ones. Table 2 shows values for the annual variation amplitude for pressure and PT corrected time series, as well as possibly more informative reduction of annual variation calculated relative to the amplitude of the pressure corrected muon flux.

While, time series in Figure 5 for data PT corrected using integral, LD and BDTG methods do not seem to have some unexpected fluctuations, that is not the case for MLP method, where one can observe some

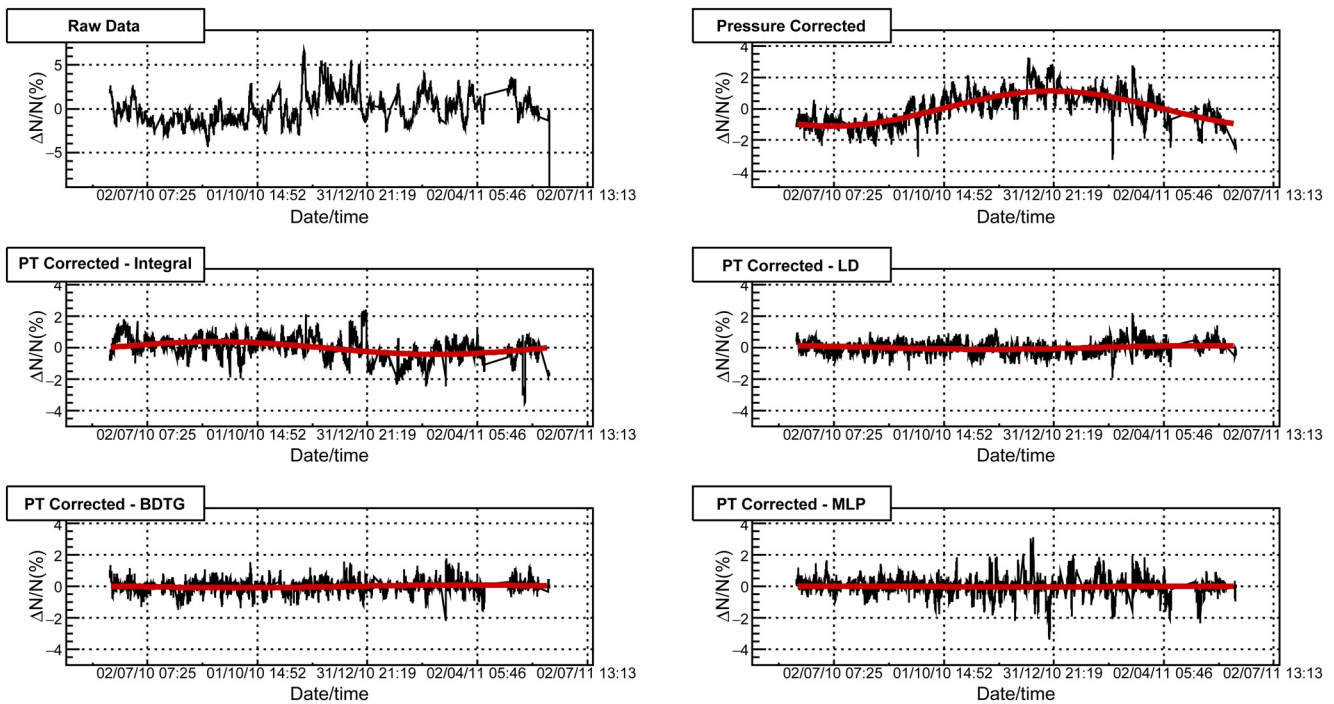


Figure 5. Muon count rate time series for the period from June 1, 2010 to May 31, 2011: raw data (top left), pressure corrected data (top right), PT corrected data using integral method (second row left) and data PT corrected using selected multivariate methods.

data that appears to deviate from the mean more significantly than what would be intuitively expected. For remaining multivariate algorithms this is even more the case. In order to try and quantify this visual comparison, we will analyze the effect corrections have on standard deviation of the data. If calculated relative to the mean muon flux for the whole period, standard deviation would be sensitive to the residual annual variation. To make standard deviation independent of the seasonal variation, we used a moving ten-day window to determine the mean value and then calculated the standard deviation relative to it.

Figure 6 shows distributions of relative variation of muon flux in respect to the moving window mean value for raw data and PT corrected data using integral, LD and MLP methods. It is based on these distributions that standard deviation was determined and results are presented in Table 3. Comparing standard deviations for PT corrected muon flux obtained by multivariate methods with the one obtained by the integral method, we can see that for LD, BDT, and BDTG algorithms they have comparable values. The difference is somewhat larger in the case of MLP, which is in accordance with features observed in Figure 6, while it is significantly larger for the remaining algorithms. This indicates that PT correction performed using KNN and PDERS (and possibly MLP) algorithms probably introduces some artificial features into PT corrected muon flux data.

One way to evaluate the effectiveness of different algorithms in reduction of the seasonal variation even better, would be to compare the PT corrected muon data to pressure corrected time series for selected neutron monitor detectors. The reasoning is based on a well-known fact that meteorological effects on the neutron component of secondary cosmic rays are dominated by the barometric effect. Temperature effect does exist for the secondary cosmic ray neutrons, but whether calculated theoretically (Dorman, 2004) or determined experimentally (Kaminer et al., 1965), it is still an order of magnitude smaller than for the muon component and typically not corrected for in neutron monitor data. Based on this, we

Table 2
Amplitude and Reduction of the Amplitude of Annual Variation Relative to Pressure Corrected Data (P Corrected) for PT Corrected Data (Using Integral and Selected Multivariate Methods)

Method	Amplitude (%)	Relative reduction (% of P corrected)
P corrected	1.11 ± 0.09	/
Integral	0.40 ± 0.03	64 ± 6
PDERS	0.09 ± 0.02	92 ± 3
KNN	0.24 ± 0.04	79 ± 5
LD	0.11 ± 0.03	90 ± 4
MLP	0.03 ± 0.01	98 ± 2
BDT	0.12 ± 0.03	89 ± 4
BDTG	0.086 ± 0.009	92 ± 2

Abbreviations: BDT, boosted decision tree; BDTG, gradient boosted decision tree; KNN, k-nearest neighbor; LD, linear discriminant.

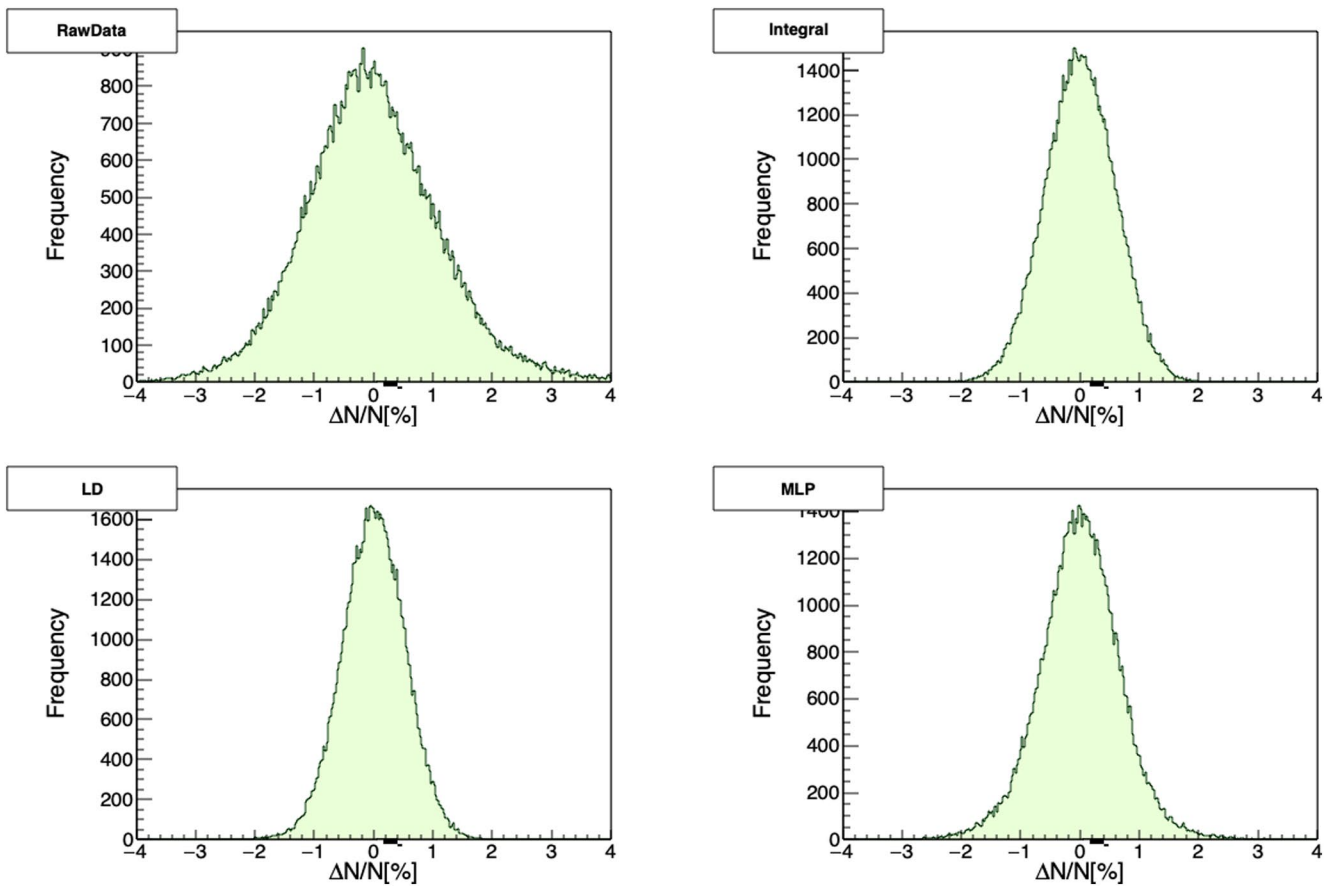


Figure 6. Relative variation of muon count rate calculated in respect to mean count in the ten-day moving window, for raw data (top left), PT corrected using integral method (top right), and data PT corrected using selected multivariate methods (second row).

believe pressure corrected neutron monitor data to be (in the first approximation) independent from meteorological effects, and hence a good reference for the evaluation of effectiveness of different methods for PT corrections of muon flux data.

For this comparison, we have chosen neutron monitors located in Athens and Rome, as they had the most consistent operation in the period we use for the analysis. Respective geomagnetic cutoff rigidities for these neutron monitors are 8.53 and 6.27 GV. Pressure and efficiency corrected relative neutron count rate was acquired via Neutron Monitor Database (NEST, 2020), presented for the said period in Figure 7. As for the muon flux data, relative neutron count rate time series were fitted with sinusoidal function, with a period of one year, to obtain the amplitude used as an estimate of the annual variation. Neutron monitors are more sensitive to lower energy secondaries than muon detectors so their time series can exhibit larger variations, which in turn can affect the fitting algorithm. However, in this case the fits seem to be dominantly affected by the relatively stable period between June and November 2010, hence we believe them to be a reliable estimate of the seasonal variation amplitude. Thus acquired annual variation amplitude for Rome neutron monitor is $(0.29 \pm 0.01)\%$, while for the Athens neutron monitor it is $(0.17 \pm 0.05)\%$.

Table 3

Standard Deviation of Relative Variation of Muon Count Rate for Raw and Data Corrected for Pressure and Temperature Effect (Using Integral and Selected Multivariate Methods)

Method	Raw	Integral	PDERS	KNN	LD	MLP	BDT	BDTG
Relative deviation (%)	1.117	0.592	0.990	0.785	0.533	0.687	0.607	0.551

Abbreviations: BDT, boosted decision tree; BDTG, gradient boosted decision tree; KNN, k-nearest neighbor; LD, linear discriminant.

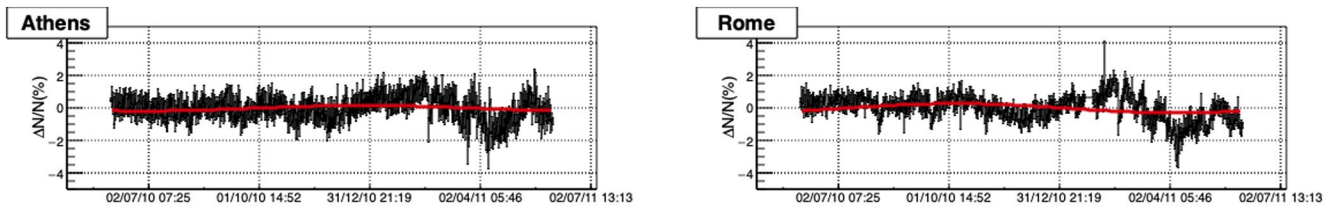


Figure 7. Relative neutron count rate time series for the period from June 1, 2010 to May 31, 2011 for Athens (left) and Rome (right) neutron monitors.

Comparing these values with the ones in Table 2, we see that methods KNN, LD, and BDT yield the most similar results. PDERS and MLP seem to underestimate the annual variation, while the integral method estimates a somewhat larger value.

Observed overall poor performance of KNN and PDERS algorithms could possibly be explained by the fact that these algorithms perform best when applied to problems involving strong nonlinear correlations, and are less efficient when dependencies between variables are dominantly linear (Hoecker et al., 2007). Additionally, these algorithms typically need a large training sample, so possibly statistics in our analysis was inadequate. However, artificial neural networks (such as MLP) should in principle be well suited for multivariate linear regression, and perform better than observed results suggest. Most likely, using minimization of the average quadratic deviation as a sole criterium for the selection of optimal parameters in the training phase may lead to overtraining (Montgomery et al., 2006), and additional qualitative criteria (i.e., ones introduced here) and more careful parameter control should also be used. BDT and BDTG algorithms performed reasonably well even though they are not optimized for treatment of linear multivariate problems, however, spectral analysis indicates a further improvement can be made. Additionally, all algorithms would probably benefit from a longer data interval of several years being used.

4.2. Effects of PT Correction on Aperiodic CR Variations

As mentioned before, apart from increasing sensitivity of muon detectors to periodic variations of primary cosmic rays, correcting raw muon flux data for meteorological parameters also affects detector sensitivity to aperiodic events which occur due to heliospheric modulation of primary cosmic rays. Here, we will analyze the effect PT correction, performed by application of different multivariate algorithms, has on detection of Forbush decrease events. We have chosen to concentrate on Forbush decreases as our muon detector is much less sensitive to other aperiodic events, such as ground level enhancements (GLE).

Forbush decrease (FD) events are typically characterized by their amplitude, so it could be a natural choice for a parameter to be used as a measure of detection sensitivity. However, another requirement for definition of sensitivity could be that detected signal significantly deviates from random fluctuations. That is, why we have decided to use the ratio of the amplitude to the standard deviation of muon flux, or relative amplitude, as an estimate of sensitivity to aperiodic events, rather than the actual amplitude. As we primarily focus on the magnitude of Forbush decreases, when we mention an FD event in the following text it mainly refers to the decrease phase and not the recovery phase.

To determine the amplitude, we have used a method proposed by Barbashina et al. (2009). The idea is to make the result independent from different trends leading up to, and following the actual FD. To do this, two intervals are defined: one i days before the onset of the FD, where i can have value $(1, \dots, n)$ days, and the other p days after the end of the decrease, where p can have value $(1, \dots, m)$ days. These intervals are then detrended using fit parameters obtained from linear regression. Mean count is determined for the detrended time series before the onset of FD for j days (where $j = 1, \dots, i$), and for the detrended time series during recovery stage for q days (where $q = 1, \dots, p$). Thus, in total we obtain $n!$ values for mean detrended count before the onset of FD, and $m!$ values for mean detrended count for the recovery stage. FD amplitude estimate is then calculated for each combination of “before” and “after” values according to the following formula:

$$A_{ij}^{pq} = \frac{\langle I_{before}^{(i,j)} \rangle - \langle I_{after}^{(p,q)} \rangle}{\langle I_{before}^{(i,j)} \rangle} \times 100\%, \quad (5)$$

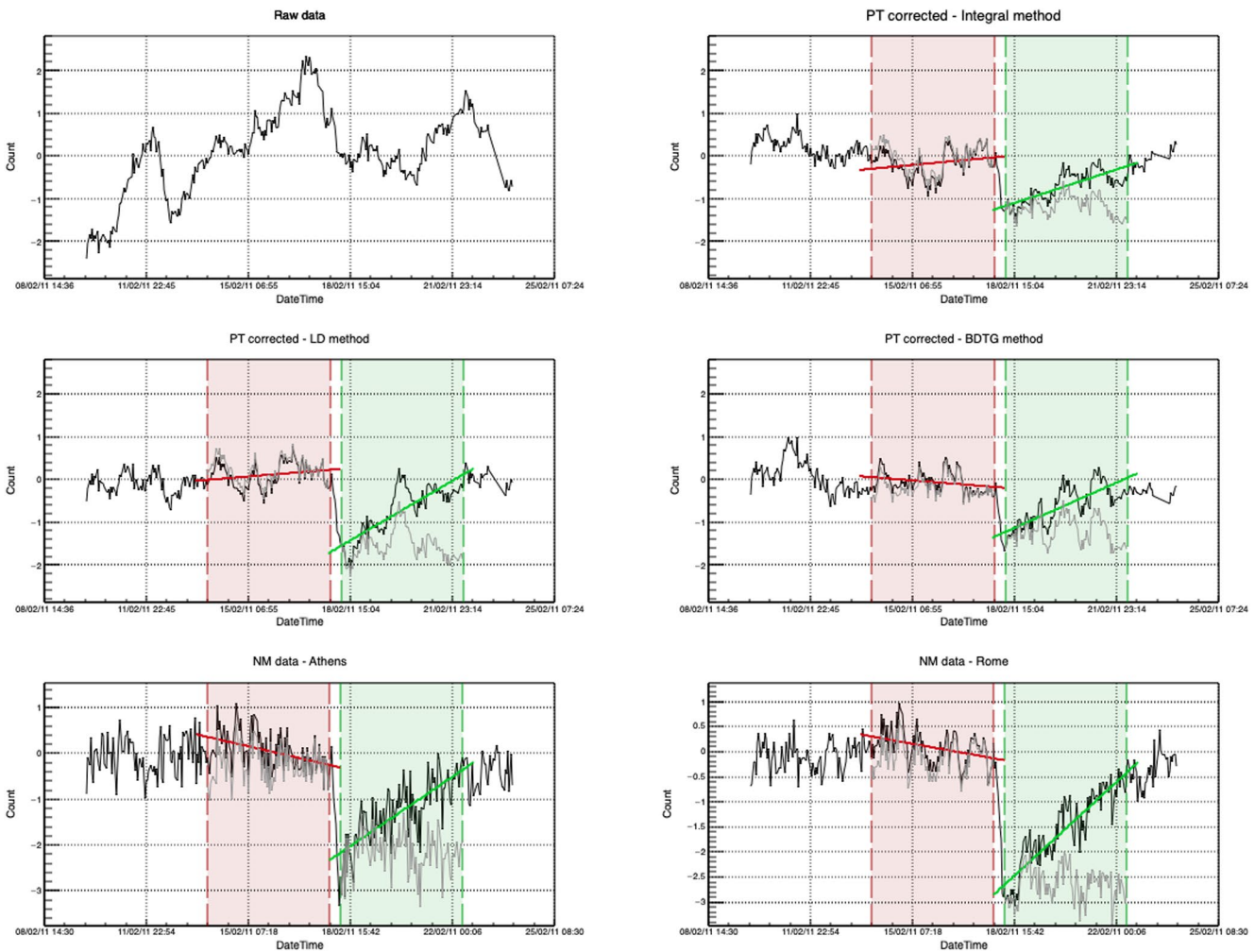


Figure 8. Time series for the interval around Forbush decrease of February 18, 2011: raw muon data (top left), PT corrected muon data using integral (top right), linear discriminant (center left) and gradient boosted decision tree (center right) methods, and neutron monitor data for Athens (bottom left) and Rome (bottom right) neutron monitors. Interval leading into (red) and following the Forbush decrease (FD) (green) are highlighted, as well as detrended intervals used to determine FD amplitude (gray).

where I_{before} and I_{after} are respective values for mean detrended count for intervals before the onset and after the end of the Forbush decrease. Finally, FD amplitude is calculated as the average of individual A_{ij}^{pq} values, rms deviation from the mean of the distribution used as an error estimate.

During the one-year period we used for the analysis there was a large number of Forbush events, but most of them had rather small amplitudes. We have analyzed several, however, here we will focus on the one with the largest magnitude as the results are most easily interpreted. The event is a Forbush decrease that occurred on February 18, 2011 in relation to X2.2 solar flare, and according to IZMIRAN space weather database (IZMIRAN, 2020) had 10 GV rigidity particle variation magnitude of 5.4. In Figure 8, we have shown plots that represent procedure described in the previous paragraph, applied to PT corrected datasets using integral method and selected multivariate algorithms. Procedure is also applied to pressure and efficiency corrected data for Athens and Rome neutron monitors, raw data also presented for reference. On the plots, interval leading to the onset of FD is indicated by red dashed lines, while recovery interval after the decrease is indicated by green dashed lines. We have chosen the lengths of both intervals to be four days ($n = m = 4$). Linear fits are represented by solid red and green lines, respectively, while detrended intervals are plotted using gray lines. Amplitudes and relative amplitudes calculated from the differences of means of detrended intervals are shown in Table 4.

Table 4
Amplitudes and Relative Amplitudes for the Forbush Decrease of February 18, 2011 for PT Corrected Muon Data and Selected Neutron Monitors

Method/NM monitor	Integral	LD	BDTG	Athens	Rome
FD amplitude (%)	1.38 ± 0.14	1.96 ± 0.18	1.10 ± 0.13	1.97 ± 0.15	2.68 ± 0.15
Relative FD amplitude	4.31 ± 0.44	7.09 ± 0.65	4.78 ± 0.56	5.30 ± 0.40	8.65 ± 0.48

Abbreviations: BDTG, gradient boosted decision tree; FD, Forbush decrease; LD, linear discriminant.

We see that relative amplitudes for this Forbush decrease, calculated based on data corrected for pressure and temperature using LD and BDTG algorithms, have sensitivity that is comparable or better than the sensitivity of integral method, even approaching the sensitivity of reference neutron monitors in the case of LD algorithm. However, when LD algorithm is concerned, such result can be at least in part explained by the fact that the calculated absolute FD amplitude is larger than expected for a muon detector. We would expect this value to be comparable to the value calculated based on the integral method. The reason for this discrepancy could be systematic, but also could be somewhat related to features of the studied FD event. Ideally, we should extend this analysis to more events, but selected time period was relatively calm in terms of solar activity, and February 2011 event was the only significant one with magnitude for 10 GV rigidity particles larger than five. Preliminary analysis done on Forbush decrease events of larger magnitude, that are outside the period used for analysis in this work, does show somewhat smaller effect for LD method, so that could be one of the focuses in the continuation of this work. We have excluded plots for the remaining multivariate algorithms as the results were either poorer (in the case of BDT and MLP) or inconsistent (in the case of PDERS and KNN).

5. Conclusions

We have selected a number of multivariate algorithms included in the TMVA package to apply for the correction of barometric and temperature effect on cosmic ray muons. Optimal parameters were determined for each algorithm based on the average quadratic deviation of modeled from measured data. Different distributions of modeled data for training phase and after the application of trained methods were compared to estimate the performance of selected algorithms. Pressure and temperature correction was done and spectral analysis performed to further test the algorithm consistency. The effect of the correction was analyzed for long-term (annual) and short-term (Forbush decrease) cosmic ray variations. In both cases, the efficiency of multivariate algorithms was compared to integral method and pressure corrected neutron monitor data.

Multidimensional probability density estimator algorithms (PDERS and KNN) appear not to be well suited for the modeling of pressure and temperature effect, most likely due to highly linear correlations between variables. MLP seems to have underperformed, while methods based on boosted decision trees (particularly BDTG) proved to be more successful, especially when effect on aperiodic variations was concerned. It should be expected that both MLP and BDT(G) methods can be improved if a longer period is used for analysis and parameters beyond average quadratic deviation of modeled data are used for algorithm optimization during training phase. Out of presented algorithms, LD proved to be the most consistent and effective in removing the pressure and temperature effects. In terms of the effect of PT correction on annual and aperiodic variations, this method matched or outperformed the integral method, while the effect it had on aperiodic effects was somewhat overestimative. This could give us grounds to assume at least part of the temperature effect is not taken into account by the integral method, and that there could be room for further improvement in modeling of meteorological effects beyond what theory currently provides.

Data Availability Statement

Raw muon count rate data set used in this study are publicly available online on the Belgrade Cosmic Ray Station site (<http://www.cosmic.ipb.ac.rs/>). Modeled atmospheric temperature data are available online on the NOAA GFS page (<https://www.ncdc.noaa.gov/data-access/model-data/model-datasets/global-forecast>

system-gfs). Latest atmospheric pressure and ground temperature data are available online on the site of Republic Hydro-meteorological Service of Serbia (<http://www.hidmet.gov.rs/>). List of international geomagnetically quiet days can be downloaded from the GFZ site (<https://www.gfz-potsdam.de/en/kp-index/>). Neutron monitor data can be accessed online via NEST browser interface (<http://www01.nmdb.eu/nest/>).

Acknowledgments

The authors acknowledge funding provided by the Institute of Physics Belgrade, through the grant by the Ministry of Education, Science and Technological Development of the Republic of Serbia.

References

- Barbashina, N., Dmitrieva, A., Kompaniets, K., Petrukhin, A., Timashkov, D., Shutenko, V., et al. (2009). Specific features of studying Forbush decreases in the muon flux. *Bulletin of the Russian Academy of Sciences: Physics*, 73, 343–346. <https://doi.org/10.3103/S1062873809030198>
- Barrett, P. H., Bollinger, L. M., Cocconi, G., Eisenberg, Y., & Greisen, K. (1952). Interpretation of cosmic-ray measurements far underground. *Reviews of Modern Physics*, 24, 133–178. <https://doi.org/10.1103/RevModPhys.24.133>
- Belov, A., Blokh, Y., Dorman, L., & Rogovaya, S. (1987). The temperature diagnostics of the atmosphere allowing for the temperature of the near-surface layer. *International Cosmic Ray Conference*, 4, 263.
- Berkova, M., Belov, A., Eroshenko, E., & Yanke, V. (2012). Temperature effect of muon component and practical questions of how to take into account in real time. *Astrophysics and Space Sciences Transactions*, 8, 41–44. <https://doi.org/10.5194/astra-8-41-2012>
- Blackett, P. M. S. (1938). On the instability of the Barytron and the temperature effect of cosmic rays. *Physical Review*, 54, 973–974. <https://doi.org/10.1103/PhysRev.54.973>
- Carli, T., & Koblitz, B. (2003). A multi-variate discrimination technique based on range-searching. *Nuclear Instruments and Methods in Physics Research Section A: Accelerators, Spectrometers, Detectors and Associated Equipment*, 501, 576–588. [https://doi.org/10.1016/S0168-9002\(03\)00376-0](https://doi.org/10.1016/S0168-9002(03)00376-0)
- Dorman, L. I. (1954). On the temperature effect of the hard component of cosmic rays. *Reports of Academy of Sciences of USSR (DAN SSSR)*, 95, 49–52.
- Dorman, L. I. (2004). *Cosmic rays in the Earth's atmosphere and underground*. Springer. Retrieved from <https://books.google.rs/books?id=mKLv68WBu5kC>
- Dragić, A., Joković, D., Banjanac, R., Udovičić, V., Panić, B., Puzović, J., & Aničin, I. (2008). Measurement of cosmic ray muon flux in the Belgrade ground level and underground laboratories. *Nuclear Instruments and Methods in Physics Research Section A: Accelerators, Spectrometers, Detectors and Associated Equipment*, 591(3), 470–475.
- Dragic, A. L., Udovicic, V. I., Banjanac, R., Jokovic, D. R., Maletic, D. M., Veselinovic, N. B., et al. (2011). The new set-up in the Belgrade low-level and cosmic-ray laboratory. *Nuclear Technology & Radiation Protection*, 26(3), 181–192. <https://doi.org/10.2298/NTRP1103181D>
- Duperier, A. (1949). The meson intensity at the surface of the Earth and the temperature at the production level. *Proceedings of the Physical Society Section A*, 62(11), 684–696. <https://doi.org/10.1088/0370-1298/62/11/302>
- Dvornikov, V. M., Krestyannikov, Y. Y., & Sergeev, A. (1976). Determination of the mass-average temperature on the cosmic ray intensity data. *Geomagnetism and Aeronomy*, 16, 923–925.
- Feinberg, E. L. (1946). On the nature of cosmic ray barometric and temperature effects. *Reports of Academy of Sciences of USSR (DAN SSSR)*, 53, 421–424. <https://doi.org/10.1038/157421a0>
- Forbush, S. E. (1937). On the effects in cosmic-ray intensity observed during the recent magnetic storm. *Physical Review*, 51, 1108–1109. <https://doi.org/10.1103/PhysRev.51.1108.3>
- Forró, M. (1947). Temperature effect of cosmic radiation at 1000-m water equivalent depth. *Physical Review*, 72, 868–869. <https://doi.org/10.1103/PhysRev.72.868>
- GFS. (2020). Retrieved from <https://www.ncdc.noaa.gov/data-access/model-data/model-datasets/global-forecast-system-gfs>
- GFZ Potsdam. (2020). Retrieved from <https://www.gfz-potsdam.de/en/kp-index/>
- Hess, V. F. (1940). On the seasonal and the atmospheric temperature effect in cosmic radiation. *Physical Review*, 57, 781–785. <https://doi.org/10.1103/PhysRev.57.781>
- Hoecker, A., Speckmayer, P., Stelzer, J., Therhaag, J., von Toerne, E., Voss, H., & Zemla, A. (2007). *Tmva—Toolkit for multivariate data analysis*. Ithaca, NY: Cornell University.
- IZMIRAN. (2020). Retrieved from <http://spaceweather.izmiran.ru/eng/dbs.html>
- Joković, D. (2011). *Detekcija i spektroskopija miona iz kosmičkog zračenja plastičnim scintilacionim detektorima (Detection and spectroscopy of cosmic ray muons with plastic scintillation detectors) (Doctoral dissertation)*. Faculty of Physics, University of Belgrade. Retrieved from <http://www.cosmic.ipb.ac.rs/documents/jokovic-thesis.pdf>
- Kaminer, N. S., Ilgatch, S. F., & Khadakhanova, T. S. (1965). Temperature effect of the cosmic ray neutron component. In *Proceedings of the 9th International Cosmic Ray Conference* (Vol. 1, p. 486).
- Kohno, T., Imai, K., Inue, A., Kodama, M., & Wada, M. (1981). Estimation of the vertical profile of atmospheric temperature from cosmic-ray components. In *Proceedings of the 17th International Cosmic Ray Conference* (Vol. 10, p. 289).
- Lalchand, V. (2020). Extracting more from boosted decision trees: A high energy physics case study. In *33rd Annual Conference on Neural Information Processing Systems* (Vol. 1).
- Low Background Laboratory for Nuclear Physics. (2020). Retrieved from <http://www.cosmic.ipb.ac.rs/>
- Maeda, K., & Wada, M. (1954). Atmospheric temperature effect upon the cosmic ray intensity at sea level. *Journal of the Scientific Research Institute*, 48, 71–79.
- Montgomery, D. C., Peck, E. A., & Vining, G. G. (2006). *Introduction to linear regression analysis* (4th ed.). Hoboken, NJ: Wiley & Sons.
- Morozova, A. L., Blanco, J. J., & Ribeiro, P. (2017). Modes of temperature and pressure variability in midlatitude troposphere and lower stratosphere in relation to cosmic ray variations. *Space Weather*, 15(5), 673–690. <https://doi.org/10.1002/2016SW001582>
- Myssowsky, L., & Tuwim, L. (1926). Unregelmäßige intensitätsschwankungen der höhenstrahlung in geringer seehöhe. *Zeitschrift für Physik*, 39, 146–150. <https://doi.org/10.1007/BF01321981>
- NEST. (2020). Retrieved from <http://www01.nmdb.eu/nest/>
- Press, W. H., Teukolsky, S. A., Vetterling, W. T., & Flannery, B. P. (2007). *Numerical recipes 3rd edition: The art of scientific computing* (3rd ed.). New York: Cambridge University Press.
- Quenby, J. J., & Thambayahpillai, T. (1960). Atmospheric temperature effects on the solar daily variation of cosmic ray intensity. *The Philosophical Magazine: A Journal of Theoretical Experimental and Applied Physics*, 5(54), 585–600. <https://doi.org/10.1080/14786436008241210>
- RHMZ. (2020). Retrieved from <http://www.hidmet.gov.rs/index-eng.php>

- Savic, M., Dragic, A., Veselinovic, N., Udovicic, V., Banjanac, R., Jokovic, D., & Maletic, D. (2016). Effect of pressure and temperature corrections on muon flux variability at ground level and underground. In *25th European cosmic ray Symposium*.
- Savic, M. R., Dragic, A. L., Maletic, D. M., Veselinovic, N. B., Banjanac, R. M., Jokovic, D. R., & Udovicic, V. I. (2019). A novel method for atmospheric correction of cosmic-ray data based on principal component analysis. *Astroparticle Physics*, *109*, 1–11. <https://doi.org/10.1016/j.astropartphys.2019.01.006>
- Veselinović, N., Dragić, A., Savić, M., Maletić, D., Joković, D., Banjanac, R., & Udovičić, V. (2017). An underground laboratory as a facility for studies of cosmic-ray solar modulation. *Nuclear Instruments and Methods in Physics Research Section A: Accelerators, Spectrometers, Detectors and Associated Equipment*, *875*, 10–15. <https://doi.org/10.1016/j.nima.2017.09.008>
- Wada, M. (1962). Atmospheric effects on the cosmic-ray meson intensity. *Journal of the Physical Society of Japan Supplement*, *17*, 508. <https://doi.org/10.1143/jpsj.17.1805>

New insights from cross-correlation studies between solar activity indices and cosmic-ray flux during Forbush decrease events

Mihailo Savić, Nikola Veselinović*, Aleksandar Dragić, Dimitrije Maletić, Dejan Joković
Vladimir Udovičić, Radomir Banjanac, David Knežević

Institute of Physics Belgrade, University of Belgrade, Pregrevica 118, 11080 Belgrade, Serbia

Received 1 April 2022; received in revised form 12 September 2022; accepted 27 September 2022

Available online 3 October 2022

Abstract

Observed galactic cosmic ray intensity can be subjected to a transient decrease. These so-called Forbush decreases are driven by coronal mass ejection induced shockwaves in the heliosphere. By combining in situ measurements by space borne instruments with ground-based cosmic ray observations, we investigate the relationship between solar energetic particle flux, various solar activity indices, and intensity measurements of cosmic rays during such an event. We present cross-correlation study done using proton flux data from the SOHO/ERNE instrument, as well as data collected during some of the strongest Forbush decreases over the last two completed solar cycles by the network of neutron monitor detectors and different solar observatories. We have demonstrated connection between the shape of solar energetic particles fluence spectra and selected coronal mass ejection and Forbush decrease parameters, indicating that power exponents used to model these fluence spectra could be valuable new parameters in similar analysis of mentioned phenomena. They appear to be better predictor variables of Forbush decrease magnitude in interplanetary magnetic field than coronal mass ejection velocities.

© 2022 COSPAR. Published by Elsevier B.V. All rights reserved.

Keywords: Cosmic rays; Forbush decrease; Solar energetic particles; Solar activity

1. Introduction

Cosmic rays (CRs) are high-energy charged particles that arrive at Earth from space, mainly originating from outside of our Solar system. CRs are modulated in the heliosphere (Heber et al., 2006) due to interaction with the interplanetary magnetic field (IMF) frozen in a constant stream of charged particles from Sun - the solar wind (SW). Transients in the heliosphere additionally modulate CRs. One type of transients are interplanetary coronal mass ejections (ICMEs), closely related to coronal mass ejections (CMEs).

ICMEs interact with SW, and as the speed of particles in ICME is different than the speed of SW particles, a bow shock can be created, affecting the CR flux (Belov et al., 2014). This interaction between ICMEs and residual solar wind can be one of the causes of short-term depression in CR flux, detectable at Earth (Subramanian et al., 2009). Such transient decrease in observed flux is known as a Forbush decrease (FD), a type of CR flux modulation that has been studied extensively since its initial discovery in the 1930s (Gopalswamy (2016) and references therein). There are two clearly distinguishable classes of Forbush decreases: recurrent and non-recurrent. Non-recurrent FDs, typically caused by ICMEs (Dumbovic et al., 2012), are mostly characterized by a sudden offset, which lasts about a day, followed by a gradual recovery phase within several days (Cane, 2000). Due to ICME sub-structures

* Corresponding author.

E-mail address: veselinovic@ipb.ac.rs (N. Veselinović).

(the sheath and the associated shock and magnetic cloud) FD can have one or two-step profile, which depends on transit of one or both structures to the observer (Richardson and Cane, 2011). Recurrent FDs have different profile, with gradual onset and decrease and symmetrical recovery caused by high-speed streams from coronal holes (Melkumyan et al., 2019). In this paper we will focus on non-recurrent ICME induced FDs.

Apart from FD profile, one of the main parameters that is used to describe a Forbush decrease is its magnitude. The effect is not the same for all CR particles, as it depends on their rigidity. Rigidity is defined as $R \equiv B\rho = p/q$, where ρ is gyroradius of the particle due to magnetic field B , p is particle momentum, and q is its charge. The higher the rigidity of a particle, the less it is affected by heliospheric inhomogeneities, hence the reduction in flux is less pronounced.

Another phenomenon that can accompany violent events on the Sun is emission of fast-moving particles, commonly known as solar energetic particles (SEP). The occurrence of such particles is typically related to eruptions on the surface of the Sun, which can be characterized by bursts of X-rays - solar flares (SF), and/or emission of coronal plasma - already mentioned CMEs. When excess of these solar energetic particles with high energy penetrates the geomagnetic field, it can cause a sudden and brief increase in measured CR flux at Earth - a ground level enhancement (GLE). Because GLEs can be harmful to human infrastructures (potentially damaging power lines, satellites in orbit, etc.), they have been studied in detail for decades.

Variations of CR flux have been monitored at Earth for decades using ground and underground-based detectors, primarily neutron monitors (NM) (Belov et al., 2000; Koldobskiy et al., 2019) and muon detectors (Mendonça et al., 2016; Veselinović et al., 2015). Different types of ground-based detectors complement each other in terms of their CR energy domain (Veselinovic et al., 2017), muon detectors being sensitive to energies higher than those detectable by NMs. In addition, CR flux is also (especially in the last couple of decades) directly measured in space using space-borne instruments (Dumbovic et al., 2020; von Forstner et al., 2020). In the MeV energy range most space probe particle detectors are sensitive to, enhancement of SEP flux can enshroud CR flux, thus making a task of establishing decoupled event-integrated energy spectra (or spectral fluences) for SEP and CRs a laborious task (Koldobskiy et al., 2021; Bruno and Richardson, 2021).

Many authors have studied the connection between SFs, CMEs/ICMEs and SEP, consequential effects on the geomagnetic field and compound effect of the IMF and geomagnetic field disturbances on CRs. Most relevant for our analysis is work that studied connection between different FD and ICME parameters (Belov et al. (2000), Belov (2008), Papaioannou et al. (2020) and references therein), which has among other, shown significant correlation between CME speeds and FD magnitudes. More precisely, CME speeds have been established as the best predictor

variables of FD magnitudes for primary CR particles with 10GV rigidity detected at Earth. Also of interest is the work that studied the connection between the disturbance of geomagnetic field and CR flux measured at Earth (Alhassan et al., 2021; Badruddin et al., 2019), where a significant correlation between FD magnitude and different geomagnetic parameters due to common solar or interplanetary origin has been established.

SF, CME/ICME, SEP and FD events are very often related processes that occur either simultaneously or in succession, in which case can be thought of as different components of one more complex event. CMEs (along with their interplanetary counterparts ICMEs) have been recognized as the main driver of FDs, while on the other hand there has been plenty of evidence for the relationship between CMEs with SEP. Namely, there are two different known mechanism for SEP acceleration: acceleration during magnetic-reconnection events usually resulting in solar flares (which produce short impulsive SEP events), and acceleration caused by CME induced shock waves (which result in gradual SEP events) (Reames, 1999). For this study the second class is of interest. Another type of closely related events that are important for this analysis are energetic storm particle (ESP) events, which represent particles accelerated locally by interplanetary shocks driven by fast CMEs (Desai and Giacalone, 2016). Even though details of the mechanism and the precise role of CME induced shock in the evolution of SEP events are not fully understood (Anastasiadis et al., 2019), we believe that analysis of how SEP/ESP events relate to CME, geomagnetic and FD events could provide some valuable new insight. We are especially interested in, and will concentrate the most on, the possibility of the last of these connections. To do so, we have decided to look into the shape of SEP/ESP fluence spectra and analyze how it relates to different CME, geomagnetic and especially FD parameters.

It should be noted that different mentioned types of events, even when related, do not need to occur at the same place nor at the same time. This is due to the fact that SEP travel along magnetic field lines, while CME/ICME shocks travel mostly directly away from the Sun. Furthermore, modulation of primary CR, detected as FD upon their arrival at Earth, can happen anywhere in the heliosphere. Hence, in general case, detection of these events should not necessarily be simultaneous. However, we believe that for the class of events selected for this analysis we can assume that they occur and are detected within a certain time window. We will elaborate more on this in Section 2.3.

The article is structured as follows: first we list various sources of data and justify the selection of solar cycle 23 and 24 FD events to be used in the analysis; then we describe parametrization of SEP events (involving calculation and parametrization of SEP fluence spectra); finally we perform correlative analysis between established SEP parameters and various CME, FD and geomagnetic indices and discuss the observed dependencies.

2. Data

Sources of SEP proton flux, various solar and space weather parameters, as well as ground CR measurements and different FD parameters used in this study are listed below. Different criteria for FD event selection are also described.

2.1. Solar energetic particle flux data

The source for SEP flux data was the ERNE instrument (Torsti et al., 1995) onboard the Solar and Heliospheric Observatory (SOHO). Instrument consists of two separate particle detectors. The Low-Energy Detector (LED) and the High-Energy Detector (HED). Former covers ion fluxes and count rates in the 1.3 – 13 MeV/nucleon energy range, and latter ion fluxes and count rates in the 13 – 130 MeV/nucleon energy range. Both ranges are separated in ten energy channels. SOHO has been making in situ observation from Lagrangian point L1 for the last three solar cycles (data available at https://omniweb.gsfc.nasa.gov/ftpbrowser/flux_spectr_m.html). ERNE data for solar cycles 23, 24 and current cycle 25 allows the study of variations of proton fluences in SEP events during this period (Paassilta et al., 2017; Belov et al., 2021). Higher channels are more correlated with measured CR flux (Veselinovic et al., 2021) and it appears as if flux in these channels is a mixture of CR and energetic proton fluxes of particles with the same energy. Important feature of HED detector is that, due to rather large geometric factor, during large intensity proton events SOHO/ERNE data have been subject to saturation effects in higher energy channels (Valtonen and Lehtinen, 2009; Miteva et al., 2020).

2.2. IZMIRAN directory of Forbush decreases

IZMIRAN database is an online repository developed at the Institute of Terrestrial Magnetism, Ionosphere and Radiowave Propagation (IZMIRAN) at Moscow Troitsk, Russia. It contains an extensive list of Forbush decreases and various parameters from solar, space weather, cosmic ray and geomagnetic measurements, spanning from the late 1950s (<http://spaceweather.izmiran.ru/eng/dbs.html>). Database has been compiled from a number of sources, such as measurements by ground-based detectors, instruments mounted on various satellites, as well as public data provided by different agencies specializing in monitoring solar, space and atmospheric weather and geomagnetism. Extensive list of sources and data repositories used to compile this database are referenced in a number of publications listed on the IZMIRAN internet site (IZMIRAN Space Weather Prediction Center, 2016).

We have decided to use IZMIRAN database as our primary source of data for Forbush decrease parameters as well as for selected variables, parameters and indices that describe associated space weather and geomagnetic

phenomena. Selection of parameters pertinent to our analysis was mostly based on previous work by other authors (i.e. Belov (2008), Lingri et al. (2016)), where they established which quantities are most relevant in these types of studies.

Chosen parameters fall into three categories (abbreviations to be used throughout the text are given in parentheses). First category are FD related parameters - Forbush decrease magnitude for 10GV rigidity primary particles (M) and Forbush decrease magnitude for 10GV rigidity primary particles corrected for magnetospheric effect using Dst index (M_M). These magnitudes are determined using global survey method (GSM). GSM combines measurements from a world-wide network of neutron monitors (NMs), takes into account different anisotropies, disturbances of atmospheric and geomagnetic origin, as well as apparatus-specific features, and produces an estimated hourly variation of CR flux outside Earth's atmosphere and magnetosphere (Belov et al., 2018). Specifically, correction for magnetospheric effect takes into account the fact that geomagnetic disturbances affect the effective cutoff threshold rigidities and effective asymptotic directions of primary particles for different NM stations (Belov et al., 2005).

Second group of parameters used from IZMIRAN database are CME and SW related parameters - the average CME velocity between the Sun and the Earth, calculated using the time of the beginning of the associated X-ray flare (V_{mean}), the average CME velocity between the Sun and the Earth, calculated using the time of the beginning of the associated CME observations (V_{meanC}) and maximal hourly solar wind speed in the event (V_{max}). Izmiran DB authors have matched detected FD events with associated CMEs using a SOHO LASCO CME catalog (Belov et al., 2014). Catalog includes a comprehensive list of CME events along with some of most relevant parameters, i.e. speeds calculated by tracking CME leading edge (as described in Yashiro et al. (2004), further sources available at https://cdaw.gsfc.nasa.gov/CME_list/catalog_description.htm).

Final group of parameters from IZMIRAN database used in this analysis are related to geomagnetic field - maximal Kp index in the event (Kp_{max} - based on data from NOAA Space Weather Prediction Center, <https://www.swpc.noaa.gov/products/planetary-k-index>), maximal 3-h Ap index in the event (Ap_{max} - defined as the mean value of the variations of the terrestrial magnetic field, derived from Kp index) and minimal Dst index in the event (Dst_{min} - calculated using data provided by World Data Center for Geomagnetism, Kyoto, <http://wdc.kugi.kyoto-u.ac.jp/dst/dir/index.html>).

2.3. Selection of FD events

Time interval used for this analysis was dictated by the period of operation of SOHO/ERNE device, which was commissioned in December 1995 (data available from June 1996) and is still operational. That coincides with the

beginning of solar cycle 23 and lasts through cycle 24, so we considered all FD events that occurred in this period, concentrating on events with magnitudes for 10 GV particles larger 4% in the analysis. There are several reasons for such magnitude cut, primary reason being that even though we often reference neutron monitor data in the analysis, CR related research in our laboratory is mainly based on muons detectors, which are generally less sensitive to FDs of smaller magnitude and GLE events. Additionally, it is known that all larger FDs (i.e. with magnitudes greater than 5%) are caused by CMEs (Belov, 2008). Since we use CME speed as a reference parameter in the analysis, introducing such cut made event selection simpler, as practically all considered FD events would have an associated CME. Finally, CME speed is less reliably determined in the case of weaker CME events (Yashiro et al., 2004).

One important step in the event selection procedure is to make sure that for each global event both proton flux increase detected by SOHO/ERNE and FD are related to the same CME. As mentioned in the introduction, detection of these separate events is not necessarily simultaneous. However, we have checked the direction of CMEs/ICMEs for all events for which such information was available, and in all these cases they moved directly toward Earth. This would imply that detection of the increase of energetic particles, Forbush decrease and geomagnetic storm associated with a given CME should be detectable within a relatively small time window. To illustrate this, on Fig. 1 we have shown time series for proton flux (in

one selected energy channel), CR flux and Dst index for one such event. Furthermore, because of large magnitudes of FDs selected for the analysis, we believe it to be the case for all events.

Another important point is that we cannot say with certainty what is the exact origin of detected proton flux solely based on SOHO/ERNE data. They could be of solar origin (SEP), particles accelerated locally at shock in interplanetary space (ESP), or combination of both. For the sake of simplicity we have decided to use the somewhat more general term SEP for these energetic particles, having mentioned limitation of its use in mind.

As determination of SEP fluence is not a straightforward procedure (as explained in more detail in Section 3.1), from the initial set of events we discarded all for which fluence value was difficult to determine or had a large uncertainty due to overlap and unclear separation of proton flux time series of successive events. That set was then further reduced based on the quality of FD identification flag assigned to each event in the IZMIRAN database, taking into account only events where identification was confident or reliable enough. Applying mentioned selection criteria resulted in the final set of 21 events, presented in Table 1 with some of the parameters of interest.

3. Parametrization of SEP fluence energy spectra

Parametrization procedure for any of the selected FD events can be broken down into two steps: 1 - calculation

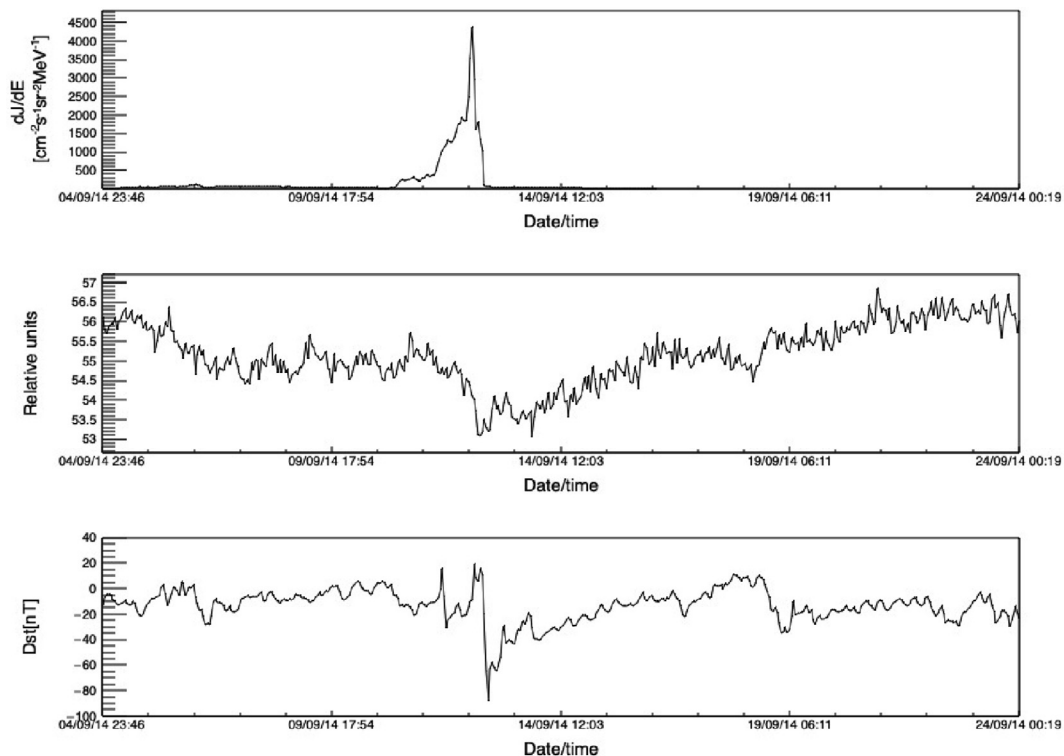


Fig. 1. Time series of hourly data for the same time interval around FD event of 12 September 2014: proton flux in the 1.3 – 1.6 MeV channel (top), Athens neutron monitor count rate (middle), and Dst index (bottom).

Table 1

Forbush decrease events from solar cycles 23 and 24 selected for the analysis, along with some of the FD, CME and geomagnetic field parameters of interest.

Date/Time	M [%]	M_M [%]	X flare	V_{mean} [km s ⁻¹]	V_{meanC} [km s ⁻¹]	V_{max} [km s ⁻¹]	Kp_{max}	Ap_{max}	Dst_{min} [nT]
2001.09.29 09:40:00	4.3	4.4	M 1.0/	852.0	831	694.0	5.33	56.0	-56.0
2001.10.11 17:01:00	7.0	6.9	M 1.4/2F	766.0	769	572.0	6.0	80.0	-71.0
2001.10.21 16:48:00	5.4	7.3	X 1.6/2B	855.0	858	677.0	7.67	179.0	-187.0
2001.11.24 05:56:00	9.2	9.8	M 9.9/	1323.0	1366	1024.0	8.33	236.0	-221.0
2002.04.17 11:07:00	6.2	7.0	M 1.2/SF	742.0	745	611.0	7.33	154.0	-127.0
2002.09.07 16:36:00	4.6	5.1	C 5.2/SF	860.0	863	550.0	7.33	154.0	-181.0
2003.10.30 16:19:00	14.3	9.4	X10.0/2B	2109.0	2140	1876.0	9.0	400.0	-383.0
2003.11.20 08:03:00	4.7	6.8	M 3.2/2N	854.0	872	703.0	8.67	300.0	-422.0
2004.07.26 22:49:00	13.5	14.4	M 1.1/1F	1279.0	1290	1053.0	8.67	300.0	-197.0
2004.09.13 20:03:00	5.0	5.3	M 4.8/SX	945.0	948	613.0	5.33	56.0	-50.0
2005.05.15 02:38:00	9.5	12.2	M 8.0/SX	1207.0	1231	987.0	8.33	236.0	-263.0
2006.12.14 14:14:00	8.6	9.6	X3.4/4B	1154.0	1165	955.0	8.33	236.0	-146.0
2011.02.18 01:30:00	5.2	4.7	X2.2/	579.0	579	691.0	5.0	48.0	-30.0
2011.08.05 17:51:00	4.3	4.8	M 9.3/	1089.0	1104	611.0	7.67	179.0	-115.0
2011.10.24 18:31:00	4.9	6.5	-	-	633	516.0	7.33	154.0	-147.0
2012.03.08 11:03:00	11.7	11.2	X5.4/	1187.0	1188	737.0	8.0	207.0	-143.0
2012.07.14 18:09:00	6.4	7.6	X 1.4/	822.0	834	667.0	7.0	132.0	-127.0
2013.06.23 04:26:00	5.9	5.3	M 2.9/	832.0	844	697.0	4.33	32.0	-49.0
2014.09.12 15:53:00	8.5	5.9	X1.6/2B	893.0	897	730.0	6.33	94.0	-75.0
2015.06.22 18:33:00	8.4	9.1	M2.6/	1027.0	1040	742.0	8.33	236.0	-204.0
2017.09.07 23:00:00	6.9	7.7	X9.3/	-	1190	817.0	8.33	236.0	-124.0

of SEP fluence in different energy channels and 2 - determination of power exponents for SEP fluence spectra.

3.1. SEP fluence calculation

SEP fluence is calculated by integrating SOHO/ERNE proton flux time series in separate energy channels over time period associated with a given FD event. First step in this procedure is to determine this time period (and hence integration boundaries) as precisely as possible. Most more energetic events we considered for this analysis have a strong SF associated with them. This may lead to a complex picture, as FD event of interest often occurs in the middle of a turbulent period where additional FDs (sometimes associated with other CMEs) precede or follow it. As a consequence, clear separation of successive events and determination of optimal integration boundaries may not be simple nor straightforward. To make this procedure more reliable, we have used IZMIRAN database and neutron monitor data (courtesy of the Neutron Monitor Database ([Neutron Monitor Database, 2022](#))) in parallel with SOHO/ERNE proton time series, trying to identify prominent features in all three sources, so we could separate events of interest in all energy channels as clearly as possible.

Baseline for integration was determined based on a data interval of at least one (but preferably several) days, where proton flux was negligibly different from zero relative to the flux during the event. If possible, time interval before the event was taken for the calculation of baseline unless there was a preceding disturbance, in which case quiet interval following the event was taken instead. Integration of fluence for several selected SOHO/ERNE energy channels

for the event of 12 September 2014 is shown on [Fig. 2](#). Integration interval is indicated with vertical dashed lines and baseline value with a horizontal dashed line.

One interesting feature that can be observed in SOHO/ERNE data time series is that in some cases proton flux in the highest energy channels can dip below the baseline after the initial increase. For a number of events such behavior is even more pronounced, where in extreme cases it can happen that no flux increase is observed, but rather just the decrease. We believe this indicates that the highest energy channels have non-negligible contribution of low-energy cosmic rays, which can increase uncertainty for fluence calculation. We will refer to this again when discussing fluence spectra in [Section 3.2](#).

To make fluence calculation procedure more reliable we have assigned a quality flag to each event, based on our estimate of the uncertainty of integration, and decided on a quality cut we deemed acceptable for further analysis. As mentioned in [Section 2.3](#), 21 events have passed this criterion. Even then, for a number of events calculated fluence proved to be sensitive to small variations of integration boundaries, which makes it especially difficult to give a reliable estimate of the error for the integration procedure and should be kept in mind when discussing the results.

3.2. Determination of SEP fluence spectra power exponents

Fluence energy spectra for all selected events were formed using values for different energy channels, calculated as explained in the previous section. The choice of parameters to be used to describe their shape and characteristics depends on the analytic expression used to model

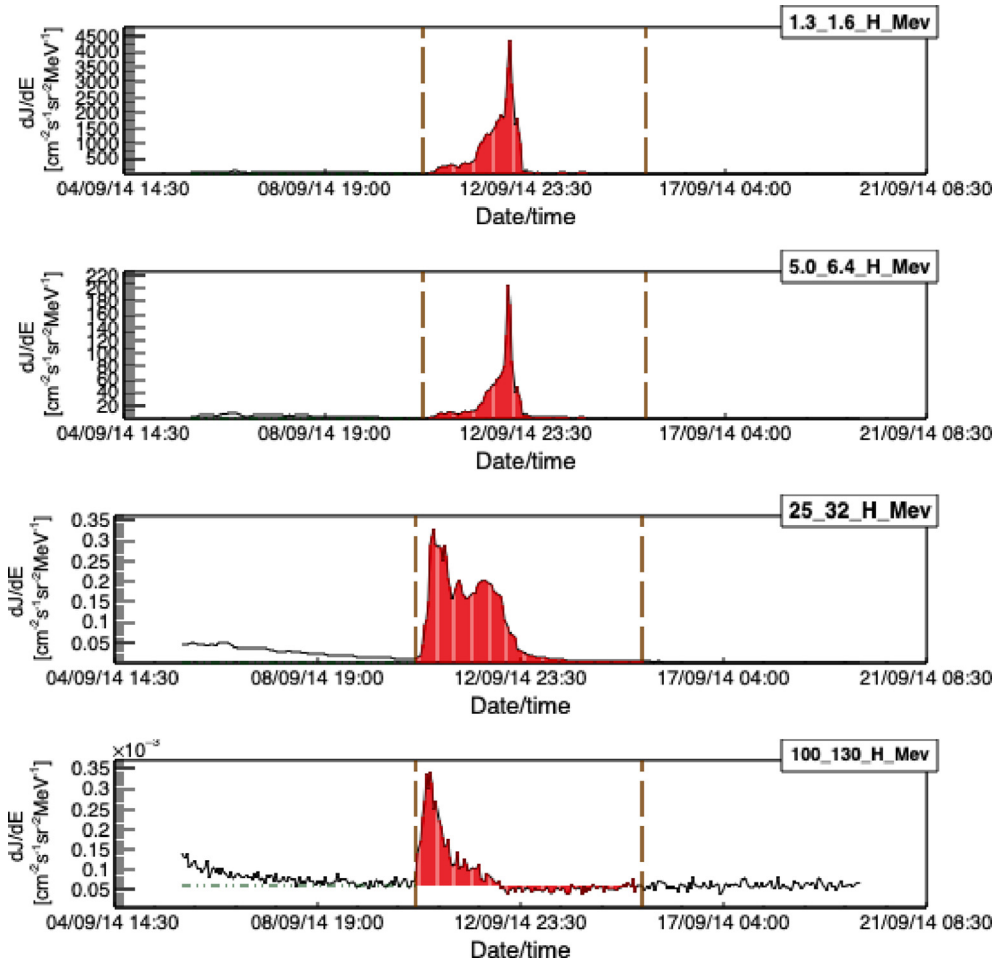


Fig. 2. Solar proton flux for four selected energy channels during FD event of 12 September 2014. Vertical dashed lines indicate integration interval, horizontal dashed line indicates the baseline value, while areas shaded red correspond to result of the integration used to calculate the SEP fluence.

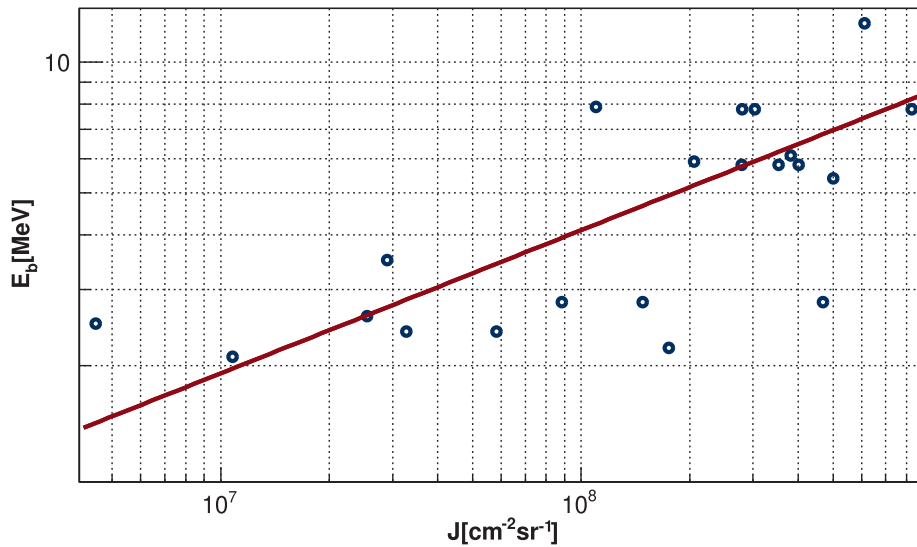


Fig. 3. “Knee” energy dependence on SEP fluence (integrated over full energy range) for selected events. Power function fit is indicated by the red line.

the spectrum. In general, during a SEP event spectra exhibit a characteristic “bend” or a “knee”, which is not so straightforward to describe theoretically. Various expressions were proposed to model this observed feature (Ellison and Ramaty, 1985; Mottl et al., 2001), out of which we have decided to use the following double power law one (Band et al., 1993; Zhao et al., 2016), as we feel it is well suited for our analysis:

$$\frac{dJ}{dE} = \begin{cases} E^{-\alpha} \exp\left(-\frac{E}{E_b}\right) & E \leq (\beta - \alpha)E_b, \\ E^{-\beta} [(\beta - \alpha)E_b]^{\beta - \alpha} \exp(\alpha - \beta) & E > (\beta - \alpha)E_b, \end{cases} \quad (1)$$

where E_b is knee energy at which the break occurs, while α and β are power-law exponents that describe energy ranges below and above the break respectively, and consequently are variables we chose to parametrize the SEP event.

These power-law exponents obtained by fitting fluence spectra with Expression 1 can be very sensitive to variation of knee energy, so some care needs to be taken in order to determine E_b as accurately as possible.

Determination of knee energy using “by eye” method proved to be uncertain enough for us to decide on using a more quantitative approach, which is based on the fact that knee energy generally depends on the integral fluence of the event (as described in Nymmik (2013) and Miroshnichenko and Nymmik (2014)). In accordance with this, we firstly determined the knee energy “by eye”, plotted it against integral fluence and then fitted this dependence with a power function in the form of $E_b = aJ^b$ (Fig. 3), where E_b is the knee energy, J integral fluence, and a and b are fit parameters. We then used these fit parameters to determine E_b for each event. In several cases where there has been some overlap of proton flux time series profiles associated with different successive events, small correction for integral fluence was introduced, which also affected the knee energy value.

Fluence spectra were then fitted with expression given in Eq. 1, using thusly calculated knee energy. On Fig. 4 we can see two characteristic examples that illustrate how well this expression actually models the fluence spectrum during a SEP event. In case of 11 October 2001 event (Fig. 4a) we see that the theoretical model fits the experimental data reasonably well, except for some small disagreement in the highest energy channels (feature we believe can be explained by our assumption that there is a non-negligible contribution of low-energy CR in this energy range). On the other hand, for a number of events with greater SEP flux higher energy channels tend to get saturated (as mentioned in Section 2.1). This in turn leads to an underestimated fluence and consequently poorer fit in this energy range, as can be seen for the 24 November 2001 event shown on Fig. 4b. Contribution of flux in these high-energy channels to integral fluence is very small, so this underestimated value does not significantly affect the value of knee energy or uncertainty of the exponent α . However,

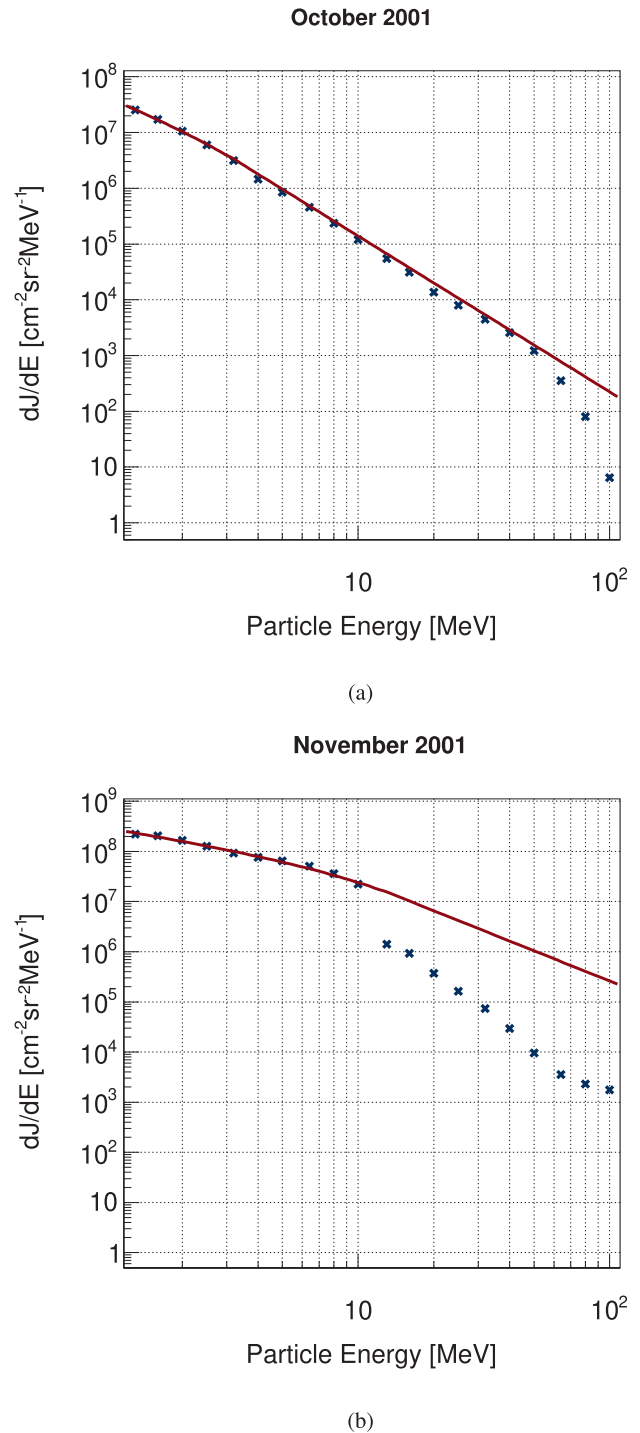


Fig. 4. SEP fluence energy spectra for the: (a) 11 October 2001 event, (b) 24 November 2001 event. Red lines indicate the double power law fit.

the uncertainty of exponent β is more significantly affected and for this reason in further analysis we will rely on exponent α more for the parametrization of fluence spectra.

4. Correlative analysis

We have performed correlative analysis between power exponents chosen to parametrize SEP fluence and selected

Table 2

Correlation coefficients (r) between SEP fluence spectra power exponents and selected FD, CME and geomagnetic field indices.

	α	β	M	M_M	V_{meanC}	V_{mean}	V_{max}	Kp_{max}	Ap_{max}	Dst_{min}
α	1.00	0.96	0.67	0.64	0.77	0.75	0.66	0.40	0.53	-0.40
β	0.96	1.00	0.67	0.67	0.72	0.70	0.60	0.44	0.50	-0.38
M	0.67	0.67	1.00	0.84	0.79	0.79	0.79	0.53	0.65	-0.41
M_M	0.64	0.67	0.84	1.00	0.57	0.57	0.53	0.69	0.69	-0.46
V_{meanC}	0.77	0.72	0.79	0.57	1.00	1.00	0.92	0.61	0.77	-0.58
V_{mean}	0.75	0.70	0.79	0.57	1.00	1.00	0.92	0.62	0.78	-0.60
V_{max}	0.66	0.60	0.79	0.53	0.92	0.92	1.00	0.49	0.71	-0.58
Kp_{max}	0.40	0.44	0.53	0.69	0.61	0.62	0.49	1.00	0.94	-0.78
Ap_{max}	0.53	0.50	0.65	0.69	0.77	0.78	0.71	0.94	1.00	-0.87
Dst_{min}	-0.40	-0.38	-0.41	-0.46	-0.58	-0.60	-0.58	-0.78	-0.87	1.00

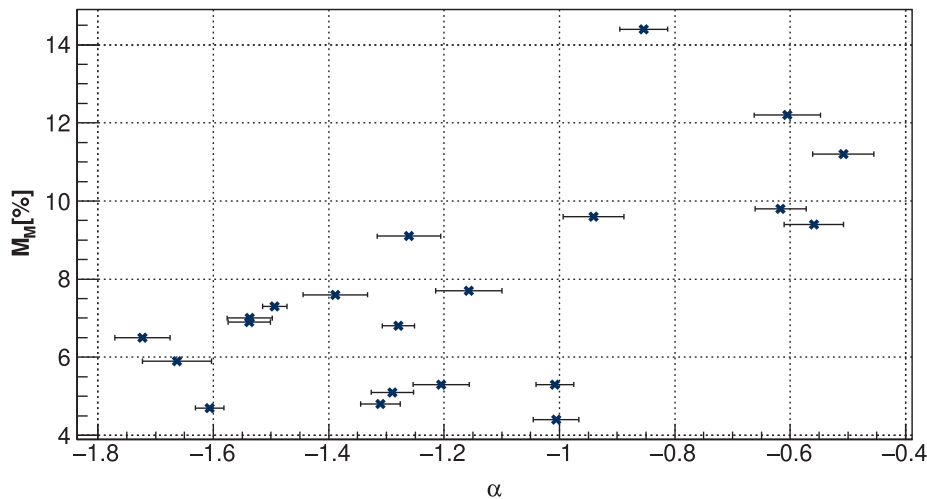


Fig. 5. Dependence of FD magnitude for particles with 10GV rigidity corrected for magnetospheric effects (M_M) on power exponent α .

parameters from Izmiran database. The results are presented in Table 2. Worth noting is the slightly lower statistics for V_{mean} due to exclusion of two events for which this parameter was not available.

Strong correlation between FD magnitude for particles with 10GV rigidity (M) and mean CME (V_{meanC} , V_{mean}) and maximum SW (V_{max}) velocities illustrates the important role these parameters have in driving FD events, as has been discussed in detail by several authors (i.e. Belov et al. (2014)). On the other hand, correlation between these velocities and parameter M_M is noticeably smaller. M_M is FD magnitude for particles with 10GV rigidity corrected for magnetospheric effect (using Dst index), so we could approximate it as an estimated measure of the FD magnitude in interplanetary magnetic field.

If we now look at how SEP fluence spectra power exponents relate to other parameters in Table 2, we observe the best correlation with mean CME velocities, while it is somewhat smaller with maximum SW velocity. Correlation with FD magnitude (M) is smaller than for CME velocities, however interestingly the correlation with the corrected FD magnitude (M_M) appears larger than in the case of CME velocities. One possible explanation for this could be that the shape of SEP fluence spectrum is more related to CR disturbance induced in interplanetary magnetic and less

to one induced in geomagnetic field. What could support this assumption further is the fact that we observe smaller correlation between α and β exponents and geomagnetic indices Kp_{max} , Ap_{max} and Dst_{min} than between these indices and CME velocities.

It should be said that even though SEP fluence spectra power exponents are not directly measured independent variables, the procedure to calculate them is relatively simple, while procedure used to calculate FD magnitudes (using GSM approach) is somewhat less straightforward and accessible. Hence, these exponents could be used to give a first estimate of Forbush decrease magnitudes outside atmosphere and magnetosphere. Having this in mind, we could conclude that SEP fluence power exponents could be better predictor variables (in the sense described above) of FD magnitude in interplanetary space than CME velocities are, while they are less reliable predictor variables of FD magnitude observed at Earth. If true, this could possibly lead us a small step closer to empirically decoupling the effects of IMF and geomagnetic fields on CR.

To further examine how FD magnitude corrected for magnetospheric effects is related to the shape of SEP fluence spectra, we have analyzed their dependence, which is plotted on Fig. 5. Both power exponents exhibit similar dependence, but only plot for α is shown, as it has consid-

Table 3

Correlation coefficients (r) between FD magnitudes for particles with 10GV rigidity (uncorrected M and corrected for magnetospheric effect M_M) and SEP fluence spectra power exponents, selected FD, CME and geomagnetic field indices for particles with $M_M \geq 6\%$ (left) and particles with $M_M < 6\%$ (right).

	$M_M \geq 6\%$					$M_M < 6\%$				
	α	β	V_{meanC}	V_{mean}	V_{max}	α	β	V_{meanC}	V_{mean}	V_{max}
M	0.82	0.76	0.84	0.85	0.78	-0.55	-0.25	-0.08	-0.10	0.62
M_M	0.77	0.76	0.52	0.49	0.55	-0.38	0.01	0.23	0.19	0.17

erably smaller uncertainty (as mentioned in Section 3.2) and we believe it to be a more reliable parameter. We can see that the graph is fairly linear, as could be expected based on the correlation coefficients, but on closer inspection it appears as if there are two separate classes of events with somewhat different behavior. If we loosely divide all FD events into low-magnitude set (with M_M less than 6%) and high-magnitude set (with M_M greater or equal to 6%), we can observe much weaker dependence of corrected FD magnitude on power exponent α for the first class than for the second one.

To check if this observation is well founded, we look into the correlation coefficients for these two separate classes, which are shown in Table 3.

We can see that correlation coefficients for these two sets are indeed very different. While in case of FDs with M_M equal or greater than 6% we observe an even larger correlation than before between power exponents α and β and both FD magnitude and corrected FD magnitude (approaching the values of correlation coefficients for CME velocities), coefficients for FDs with M_M less than 6% have very different values, correlation even being negative. Although statistics for this second set of events is rather small (and hence the uncertainty for correlation coefficients might be large), it appears that the assumption about two classes of events does stand. What is more, we observe a similarly drastic difference in correlation coefficients between FD magnitudes and mean CME velocities (with little to none correlation for events with $M_M < 6\%$), also pointing to the existence of two separate classes of events. This could need to be further confirmed using larger statistics, i.e. by including FD events with magnitudes smaller than 4%.

5. Conclusions

We analyzed the connection between CME, SEP and FD events, investigating how the shape of SEP fluence spectra during the global disturbance relates to different CME and FD parameters typically used in such analysis. We fitted SEP fluence spectra with double power law and used power exponents (α and β) from these fits to parameterize the shape of SEP fluence spectra.

By the means of correlative analysis we investigated the connection between SEP fluence spectra power exponents and selected CME and SW parameters (mean CME and maximum SW velocities), as well as selected FD parameters (magnitude for 10GV particles and magnitude for

10GV particles corrected for magnetospheric effect) and various parameters of geomagnetic activity (Kp , Ap and Dst indices).

We observed largest correlation between power exponents and CME velocities. The correlation between power exponents and FD magnitude (M) is significant yet smaller than in case of mean CME velocities (V_{meanC} , V_{mean}) and FD magnitude. On the other hand, the correlation between FD magnitude corrected for magnetospheric effects (M_M) and power exponents is larger than between these magnitudes and mean CME velocities.

The dependence of corrected FD magnitude on power exponent α possibly indicates two separate classes of events in terms of corrected magnitude value, rough boundary being corrected FD magnitude value of 6%. Events with corrected FD magnitude larger than 6% show increased correlation with power exponent α , while for the set of events with this magnitude smaller than 6% correlation even has opposite sign. Similarly considerable difference between two classes of events can be observed in correlations of mean CME velocities and corrected FD magnitude. Even taking into account smaller number of events used in the analysis, this could be an indication of these two groups of events exhibiting different behavior.

With everything considered, we believe we have demonstrated an important connection of the shape of SEP fluence spectra with CME and FD events, and that power exponents α and β can be valuable new parameters to be used in the future study of mentioned phenomena. They seem to be better predictor variables of FD magnitude (and hence CR disturbance) in interplanetary magnetic field than CME velocities, especially in the case of events where FD magnitude corrected for magnetospheric effect is larger than 6%.

Declaration of Competing Interest

The authors declare that they have no known competing financial interests or personal relationships that could have appeared to influence the work reported in this paper.

Acknowledgments

The authors acknowledge funding provided by the Institute of Physics Belgrade, through the grant by the Ministry of Education, Science and Technological Development of the Republic of Serbia.

OMNI data was made available by NASA/GSFC's Space Physics Data Facility's OMNIWeb service. Data from the SOHO experiment, an international collaboration between ESA and NASA, was kindly provided by ERNE team from Turku University, Finland. Neutron monitor data is available online through the use of excellent NEST tool, provided by the Neutron Monitor Database. We would also like to express our gratitude to the cosmic ray group at the IZMIRAN Space Weather Prediction Center at Pushkov Institute of Terrestrial Magnetism, Ionosphere and Radio Wave Propagation of the Russian Academy of Sciences for kindly providing catalogue of Forbush-effects and interplanetary disturbances.

Finally, we would like to thank the Reviewers for constructive comments and useful suggestions that significantly contributed to the quality of the manuscript.

References

- Alhassan, J.A., Okike, O., Chukwude, A.E., 2021. Testing the effect of solar wind parameters and geomagnetic storm indices on galactic cosmic ray flux variation with automatically-selected forbush decreases. *Res. Astron. Astrophys.* 21 (9), 234. <https://doi.org/10.1088/1674-4527/21/9/234>.
- Anastasiadis, A., Lario, D., Papaioannou, A., et al., 2019. Solar energetic particles in the inner heliosphere: status and open questions. *Philosoph. Trans. Roy. Soc. A: Mathe. Phys. Eng. Sci.* 377 (2148), 20180100. <https://doi.org/10.1098/rsta.2018.0100>, URL: <https://royalsocietypublishing.org/doi/abs/10.1098/rsta.2018.0100>.
- Badruddin, B., Aslam, O.P. M., Derouich, M. et al., 2019. Forbush decreases and geomagnetic storms during a highly disturbed solar and interplanetary period, 4–10 september 2017. *Space Weather*, 17(3), 487–496. URL: <https://agupubs.onlinelibrary.wiley.com/doi/abs/10.1029/2018SW001941>. <https://doi.org/10.1029/2018SW001941>.
- Band, D., Matteson, J., Ford, L., et al., 1993. BATSE Observations of Gamma-Ray Burst Spectra. I. Spectral Diversity. *Astrophys. J.* 413, 281–292. <https://doi.org/10.1086/172995>.
- Belov, A., 2008. Forbush effects and their connection with solar, interplanetary and geomagnetic phenomena. *Proc. Int. Astron. Union* 4 (S257), 439–450. <https://doi.org/10.1017/S1743921309029676>.
- Belov, A., Abunin, A., Abunina, M., et al., 2014. Coronal mass ejections and non-recurrent forbush decreases. *Sol. Phys.* 289, 3949–3960. <https://doi.org/10.1007/s11207-014-0534-6>.
- Belov, A., Baisultanova, L., Eroshenko, E., et al., 2005. Magnetospheric effects in cosmic rays during the unique magnetic storm on november 2003. *J. Geophys. Res.: Space Phys.* 110 (A09S20). <https://doi.org/10.1029/2005JA011067>.
- Belov, A., Eroshenko, E., Oleneva, V., et al., 2000. What determines the magnitude of forbush decreases? *Adv. Space Res.* 27 (3), 625–630. [https://doi.org/10.1016/S0273-1177\(01\)00095-3](https://doi.org/10.1016/S0273-1177(01)00095-3), URL: <https://www.sciencedirect.com/science/article/pii/S0273117701000953>.
- Belov, A., Eroshenko, E., Yanke, V., et al., 2018. The Global Survey Method Applied to Ground-level Cosmic Ray Measurements. *Sol. Phys.* 293 (4), 68. <https://doi.org/10.1007/s11207-018-1277-6>.
- Belov, A., Papaioannou, A., Abunina, M., et al., 2021. On the rigidity spectrum of cosmic-ray variations within propagating interplanetary disturbances: Neutron monitor and SOHO/EPHIN observations at ~1–10 GV. *Astrophys. J.* 908 (1), 5. <https://doi.org/10.3847/1538-4357/abd724>.
- Bruno, A., Richardson, I.G., 2021. Empirical model of 10–130 mev solar energetic particle spectra at 1 au based on coronal mass ejection speed and direction. *Sol. Phys.* 296 (36). <https://doi.org/10.1007/s11207-021-01779-4>.
- Cane, H., 2000. Coronal mass ejections and forbush decreases. *Space Sci. Rev.* 93 (1), 55–77. <https://doi.org/10.1023/A:1026532125747>.
- Desai, M., Giacalone, J., 2016. Large gradual solar energetic particle events. *Living Rev. Sol. Phys.* 13 (3). <https://doi.org/10.1007/s41116-016-0002-5>.
- Dumbovic, M., Vršnak, B., Calogovic, J., et al., 2012. Cosmic ray modulation by different types of solar wind disturbances. *A&A* 538, A28. <https://doi.org/10.1051/0004-6361/201117710>.
- Dumbovic, M., Vršnak, B., Guo, J., et al., 2020. Evolution of coronal mass ejections and the corresponding forbush decreases: Modeling vs. multi-spacecraft observations. *Sol. Phys.* 295 (104). <https://doi.org/10.1007/s11207-020-01671-7>.
- Ellison, D.C., Ramaty, R., 1985. Shock acceleration of electrons and ions in solar flares. *Astrophys. J.* 298, 400–408. <https://doi.org/10.1086/163623>.
- Freiherr von Forstner, J.L., Guo, J., Wimmer-Schweingruber, R.F., et al., 2020. Comparing the properties of icme-induced forbush decreases at earth and mars. *J. Geophys. Res.: Space Phys.* 125(3), e2019JA027662. URL: <https://agupubs.onlinelibrary.wiley.com/doi/abs/10.1029/2019JA027662>. <https://doi.org/10.1029/2019JA027662>. E2019JA027662 10.1029/2019JA027662.
- Gopalswamy, N., 2016. History and development of coronal mass ejections as a key player in solar terrestrial relationship. *Geosci. Lett.* 3 (8), 18. <https://doi.org/10.1186/s40562-016-0039-2>.
- Heber, B., Fichtner, H., Scherer, K., 2006. Solar and heliospheric modulation of galactic cosmic rays. *Space Sci. Rev.* 125 (1), 81–91. <https://doi.org/10.1007/s11214-006-9048-3>.
- IZMIRAN Space Weather Prediction Center, 2016. Izmiran space weather prediction center. URL: <http://spaceweather.izmiran.ru/eng/about.html> [Online; accessed 29-January-2022].
- Koldobskiy, S.A., Bindi, V., Corti, C., et al., 2019. Validation of the neutron monitor yield function using data from ams-02 experiment, 2011–2017. *J. Geophys. Res.: Space Phys.* 124 (4), 2367–2379. <https://doi.org/10.1029/2018JA026340>, URL: <https://agupubs.onlinelibrary.wiley.com/doi/abs/10.1029/2018JA026340>.
- Koldobskiy, S., Raukunen, O., Vainio, R., et al., 2021. New reconstruction of event-integrated spectra (spectral fluences) for major solar energetic particle events. *Astron. Astrophys.* 647, A132. <https://doi.org/10.1051/0004-6361/202040058>.
- Lingri, D., Mavromichalaki, H., Belov, A., et al., 2016. Solar activity parameters and associated forbush decreases during the minimum between cycles 23 and 24 and the ascending phase of cycle 24. *Sol. Phys.* 291, 1025–1041. <https://doi.org/10.1007/s11207-016-0863-8>.
- Melkumyan, A., Belov, A., Abunina, M., et al., 2019. On recurrent Forbush Decreases. In: Lagutin, A., Moskalenko, I., Panasyuk, M. (Eds.), *Journal of Physics Conference Series*, IOP Publishing, Bristol, United Kingdom volume 1181 of *Journal of Physics Conference Series*. p. 012009, <https://doi.org/10.1088/1742-6596/1181/1/012009>.
- de Mendonça, R.R. S., Braga, C.R., Echer, E., et al., 2016. The temperature effect in secondary cosmic rays (Muons) observed at the ground: analysis of the global muon detector network data. *Astrophys. J.* 830(2), 88. <https://doi.org/10.3847/0004-637x/830/2/88>.
- Miroshnichenko, L., Nymmik, R., 2014. Extreme fluxes in solar energetic particle events: Methodological and physical limitations. *Radiation Measur.* 61, 6–15. <https://doi.org/10.1016/j.radmeas.2013.11.010>, URL: <https://www.sciencedirect.com/science/article/pii/S1350448713003806>.
- Miteva, R., Samwel, S.W., Zabunov, S., et al., 2020. On the flux saturation of SOHO/ERNE proton events. *Bulgarian Astron. J.* 33, 99.
- Mottl, D.A., Nymmik, R. A., Sladkova, A.I., 2001. Energy spectra of high-energy SEP event protons derived from statistical analysis of experimental data on a large set of events. In: El-Genk, M.S., Bragg, M.J. (Eds.), *Space Technology and Applications International Forum - 2001*, AIP Publishing LLC., New York volume 552 of *American Institute of Physics Conference Series*, pp. 1191–1196, <https://doi.org/10.1063/1.1358071>.

- Neutron Monitor Database, 2022. Neutron Monitor Database. URL: <https://www.nmdb.eu/>.
- Nymmik, R., 2013. Charge states of heavy ions, as determined from the parameters of solar energetic particle spectra. *Bull. Russian Acad. Sci.: Phys.* 77, 490–492. <https://doi.org/10.3103/S1062873813050419>.
- Paassilta, Miiikka, Raukunen, Osku, Vainio, Rami, et al., 2017. Catalogue of 55–80 mev solar proton events extending through solar cycles 23 and 24. *J. Space Weather Space Clim.* 7, A14. <https://doi.org/10.1051/swsc/2017013>.
- Papaioannou, A., Belov, A., Abunina, M., et al., 2020. Interplanetary coronal mass ejections as the driver of non-recurrent forrush decreases. *Astrophys. J.* 890 (2), 101. <https://doi.org/10.3847/1538-4357/ab6bd1>.
- Reames, D.V., 1999. Particle acceleration at the sun and in the heliosphere. *Space Sci. Rev.* 90 (3), 413–491. <https://doi.org/10.1023/A:1005105831781>.
- Richardson, I.G., Cane, H.V., 2011. Galactic Cosmic Ray Intensity Response to Interplanetary Coronal Mass Ejections/Magnetic Clouds in 1995–2009. *Sol. Phys.* 270 (2), 609–627. <https://doi.org/10.1007/s11207-011-9774-x>.
- Subramanian, P., Antia, H.M., Dugad, S.R., et al., 2009. Forrush decreases and turbulence levels at coronal mass ejection fronts. *A&A* 494 (3), 1107–1118. <https://doi.org/10.1051/0004-6361:200809551>.
- Torsti, J., Valtonen, E., Lumme, M., et al., 1995. Energetic particle experiment erne. *Sol. Phys.* 162 (1–2), 505–531. <https://doi.org/10.1007/BF00733438>.
- Valtonen, E., Lehtinen, I.-V., 2009. Solar energetic particle fluences from soho/erne. *Acta Geophys.* 57, 116–124. <https://doi.org/10.2478/s11600-008-0056-4>.
- Veselinovic, N., Dragic, A., Savić, M., et al., 2017. An underground laboratory as a facility for studies of cosmic-ray solar modulation. *Nucl. Instrum. Methods Phys. Res. Section A: Accelerat. Spectromet. Detectors Assoc. Equip.* 875, 10–15. URL: <https://www.sciencedirect.com/science/article/pii/S0168900217309634>. <https://doi.org/10.1016/j.nima.2017.09.008>.
- Veselinovic, Nikola, Savić, Mihailo, Dragic, Aleksandar, et al., 2021. Correlation analysis of solar energetic particles and secondary cosmic ray flux. *Eur. Phys. J. D* 75 (6), 173. <https://doi.org/10.1140/epjd/s10053-021-00172-x>.
- Veselinović, N., Dragić, A., Maletić, D., et al., 2015. Cosmic rays muon flux measurements at Belgrade shallow underground laboratory. In: Trache, L., Chesneanu, D., Alexandru Ur, C. (Eds.), *Exotic Nuclei and Nuclear/Particle Astrophysics (V) From Nuclei to Stars: Carpathian Summer School of Physics 2014*, AIP Publishing LLC., New York volume 1645 of American Institute of Physics Conference Series, pp. 421–425. <https://doi.org/10.1063/1.4909614>.
- Yashiro, S., Gopalswamy, N., Michalek, G., et al., 2004. A catalog of white light coronal mass ejections observed by the soho spacecraft. *J. Geophys. Res.: Space Phys.* 109 (A7). <https://doi.org/10.1029/2003JA010282>.
- Zhao, L., Zhang, M., Rassoul, H.K., 2016. Double power laws in the event-integrated solar energetic particle spectrum. *Astrophys. J.* 821 (1), 62. <https://doi.org/10.3847/0004-637x/821/1/62>.



Article

Impacts of Extreme Space Weather Events on September 6th, 2017 on Ionosphere and Primary Cosmic Rays

Aleksandra Kolarski , Nikola Veselinović , Vladimir A. Srećković , Zoran Mijić * , Mihailo Savić
and Aleksandar Dragić

Institute of Physics Belgrade, University of Belgrade, Pregrevica 118, 11080 Belgrade, Serbia

* Correspondence: zoran.mijic@ipb.ac.rs; Tel.: +381-11-3713134

Abstract: The strongest X-class solar flare (SF) event in 24th solar cycle, X9.3, occurred on 6 September 2017, accompanied by earthward-directed coronal mass ejections (CMEs). Such space weather episodes are known to cause various threats to human activities ranging from radio communication and navigation disturbances including wave blackout to producing geomagnetic storms of different intensities. In this study, SFs' ionospheric impacts and effects of accompanied heliospheric disturbances on primary cosmic rays (CR) are investigated. This work offers the first detailed investigation of characteristics of these extreme events since they were inspected both from the perspective of their electromagnetic nature, through very low frequency (VLF) radio waves, and their corpuscular nature of CR by multi-instrumental approach. Aside data recorded by Belgrade VLF and CR stations, data from GOES and SOHO space probes were used for modeling and analysis. Conducted numerical simulations revealed a significant change of ionospheric parameters (sharpness and effective reflection height) and few orders of magnitude increase of electron density. We compared our findings with those existing in the literature regarding the ionospheric response and corresponding parameters. In addition, Forbush decrease (FD) magnitude, corrected for magnetospheric effect, derived from measurements, and one predicted from power exponents used to parametrize the shape of energetic proton fluence spectra at L1 were compared and found to be in good agreement. Presented findings could be useful for investigation of atmospheric plasma properties, particles' modeling, and prediction of extreme weather impacts on human activities.

Keywords: solar flares; coronal mass ejections; atmospheric ionization; sudden ionospheric disturbances; ionospheric parameters; solar energetic particles; secondary cosmic ray flux; Forbush decreases



Citation: Kolarski, A.; Veselinović, N.; Srećković, V.A.; Mijić, Z.; Savić, M.; Dragić, A. Impacts of Extreme Space Weather Events on September 6th, 2017 on Ionosphere and Primary Cosmic Rays. *Remote Sens.* **2023**, *15*, 1403. <https://doi.org/10.3390/rs15051403>

Academic Editors: Dario Sabbagh and Saioa A. Campuzano

Received: 17 January 2023

Revised: 23 February 2023

Accepted: 28 February 2023

Published: 2 March 2023



Copyright: © 2023 by the authors. Licensee MDPI, Basel, Switzerland. This article is an open access article distributed under the terms and conditions of the Creative Commons Attribution (CC BY) license (<https://creativecommons.org/licenses/by/4.0/>).

1. Introduction

As an important aspect of space weather applications, ionospheric responses to intense solar flares (SFs) and coronal mass ejections (CMEs) have been investigated for several decades [1–3]. Short in duration but huge explosive events on the Sun release high-energy particles and intense broad range radiation influencing the state of the Earth's upper atmosphere. While enhanced EUV radiation disturbs E and F regions of the ionosphere, during solar flares, X-ray radiation can increase by several orders of magnitude and cause an extra ionization within the ionospheric D-layer [4,5]. The increase in the rate of change of atmospheric ionization depends on both the flare class and the rate of change in flare radiations [6]. For the investigation of D-region behavior, radio wave measurements at very low and low frequencies (VLF-LF) are widely used [7–9]. SFs have a direct radio wave interference effect on Global Navigation Satellite System (GNSS) transmission and other radio systems [10–12]. High-frequency (HF) radio wave blackout and magnetic field variation have also been documented and studied [11,13].

Solar activity can produce extreme phenomena which are more likely around the maximum of the 11-year cycle. One such type of events are SFs that are, in most cases, followed by CMEs [14]. CME releases a large-scale flux of charged particles from solar

corona with an accompanying embedded magnetic field. This additional flux of charged particles emerging in interplanetary space is defined as interplanetary coronal mass ejection (ICME). When propagating with speed greater than magnetosonic wave speed (in solar wind reference frame), ICME can form a shock due to interaction with ambient solar wind. In situ measurements of the environment performed by space probes at different locations in the heliosphere can provide information about various solar weather parameters. They also include direct measurements of fast-moving energetic particles that can be in temporal correlation with CMEs and SFs [15]. These particles can originate from the Sun, in which case they are called solar energetic particles (SEPs) or can be accelerated locally by an ICME related shock when they are referred to as energetic storm particles (ESPs). Several space probes placed at Lagrange point 1 (L1) between the Sun and the Earth constantly monitor this flux, in addition to a number of probes at Earth's vicinity and elsewhere throughout the heliosphere [16]. Enhancement of interplanetary magnetic field (IMF) creates additional modulation of cosmic ray (CR) and can lead to one of the transient phenomena, Forbush decrease (FD). FD is a rapid depression of measured CR flux (typically occurring within a day), followed by a gradual recovery that can last for several days [17]. Correlation between FD parameters (magnitude of decrease, duration, time evolution) and various parameters of solar wind plasma have been studied in the past [18–20].

Extreme space weather events can have severe impacts on wide areas of human activities. Historically, such events are not very frequent, but the probability of their occurrence over the next decade is not negligible (i.e., for geomagnetic storms, it has been estimated to be about 12% [21]). Extreme events can cause significant damage to sensitive satellite components and increase absorbed radiation dose in space, which can pose a serious health hazard to astronauts. Energetic particle flux during extreme solar activity events is studied and different models of the space environment are proposed for forecasting schemes. Even though many studies have been carried out, still, only limited information is available on an approximate assessment of the direct impact such events can have on technological infrastructure and what the indirect associated expenses would be [22].

Study of ionospheric reaction to SFs is currently very relevant research, given the prospect of improving the capacity and reliability of anticipating space weather disturbances, which might affect the performance of a wide range of space-borne and ground-based technological systems and pose a danger to human health and safety [23,24].

The 24th solar cycle began in December 2008 and although approaching the solar minimum and the low solar activity, several strong SFs occurred in September 2017, including the X9.3 class flare, the strongest one in that cycle [25,26]. A lot of studies have been published analyzing different aspects of these extreme weather events. The SF effect on the chemical structure of the upper and middle atmosphere is reported in [27]. In the study presented in [28], the analysis of total electron content (TEC) and rate of change of TEC index to probe the storm-time ionospheric TEC irregularities in the Indian longitude sector during the space weather events of 6–10 September 2017 was presented. During the flares, the total radio fade-out in the range of 30 to 90 min at the Hermanus and Sao Luis ionosondes is reported [29]. It is also observed that SFs' effects on the ionosphere last longer than the effects on the Earth's magnetic field [30]. The effects of the strong X9.3 flare of 6 September 2017, following its impact on the ionosphere and the resulting difficulties for existing (e.g., precise positioning and GNSS navigation support services) and future technologies (e.g., autonomous car navigation) have been analyzed [10].

In this paper, X-class SFs of 6 September 2017 ionospheric impacts and the effects of accompanied heliospheric disturbances on primary cosmic rays are investigated. The atmospheric D-region parameters and electron density are obtained and analyzed along with various heliospheric parameters (associated with the accompanying ICME) measured in-situ at L1, as well as flux of secondary cosmic ray muons measured on the ground and shallow-underground levels. Since all empirical models are based upon data obtained through numerous studies, such as International Reference Ionosphere model [31], each

case study of extreme weather events is of great significance, not only for the atmospheric plasma properties investigations, but also for the particles' modeling procedures. With that goal, modulation of ionosphere and CR flux by intense X-class SF events was investigated through a multi-instrumental approach, by employing space- and ground-based observations on one hand, and by conducting proposed numerical simulations on the other hand, using both original VLF and CR measurements (from the same location in Belgrade) as well as data and results from other observing stations worldwide. Through extensive comparison, noticed agreements and disagreements between results are highlighted as well.

2. Materials and Methods

Galactic cosmic rays interact with interplanetary magnetic fields as they traverse our solar system. IMF is a solar magnetic field carried by the solar wind, a stream of charged particles propagating outward from the Sun. Interaction of CRs with IMF modulates CR flux as is also evident from measurements of CR flux intensity with Earth-based CR detectors [32]. Galactic cosmic rays, upon reaching Earth, interact with atmospheric atoms and molecule nuclei, generating a shower of secondary particles. Secondary CRs vertical flux, at the bottom of the atmosphere (at atmospheric depth 1000 g cm^{-2}), for particles' energies larger than 1 GeV, is composed mainly of muons ($\approx 90 \text{ m}^{-2} \text{ s}^{-1} \text{ sr}^{-1}$), protons and neutrons ($\approx 2 \text{ m}^{-2} \text{ s}^{-1} \text{ sr}^{-1}$), electrons and positrons ($\approx 0.2 \text{ m}^{-2} \text{ s}^{-1} \text{ sr}^{-1}$), and charged pions ($\approx 0.04 \text{ m}^{-2} \text{ s}^{-1} \text{ sr}^{-1}$) as well as neutrinos [33]. Observation of these secondary CRs can be conducted in the atmosphere, on the ground or even underground, detecting one or several different types of produced particles. A worldwide network of neutron monitors (NM) and ground detectors that detect hadronic components of secondary CRs have been in use for decades. NMs are sensitive to primary CRs with energies of about 0.5–20 GeV. Another type of widely used Earth-based CR detectors are muon monitors, focused on detecting the muon component of secondary CRs. Muon monitors are sensitive to higher energies of primary CRs, thus complementing NMs measurements [34].

Belgrade CRs station is a part of the Low-background Laboratory for Nuclear Physics (LBLNP) at the Institute of Physics Belgrade (IPB), Serbia. It has two identical detector set-ups placed on two different levels, one on ground level (GLL) and the other in shallow-underground (UL). Underground level is situated below 12 m of loess overburden (25-m water equivalent). This setup allows for monitoring of secondary CR's muons flux that originates from two different energy ranges under the same environmental conditions (such as geomagnetic location, atmospheric parameters, experimental setup). Altitude of the station is 78 m above sea level, with a geomagnetic latitude of $39^{\circ}32' \text{ N}$. Relation between the measured count rate of these energy-integrating detectors with flux of primary CRs at the top of the atmosphere was found using a calculated detector yield function. Additionally, due to the sensitivity of secondary muons to varying properties of the atmosphere, which acts as a moderator, correction of measured flux for atmospheric pressure and variation of temperature throughout the whole atmospheric column from the top of the atmosphere to the ground is needed. Details of the detector systems and response function of Belgrade CR station acquired using Monte Carlo simulation of CR transport, along with the description and results of atmospheric and efficiency corrections are presented in [35,36].

For inspection of the Earth's lower ionospheric response to intense solar activity during events of energetic solar outbursts (such as SFs and CMEs) during the descending branch of the 24th solar cycle, as in September 2017, VLF radio signal registrations from Belgrade's (BEL; 44.85° N , 20.38° E) Absolute Phase and Amplitude Logger (AbsPAL) station database were used. This system is a part of the Laboratory for Astrophysics and Physics of Ionosphere at the IPB, Serbia. Numerical simulations conducted in this paper rely on application of the well known and widely exploited technique of Long Wavelength Propagation Capability (LWPC) software [37] utilization on one hand, based on hop wave theory and the ionospheric exponential model [38,39], and on the FlarED' Method and Approximate Analytic Expression application [5,40] on the other hand: the novel approach based on retrieving ionospheric parameters directly from solar X-ray radiation spectral

components of soft range. Here, novel approach is applied on two cases of SF events within the strongest X-class (the weaker X2.2 and stronger X9.3), making the validation of the proposed approximate method firmly applicable and reliable across the entire X-class range, in addition to some previous recent research all regarding cases of weaker X-class SFs from the lower section of X-class range [5,8,40]. The methodology used relies on simultaneous monitoring of several VLF signals during regular and irregular ionospheric conditions, both for amplitude and phase, and obtaining properties of perturbations directly from observed recorded VLF data, by signal values' comparison between unperturbed and perturbed states. The details are presented in Section 3.2 and Supplementary Material.

3. Results

3.1. Solar Energetic Particles and Secondary Cosmic Ray Flux during and after Intense SF Events

The strongest flare of solar cycle 24 (classified as X9.3) happened in early September 2017 during the declining phase of this solar cycle. Active region AR12673 [41] was the cause of unusual and intensive solar activity. This region produced several more SFs around that time with the most intense one occurring on 6 September 2017. The flare was closely followed by a severe geomagnetic storm that began on 7 September. In total, four different possibly related CMEs erupted within several days. The first of these was a halo CME that happened on 4 September which, together with the second one, affected CR flux and produced an intense Forbush decrease on 7 September. Magnitude of FD for 10 GV rigidity primary CR corrected for magnetospheric effect (M_M) [18] was -7.7% (quoted from IZMIRAN database of FD parameters [42]).

Solar activity and the accompanying heliospheric disturbance during early September 2017 have been studied in detail in a number of published articles that indicate that successive CMEs between 4–6 September produced complex transients. Complex interactions caused by the passage of ICME are not so simple to model, one consequence being that it is not so straightforward to predict time of arrival of the disturbance on Earth [43]. However, in-situ measurements by space probes at L1 can help in this regard. Based on data from Solar and Heliospheric Observatory (SOHO)/Large Angle and Spectrometric Corona-graph (LASCO)/C2 [44] and analysis given in [45], the first CME from AR12673 with a moderate speed of approximately 710 km s^{-1} appeared on 4 September followed by a much faster (approx. 1350 km s^{-1}) second CME. These two CMEs merged in lower solar corona into a single structure producing single shock followed by a prolonged sheath region which was detected at L1 on 6 September. The second shock arrived at L1 on 7 September as a result of CME that occurred on 6 September. This CME had a high velocity of 1480 km s^{-1} and its eruption coincides with the X9.3 SF. This shock was followed by a turbulent sheath region and a magnetic cloud. One repository where such measurements can be found compiled in the form of low- and high-resolution OMNI data can be found at GSFC/Space Physics Data Facility [46]. Low-resolution OMNI data (used in this study) contains hourly values for various heliospheric and geomagnetic indices. One of the probes that monitors variation of energetic proton flux at L1 is the ERNE instrument onboard SOHO probe [47]. It consists of two separate particle detectors with complementing detector energy ranges (for lower and higher particle energies) and provides energetic particle flux measurements in 20 energy bins (ranging from 1.3 up to 130 MeV per nucleon) with a time resolution of one hour (data are available at [48]). Apart from providing insight into SF/CME/ICME induced disturbance in the heliosphere, measurements done by this instrument could be useful for predicting the effects that these phenomena have on cosmic rays, as some studies have shown [49]. Proton flux recorded during early September 2017 is showed in Figure 1 and Figures S1 and S2 in Supplementary Material. As it is often difficult to determine the acceleration mechanism related to violent events on the Sun (especially when accelerated particles are detected near Earth), for the sake of simplicity, going forward, we will refer to both solar energetic particles (accelerated near the Sun) and energetic storm particles (accelerated in interplanetary space) as SEP.

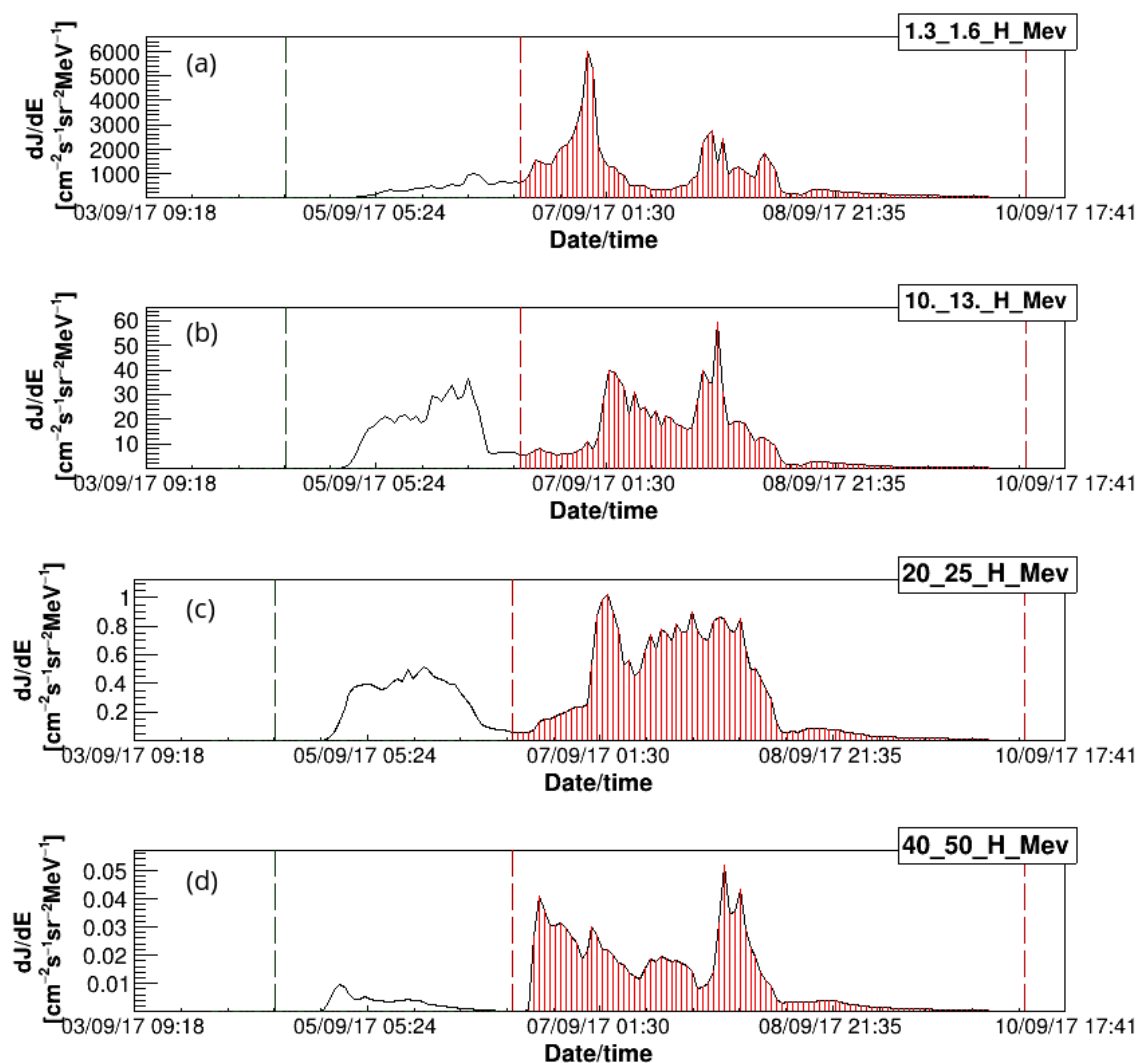


Figure 1. Hourly time series (UT) for several different proton channels from SOHO/ERNE ((a) 1.3–1.6 MeV, (b) 10–13 MeV, (c) 20–25 MeV, (d) 40–50 MeV channels' energy bands) for September 2017. Integration interval for spectral fluence is indicated with red vertical dashed lines.

In order to determine SEP fluence related to heliospheric disturbances and FD events during early September 2017, integration of SOHO/ERNE proton flux time series in separate energy channels is needed over the time period associated with a given FD event. Determination of this time period during complex solar activity in September 2017 is not simple or straightforward. Using procedures described in [36] that rely on the IZMIRAN database, as well as neutron monitor data and data measured at Belgrade muon station, we can determine optimal integration intervals more reliably.

Generally, SEP fluence spectrum exhibits a change of slope (sometimes referred to as a “knee”). Several different models are proposed to describe this characteristic shape [50–52]. We chose to use the double power law proposed in [53] given by Equation (1):

$$f(E) = \begin{cases} E^{-a} \exp\left(-\frac{E}{E_k}\right), & E < (b-a)E_k \\ E^{-b} [(b-a)E_k]^{b-a} \exp(a-b), & E > (b-a)E_k \end{cases} \quad (1)$$

where E is the particle energy, E_k is the “knee” energy (at which the break in the spectrum occurs), a and b are power exponents related to energy ranges below and above E_k , respectively. Exponents a and b are determined by fitting the proton fluence spectrum using Equation 1 and are used to parameterize its shape. E_k is set as a fixed parameter and

is determined from the known dependence of “knee” energy on integral fluence. More detailed description of the procedure can be found in [49]. The shape of fluence spectrum and fitted double power law for the September event are shown in Figure 2. Obtained values were -1.16 for exponent a and -2.5 for exponent b (taking 6.8 MeV as value for “knee” energy).

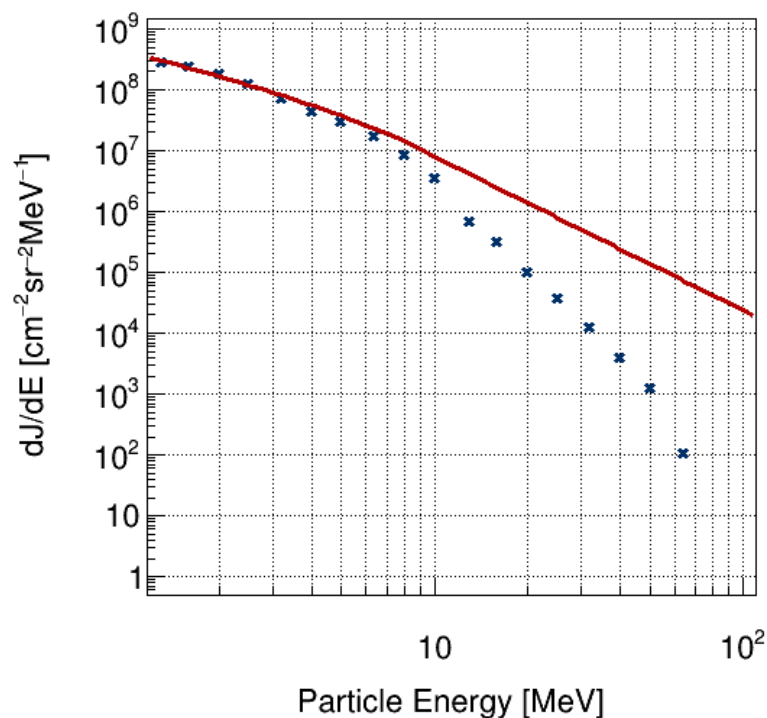


Figure 2. Fluence spectrum for energetic protons measured by SOHO/ERNE at L1 during FD in September 2017. Data points represent fluence integrated in different energy channels over time of duration of the event, while red line represents the fitted double power law.

Observed underestimate of fluence in higher energy channels can be explained by the assumption that there are contributions of low energy CR in these energy ranges that are suppressed with additional heliospheric disturbance and can be more pronounced for more extreme solar activity events. Additionally, this discrepancy between model and measured fluence can be due to saturation of high energy channels during events with greater SEP flux [54].

Contribution of these higher energy channels to integral flux is rather small and it does not significantly affect total flux, however, it does add to higher uncertainty of b , which is why this exponent is seldom used in analysis. Based on the established correlation between a exponent and FD magnitude corrected for magnetospheric effect [49], an estimated value of 8.3% was obtained for M_M , which is in reasonably good agreement with the value found in the IZMIRAN database. Large disturbances in the heliosphere in early September 2017 that cause large FD are part of a complex event that can lead to disturbance in the magnetosphere and primary CR flux variability, but also influence dynamic processes in the ionosphere.

3.2. Monitoring Low Altitude Mid-Latitude Ionosphere during intense SF events

Monitoring of the mid-latitude ionospheric D-region (50–90 km) from BEL station during September 2017 were simultaneously conducted for all VLF signals recorded by the AbsPAL system. Geographical position of BEL VLF system and the VLF transmitters (GQD/22.10 kHz, Anthorn UK and TBB/26.70 kHz, Bafa Turkey) are given in Figure S3. Both shown signals are of short great circle paths (GCPs) propagating mostly over land. In general, the GQD signal arrives to Belgrade from the north, in NW-SE direction, with

GCPGQD = 1982 km covering almost two time zones, while TBB signal arrives from the south, in SE-NW direction, with GCPTBB = 1020 km covering one time zone (Table 1). Corresponding incident solar X-ray flux data were obtained from the Geostationary Operational Environmental Satellite (GOES) database [55].

Table 1. VLF transmitting sites.

	Freq. (kHz)	Country	Latitude (°)	Longitude (°)	GCP (km)	Prop. Path Direction
Transmitter:						
GQD	22.10	UK	54.73 N	2.88 W	1982	NW to SE
TBB	26.70	Turkey	37.43 N	27.55 E	1020	SE to NW

We studied data from 6 September 2017 belonging to the descending branch of the 24th solar cycle, with the strongest SF event X9.3 reported during the last solar cycle and the earth-directed CME which produced FD. September 2017 was the most active month during 2017, with a total of 99 SFs reported, of which there were 68 C, 27 M, and four X class events. During 6 September 2017, there were seven SFs reported in total, of which there were two C, three M, and two X-class SFs. Such intense solar activity significantly affected Earth's lower ionosphere, which can be clearly observed both as amplitude and phase perturbations on sub-ionospheric propagating VLF signals and was documented on BEL AbsPAL recordings. The two strongest SFs reported on 6 September 2017, i.e., X2.2 and X9.3—overall the strongest SF from the last solar cycle, as observed on GQD and TBB signal traces, practically occurred during the established stable daytime ionospheric conditions, when both traces were entirely sunlit. BEL GQD data during the entire day of 6 September 2017, with the accompanying incident solar X-ray flux from soft spectral range (0.1–0.8 nm) are given in Figure S4. As the best representative quiet day, 3 September 2017 was chosen. As observed on GQD signal, solar-induced sudden ionospheric disturbances (SIDs) are denoted by black arrows accompanied with the time of each SF event's occurrence in UT. Both amplitude and phase perturbation follow the SF events' evolution, with time delays corresponding to the sluggishness of the ionosphere [56]. Oscillatory character of the perturbations characteristic for GQD signal registered by BEL station, can still be recognized on the signal's phase, especially in the case of the weaker SF, while in the case of the amplitude, this feature is no longer observable mostly due to inducing SF's intensity [5,7,57–59]. Although these two SF occurred back-to-back, it is possible to determine individual contributions of each SF on signal recordings. It can be stated that, although these SFs strongly impacted the Earth-ionosphere waveguide for several hours, as observed from BEL station, the mid-latitude lower ionosphere fully recovered and went back to its regular conditions. Preflare ionospheric state can be treated as quiet.

Comparison between GQD and TBB signal recordings, arriving from opposite directions to the BEL station, but both of short GCPs, is given in Figure 3, as an enlarged section related to time evolution of X2.2 and X9.3 SFs.

Amplitude change in both signals is of similar behavior, simply following the incident solar X-ray radiation, with similar relative change in the amplitude amount compared to unperturbed conditions $\Delta A \approx 7$ dB. However, in the case of the TBB signal, there is a more rapid decreasing trend after the peak value corresponding to the maximal amplitude change in both SF cases. In the case of the GQD signal, relative change in the phase amount compared to unperturbed conditions ΔPh (°) is several tens of degrees, with still recognizable oscillatory behavior characteristic for BELGQD. Unfortunately, in the case of the TBB signal, phase data were unusable so that further analysis, neither qualitative nor quantitative and neither any of the numerical simulations, were not possible to conduct. The TBB signal recordings given are purely interesting from the point of view of amplitude comparison with the GQD signal, with total opposite GCPs as recorded in Belgrade.

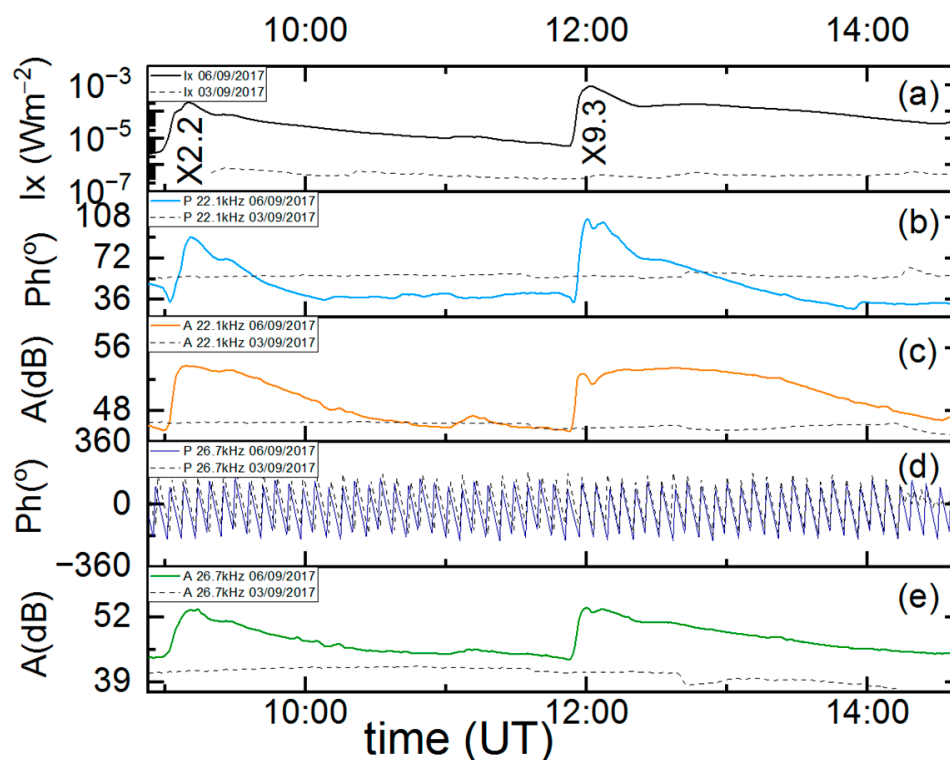


Figure 3. Simultaneous variations of X-ray flux (a) with phase delay, (b) amplitude delay, (c) variations of GQD/22.10 kHz and phase delay, (d) amplitude delay, (e) variations of TBB/26.70 kHz signals versus universal time UT during occurrence of X2.2 and X9.3 class SFs of 6 September 2017. Observed amplitude and phase perturbations with the quiet signal of 3 September 2017 (dashed black) are measured at Belgrade station. Time variation of soft X-ray irradiance is measured by GOES-15 satellite.

3.3. Analysis of Signal Propagation Parameters during Intense SF Events

SFs' occurrence time and evolution were both favorable regarding applied modeling procedures, due to stable daytime GQD waveguide conditions. This was particularly significant for application of the first of previously mentioned numerical procedures in the Methods section, i.e., application of Wait's theory through LWPC software utilization, based upon the two-component exponential model. VLF sub-ionospheric propagation simulations, depending on pair of so-called Wait's parameters β (km^{-1}) and H' (km) (representing time-dependent parameter of lower ionospheric boundary sharpness and VLF signal's reflection height), are conducted using Equation (2) valid for daytime ionosphere [39]:

$$N_e(h, H', \beta) = 1.43 \cdot 10^{13} \cdot e^{(-0.15 \cdot H')} \cdot e^{[(\beta - 0.15) \cdot (h - H')]} \text{, (m}^{-3}\text{)} \quad (2)$$

Parameters β and H' for unperturbed daytime ionospheric conditions are within software predefined as 0.3 km^{-1} and 74 km , respectively, while for each case of perturbed conditions, they must be individually modeled as input parameter pairs along GCP, depending on determined measured amplitude and phase perturbations. Modeling procedure is based on trial-and-error technique, with the goal of achieving the best fit between measured and simulated values of amplitude and phase perturbations obtained through modeling. Results from this numerical procedure in the case of X2.2 and X9.3 SFs of 6 September 2017, for their entire time evolution, are given in Figure 4. Both sharpness (Figure 4b) and effective reflection height (Figure 4a) are in correlation with incident soft X-ray flux (Figure 4c).

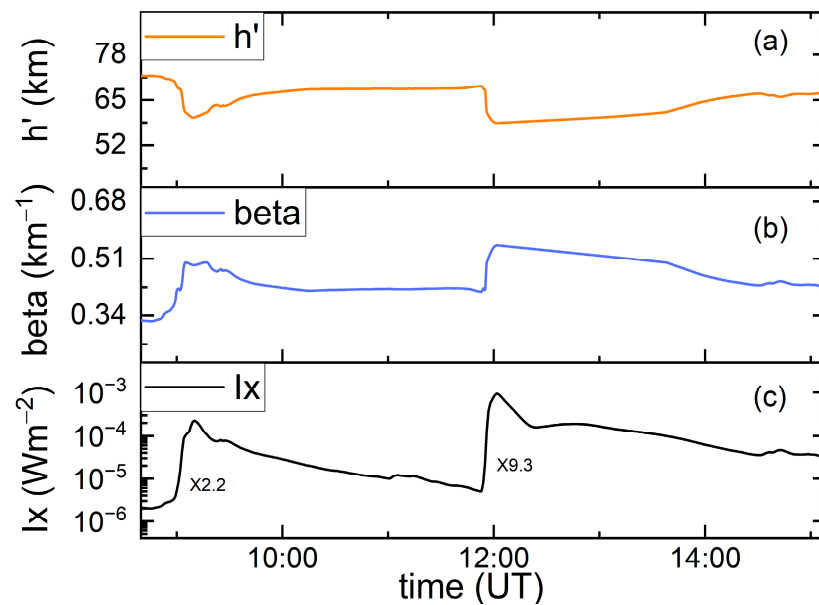


Figure 4. Simultaneous variations of the effective reflection height h' , (a) sharpness β , (b) and X-ray flux (c) during the occurrence of two successive X-ray flares of 6 September 2017.

Obtained modeled values of sharpness and reflection heights corresponding to X-ray flux peaks revealed: in the case of X2.2 SF at 09:10 UT with $I_{x_{\max}} = 2.2658 \cdot 10^{-4} \text{ Wm}^{-2}$, sharpness increased for amount of 0.13 km^{-1} and reflection height was lowered for 14 km, while in the case of X9.3 SF at 12:02 UT with $I_{x_{\max}} = 9.3293 \cdot 10^{-4} \text{ Wm}^{-2}$, sharpness increased for the amount of 0.25 km^{-1} and reflection height was lowered for 15.6 km, compared with their predefined unperturbed values.

Electron density was calculated at the reflection height, when $h = H'$ throughout altitude range corresponding to lower ionosphere (50–90 km), but it must be noted that at the range boundaries, results obtained from calculations should be taken with caution due to possible model failure. Electron density profiles corresponding to the influence of two X-class SFs from 6 September 2017, as observed on the GQD signal at BEL station, are given in Figure 5, in black and red for X2.2 and X9.3 SFs respectively, while quiet ionospheric conditions are given in blue. Conducted calculations indicate that N_e for these two SFs differ within one order of magnitude throughout the entire altitude range. Looking separately, at a height of 74 km, compared to unperturbed ionospheric state, N_e increased by almost three and about 3.5 orders of magnitude during the cases of weaker and stronger SF events respectively.

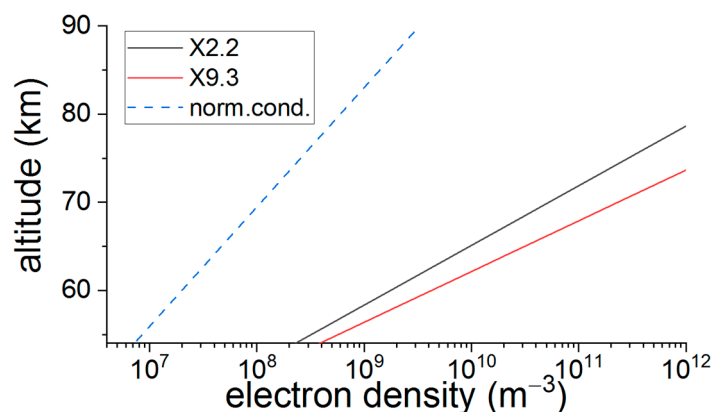


Figure 5. The height profile of electron density at peak time for two successive X-class SFs of 6 September 2017.

For time evolution of X2.2 and X9.3 SFs of 6 September 2017, during about 12 h, a novel approach for obtaining GQD signal propagation parameters, sharpness β and reflection height H' from incident solar X-ray irradiance, was applied by employing the FlarED' Method and Approximate Analytic Expression application, where electron density is calculated with simple logarithmic second-degree polynomial Equation (3) specially designed to take ionospheric response time delay through height-dependent coefficients into calculations (for more details see [5,40]):

$$\log Ne(h, Ix) = a_1(h) + a_2(h) \cdot \log Ix + a_3(h) \cdot (\log Ix)^2 \quad (3)$$

where $a_1(h)$, $a_2(h)$, and $a_3(h)$ are height-dependent coefficients, Ix is solar X-ray flux (Wm^{-2}), and h is height (km). Such calculated Ne values are in good agreement with those obtained using other simulation methods related to the two-component exponential model and VLF sub-ionospheric propagation simulations conducted through the use of LWPC software [40]. Figure 6 presents a 12-h variation of solar X-ray flux within two spectral bands provided by GOES-15 and -13 satellites (Figure 6a) and the corresponding Ne (m^{-3}) during these two X-class SFs (Figure 6b).

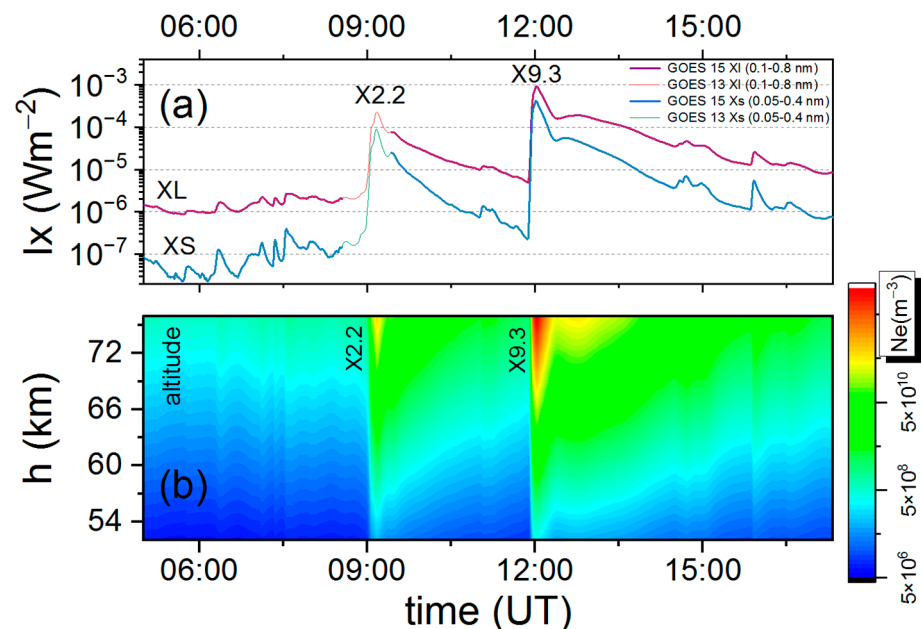


Figure 6. Variation of X-ray flux (a) as measured by GOES-15 and -13 satellites and the surface plot of corresponding electron density profile (b) versus universal time UT during two successive X-class SFs of 6 September 2017. The results are obtained using simple approximative Equation (3).

3.4. Analysis of Cosmic Ray Flux Registered by Belgrade Station during Early September 2017

As a result of solar activity at the beginning of September 2017, a strong FD was detected, resulting in a decrease of CR flux of close to 15% (as observed on the South Pole [60]). The effect was also detected on lower latitudes, being intense enough to be detected by underground muon monitors that are generally sensitive to higher energies of galactic CRs. To get a better perspective of data recorded by Belgrade muon station during this period (both by GLL and UL), we compared it against selected neutron monitor measurements (provided by the Neutron Monitor Database [61]). For this purpose, we chose three NMs: one on the opposite hemisphere with low effective vertical geomagnetic cutoff rigidity R_c , one near the North Pole, and one relatively close to Belgrade muon station with a comparable R_c . All selected stations have different asymptotic directions, R_c , and altitude and are generally sensitive to primary CR with lower median rigidity than CR detected by Belgrade muon station. Median rigidity (R_m) is the rigidity of primary CR where half of all contributions to detector count rate originates from primary CR with

rigidity lower than that specific value. Basic characteristics for NM stations are as follows: South Pole (SOPO, 90.00°S, altitude 2820 m, $R_c = 0.1$ GV, median rigidity $R_m = 10$ GV), Thule (THUL, 76.5°N, 68.7°W, 26 m, $R_c = 0.3$ GV, $R_m = 12.6$ GV), and Athens (ATHN, 37.97°N, 23.78°E, 260 m, $R_c = 8.53$ GV, $R_m = 25.1$ GV). Belgrade muon station, as mentioned before, measures muon flux on ground level (GLL, 44.85°N, 20.38°E, 75 m, $R_c = 5.3$ GV, $R_m = 63$ GV) and underground level (UL, 44.85°N, 20.38°E, 75 m, $R_c = 12$ GV, $R_m = 122$ GV). Median rigidity for NM stations is retrieved from [62]. For Belgrade muon station, R_m values for GLL and UL were determined using the response function obtained by means of Monte Carlo simulation for CR transport. Time series of detected flux for all stations during early September 2017 are given in Figure 7. Flux is normalized using a ten-day average before the FD. This longer interval was chosen due to unusually high solar activity during the period of interest.

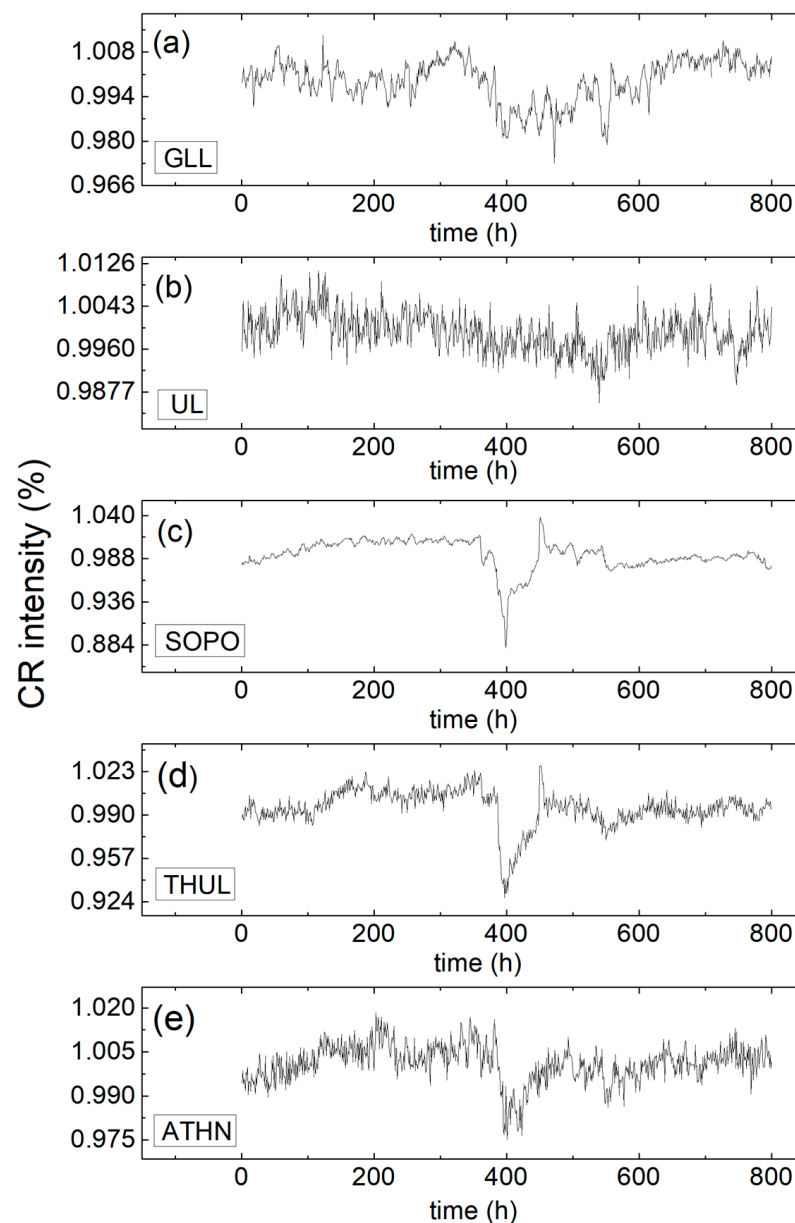


Figure 7. Normalized time series of secondary CR flux detected at several ground and one shallow-underground monitors: (a) ground (GLL) and (b) underground (UL) detector at Belgrade muon station, (c) South pole NM (SOPO), (d) Thule NM (THUL), and (e) Athens NM (ATHN).

Hourly time series show that all stations detected FD around the same time, however, time profiles are not the same. This is due to the specific sensitivity of selected CR stations to primary CR with different rigidities. Additionally, the measured magnitude of the FD is not the same for all detector stations. As expected, UL, GLL, and Athens, with higher cutoff and median rigidity, recovered from sharp depression sooner than stations at higher latitudes (with lower R_c). For a more quantitative description of the relationship between observations from selected monitors, cross-correlation analysis of hourly time series for different stations can be applied using Pearson coefficient with a 2-tail test for significance. Correlation coefficients between data recorded by these ground stations during September 2017 are given in Table 2.

Table 2. Statistical correlation between ground stations during September 2017.

Pearson Corr.	ATHN	SOPO	GLL	UL	THUL
ATHN	1	0.55084	0.43443	0.5056	0.61535
SOPO		1	0.18941	0.45194	0.81747
GLL			1	0.69325	0.36496
UL				1	0.51526
THUL					1

These ground (and one shallow-underground) stations have different locations, different cut-off rigidities, and different energy-dependent detection efficiency of the detectors. All these differences can lead to better understanding of these different correlation coefficients.

Further insight can be gathered by comparing variability of CR flux measured by different stations, as well as geomagnetic activity and selected space weather parameters for the early part of September, which are presented in Figure 8. One-hour time resolution was used for all data. The ICME list compiled by Richardson and Cane [63] and the CME list provided by SOHO/LASCO [64] were used to precisely time the near Earth passage of two ICMEs observed during this period (respective time intervals indicated in Figure 8 by dashed blue lines).

In the days following early September X-flares, two sudden storm commencements (SSCs), or two shocks, arrived during the last hours of 6–7 September (indicated by solid blue lines in Figure 8). They were followed by a sheath region and ICME ejecta. Interaction of shock and sheath region of ICME2 with ICME1 ejecta, visible in the sudden change of solar wind parameters, led to the observed intense geomagnetic activity and consequent FD. This CME-CME interaction with its complex structure was the main reason for the extensive geomagnetic storm [65] and a strong detected FD. With arrival of the first ICME, CR flux showed a small decrease detected as a low-magnitude FD by NM stations [66] (at 23:43:00 UT on 6 September, with magnitude of 1.8% according to IZMIRAN database).

When the second fast interplanetary shock arrived and interacted with ejecta from the previous ICME, a sharp decrease in CR flux and one of the largest FDs in solar cycle 24 was detected (at 23:00:00 UT on 7 September, with magnitude of 7.7% according to IZMIRAN database). Main FD was clearly visible even with muon detectors, which leads to the conclusion that inhomogeneities in the heliosphere created by interaction of these two ICMEs modulated CR extensively. The recovery phase of this FD was influenced by disturbed interplanetary condition, the effect being dependent on particle energy as was evident by comparing profiles of CR time series recorded by different stations. Before the end of the recovery phase, another flare (X8.2 of 10 September) led to a small ground level enhancement (GLE), the last one of solar cycle 24 (GLE #72). Recovery time of the main FD was approximately three days in total, which is a relatively short period for such a large CR modulation. Cross-correlation coefficients between CR time series measured by Belgrade muon station and selected space weather parameters for the period of six days (during 5–10 September) are given in Table 3.

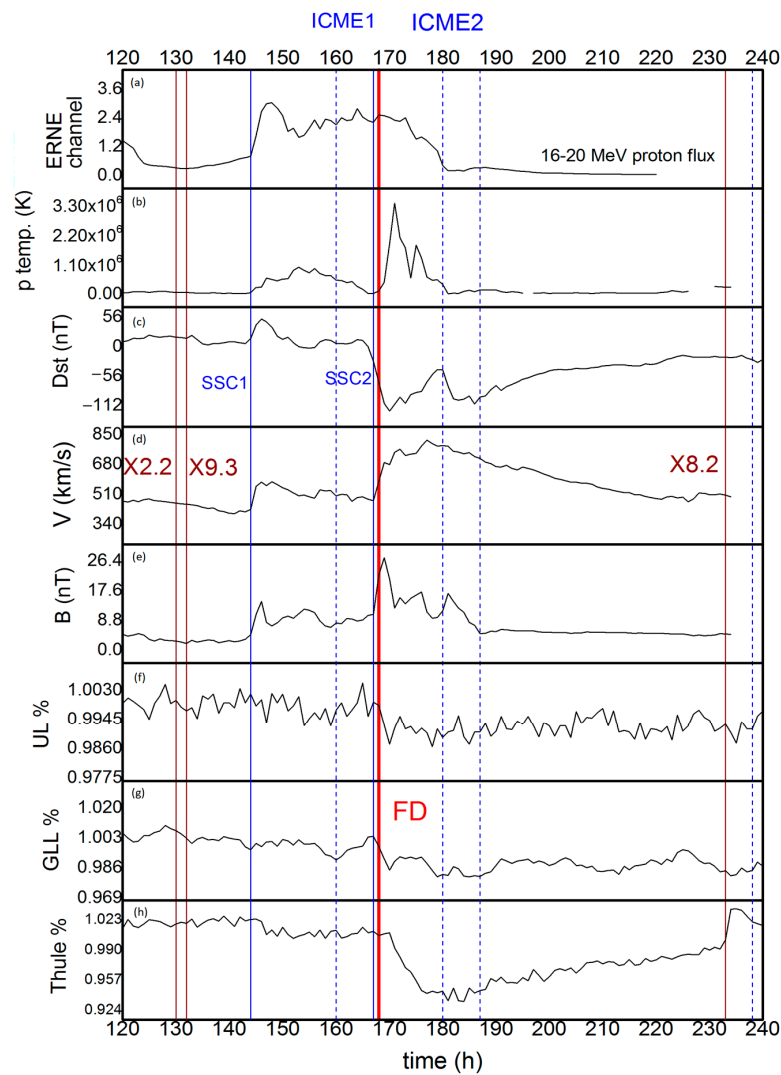


Figure 8. Hourly variation in CR intensity measured at ground station ((f) UL, (g) GLL, (h) Thule), (e) magnitude of interplanetary magnetic field B, (d) velocity of solar wind V, (c) Dst index, (b) proton temperature, and (a) one of the proton channels measured by ERNE/SOHO during early September 2017 (period 4th–10th).

Table 3. Statistical correlation (with significance) between time series of CR flux measured at ground stations and selected space weather parameters during 5–10 September 2017.

Pearson Corr.	Thule		GLL		UL	
Thule	1					
GLL	0.67213	(<10 ⁻⁶)	1			
UL	0.62741	(<10 ⁻⁶)	0.75552	(<10 ⁻⁶)	1	
Average B	-0.238	(<0.008)	-0.242	0.007	-0.243	<0.007
SW speed	-0.80562	(<10 ⁻⁶)	-0.62829	(<10 ⁻⁶)	-0.58503	(<10 ⁻⁶)
Dst Index	0.77923	(<10 ⁻⁶)	0.6979	(<10 ⁻⁶)	0.65494	(<10 ⁻⁶)
Proton Channel 16–20 MeV	0.43083	<10 ⁻⁵	0.38276	<10 ⁻⁴	0.31715	<10 ⁻³

During this period, apparent correlation can be established between selected parameters. This correlation is larger for Thule NM than in the case of Belgrade Muon monitor. Due to the short period, correlation between proton flux at L1 and detected CR flux on all stations is exaggerated.

4. Discussion

The cascade of strong solar activity from AR12673 that occurred in early September 2017 was among others characterized by a number of SFs. Several concurrent interconnecting CMEs/ICMEs emerged in a relatively short period, inducing a disturbance in the heliosphere. The complex structure of interacting CMEs/ICMEs produced an extensive geomagnetic storm and ionospheric disturbance and affected the flux of primary CR (visible as a FD). Additionally, the mentioned phenomena were responsible for the increased flux of energetic particles in interplanetary space. The origin and acceleration mechanism for energetic protons measured at L1 is not so straightforward to determine due to complicated interactions of all effects potentially involved. In case these particles originate from the Sun, correlation between SF properties and SEP fluence is supposed to be rather poor, although it is suggested that primary acceleration of SEP to higher energies occur in close proximity to the flare site [67,68]. If, on the other hand, these particles are accelerated in interplanetary space due to the passage of ICME shock, some correlation can be established (i.e., between measured proton fluence and CME/ICME velocity). However, regardless of their origin, the shape of energetic proton fluence spectrum can hold useful information about heliospheric disturbance and can even provide insight into the effect that this disturbance has on the flux of primary CR in interplanetary space (especially when more intense events are concerned). That was also demonstrated in this case, where the magnitude of the corresponding FD corrected for magnetospheric effect estimated from proton fluence spectra was in good agreement with the value for M_M calculated based on NM measurements.

Impacts of the soft range X-ray solar electromagnetic radiation released from two powerful SF events from 6 September 2017 onto the European mid-latitude ionospheric D-region were monitored and inspected based on recordings from BEL narrowband VLF receiving station, belonging to a global ground-based VLF network system. Lower ionospheric disturbances induced by incident soft range X-ray radiation were indirectly examined regarding simultaneous perturbations of VLF radio signals' propagation parameters within the Earth-ionosphere waveguide, with analysis conducted for signals with short GCPs (Table 1; Figure S3).

Aside from quiet ionospheric preflare conditions, SFs' occurrence times were also favorable in terms of applied modeling procedure using the LWPC software package, since analyzed signals on their GCPs towards BEL station were transmitted through waveguides under already established stable daytime ionospheric conditions. Since this procedure relies on trial-and-error technique in acquiring the best fitting pair of Wait's parameters for depicting real measured data with the modeled data, and from that, by obtaining information regarding lower ionospheric conditions based on modeled ones, both of these prerequisites significantly eased an already highly challenging task of modeling X-class SFs and especially those most energetic among them. In such disturbed conditions, both ionospheric plasma properties and related corresponding VLF signal propagation parameters are drastically changed compared with the regular state. Accordingly, electron density height profiles are also changed in regard to both time and space distributions. As expected, the evolution of observed VLF signals' perturbations was with similar characteristics, following a lower ionospheric response to incident solar X-ray flux with delay times corresponding to the sluggishness of the ionosphere and were of amounts expected for cases of such powerful events (Figure 3). Their back-to-back occurrence did not allow for individual duration specification of each SF's impact on analyzed VLF signals, however, their individual contribution was possible to determine. According to registered VLF BEL data, after a several-hour lasting disturbance, the lower ionosphere fully recovered (Figure S4).

For the state of maximal perturbation that corresponds to SFs' X-ray flux peaks, perturbed GQD signal's amplitudes are 118% and 117% of unperturbed, while phases are 165% and 192% of unperturbed. Wait's parameters are in correlation with incident soft X-ray flux and modeling results based upon exponential conductivity increase with height within the ionosphere suggesting that perturbed sharpnesses are 143.3% and 183.3% of unperturbed, while perturbed reflection heights are 81% and 78.9% of unperturbed,

respectively to SFs (Figure 4). As expected, in the case of the stronger SF event, propagation was more affected by the induced disturbance, causing the reflecting edge boundary to become significantly sharper, while reflecting edge height descended for 1.6 km^{-1} more than in case of the weaker one. Numerically, simulated ionospheric conditions fit well with observed ones, as indirectly obtained through GQD signal's amplitude and phase measurements. Due to its short GCP and stable daytime ionospheric conditions, averaged conditions that were held within the waveguide during the modeling procedure can be considered reliable. Electron densities calculated using Equation (2) for the D-region altitude range show about one order of magnitude difference between analyzed SFs at their peak, giving a reflection height of 74 km an increase in electron density of 82.1% compared between stronger and weaker events (Figure 5).

The effects on the ionosphere of the largest SF event of the last decade, X9.3 together with X2.2, occurred on 6 September 2017, observed through GQD VLF signal response in relation to the SF class, were compared with some other cases of strong SF events, including several major SFs (2003–2011 of class X28+–X6.9) and other SFs (from 2006–2017 of class X1–X9.3 and from period 1994–1998 in range X1–X5). Figure S5 provides a comparison of the results obtained in this study (black stars) and those available in the literature [5,7,8,69–77]. Presented ionospheric parameters (β and H') and corresponding electron densities are related to results from two hundred cases of SF events recorded in Belgrade on GQD trace in the period of 2003–2017 in other mid-latitudinal ionospheric sectors and the low-latitudinal ionospheric sector. In order to ensure better insight into the tendency of parameters with the SF events' strength, smaller diagrams containing the entire C–X-class range are embedded in Figure S5. It can be seen that values of signal parameters for some X-class events are quite scattered.

Our results fit well with the general trend (linear fit), considering that most of the available cases taken into consideration are from the mid-latitudinal sector. A significant discrepancy notable in the enlarged X-class section, related to results from [69] and [70], is probably caused by latitudinal factor (due to low-latitudinal observations likewise as suggested in [71] and similarly due to observations obtained more towards higher-latitude compared with Belgrade receiver site, respectively). A novel proposed approximate method that employs approximative Equation (3) for obtaining ionospheric parameters was validated both for cases of weaker and stronger SFs and expanded further towards the upper boundary of X-class range, as compared to recent previous studies employing this technique. Applied novel approach provides mapping of the entire ionospheric altitude range (Figure 6) in a simpler and easier to conduct manner. Results obtained in this study using this novel approach applied to X-class SFs could be useful for validation of the available ionospheric models and as input data for other climate models.

Furthermore, increased solar activity at the beginning of September 2017 had a significant effect on cosmic rays observed as a decrease in measured flux by all relevant CR stations. Intensity of the event was such that the energy range of affected primary CR was wide enough for the effect to be detected both by neutron monitors and muon detectors. The decrease was even observable in shallow-underground muon measurements, although to a much lesser extent. Temporal agreement between measurements taken by different detectors was good, while the shape of detected FD varied, as would be expected due to difference in location, instrument design, and sensitivity. Cross-correlation analysis of hourly time series for different stations (presented in Table 2) shows expected positive correlation, where obtained coefficients are consistent with values expected based on differences in detector location, particular setups, station specific environmental conditions, and most importantly, the energy (rigidity) range of primary CR they are sensitive to. GLL and UL have the same position, however, correlation is not so high (≈ 0.7) due to different R_c and R_m . Nevertheless, this correlation is higher than that between either of the detectors and any of the neutron monitor stations. NMs have more similar R_c and R_m values, so this correlation is greater despite their different location. As far as correlation between measured CR flux and selected space weather and geomagnetic parameters is concerned,

a larger correlation observed for NM (Table 3) can almost certainly be attributed to the fact that muon detectors are sensitive to higher energy CR (which are less modulated by disturbances in the heliosphere). Correlation between selected proton channel (particles with energy between 16 and 20 MeV) and CR flux is exaggerated as it is a consequence of a relatively short time interval taken for analysis. This value is greatly reduced if a longer interval is taken into consideration, even appearing as a small anticorrelation. This is expected as proton flux with its turbulent magnetic field scatters CR and thus can produce a decrease in detected CR flux. Inverse correlation of magnetic field and solar wind speed with CR flux is anticipated due to the same reason.

Forbush decrease in early September 2017 was caused by compound solar wind disturbance formed due to the interaction of several ICMEs. This time interval is particularly interesting because it happens in a descending-to-minimum phase of a solar cycle. The apparent multitude of solar activity is more characteristic to other phases. For example, similar series of successive CMEs led to FD in March 2012 [78] during the ascending phase of the solar cycle, but this heightened activity of the Sun, isolated between relatively quiet periods, allows for better study of the phenomena. Forecasting these multiple CME interaction events and predicting time of arrival is very difficult [45] but needed, so this series of events can be a good case study.

Although no apparent correlation between SF intensity and solar wind and FD parameters is clearly demonstrable, the majority of more intense FDs are caused by a CME/ICME following a significant SF, thus indicating a likely connection. For one such complex event, accompanying disturbances induced in the heliosphere, magnetosphere, and ionosphere are generally directly attributed to different sources and establishing clear relationships between various parameters used to describe them is far from straightforward. Yet, based on some general features, it is possible to make rudimentary event classification, where within certain classes, some of these relationships may be more pronounced. Strong flares do not necessarily produce a significant FD (although can have an associated GLE, as is the case for X14.4 flare that occurred on 15 April 2001), can produce both strong FDs and GLEs (e.g., GLE #69 on 20 January 2005, GLE #66 on 28 October and GLE #67 on 2 November 2003), or can produce strong FD but without associated GLE (e.g., 7 March 2012, related to X5.4 flare and September 2017 event studied here). It has been shown [49,79] that events that fall in this last category exhibit stronger correlations between FD magnitude and some space weather parameters, specifically average CME speed. More recently, a correlation between FD magnitude (especially in the case of more intense FDs) and shape of energetic proton spectra measured at L1 has been reported for this class of events. As the number of such events is relatively low, it is of significance that results presented in this work are consistent with the indicated relationship. For reference, dependence of FD magnitude on selected SF, CME, and geomagnetic parameters for some of the mentioned events is given in Figure S6.

5. Conclusions

The influence of severely disturbed space weather conditions of 6 September 2017 on parameters of the Earth's atmosphere was studied, in relation to the relatively close and far surroundings of the Earth. The influence of strong X-class SFs on the ionosphere and primary cosmic rays, based on space- and ground-based observations on one hand and simulations on the other hand, are presented. It contributes to better understanding of solar-terrestrial coupling processes and how primary cosmic rays and the ionosphere respond under conditions during the X-class SF events. Based on the results presented, the following conclusions can be drawn:

- SEP fluence during strongly disturbed conditions of the heliosphere in early September 2017 was calculated from SOHO/ERNE data and modeled using double power law. Relationships between power exponents used to parameterize the shape of fluence spectrum and FD magnitude corrected for magnetospheric effect are consistent with ones expected for this type of event. Hourly time series of secondary CR flux, detected by several ground-based monitors and one shallow-underground monitor, show that

- all stations detected FD at the same time. Cross-correlation between these time series, and between CR time series and some geomagnetic activity indices, as well as selected IMF and solar wind parameters, are presented. Sensitivity of different stations to primary CR with different rigidity results in different time profiles, maximal decreases, and duration of recovery phase of FD;
- We observed that a correlation between heliospheric and geomagnetic parameters decreases with increase of median energy of the CR detected by different stations and that shows an extension of CR modulation of complex CME-CME interaction structure initiated with strong SFs;
 - Impact of intense solar activity onto the Earth's lower ionosphere, through analyzed X-class SFs, was clearly observed (perturbed amplitudes are 118% and 117% of unperturbed, while perturbed phases are 165% and 192% of unperturbed, for X2.2 and X9.3, respectively). BEL AbsPAL recordings of registered VLF signals during SF events are in correlation with X-ray flux (with time delays corresponding to the sluggishness of the ionosphere). Although X2.2 and X9.3 occurred back-to-back, it was possible to determine individual contributions of each SF based upon registered VLF signals;
 - Numerical simulations were conducted through the application of the LWPC software package and the FlarED' Method and Approximate Analytic Expression application's novel approach. The ionospheric parameters (sharpness and effective reflection height) and electron density are in correlation with incident X-ray flux of soft range. N_e for these two SFs revealed the difference within one order of magnitude throughout the entire altitude range considered. Compared to quiet ionospheric conditions, N_e at the reference height increased by several orders of magnitude during both SF events. As monitored by BEL VLF station in the mid-latitudinal sector, both presented X-class SFs are common in properties and behavior, as could be expected for intense SF events, according to their strength. However, there is a significant difference in estimations of ionospheric parameters related to some other cases of reported X-class SFs from different sectors.

Although there are numerous papers related to the influence of SF events on Earth's ionosphere, the vast majority of present case studies of selected SF events, more or less are extensively related to numbers of examined cases. X-class SF events have never been systematically studied in terms of lower ionospheric response. Coupling processes between such extreme space weather events and the lower ionosphere are not well understood. In addition, many intense SF events are related to other energetic solar events like CMEs and SEPs. Comprehensive research is needed especially in terms of retrieving a global (worldwide) lower ionospheric response to such strong events from propagation parameters of radio signals as a remote sensing technique. Case studies, although restricted to some selected events and with great contribution of "local" components contained within obtained and presented results, would provide substantial contributions.

This study emphasized the relevance of the ionospheric response, which was analyzed using a multi-instrument method, and gave a comprehensive examination of the events from the Sun to the Earth. It gave an insight into the sudden increase in ionization during the storm and strong SFs from the beginning of September 2017 and the potential effects on radio communication. Since conditions in the D-region of the ionosphere have a dramatic effect on high frequency communications and low frequency navigation systems, the ionospheric responses (and its parameters like β , H' and N_e) to severe SFs are a key topic of study in ionospheric physics and are considered to be an important factor for space weather predictions, improvement of empirical models, and applications of machine learning techniques in atmospheric sciences.

Supplementary Materials: The following supporting information can be downloaded at: <https://www.mdpi.com/article/10.3390/rs15051403/s1>, Figure S1: Differential SEP fluxes during extreme solar event in September 2017, measured by SOHO/ERNE energetic particle sensors LET (Low Energy Detector) proton channels. Red vertical dashed lines indicate the time for the start and the end

of interval used to calculate the integral flux.; Figure S2: Differential SEP fluxes during extreme solar event in September 2017, measured by SOHO/ERNE energetic particle sensors HET (High Energy Detector) proton channels. Red vertical dashed lines indicate the time for the start and the end of interval used to calculate the integral flux.; Figure S3: The geographic position of Belgrade (BEL) VLF receiver and the GQD transmitter (54.73°N, 2.88°W), Anthorn UK and TBB transmitter (37.43°N, 27.55°E) Bafa Turkey with GCP of sub-ionospheric propagating VLF signals.; Figure S4: Simultaneous variations of X-ray flux (red), phase (blue), and amplitude (orange) of GQD/22.10 kHz signal versus universal time UT during occurrence of X2.2 and X9.3 class solar flares of 6 September 2017 (from upper to lower panel). Observed amplitude and phase perturbations on GQD radio signal, as well as quiet signal (dashed black), are measured at Belgrade station. Time variation of soft X-ray irradiance is measured by GOES-15 satellite.; Figure S5: Lower ionospheric response to SF events of different strength across X-class (shaded gray area), obtained indirect modeling of VLF signals' propagation parameters: (a) sharpness β (km^{-1}), and (b) effective reflection height H' , (km) and (c) estimated corresponding electron densities N_e (m^{-3}), in function of X-ray flux; results from our research are presented by black stars.; Figure S6: Magnitude of the FD versus the average CME velocity between the Sun and the Earth, calculated using the time of the beginning of the associated CME observations (a) Minimal Dst-index in the event, (b) maximal X-ray flare power (c) with associated flare indicated in red.

Author Contributions: Conceptualization, V.A.S.; writing—original draft preparation, V.A.S., A.K. and N.V.; writing—review and editing A.K., N.V., V.A.S., Z.M., M.S. and A.D. The authors had full access to the data and took responsibility for their integrity. All authors have read and agreed to the published version of the manuscript.

Funding: This work was funded by the Institute of Physics Belgrade, University of Belgrade, through a grant by the Ministry of Science, Technological Development and Innovations of the Republic of Serbia.

Data Availability Statement: VLF data were recorded at the Institute of Physics Belgrade, University of Belgrade and can be obtained upon request. Please contact V.A.S.

Acknowledgments: The article is based upon work from COST Action CA18212—Molecular Dynamics in the GAS phase (MD-GAS), supported by COST (European Cooperation in Science and Technology). Authors thank D. Šulić for instrumental set-up and useful discussions. OMNI data was made available by NASA/GSFC's Space Physics Data Facility's OMNIWeb service. This CME catalog is generated and maintained at the CDAW Data Center by NASA and The Catholic University of America in cooperation with the Naval Research Laboratory. SOHO is a project of international cooperation between ESA and NASA. We acknowledge the NMDB database, founded under the European Union's FP7 program (contract no.213007) for providing data. We also gratefully acknowledge using data from the catalogue of Forbush effects and interplanetary disturbances provided by Cosmic Ray Group at the IZMIRAN Space Weather Prediction Center at Pushkov Institute of Terrestrial Magnetism, Ionosphere, and Radio Wave Propagation of the Russian Academy of Sciences.

Conflicts of Interest: The authors declare no conflict of interest. The funders had no role in the design of the study; in the collection, analyses, or interpretation of data; in the writing of the manuscript, or in the decision to publish the results.

References

1. Manju, G.; Pant, T.K.; Devasia, C.V.; Ravindran, S.; Sridharan, R. Electrodynamical response of the Indian low-mid latitude ionosphere to the very large solar flare of 28 October 2003—A case study. *Ann. Geophys.* **2009**, *27*, 3853–3860. [[CrossRef](#)]
2. Fu, H.; Zheng, Y.; Ye, Y.; Feng, X.; Liu, C.; Ma, H. Joint Geoeffectiveness and Arrival Time Prediction of CMEs by a Unified Deep Learning Framework. *Remote Sens.* **2021**, *13*, 1738. [[CrossRef](#)]
3. Sahai, Y.; Becker-Guedes, F.; Fagundes, P.R.; Lima, W.L.C.; de Abreu, A.J.; Guarnieri, F.L.; Candido, C.M.N.; Pillat, V.G. Unusual ionospheric effects observed during the intense 28 October 2003 solar flare in the Brazilian sector. *Ann. Geophys.* **2007**, *25*, 2497–2502. [[CrossRef](#)]
4. Le, H.; Liu, L.; Chen, Y.; Wan, W. Statistical analysis of ionospheric responses to solar flares in the solar cycle 23. *J. Geophys. Res. Space Phys.* **2013**, *118*, 576–582. [[CrossRef](#)]
5. Srećković, V.A.; Šulić, D.M.; Ignjatović, L.; Vujčić, V. Low Ionosphere under Influence of Strong Solar Radiation: Diagnostics and Modeling. *Appl. Sci.* **2021**, *11*, 7194. [[CrossRef](#)]
6. Kelley, M.C. *The Earth's Ionosphere: Plasma Physics and Electrodynamics*; Academic Press: Cambridge, MA, USA, 2009.

7. Barta, V.; Natras, R.; Srećković, V.; Koroncay, D.; Schmidt, M.; Šulic, D. Multi-instrumental investigation of the solar flares impact on the ionosphere on 05–06 December 2006. *Front. Environ. Sci.* **2022**, *10*, 904335. [[CrossRef](#)]
8. Kolarski, A.; Srećković, V.A.; Mijić, Z.R. Response of the Earths Lower Ionosphere to Solar Flares and Lightning-Induced Electron Precipitation Events by Analysis of VLF Signals: Similarities and Differences. *Appl. Sci.* **2022**, *12*, 582. [[CrossRef](#)]
9. Nina, A. Modelling of the Electron Density and Total Electron Content in the Quiet and Solar X-ray Flare Perturbed Ionospheric D-Region Based on Remote Sensing by VLF/LF Signals. *Remote Sens.* **2022**, *14*, 54. [[CrossRef](#)]
10. Berdermann, J.; Kriegel, M.; Banyś, D.; Heymann, F.; Hoque, M.M.; Wilken, V.; Borries, C.; Heßelbarth, A.; Jakowski, N. Ionospheric Response to the X9.3 Flare on 6 September 2017 and Its Implication for Navigation Services Over Europe. *Space Weather* **2018**, *16*, 1604–1615. [[CrossRef](#)]
11. Yasyukevich, Y.; Astafyeva, E.; Padokhin, A.; Ivanova, V.; Syrovatskii, S.; Podlesnyi, A. The 6 September 2017 X-Class Solar Flares and Their Impacts on the Ionosphere, GNSS, and HF Radio Wave Propagation. *Space Weather* **2018**, *16*, 1013–1027. [[CrossRef](#)]
12. De Paula, V.; Segarra, A.; Altadill, D.; Curto, J.J.; Blanch, E. Detection of Solar Flares from the Analysis of Signal-to-Noise Ratio Recorded by Digisonde at Mid-Latitudes. *Remote Sens.* **2022**, *14*, 1898. [[CrossRef](#)]
13. Demyanov, V.V.; Yasyukevich, Y.V.; Ishin, A.B.; Astafyeva, E.I. Ionospheric super-bubble effects on the GPS positioning relative to the orientation of signal path and geomagnetic field direction. *GPS Solut.* **2012**, *16*, 181–189. [[CrossRef](#)]
14. Yashiro, S.; Gopalswamy, N. Statistical relationship between solar flares and coronal mass ejections. *Proc. Int. Astron. Union* **2008**, *4*, 233–243. [[CrossRef](#)]
15. Desai, M.; Giacalone, J. Large gradual solar energetic particle events. *Living Rev. Sol. Phys.* **2016**, *13*, 3. [[CrossRef](#)]
16. Freiherr von Forstner, J.L.; Guo, J.; Wimmer-Schweingruber, R.F.; Dumbović, M.; Janvier, M.; Démoulin, P.; Veronig, A.; Temmer, M.; Papaioannou, A.; Dasso, S.; et al. Comparing the Properties of ICME-Induced Forbush Decreases at Earth and Mars. *J. Geophys. Res. Space Phys.* **2020**, *125*, e2019JA027662. [[CrossRef](#)]
17. Cane, H.V. Coronal Mass Ejections and Forbush Decreases. *Space Sci. Rev.* **2000**, *93*, 55–77. [[CrossRef](#)]
18. Belov, A.V.; Eroshenko, E.A.; Oleneva, V.A.; Struminsky, A.B.; Yanke, V.G. What determines the magnitude of forbush decreases? *Adv. Space Res.* **2001**, *27*, 625–630. [[CrossRef](#)]
19. Papaioannou, A.; Belov, A.; Abunina, M.; Eroshenko, E.; Abunin, A.; Anastasiadis, A.; Patsourakos, S.; Mavromichalaki, H. Interplanetary Coronal Mass Ejections as the Driver of Non-recurrent Forbush Decreases. *Astrophys. J.* **2020**, *890*, 101. [[CrossRef](#)]
20. Belov, A.; Shlyk, N.; Abunina, M.; Belova, E.; Abunin, A.; Papaioannou, A. Solar Energetic Particle Events and Forbush Decreases Driven by the Same Solar Sources. *Universe* **2022**, *8*, 403. [[CrossRef](#)]
21. Riley, P.; Love, J.J. Extreme geomagnetic storms: Probabilistic forecasts and their uncertainties. *Space Weather* **2017**, *15*, 53–64. [[CrossRef](#)]
22. Eastwood, J.P.; Biffis, E.; Hapgood, M.A.; Green, L.; Bisi, M.M.; Bentley, R.D.; Wicks, R.; McKinnell, L.A.; Gibbs, M.; Burnett, C. The Economic Impact of Space Weather: Where Do We Stand? *Risk Anal.* **2017**, *37*, 206–218. [[CrossRef](#)] [[PubMed](#)]
23. Kumar, A.; Kashyap, Y.; Kosmopoulos, P. Enhancing Solar Energy Forecast Using Multi-Column Convolutional Neural Network and Multipoint Time Series Approach. *Remote Sens.* **2023**, *15*, 107. [[CrossRef](#)]
24. Alabdulgader, A.; McCraty, R.; Atkinson, M.; Dobyns, Y.; Vainoras, A.; Ragulskis, M.; Stolc, V. Long-Term Study of Heart Rate Variability Responses to Changes in the Solar and Geomagnetic Environment. *Sci. Rep.* **2018**, *8*, 2663. [[CrossRef](#)] [[PubMed](#)]
25. Bruno, A.; Christian, E.R.; de Nolfo, G.A.; Richardson, I.G.; Ryan, J.M. Spectral Analysis of the September 2017 Solar Energetic Particle Events. *Space Weather* **2019**, *17*, 419–437. [[CrossRef](#)]
26. Chamberlin, P.C.; Woods, T.N.; Didkovsky, L.; Eparvier, F.G.; Jones, A.R.; Machol, J.L.; Mason, J.P.; Snow, M.; Thiemann, E.M.B.; Viereck, R.A.; et al. Solar Ultraviolet Irradiance Observations of the Solar Flares During the Intense September 2017 Storm Period. *Space Weather* **2018**, *16*, 1470–1487. [[CrossRef](#)]
27. Pikulina, P.; Mironova, I.; Rozanov, E.; Karagodin, A. September 2017 Solar Flares Effect on the Middle Atmosphere. *Remote Sens.* **2022**, *14*, 2560. [[CrossRef](#)]
28. Vankadara, R.K.; Panda, S.K.; Amory-Mazaudier, C.; Fleury, R.; Devanaboyina, V.R.; Pant, T.K.; Jamjareegulgarn, P.; Haq, M.A.; Okoh, D.; Seemala, G.K. Signatures of Equatorial Plasma Bubbles and Ionospheric Scintillations from Magnetometer and GNSS Observations in the Indian Longitudes during the Space Weather Events of Early September 2017. *Remote Sens.* **2022**, *14*, 652. [[CrossRef](#)]
29. Amaechi, P.O.; Akala, A.O.; Oyedokun, J.O.; Simi, K.G.; Aghogho, O.; Oyeyemi, E.O. Multi-Instrument Investigation of the Impact of the Space Weather Events of 6–10 September 2017. *Space Weather* **2021**, *19*, e2021SW002806. [[CrossRef](#)]
30. Curto, J.J.; Marsal, S.; Blanch, E.; Altadill, D. Analysis of the Solar Flare Effects of 6 September 2017 in the Ionosphere and in the Earth's Magnetic Field Using Spherical Elementary Current Systems. *Space Weather* **2018**, *16*, 1709–1720. [[CrossRef](#)]
31. Bilitza, D. IRI the International Standard for the Ionosphere. *Adv. Radio Sci.* **2018**, *16*, 1–11. [[CrossRef](#)]
32. Moraal, H. Cosmic-Ray Modulation Equations. *Space Sci. Rev.* **2013**, *176*, 299–319. [[CrossRef](#)]
33. Dorman, L.I. *Cosmic Rays in the Earth's Atmosphere and Underground*; Springer: Dordrecht, The Netherlands, 2004; Volume 303, p. 862.
34. Zhang, J.L.; Tan, Y.H.; Wang, H.; Lu, H.; Meng, X.C.; Muraki, Y. The Yangbajing Muon–Neutron Telescope. In *Nuclear Instruments and Methods in Physics Research Section A: Accelerators, Spectrometers, Detectors and Associated Equipment*; Elsevier: Amsterdam, The Netherlands, 2010; Volume 623, pp. 1030–1034. [[CrossRef](#)]

35. Veselinović, N.; Dragić, A.; Savić, M.; Maletić, D.; Joković, D.; Banjanac, R.; Udovičić, V. An underground laboratory as a facility for studies of cosmic-ray solar modulation. In *Nuclear Instruments and Methods in Physics Research Section A: Accelerators, Spectrometers, Detectors and Associated Equipment*; Elsevier: Amsterdam, The Netherlands, 2017; Volume 875, pp. 10–15.
36. Savić, M.; Maletić, D.; Dragić, A.; Veselinović, N.; Joković, D.; Banjanac, R.; Udovičić, V.; Knežević, D. Modeling Meteorological Effects on Cosmic Ray Muons Utilizing Multivariate Analysis. *Space Weather* **2021**, *19*, e2020SW002712. [[CrossRef](#)]
37. Ferguson, J. *Computer Programs for Assessment of Long-Wavelength Radio Communications, Version 2.0: User's Guide and Source Files*; Space and Naval Warfare Systems Center: San Diego, CA, USA, 1998.
38. Mitra, A.P. *Ionospheric Effects of Solar Flares*; Springer: Berlin/Heidelberg, The Netherlands, 1974; Volume 46.
39. Wait, J.R.; Spies, K.P. *Characteristics of the Earth-Ionosphere Waveguide for VLF Radio Waves*; US Department of Commerce, National Bureau of Standards: Gaithersburg, MD, USA, 1964; Volume 13.
40. Srećković, V.A.; Šulić, D.M.; Vujčić, V.; Mijić, Z.R.; Ignjatović, L.M. Novel Modelling Approach for Obtaining the Parameters of Low Ionosphere under Extreme Radiation in X-Spectral Range. *Appl. Sci.* **2021**, *11*, 11574. [[CrossRef](#)]
41. AR12673 History. Available online: http://helio.mssl.ucl.ac.uk/helio-vo/solar_activity/arstats/arstats_page4.php?region=12673 (accessed on 14 December 2022).
42. Space Weather Prediction Center (IZMIRAN). Available online: <http://spaceweather.izmiran.ru/eng/dbs.html> (accessed on 22 January 2022).
43. Wold, A.M.; Mays, M.L.; Taktakishvili, A.; Jian, L.K.; Odstrcil, D.; MacNeice, P. Verification of real-time WSA–ENLIL+Cone simulations of CME arrival-time at the CCMC from 2010 to 2016. *J. Space Weather Space Clim.* **2018**, *8*, A17. [[CrossRef](#)]
44. Gopalswamy, N.; Yashiro, S.; Michalek, G.; Stenborg, G.; Vourlidas, A.; Freeland, S.; Howard, R. The SOHO/LASCO CME Catalog. *Earth Moon Planets* **2009**, *104*, 295–313. [[CrossRef](#)]
45. Werner, A.L.E.; Yordanova, E.; Dimmock, A.P.; Temmer, M. Modeling the Multiple CME Interaction Event on 6–9 September 2017 with WSA-ENLIL+Cone. *Space Weather* **2019**, *17*, 357–369. [[CrossRef](#)]
46. SPDF - OMNIWeb Service. Available online: https://spdf.gsfc.nasa.gov/pub/data/omni/low_res_omni/ (accessed on 10 November 2022).
47. Torsti, J.; Valtonen, E.; Lumme, M.; Peltonen, P.; Eronen, T.; Louhola, M.; Riihonen, E.; Schultz, G.; Teittinen, M.; Ahola, K.; et al. Energetic particle experiment ERNE. *Sol. Phys.* **1995**, *162*, 505–531. [[CrossRef](#)]
48. Multi-Source Spectral Plots (MSSP) of Energetic Particle. Available online: https://omniweb.gsfc.nasa.gov/ftpbrowser/flux_spectr_m.html (accessed on 25 October 2022).
49. Savić, M.; Veselinović, N.; Dragić, A.; Maletić, D.; Joković, D.; Udovičić, V.; Banjanac, R.; Knežević, D. New insights from cross-correlation studies between solar activity indices and cosmic-ray flux during Forbush decrease events. *Adv. Space Res.* **2022**, *71*, 2006–2016. [[CrossRef](#)]
50. Band, D.; Matteson, J.; Ford, L.; Schaefer, B.; Palmer, D.; Teegarden, B.; Cline, T.; Briggs, M.; Paciesas, W.; Pendleton, G.; et al. BATSE Observations of Gamma-Ray Burst Spectra. I. Spectral Diversity. *Astrophys. J.* **1993**, *413*, 281. [[CrossRef](#)]
51. Ellison, D.C.; Ramaty, R. Shock acceleration of electrons and ions in solar flares. *Astrophys. J.* **1985**, *298*, 400–408. [[CrossRef](#)]
52. Mottl, D.A.; Nymmik, R.A.; Sladkova, A.I. Energy spectra of high-energy SEP event protons derived from statistical analysis of experimental data on a large set of events. *AIP Conf. Proc.* **2001**, *552*, 1191–1196. [[CrossRef](#)]
53. Zhao, L.; Zhang, M.; Rassoul, H.K. Double power laws in the event-integrated solar energetic particle spectrum. *Astrophys. J.* **2016**, *821*, 62. [[CrossRef](#)]
54. Miteva, R.; Samwel, S.W.; Zabunov, S.; Dechev, M. On the flux saturation of SOHO/ERNE proton events. *Bulg. Astron. J.* **2020**, *33*, 99.
55. NOAA National Centers for Environmental Information. Available online: <https://satdat.ngdc.noaa.gov/sem/goes/data/avg/> (accessed on 10 October 2022).
56. Žigman, V.; Grubor, D.; Šulić, D. D-region electron density evaluated from VLF amplitude time delay during X-ray solar flares. *J. Atmos. Sol.-Terr. Phys.* **2007**, *69*, 775–792. [[CrossRef](#)]
57. Kolarski, A.; Grubor, D. Sensing the Earth's low ionosphere during solar flares using VLF signals and goes solar X-ray data. *Adv. Space Res.* **2014**, *53*, 1595–1602. [[CrossRef](#)]
58. Kolarski, A.; Srećković, V.A.; Mijić, Z.R. Monitoring solar activity during 23/24 solar cycle minimum through VLF radio signals. *Contrib. Astron. Obs. Skaln. Pleso* **2022**, *52*, 105. [[CrossRef](#)]
59. Šulić, D.; Srećković, V.A.; Mihajlov, A.A. A study of VLF signals variations associated with the changes of ionization level in the D-region in consequence of solar conditions. *Adv. Space Res.* **2016**, *57*, 1029–1043. [[CrossRef](#)]
60. Dorman, L.; Tassev, Y.; Velinov, P.I.Y.; Mishev, A.; Tomova, D.; Mateev, L. Investigation of exceptional solar activity in September 2017: GLE 72 and unusual Forbush decrease in GCR. *J. Phys. Conf. Ser.* **2019**, *1181*, 012070. [[CrossRef](#)]
61. Neutron Monitor Database. Available online: <https://www.nmdb.eu/> (accessed on 20 October 2022).
62. Kojima, H.; Shibata, S.; Oshima, A.; Hayashi, Y.; Antia, H.; Dugad, S.; Fujii, T.; Gupta, S.K.; Kawakami, S.; Minamino, M.; et al. Rigidity Dependence of Forbush Decreases. In *Proceedings of the 33rd International Cosmic Ray Conference, Rio de Janeiro, Brazil, 2–9 July 2013*.
63. Near-Earth Interplanetary Coronal Mass Ejections Since January 1996. Available online: <https://izw1.caltech.edu/ACE/ASC/DATA/level3/icmetable2.htm> (accessed on 15 October 2022).

64. Soho Lasco Cme Catalog Cdaw Data Center. Available online: https://cdaw.gsfc.nasa.gov/CME_list/ (accessed on 10 November 2022).
65. Scolini, C.; Chané, E.; Temmer, M.; Kilpua, E.K.J.; Dissauer, K.; Veronig, A.M.; Palmerio, E.; Pomoell, J.; Dumbović, M.; Guo, J.; et al. CME–CME Interactions as Sources of CME Geoeffectiveness: The Formation of the Complex Ejecta and Intense Geomagnetic Storm in 2017 Early September. *Astrophys. J. Suppl. Ser.* **2020**, *247*, 21. [[CrossRef](#)]
66. Badruddin, B.; Aslam, O.P.M.; Derouich, M.; Asiri, H.; Kudela, K. Forbush Decreases and Geomagnetic Storms During a Highly Disturbed Solar and Interplanetary Period, 4–10 September 2017. *Space Weather* **2019**, *17*, 487–496. [[CrossRef](#)]
67. Miteva, R.; Klein, K.L.; Malandraki, O.; Dorrian, G. Solar Energetic Particle Events in the 23rd Solar Cycle: Interplanetary Magnetic Field Configuration and Statistical Relationship with Flares and CMEs. *Sol. Phys.* **2013**, *282*, 579–613. [[CrossRef](#)]
68. Ravishankar, A.; Michałek, G. Non-interacting coronal mass ejections and solar energetic particles near the quadrature configuration of Solar TERrestrial RELations Observatory. *Astron. Astrophys.* **2020**, *638*, A42. [[CrossRef](#)]
69. Pandey, U.; Singh, B.; Singh, O.P.; Saraswat, V.K. Solar flare induced ionospheric D-region perturbation as observed at a low latitude station Agra, India. *Astrophys. Space Sci.* **2015**, *357*, 35. [[CrossRef](#)]
70. Gavrilov, B.G.; Ermak, V.M.; Lyakhov, A.N.; Poklad, Y.V.; Rybakov, V.A.; Ryakhovsky, I.A. Reconstruction of the Parameters of the Lower Midlatitude Ionosphere in M- and X-Class Solar Flares. *Geomagn. Aeron.* **2020**, *60*, 747–753. [[CrossRef](#)]
71. Venkatesham, K.; Singh, R. Extreme space-weather effect on D-region ionosphere in Indian low latitude region. *Curr. Sci.* **2018**, *114*, 1923–1926. [[CrossRef](#)]
72. Thomson, N.R.; Rodger, C.J.; Clilverd, M.A. Large solar flares and their ionospheric D region enhancements. *J. Geophys. Res. Space Phys.* **2005**, *110*. [[CrossRef](#)]
73. Grubor, D.; Šulić, D.; Žigman, V. The response of the Earth-ionosphere VLF waveguide to the January 15–22 2005 solar events. In Proceedings of the IUGG XXIV General Assembly, Perugia, Italy, 2–13 July 2007.
74. Kolarski, A.; Grubor, D. Monitoring VLF signal perturbations induced by solar activity during January 2005. In Proceedings of the The XIX Serbian Astronomical Conference, Belgrade, Serbia, 13–17 October 2020; pp. 387–390.
75. Kumar, S.; Kumar, A.; Menk, F.; Maurya, A.K.; Singh, R.; Veenadhari, B. Response of the low-latitude D region ionosphere to extreme space weather event of 14–16 December 2006. *J. Geophys. Res. Space Phys.* **2015**, *120*, 788–799. [[CrossRef](#)]
76. Tan, L.M.; Thu, N.N.; Ha, T.Q.; Marbouti, M. Study of solar flare induced D-region ionosphere changes using VLF amplitude observations at a low latitude site. *Indian J. Radio Space Phys.* **2014**, *43*, 197–246.
77. McRae, W.M.; Thomson, N.R. Solar flare induced ionospheric D-region enhancements from VLF phase and amplitude observations. *J. Atmos. Sol.-Terr. Phys.* **2004**, *66*, 77–87. [[CrossRef](#)]
78. Zhao, L.L.; Zhang, H. Transient galactic cosmic-ray modulation during solar cycle 24: A comparative study of two prominent forbush decrease events. *Astrophys. J.* **2016**, *827*, 13. [[CrossRef](#)]
79. Lingri, D.; Mavromichalaki, H.; Belov, A.; Eroshenko, E.; Yanke, V.; Abunin, A.; Abunina, M. Solar Activity Parameters and Associated Forbush Decreases During the Minimum between Cycles 23 and 24 and the Ascending Phase of Cycle 24. *Sol. Phys.* **2016**, *291*, 1025–1041. [[CrossRef](#)]

Disclaimer/Publisher’s Note: The statements, opinions and data contained in all publications are solely those of the individual author(s) and contributor(s) and not of MDPI and/or the editor(s). MDPI and/or the editor(s) disclaim responsibility for any injury to people or property resulting from any ideas, methods, instructions or products referred to in the content.

Multiple Coulomb scattering of muons in lithium hydride

M. Bogomilov,¹ R. Tsenov,¹ G. Vankova-Kirilova,¹ Y. P. Song,² J. Y. Tang,² Z. H. Li,³ R. Bertoni,⁴ M. Bonesini,⁴ F. Chignoli,⁴ R. Mazza,⁴ V. Palladino,⁵ A. de Bari,⁶ D. Orestano,⁷ L. Tortora,⁷ Y. Kuno,⁸ H. Sakamoto,⁸ A. Sato,⁸ S. Ishimoto,⁹ M. Chung,¹⁰ C. K. Sung,¹⁰ F. Filthaut,¹¹ M. Fedorov,¹² D. Jokovic,¹³ D. Maletic,¹³ M. Savic,¹³ N. Jovancevic,¹⁴ J. Nikolov,¹⁴ M. Vretenar,¹⁵ S. Ramberger,¹⁵ R. Asfandiyarov,¹⁶ A. Blondel,¹⁶ F. Drielsma,¹⁶ Y. Karadzhov,¹⁶ G. Charnley,¹⁷ N. Collomb,¹⁷ K. Dumbell,¹⁷ A. Gallagher,¹⁷ A. Grant,¹⁷ S. Griffiths,¹⁷ T. Hartnett,¹⁷ B. Martlew,¹⁷ A. Moss,¹⁷ A. Muir,¹⁷ I. Mullacrane,¹⁷ A. Oates,¹⁷ P. Owens,¹⁷ G. Stokes,¹⁷ P. Warburton,¹⁷ C. White,¹⁷ D. Adams,¹⁸ V. Bayliss,¹⁸ J. Boehm,¹⁸ T. W. Bradshaw,¹⁸ C. Brown,¹⁸ M. Courthold,¹⁸ J. Govans,¹⁸ M. Hills,¹⁸ J.-B. Lagrange,¹⁸ C. Macwaters,¹⁸ A. Nichols,¹⁸ R. Preece,¹⁸ S. Ricciardi,¹⁸ C. Rogers,¹⁸ T. Stanley,¹⁸ J. Tarrant,¹⁸ M. Tucker,¹⁸ S. Watson,¹⁸ A. Wilson,¹⁸ R. Bayes,¹⁹ J. C. Nugent,¹⁹ F. J. P. Soler,¹⁹ R. Gamet,²⁰ P. Cooke,²⁰ V. J. Blackmore,²¹ D. Colling,²¹ A. Dobbs,²¹ P. Dornan,²¹ P. Franchini,²¹ C. Hunt,²¹ P. B. Jurj,²¹ A. Kurup,²¹ K. Long,²¹ J. Martyniak,²¹ S. Middleton,²¹ J. Pasternak,²¹ M. A. Uchida,²¹ J. H. Cobb,²² C. N. Booth,²³ P. Hodgson,²³ J. Langlands,²³ E. Overton,²³ V. Pec,²³ P. J. Smith,²³ S. Wilbur,²³ G. T. Chatzitheodoridis,²⁴ A. J. Dick,²⁴ K. Ronald,²⁴ C. G. Whyte,²⁴ A. R. Young,²⁴ S. Boyd,²⁵ J. R. Greis,²⁵ T. Lord,²⁵ C. Pidcott,²⁵ I. Taylor,²⁵ M. Ellis,²⁶ R. B. S. Gardener,²⁶ P. Kyberd,²⁶ J. J. Nebrensky,²⁶ M. Palmer,²⁷ H. Witte,²⁷ D. Adey,²⁸ A. D. Bross,²⁸ D. Bowring,²⁸ P. Hanlet,²⁸ A. Liu,²⁸ D. Neuffer,²⁸ M. Popovic,²⁸ P. Rubinov,²⁸ A. DeMello,²⁹ S. Gourlay,²⁹ A. Lambert,²⁹ D. Li,²⁹ T. Luo,²⁹ S. Prestemon,²⁹ S. Virostek,²⁹ B. Freemire,³⁰ D. M. Kaplan,³⁰ T. A. Mohayai,³⁰ D. Rajaram,³⁰ P. Snopok,³⁰ Y. Torun,³⁰ L. M. Cremaldi,³¹ D. A. Sanders,³¹ D. J. Summers,³¹ L. R. Coney,³² G. G. Hanson,³² and C. Heidt³²

(MICE Collaboration)

¹*Department of Atomic Physics, St. Kliment Ohridski University of Sofia,
5 James Bourchier Blvd, Sofia, Bulgaria*

²*Institute of High Energy Physics, Chinese Academy of Sciences,
19 Yuquan Rd, Shijingshan District, Beijing, China*

³*Sichuan University, 252 Shuncheng St, Chengdu, China*

⁴*Sezione INFN Milano Bicocca and Dipartimento di Fisica G. Occhialini,
Piazza della Scienza 3, Milano, Italy*

⁵*Sezione INFN Napoli and Dipartimento di Fisica, Università Federico II,
Complesso Universitario di Monte S. Angelo, via Cintia, Napoli, Italy*

⁶*Sezione INFN Pavia and Dipartimento di Fisica, Università di Pavia, Via Agostino Bassi 6, Pavia, Italy*

⁷*Sezione INFN Roma Tre and Dipartimento di Matematica e Fisica, Università Roma Tre,
Via della Vasca Navale 84, Roma, Italy*

⁸*Osaka University, Graduate School of Science, Department of Physics, 1-1 Machikaneyamacho,
Toyonaka, Osaka, Japan*

⁹*High Energy Accelerator Research Organization (KEK), Institute of Particle and Nuclear Studies,
Tsukuba, Ibaraki, Japan*

¹⁰*Department of Physics, UNIST, 50 UNIST-gil, Ulsan, South Korea*

¹¹*NIKHEF, Science Park 105, Amsterdam, Netherlands*

¹²*Radboud University, Houtlaan 4, Nijmegen, Netherlands*

¹³*Institute of Physics, University of Belgrade, Serbia*

¹⁴*Faculty of Sciences, University of Novi Sad, Trg Dositeja Obradovića 3, Novi Sad, Serbia*

¹⁵*CERN, Esplanade des Particules 1, Geneva, Switzerland*

¹⁶*DPNC, Section de Physique, Université de Genève, 24 Quai Ernest-Ansermet, Geneva, Switzerland*

¹⁷*STFC Daresbury Laboratory, Keckwick Ln, Daresbury, Cheshire, United Kingdom*

¹⁸*STFC Rutherford Appleton Laboratory, Harwell Campus, Didcot, United Kingdom*

¹⁹*School of Physics and Astronomy, Kelvin Building, University of Glasgow, Glasgow, United Kingdom*

²⁰*Department of Physics, University of Liverpool, Oxford St, Liverpool, United Kingdom*

²¹*Department of Physics, Blackett Laboratory, Imperial College London,
Exhibition Road, London, United Kingdom*

²²*Department of Physics, University of Oxford,*

Denys Wilkinson Building, Keble Rd, Oxford, United Kingdom

²³*Department of Physics and Astronomy, University of Sheffield, Hounsfield Rd, Sheffield, United Kingdom*

²⁴*SUPA and the Department of Physics, University of Strathclyde,
107 Rottenrow, Glasgow, United Kingdom*

²⁵*Department of Physics, University of Warwick, Gibbet Hill Road, Coventry, United Kingdom*

²⁶*College of Engineering, Design and Physical Sciences, Brunel University, Kingston Lane, Uxbridge, United Kingdom*

²⁷*Brookhaven National Laboratory, 98 Rochester Street, Upton, New York, USA*

²⁸*Fermilab, Kirk Rd and Pine Street, Batavia, Illinois, USA*

²⁹*Lawrence Berkeley National Laboratory, 1 Cyclotron Road, Berkeley, California, USA*

³⁰*Illinois Institute of Technology, 10 West 35th Street, Chicago, Illinois, USA*

³¹*University of Mississippi, University Avenue, Oxford, Mississippi, USA*

³²*University of California, 900 University Avenue, Riverside, California, USA*

 (Received 21 September 2022; accepted 27 October 2022; published 14 November 2022)

Multiple Coulomb scattering (MCS) is a well-known phenomenon occurring when charged particles traverse materials. Measurements of muons traversing low Z materials made in the MuScat experiment showed that theoretical models and simulation codes, such as GEANT4 (v7.0), over-estimated the scattering. The Muon Ionization Cooling Experiment (MICE) measured the cooling of a muon beam traversing a liquid hydrogen or lithium hydride (LiH) energy absorber as part of a programme to develop muon accelerator facilities, such as a neutrino factory or a muon collider. The energy loss and MCS that occur in the absorber material are competing effects that alter the performance of the cooling channel. Therefore measurements of MCS are required in order to validate the simulations used to predict the cooling performance in future accelerator facilities. We report measurements made in the MICE apparatus of MCS using a LiH absorber and muons within the momentum range 160 to 245 MeV/ c . The measured RMS scattering width is about 9% smaller than that predicted by the approximate formula proposed by the Particle Data Group, but within the latter's stated uncertainty. Data at 172, 200 and 240 MeV/ c are compared to the GEANT4 (v9.6) default scattering model. These measurements show agreement with this more recent GEANT4 (v9.6) version over the range of incident muon momenta.

DOI: [10.1103/PhysRevD.106.092003](https://doi.org/10.1103/PhysRevD.106.092003)

I. INTRODUCTION

Multiple Coulomb scattering (MCS) describes the multiple interactions of charged particles in the Coulomb field of the nuclei and electrons of a material. Rossi and Greisen derived a simple expression for the root-mean-square (RMS) scattering angle in the small angle approximation [1] by integrating the Rutherford cross section [2]. The mean square scattering angle $\langle\theta^2\rangle$ after multiple collisions traversing a thickness dz of material can be expressed as a function of radiation length X_0

$$\frac{d\langle\theta^2\rangle}{dz} = \frac{E_s^2}{p^2\beta^2} \frac{1}{X_0}, \quad (1)$$

where $E_s = 21.2$ MeV/ c , p is the momentum of the charged particle and β its speed in units of the speed of light, c . The projection of the scattering angle onto a plane containing the incident track gives the RMS projected scattering angle $\theta_0 = \sqrt{\langle\theta^2/2\rangle}$ [3]

$$\theta_0 = \frac{14.85 \text{ MeV}/c}{p\beta} \sqrt{\frac{\Delta z}{X_0}}. \quad (2)$$

Molière [4,5] developed a theory of MCS based on the scattering of fast charged particles from atomic nuclei that showed good agreement with data. Bethe [6] improved the treatment by taking into account interactions with electrons within the atom. The theory was subsequently improved by Fano [7] to account for elastic and inelastic scattering.

Most of the models of MCS mentioned above reproduce data very well [8] for small angle scatters and when the atomic number, Z , of the target nuclei is large. Highland [9] compared the Molière theory with the simple formula by Rossi and Greisen Eq. (1), and found a distinct Z dependence of the value of E_s . As a consequence, Highland recommended that a logarithmic term be added to the Rossi-Greisen formula to improve the agreement with Molière's theory, especially at low Z such as for liquid hydrogen or lithium hydride. The formula for θ_0 , the RMS width of the Gaussian approximation for the central 98% of the projected scattering angle distribution on a plane, was reviewed by Lynch and Dahl [10] and is now recommended by the Particle Data Group [3] as

$$\theta_0 = \frac{13.6 \text{ MeV}/c}{p\beta} \sqrt{\frac{\Delta z}{X_0}} \left(1 + 0.038 \ln \frac{\Delta z}{X_0\beta^2} \right), \quad (3)$$

Published by the American Physical Society under the terms of the [Creative Commons Attribution 4.0 International license](https://creativecommons.org/licenses/by/4.0/). Further distribution of this work must maintain attribution to the author(s) and the published article's title, journal citation, and DOI. Funded by SCOAP³.

claimed to be accurate to 11% over the full range of values of Z .

Multiple scattering has not been well modeled for low Z materials in standard simulations. Data collected by the MuScat experiment [8] indicate that GEANT4 v7.0 [11] and the Molière model overestimate MCS for these materials. However, a simple Monte Carlo method, which samples the Wentzel scattering cross section [12] to generate the MCS distributions, was shown by Carlisle and Cobb in [13] to agree very well with muon scattering data from the MuScat experiment. Since the time of MuScat, GEANT4 has evolved through several versions and the comparison to data made in this analysis uses GEANT4 v9.6.

Emittance is a measure of the average spread of particle coordinates in position and momentum phase space and has dimensions of length times angle, e.g., mm · radians, usually written as just mm. The Muon Ionization Cooling Experiment (MICE) made measurements of emittance reduction in low Z absorbers, i.e., those materials that can be used to reduce muon-beam emittance via ionization cooling [14], thus providing the first observation of the ionization cooling process [15] that can be used to cool beams of muons for a neutrino factory [16] or a muon collider [17–20]. The normalized transverse emittance of the MICE muon beam [21] is reduced due to energy loss and increased by the scattering in the absorber material. The rate of change in the normalized emittance, ϵ_n , [14] is given by

$$\frac{d\epsilon_n}{dz} \approx -\frac{\epsilon_n}{p_\mu \beta} \left\langle \frac{dE_\mu}{dz} \right\rangle + \frac{\beta_\perp p_\mu}{2m_\mu} \frac{d\theta_0^2}{dz}, \quad (4)$$

where $\frac{dE_\mu}{dz}$ is the energy loss of muons per unit distance, m_μ the muon mass, p_μ the muon momentum and β_\perp the betatron function.

To make accurate predictions of the emittance in the absorber materials, the model in the simulation must be validated. This is particularly important for the prediction of the equilibrium emittance, the case when $d\epsilon_n/dz = 0$ and

$$\epsilon_n = \frac{\beta_\perp p_\mu^2 \beta}{2m_\mu} \frac{d\theta_0^2}{dz} \left\langle \frac{dE_\mu}{dz} \right\rangle^{-1}. \quad (5)$$

This provides the minimum emittance for which cooling is effective and is lowest for low Z absorbers. There is thus great interest in performing a detailed measurement of MCS of muons traversing low Z absorbers, such as liquid hydrogen or lithium hydride (LiH). Here, we report the first measurement of MCS of muons in lithium hydride in the muon momentum range 160 to 245 MeV/ c , using the MICE apparatus. Accurate MCS modeling will ensure design studies for future facilities are as informative as possible [22]. This paper is divided as follows: Sec. II outlines the MICE experiment, describes the analysis method and defines the relevant measurement angles, Sec. III describes the data collected and the event selection and Sec. IV describes the data deconvolution method and the multiple scattering results, with a final short conclusion in Sec. V.

II. METHOD

The MICE configuration for the MCS measurements presented here consisted of two scintillating fiber trackers, one upstream (US) and one downstream (DS) of a lithium hydride absorber. Each tracker contained five stations, each composed of three planes of scintillating fiber employing 120° stereo views, immersed in helium gas [23]. Thin aluminum windows separated the helium volume from the vacuum containing the absorber. The tracker position resolution was determined to be 470 μm [24]. The solenoid magnets surrounding the trackers were turned off for these measurements to allow straight-track reconstruction of the muons before and after the absorber.

The muon beam was generated by protons with a kinetic energy of 700 MeV at the STFC Rutherford Appleton Laboratory ISIS synchrotron facility [21,25] impinging on a titanium target [26,27]. The beam line is described in [21].

A schematic diagram of the MICE cooling channel and detectors is shown in Fig. 1. A time of flight (TOF) system, consisting of three detectors (TOF0 and TOF1 upstream and TOF2 downstream of the apparatus), was used to measure the momentum of reconstructed muons [28]. The Cherenkov detector, preshower system (KL) and electron-muon ranger (EMR) were used to confirm the TOF's particle identification performance [21,29,30]. The MICE coordinate system is defined with $+z$ pointing along the

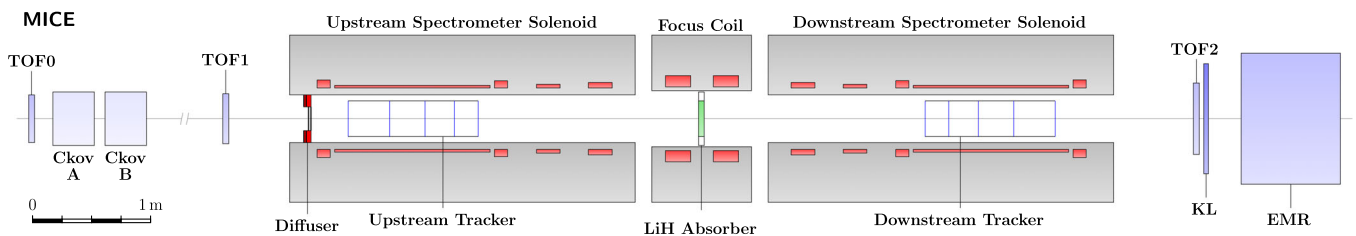


FIG. 1. Schematic of the MICE cooling channel. The spectrometer solenoids and focus coils were not powered during the measurements described here. A variable thickness diffuser upstream of the trackers was fully retracted during the measurements. Acronyms are defined in the text.

beam direction toward the downstream region, $+y$ pointing upward and $+x$ defined to be consistent with a right-handed coordinate system.

The MICE LiH absorber was a disk, 65.37 ± 0.02 mm thick (along the z -axis) and 550 mm in diameter. The absorber was coated with a thin parylene layer to prevent the ingress of water or oxygen. The composition of the LiH disk by weight was 81% ${}^6\text{Li}$, 4% ${}^7\text{Li}$ and 14% ${}^1\text{H}$ with some trace amounts of carbon, oxygen and calcium. The density of the disk was measured to be 0.6957 ± 0.0006 g/cm³, and the radiation length was calculated to be 70.38 g/cm².

Multiple scattering is characterized using either the three-dimensional (3D) angle between the initial and final momentum vectors, θ_{scatt} , or the 2D projected angle of scattering. The projected angles between the track vectors in the x - z (θ_Y) and y - z (θ_X) planes of the experimental coordinate system can be used, but these are only the true projected angles if the incident muon has no component of momentum in a direction perpendicular to these planes, i.e., the y or x direction respectively. To obtain the correct projected angle, a plane of projection must be defined for each incoming muon. The rotation calculated about an axis in the plane defined for each incoming muon is, to a very good approximation, the rotation around the specified axis. The precise definitions of θ_X and θ_Y are given in the Appendix.

Table I shows the expected RMS projected scattering angles, θ_0 , obtained using Eq. (3), for the LiH absorber and the material in each of the trackers. The number of radiation lengths traversed by a muon as it passes through the absorber was larger than that which it traversed as it passed through the trackers hence the majority of the scattering occurs in the absorber. Nevertheless the scattering in the trackers is significant and must be corrected for.

III. DATA SELECTION AND RECONSTRUCTION

A coincidence of two PMTs firing in TOF1 was used to trigger readout of the detector system including the trackers. The muon rate was such that only a single incident particle was observed in the apparatus per readout. Data reconstruction and simulation were carried out using MAUS

(MICE Analysis and User Software) v3.3.2 [31] (which uses GEANT4 v9.6.p02). Position and angle reconstruction was performed using data from the MICE trackers while momentum reconstruction was performed using data from the TOF detectors.

A. Position and angle reconstruction

Space points were created from the signals generated in the three scintillating fiber planes contained in a tracker station. Multiple space points that formed a straight line through the tracker were associated together. Space points that did not match a possible track were rejected. A Kalman filter [32] was used to provide an improved estimate of the track position and angle in each tracker at the plane nearest to the absorber.

An upstream track was required for the event to be considered for analysis, with a minimum of three space points among the five stations of the upstream tracker. No requirement was made on the presence of a downstream track. All scattering distributions were normalized to the number of upstream tracks selected in the analysis. The efficiency of the trackers has been shown to be very close to 100% [33].

A residual misalignment between the upstream and downstream trackers was corrected by rotating all upstream tracks by a fixed angle in the range 1–7 mrad. The final uncertainty in the rotation angles following the alignment procedure was 0.07 mrad.

B. Momentum reconstruction

Time of flight was used to measure the momentum of the muon at the absorber. Two time of flight measurements were used, designated as TOF01, the time of flight between TOF0 and TOF1, and TOF12, the time of flight between TOF1 and TOF2. The average momentum between time of flight detectors was calculated by evaluating

$$p = \frac{m_\mu c}{\sqrt{\frac{t_u^2}{t_e^2} - 1}} - \Delta p_{BB} - p_{MC}, \quad (6)$$

TABLE I. Material budget affecting particles passing through the MICE LiH absorber. The material thickness normalized by the radiation length is given with the RMS width of the scattering distribution calculated from the full PDG formula [3] in Eq. (3). Note that the thickness shown for the tracker materials (He, Al windows, and scintillating fibers) includes both trackers.

Material	z (cm)	z/X_0	ρ (g cm ⁻³)	θ_0 (mrad)		
				172 MeV/ c	200 MeV/ c	240 MeV/ c
Tracker He	226	0.00030	1.663×10^{-4}	1.09	0.91	0.73
Al Window	0.032	0.0036	2.699	4.31	3.58	2.89
Scintillating Fibers	1.48	0.036	1.06	14.9	12.4	10.0
Total Tracker		0.038		15.8	13.2	10.6
LiH	6.5	0.0641	0.6957	21.3	17.7	14.3
Total with LiH		0.1058		29.9	24.8	20.0

which assumes the mass of the electron to be ≈ 0 and where t_μ is the time of flight of the muon and t_e is the average time of flight of positrons ($t_e = 25.40$ ns for TOF01 and 27.38 ns for TOF12). Δp_{BB} was an additional term which accounted for the Bethe-Bloch most probable energy loss [34] of the muon as it passes through matter and was chosen to yield an optimal reconstructed momentum at the center of the absorber. When measuring the momentum using TOF01, accounting for the material upstream of the LiH absorber, Δp_{BB} was of order ~ 25 MeV/c (the correction varied as a function of muon momentum and was calculated separately for each selected sample of muons). p_{MC} accounted for the bias between the reconstructed and true momentum observed in the Monte Carlo (MC) simulation; this arises primarily due to the simplifying assumptions intrinsic to Eq. (6), e.g., that the path length between the TOF detectors can be approximated to the straight line on-axis distance between the two detectors when in fact the particle's trajectory may have curved through various magnetic fields or scattered in material. p_{MC} was used when calculating the momentum with both TOF01 and TOF12 and the correction, p_{MC} , was ~ 2 – 6 MeV/c. After correction, the reconstructed data were well described by the MC as shown in Fig. 2.

For muons reaching the end of the channel, the momentum measurement was made using TOF1 and TOF2. In this case the absorber sits near the midpoint between the detectors and the distance between them was larger than the distance between TOF0 and TOF1 which results in a slightly smaller uncertainty. In the selected samples, $\sim 90\%$ of muons reach TOF2. If no hit was recorded in TOF2, the momentum measurement was made using TOF0 and TOF1. The TOF01 distribution is shown in Fig. 3.

Characteristics of the time-of-flight samples selected using TOF01 are shown in Table II. The resolution of the TOF system was ≈ 70 ps which corresponds to ~ 4 – 10 MeV/c depending on the momentum setting. The agreement between the reconstructed momentum and the simulated true muon momentum at the center of the absorber is shown in Fig. 2(a) and a residual plot ($p_{\text{Reconstructed}} - p_{\text{Truth}}$) is shown in Fig. 2(b).

C. Data collection

Six datasets were collected during the ISIS user cycle 2015/04 using muon beams with a nominal 3 mm emittance, at three nominal momenta (172, 200 and 240 MeV/c). The three datasets collected with the LiH absorber in place are referred to as ‘LiH’ data while the three datasets with no absorber in place are referred to as ‘no absorber’ data. The beams typically had RMS widths of 30–36 mm and divergences of 9.0–9.4 mrad, after the selection described in Sec. III D. The no absorber datasets were used to determine the scattering attributable to the tracking detectors and thus to extract the true MCS distribution due to the LiH absorber. Two methods,

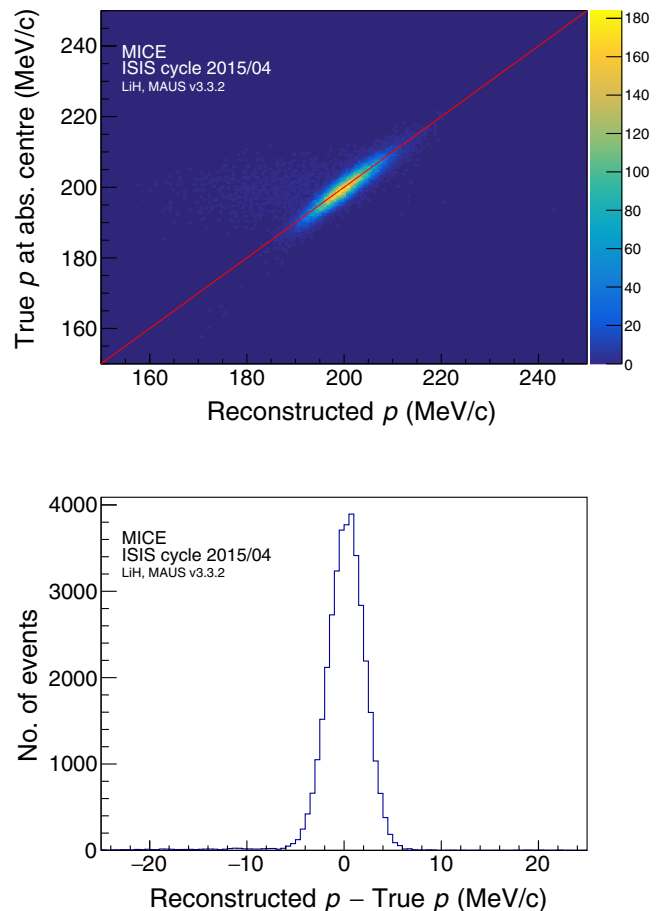


FIG. 2. Top: comparison of the reconstructed and true momentum for the MC sample, for the bin with average momentum 200 MeV/c. Bottom: residual between reconstructed and true momentum for the MC sample. The systematic error associated with the momentum reconstruction is discussed in Sec. IV D.

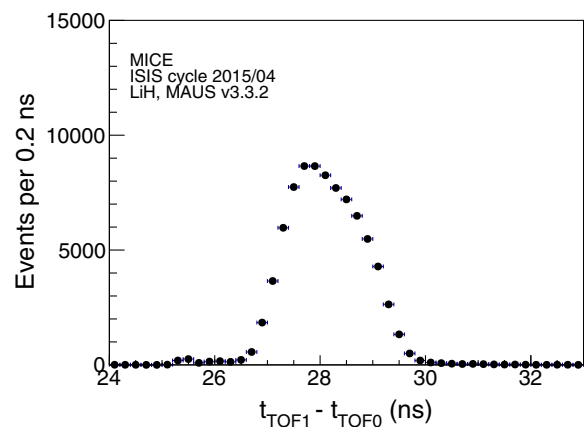


FIG. 3. Combined time-of-flight between TOF0 and TOF1 distribution of LiH data for all beam line settings after all selection cuts.

TABLE II. Characteristics of the samples selected for model comparison; the standard deviation of the reconstructed momenta are compared with the spread of true momenta of equivalent samples selected from the simulation.

Desired momentum (MeV/ <i>c</i>)	Lower TOF limit (ns)	Upper TOF limit (ns)	Measured $\langle p \rangle$ (MeV/ <i>c</i>)	Standard deviation (MeV/ <i>c</i>)	True MC momentum spread (MeV/ <i>c</i>)
172	28.60	28.80	171.55 ± 0.06	4.37 ± 0.06	4.82
200	27.89	28.09	199.93 ± 0.07	5.92 ± 0.05	5.97
240	27.16	27.36	239.76 ± 0.13	8.95 ± 0.09	8.21

TABLE III. Particle selection criteria and survival rates for the muon sample with a LiH absorber.

Selection	Description	Fraction events surviving each cut
Upstream track selection	Exactly one TOF0 space point, exactly one TOF1 space point and one upstream track.	100.0%
Diffuser cut	Upstream tracks were projected to the diffuser position. Any track outside the radius of the diffuser aperture was rejected.	81.7%
Fiducial selection	Upstream tracks, when projected to the far end of the downstream tracker, have a projected distance from axis less than 90 mm.	3.7%

described in Sec. IV, were used. Positively charged muon beams were used to minimize pion contamination, which was measured to be less than 1.4% [29]. Positron contamination was identified and rejected using the time-of-flight system.

D. Event selection

The data from the three nominal muon beams were merged into one sample and all muons in the sample were treated identically. Unbiased scattering distributions were selected from the data samples using the cuts listed in Table III. The fraction of events selected by each cut is also shown. Events that produced one space point in TOF0 and one space point in TOF1 were selected. A beam diffuser, otherwise used to increase the beam emittance, was fully retracted for all of the runs used in this analysis. A fraction of the muon beam traversed the diffuser ring in its retracted position, adding additional energy loss. Any upstream tracks that traversed the outer ring of the diffuser were removed.

A fiducial selection to ensure that the unscattered downstream track was likely to have been within the volume of the downstream tracker was also applied. If the upstream track, when projected to the downstream end of the downstream tracker, passed outside of the fiducial radius $r_0 = 90$ mm the track was rejected.

Finally, particles with a time of flight between stations TOF0 and TOF1 compatible with the passage of a muon (above 26 ns) were selected. The data were then binned in 200 ps Δt_{01} bins (Fig. 3) to yield eleven quasi-monochromatic samples. Most positrons, which had a TOF between 25 and 26 ns, were excluded by this binning. Three of these samples, with mean momentum of 172, 200

TABLE IV. Sample size after selection.

Absorber	p (MeV/ <i>c</i>)	No. of events US	No. of events DS
LiH	172	6479	5906
	200	8589	8112
	240	5612	5445
No Absorber	172	1500	1469
	200	2025	1995
	240	1394	1378

and 240 MeV/*c* and containing 0.19, 0.25 and 0.19% of the total number of events respectively, were compared to the GEANT4 and Molière models. The sample at 172 MeV/*c* enabled comparison with MuScat while samples at 200 and 240 MeV/*c* were of interest for the MICE experiment. The selected sample sizes are shown in Table IV.

E. Acceptance correction

The simulated geometric acceptance of the downstream tracker as a function of the projected scattering angles θ_x and θ_y is shown in Fig. 4. The acceptance depends on the scattering angle so the scattering angle distributions must be corrected by the acceptance determined from simulation. The acceptance data were fitted by a seventh order polynomial,

$$\epsilon = a + b\theta_i^2 + c\theta_i^4 + d\theta_i^6 + e\theta_i^7,$$

where i is the bin number and a , b , c , d and e are fit parameters. This smoothed fluctuations in the tails of the acceptance function.

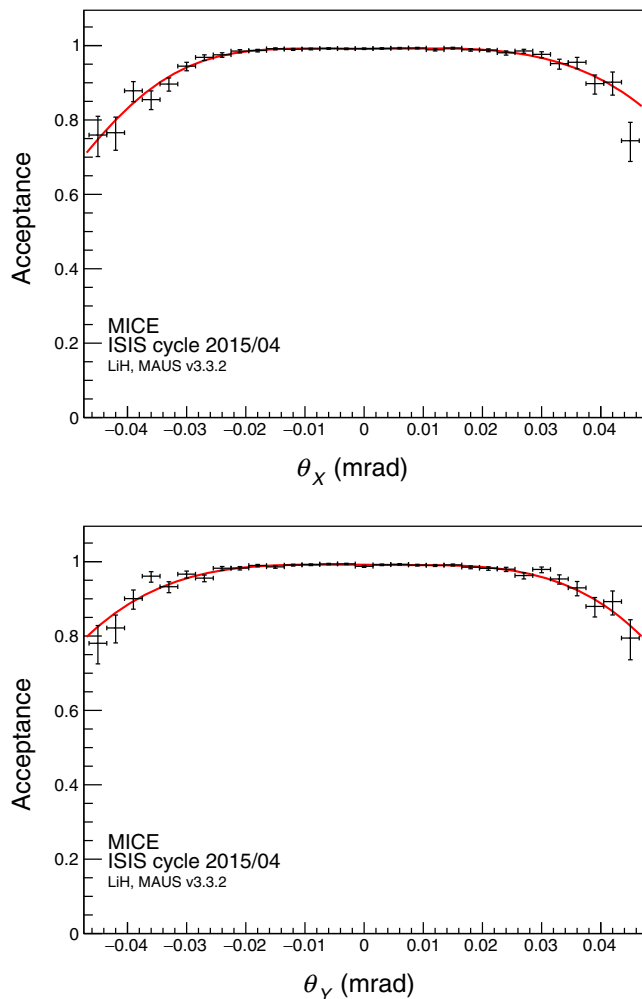


FIG. 4. The simulated fraction of events reconstructed by the trackers as a function of scattering angle after event selection. The red curve is an asymmetric seventh order polynomial fitted to the points and used for the acceptance correction.

F. Comparison to simulation

The MICE MC simulation models particles arising from protons incident on the target. G4beamline [35] was used to simulate particles from immediately after the target to just upstream of TOF0. The remainder of MICE, including

the downstream portion of the beam line and cooling channel, was simulated using MAUS [31]. The simulation is handled in this way to reduce the computing resources required, as only a small subset of particles at the target is transported to the end of the cooling channel.

A comparison between the momentum distributions for reconstructed MC and data for the selected samples at three momenta (172, 200 and 240 MeV/c) is shown in Fig. 5. The measured distributions of x and y positions and slopes for the selected upstream muon samples are well described by the GEANT4 (v9.6) MC, as illustrated in Fig. 6. All MC scattering distributions include both statistical and systematic errors.

IV. RESULTS

A. Raw data MC comparison

The θ_x and θ_y distributions from the LiH and no absorber data are compared to GEANT4 (v9.6) simulations in Figs. 7–9 and the θ_{Scatt}^2 distribution in Fig. 10, at three momenta: 172, 200 and 240 MeV/c. The simulation gives an adequate description of the data; a summary of the comparison given in Table V. The integrals of these distributions are between 88% and 96% demonstrating that the selection criteria ensure high transmission for the selected sample. In this analysis GEANT4 (v9.6) is used with the QGSP_BERT (v4.0) physics list. In this configuration, multiple Coulomb scattering is modelled by the G4WentzelVI model [36,37]. The G4WentzelVI model is a mixed algorithm simulating both the hard collisions one by one and using a multiple scattering theory to treat the effects of the soft collisions at the end of a given step; this prevents the number of steps in the simulation from becoming too large and also reduces the dependence on the step length. This model is expected to provide results similar in accuracy to single scattering but in a computationally efficient manner. Single scattering is based on the assumption that the effect of multiple scattering can be modeled as if the hard scatters are the sum of many individual scatters while soft scatters are sampled from a distribution. “Hard” scatters are inelastic and result in large-angle deflections and large energy transfers. “Soft” scatters

TABLE V. Distribution widths of multiple scattering in lithium hydride and the χ^2 comparisons between data and the GEANT4 simulation. The χ^2/NDF were calculated using the number of bins as the number of degrees of freedom. Statistical and systematic uncertainties are given for the data distributions. Only statistical uncertainties are given for the model.

p (MeV/c)	Angle	θ_{Data} (mrad)	θ_{G4} (mrad)	χ^2/NDF	P-value
171.55	θ_x	$21.16 \pm 0.28 \pm 0.48$	21.87 ± 0.25	23.67/31	0.79
171.55	θ_y	$20.97 \pm 0.27 \pm 0.48$	21.51 ± 0.25	37.86/31	0.15
199.93	θ_x	$18.38 \pm 0.18 \pm 0.33$	18.76 ± 0.09	17.75/31	0.96
199.93	θ_y	$18.35 \pm 0.18 \pm 0.33$	18.89 ± 0.09	27.93/31	0.57
239.76	θ_x	$15.05 \pm 0.17 \pm 0.21$	15.69 ± 0.06	8.07/31	1.00
239.76	θ_y	$15.03 \pm 0.16 \pm 0.21$	15.55 ± 0.06	8.23/31	1.00

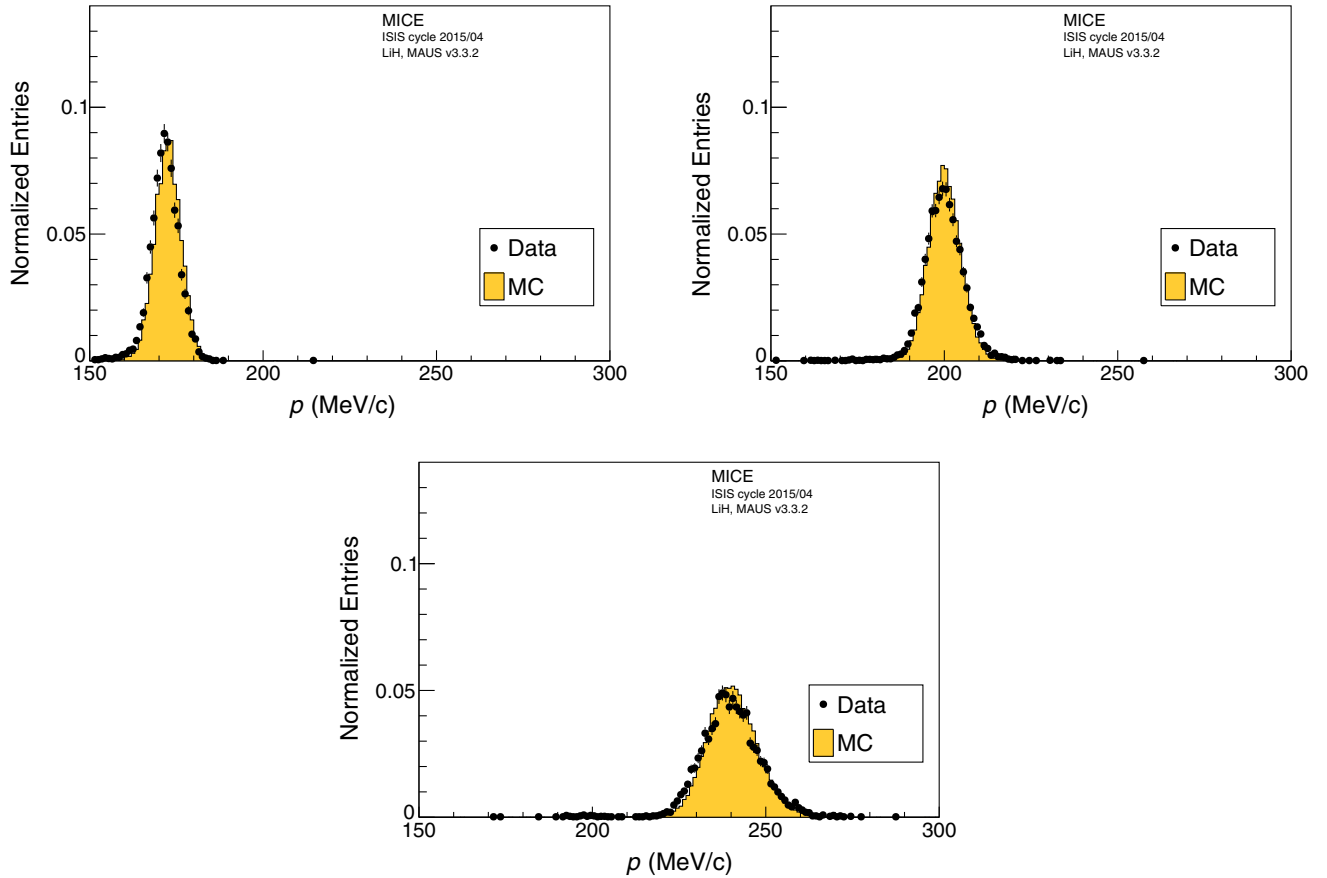


FIG. 5. Comparison of reconstructed muon momentum at the center of the absorber for the 172, 200 and 240 MeV/ c samples for data and simulation.

are elastic and result in small-angle deflections with small energy transfers.

B. Convolution with scattering models

The data collected with the absorber were compared to GEANT4 and the Molière scattering models by performing a convolution of the scattering model with no absorber data. The convolution,

$$n_{\text{conv}}(\theta) = n_{\text{NA}}(\theta) * n_{\text{model}}(\theta), \quad (7)$$

where $n_{\text{conv}}(\theta)$ is the forward convolved distribution, $n_{\text{NA}}(\theta)$ is the scattering distribution measured with the no absorber data and $n_{\text{model}}(\theta)$ is the scattering distribution predicted by the model, is performed by adding an angle sampled from the predicted scattering distribution in the absorber for a given model (GEANT4 or Molière) to the angle determined from a given trajectory selected from the no absorber data. This takes into account scattering in the measurement system. The trajectories described by the sum of angles are extrapolated to the downstream tracker and if the track would not have been contained within the downstream tracker then it is not shown in the scattering distribution but the event is still counted in the

normalization. The net effect is a distribution, $n_{\text{conv}}(\theta)$, that is the convolution of the raw scattering model $n_{\text{model}}(\theta)$ with the detector effects given by the no absorber distribution $n_{\text{NA}}(\theta)$. Plots of the lithium hydride absorber data and the no absorber data convolved with either the GEANT4 simulation or the Molière model are shown in Fig. 11, with the residuals shown in Fig. 12, and the results are summarized in Table VI.

The Molière distributions for the lithium hydride absorber were calculated using the procedure described by Gottschalk [38] for mixtures and compounds. Pure ${}^6\text{LiH}$ with a thickness of 4.498 g cm^{-2} was assumed. Distributions were calculated for monoenergetic muons of 172, 200 and 240 MeV/ c . Because the muon energy loss is small—about 11 MeV—the muon momentum was taken to be constant through the absorber.

Fano's correction to the Molière distribution was used to account for the scattering by atomic electrons. The values of the parameter U_{in} , which appears in the correction, were $-U_{\text{in}} = 3.6$ for hydrogen, as calculated exactly by Fano, and $-U_{\text{in}} = 5.0$ for lithium as suggested by Gottschalk for other materials.

A cubic spline was used to interpolate between the tabulated points of the functions given by Molière and

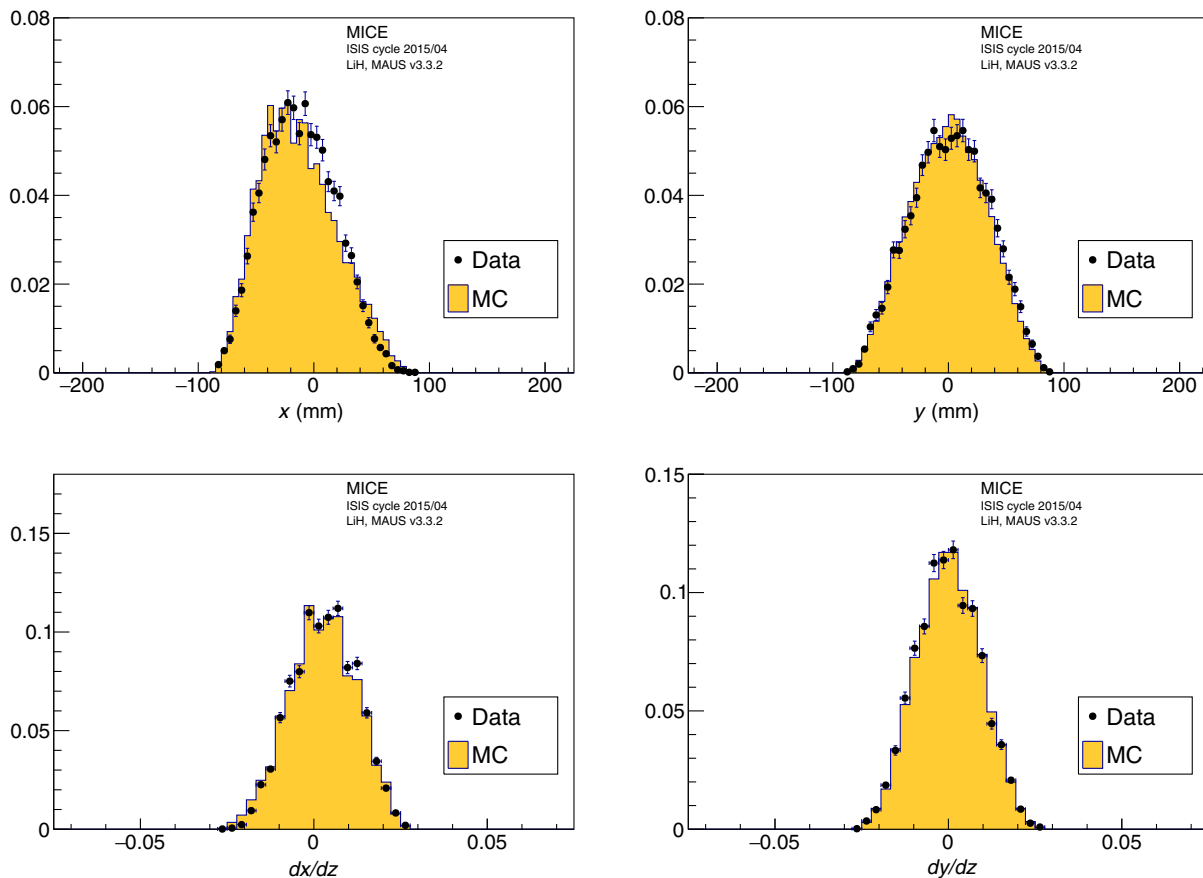


FIG. 6. Comparison between Monte Carlo simulations and data for muons in the 200 MeV/ c sample with the LiH absorber installed. All distributions are for the selected muons at the upstream reference plane. Top left: x distribution, top right: y distribution, bottom left: dx/dz distribution and bottom right: dy/dz distribution.

TABLE VI. Distribution widths of multiple scattering in lithium hydride data compared to no absorber data convolved with two different models of scattering (GEANT4 and Molière). The χ^2/NDF were calculated using the number of bins as the number of degrees of freedom. Statistical and systematic uncertainties are given for the data distributions.

p (MeV/ c)	Angle	θ_{Data} (mrad)	θ_{G4} (mrad)	χ^2/NDF	P-value	θ_{Mol} (mrad)	χ^2/NDF	P-value
171.55	θ_X	$21.16 \pm 0.28 \pm 0.48$	21.36 ± 0.05	30.29/31	0.45	22.64 ± 0.06	34.72/31	0.25
171.55	θ_Y	$20.97 \pm 0.27 \pm 0.48$	21.32 ± 0.05	29.10/31	0.51	22.58 ± 0.06	41.14/31	0.08
199.93	θ_X	$18.38 \pm 0.18 \pm 0.33$	18.09 ± 0.03	21.78/31	0.86	19.00 ± 0.04	28.04/31	0.57
199.93	θ_Y	$18.35 \pm 0.18 \pm 0.33$	18.02 ± 0.03	26.98/31	0.62	18.98 ± 0.04	35.41/31	0.23
239.76	θ_X	$15.05 \pm 0.17 \pm 0.21$	15.07 ± 0.02	4.08/31	1.00	15.62 ± 0.02	9.48/31	1.00
239.76	θ_Y	$15.03 \pm 0.16 \pm 0.21$	15.11 ± 0.02	3.44/31	1.00	15.70 ± 0.02	8.62/31	1.00

Bethe. Systematic errors in the calculation arising from, for example, the description of the absorber as pure ${}^6\text{LiH}$ were estimated to be of the order of one percent.

The calculated widths, θ_m , of the central Gaussian term of the projected Molière distributions are given in Table VII. If scattering by electrons is not included, i.e., Fano's electron correction is set to zero, the distributions are approximately twenty percent narrower. We note that Bethe's *ansatz* $Z^2 \rightarrow Z(Z+1)$ [6] to describe

the electron contribution is inappropriate here because the maximum kinematically allowed scattering angle of a 200 MeV/ c muon by an electron is of the order of 4 milliradians, much less than the width of the scattering distribution. The Molière predictions shown in Table VII differ from those shown in Table VI as these are the predictions solely from the Molière calculation not the Molière prediction convolved with MICE no absorber scattering data.

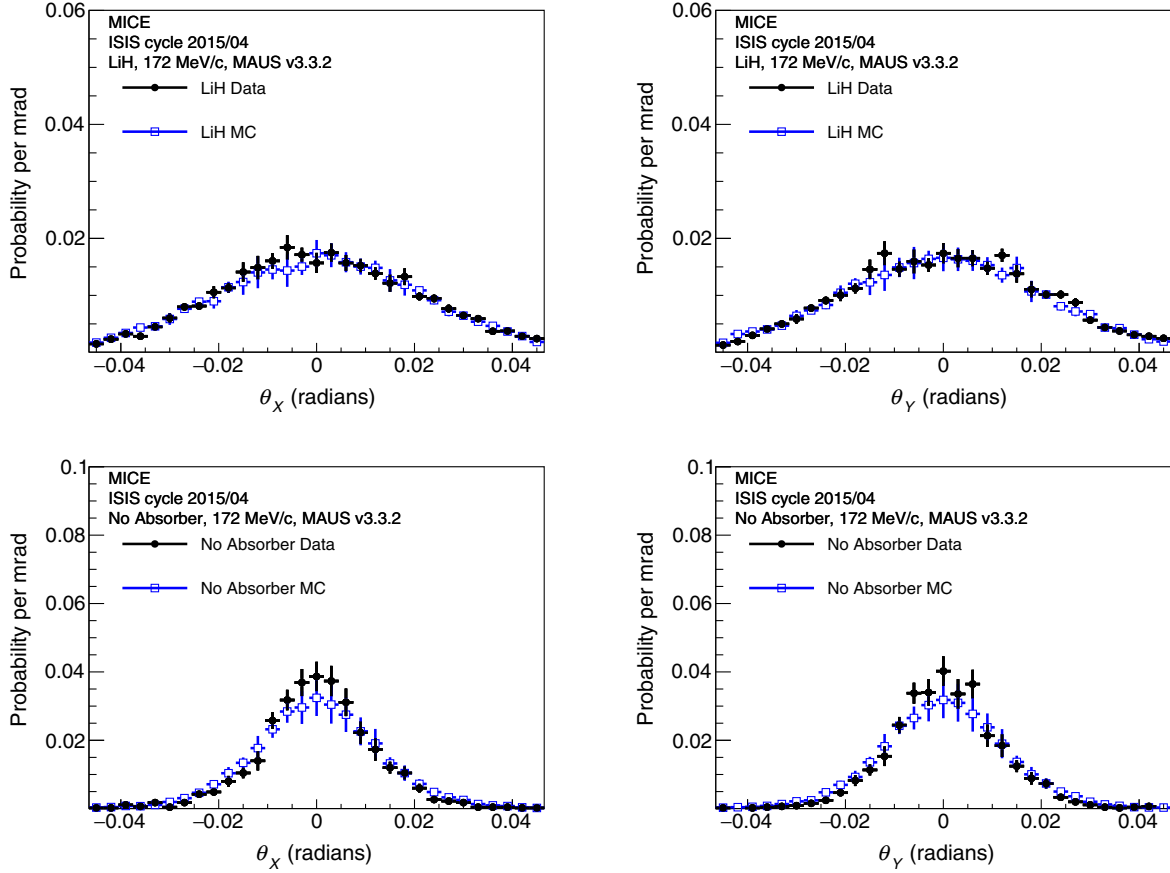


FIG. 7. Scattering probability functions θ_x and θ_y reconstructed from the 172 MeV/c muon beam with (top) and without (bottom) the LiH absorber in place compared to reconstructed MC scattering distributions. The black points are the real data and the blue open squares are the simulated data.

TABLE VII. Calculated widths, θ_m , of the central Gaussian term of the projected Molière distribution for the lithium hydride absorber at each selected muon momentum.

Momentum MeV/c	θ_m milliradians
172	20.03
200	16.87
240	13.60

C. Deconvolution

To determine the underlying scattering distribution in the absorber, the effects of scattering in nonabsorber materials and the detector resolution must be deconvolved from the measured scattering distribution. The measured scattering distribution with the absorber in the MICE channel can be written

$$s'(i) = A(i) \sum_{k=0}^{k=31} s(k) (h(i-k)/A(i-k)), \quad (8)$$

where $s'(i)$ is the number of events measured in the i th bin with the absorber in the channel, $s(k)$ is the scattering

distribution due only to the absorber material without the detector, $h(i-k)$ is the no absorber scattering distribution which includes the detector resolution and $A(i)$ is the acceptance function at bin (i). This system of linear equations can be written in matrix form as

$$\vec{s}' = \mathbf{H}\vec{s} \quad (9)$$

where \vec{s}' is the a vector where each entry is the number of events in a bin of the scattering distribution of all material in the channel. Similarly for \vec{s} but for a scattering distribution of only the absorber and \mathbf{H} is a matrix which transforms one to the other. The unfolding step employs Gold's [39] deconvolution algorithm to extract the true scattering distribution (s) solely due to the absorber material, as described in [40] and implemented in the ROOT [41] TSpectrum class. The advantages of using the Gold deconvolution algorithm are that it does not rely on simulated data or scattering models and is a purely data-driven technique making use of all of the data collected. The output of the deconvolution is compared to the GEANT4 and Molière prediction in Fig. 13.

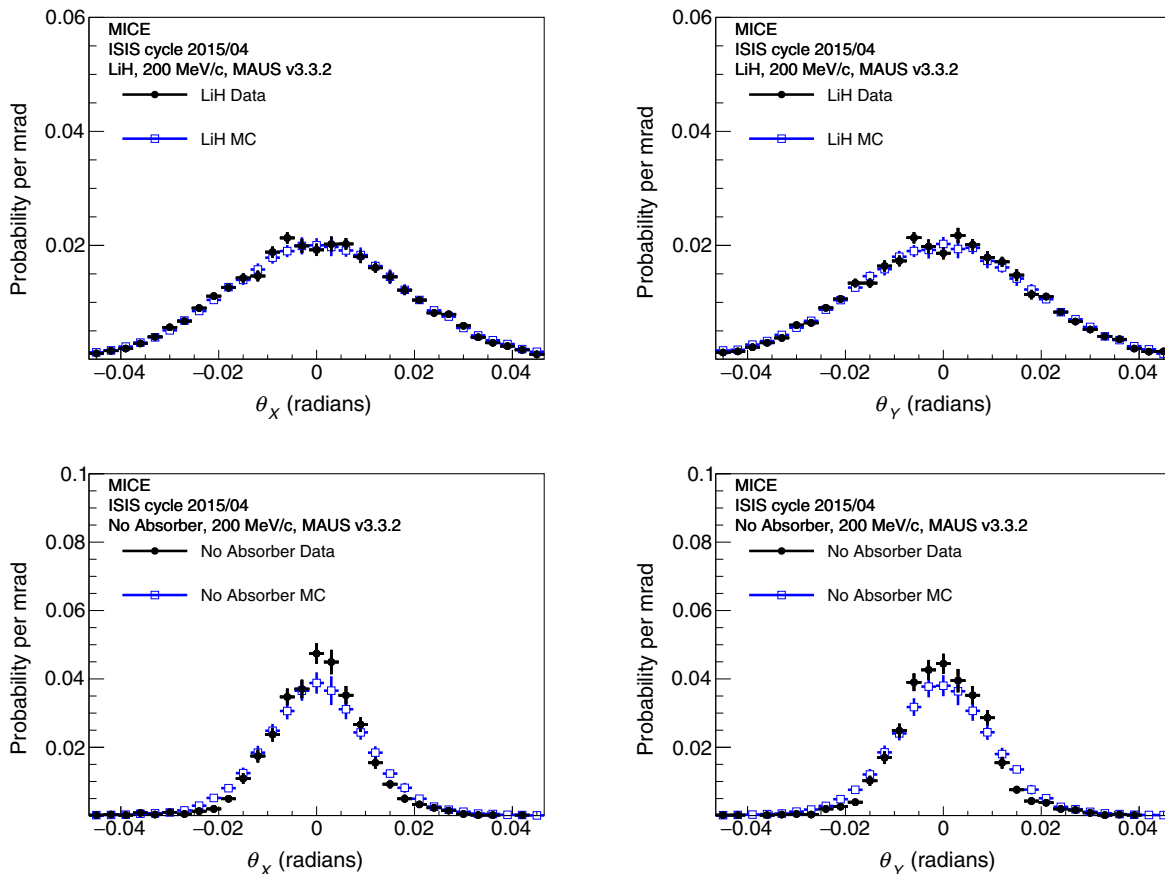


FIG. 8. Scattering probability functions θ_x and θ_y reconstructed from the 200 MeV/c muon beam with (top) and without (bottom) the LiH absorber in place compared to reconstructed MC scattering distributions. The black points are the real data and the blue open squares are the simulated data.

D. Systematic uncertainties

Six contributions to the systematic uncertainty in the scattering distributions are considered here; uncertainties in the time of flight; measured alignment; fiducial radius; choice of plane in which to measure scattering; effect of pion contamination; and in the deconvolution procedure. To calculate the systematic uncertainty for the individual bins of the scattering plots shown in Figs. 7–10 and 13 the numerical derivative is calculated with the expression

$$\sigma_{\text{sys},i} = \frac{dn_i}{d\alpha} \sigma_\alpha \approx \frac{\Delta n_i}{\Delta \alpha} \sigma_\alpha, \quad (10)$$

where Δn_i is the change in the number of entries in a bin that results from altering a parameter α with a known uncertainty σ_α in the analysis or simulation by an amount $\Delta \alpha$. The uncertainty in the measured width of the distribution is calculated in a similar way using

$$\sigma_{\text{sys}} \approx \frac{\Delta \theta_0}{\Delta \alpha} \sigma_\alpha, \quad (11)$$

where $\Delta \theta_0$ is the change in the width of the scattering distribution when measured in either the x or y projection. The systematic uncertainties are reported for the RMS width of the θ_x distribution ($\theta_{0,x}$) and the width of the θ_y distribution ($\theta_{0,y}$) separately.

A significant systematic uncertainty is due to the TOF selection criteria which directly impact the momentum range of the particles used in the scattering measurement. The scale is set using the measured 70 ps uncertainty on the time-of-flight measurement. The effect of particles incorrectly appearing inside or outside of the 200 ps bin selection window is determined by offsetting the no absorber data by 200 ps and the change in the measured scattering width is treated as the systematic uncertainty.

Uncertainties in the alignment have a direct effect on the angles measured by the tracker. The alignment of the MICE trackers is characterized by offsets parallel to x and y , with an uncertainty of 0.2 mm, and angles of rotation about the x and y axes, with an uncertainty of 0.07 mrad. The uncertainties in the width of the scattering distributions were extracted from a number of pseudo-experiments, where the alignment parameters were varied in each iteration.

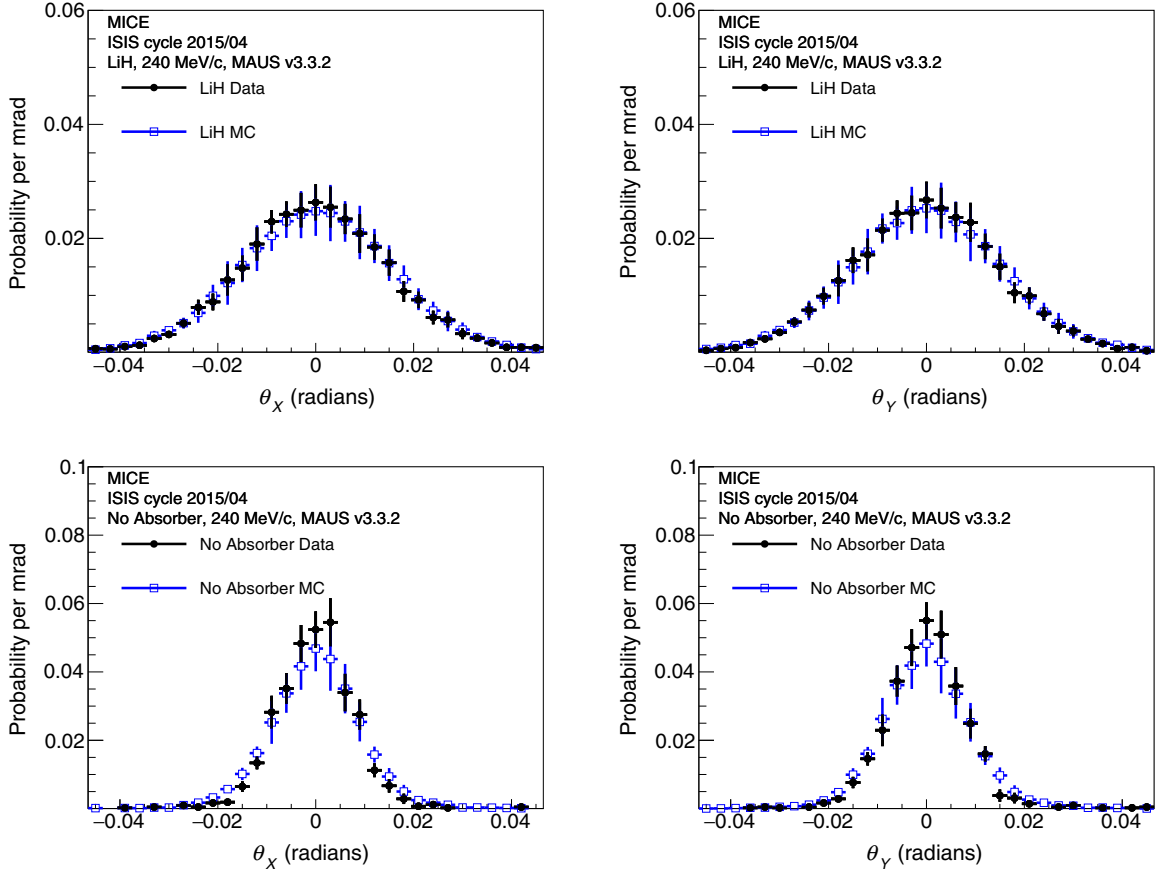


FIG. 9. Scattering probability functions θ_x and θ_y reconstructed from the 240 MeV/c muon beam with (top) and without (bottom) the LiH absorber in place compared to reconstructed MC scattering distributions. The black points are the real data and the blue open squares are the simulated data.

The choice of the fiducial region may systematically affect the results. A scan over the possible values of the fiducial radius was completed and the variation in the width of the scattering distributions for samples adjacent to the selected value of 90 mm was used to set the uncertainty.

The definitions of the scattering angles are given in Sec. II and the Appendix. In the definition of the projected scattering angles, θ_x and θ_y , $\hat{\mathbf{v}}$ is the unit vector mutually orthogonal to the y direction and the momentum vector and $\hat{\mathbf{u}}$ is the unit vector parallel to the upstream momentum vector. They are related via the formula

$$\hat{\mathbf{v}} = \hat{\mathbf{s}} \times \hat{\mathbf{u}}, \quad (12)$$

where $\hat{\mathbf{s}}$ is arbitrarily defined as $\hat{\mathbf{s}} = (0, -1, 0)$. This expression defines a direction perpendicular to a plane containing the upstream track. There are an infinite number of planes that contain this track, so we consider the uncertainty introduced by the definition of $\hat{\mathbf{s}}$ by rotating it between 0° and 180° , in increments of 1° , around the x -axis, with the analysis repeated after each increment. The

resulting maximum change in measured scattering angle is included in the systematic uncertainties in Table VIII.

The MICE muon beam has pion contamination with an upper limit $f_\pi < 1.4\%$ at 90% C.L. [29]. To measure the effect of this contamination on the scattering measurement for muons, a Monte Carlo study was performed. The measurement was simulated with the MICE beam, including simulated impurities, and a pure muon sample, with the systematic error being the difference between the two results.

The difference between the deconvolved result and the true scattering distribution from a GEANT4 simulation was taken to be an additional source of systematic error. This accounts for any bias introduced by the Gold deconvolution procedure. The systematic uncertainties for the deconvolution procedure showed significant variation from bin to bin so a parabolic smoothing function was used to assign the systematic uncertainty to each bin.

All systematic uncertainties, and their quadratic combination, for the three selected momenta of 172, 200 and 240 MeV/c are included in Table VIII. The dominant systematic uncertainties are those in the momentum scale of the TOF system and the deconvolution procedure.

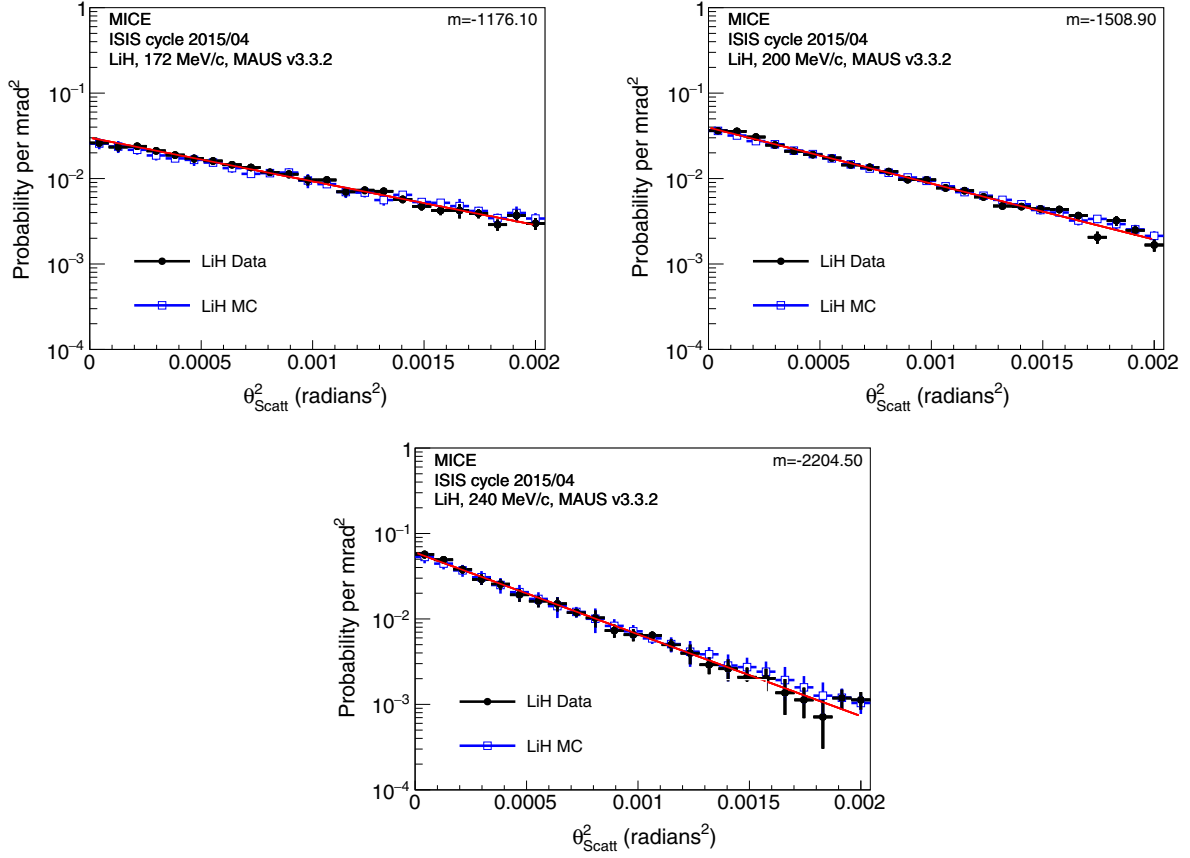


FIG. 10. θ_{Scatt}^2 distributions reconstructed from the 172, 200 and 240 MeV/c muon samples. The LiH absorber was in the beamline in these samples. The black points are the real data and the blue open squares are the reconstructed simulated data. A function $Ae^{-m\theta_{\text{Scatt}}^2}$ was fitted to the data distribution and is shown by the red line with m displayed on the plot.

E. Model comparisons

The residual between the scattering distribution in data and that predicted by the models is used to quantify the level of agreement between data and simulation. The normalized residual is defined as

$$\text{residual} = \frac{p_{\text{data}}(\theta_i) - p_{\text{simulation}}(\theta_i)}{\sqrt{\sigma_{\text{stat}}^2 + \sum \sigma_{\text{sys},i}^2}} \quad (13)$$

where $p_{\text{data}}(\theta_i)$ is the probability of scattering at angle θ_i measured with the MICE data and $p_{\text{simulation}}(\theta_i)$ is the probability of scattering predicted by the corresponding model. The systematic uncertainties $\sigma_{\text{sys},i}^2$, discussed in Sec. IV D, are calculated and summed in quadrature on a bin by bin level. The χ^2 derived from these residuals appears in Table V. The χ^2 between the scattering distribution from the data and that predicted by the model is calculated using

$$\chi^2 = \sum_{i=0}^N \frac{(p_{\text{data}}(\theta_i) - p_{\text{simulation}}(\theta_i))^2}{\sigma_{\text{stat}}^2 + \sum_{\text{sys}} \sigma_{\text{sys},i}^2} \quad (14)$$

where N is the number of bins and sys is the number of systematic errors. The χ^2 was calculated using 31 data points and demonstrates good agreement between data and MC. The χ^2 calculation in Eq. (14) was repeated for both the forward convolution comparison to real data and for the comparison between the deconvolved data and the GEANT4 and Molière models. The systematic uncertainties are added on a bin by bin basis in the calculation of the χ^2 in Eq. (14).

There is very little difference between the GEANT4 simulation, the Molière calculations and the deconvolved data. The deconvolved θ_X and θ_Y multiple scattering distributions on lithium hydride for the 172, 200 and 240 MeV/c muon samples are shown in Fig. 13, and these are compared with a GEANT4 LiH simulation and the Molière calculation.

The distributions of the projections in θ_X and θ_Y were characterized using a Gaussian fit within a ± 45 mrad range, with the results shown in Table IX for deconvolved data using the Gold deconvolution algorithm and the true distributions extracted from the GEANT4 simulation and the Molière model calculation. The table shows that the deconvolved θ_X and θ_Y projections of the scattering

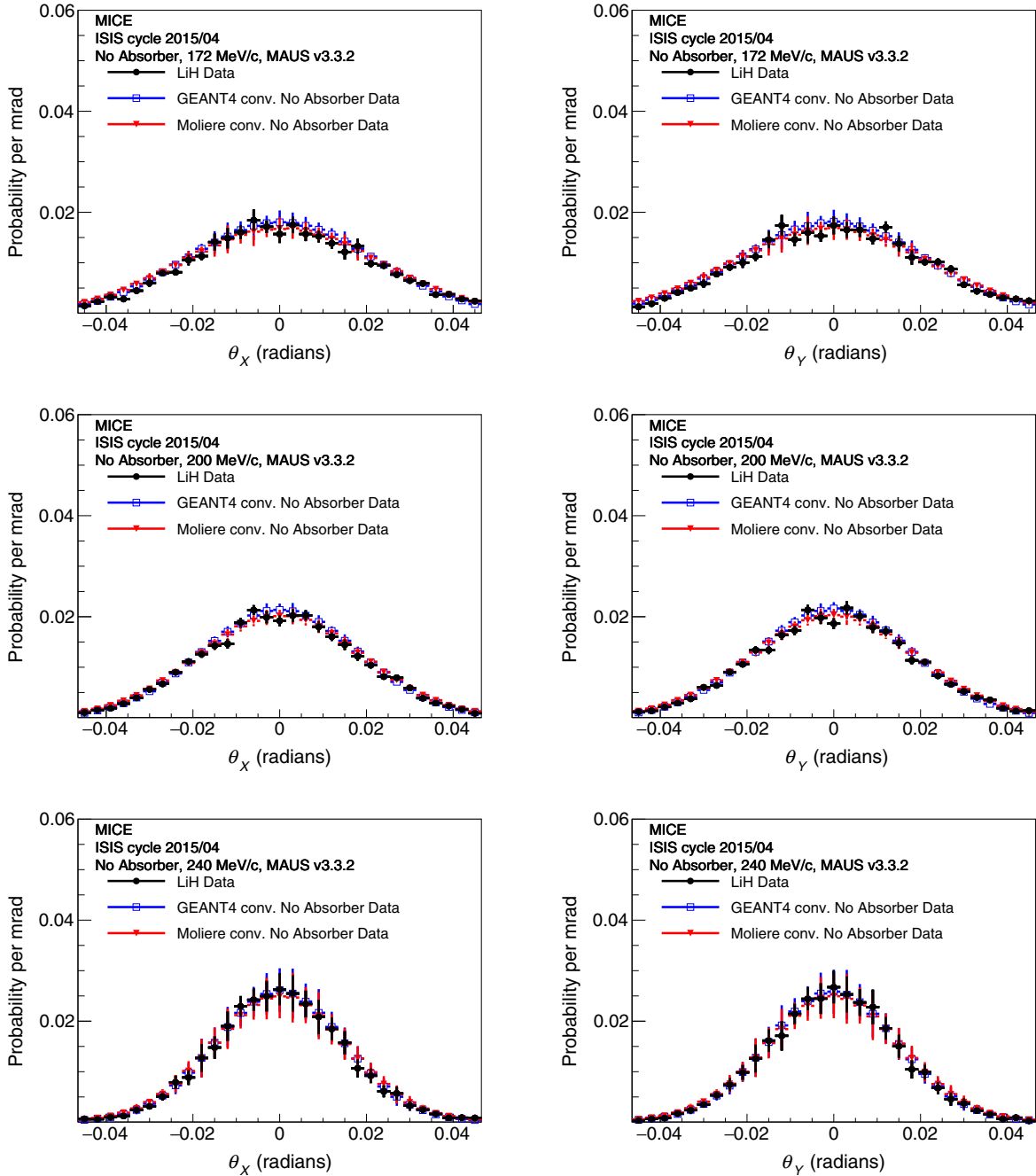


FIG. 11. Scattering probability functions reconstructed from the 172, 200 and 240 MeV/c muon beams with the LiH absorber in place (black dots) compared to the GEANT4 scattering model (blue dots) and the Molière model (red dots) in LiH convolved with the no absorber distribution.

distributions are approximately consistent with the GEANT4 and Molière distributions, but the Molière distribution is systematically wider than the rest and significantly wider than that given by GEANT4.

F. Momentum-dependent measurements

The selected samples are plotted as a function of mean momentum for each sample, to confirm the dependence of

the widths of the scattering distributions on momentum. The number of events contained in each TOF bin is between 3500 and 9000 events. The deconvolved scattering widths as a function of momentum are shown in Fig. 14. The widths, θ_0 , are fitted to

$$\theta_0 = \frac{13.6 [\text{MeV}/c]a}{p\beta}, \quad (15)$$

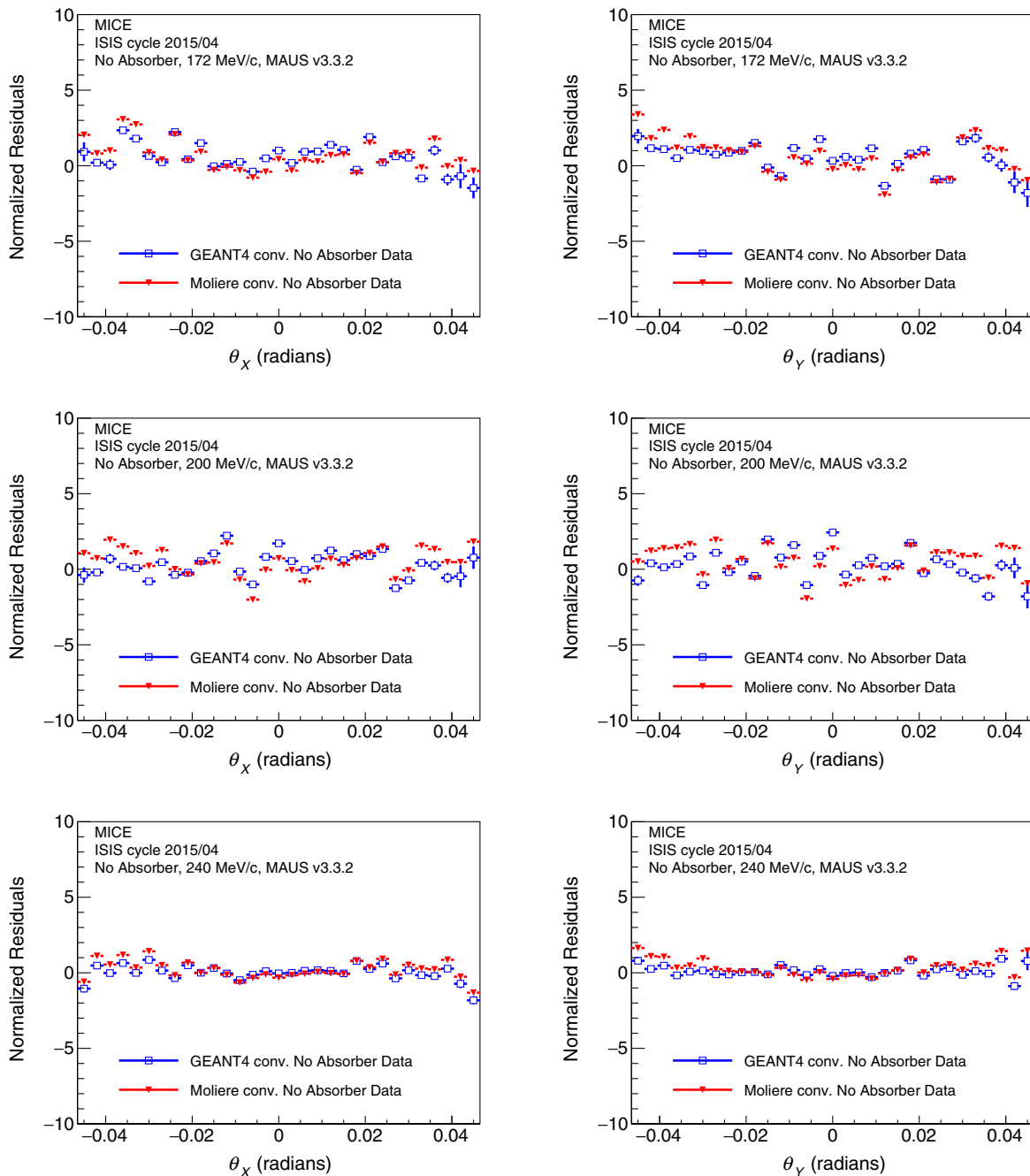


FIG. 12. Scattering residuals between data with the LiH absorber and no absorber data convolved with either GEANT4 or the Molière scattering models in LiH for the 172, 200 and 240 MeV/ c samples. The residuals are normalized to the estimated uncertainty in the data in each bin. The agreement improves at higher momentum where the scattering distributions are narrower.

where a is a fit coefficient, motivated by Eq. (3), where the β dependence of the log term is negligible, changing the calculated value by less than 1%.

The coefficient, a , is compared with the prediction from the PDG formula in Eq. (3). The values of the coefficients, a , determined from the fits to the $\theta_{0,X}$ and $\theta_{0,Y}$ distributions are shown in Table X. The numerical derivative of the

momentum with respect to TOF of the sample was calculated and used to assess the systematic uncertainty associated with the measurement.

Measurements using the projected angles are systematically smaller than the PDG prediction. The average of the two fits to the $\theta_{0,X}$ and $\theta_{0,Y}$ muon scattering widths as a function of momentum yields $a = 208.1 \pm 1.5$ mrad,

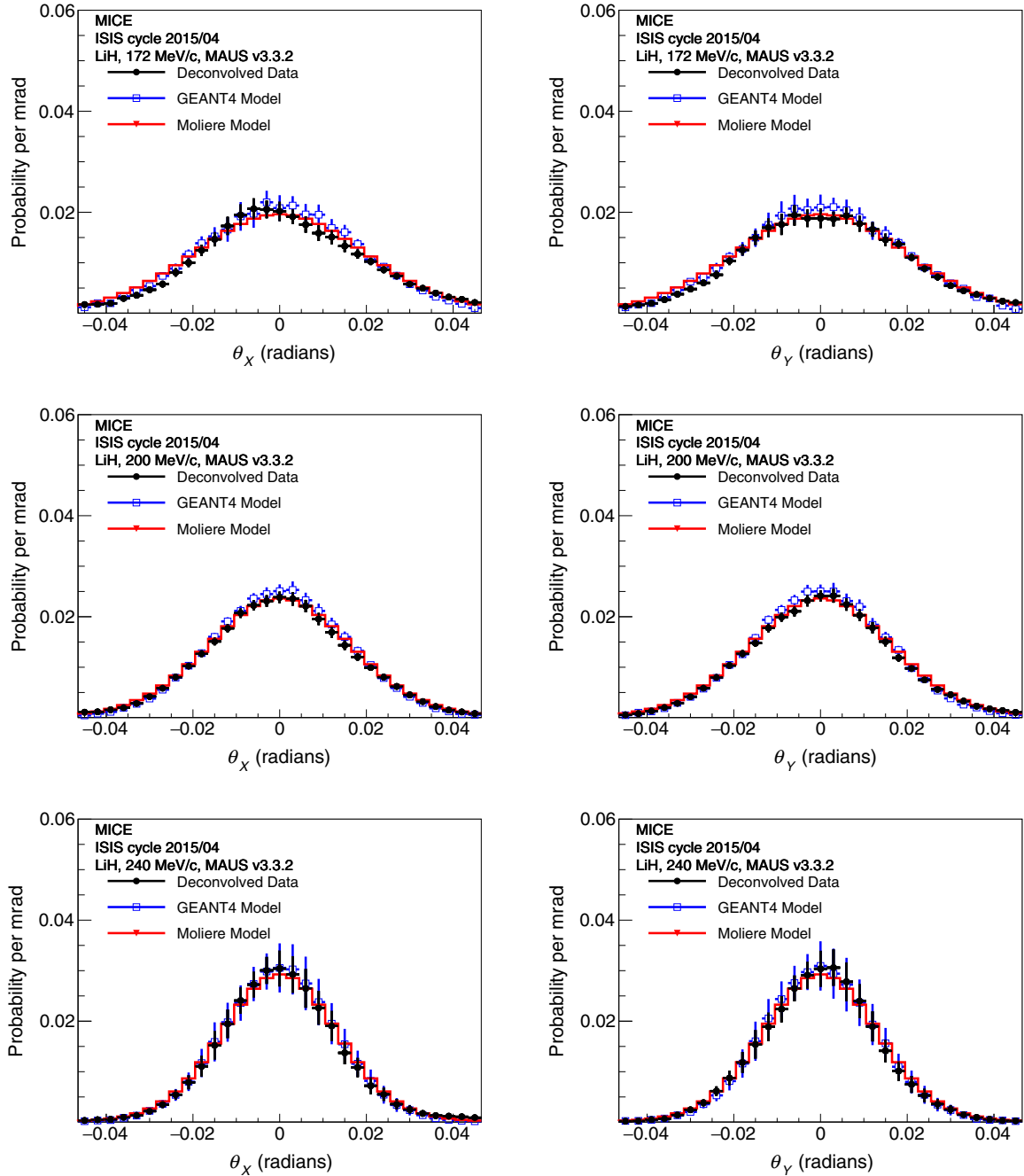


FIG. 13. Projected θ_x and θ_y multiple scattering probability functions at 172, 200 and 240 MeV/c after deconvolution. The GEANT4 and Molière scattering distributions in LiH are provided for comparison.

which is 9% smaller than the value proposed by the PDG formula, $a = 226.7$ mrad, but still within the uncertainties of that approximate formula, Eq. (3), which is quoted as accurate to 11%.

V. CONCLUSIONS

Presented here is an analysis of the LiH multiple Coulomb scattering data taken during ISIS user run

2015/04 using MICE. These data were compared to the GEANT4 (v9.6) default scattering model [11] and the full Molière calculation [4,5]. A χ^2 statistic was used to make quantitative statements about the validity of the proposed models. Three approaches are taken; the measured LiH and no absorber scattering distributions were compared to GEANT4, the forward convolution using the no absorber data was compared to both GEANT4 and the Molière model and the deconvolution of the LiH scattering data using the

TABLE VIII. Systematic uncertainties associated with the width of the scattering distributions of $\theta_{0,X}$ and $\theta_{0,Y}$ in three representative momentum bins.

p (MeV/c)	Type	$\Delta\theta_{0,X}$ (mrad)	$\Delta\theta_{0,Y}$ (mrad)
171.55	TOF selection	0.64	0.64
	Alignment	< 0.01	0.01
	Fiducial radius	< 0.01	< 0.01
	θ angle definition	< 0.01	< 0.01
	π contamination	< 0.01	< 0.01
	Deconvolution	1.25	1.19
	Total sys.	1.39	1.35
199.93	TOF selection	0.29	0.29
	Alignment	0.02	< 0.01
	Fiducial radius	0.01	0.01
	θ definition	< 0.01	< 0.01
	π contamination	< 0.01	< 0.01
	Deconvolution	0.70	0.47
	Total sys.	0.73	0.54
239.76	TOF selection	0.27	0.27
	Alignment	< 0.01	< 0.01
	Fiducial radius	0.01	0.01
	θ definition	< 0.01	< 0.01
	π contamination	0.01	0.01
	Deconvolution	0.27	0.41
	Total sys.	0.36	0.49

no absorber data was compared to both GEANT4 and the Molière model. In all cases the GEANT4 scattering widths agreed with the measured data at each of the nominal momenta, but the Molière model produces systematically wider distributions.

The momentum dependence of scattering was examined by selecting 200 ps time of flight samples from the muon beam data. The momentum dependence from 160 to 245 MeV/c was compared to the dependence in Eq. (3), from the PDG [3], and it was found that the measured RMS scattering width is about 9% smaller than the approximate PDG estimation, but within the latter's stated uncertainty.

 TABLE IX. Widths of best fit Gaussian fitted to central ± 45 mrad of scattering distributions after deconvolution compared to GEANT4 and Molière models. Statistical and systematic uncertainties are given for the data distributions. Only statistical uncertainties are given for the GEANT4 model.

p (MeV/c)	Angle	$\theta_{\text{Gold}}^{\text{meas}}$ (mrad)	$\theta_{G4}^{\text{true}}$ (mrad)	$\theta_{\text{Molière}}^{\text{true}}$ (mrad)
171.55	θ_X	$19.03 \pm 0.26 \pm 1.39$	18.62 ± 0.13	20.03
171.55	θ_Y	$18.95 \pm 0.24 \pm 1.35$	18.59 ± 0.12	20.03
199.93	θ_X	$16.59 \pm 0.17 \pm 0.73$	15.82 ± 0.05	16.87
199.93	θ_Y	$16.36 \pm 0.17 \pm 0.55$	15.82 ± 0.05	16.87
239.76	θ_X	$13.29 \pm 0.17 \pm 0.37$	13.16 ± 0.04	13.60
239.76	θ_Y	$13.21 \pm 0.16 \pm 0.49$	13.10 ± 0.04	13.60

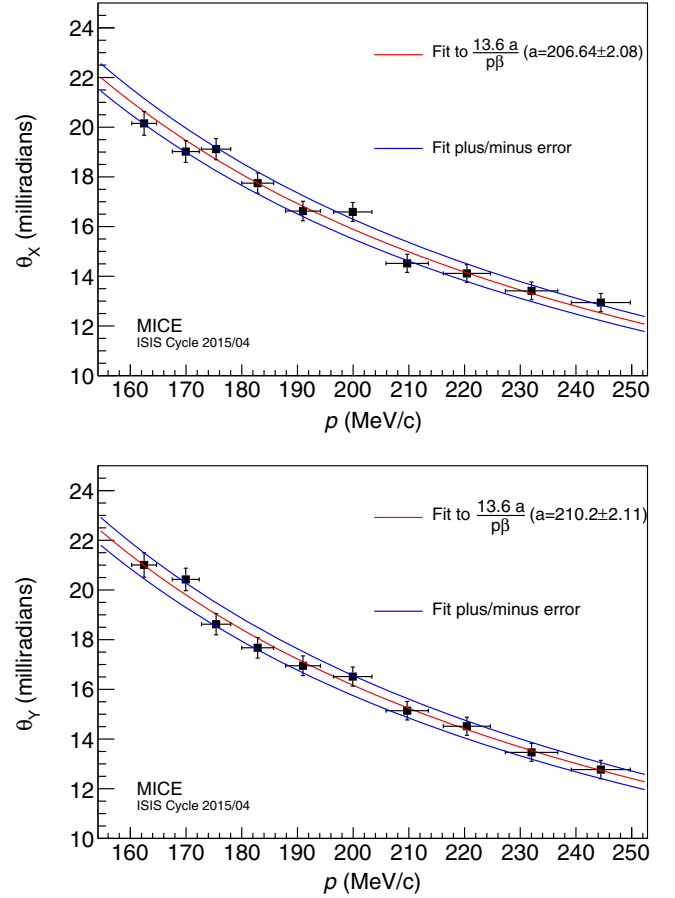


FIG. 14. The results of the scattering analysis using data in a number of momentum bins. Scattering widths are reported after application of the Gold deconvolution.

TABLE X. Results of the fit to the scattering widths as a function of momentum, given by Eq. (15). The value predicted by the PDG is also shown.

Angle	a (mrad)
$\theta_{0,X}$	206.6 ± 2.1
$\theta_{0,Y}$	210.2 ± 2.1
PDG	226.7

ACKNOWLEDGMENTS

The work described here was made possible by grants from the Science and Technology Facilities Council (UK), the Department of Energy and the National Science Foundation (USA), the Istituto Nazionale di Fisica Nucleare (Italy), the European Union under the European Union's Framework Programme 7 (AIDA project, Grant Agreement No. 262025; TIARA project, Grant Agreement No. 261905; and EuCARD), the Japan Society for the Promotion of Science, the National Research Foundation of Korea (No. NRF-2016R1A5A1013277), the Ministry of Education, Science and Technological Development of the Republic of Serbia, the Institute of High Energy Physics/Chinese Academy of Sciences fund for collaboration between the People's Republic of China and the USA, and the Swiss National Science Foundation in the framework of the SCOPES program. We gratefully acknowledge all sources of support. We are grateful for the support given to us by the staff of the STFC Rutherford Appleton and Daresbury laboratories. We acknowledge the use of Grid computing resources deployed and operated by GridPP in the UK [42].

APPENDIX: DEFINITION OF SCATTERING ANGLES

The projections of the scattering angle onto the y - z or x - z plane, angles θ_X and θ_Y , are defined by considering the inner product of the downstream momentum \mathbf{p}_{DS} with the component of the upstream momentum vector \mathbf{p}_{US} , perpendicular to the projection plane. The scattering projection into the plane defined by the momentum vector and the y -axis is

$$\theta_Y = \arctan\left(\frac{\mathbf{p}_{DS} \cdot \hat{\mathbf{v}}}{\mathbf{p}_{DS} \cdot \hat{\mathbf{u}}}\right) = \arctan\left(\frac{\mathbf{p}_{DS} \cdot (\hat{\mathbf{y}} \times \mathbf{p}_{US})|\mathbf{p}_{US}|}{(\mathbf{p}_{DS} \cdot \mathbf{p}_{US})|\hat{\mathbf{y}} \times \mathbf{p}_{US}|}\right), \quad (\text{A1})$$

where $\hat{\mathbf{y}}$ is the unit vector in the y direction, $\hat{\mathbf{v}} = \hat{\mathbf{y}} \times \mathbf{p}_{US}/|\hat{\mathbf{y}} \times \mathbf{p}_{US}|$ is the unit vector mutually orthogonal to the y direction and the momentum vector and $\hat{\mathbf{u}} = \mathbf{p}_{US}/|\mathbf{p}_{US}|$ is the unit vector parallel to the upstream momentum

vector. A scattering angle in the perpendicular plane must then be defined as

$$\theta_X = \arctan\left(\frac{|\mathbf{p}_{US}| \frac{\mathbf{p}_{DS} \cdot (\mathbf{p}_{US} \times (\hat{\mathbf{y}} \times \mathbf{p}_{US}))}{|\mathbf{p}_{US} \times (\hat{\mathbf{y}} \times \mathbf{p}_{US})| |\mathbf{p}_{DS} \cdot \mathbf{p}_{US}|}}{|\mathbf{p}_{US} \times (\hat{\mathbf{y}} \times \mathbf{p}_{US})| |\mathbf{p}_{DS} \cdot \mathbf{p}_{US}|}\right), \quad (\text{A2})$$

where the downstream vector is now projected onto the unit vector $\hat{\mathbf{v}} = \mathbf{p}_{US} \times (\hat{\mathbf{y}} \times \mathbf{p}_{US})/|\mathbf{p}_{US} \times (\hat{\mathbf{y}} \times \mathbf{p}_{US})|$. These two expressions can be expressed in terms of the gradients of the muon tracks before and after the scatters,

$$\theta_Y = \arctan\left\{\frac{\sqrt{1 + \left(\frac{dx}{dz}\right)_{US}^2 + \left(\frac{dy}{dz}\right)_{US}^2}}{\sqrt{1 + \left(\frac{dx}{dz}\right)_{US}^2}} \times \left(\frac{\left(\frac{dx}{dz}\right)_{DS} - \left(\frac{dx}{dz}\right)_{US}}{1 + \left(\frac{dx}{dz}\right)_{US} \left(\frac{dx}{dz}\right)_{DS} + \left(\frac{dy}{dz}\right)_{US} \left(\frac{dy}{dz}\right)_{DS}}\right)\right\}, \quad (\text{A3})$$

$$\theta_X = \arctan\left\{\sqrt{\frac{1 + \left(\frac{dx}{dz}\right)_{US}^2 + \left(\frac{dy}{dz}\right)_{US}^2}{\left(1 + \left(\frac{dx}{dz}\right)_{US}^2 + \left(\frac{dy}{dz}\right)_{US}^2\right)\left(1 + \left(\frac{dx}{dz}\right)_{US}^2\right)}} \times \left(\frac{\left(\frac{dy}{dz}\right)_{DS} \left(1 + \left(\frac{dx}{dz}\right)_{US}^2\right) + \left(\left(\frac{dx}{dz}\right)_{DS} \left(\frac{dx}{dz}\right)_{US} - 1\right) \left(\frac{dy}{dz}\right)_{US}}{1 + \left(\frac{dx}{dz}\right)_{US} \left(\frac{dx}{dz}\right)_{DS} + \left(\frac{dy}{dz}\right)_{US} \left(\frac{dy}{dz}\right)_{DS}}\right)\right\}. \quad (\text{A4})$$

In the approximation of small angles (i.e., $\frac{dx}{dz} \approx \frac{dy}{dz} \ll 1$) these produce the more familiar forms

$$\theta_X = \left(\frac{dy}{dz}\right)_{DS} - \left(\frac{dy}{dz}\right)_{US} \quad (\text{A5})$$

for scattering about the x -axis or

$$\theta_Y = \left(\frac{dx}{dz}\right)_{DS} - \left(\frac{dx}{dz}\right)_{US} \quad (\text{A6})$$

for scattering about the y -axis. The more exact expressions, Eqs. (A3) and (A4), are used throughout for this analysis.


-
- [1] B. Rossi and K. Greisen, Cosmic-ray theory, *Rev. Mod. Phys.* **13**, 240 (1941).
 [2] E. Rutherford, LXXIX. The scattering of α and β particles by matter and the structure of the atom, *Philos. Mag. Ser. 6* **21**, 669 (1911).
 [3] P. Zyla *et al.* (Particle Data Group), Review of particle physics, *Prog. Theor. Exp. Phys.* **2020**, 083C01 (2020).

- [4] G. Molière, Theorie der Streuung schneller geladener Teilchen I. Einzelstreuung am abgeschirmten Coulomb-Feld, *Z. Naturforsch.* **A2**, 133 (1947).
 [5] G. Molière, Theory of the scattering of fast charged particles. 2. Repeated and multiple scattering, *Z. Naturforsch.* **A3**, 78 (1948).
 [6] H. A. Bethe, Molière's theory of multiple scattering, *Phys. Rev.* **89**, 1256 (1953).

- [7] U. Fano, Inelastic collisions and the Molière theory of multiple scattering, *Phys. Rev.* **93**, 117 (1954).
- [8] D. Attwood *et al.*, The scattering of muons in low Z materials, *Nucl. Instrum. Methods Phys. Res., Sect. B* **251**, 41 (2006).
- [9] V. L. Highland, Some practical remarks on multiple scattering, *Nucl. Instrum. Methods* **129**, 497 (1975).
- [10] G. R. Lynch and O. I. Dahl, Approximations to multiple Coulomb scattering, *Nucl. Instrum. Methods Phys. Res., Sect. B* **58**, 6 (1991).
- [11] S. Agostinelli *et al.* (GEANT4 Collaboration), GEANT4: A Simulation toolkit, *Nucl. Instrum. Methods Phys. Res., Sect. A* **506**, 250 (2003).
- [12] G. Wentzel, Zwei Bemerkungen über die Zerstreung korpuskularer Strahlen als Beugungserscheinung, *Z. Phys.* **40**, 590 (1926).
- [13] T. Carlisle, Step IV of the Muon Ionization Cooling Experiment (MICE) and the multiple scattering of muons, Ph.D. thesis, Oxford U., 2013.
- [14] D. Neuffer, Principles and applications of muon cooling, *Part. Accel.* **14**, 75 (1983).
- [15] M. Bogomilov *et al.* (MICE Collaboration), Demonstration of cooling by the muon ionization cooling experiment, *Nature (London)* **578**, 53 (2020).
- [16] M. Bogomilov *et al.*, Neutrino factory, *Phys. Rev. ST Accel. Beams* **17**, 121002 (2014).
- [17] D. Neuffer, P. Snopok, and Y. Alexahin, Front end for a neutrino factory or muon collider, *J. Instrum.* **12**, T11007 (2017).
- [18] C. T. Rogers, D. Stratakis, G. Prior, S. Gilardoni, D. Neuffer, P. Snopok, A. Alekou, and J. Pasternak, Muon front end for the neutrino factory, *Phys. Rev. ST Accel. Beams* **16**, 040104 (2013).
- [19] D. Stratakis and R. B. Palmer, Rectilinear six-dimensional ionization cooling channel for a muon collider: A theoretical and numerical study, *Phys. Rev. ST Accel. Beams* **18**, 031003 (2015).
- [20] D. Neuffer, H. Sayed, J. Acosta, T. Hart, and D. Summers, Final cooling for a high-energy high-luminosity lepton collider, *J. Instrum.* **12**, T07003 (2017).
- [21] M. Bogomilov *et al.* (MICE Collaboration), The MICE Muon Beam on ISIS and the beam-line instrumentation of the Muon Ionization Cooling Experiment, *J. Instrum.* **7**, P05009 (2012).
- [22] K. Long, D. Lucchesi, M. Palmer, N. Pastrone, D. Schulte, and V. Shiltsev, Muon colliders to expand frontiers of particle physics, *Nat. Phys.* **17**, 289 (2021).
- [23] M. Ellis *et al.*, The design, construction and performance of the MICE scintillating fibre trackers, *Nucl. Instrum. Methods Phys. Res., Sect. A* **659**, 136 (2011).
- [24] M. Bogomilov *et al.* (MICE Collaboration), Performance of the MICE diagnostic system, *J. Instrum.* **16**, P08046 (2021).
- [25] D. Adams *et al.* (MICE Collaboration), Characterisation of the muon beams for the Muon Ionisation Cooling Experiment, *Eur. Phys. J. C* **73**, 2582 (2013).
- [26] C. N. Booth *et al.*, The design, construction and performance of the MICE target, *J. Instrum.* **8**, P03006 (2012).
- [27] C. N. Booth *et al.*, The design and performance of an improved target for MICE, *J. Instrum.* **11**, P05006 (2016).
- [28] R. Bertoni, A. Blondel, M. Bonesini, G. Cecchet, A. de Bari, J. Graulich, Y. Karadzhov, M. Rayner, I. Rusinov, R. Tsenov, S. Terzo, and V. Verguilo, The design and commissioning of the mice upstream time-of-flight system, *Nucl. Instrum. Methods Phys. Res., Sect. A* **615**, 14 (2010).
- [29] M. Bogomilov *et al.* (MICE Collaboration), Pion contamination in the MICE muon beam, *J. Instrum.* **11**, P03001 (2015).
- [30] D. Adams *et al.* (MICE Collaboration), Electron-Muon Ranger: Performance in the MICE Muon Beam, *J. Instrum.* **10**, P12012 (2015).
- [31] R. Asfandiyarov *et al.*, MAUS: The MICE analysis user software, *J. Instrum.* **14**, T04005 (2018).
- [32] R. Kalman, A new approach to linear filtering and prediction problems., *J. Basic Eng.* **82**, 35 (1960).
- [33] A. Dobbs, C. Hunt, K. Long, E. Santos, M. A. Uchida, P. Kyberd, C. Heidt, S. Blot, and E. Overton, The reconstruction software for the MICE scintillating fibre trackers, *J. Instrum.* **11**, T12001 (2016).
- [34] H. Bichsel, Shell corrections in stopping powers, *Phys. Rev. A* **65**, 052709 (2002).
- [35] T. J. Roberts, K. B. Beard, D. Huang, S. Ahmed, D. M. Kaplan, and L. K. Spentzouris, G4Beamline particle tracking in matter-dominated beam lines, *Conf. Proc. C* **0806233**, WEPP120 (2008).
- [36] J. Allison *et al.*, Recent developments in GEANT4, *Nucl. Instrum. Methods Phys. Res., Sect. A* **835**, 186 (2016).
- [37] V. N. Ivanchenko, O. Kadri, M. Maire, and L. Urban, GEANT4 models for simulation of multiple scattering, *J. Phys. Conf. Ser.* **219**, 032045 (2010).
- [38] B. Gottschalk, A. M. Koehler, R. J. Schneider, J. M. Sisterson, and M. S. Wagner, Multiple Coulomb scattering of 160 MeV protons, *Nucl. Instrum. Methods Phys. Res., Sect. B* **74**, 467 (1993).
- [39] R. Gold, An iterative unfolding method for response matrices, Technical Report No. ANL-6984.
- [40] M. Morháč, J. Kliman, V. Matoušek, M. Veselský, and I. Turzo, Efficient one- and two-dimensional Gold deconvolution and its application to γ -ray spectra decomposition, *Nucl. Instrum. Methods Phys. Res., Sect. A* **401**, 385 (1997).
- [41] R. Brun and F. Rademakers, ROOT: An object oriented data analysis framework, *Nucl. Instrum. Methods Phys. Res., Sect. A* **389**, 81 (1997).
- [42] <http://www.gridpp.ac.uk/>



Application of Geant4 simulation in measurement of cosmic-ray muon flux and studies of muon-induced background

Dejan Joković^a , Dimitrije Maletić, Aleksandar Dragić, Nikola Veselinović, Mihailo Savić, Vladimir Udovičić, Radomir Banjanac, David Knežević

Institute of Physics, University of Belgrade, Pregrevica 118, Belgrade 11080, Serbia

Received: 3 May 2023 / Accepted: 28 October 2023

© The Author(s), under exclusive licence to Società Italiana di Fisica and Springer-Verlag GmbH Germany, part of Springer Nature 2023

Abstract The low-level underground laboratory at the Institute of Physics Belgrade is a facility for gamma-ray spectroscopy measurements and for measurements of cosmic-ray muon intensity. Related to the two research subjects, studies of cosmic-ray muon-induced background in gamma spectroscopy are of particular interest. Continuous measurements of cosmic muon intensity at the ground level and underground sites have been carried out by means of plastic scintillation detectors. The detector response, interpretation of the experimental spectra and their calibration were obtained and verified using a Geant4-based simulation. The results of the simulation were used in measurement of muon flux at the surface and shallow underground (25 m w e)—the measured fluxes are $(170 \pm 6) \text{ m}^{-2} \text{ s}^{-1}$ and $(44 \pm 1) \text{ m}^{-2} \text{ s}^{-1}$, respectively. An underground muon detector can operate in coincidence with a high-purity germanium gamma-ray detector, which allows investigations of muon-induced processes in germanium spectrometers. In low-level gamma spectroscopy, neutrons produced by muons in the lead shielding of a germanium detector contribute to the detector background. Simulation of prompt muon-induced background as well as simulation of neutron production by cosmic muons in lead were carried out. Estimated neutron yield in lead is $(3.1 \pm 0.4) \times 10^{-5}$ neutrons per g/cm^2 , per tagged muon. Also the average neutron multiplicity is calculated.

1 Introduction

The low-background underground laboratory at the Institute of Physics Belgrade has been designed as a multi-purpose facility for gamma-ray spectroscopy measurements of low activities, as well as for measurements of cosmic-ray intensity. The two main research objectives intersect in studies of cosmic-ray muon-induced background in gamma spectroscopy measurements. The laboratory is located at near-sea level, at the altitude of 78 m. It consists of two separate parts—the ground level and the underground; the shallow underground part is dug at the depth of about 12 m beneath the surface. The earth above the underground site consists of four layers of loess with average density of $(2.0 \pm 0.1) \text{ g}/\text{cm}^3$. With the 30 cm thick concrete ceiling, the overburden is approximately equal to 25 m of water equivalent (m w e; 1 m w e gives an interaction depth of $1 \text{ hg}/\text{cm}^2$). It provides a good environment for gamma spectroscopy—the overburden soil layer absorbs almost all nucleonic component of cosmic rays and reduces muon flux by about four times. Radon concentration is kept low by preventing diffusion from the soil and by maintaining constant overpressure in the room. One shielded high-purity germanium (HPGe) spectrometer is dedicated for low-level gamma measurements in the underground laboratory. It can operate in coincidence with a muon scintillation detector, which enables investigations of muon-induced events in the germanium detector. More details on the laboratory can be found in [1].

Cosmic-ray muon intensity has been continuously measured at both the ground level and underground sites since 2002. The current experimental set-up, described in the next section, was upgraded and commissioned in 2008. Measurements of muon intensity and its temporal variations can give some information on primary cosmic radiation, interaction processes in the atmosphere and solar modulation. Low-energy primary cosmic rays are under large influence of interplanetary magnetic field, whose structure varies because of solar activity, which has various periodic and aperiodic features. Therefore, temporal variations of cosmic muon flux are expected to be a good indicator of solar activity. These measurements yielded some results on muon flux and its variations [2–5]. In shallow and deep underground laboratories cosmic muons represent an important source of background, either directly or by generating high-energy neutrons in interactions in rock or detector and its surroundings [6–8]. Results of a preliminary study on muon-induced neutron production rate were published in [9].

Today applications of various Monte Carlo simulation methods make an essential part of experimental research. These simulation methods are found to be very useful for modeling detector response, accurate interpretation of experimental data, particularly

^a e-mail: yokovic@ipb.ac.rs (corresponding author)

experimental spectra and their features, as well as for detector calibration. There is a handful of Monte Carlo toolkits used in nuclear and particle physics studies, one of the most commonly used is Geant4 (Geometry aNd Tracking), which has been developed and maintained at CERN [10–12]. Geant4 is a framework for accurate Monte Carlo simulations of particle transport through matter. It contains a complete set of routines for modeling particle trajectories and interactions: detector geometry and materials, physics processes, event generation, detector response and analysis and visualization. Versatility and flexibility of Geant4 allow users to build customized simulation programmes that fit their specific needs. Another advantage of the toolkit is that a built simulation can be easily modified, so as to be suitable for different detector configurations. Increase in computational power enabled Geant4 simulations to be no longer time demanding in order to achieve good statistical uncertainties, due to use of parallel computing, multithreading, etc. Uses of Geant4 span from high energy, nuclear and accelerator physics to medical and space science.

In experiments carried out in the Belgrade underground laboratory, Geant4-based simulations have been developed in order to obtain detector response for various detector configurations, as well as for interpretation of the experimental spectra and their calibration. They include simulations of response of the plastic scintillation detectors for cosmic-ray muon studies and simulations of the germanium detector for gamma spectroscopy. Here we present an overview of applications of Geant4 simulations in measurement of cosmic-ray muon fluxes at the ground level and underground sites and for estimation of muon-induced background in the lead shield of the HPGe detector.

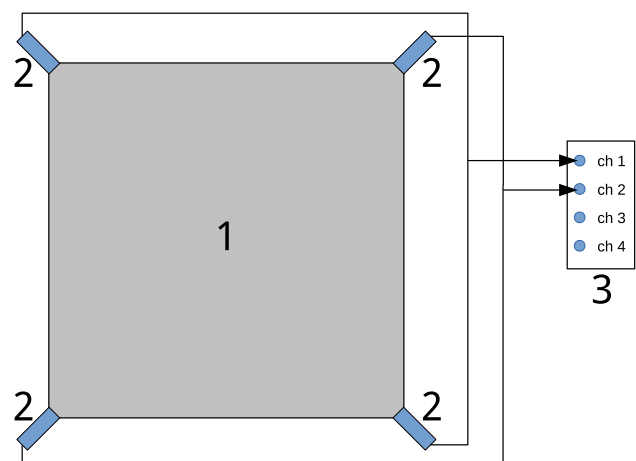
2 Experimental set-up

Measurements of cosmic-ray muon intensity have been performed by means of plastic scintillation detectors, situated in both the ground level and underground parts of the laboratory. Each detector configuration consists of one large scintillator with an accompanying data acquisition system. The two experimental set-ups are identical but they operate independently, each detector has its dedicated data acquisition module. A sketch of the detector set-up is displayed in Fig. 1.

The polystyrene-based scintillator (similar to NE102) has a rectangular shape with base area $100\text{ cm} \times 100\text{ cm}$ and thickness 5 cm, housed in 1 mm thick aluminum. It lies horizontally on its largest side. At each corner of the scintillator a 2-inch photomultiplier tube (PMT) is attached, pointing at the detector's diagonal. Individual signals from the photomultiplier tubes looking at the same diagonal, i.e., two opposite photomultipliers, are summed in one output signal. Hence two output signals from the two detector's diagonals are recorded and stored on tape. The data acquisition system is based on a fast 4-channel analog-to-digital converter (ADC), model CAEN N1728B, which has 100 MHz sampling frequency (time resolution 10 ns). Two input ADC channels are used for the summed signals from the two diagonals of the scintillator, respectively, there are two signals per scintillator, each feeding one ADC channel. The third and/or fourth ADC channels are reserved for other detectors, such as germanium detector. Information about each event (input channel, time tag, amplitude) whose amplitude is above threshold is stored in an event list, which allows offline analyses of single and coincidence events between different channels within a chosen time window. Time and amplitude spectra are formed by histogramming data from the event list, for single ADC channels or for two or more coinciding channels.

Single spectra of the plastic scintillators result from the summed signals from the PMTs on the same diagonal, which are fed to two ADC channels separately; hence two single spectra are produced for each detector. The typical experimental spectra, for both the surface and underground detectors, are presented in Fig. 2. They are mainly composed of energy deposit spectra of cosmic rays that pass through the scintillator and of Compton scattered environmental gamma radiation, as a dominant source of background. The main feature in the spectra is a peak that should correspond to muon and electron energy loss in the 5 cm thick scintillator. However, this energy loss peak, and subsequently cosmic events, cannot be separated from the background, which is quite significant because of the detector's large size and its four PMTs (Fig. 2).

Fig. 1 Experimental set-up for cosmic-ray intensity measurements: plastic scintillation detector (1), photomultiplier tubes (2), analog-to-digital converter (3)



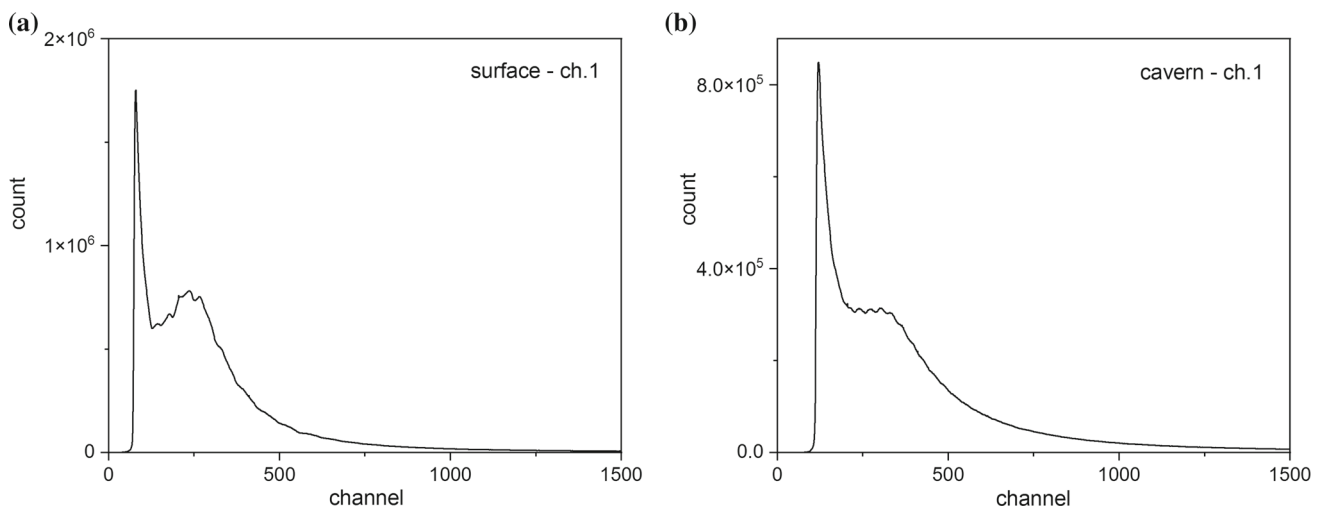
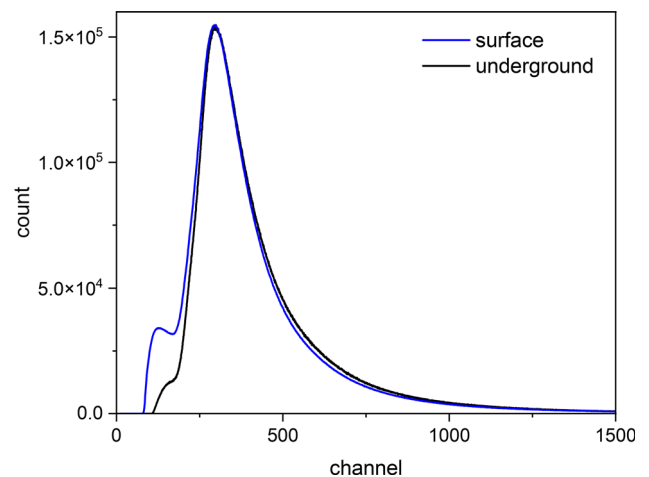


Fig. 2 Typical single spectra of the surface (left) and underground (right) scintillation detectors, produced by the summed signals from the PMTs looking at the same detector's diagonal. They are composed of energy deposit spectra of cosmic rays and of environmental gamma radiation

Fig. 3 Normalized coincidence spectra of the surface and underground detectors. The spectra are considered as solely energy deposit spectra of cosmic-ray charged particles. Both spectra exhibit a peak that corresponds to charged particle energy loss in the 5 cm thick plastic scintillator



Investigation of responses of the single PMTs have shown that cosmic events can be selected by coinciding events that promptly trigger all four PMTs, i.e., both detector's diagonals. Time interval spectra of coincidences between the ADC channels that are fed by the two diagonals, have a sharp peaked distribution that is 40 ns wide and stretches up to ± 50 ns upon the peak (given the 10 ns time resolution of the ADCs). Prompt coincidences selected within a time window of 100 ns are associated to cosmic rays. This procedure virtually removes background, as environmental gamma rays cannot trigger both diagonals. The coincidence spectra are considered as solely due to energy losses by charged particles in the scintillator. These interpretations of the experimental spectra have been supported by Geant4 simulations. The individual coincidence spectra per the diagonal are then summed into one energy deposit spectrum, per the detector; the coincidence spectra for both the surface and underground detectors are presented in Fig. 3.

The coincidence spectra of the scintillators show a well-defined peak of the charged particle energy losses, while the low-energy background present in the single spectra vanishes (Figs. 2, 3). Since the specific energy loss for muons is ~ 2 MeV per g/cm^2 , the spectral peak should be at the energy ~ 11 MeV, for the 5 cm thick plastic scintillator. Comparing the spectra of the detectors at the surface and in the underground laboratory one can notice the difference in their shape at lower energies. This difference points to the contribution of electromagnetic component of cosmic rays (electrons, positrons and photons), whose flux is significant at the surface. It is absent underground, where practically only muon component is present. Hence, it is plausible to assume that events recorded by the underground detector are only muon events, while for the surface detector they include electromagnetic component. Moreover, due to edge effects there are some cosmic events that fall below the instrumental cuts. The amount of these lost events can be found by comparing experimental results with simulations (Sect. 3).

3 Measurement of cosmic-ray muon flux

3.1 Simulation

With the aim of corroborating the aforementioned statements and interpretations, a Geant4-based application for modeling detector response of the scintillation detectors has been developed. It can be also used for calibration of spectra. The simulation has been done along the same lines as in the previous works [2, 13]. Latest Geant4 version used for this work is 11.0. In Geant4, an event is generated by defining primary particle, its initial position, momentum direction and energy. In the simulation of the underground detector, primary particles were muons, since it can be assumed that only muons are present at the depth of 25 m w e. Muons were gunned from the horizontal and vertical sides of the detector. Particle positions and momentum directions were generated in accordance with the muon directional intensity, which depends on zenith angle: $I(\theta) = I(0) \cos^n \theta$, where n has a value 1.85 at sea level and 1.55 at the 25 m w e depth [14, 15]. Integrated intensity of muons that pass through the horizontal surface is

$$J_h = \int_{\Omega} I(\theta) \cos \theta \sin \theta d\theta d\phi = 2\pi I(0) \int_0^{\pi/2} \cos^{(n+1)} \theta \sin \theta d\theta = 2\pi I(0) \frac{1}{n+2}, \quad (1)$$

while integrated intensity of muons that pass through the vertical surface is

$$J_v = \int_{\Omega} I(\theta) \sin^2 \theta \cos \phi d\theta d\phi = I(0) \int_{\Omega} \cos^n \theta \sin^2 \theta \cos \phi d\theta d\phi, \quad (2)$$

latter integrated over a quarter of the sphere. From the ratio J_h/J_v it follows that muons have higher probability to hit the horizontal than the vertical surface—for $n = 1.55$, $J_h/J_v = 3.64$ per unit area, and for $n = 1.85$, $J_h/J_v = 3.88$. These probabilities were taken into account when primary positions on the horizontal and vertical detector's sides were generated.

The particle energy was calculated in two steps. First, energy at the surface was sampled from the Gaisser's formula for muon energy spectrum at sea level [16]:

$$\frac{dJ_{\mu}(E)}{dE} = 0.14E^{-2.7} \left(\frac{1}{1 + 1.1 \frac{E \cos \theta}{115 \text{ GeV}}} + \frac{0.054}{1 + 1.1 \frac{E \cos \theta}{850 \text{ GeV}}} \right), \quad (3)$$

where E is the muon energy in GeV, and $\cos \theta$ is sampled from the $\cos^{1.85} \theta$ distribution. The formula does not describe well experimental data at lower energies and larger zenith angles, so it was modified according to [17]. Muon energy loss in the earth layer was calculated from the practical equation for total energy loss of muons in standard rock, in units of MeV [18]:

$$-\left(\frac{dE}{dx}\right) = 1.84 + 4.65 \cdot 10^{-6} E + 0.076 \ln \left(\frac{E'}{m_{\mu} c^2} \right) [\text{MeV}/(\text{g}/\text{cm}^2)], \quad (4)$$

where E' is the maximum transferable energy $E' = E^2 / (E + m_{\mu}^2 c^2 / 2m_e)$, m_{μ} is the mass of the muon, and m_e is the mass of the electron. The muon path length, i.e., layer thickness, dx was calculated as $25/\cos \theta$ hg/cm². The energy loss was then subtracted from the value sampled from Eq. 3, and the deducted value was taken for the initial muon energy in the simulation. The muon energy spectrum underground is thus hardened because low-energy muons are removed.

Muons were tracked through the scintillator as a sensitive detector. When a muon passes through a material, it interacts with matter—in these interactions it deposits a portion of its energy, which adds to the overall energy deposit spectrum. Physics processes were applied through the Geant4 physics list QGSP_BERT_HP, which include all interactions leading to production of secondaries, as well as for calculation of energy losses in the detector. For the purpose of simulation of the plastic scintillators electromagnetic interactions of muons, electrons and gammas are relevant (constructor G4EmStandardPhysics_option4 was activated).

The normalized simulated and experimental spectra agree very well, thus verifying interpretation of the detector response and the experimental results (Fig. 4). Furthermore, by comparing the two spectra one can find the percentage of muon events that are not recorded due to instrumental cuts. It is equal to the ratio of counts in the two spectra, here it is approx. 6%. This correction was applied in calculation of the muon flux underground. Relative arbitrariness in estimation of the fraction of lost events contributes to the uncertainty of the measured muon flux to a large degree.

When the same simulation was applied for the surface detector, there was a large discrepancy between the simulation and experimental results. This led to a conclusion that besides muonic, electromagnetic component of cosmic rays also had to be taken into account. Therefore, the model was further extended, so as to include all secondary cosmic-ray particles at the surface. Particle fluxes at the surface were obtained using CORSIKA (COsmic Ray SIMulations for KAscade) programme [19, 20]. It is a Monte Carlo code for simulation of extensive air showers generated by primary cosmic rays in their interactions with air nuclei at the top of the atmosphere. It produces spectra of secondary cosmic rays at a chosen observation level (altitude) above the surface. The output is in a form of a list that keeps information about each particle—its type, momentum, energy and time of arrival. Geant4 provides an interface that can read output files from external event generators and use information to generate primary particles (type, momentum and energy). Hence, CORSIKA served as a primary event generator, while the detector response was modeled by the Geant4 simulation. Details on the CORSIKA simulation—primary cosmic-ray spectrum, hadron interaction models, geomagnetic field, atmospheric model, observation level—can be found in [3].

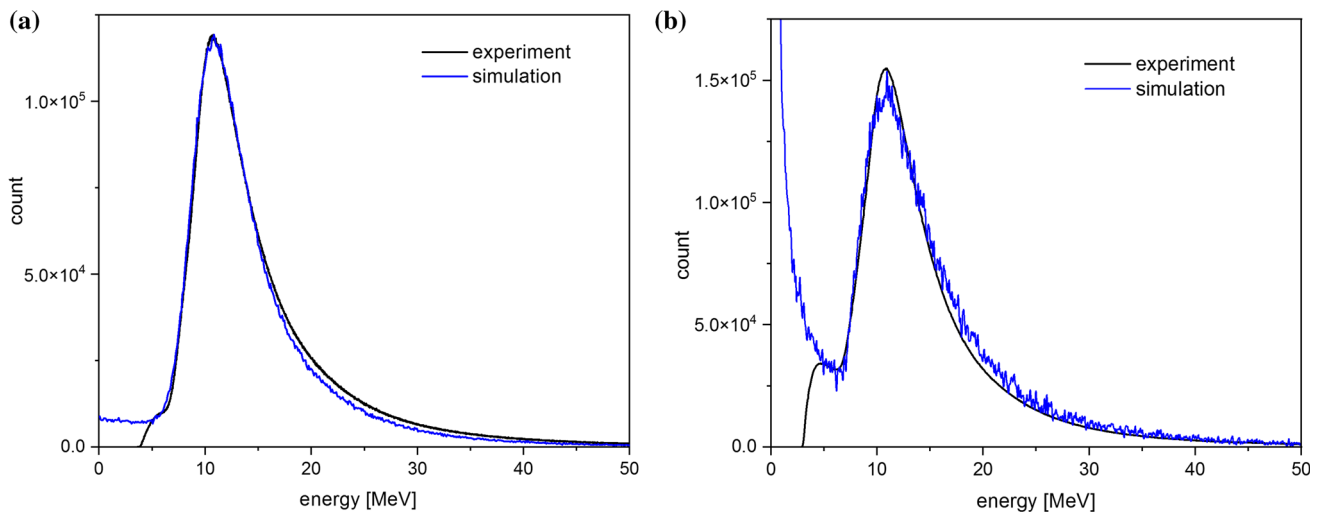


Fig. 4 Normalized experimental (black line) and simulated (blue line) energy deposit spectra of the scintillation detectors in the underground laboratory (left) and at the surface (right). Peak of charged particle energy losses in the spectra is at energy about 11 MeV, approx. equal to muon energy loss in the 5 cm thick plastic scintillator

Primary particles for the simulation of the surface detector, muons, electrons and gammas were, respectively, selected from the CORSIKA output. The energy deposit spectra were then obtained separately for the three types of particles. These individual spectra exhibit some different features, the main difference is that the muon spectrum is virtually the same as for the underground detector, while the gamma ray spectrum is mostly at lower energies [3]. The sum of the individual energy deposit spectra gives the resultant simulated spectrum, which is in good agreement with the experimental one (Fig. 4). It is clearly separated into two parts at ~ 6 MeV, which nearly corresponds to the threshold set by instrumental cuts. At energies exceeding the threshold muon events are dominant, however there is a small but non-negligible contribution of electrons and gammas. The fraction of muons in the simulated spectrum above the instrumental cut is equal to the ratio of muon counts to the total counts—muons make about 87% of the total number of events above the 6 MeV threshold.

3.2 Results

The cosmic muon flux is calculated from the equation $\Phi = N_{\mu}/(St)$, where N_{μ} is number of muons, S surface area and t measurement time. The average muon flux underground was calculated from data recorded during 289 days of measurement ($t = 2.497 \times 10^7$ s). The detection efficiency to muons for this type of detector is close to 100% [21]; the simulation confirms this assumption, but it contributes to uncertainty of the measured flux to a smaller extent. The number of muon events was corrected for events below the instrumental cuts, which was equal to the ratio of normalized counts in the simulated and experimental spectra. About 6% of muon events falls below the cuts. After correction for lost events, the total number of muons is 1.149×10^9 . The horizontal area of the detector is 1 m^2 , however muons also hit vertical sides. On the other hand, muons have higher probability to hit the horizontal than the vertical surface, due to $\cos^2\theta$ directional distribution – 3.64 times higher for the underground detector. The effective detector area is thus 1.055 m^2 . Finally, the muon flux underground, at the 25 m w e depth, is $\Phi = (44 \pm 1) \text{ m}^{-2} \text{ s}^{-1}$. Statistical uncertainties are much smaller than systematic ones, which are partially associated to experimental data treatment, such as the selection of time window for coinciding the single detector spectra and estimation of the fraction of lost muon events below instrumental cuts. Uncertainty of the simulation is roughly estimated by varying parameters of simulation, particularly angular distribution of muons (exponent n in $\cos^n\theta$), thickness of the overburden and calculation of muon energy loss (Eq. 4).

At the surface, the total cosmic-ray flux is the sum of muon and electromagnetic fluxes. First the total flux above the instrumental cut was calculated from the experimental data. Then the percentage of muons above the cut was found from the simulated data—approx. 87% of the total number of events. The flux was also corrected for muon events below the cuts (+ 6%). The effects of seasonal variations are mostly removed due to long measurement time. The total number of cosmic events is 4.079×10^9 . After all corrections applied ($N_{\mu} = N_{\text{tot}} \times 0.87 \times 1.06$), the number of muon events is 3.762×10^9 . The time of measurement is 244 days (2.108×10^7 s), and the effective detector area is 1.0515 m^2 . Finally, muon flux at the surface is $\Phi = (170 \pm 6) \text{ m}^{-2} \text{ s}^{-1}$. The uncertainty was evaluated in a similar way as for the calculation of the muon flux underground. There is also a contribution to the uncertainty that comes from the correction for the fraction of muons in the total flux, which was calculated from the simulation data.

The measured fluxes underground and at the surface are consistent with the previous work, though the muon flux at the surface gives 24% higher value [2]. Integrated muon intensity at sea level is often referred as about $1 \text{ cm}^{-2} \text{ min}^{-1}$ [22], the calculated flux at the surface is in accord with this value. The underground flux adds to the list of muon data in underground laboratories [23]. The integral flux of electromagnetic component at the surface is very approximately estimated to 30% of the total flux.

4 Simulation of muon-induced background

4.1 Muon-induced background in the germanium detector

The muon detector in the underground laboratory can operate in coincidence with a coaxial high-purity germanium detector (ORTEC GEM30). The detector is based on a cylindrical p-type crystal, with the diameter 58.5 mm and the length 56.4 mm, and the active volume 149 cm³. The relative efficiency is 35%, with respect to the efficiency of a 3 × 3 inch NaI detector. The detector is placed inside a 12 cm thick lead castle made of lead with low content of ²¹⁰Pb (specific activity 25 Bq/kg). Due to the 12 m overburden and thick lead shielding, it is suitable for gamma spectroscopy of low-activities. The muon detector is placed directly above the lead castle at the distance 44 cm, and can serve as a veto for additional background suppression. Signals from the HPGe detector are fed into an input channel of the same ADC that is used by the muon detector. The acquisition system allows up to four different inputs; here two inputs are used for signals from the muon detector and one for the HPGe detector. Events recorded by both detectors are stored in one list with information about each event (input channel, trigger time and amplitude). This allows analyses of coincidence or anticoincidence between different channels, by selecting proper time window. In the coincidence mode muon-induced events in the germanium detector can be studied. In the anticoincidence mode the scintillator can serve as an anti-cosmic veto detector.

Geant4 simulations have found wide-ranging applications in gamma spectroscopy with germanium detectors. One of the main subjects that have been studied is evaluation of muon-induced background in germanium detectors, operating at the surface and underground [24–28]. The simulation that combines the underground scintillator and the HPGe detector was performed with a goal to obtain coincidence response of the two-detector system to cosmic muons. It was used to estimate prompt muon-induced background, which originates from direct muon interaction with the germanium crystal or from electrons ionized by muons in the detector and surroundings. It can also give a prediction of background reduction by the anti-cosmic veto [13].

Configuration of an HPGe detector is more complex than a simple scintillator box, which is why the detailed knowledge of the detector geometry is an essential precondition for an accurate modeling. In this simulation the detector was constructed utilizing the detector parameters provided by the manufacturer. The geometry was tested by varying these parameters and looking at how the changes affect the detector response. This method can be also used for uncertainty estimation. Small changes of the parameters may give rise to large deviations between simulated and experimental results. In order to overcome these difficulties an optimization procedure is often performed, by tuning the detector parameters so as to achieve the best possible agreement with experimental values [29]. For use in gamma spectroscopy Geant4 provides low-energy electromagnetic packages that best model interactions of low-energy gamma rays. Here the G4EmStandardPhysics_option4 constructor class, which combines electromagnetic models for simulations with high accuracy, was activated.

First, the simulation of the germanium background generated by prompt muon interactions in the lead shield was performed. Primary muons were generated on the surface of the lead castle, the top and side surfaces. Energy and angular distributions of muons are the same as used in the simulation of muons underground, described in Sect. 3.1. Per event, initial position and momentum direction were sampled from $\cos^{\eta}\theta$ distribution ($\eta = 1.55$), while energy was sampled from the modified Gaisser's formula and subtracted for the muon energy loss (Eq. 3, 4). Here the germanium crystal is a sensitive detector for calculation of energy deposit. The energy deposit spectrum is in high-energy part due to muons that traverse through the germanium crystal, which has a broad peak at about 43 MeV [13]. For gamma spectroscopy measurements the range up to 3 MeV is mostly of interest. This part of the spectrum is due to secondary particles produced by muons in the detector's surroundings, mainly in the lead castle. The prominent annihilation peak builds upon the continuous spectrum.

Then the simulation of the scintillator and the HPGe detector working in coincidence was carried out, with primary muons now generated on the scintillator's surface, in the same way as described in Sect. 3.1. A sketch of the visualized Geant4 geometry and a muon event is displayed in Fig. 5. The coincidences were selected with a simple condition that a muon has to deposit energy in both detectors. The simulated coincidence spectrum of the germanium detector up to 3 MeV, together with the background spectrum, is shown in Fig. 6. The prominent annihilation peak builds upon the continuous spectrum. Integral of this spectrum gives the number of vetoed background events in the range of 0–3 MeV.

Relative background reduction by the anti-cosmic veto was found as a ratio of counts in the two spectra. For the given configuration the veto halves the prompt muon background in the lead shield. However, the total background of the HPGe detector would be diminished by only 15%. The new set-up has the muon detector half the distance closer to the lead castle, which should to some extent improve background reduction. A common anti-cosmic veto system consists of detectors that are placed above and to the sides of a lead castle, so that the veto is triggered by any arriving muon. This type of set-up would provide background reduction as good as possible for the HPGe detector. However, at the moment it is not planned to add more veto detectors.

4.2 Neutron production by muons in lead

Neutrons produced in interactions of cosmic-ray muons with the detector and its surroundings contribute to background, especially in sensitive experiments in deep underground laboratories searching for rare events. In interactions with the detector neutrons produce signals that may mimic signals from the events searched for. Therefore investigation of neutron-induced background is of great importance for low-background measurements. For lead-shielded germanium detectors neutrons produced by cosmic muons in lead

Fig. 5 Visualization of the Geant4 geometry of the scintillator and HPGe detector, and a coincidence muon event. Particle tracks are: blue—muon, green—photon, red—electron

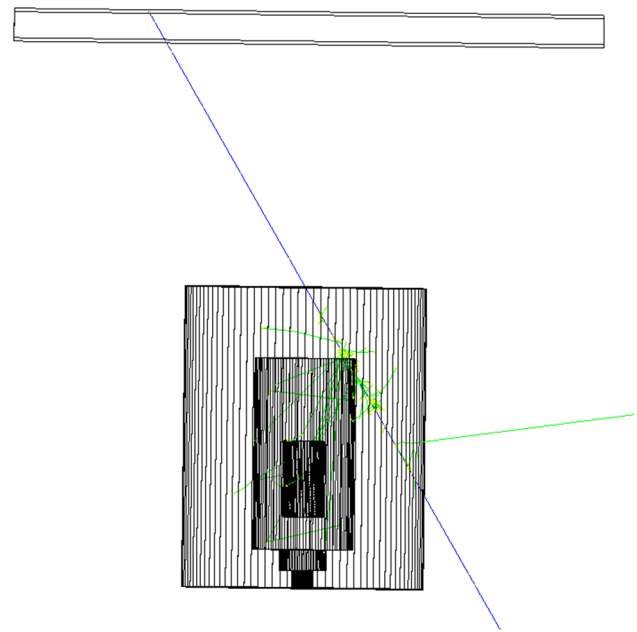
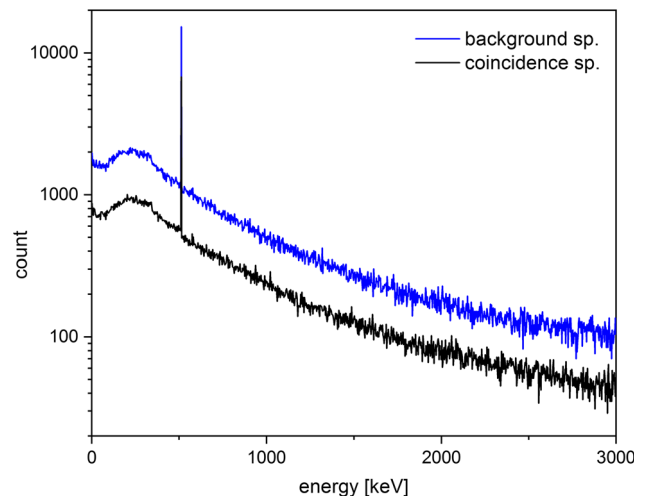


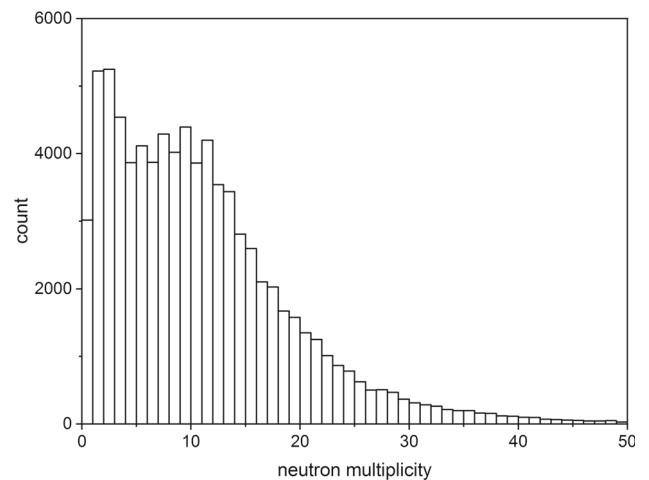
Fig. 6 Normalized background spectrum (blue line) and coincidence spectrum of the HPGe detector (black line) induced by prompt muon interactions in lead, and estimated anti-cosmic veto suppression [13]



are an unavoidable source of background. As it was already pointed out, the experimental set-up in the underground laboratory enables studies of muon-induced events in the HPGe detector, when it works in coincidence with the muon detector. Preliminary results on flux of fast neutrons produced by muons in the lead shielding of the HPGe detector were reported in [9]. Data were collected during over 400 days of measurement. Neutrons were identified from the 692 keV line in the coincidence spectrum, which arises from neutron inelastic scattering on Ge-72 isotope. Neutron production rate can be determined from count rate in the 692 keV line in the spectrum [30]. The muon-induced neutron flux, within the volume of the lead shielding, is $(3.1 \pm 0.5) \times 10^{-4} \text{ cm}^{-2} \text{ s}^{-1}$.

A variety of Geant4 simulation methods have been utilized in studies of production of neutrons by cosmic muons in lead at the surface and underground [31–33]. Here we present the first results of the simulation of muon-induced neutron production in the lead shielding of the HPGe detector. It was done in the same manner as the previous simulations. Primary muons were generated on the top and side surfaces of the lead castle. Muon energy and directional distributions followed the same procedure described in Sect. 3. Hadronic interactions were included through the Geant4 QGSP_BERT_HP physics list. It uses high precision neutron models and cross sections for low-energy neutron interactions. For electromagnetic part the G4EmStandardPhysics_option4 constructor was activated. The simulation was then repeated with the physics lists FTFP_BERT_HP and Shielding, latter is recommended for neutron transport. All three physics models invoke the same classes for neutron interactions. There was no significant difference in the results. Because energy thresholds for production of secondary particles were set at low values, large number of particles was produced. Hence all secondaries but muons and neutrons were killed, and only muons and neutrons were tracked through the lead volume.

Fig. 7 Multiplicity distribution of neutrons produced by muons in lead at the 25 m w e depth



Neutron yield in lead can be determined from the equation $Y_n = N_n / (N_\mu l_\mu \rho)$, where N_n is number of neutrons produced, N_μ is number of muons, l_μ is the mean path length of muons and ρ is density. In total 10^8 muon histories were generated, and 9.34×10^5 neutrons were produced. The mean path length that muons travel through the lead castle, obtained from the simulation, is 26.6 cm. Finally, the neutron yield in the lead volume is $(3.1 \pm 0.4) \times 10^{-5}$ neutrons per gcm^{-2} per muon. It was also looked at how many of these neutrons reach the HPGe detector inside the lead castle—it was approx. 2.4% of all neutrons, though statistics was rather poor for precise studies of neutron-induced processes in the germanium detector. Additionally, neutron multiplicity for each event was found, as number of neutrons per tagged muon. Its distribution is shown in Fig. 7, while the average multiplicity is 11.5.

5 Conclusion

The Geant4-based simulations have been extensively used in experiments carried out in the low-background underground laboratory at the Institute of Physics Belgrade. Here presented overview describes applications of Geant4 simulations in measurements of cosmic-ray muon intensity and in gamma spectroscopy studies of events which have origin in cosmic muons. Detector responses of the plastic scintillation detectors and the germanium detector were obtained in order to evaluate experimental results. In simulations of the surface scintillator primary particles were generated by CORSIKA programme, so as to include electromagnetic component, which is absent underground. Simulated energy deposit spectra showed good agreement with experimental ones. Comparing these spectra precise calculations of muon integral intensity could be calculated. The measured muon fluxes at the surface and underground are $(170 \pm 6) \text{ m}^{-2} \text{ s}^{-1}$ and $(44 \pm 1) \text{ m}^{-2} \text{ s}^{-1}$, respectively. The results are consistent with our previous work and available muon data.

Simulation studies of cosmic muon interactions with lead were performed with a goal to estimate muon-induced background in the germanium detector. Muons can cause two types of background: the first one is due to prompt interactions of muons and secondary particles produced by muons and the second one is due to delayed decays of Ge nuclei produced in neutron inelastic collisions. The prompt muon-induced background was estimated with a simulation of the scintillator and the HPGe detector in coincidence, for the given detector configuration. The two detectors can operate in coincidence or anticoincidence provided the correct selection criteria between recorded events. When they work in anticoincidence the scintillator serves as an anti-cosmic veto. Simulated prompt muon background is also an estimation of the reduction of cosmic background by the veto, which in this case is by one half. The new experimental set-up has the muon detector close to the lead castle, which should improve the background reduction. Another task that was carried out was the simulation of neutron production by cosmic muons in lead. The estimated yield in the lead volume is $(3.1 \pm 0.4) \times 10^{-5}$ neutrons per gcm^{-2} per muon. Also neutron multiplicity per tagged muon is obtained. The results make a good basis for further studies of cosmic muon-induced processes in the vicinity of germanium detectors, including production of neutrons and other particles in the overburden rocks.

Acknowledgements The authors acknowledge funding provided by the Institute of Physics Belgrade, through the grant by the Ministry for Science, Technological Development and Innovation of the Republic of Serbia. The authors thank the reviewers for valuable suggestions that improved quality of the manuscript.

Data Availability Statement This manuscript has associated data in a data repository. [Authors' comment: Data sets generated during the current study are available from the corresponding author. Time series of muon flux data are available at http://cosmic.ipb.ac.rs/muon_station/index.html. The simulation code used in this work is publicly available at the zenodo.org data repository, <https://doi.org/10.5281/zenodo.10005170>.]

Declarations

Conflict of interest The authors have no competing interests to declare that are relevant to the content of this article.

References

1. A. Dragić et al., Nucl. Technol. Radiat. Prot. **26**, 181 (2011)
2. A. Dragić et al., Nucl. Instrum. Methods Phys. Res. A **591**, 470 (2008)
3. N. Veselinović et al., Nucl. Instrum. Methods Phys. Res. A **875**, 10 (2017)
4. M. Savić et al., Astropart. Phys. **109**, 1 (2019)
5. N. Veselinović et al., Eur. Phys. J. D **75**, 173 (2021)
6. V.A. Kudryavtsev, L. Pandola, V. Tomasello, Eur. Phys. J. A **36**, 171 (2008)
7. D. Barker, D.-M. Mei, C. Zhang, Phys. Rev. D **86**, 054001 (2012)
8. H.W. Bae, E.J. Jeon, Y.D. Kim, S.W. Lee, Astropart. Phys. **114**, 60 (2020)
9. A. Dragić et al., J. Phys. Conf. Ser. **409**, 012054 (2013)
10. Geant4, <https://geant4.web.cern.ch/>
11. S. Agostinelli et al., Nucl. Instrum. Methods Phys. Res. A **506**, 250 (2003)
12. J. Allison et al., Nucl. Instrum. Methods Phys. Res. A **835**, 186 (2016)
13. D.R. Joković et al., Appl. Radiat. Isot. **67**, 719 (2009)
14. P.K.F. Grieder, *Cosmic Rays at Earth* (Elsevier, Amsterdam, 2001), p.372
15. P.K.F. Grieder, *Cosmic Rays at Earth* (Elsevier, Amsterdam, 2001), p.498
16. T.K. Gaisser, *Cosmic Rays and Particle Physics* (Cambridge University Press, Cambridge, 1990), p.71
17. M. Guan et al., *Muon Simulation at the Daya Bay Site* (Lawrence Berkeley National Laboratory, 2010)
18. P.K.F. Grieder, *Cosmic Rays at Earth* (Elsevier, Amsterdam, 2001), p.467
19. CORSIKA, <https://www.iap.kit.edu/corsika/>
20. D. Heck et al., CORSIKA: a Monte Carlo code to simulate extensive air showers, Report FZKA 6019. (Forschungszentrum Karlsruhe, 1998)
21. T. Enquist et al., Nucl. Instrum. Methods Phys. Res. A **554**, 286 (2005)
22. P.A. Zyla et al., Prog. Theor. Exp. Phys. **2020**, 083C01 (2020)
23. B. Mitrica et al., Adv. High Energy Phys. **2013**, 256230 (2013)
24. N. Jovančević et al., Nucl. Instrum. Methods Phys. Res. A **612**, 303 (2010)
25. N.Q. Hung, V.H. Hai, M. Nomachi, Appl. Radiat. Isot. **121**, 87 (2017)
26. R. Breier, M. Laubenstein, P.P. Povinec, Appl. Radiat. Isot. **126**, 188 (2017)
27. M. Baginova, P. Vojtyla, P.P. Povinec, Astropart. Phys. **143**, 102756 (2022)
28. J. Knezevic et al., Nucl. Instrum. Methods Phys. Res. A **1032**, 166624 (2022)
29. M. Travar et al., J. Radioanal. Nucl. Chem. **332**, 817 (2023)
30. G. Škoro et al., Nucl. Instrum. Methods Phys. Res. A **316**, 333 (1992)
31. L. Reichhart et al., Astropart. Phys. **47**, 67 (2013)
32. Q. Du et al., Astropart. Phys. **102**, 12 (2018)
33. R. Kneißl et al., Astropart. Phys. **111**, 87 (2019)

Springer Nature or its licensor (e.g. a society or other partner) holds exclusive rights to this article under a publishing agreement with the author(s) or other rightsholder(s); author self-archiving of the accepted manuscript version of this article is solely governed by the terms of such publishing agreement and applicable law.



Search for the evidence of $^{209}\text{Bi}(\gamma, p5n)^{203}\text{Pb}$ reaction in 60 MeV bremsstrahlung beams

M. Krmar^{1,a}, N. Jovančević¹, D. Maletić², Ž. Medić², D. Knežević², M. Savić², Yu. Teterev³, S. Mitrofanov³, K. D. Timoshenko³, S. I. Alexeev³, H. Marukyan⁴, I. Kerobyan⁴, R. Avetisyan⁴, L. Poghosyan⁴, R. Dallakyan⁴, A. Hakobyan⁴, L. Vahradyan⁴, H. Mkrtchyan⁴, A. Petrosyan⁴

¹ Physics Department, Faculty of Science, University Novi Sad, Novi Sad, Serbia

² Institute of Physics, Belgrade, Serbia

³ Flerov Laboratory of Nuclear Reactions, Joint Institute for Nuclear Research, Dubna, Russia

⁴ A. Alikhanyan National Science Laboratory (Yerevan Physics Institute), Yerevan, Armenia

Received: 2 June 2023 / Accepted: 11 July 2023 / Published online: 26 July 2023

© The Author(s), under exclusive licence to Società Italiana di Fisica and Springer-Verlag GmbH Germany, part of Springer Nature 2023

Communicated by Jose Benlliure

Abstract Samples made from natural bismuth were exposed in 60 MeV end-point bremsstrahlung beam. In this paper, a simple model for determination the share of two ways of ^{203}Pb formation: by the decay of ^{203}Bi , produced in $^{209}\text{Bi}(\gamma, 6n)^{203}\text{Bi}$ reaction and by $^{209}\text{Bi}(\gamma, p 5n)^{203}\text{Pb}$ reaction is described. The method employs the ratio of ^{203}Pb and ^{203}Bi nuclei numbers and activities at the end of the exposure as the input value. This ratio was estimated from gamma spectra measured after irradiation of natural Bi sample. It was found that the rate of production of ^{203}Pb by $^{209}\text{Bi}(\gamma, p 5n)^{203}\text{Pb}$ reaction is about 6% of the ^{203}Bi production rate in the $^{209}\text{Bi}(\gamma, 6n)^{203}\text{Bi}$ reaction. Obtained result is compared with TALYS based estimation.

1 Introduction

The simplest photonuclear reaction (γ, n) usually takes place through the well-known mechanism of giant dipole resonance. For a large number of stable nuclei, the energy differential cross section of this reaction has been successfully measured [1, 2]. Data on photonuclear reactions can be found in available databases [3] also. The experimental evidence for the ($\gamma, 2n$) reaction is much poorer, while for reactions when three or more neutrons are emitted (usually denoted by (γ, xn)), the reaction cross sections can be obtained by mainly by theoretical calculations [4]. For reactions in which a charged particle, such as proton in the simplest case, is emitted (single or in addition to one or more neutrons) there is a much poorer experimental evidence. In the interactions of

high energy photons with nuclei, the probability of emission of a charged particle is significantly lower than the emission of neutrons due to the existence of the Coulomb barrier. It is a reason why experimental data concerning ($\gamma, p xn$) are insufficient in literature.

Cross sections for photonuclear reactions on natural bismuth (monoisotope ^{209}Bi) with emission of one and two neutrons can be found in the reference [5]. In several recently published papers [6–11], photonuclear reactions with Bi target exposed in bremsstrahlung photon beams having end-point energies up to 70 MeV were studied. Irradiation of such a heavy element by the high energy photons can give several products of (γ, xn) reactions. In these publications, the relative yield of photonucleated reactions on ^{209}Bi was analyzed, while in reference [12] the cross section results for reactions (γ, n), ($\gamma, 2n$), ($\gamma, 3n$) and ($\gamma, 4n$) were presented. The authors of reference [12] used natural bismuth target and quasimonochromatic laser Compton-scattering γ -ray beams with energies up to 40 MeV. In reference [11], reaction channel (γ, pxn) with emission of one proton along with several neutrons is accounted for.

In this paper, an attempt was made to establish experimental evidence for $^{209}\text{Bi}(\gamma, p 5n)^{203}\text{Pb}$ nuclear reaction by comparison of intensities of gamma lines following EC decay of ^{203}Bi and ^{203}Pb . Lead-203 can be formed by ($\gamma, p 5n$) nuclear reaction, but it is certainly created after decay of ^{203}Bi , obtained in $^{209}\text{Bi}(\gamma, 6n)^{203}\text{Bi}$ reaction. After activation of the target made from natural bismuth by 60 MeV end-point energy bremsstrahlung beam, several gamma spectra were successively measured. Gamma lines from the measured spectra were selected in order to estimate the ratio of created nuclei numbers of ^{203}Bi and ^{203}Pb in the moment

^a e-mail: krmar@df.uns.ac.rs (corresponding author)

Fig. 1 Part of the chart containing relevant nuclides

Bi202 1.72 h 5+ EC, α	Bi203 11.76 h 9/2- EC, α	Bi204 11.22 h 6+ EC	Bi205 15.31 d 9/2- EC	Bi206 6.243 d 6(+) EC	Bi207 31.55 y 9/2+ EC	Bi208 3.68E5 y (5)+ EC	Bi209 Stable 9/2- 100%
Pb201 9.33 h 5/2- EC	Pb202 5.24E4 y 0+ EC	Pb203 51.873 h 5/2- EC	Pb204 1.4E17 y 0+ 1.4%	Pb205 1.53E7 y 5/2- EC	Pb206 Stable 0+ 24.1%	Pb207 Stable 1/2- 24.1%	Pb208 Stable 0+ 52.4%

when irradiation was stopped. Probability ratio for the occurrence of $(\gamma,6n)$ and $(\gamma,p5n)$ nuclear reactions can be obtained from these data.

For the purposes of this paper, the cross sections for the observed nuclear reactions were extracted using the TALYS code. These cross-sections were used to estimate the ratio of probabilities of nuclear reactions of interest in order to compare them with the values obtained by measurements.

2 Materials and methods

Considering that lead isotopes ^{206}Pb , ^{207}Pb and ^{208}Pb are stable (Fig. 1), $^{209}\text{Bi}(\gamma,p3n)^{205}\text{Pb}$ is the very first photonuclear reaction on ^{209}Bi which can give active lead as a product. However, half life of ^{205}Pb is $1.57 \cdot 10^7$ y and small amount of produced ^{205}Pb , would be very difficult to detect. Moreover, this isotope does not emit gamma radiation.

The next candidate which can be used to verify if (γ,pxn) on natural bismuth can yield measurable amounts of reaction products is ^{204m}Pb . Half life of ^{204m}Pb is 67.2 min and de-excitation of isomer state takes place through several gamma transitions having high quantum yield. However, ^{204m}Pb can be created by decay of ^{204}Bi , produced in $(\gamma,5n)$ photonuclear reaction. This means that de-excitation of the isomeric state of ^{204m}Pb created in $(\gamma,p4n)$ results in gamma transitions that are almost the same as those occurred after the ^{204}Bi decay. It is very difficult to estimate how ^{204}Bi decay and ^{204m}Pb de-excitation contribute to the total intensity of some of measured gamma lines.

Another possibility to check if irradiation of ^{209}Bi by high-energy photons results in proton emission together with several neutrons is lead isotope ^{203}Pb . This isotope can be created by $(\gamma,p5n)$ reaction. Half-life of ^{203}Pb is 51.873 h and after decay two intensive lines in gamma spectra can be observed. A study of gamma photons originating from the decay of ^{203}Pb could be a good way to determine if $(\gamma,p5n)$ reaction can give measurable amount of ^{203}Pb during irradiation of the natural bismuth target by high energy photons. But in order to do that, it is necessary to estimate, in some way, how much of the ^{203}Pb activity comes from decay of ^{203}Bi .

2.1 Irradiation

In interactions of ^{209}Bi nuclei with high energy photons, several bismuth isotopes can be created through (γ,xn) reactions. Suppose that a bismuth isotope ^{203}Bi , we have chosen to analyze, is formed at a constant rate q in a photon beam. The change of the number of nuclei of observed bismuth isotope can then be described by the following differential equation:

$$\frac{dN_{Bi}}{dt} = q - \lambda_{Bi}N_{Bi} \quad (1)$$

λ_{Bi} is decay constant of ^{203}Bi , created in $(\gamma,6n)$ photonuclear reaction. The number of created ^{203}Bi nuclides after irradiation time t_{irr} is:

$$N_{Bi} = \frac{q}{\lambda_{Bi}}(1 - \exp(-\lambda_{Bi}t_{irr})) \quad (2)$$

The dynamics of the number of ^{203}Pb nuclei created exclusively by the decay of ^{203}Bi can be expressed as:

$$\frac{dN_{Pb}}{dt} = \lambda_{Bi}N_{Bi} - \lambda_{Pb}N_{Pb} \quad (3)$$

The very same ^{203}Pb isotope can additionally be produced through the $(\gamma,p5n)$ nuclear reaction. In the case when the production of ^{203}Pb occurs, process can be described by the following equation:

$$\frac{dN_{Pb}}{dt} = \lambda_{Bi}N_{Bi} + p - \lambda_{Pb}N_{Pb} \quad (4)$$

where p denotes a constant rate of ^{203}Pb production through the $(\gamma,p5n)$ nuclear reaction. It can be considered that at the very beginning ($t = 0$), there were no ^{203}Pb nuclei. The solutions of differential Eqs. 3 and 4 describing time evolution of the number of ^{203}Pb isotopes are:

$$N_{Pb} = q \left[\frac{1}{\lambda_{Pb}}(1 - \exp(-\lambda_{Pb}t_{irr})) + \frac{1}{\lambda_{Pb} - \lambda_{Bi}}(\exp(-\lambda_{Pb}t_{irr}) - \exp(-\lambda_{Bi}t_{irr})) \right] \quad (5)$$

in the case when ^{203}Pb originates from the decay of ^{203}Bi , and

$$N_{Pb} = q \left[\frac{1 + \frac{p}{q}}{\lambda_{Pb}} (1 - \exp(-\lambda_{Pb}t_{irr})) + \frac{1}{\lambda_{Pb} - \lambda_{Bi}} (\exp(-\lambda_{Pb}t_{irr}) - \exp(-\lambda_{Bi}t_{irr})) \right] \quad (6)$$

when production of ^{203}Pb through $(\gamma, p \ 5n)$ can not be neglected.

Using Eqs. 2 and 5 ratio $N_{Pb}(t_{irr})/N_{Bi}(t_{irr})$ of produced numbers of ^{203}Pb and ^{203}Bi nuclei, in the case when ^{203}Pb is produced only by the ^{203}Bi decay, can be determined as:

$$\frac{N_{Pb}(t_{irr})}{N_{Bi}(t_{irr})} = \frac{\frac{\lambda_{Bi}}{\lambda_{Pb}} (1 - \exp(-\lambda_{Pb}t_{irr})) + \frac{\lambda_{Bi}}{\lambda_{Pb} - \lambda_{Bi}} (\exp(-\lambda_{Pb}t_{irr}) - \exp(-\lambda_{Bi}t_{irr}))}{1 - \exp(-\lambda_{Bi}t_{irr})} \quad (7)$$

It can be seen from Eq. 7 that the ratio of ^{203}Pb and ^{203}Bi nuclei numbers does not depend on the rate q at which Bi is generated in photonuclear reaction.

In a similar way, using Eqs. 2 and 6, it can be determined the $^{203}\text{Pb}/^{203}\text{Bi}$ nuclei number ratio for the case when the ^{203}Pb isotope is formed by decay of ^{203}Bi and the direct $^{209}\text{Bi}(\gamma, p \ 5n)$ reaction as well.

$$\frac{N_{Pb}(t_{irr})}{N_{Bi}(t_{irr})} = \frac{(1 + \frac{p}{q}) \frac{\lambda_{Bi}}{\lambda_{Pb}} (1 - \exp(-\lambda_{Pb}t_{irr})) + \frac{\lambda_{Bi}}{\lambda_{Pb} - \lambda_{Bi}} (\exp(-\lambda_{Pb}t_{irr}) - \exp(-\lambda_{Bi}t_{irr}))}{1 - \exp(-\lambda_{Bi}t_{irr})} \quad (8)$$

From the above Eq. 8, we can see that the ratio p/q , ie. the production rate of ^{203}Bi by the emission of six neutrons and the rate of production of ^{203}Pb by $(\gamma, p \ 5n)$ nuclear reaction affects ratio of these two isobars. It can be seen that, if there is no proton emission, ie. if $p = 0$, Eq. 8 turns into Eq. 7.

All the above equations, as well as those that will follow in which the ratios of the nuclei of the observed two isotopes N_{Pb}/N_{Bi} can be written in the form where the ratios of their activities A_{Pb}/A_{Bi} appear.

2.2 Decay measurement

At the moment when the irradiation is completed, there will be some number of both radionuclides in the bismuth sample: $N_{Pb}(t_{irr})$ and $N_{Bi}(t_{irr})$. After the end of the irradiation, it is possible to register gamma spectra of irradiated sample and $N_{Pb}(t_{irr})$ and $N_{Bi}(t_{irr})$ can be considered as the initial numbers of ^{203}Bi and ^{203}Pb . Let's denote them as N_{Bi}^0 and N_{Pb}^0 . Starting from the end of irradiation, activity of ^{203}Bi

will decrease according to a well-known exponential law

$$N_{Bi}(t) = N_{Bi}^0 \exp(-\lambda_{Bi}t) \quad (9)$$

while the dynamics of the time change of ^{203}Pb activity will be determined by the rate of its simultaneous decay and creation from ^{203}Bi . It is well known that a number of daughter nuclei in the case of simultaneous decay can be described as:

$$N_{Pb}(t) = \frac{\lambda_{Bi}}{\lambda_{Pb} - \lambda_{Bi}} N_{Bi}^0 (\exp(-\lambda_{Bi}t) - \exp(-\lambda_{Pb}t)) + N_{Pb}^0 \exp(-\lambda_{Pb}t) \quad (10)$$

Let's assume that the recording of the gamma spectrum started at the moment t_1 after the end of the irradiation, and that the measurement was stopped at the moment t_2 . In that time interval, the number of decayed ^{203}Bi nuclei is:

$$N_{Bi}^D = N_{Bi}^0 (\exp(-\lambda_{Bi}t_1) - \exp(-\lambda_{Bi}t_2)) \quad (11)$$

By integrating the function that describes the temporal change of ^{203}Pb activity within the same time limits, it is obtained that the total number of ^{203}Pb nuclei that decayed is:

$$N_{Pb}^D = \frac{\lambda_{Bi}}{\lambda_{Bi} - \lambda_{Pb}} N_{Bi}^0 (\exp(-\lambda_{Pb}t_1) - \exp(-\lambda_{Pb}t_2)) - \frac{\lambda_{Pb}}{\lambda_{Bi} - \lambda_{Pb}} N_{Bi}^0 (\exp(-\lambda_{Bi}t_1) - \exp(-\lambda_{Bi}t_2)) + N_{Pb}^0 (\exp(-\lambda_{Pb}t_1) - \exp(-\lambda_{Pb}t_2)) \quad (12)$$

From Eqs. 11 and 12 the values of N_{Bi}^0 and N_{Pb}^0 can be estimated, but in some cases it is more convenient to analyze the ratio of the number of decays of the observed two nuclides:

$$\frac{N_{Pb}^D}{N_{Bi}^D} = \frac{\lambda_{Bi}}{\lambda_{Bi} - \lambda_{Pb}} \frac{\exp(-\lambda_{Pb}t_1) - \exp(-\lambda_{Pb}t_2)}{\exp(-\lambda_{Bi}t_1) - \exp(-\lambda_{Bi}t_2)} - \frac{\lambda_{Pb}}{\lambda_{Bi} - \lambda_{Pb}} + \frac{N_{Pb}^0}{N_{Bi}^0} \frac{\exp(-\lambda_{Pb}t_1) - \exp(-\lambda_{Pb}t_2)}{\exp(-\lambda_{Bi}t_1) - \exp(-\lambda_{Bi}t_2)} \tag{13}$$

As can be seen from Eq. 13, if the ratio of the decay numbers of ²⁰³Pb and ²⁰³Bi is known, it is possible to estimate the ratio of the initial numbers of these two nuclides N_{Pb}^0/N_{Bi}^0 .

In order to determine the ratio of the number of decays N_{Pb}^D/N_{Bi}^D in a selected time interval, two gamma lines, one from ²⁰³Pb and another from ²⁰³Bi should be selected their intensities should be determined. Let's denote registered intensities with N_{Bi}^R and N_{Pb}^R . Ratio N_{Pb}^D/N_{Bi}^D can be determined as:

$$\frac{N_{Pb}^D}{N_{Bi}^D} = \frac{N_{Pb}^R}{N_{Bi}^R} \frac{\varepsilon_{Bi} p_{\gamma}^{Bi}}{\varepsilon_{Pb} p_{\gamma}^{Pb}} \tag{14}$$

The quantum yields of the observed gamma transitions of ²⁰³Bi and ²⁰³Pb are denoted by p_{γ}^{Bi} and p_{γ}^{Pb} while ε_{Bi} and ε_{Pb} are the absolute detection efficiency at the selected energies. From Eq. 14 it can be seen that it is sufficient to know the relative efficiency of the detector system for the used geometry.

2.3 Procedure of the results extraction

And finally, let's summarize the procedure that can be used to prove whether a measurable contribution of (γ,p 5n) reaction could be expected:

- (a) the ratio of ²⁰³Pb and ²⁰³Bi nuclei numbers, expected at the end of irradiation, without contribution of (γ,p 5n) reaction, could be calculated using Eq. 7;
- (b) intensities of selected gamma lines should be obtained. The N_{Pb}^D/N_{Bi}^D ratio can be calculated using Eq. 14;
- (c) Equation 13 should be used to obtain the ratio of initial nuclei numbers N_{Pb}^0/N_{Bi}^0 , created during exposition in the photon beam;
- (d) obtained N_{Pb}^0/N_{Bi}^0 ratio can be compared with the result derived from Eq. 7. If the obtained values coincide within the interval of experimental error, it can be concluded that the reaction (γ,p 5n) does not give a measurable contribution to the activity of ²⁰³Pb. However, if the contribution of the reaction (γ,p 5n) to the total number of ²⁰³Pb cannot be neglected, the N_{Pb}^0/N_{Bi}^0 ratio obtained by Eq. 13 should be greater than the ratio acquired from Eq. 7
- e) and finally, if the ratios N_{Pb}^0/N_{Bi}^0 differ, it is possible to find the value of the parameter p/q in Eq. 8 which gives the N_{Pb}^0/N_{Bi}^0 ratio experimentally established.

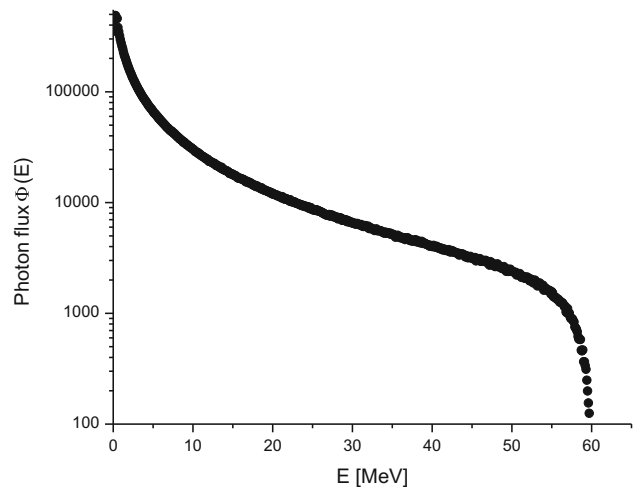


Fig. 2 The shape of the photon spectrum $\Phi(E)$ obtained for 30 M incident electrons

The described procedure can give confirmation about contribution of the (γ,p 5n) reaction to the total activity of ²⁰³Pb and to estimate the value p/q .

2.4 Theoretical calculations

The rate of some nuclear reaction at the selected target is directly proportional to the product of the cross section and the number of incident particles. This means that the quantities p and q would be proportional to the saturation activities of observed reactions:

$$q \sim \int_{E_t}^{E_{max}} \sigma_{6n}(E)\Phi(E)dE \tag{15}$$

$$p \sim \int_{E_t}^{E_{max}} \sigma_{p,5n}(E)\Phi(E)dE \tag{16}$$

where $\Phi(E)$ is photon fluency, E_t is energy threshold for observed nuclear reaction and E_{max} is end-point energy of the photon spectra (in our case 60 MeV). By $\sigma_{6n}(E)$ and $\sigma_{p,5n}(E)$ cross-sections for (γ,6n) and (γ,p 5n) nuclear reactions are denoted respectively.

The simplest way to check the obtained result for the p/q ratio would be to calculate the saturation activities for these two reactions using Eqs. 15 and 16 and compare them with the experimental result.

The shape of the photon spectrum $\Phi(E)$ is obtained by using Geant4 software package [13], version v11.1.0, with standard G4 electromagnetic physics option selected. The simulation starts with creating 30 M of 60 MeV electrons in the beam, with very small Gaussian spread in energy of 0.01 MeV. The photon spectrum, obtained at the place of irradiated sample based on the geometry described in the next section is presented in Fig. 2.

There is no experimental evidence of the cross sections of $^{209}\text{Bi}(\gamma,6n)$ and $^{209}\text{Bi}(\gamma,p\ 5n)$ nuclear reactions in literature. Related information can be obtained using some numerical code for evaluation of the cross sections for nuclear reactions. In this experiment, TALYS 1.9 code was used to estimate cross sections for $^{209}\text{Bi}(\gamma,p\ 5n)^{203}\text{Pb}$ and $^{209}\text{Bi}(\gamma,6n)^{203}\text{Bi}$ reactions. It was decided to use SMLO model for a strength function. It can be expected that the choice of the strength function model has an impact on the estimation of the cross section, but that analysis is beyond the scope of this paper. Six different models of level density were employed in calculations. Cross sections were calculated using phenomenological (1. The Fermi Gas Model + Constant Temperature Model, 2. The Back-shifted Fermi gas Model, 3. The Generalized Superfluid Model) and microscopic (4. Skyrme-Hartree-Fock-Bogoluybov, 5. Gogny-Hartree-Fock-Bogoluybov and temperature-dependent 6. Gogny-Hartree-Fock-Bogoluybov models) of level density [14].

3 Measurements

One coin-shaped sample of natural bismuth (high purity 99.999%), 1 cm diameter and mass of 1.1 g, was exposed in bremsstrahlung photon beam having maximal energy of 60 MeV. The source of the photon beams was the linear electron accelerator LUE-75 located at A. Alikhanyan National Science Laboratory in Yerevan, Armenia. Accelerated electrons, after passing through a cylindrical collimator (length of 20 mm and a diameter of 15 mm) strike a pure tungsten converter. The thickness of the converter was 2 mm, and a 30 mm long aluminum cylinder was placed directly behind it. The function of the aluminum was to stop the electrons that passed through the tungsten. At a distance of 60 mm from the tungsten plate, a Bi coin was placed. Duration of exposition was 30 min.

After 22 min., exposed Bi coin was placed 86 mm from the end cap of HPGe detector. Measurement setup is presented in Fig. 3. Activity of measured samples was high enough and no detector shielding was used. Sample was fixed by tape to the holder ring above detector. First 5400 s spectrum was measured and second one was collected during 79,463 s. In the measured spectra, gamma lines from several Bi isotopes were identified. The lightest one was ^{202}Bi . Gamma line intensities were determined using the GENIE software package.

The most intense ^{203}Pb gamma transition of 279.2 keV (quantum yield 81%) was selected for calculation procedure. In both collected spectra, a prominent single 279.2 keV gamma line appeared. For example, in the first spectrum, intensity of this line was $5.87(28)\cdot 10^3$ counts. In the second spectrum, intensity of this line was $3.71(2)\cdot 10^5$ detected

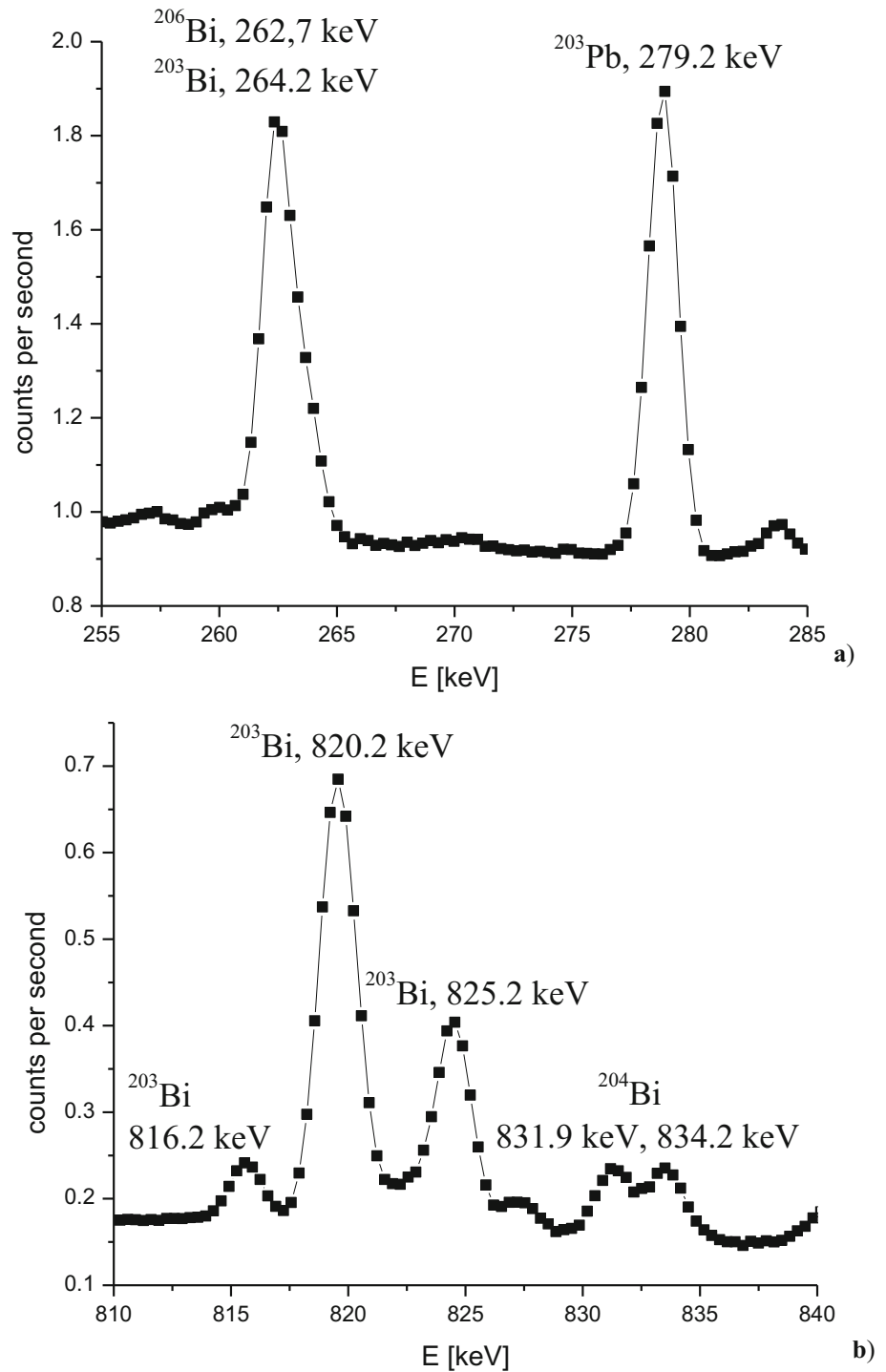


Fig. 3 Measurement setup

counts. Several strong gamma lines of ^{203}Bi were identified in spectra, however almost all of them are parts of doublets or even multiplets. In order to avoid errors caused during the numerical procedure in separation of the intensity of individual lines in doublets, several gamma transitions of ^{203}Bi were chosen for calculation. Ratio of decayed nuclei $N_{\text{Pb}}^D/N_{\text{Bi}}^D$ was calculated using Eq. 14 and intensities of 264.2 keV, 816.2 keV and 1033.8 keV gamma lines of ^{203}Bi and mean average was calculated. For example, in the first spectrum intensity of 264.2 keV gamma line was $3.63(7)\cdot 10^4$ detected counts. Considering that activity of ^{203}Bi decreased all the time, while the activity of ^{203}Pb increased, intensity 264.2 keV gamma line was smaller than 279.2 keV gamma line of ^{203}Pb in second spectra. Intensity of 264.2 keV gamma line was $1.015(15)\cdot 10^4$ counts. Two segments of measured gamma spectra are depicted in Fig. 4.

It can be seen from the Eq. 14 that the $N_{\text{Pb}}^D/N_{\text{Bi}}^D$ ratio can be obtained using the relative efficiency of the detection system. The best way to get relative efficiency is to use gamma lines of ^{206}Bi . Half-life of this isotope is 6.243 days and there are many intensive gamma transitions from 183.98 to 2 MeV. The longer spectrum was used and 16 gamma lines of ^{206}Bi , starting from 183.98 keV to 1878.65 keV were selected to get relative efficiency. Combination of an exponential function and a second order polynomial was used in fit procedure.

Fig. 4 Two parts of gamma spectra: **a)** low energy part containing ^{203}Pb gamma line (279.2 keV) and $^{203}\text{Bi}/^{206}\text{Bi}$ doublet; **b)** multiplet containing three ^{203}Bi lines



4 Results and discussion

4.1 Experiment

The estimation of the $N_{\text{Pb}}(t_{\text{irr}})/N_{\text{Bi}}(t_{\text{irr}})$ ratio at the moment when irradiation was stopped can be obtained from the Eq. 7.

This equation describes output of the $(\gamma,6n)$ reaction, without proton emission. It was obtained that the ratio of created ^{203}Pb and ^{203}Bi nuclei is $N_{\text{Pb}}(t_{\text{irr}})/N_{\text{Bi}}(t_{\text{irr}}) = 0.0148$. If no $(\gamma,p5n)$ reaction occurs, it could be expected that number of ^{203}Pb created nuclei is 1.48% of the number of ^{203}Bi nuclei, after 30 min of irradiation. Ratio of activities of two

Table 1 $^{203}\text{Pb}/^{203}\text{Bi}$ activity ratio at the end of irradiation

	$N_{\text{Pb}(t_{\text{irr}})}/N_{\text{Bi}(t_{\text{irr}})}$	$A_{\text{Pb}(t_{\text{irr}})}/A_{\text{Bi}(t_{\text{irr}})}$
Without proton emission ($(\gamma,6n)$ only), Eq. 7	0.0148	0.00335
Experimental based values, Eq. 13	0.0758(8)	0.0172(2)

mentioned nuclei after irradiation is $A_{\text{Pb}(t_{\text{irr}})}/A_{\text{Bi}(t_{\text{irr}})} = 0.00335$.

The intensities of the selected gamma lines were determined in both measured spectra. Relative efficiency of detection was calculated using gamma lines of ^{206}Bi . Ratio of ^{203}Pb and ^{203}Bi nuclei that decayed in the observed time interval was evaluated as shown in Eq. 14. Obtained $N_{\text{Pb}}^D/N_{\text{Bi}}^D$ ratio was used to calculate value of $N_{\text{Pb}}^0/N_{\text{Bi}}^0$ ratios by Eq. 13. The ratio of activities at the moment when irradiation was stopped was calculated as well. Both registered spectra gave ratio results that agreed within experimental error. In the continuation of the paper, the results obtained from gamma lines measured in a longer spectrum will be presented, due to better counting statistics. The calculated and experimental values are presented in Table 1.

It can be seen from the data presented in Table 1 that the ratio of the numbers of created ^{203}Pb and ^{203}Bi nuclei, as well as their activity ratio, at the end of irradiation, extracted from the measured spectra, differs significantly from the estimation based on the assumption that no proton is emitted in photonuclear reaction. This leads us to the conclusion that the production of ^{203}Pb by some other process, probably $(\gamma, p 5n)$, in addition to the decay of ^{203}Bi can have a significant contribution.

After the experimental confirmation of the possibility that $(\gamma, p 5n)$ nuclear reaction can make a measurable contribution to total ^{203}Pb activity, the very next step is to estimate p/q ratio. Equation 8 gives such a possibility. If the irradiation time was 30 min and experimentally obtained ratio of ^{203}Pb and ^{203}Bi nuclei is 0.0758(8), it was estimated using Eq. 8, that p/q factor is 0.060(1). This means that the rate of production of ^{203}Pb by $^{209}\text{Bi}(\gamma, p 5n)$ reaction is 6% of the rate of $^{209}\text{Bi}(\gamma, 6n)$ ^{203}Bi (Fig. 5).

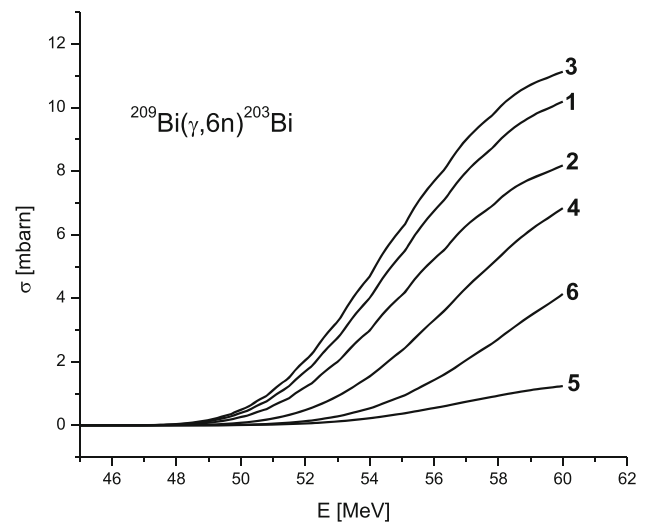


Fig. 5 TALYS estimations for cross section of $^{209}\text{Bi}(\gamma,6n)^{203}\text{Bi}$ reaction. The numbers indicate the level density model as numbered in Sect. 2.4

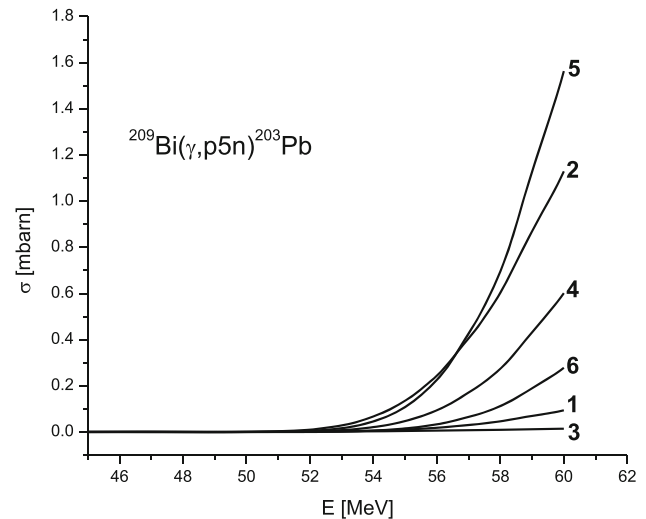


Fig. 6 TALYS estimations for cross section of $^{209}\text{Bi}(\gamma, p 5n)^{203}\text{Pb}$ reaction. The numbers indicate the level density model as numbered in Sect. 2.4

4.2 Calculated ratio of $^{209}\text{Bi}(\gamma, p 5n)$ and $^{209}\text{Bi}(\gamma, 6n)$ reaction probabilities

And finally, in order to estimate ratio of probabilities of $^{209}\text{Bi}(\gamma, p 5n)$ and $^{209}\text{Bi}(\gamma, 6n)$ reactions, denoted as p and q , it is necessary to calculate the energy differential cross section for both reactions using the TALYS code. The obtained results, for all six models of level densities are shown in Figs. 5 and 6. As might be expected, the cross section for a reaction without emission of positive charged particle is significantly larger than cross section for emission of one proton in addition to five neutrons. It should also be noted that the

Table 2 Ratio p/q obtained using measured activities and simulation performed with six different models of level densities (in the same order as stated in Sect. 2.4)

	p/q ratio
Estimated using TALYS cross sections	0.00278
	0.0472
	0.000698
	0.0329
	0.5077
	0.0295
Estimated from Eq. 8	0.060(1)

estimated cross sections for both observed reactions can be very different from each other, depending on which density of states model is chosen.

With the obtained values of cross section and chosen bremsstrahlung function it is possible to calculate p/q ratio using both Eqs. 15 and 16. The result of TALYS estimations are depicted in Table 2, together with results of calculations based on measured data.

It is referred that the results obtained in the photo-activation experiments on ^{208}Pb and ^{209}Bi [7, 8] are in good agreement with the calculations performed using the TALYS code. Some examples can be found in the literature [15, 16] that the results of TALYS calculations do not completely match the results of measurements. For the purpose of analyzing the obtained results, it is particularly important to emphasize that one of the conclusions presented in reference [11] is that the shares of $^{209}\text{Bi}(\gamma, p 4n)$ and $^{209}\text{Bi}(\gamma, p 5n)$ reaction are not negligible. The authors estimated that the yield of the $^{209}\text{Bi}(\gamma, p 4n)$ reaction obtained experimentally at 55.6 MeV bremsstrahlung beam was almost 15 times higher than the yield estimated using the TALYS code. In the case of $^{209}\text{Bi}(\gamma, p 5n)$ reaction, this difference is even greater.

Here, it is particularly important to point out that, based on the results presented in reference [11], it can be concluded that the yield of $^{209}\text{Bi}(\gamma, p 5n)^{203}\text{Pb}$ reaction is about 9.4 times higher than the yield of reaction $^{209}\text{Bi}(\gamma, 6n)^{203}\text{Bi}$. As can be seen from Table 2, in this paper it is estimated that the yield of $^{209}\text{Bi}(\gamma, 6n)^{203}\text{Bi}$ reaction is over 16 times higher than the yield of $^{209}\text{Bi}(\gamma, p 5n)^{203}\text{Pb}$ reaction. It is most likely that the Coulomb barrier significantly reduces the probability of reactions in which a charged particle is emitted.

According to the data presented in Table 2, it is difficult to get general conclusion concerning agreement between TALYS estimation and experimental results. As can be seen, TALYS estimations can be almost two orders of magnitude smaller than the experimentally obtained p/q value, as well as one order of magnitude higher.

5 Conclusions

In this study, an attempt was made to check if ^{203}Pb is formed in photonuclear reactions on ^{209}Bi exclusively from the decay of ^{203}Bi formed in $(\gamma, 6n)$ reaction or $(\gamma, p 5n)$ reaction also plays a part in it, as indicated in reference [11]. It has been shown that this estimation can be made if the ratio of ^{203}Pb and ^{203}Bi nuclei numbers, at the moment when the exposure of the Bi target in the photon beam is completed, is known.

Irradiation of the target from natural bismuth was performed at 60 MeV bremsstrahlung beam. Induced activity was measured in standard off-beam experiment. Registered spectra were used to extract numbers of created ^{203}Bi and ^{203}Pb nuclei. The obtained ratio of nuclei numbers indicates that ^{203}Pb is formed in some other way, other than from the decay of ^{203}Bi . The most likely mechanism is the $(\gamma, p 5n)$ reaction. Based on the experimentally estimated $^{203}\text{Pb}/^{203}\text{Bi}$ nuclei number (or activity) ratio at the moment when the irradiation was stopped, it is possible to estimate how much of the ^{203}Pb activity originates from $(\gamma, p 5n)$ reaction. It was obtained that the number of produced ^{203}Pb nuclei is about 7.6% of the number of ^{203}Bi nuclei. Based on this value, it was established that the rate of production of ^{203}Pb through $(\gamma, p 5n)$ reactions is about 6% of the rate of production of ^{203}Bi by $(\gamma, 6n)$ reaction. This is significantly less than presented in reference [11].

In order to verify the obtained results, a TALYS simulation of cross-sections for $(\gamma, p 5n)$ and $(\gamma, 6n)$ reaction was performed. According to the obtained cross-sections, ratio of reaction rates of both reactions was calculated using one model of strength function and six models of level density function. Due to large scatter of TALYS cross sections for both reactions obtained results of ratios of reaction rates differ significantly.

This approach neither verified nor contradicted certain indications [11] that TALYS code underestimates the probability of photonuclear events in which a proton is realized in addition to neutrons. A new experiment that primarily makes advantage of wider range of energies, preferably higher than 60 MeV and a more detailed analysis of theoretical results and TALYS simulations may eliminate this doubt. The new measurements will also help to resolve the dilemma of whether the yield of $^{209}\text{Bi}(\gamma, p 5n)^{203}\text{Pb}$ reaction is significantly higher than the yield of the $^{209}\text{Bi}(\gamma, 6n)^{203}\text{Bi}$ reaction, as stated in reference [11], or whether this ratio is significantly lower, as obtained in the measurements described in this paper. The method described in this study is not limited to the case of ^{209}Bi , and can be applied to other targets and products of photonuclear reactions.

Data Availability Statement This manuscript has no associated data or the data will not be deposited. [Authors' comment: This manuscript has no associated data.]

References

1. Handbook on Nuclear Activation Data, Technical Report Series 273, IAEA Vienna (1987)
2. Handbook of photonuclear data for applications: Cross sections and spectra, IAEA TECDOC 1178, IAEA Vienna (2000)
3. Experimental Nuclear Reaction Data (EXFOR) <https://www-nds.iaea.org/exfor/>
4. A.J. Koning, D. Rochman, Nucl. Data Sheets **113**(12), 2841–2934 (2012)
5. R.R. Harvey, J.T. Caldwell, R.L. Bramblett, S.C. Fultz, Phys. Rev. **136**(1B), 126–131 (1964)
6. H. Naik, A.V.R. Reddy, S. Ganesan, D. Raj, K. Kim, G. Kim, Y.D. Oh, D.K. Pham, M.H. Cho, I.S. Ko, W. Namkung, J. Korean Phys. Soc. **52**(3), 934–939 (2008)
7. H. Naik, S. Singh, A.V.R. Reddy, V.K. Manchanda, S. Ganesan, D. Raj, M.S. Rahman, K.S. Kim, G. Kim, Y.D. Oh, H.-S. Lee, M.-H. Cho, I.S. Ko, W. Namkung, Eur. Phys. J. A **41**, 323–334 (2009)
8. H. Naik, S. Singh, A. Goswami, V.K. Manchanda, G. Kim, K.S. Kim, M.-W. Lee, M.S. Rahman, D. Raj, S. Ganesan, S. Suryanarayana, M.-H. Cho, W. Namkung, Nucl. Instrum. Methods Phys. Res. B **269**, 1417–1424 (2011)
9. A.N. Ermakov, B.S. Ishkhanov, I.M. Kapitonov, I.V. Makarenko, V.N. Orlin, Phys. At. Nucl. **73**(5), 737–745 (2010)
10. S.S. Belyshev, A.N. Ermakov, B.S. Ishkhanov, V.V. Khankin, A.S. Kurilik, A.A. Kuznetsov, V.I. Shvedunov, K.A. Stopani, Nucl. Instrum. Methods Phys. Res. A **745**, 133–137 (2014)
11. S.S. Belyshev, D.M. Filipescu, I. Gheoghe, B.S. Ishkhanov, V.V. Khankin, A.S. Kurilik, A.A. Kuznetsov, V.N. Orlin, N.N. Peskov, K.A. Stopani, O. Tesileanu, V.V. Varlamov, Eur. Phys. J. A **51**, 67 (2015)
12. I. Gheorghe, H. Utsunomiya, S. Katayama, D. Filipescu, S. Belyshev, K. Stopani, V. Orlin, V. Varlamov, T. Shima, S. Amano, S. Miyamoto, Y.-W. Lui, T. Kawano, S. Goriely, Phys. Rev. C **96**, 044604 (1917) Erratum Physical Review C **99**, 059901 (2019)
13. S. Agostinelli et al., Geant4—a simulation toolkit. Nucl. Instrum. Meth. A **506**, 250–303 (2003)
14. A. Koning, S. Hilaire, S. Goriely, Simulation of nuclear reactions, TALYS-1.96/2.0, https://www-nds.iaea.org/talys/tutorials/talys_v1.96.pdf
15. O.S. Deiev, I.S. Timoshenko, S.N. Olejnik, V.A. Kushnir, V.V. Mytrochenko, S.A. Perezhogin, Phys. Rev. C **106**, 024617 (2022)
16. A.N. Vodin, O.S. Deiev, I.S. Timoshenko, S.N. Olejnik, M.I. Ayzatskiy, V.A. Kushnir, V.V. Mytrochenko, S.A. Perezhogin, Eur. Phys. J. A **57**, 208 (2021)

Springer Nature or its licensor (e.g. a society or other partner) holds exclusive rights to this article under a publishing agreement with the author(s) or other rightsholder(s); author self-archiving of the accepted manuscript version of this article is solely governed by the terms of such publishing agreement and applicable law.

Article

Further Study of the Relationship between Transient Effects in Energetic Proton and Cosmic Ray Fluxes Induced by Coronal Mass Ejections

Mihailo Savić ^{1,*} , Nikola Veselinović ¹ , Darije Maričić ², Filip Šterc ², Radomir Banjanac ¹, Miloš Travar ¹ and Aleksandar Dragić ¹ 

- ¹ Institute of Physics Belgrade, University of Belgrade, Pregrevica 118, 11080 Belgrade, Serbia; veselinovic@ipb.ac.rs (N.V.); banjanac@ipb.ac.rs (R.B.); mtravar@ipb.ac.rs (M.T.); dragic@ipb.ac.rs (A.D.)
² Astronomical Observatory Zagreb, Opatička 22, 10000 Zagreb, Croatia; dmaricic@zvjezdarnica.hr (D.M.); fsterc@zvjezdarnica.hr (F.Š.)
* Correspondence: msavic@ipb.ac.rs

Abstract: The study and better understanding of energetic transient phenomena caused by disturbances occurring on our Sun are of great importance, primarily due to the potential negative effects those events can have on Earth's environment. Here, we present the continuation of our previous work on understanding the connection between disturbances in the flux of energetic particles induced in the near-Earth environment by the passage of interplanetary coronal mass ejections and related Forbush decrease events. The relationship between the shape of fluence spectra of energetic protons measured by the instruments on the SOHO/ERNE probe at Lagrange point L1, Forbush decrease parameters measured by the worldwide network of neutron monitors, and coronal mass ejection parameters measured in situ is investigated. Various parameters used to characterize transient phenomena and their impact on the heliosphere, provided by the WIND spacecraft, were utilized to improve the accuracy of the calculation of the associated energetic proton fluence. The single and double power laws with exponential rollover were used to model the fluence spectra, and their effectiveness was compared. Correlation analysis between exponents used to characterize the shape of fluence spectra and Forbush decrease parameters is presented, and the results obtained by the two models are discussed.

Keywords: coronal mass ejections; solar energetic particles; solar wind; space weather; cosmic rays; Forbush decreases



Citation: Savić, M.; Veselinović, N.; Maričić, D.; Šterc, F.; Banjanac, R.; Travar, M.; Dragić, A. Further Study of the Relationship between Transient Effects in Energetic Proton and Cosmic Ray Fluxes Induced by Coronal Mass Ejections. *Universe* **2024**, *10*, 283. <https://doi.org/10.3390/universe10070283>

Academic Editor: Alexandre Marcowith

Received: 14 March 2024

Revised: 24 June 2024

Accepted: 25 June 2024

Published: 29 June 2024



Copyright: © 2024 by the authors. Licensee MDPI, Basel, Switzerland. This article is an open access article distributed under the terms and conditions of the Creative Commons Attribution (CC BY) license (<https://creativecommons.org/licenses/by/4.0/>).

1. Introduction

The study of eruptive events on the sun and associated disturbances in the heliosphere is of great importance, largely due to the potential hazards they can pose to many areas of modern life. This is especially true at the present time, given the increased likelihood of their occurrence in the rising phase of solar cycle 25.

Magnetic reconnection on the sun involves violent processes through which magnetic energy is transformed into other forms of energy, often resulting in solar flares (SFs) or coronal mass ejections (CMEs). SFs are sudden eruptive phenomena in the solar atmosphere's active regions, observed as a flash of electromagnetic radiation, and are frequently associated with CMEs [1,2]. CMEs are large-scale eruptions of magnetized plasma from the sun's corona into the interplanetary medium, where they can be referred to as interplanetary coronal mass ejections (ICMEs).

Solar flares and coronal mass ejections may induce complex disturbances in the heliosphere and Earth's magnetosphere. One such phenomenon includes particle acceleration that results in a flux enhancement of protons, electrons, and ions. These enhancements, typically referred to as solar energetic particle (SEP) events, can be measured in interplanetary

space by detectors onboard space probes, and in extreme cases, by Earth-based detectors. High-energy particles can be ejected and accelerated from the sun during SF events [3,4], or they can be accelerated by CME- and ICME-induced shock waves. These phenomena can accelerate SEPs to MeV or even GeV energies, reaching Earth usually within a day after their occurrence or even faster [5]. It is important to study not just the strong SEP events, which have the potential to affect our civilization [6], but also the weaker and more frequent ones. It is crucial to understand the circumstances under which they occur but also the parameters that describe the propagation and strength of these events [7].

Another way eruptive events on the sun can affect the near-Earth environment is through their impact on cosmic rays (CRs). Cosmic rays are high-energy charged particles that predominantly originate from outside our solar system, although some of these particles can originate from the sun. In the heliosphere, CRs interact with the interplanetary magnetic field (IMF), which is carried by the stream of supersonic plasma blowing outward from the sun known as the solar wind. Transients such as CMEs and ICMEs with accompanied bow shocks, created due to the interaction of faster ICME with slower solar wind, can modulate CRs [8,9]. This modulation of CRs can be detected on Earth as a sudden offset in the CR flux, followed by a gradual recovery phase that can last several days [10,11], an effect commonly known as a nonrecurrent Forbush decrease (FD). Thus, the observed change in CR flux can be used as a proxy for solar activity.

These are just some of the numerous phenomena that can occur in the heliosphere and are associated with the sun's activity. To maximize our understanding of such complex events, we must investigate all the interconnections among the various induced processes. In this work, we expand on our previous study of one such relationship [12], specifically the connection between the enhanced flux of solar energetic particles and the properties of concurrent Forbush decreases, which have also been observed and studied by other authors [13,14]. The main idea behind the study is that, on one hand, the passage of a CME/ICME can lead to particle acceleration and an increase in the detected flux of energetic particles, while on the other hand, it may cause a decrease in the observed flux of CRs or the aforementioned Forbush decrease. To investigate the connection between these two phenomena, we examined the correlation between the shape of the event-integrated differential SEP flux, or differential fluence, measured at Lagrange point 1 (L1), and the magnitudes of associated FDs. To extend and potentially refine our previous study, we implemented several improvements. These features include the utilization of high-resolution data for the IMF, solar wind, and CME speeds in order to increase the precision in determining the onset and duration of events. Furthermore, we introduced an additional model for the description of the fluence spectra to be used alongside and compared with the previously used one. Finally, we applied a new fitting procedure based on the Monte Carlo approach. We believe these improvements lead to noticeably more precise and reliable results that further support the proposed relationship between the shape of the differential fluence spectra and the magnitudes of FDs.

In the article, we first discuss various data sources used in the analysis and justify the selection of events from solar cycles 23 and 24. We then describe in detail the procedure used to determine the differential SEP fluence spectra. In the next section, we introduce two models that were used to parameterize the fluence spectra and compare how well they were able to fit the data. Finally, we perform the correlation analysis to study the dependence between FD parameters and the spectral indices of SEP fluence spectra, as well as the selected CME parameters. We discuss the results in terms of the models applied and evaluate the usefulness of obtained indices as predictors of FD properties.

2. Data and Event Selection

2.1. Data Sources

Various types of data were necessary for the presented study, including energetic proton data measured near Earth, selected IMF, CME, solar wind, and geomagnetic field parameters, as well as CR measurements by Earth-based detectors. The data are available

either in the form of time series or as extreme and averaged values over the duration of the event. Two main repositories were used to acquire these data: the OMNIWeb Plus repository provided by the NASA/Goddard Space Flight Center [15] (for energetic proton data and time series of IMF and solar wind speeds) and the IZMIRAN Forbush decrease database provided by the Pushkov Institute of Terrestrial Magnetism, Ionosphere, and Radio Wave Propagation, Russian Academy of Sciences [16] (for Forbush decrease and averaged space weather parameters).

Energetic proton data in the OMNIWeb Plus repository are provided by the Energetic and Relativistic Nuclei and Electron (ERNE) sensor unit onboard the Solar and Heliospheric Observatory (SOHO) [17]. SOHO is situated in a halo orbit around L1. SOHO/ERNE has two energetic particle sensors: the Low-Energy Detector (LED) and the High-Energy Detector (HED), each with ten energy channels measuring ion fluxes and count rates in the ranges of 1.3–13 MeV/nucleon and 13–130 MeV/nucleon, respectively. This setup has been actively monitoring differential proton flux over the course of the last three solar cycles [18,19]. For this study, hourly data of energetic protons were used.

IMF and solar wind speed data in the OMNIWeb Plus repository were provided by the Global Geospace Science (GGS) WIND spacecraft. The spacecraft was positioned upstream of Earth at L1, initially in a Lissajous orbit and then, more recently, inserted into a halo orbit around L1. The primary goal of the mission has been to monitor the properties of the solar wind, a task that its onboard instruments have successfully performed over the last three decades [20].

Various space weather parameters associated with a specific FD event were taken from the database of Forbush decreases compiled by researchers from IZMIRAN. FD magnitudes in the database are obtained using measurements from the worldwide network of neutron monitors (the most widely used type of ground-level CR detectors). Neutron monitor data were corrected for efficiency and atmospheric effects. Other space weather data in the IZMIRAN database were assembled from various sources to produce a comprehensive repository containing various associated parameters of FDs, the heliosphere, and the geomagnetic field. In this study, we used parameters related to CMEs and solar wind, such as average CME speed and maximum solar wind speed, as well as the minimal Disturbance Storm-Time index (Dst) over the duration of the FD event. We also used FD magnitudes calculated by the IZMIRAN researchers using the global survey method (GSM) technique [21]. GSM integrates measurements from a worldwide network of neutron monitors, accounting for all effects caused by various anisotropies and disturbances of atmospheric and geomagnetic origin, to derive the hourly variation of primary cosmic ray flux outside Earth's atmosphere. In addition to FD magnitudes measured at Earth, they also provide the values of FD magnitudes corrected for the magnetospheric effect, which should remove the contribution of the disturbances introduced by variations in the geomagnetic field.

2.2. Event Selection

In this study, we focused on the events that occurred during most of the solar cycle 23 and 24. To establish the connection between the shape of energetic proton fluence spectra and the properties of concurrent Forbush decrease (FD) events, we decided to focus on events with larger magnitudes, expecting the correlation to be more pronounced in such cases due to less noise from noncontributing processes. The lower boundary for FD magnitude for event selection was somewhat arbitrarily set to 4%. Further lowering this bound would certainly increase the statistics in the analysis, but we do not believe it would add much support to the proposed relationship, due to the non-negligible likelihood that events of lower magnitude may exhibit different behavior from events of larger magnitudes (which is further discussed in Section 5). However, there are plans to investigate this in more detail in the future and possibly extend the analysis to include events of lower magnitudes.

The term SEP event can be somewhat misleading due to two possible processes leading to particle acceleration, so we feel we should clarify the nature of the events used in this

work. Evidence of two distinctive physical mechanisms of SEP acceleration has been accumulating for the last half-century [4]. The first of the two mechanisms is associated with type II radio bursts from coronal and interplanetary shock waves, while the second is associated with type III radio bursts produced by streaming electrons. The former is driven by fast CMEs, is proton-dominated, and produces “gradual” SEP events (sometimes also referred to as Energetic Storm Particle, or ESP events) that have high SEP flux intensity near Earth. The latter mechanism is predominantly connected to magnetic reconnection with open magnetic field lines and resonant wave–particle interactions in impulsive SFs and jets. It produces “impulsive” SEP events that last for hours, in contrast to gradual events, which can last for days partly due to the continuing acceleration of the shock. Even though all of the CMEs used in the analysis can be associated with SFs, we believe all of them belong to the gradual SEP event class.

Determining event-integrated SEP fluence was not always simple, especially in the case of complex events where structures that appear to have different sources are superimposed. That is why we have decided to eliminate all events for which we did not find a clear association with the passage of a specific CME, leaving us with 20 events to be used in the analysis. Selected FD events and their respective parameters from the IZMIRAN database are shown in Table 1.

Table 1. Selected parameters from the IZMIRAN database associated with FD events: FD magnitude for particles with 10 GV rigidity (M), FD magnitude for particles with 10 GV rigidity corrected for magnetospheric effect (M_M), average CME speed between the Sun and the Earth calculated from the beginning of the associated CME (V_{meanC}), maximal hourly solar wind speed during the event (V_{max}), and minimal Dst index during the event (Dst_{min}).

Date/Time of FD Onset	M [%]	M_M [%]	V_{meanC} [kms ⁻¹]	V_{max} [kms ⁻¹]	Dst_{min} [nT]
29–Sep–2001 09:40:00	4.3	4.4	831	694.0	–56.0
11–Oct–2001 17:01:00	7.0	6.9	769	572.0	–71.0
21–Oct–2001 16:48:00	5.4	7.3	858	677.0	–187.0
24–Nov–2001 05:56:00	9.2	9.8	1366	1024.0	–221.0
17–Apr–2002 11:07:00	6.2	7.0	745	611.0	–127.0
07–Sep–2002 16:36:00	4.6	5.1	863	550.0	181.0
30–Oct–2003 16:19:00	14.3	9.4	2140	1876.0	383.0
20–Nov–2003 08:03:00	4.7	6.8	872	703.0	422.0
26–Jul–2004 22:49:00	13.5	14.4	1290	1053.0	197.0
13–Sep–2004 20:03:00	5.0	5.3	948	613.0	50.0
15–May–2005 02:38:00	9.5	12.2	1231	987.0	263.0
14–Dec–2006 14:14:00	8.6	9.6	1165	955.0	146.0
05–Aug–2011 17:51:00	4.3	4.8	1104	611.0	–115.0
24–Oct–2011 18:31:00	4.9	6.5	633	516.0	–147.0
08–Mar–2012 11:03:00	11.7	11.2	1188	737.0	143.0
14–Jul–2012 18:09:00	6.4	7.6	834	667.0	–127.0
23–Jun–2013 04:26:00	5.9	5.3	844	697.0	–49.0
12–Sep–2014 15:53:00	8.5	5.9	897	730.0	–75.0
22–Jun–2015 18:33:00	8.4	9.1	1040	742.0	–204.0
07–Sep–2017 23:00:00	6.9	7.7	1190	817.0	–124.0

3. Determination of Energetic Proton Fluence Spectra

Establishing a clear connection between a CME originating on the sun and a consequent FD is often not straightforward [22]. Due to the many potential interactions that can occur in the heliosphere, the same can be true when one tries to establish the effect of an ICME passage on the observed flux of energetic protons in interplanetary space.

Complex events on the sun and related disturbances in the heliosphere include various processes that can lead to particle acceleration and contribute to an increased flux of energetic protons [23]. Hence, the direct link between the structures observed in the energetic proton flux time series and the passage of an ICME is not always obvious. To establish this link as reliably as possible, we utilized data provided by various instruments onboard the WIND spacecraft. As our primary interest was the determination of the precise timing of the onset and duration of the interaction, we found the time series of the IMF and CME velocity to be the most useful parameters for this purpose available in the WIND data.

To illustrate the usefulness of WIND data for this purpose, Figure 1 shows the time series for the IMF (both the total magnitude and its components), solar wind velocity, and the flux of energetic protons for one selected channel (1.3–1.6 MeV/nucleon) measured by the SOHO/ERNE instrument for the November 2001 event. Vertical dashed lines indicate the time intervals associated with the shock-sheath region and the ICME itself (from left to right, respectively). Some of the analyzed events are forming complex magneto-plasma structures, which can be explained by interactions with high-speed solar wind streams or other ICMEs.

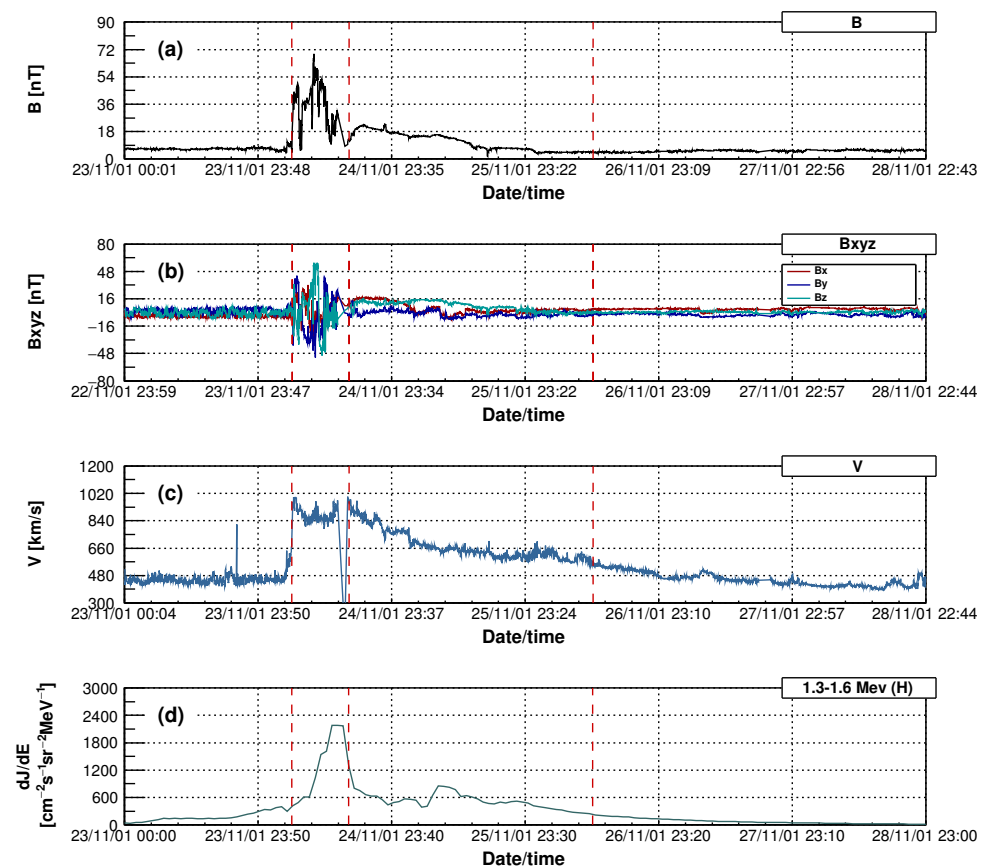


Figure 1. Time series for selected WIND parameters and SOHO/ERNE proton flux data for the November 2001 event: (a) IMF, (b) IMF components, (c) solar wind speed, and (d) energetic proton flux in 1.3–1.6 MeV energy channel.

Considering the different time resolutions of WIND (92 s) and SOHO/ERNE data (1 h), which can result in slight hour-round-off time shifts of the time series for the latter,

we observe a clear impact of the arrival of the ICME shock on the flux of energetic protons. In addition to the increase in proton flux attributed to the passage of the ICME, there is a noticeable structure that seemingly precedes the ICME shock. This structure does not appear to be directly related to the variations in the IMF or solar wind velocity. Due to the general complexity of events on the sun, which typically lead to the formation of CMEs, and the different mechanisms of particle acceleration and interaction with the solar wind, it is possible that the detected increase in proton flux preceding the shock is induced by some other aspect of such phenomena or could be some kind of event precursor. We discuss the possible nature of this structure below; however, we believe that the absence of a detailed explanation of the mechanism behind its origin will not critically affect the procedure of determining differential proton fluence and the presented results. Nonetheless, it is definitely a feature that we will try to investigate in our future work, as we believe it will lead to a better overall understanding of complex space weather phenomena.

The times marking the shock and the end of ICME interaction, determined as explained in the previous paragraphs, are now used as integration bounds to calculate event-integrated flux (or differential fluence) for each of the SOHO/ERNE energy channels. An illustration of this procedure is shown in Figure 2 for four selected SOHO/ERNE channels.

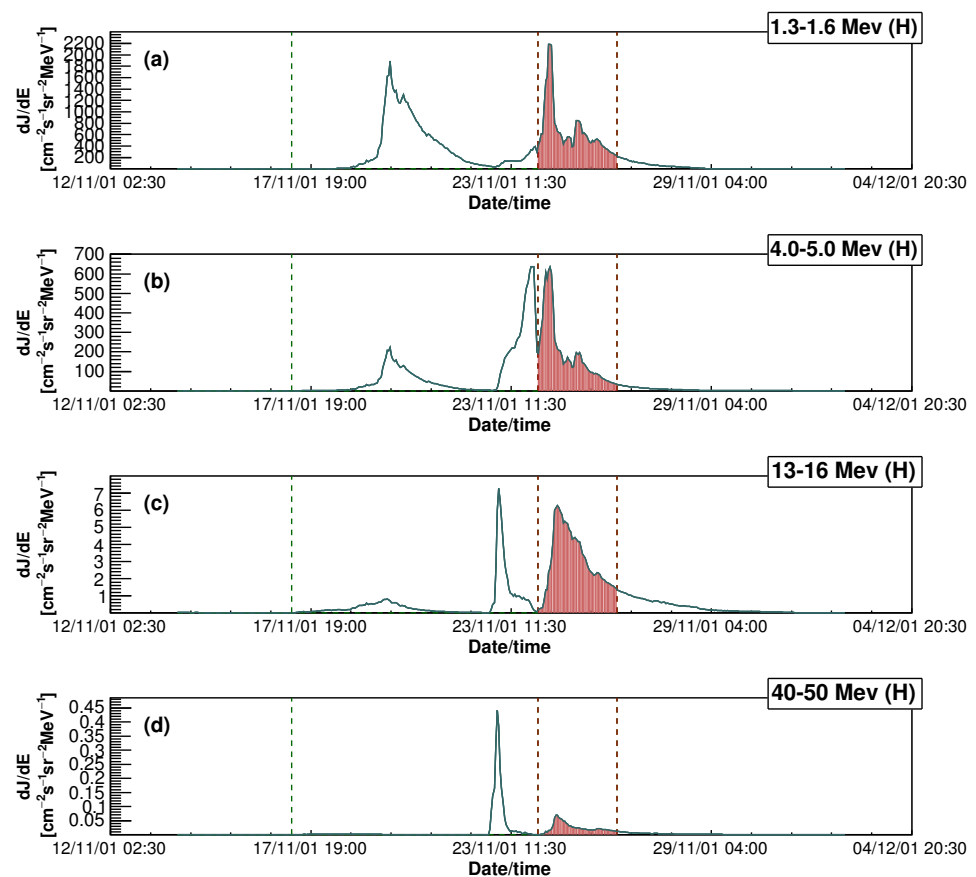


Figure 2. Energetic proton flux in four selected SOHO/ERNE energy channels for the November 2001 event: (a) 1.3–1.6 MeV, (b) 4.0–5.0 MeV, (c) 13–16 MeV, (d) 40–50 MeV. Green dashed line marks the end of the interval used to calculate the baseline, while the two red dashed lines indicate the bounds of the time interval used for integration.

Among the three vertical dashed lines, the second and the third ones mark the integration bounds, while the first one indicates the end of the time interval used to calculate the baseline value (the beginning of the baseline interval being the same as the beginning of the interval shown on the graph). In several cases where energetic proton flux preceding the event was disturbed for a longer period of time, a time interval after the event, when the

flux has recovered and was stable, was used. The duration of time intervals used for baseline determination ranged from a day and a half to several days. The filled area under the graph represents the differential fluence value for a given channel calculated relative to the baseline.

One can observe that part of the proton flux time series associated with the structure preceding the arrival of the shock exhibits a different energy dependence to the part we assume is induced by the passage of the ICME and its interaction with the local particles [24], as the relative ratio of the areas under respective profiles increases with increasing energy. This could indicate that the observed structure is not related to the CME but is a consequence of some other interaction.

In our previous work [12], due to the lack of high-resolution WIND data, integration intervals were more loosely defined. We were unable to precisely separate only the CME-induced part of the energetic proton flux, often including the precursor structure. We believe the new approach is a significant improvement and should lead to more reliable results.

4. Parametrization of Fluence Spectra

Using the values for differential energetic proton flux in different energy channels integrated over the duration of the event (as detailed in Section 3), we form the differential fluence spectra for selected events. The average energy in MeV was used for particle energy bin values [25].

Several models have been proposed over the years to describe the observed spectra [26]. One feature that has proven somewhat challenging to accurately describe is the characteristic brake or “knee”, which can be prominent in extreme events [27,28], possibly occurring due to the effect of interplanetary transport [29]. Previously [12], we relied on the model proposed by Band et al. [29,30] to fit the event-integrated fluence spectra. The model, originally developed to describe gamma-ray burst spectra but also successfully used to model fluence spectra [31], is based on the double power law in the following form:

$$\frac{dJ}{dE} = \begin{cases} AE^\alpha \exp\left(-\frac{E}{E_B}\right) & E \leq (\alpha - \beta)E_B, \\ AE^\beta [(\alpha - \beta)E_B]^{\alpha - \beta} \exp(\beta - \alpha) & E > (\alpha - \beta)E_B, \end{cases} \quad (1)$$

where E is the particle energy, E_B is the “knee” energy, α is the power law index that characterizes the low-energy part of the spectrum, β is the power law index that characterizes the high-energy part of the fluence spectrum, and A is the spectral coefficient.

While this model reasonably described the observed spectra for a number of events, in some cases, it seemed that the agreement could be better. Attempting to use the “knee” energy as a free parameter in the fitting procedure resulted in either fit instability or divergent fits. We believed this to be a consequence of the limitations of standard minimizers in handling a relatively large number of free parameters. To overcome this issue, in our previous analysis, we decided to treat the “knee” energy as a fixed parameter, determining E_B by relying on the dependence of this parameter on the integral fluence reported by some authors [28,32]. Additionally, the range conditions in Equation (1) were approximated using the expected values for indices α and β of -1 and -2 , respectively, as suggested in [30], effectively reducing the conditions for the low-energy and high-energy ranges to $E \leq E_B$ and $E > E_B$. However, the number of approximations needed to stabilize the fitting procedure seemed excessive, so considering an alternative approach seemed advisable.

To reduce potentially significant uncertainties and to increase the reliability of the fitting, in this study, we resorted to employing the procedure based on the Monte Carlo approach, specifically utilizing the *emcee* Python package. *emcee* is a robust, well-tested, and user-friendly MIT-licensed tool for Bayesian inference, which uses Markov Chain Monte Carlo (MCMC) sampling. It is based on the affine-invariant ensemble sampler and is widely and successfully applied in various research disciplines and data science domains, including astrophysics, biostatistics, and machine learning. We performed the fitting procedure using Equation (1) and setting all four parameters as free variables.

The fitting algorithm performed exceptionally well, rapidly and reliably converging to optimal parameter values with very high precision and minimal deviation between independent walkers. The approach led to a significantly improved and more stable fitting procedure, ultimately resulting in noticeably more reliable outcomes compared with our previous method.

Although fitting the energetic proton fluence spectra with the Band function using the MCMC method eventually performed remarkably well, the function was not so straightforward to implement when the fitting procedure was based on standard minimizer algorithms. Hence, we were interested in investigating whether a simpler and more robust model could be comparably effective in describing energetic proton spectra while also being easier to implement. One such model, proposed by Ellison and Ramaty, was developed based on observations of particle acceleration at interplanetary shocks [33], and was successfully used to model spectra of several particle species during large SEP events [34]. In these studies, it was concluded that for strong events it mainly fits the lower energy range satisfactorily. However, we felt it performed well enough to test it on the set of events we selected for the presented analysis. The model assumes the form of a power law with an exponential rollover to describe the energetic particle fluence spectra:

$$\frac{dJ}{dE} = AE^\gamma \exp\left(-\frac{E}{E_0}\right), \quad (2)$$

where E is the particle energy, E_0 is the cutoff exponent parameter, γ is the spectral index, and A is the spectral coefficient.

Even though it is one of the older proposed models, and some authors had objections to the somewhat arbitrary introduction of the rollover correction [32], we found the Ellison–Ramaty model to be mostly in good agreement with the observed data. Additionally, it proved to be robust in terms of the convergence of the fit. Hence, we felt it is a good candidate to compare against the model proposed by Band et al. to possibly determine if one is more suited than the other for the purpose of our analysis.

We fitted the fluence data with both Band and Ellison–Ramaty models and compared how accurately they described the observed spectra. The Ellison–Ramaty model mostly converged stably and performed reasonably well when used with standard minimizers. However, for a more accurate comparison of both models, we utilized the aforementioned implementation using the *emcee* package for the Ellison–Ramaty function as well. This indeed led to further improvements, greater accuracy, and increased precision of the fit results.

In direct comparison, the Band function proved to be an overall more flexible model, describing the spectra more accurately, particularly apparent in its ability to effectively model the “knee” feature. While in some cases this difference in performance was more evident, for the majority of events, the Ellison–Ramaty model seemed to describe the spectra sufficiently well, offering only a moderately poorer fit. In Figures 3 and 4, we show two events that best illustrate the different cases of the level of agreement between the two models.

The green line in Figures 3 and 4 represents the fit function given by Equation (1) (Band et al.), and the magenta line represents the fit function given by Equation (2) (Ellison–Ramaty). The left panels on both figures show the fluence spectrum in log–log scale, while the right panels zoom in on the region around the “knee” energy in linear scale, which proved to be the most demanding to fit adequately.

An example where the difference in performance between the two models is most apparent is the second event in October 2001 (occurring around October 21), shown in Figure 3. Here, the observed spectrum is clearly better described by Equation (1). The Ellison–Ramaty fit starts to diverge just after the “knee”, and although the divergence is not dramatic, it is still noticeable. However, in the case of the June 2013 event (Figure 4), the difference between the two models is much smaller, with Ellison–Ramaty providing only a marginally less accurate fit. We believe that the fact that the second situation is encountered more

often provides sufficient justification for continuing to use both models in the remainder of the analysis.

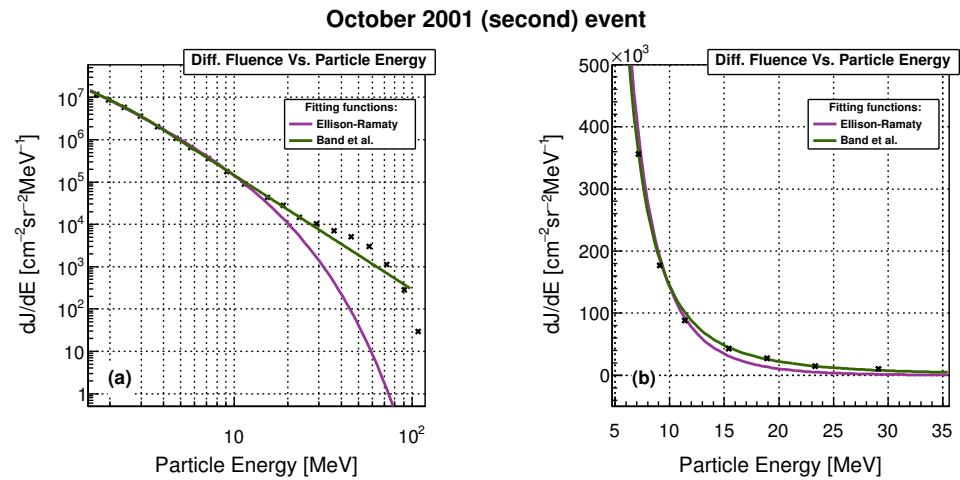


Figure 3. Fluence spectrum associated with the FD that occurred on 21 October 2001: (a) full range in log–log scale and (b) interval around the “knee” energy in linear scale. The green line indicates the fit by the Band et al. function, while the magenta line indicates the fit by the Ellison–Ramaty function.

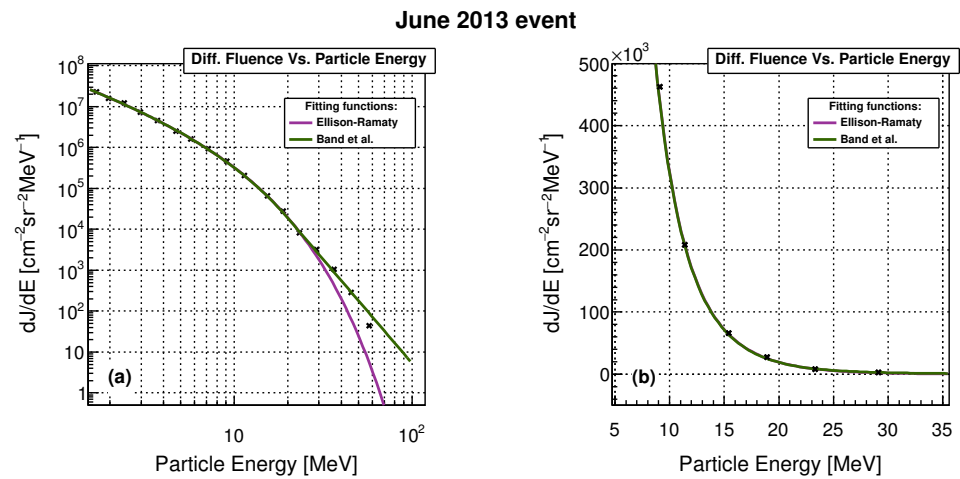


Figure 4. Fluence spectrum associated with the FD that occurred on 23 June 2013: (a) full range in log–log scale and (b) interval around the “knee” energy in linear scale. The green line indicates the fit by the Band et al. function, while the magenta line indicates the fit by the Ellison–Ramaty function.

The obtained spectral indices α , β , and γ , as well as the values for the ‘knee’ and roll-over energies, are shown in Table 2. Fit errors for all parameters are given in parentheses.

To further study and compare the usefulness of the models in describing the measured spectra, we performed a correlative analysis, presenting the results of both models in parallel.

Table 2. Parameters for the two models used to fit the fluence spectra for all events: spectral indices (α , β) and “knee” energy (E_B) for the Band et al. model, and spectral index (γ) and roll-over energy (E_0) for the Ellison–Ramaty model.

Date/Time of FD Onset	α	β	E_B [MeV]	γ	E_0 [MeV]
29–Sep–2001 09:40:00	−1.859(1)	−3.60(2)	11.71(5)	−1.806(1)	10.000(1)
11–Oct–2001 17:01:00	−1.229(8)	−4.130(4)	1.354(6)	−1.798(4)	1.999(6)
21–Oct–2001 16:48:00	−1.169(6)	−2.695(1)	2.44(2)	−1.918(2)	7.93(4)
24–Nov–2001 05:56:00	−0.375(1)	−5.537(5)	3.535(1)	−0.378(1)	3.548(1)
17–Apr–2002 11:07:00	−1.422(2)	−3.783(2)	2.529(4)	−1.667(1)	3.271(4)
07–Sep–2002 16:36:00	−1.866(1)	−4.73(2)	4.991(8)	−1.882(1)	5.122(7)
30–Oct–2003 16:19:00	−0.100(1)	−5.876(4)	3.271(1)	0.000(1)	3.071(1)
20–Nov–2003 08:03:00	−1.599(4)	−3.419(5)	3.45(2)	−1.801(2)	4.58(2)
26–Jul–2004 22:49:00	−1.234(1)	−4.910(7)	3.328(2)	−1.255(1)	3.404(2)
13–Sep–2004 20:03:00	−0.949(1)	−6.54(2)	3.467(1)	−0.951(1)	3.474(1)
15–May–2005 02:38:00	−0.431(1)	−7.37(4)	2.811(1)	−0.432(1)	2.813(1)
14–Dec–2006 14:14:00	−0.721(1)	−4.038(2)	2.200(1)	−0.841(1)	2.427(1)
05–Aug–2011 17:51:00	−1.532(1)	−4.70(1)	4.742(5)	−1.545(1)	4.837(5)
24–Oct–2011 18:31:00	−1.112(2)	−7.57(5)	1.641(1)	−1.119(1)	1.648(1)
08–Mar–2012 11:03:00	−0.677(1)	−3.642(1)	5.129(1)	−0.698(1)	5.286(1)
14–Jul–2012 18:09:00	−1.246(1)	−9.999(1)	2.496(1)	−1.245(1)	2.494(1)
23–Jun–2013 04:26:00	−1.560(1)	−5.08(3)	5.71(1)	−1.564(1)	5.752(9)
12–Sep–2014 15:53:00	−0.551(3)	−3.350(1)	1.287(2)	−1.699(1)	3.232(4)
22–Jun–2015 18:33:00	−1.382(1)	−6.21(2)	3.424(1)	−1.386(1)	3.437(1)
07–Sep–2017 23:00:00	−1.210(1)	−5.11(1)	4.553(3)	−1.216(1)	4.590(2)

5. Correlation between Spectral Indices and Forbush Decrease Parameters

To study the relationship between the enhanced flux of energetic protons accelerated by a CME/ICME-related interplanetary shock and the effect of the passage of these disturbances on cosmic rays, we investigate the correlation between spectral indices used to parameterize the shape of the energetic proton fluence spectra and the magnitudes of coincident Forbush decreases. FD magnitudes for 10 GV rigidity particles, calculated using GSM applied to neutron monitor data provided by the global neutron monitor network [35], are available in the IZMIRAN database. In addition to FD magnitudes measured at Earth, the database offers calculated values of FD magnitudes for 10 GV rigidity particles corrected for magnetospheric effects using the Dst index.

Figure 5 shows the dependence between the spectral index α , obtained by fitting the fluence spectra with the function proposed by Band et al., and FD magnitudes. The dependence for the measured FD magnitude (M) is shown in the left panel, while the dependence for FD magnitude corrected for magnetospheric effects (M_M) is shown in the right panel.

Equivalent plots for spectral index β are shown in Figure 6.

Figure 7 shows the relationship between FD magnitude and the spectral index γ , obtained by fitting the fluence spectra with the Ellison–Ramaty function. As in the previous figure, the dependence for the measured FD magnitude is shown on the left panel, while one for the FD magnitude corrected for magnetospheric effects is shown on the right panel.

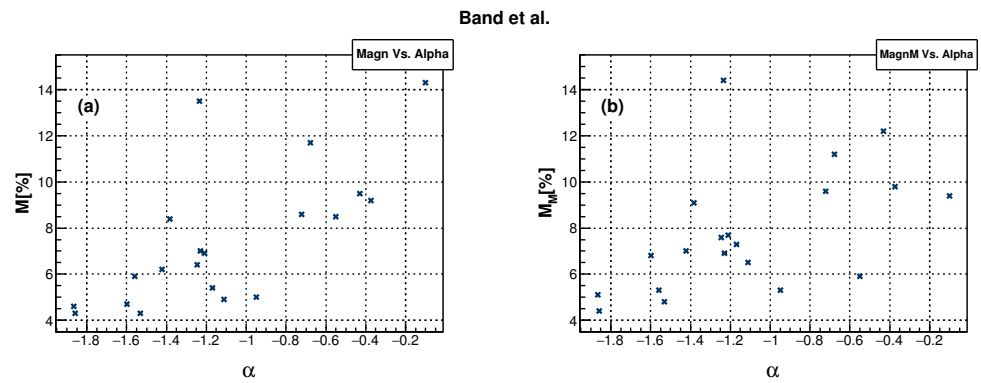


Figure 5. Dependence of FD magnitudes on the spectral index α for (a) FD magnitude for particles with 10 GV rigidity and (b) FD magnitude for particles with 10 GV rigidity corrected for magnetospheric effect.

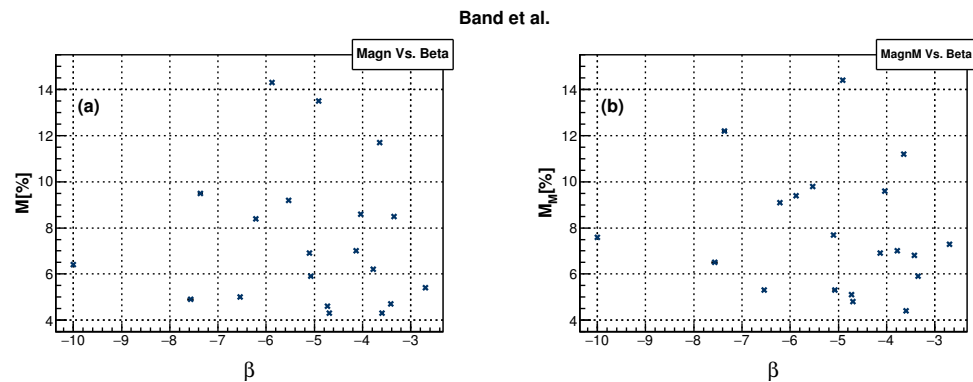


Figure 6. Dependence of FD magnitudes on the spectral index β for (a) FD magnitude for particles with 10 GV rigidity and (b) FD magnitude for particles with 10 GV rigidity corrected for magnetospheric effect.

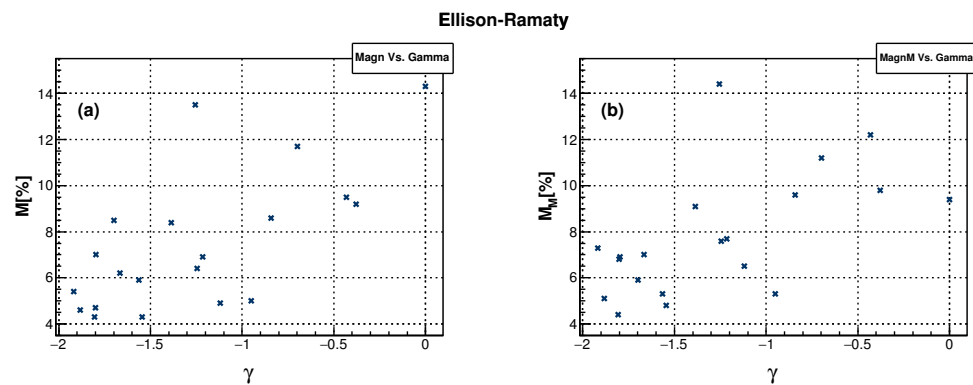


Figure 7. Dependence of FD magnitudes on the spectral index γ for (a) FD magnitude for particles with 10 GV rigidity and (b) FD magnitude for particles with 10 GV rigidity corrected for magnetospheric effect.

The new fitting procedure has undoubtedly improved the reliability with which spectral index α is determined, and for some events, the newly obtained values have changed non-negligibly. However, the effect of the new results on the dependence shown in Figure 5 was not dramatic. A much larger change was observed in new values for the parameter β (Figure 6). Where before it exhibited similar dependence as spectral index α in relation to FD magnitudes, now it is clear there is little correlation between these quantities. A few reasons come to mind to explain this observation, which could be related to the origin, acceleration mechanisms, and potential transport effects of the higher energy

protons. However, we feel such a discussion is probably beyond the scope of this study, so for now this feature should be noted and further investigation left for future analysis. When it comes to the spectral index obtained from the Ellison–Ramaty fit, we observe a very similar relationship between γ and FD magnitudes as we do for α . This could indicate that the poorer fit of the Ellison–Ramaty function does not have a significant impact on this relationship. The observation seems consistent with our assumption, based on the negligible correlation between the spectral index β and FD magnitudes, that the importance of the shape of the high-energy part of the spectrum appears to be less significant for the relationship we are investigating.

It is worth noting that in the distributions shown in Figures 5 and 7, we observe what could be an outlier event (the July 2004 event with the value for M slightly below and the value for M_M slightly above 14%) A potential reason for the deviation could be the overestimation of the FD magnitude for this event. The July 2004 event occurred on 26 July at 22:49:00 (according to the IZMIRAN database). It was preceded by two other events: one on 22 July at 10:36:00 (with a magnitude of 5.2%) and the second one on 24 July at 06:13:00 (with a magnitude of 4.6%). Cosmic ray flux had not yet recovered from these two events before the occurrence of the 26 July FD. We believe that if that was not the case, the magnitude for this event would be several percent smaller, hence it would deviate less in distributions presented in Figures 5 and 7.

Previously [12], we noticed the possibility of the existence of two classes of events, where a different trend was observed for the events of smaller and events of larger FD magnitude, the boundary between them somewhat arbitrarily set to a magnitude of 6%. After refining the analysis in this work, the possibility of such classification is not eliminated but is somewhat less evident, and it appears to require a more careful analysis, which could be considered in a possible future extension of this study.

To quantify the proposed correlations between the spectral indices and FD magnitudes, we have performed a standard correlation analysis. Pearson correlation coefficients between FD magnitudes and spectral indices α , β , and γ , as well as several selected space weather parameters, are shown in Table 3. We omitted to include the results for the parameters E_B and E_0 , as they exhibited an insignificant correlation with other parameters of interest. Additionally, aside from a relatively modest correlation between γ and E_0 of -41% , they also showed negligible correlations with the spectral indices themselves.

Table 3. Correlation coefficients between FD magnitudes and spectral indices, as well as selected space weather parameters.

	α	β	γ	V_{meanC} [kms ⁻¹]	V_{max} [kms ⁻¹]	Dst_{min} [nT]
M [%]	0.70	−0.05	0.68	0.78	0.79	−0.38
M_M [%]	0.54	−0.15	0.59	0.54	0.53	−0.42

The correlation between spectral index α and FD magnitude M is roughly the same as previously reported (70% instead of 67%), while the correlation with FD magnitude corrected for the magnetospheric effect M_M is somewhat smaller (54% instead of 64%). There is barely any correlation between spectral index β with any of the FD magnitudes, as was indicated by the plots in Figure 6. Correlation coefficients for the spectral index γ have values comparable to those obtained for α —68% and 59% for M and M_M , respectively. We believe that these results are non-negligibly affected by the observed deviation of the July 2004 event and that the actual correlations are stronger. Indeed, if the July 2004 event is removed, the correlations increase for both spectral indices α and γ , as shown in Table 4.

Table 4. Correlation coefficients between FD magnitudes, spectral indices, as well as selected space weather parameters, with the July 2004 event excluded.

	α	β	γ	V_{meanC} [kms ⁻¹]	V_{max} [kms ⁻¹]	Dst_{min} [nT]
M [%]	0.83	−0.07	0.77	0.81	0.80	−0.39
M_M [%]	0.71	−0.20	0.73	0.54	0.52	−0.47

Based on the results in Table 3, we see that the correlation between FD magnitude M and spectral indices α and γ are only slightly smaller than the correlations between M and the maximum hourly solar wind speed (V_{max}) and average CME velocity (V_{meanC}), which are quantities that typically show the largest correlation with FD magnitudes [36], and could be considered as the best predictors for FD magnitudes among space weather parameters. On the other hand, the correlations between the corrected FD magnitude M_M and spectral indices are comparable to the correlations between M_M and V_{max} and V_{meanC} . If the July 2004 event is not taken into account (results presented in Table 4), the correlations with M for both spectral indices become comparable to those for V_{max} and V_{meanC} . More importantly, for M_M , the correlations are significantly larger for both indices, indicating the extent to which the results in Table 3 were negatively influenced by the deviation of the July 2004 event.

Presented results, particularly the ones in Table 4, indicate even more strongly than in our previous work the significant correlation between spectral indices used to parameterize the shape of fluence spectra of energetic protons and FD magnitudes. The level of correlation for magnitude M suggests that spectral indices α and γ serve as equally effective predictors of FD magnitude for particles with 10 GV rigidity obtained by the GSM model (M) as other space weather parameters, while for the FD magnitude for particles with 10 GV rigidity corrected for magnetospheric effects (M_M), they appear to be better predictors than other parameters. The results for both α and γ are largely comparable, and they seem to be almost equally useful for our study. However, if we had to choose the recommended model for use in this type of analysis, it would be the model proposed by Band et al. This model proved to be more flexible, especially in modeling the “knee” and the higher energy part of the energetic proton fluence spectra. The potential downside of this model is that it requires some effort in implementation. In that sense, we believe the Ellison–Ramaty model remains a useful tool due to its robustness and ‘out-of-the-box’ applicability.

It was shown [1] that even during complex heliospheric events, involving multiple CMEs in succession, it was possible to calculate with sufficient accuracy the magnitude of the FD outside the geomagnetic field (corrected for the magnetospheric effect) using the established correlation. The obtained value for the FD magnitude corrected for magnetospheric effects was -8.3% , which was in good agreement with the value of -7.7% obtained from the GSM (the relative difference between the two methods being 7%). In the case of the FD magnitude measured at Earth relative difference was somewhat larger (15%), where we obtained the value of -8.1% , while the value calculated based on the GSM was -6.9% . These results indicate that the established correlations, even without additional refinement, can reliably predict FD amplitudes.

6. Conclusions

We presented an extension of our work, focusing on studying the connection between disturbances in the flux of energetic particles in the heliosphere and concurrent variations in the cosmic ray flux induced by the passage of a CME/ICME. Energetic proton flux, measured by the SOHO/ERNE instrument at L1 in twenty energy channels, was integrated over the duration of the event to obtain differential fluence spectra. To enhance the accuracy of this procedure, IMF and CME speed data provided by the WIND satellite were utilized. Fluence spectra were fitted with both the Ellison–Ramaty model and the model proposed by Band et al., and their effectiveness was compared. Cross-correlation between the spectral power indices obtained from the models and FD magnitudes, calculated by the GSM model

for 10 GV particles from the IZMIRAN database, was performed. The correlation between spectral indices and FD magnitude for events of moderate-to-high magnitude proved to be significant and, with the exception of the July 2004 event, comparable to the correlation with other space weather parameters that could be considered good predictors of FD magnitude. In the case of FD magnitude corrected for magnetospheric effects, the correlation with spectral indices is greater than for any other space weather parameter. Even though the Ellison–Ramaty model was able to model the energetic proton fluence spectra well in many cases, the model proposed by Band et al. performed better overall. Therefore, in our opinion, it should be the recommended model for similar studies.

Author Contributions: Conceptualization, M.S. and N.V.; methodology, M.S., N.V., D.M., F.Š., and A.D.; software, M.S., N.V., D.M. and F.Š.; validation, M.S., N.V., D.M., F.Š. and A.D.; formal analysis, M.S., N.V., D.M. and F.Š.; investigation, M.S., N.V., D.M. and F.Š.; resources, M.T. and M.S.; data curation, R.B., M.T. and M.S.; writing—original draft preparation, M.S. and N.V.; writing—review and editing, M.S., N.V., D.M., F.Š. and A.D. visualization, M.S. and N.V. All authors have read and agreed to the published version of the manuscript.

Funding: This work was funded by the Institute of Physics Belgrade, University of Belgrade, through a grant by the Ministry of Science, Technological Development and Innovations of the Republic of Serbia.

Data Availability Statement: Energetic proton data from SOHO/ERNE instrument are publicly available via OMNIWeb FTP page https://omniweb.gsfc.nasa.gov/ftpbrowser/soho_erne_flux_hr.html (accessed on 31 May 2024). IMF and solar wind speed time series measured by the WIND spacecraft are openly available at https://omniweb.gsfc.nasa.gov/ftpbrowser/wind_swe_2m.html (accessed on 31 May 2024). IZMIRAN database of Forbush decreases is free for public access at <http://spaceweather.izmiran.ru/eng/dbs.html> (accessed on 31 May 2024).

Acknowledgments: We would like to express our gratitude to the Reviewers for constructive comments and useful suggestions that significantly contributed to the quality of the manuscript. OMNI data were made available by NASA/GSFC’s Space Physics Data Facility’s OMNIWeb service. We acknowledge SOHO, a project of international cooperation between ESA and NASA. Additionally, we gratefully acknowledge the Cosmic Ray Group at the IZMIRAN Space Weather Prediction Center at the Pushkov Institute of Terrestrial Magnetism, Ionosphere, and Radio Wave Propagation of the Russian Academy of Sciences for providing the data used in our study.

Conflicts of Interest: The authors declare no conflicts of interest.

Abbreviations

The following abbreviations are used in this manuscript:

SF	Solar Flare
CME	Coronal Mass Ejection
ICME	Interplanetary coronal mass ejections
SEP	Solar Energetic Particles
CR	Cosmic Rays
FD	Forbush decrease
L1	Lagrange Point 1
IMF	Interplanetary Magnetic Field
Dst index	Disturbance Storm Time index
ERNE	Energetic and Relativistic Nuclei and Electron sensor unit
SOHO	Solar and Heliospheric Observatory
GSM	Global Survey Method
MCMC	Markov Chain Monte Carlo

References

1. Kolarski, A.; Veselinović, N.; Srećković, V.A.; Mijić, Z.; Savić, M.; Dragić, A. Impacts of Extreme Space Weather Events on September 6th, 2017 on Ionosphere and Primary Cosmic Rays. *Remote Sens.* **2023**, *15*, 1403. [CrossRef]
2. Yashiro, S.; Gopalswamy, N. Statistical relationship between solar flares and coronal mass ejections. *Univers. Heliophysical Processes Proc. IAU Symp.* **2008**, *4*, 233–243. [CrossRef]
3. Rotti, S.; Petrus, C.; Martens, P.C. Analysis of SEP Events and Their Possible Precursors Based on the GSEP Catalog2023. *Astrophys. J. Suppl. Ser.* **2023**, *267*, 40. [CrossRef]
4. Reames, D.V. The Two Sources of Solar Energetic Particles. *Space Sci. Rev.* **2013**, *175*, 53–92. [CrossRef]
5. Posner, A.; Strauss, R.D. Warning time analysis from SEP simulations of a two-tier RELeASE System applied to Mars exploration. *Space Weather* **2020**, *18*, e2019SW002354. [CrossRef]
6. Kataoka, R.; Sato, T.; Miyake, S.; Shiota, D.; Kubo, Y. Radiation dose nowcast for the ground level enhancement on 10–11 September 2017. *Space Weather* **2018**, *16*, 917–923. [CrossRef]
7. Waterfall, C.O.G.; Dalla, S.; Raukunen, O.; Heynderickx, D.; Jiggins, P.; Vainio, R. High energy solar particle events and their relationship to associated flare, CME and GLE parameters. *Space Weather* **2023**, *21*, e2022SW003334. [CrossRef]
8. Belov, A.; Abunin, A.; Abunina, M.; Eroshenko, E.; Oleneva, V.; Yanke, V.; Papaioannou, A.; Mavromichalaki, H.; Gopalswamy, N.; Yashiro, S. Coronal mass ejections and non-recurrent forrush decreases. *Sol. Phys.* **2014**, *289*, 3949–3960. [CrossRef]
9. Belov, A.; Shlyk, N.; Abunina, M.; Belova, E.; Abunin, A.; Papaioannou, A. Solar Energetic Particle Events and Forrush Decreases Driven by the Same Solar Sources. *Universe* **2022**, *8*, 403. [CrossRef]
10. Cane, H. Coronal mass ejections and forrush decreases. *Space Sci. Rev.* **2000**, *93*, 55–77. [CrossRef]
11. Gopalswamy, N. History and development of coronal mass ejections as a key player in solar terrestrial relationship. *Geosci. Lett.* **2016**, *3*, 8. [CrossRef]
12. Savić, M.; Veselinović, N.; Dragić, A.; Maletić, D.; Joković, D.; Udovičić, V.; Banjanac, R.; Knežević, D. New insights from cross-correlation studies between solar activity indices and cosmic-ray flux during Forrush decrease events. *Adv. Space Res.* **2023**, *71*, 2006–2016. [CrossRef]
13. Dumbovic, M.; Vrsnak, B.; Guo, J.; Heber, B.; Dissauer, K.; Carcaboso, F.; Temmer, M.; Veronig, A.; Podladchikova, T.; Möstl, C.; et al. Evolution of coronal mass ejections and the corresponding forrush decreases: Modeling vs. multi-spacecraft observations. *Sol. Phys.* **2020**, *295*, 104. [CrossRef]
14. Papaioannou, A.; Belov, A.; Abunina, M.; Eroshenko, E.; Anastasiadis, A.; Patsourakos, S.; Mavromichalaki, H. Interplanetary coronal mass ejections as the driver of non-recurrent Forrush decreases. *Astrophys. J.* **2020**, *890*, 101. [CrossRef]
15. OMNIWeb Plus Service. Available online: <https://omniweb.gsfc.nasa.gov/> (accessed on 12 February 2024).
16. IZMIRAN. Available online: <https://www.izmiran.ru/> (accessed on 12 February 2024).
17. Torsti, J.; Valtonen, E.; Lumme, M.; Peltonen, P.; Eronen, T.; Louhola, M.; Riihonen, E.; Schultz, G.; Teittinen, M.; Ahola, K.; et al. Energetic particle experiment ERNE. *Sol. Phys.* **1995**, *162*, 505–531. [CrossRef]
18. Paassilta, M.; Raukunen, O.; Vainio, R.; Valtonen, E.; Papaioannou, A.; Siipola, R.; Riihonen, E.; Dierckx, M.; Crosby, N.; Malandraki, O.; et al. Catalogue of 55–80 MeV solar proton events extending through solar cycles 23 and 24. *J. Space Weather Space Clim.* **2017**, *7*, A14. [CrossRef]
19. Belov, A.; Papaioannou, A.; Abunina, M.; Dumbovic, M.; Richardson, I.G.; Heber, B.; Kuhl, P.; Herbst, K.; Anastasiadis, A.; Vourlidas, A.; et al. On the rigidity spectrum of cosmic-ray variations within propagating interplanetary disturbances: Neutron monitor and SOHO/EPHIN observations at 1–10 GV. *Astrophys. J.* **2021**, *908*, 5. [CrossRef]
20. Wilson, L.B.; Brosius, A.L.; Gopalswamy, N.; Nieves-Chinchilla, T.; Szabo, A.; Hurley, K.; Phan, T.; Kasper, J.C.; Noé Lugaz, N.; Richardson, I.G.; et al. A quarter century of wind spacecraft discoveries. *Rev. Geophys.* **2021**, *59*, e2020RG000714. [CrossRef]
21. Belov, A.; Eroshenko, E.; Yanke, V.; Oleneva, V.; Abunin, A.; Abunina, M.; Papaioannou, A.; Mavromichalaki, H. The Global Survey Method Applied to Ground-level Cosmic Ray Measurements. *Sol. Phys.* **2016**, *293*, 578. [CrossRef]
22. Janvier, M.; Démoulin, P.; Guo, J.; Dasso, S.; Regnault, F.; Tóth, S.; Moutoussidou, S.; Gutierrez, C.; Perri, B. The Two-step Forrush Decrease: A Tale of Two Substructures Modulating Galactic Cosmic Rays within Coronal Mass Ejections. *Astrophys. J. Lett.* **2021**, *922*, 216. [CrossRef]
23. Gopalswamy, N. The Sun and Space Weather. *Atmosphere* **2022**, *13*, 1781. [CrossRef]
24. Desai, M.; Giacalone, J. Large gradual solar energetic particle events. *Living Rev. Sol. Phys.* **2016**, *13*, 3. [CrossRef]
25. Vainio, R.; Valtonen, E.; Heber, B.; Malandraki, O.E.; Papaioannou, A.L.; Klein, K.L.; Afanasiev, A.; Agueda, N.; Aurass, H.; Battarbee, M.; et al. The first SEP Server event catalogue ~68-MeV solar proton events observed at 1 AU in 1996–2010. *JSWSC* **2013**, *3*, A12.
26. Mottl, D.A.; Nymmik, R.A.; Sladkova, A.I. Energy spectra of high-energy SEP event protons derived from statistical analysis of experimental data on a large set of events. In Proceedings of the Space Technology and Applications International Forum—2001, Albuquerque, NM, USA, 11–14 February 2001; pp. 1191–1196.
27. Nymmik, R.A. Inflections (knees) in wide-range spectra of solar energetic protons and heavy ions: Their form, parameters, and regularities. *Bull. Russ. Acad. Sci. Phys.* **2011**, *75*, 761–763. [CrossRef]
28. Miroshnichenko, L.I.; Nymmik, R.A. Extreme fluxes in solar energetic particle events: Methodological and physical limitations. *Radiat. Meas.* **2011**, *61*, 6–15. [CrossRef]
29. Zhao, L.; Zhang, M.; Rassoul, H.K. Double power laws in the event-integrated solar energetic particle spectrum. *Astrophys. J.* **2016**, *821*, 62. [CrossRef]

30. Band, D.; Matteson, J.; Ford, L.; Schaefer, B.; Palmer, D.; Teegarden, B.; Cline, T.; Briggs, M.; Pacieras, W.; Pendleton, G.; et al. BATSE Observations of Gamma-Ray Burst Spectra. I. Spectral Diversity. *Astrophys. J.* **1993**, *413*, 281. [[CrossRef](#)]
31. Raukunen, O.; Vainio, R.; Tylka, A.J.; Dietrich, W.F.; Jiggins, P.; Heynderickx, D.; Dierckxsens, M.; Crosby, N.; Ganse, U.; Siipola, R. Two solar proton fluence models based on ground level enhancement observations. *J. Space Weather Spac.* **2018**, *A04*, 8. [[CrossRef](#)]
32. Nymmik, R.A. Charge states of heavy ions, as determined from the parameters of solar energetic particle spectra. *Bull. Russ. Acad. Sci. Phys.* **2013**, *77*, 490–492. [[CrossRef](#)]
33. Ellison, D.C.; Ramaty, R. Shock acceleration of electrons and ions in solar flares. *Astrophys. J.* **1985**, *298*, 400–408. [[CrossRef](#)]
34. Mewaldt, R.A.; Cohen, C.M.S.; Labrador, A.W.; Leske, R.A.; Mason, G.M.; Desai, M.I.;Looper, M.D.; Mazur, J.E.; Selesnick, R.S.; Haggerty, D.K. Proton, helium, and electron spectra during the large solar particle events of October–November 2003. *J. Geophys. Res.* **2005**, *110*, A09S18. [[CrossRef](#)]
35. NMDB: The Neutron Monitor Database. Available online: <https://www.nmdb.eu/> (accessed on 12 February 2024).
36. Lingri, D.; Mavromichalaki, H.; Belov, A.; Eroshenko, E.; Yanke, V.; Abunin, A.; Abunina, M. Solar Activity Parameters and Associated Forbush Decreases During the Minimum Between Cycles 23 and 24 and the Ascending Phase of Cycle 24. *Sol. Phys.* **2016**, *291*, 1025–1041. [[CrossRef](#)]

Disclaimer/Publisher’s Note: The statements, opinions and data contained in all publications are solely those of the individual author(s) and contributor(s) and not of MDPI and/or the editor(s). MDPI and/or the editor(s) disclaim responsibility for any injury to people or property resulting from any ideas, methods, instructions or products referred to in the content.

See discussions, stats, and author profiles for this publication at: <https://www.researchgate.net/publication/341642542>

Radon variability due to floor level in two typical residential buildings in Serbia

Article in *Nukleonika* · May 2020

DOI: 10.2478/nuka-2020-0019

CITATIONS

9

READS

111

9 authors, including:



Vladimir Udovičić

Institute of Physics Belgrade

72 PUBLICATIONS 468 CITATIONS

SEE PROFILE



Nikola Veselinović

Institute of Physics Belgrade

36 PUBLICATIONS 159 CITATIONS

SEE PROFILE



Dimitrije M Maletić

Institute of Physics Belgrade

145 PUBLICATIONS 9,355 CITATIONS

SEE PROFILE



A. Dragić

Institute of Physics Belgrade

77 PUBLICATIONS 404 CITATIONS

SEE PROFILE



Radon variability due to floor level in two typical residential buildings in Serbia

Vladimir Udovicic ,
Nikola Veselinovic,
Dimitrije Maletic,
Radomir Banjanac,
Aleksandar Dragic,
Dejan Jokovic,
Mihailo Savic,
David Knezevic,
Maja Eremic Savkovic

Abstract. It is well known that one of the factors that influence the indoor radon variability is the floor level of the buildings. Considering the fact that the main source of indoor radon is radon in soil gas, it is expected that the radon concentration decreases at higher floors. Thus at higher floors the dominant source of radon is originating from building materials, and in some cases there may be deviations from the generally established regularity. In such sense, we chose one freestanding single-family house with loft and other 16-floor high-rise residential building for this study. The indoor radon measurements were performed by two methods: passive and active. We used passive devices based on track-etched detectors: Radtrak² Radonova. For the short-term indoor radon measurements, we used two active devices: SN1029 and SN1030 (manufactured by Sun Nuclear Corporation). The first device was fixed in the living room at the ground level and the second was moved through the floors of the residential building. Every measuring cycle at the specified floor lasted seven days with the sampling time of 2 h. The results show two different indoor radon behaviours regarding radon variability due to floor level. In the single-family house with loft we registered intense difference between radon concentration in the ground level and loft, while in the high-rise residential building the radon level was almost the same at all floors, and hence we may conclude that radon originated mainly from building materials.

Keywords: Radon variability • Time series

Introduction

Radon sources in the buildings are primarily from soil, building materials and water. Considering the nature of the occurrence and all the sources, the concentration of radon is higher in the ground-floor rooms compared with that in the higher floors of the dwellings in apartments. In the literature one can find a lot of papers dealing with the influence of various factors, including the floor levels, on the radon concentration and variability. In one group of the articles, investigation of the indoor radon concentration distribution due to floor levels of the buildings is the part of the data analysis which was drawn from the national or regional radon surveys [1–6] and others are dedicated to these specific studies [7–11]. In the case of the big buildings with a several number of floors a deviation from the general regularity can be observed, since the dominant source of indoor radon at higher floors is building materials. On the other hand, the radon variability due to floor level, especially in big cities with a much higher number of high-rise buildings and population density compared with rural environments, may have an impact on the assessments of the effective dose from radon exposure at the national level. Usually, the indoor radon map represents the arithmetic mean value of indoor radon concentration on the ground floor, and thus it is not

V. Udovicic✉, N. Veselinovic, D. Maletic, R. Banjanac,
A. Dragic, D. Jokovic, M. Savic, D. Knezevic
Institute of Physics Belgrade
University of Belgrade
Pregrevica 118 St., 11080 Belgrade, Serbia
E-mail: udovicic@ipb.ac.rs

M. Eremic Savkovic
Serbian Radiation and Nuclear Safety and Security
Directorate
Masarikova 5 St., 11000 Belgrade, Serbia

Received: 30 November 2019
Accepted: 17 January 2020

representative of the radon exposure to all citizens since most people do not live on the ground floor. So, it is necessary to convert indoor radon map to a dose map. One of the examples is presented as a plan to develop models that allow correction from ground-floor dwellings to the real situation, accounting data from the national buildings database [12]. In Serbia, national typology of residential buildings is based on the results from the monography “National typology of residential buildings of Serbia” by a group of authors from the Faculty of Architecture [13]. There are six types of the residential buildings in Serbia: two for family housing – freestanding single-family house and single-family house in a row and four types for multifamily housing – freestanding residential building and residential building (lamella) (apartment block with repeated multiple lamellar cores and separate entrances), residential building in a row, and high-rise residential building. Distribution of buildings by type at the national level shows that 97% of all residential buildings are family housing. Also, for all defined types of buildings, number of floors ranges from one to eight above the ground level. Freestanding family houses are mostly ground floor (37%) or ground floor with loft in use (26%), while there is a very low representation of houses that have more than two floors (5%), with average floor level of family buildings of 1.4 [13]. In such sense, we chose one freestanding single-family house with loft with well-known radon characteristics [14] and one 16-floor high-rise residential building for this study.

Materials and methods

Two housing units were selected, one from the family housing group and one high-rise residential building from the collective housing group. The family house has a characteristic construction style in which the house has been built for several years with constant upgrading, which can potentially be a source of radon entry into such houses. The house has a basement and is made of standard materials (brick block, concrete, plaster). Finally, insulation was made using 5-cm thick styrofoam. Long-term measurements of radon concentrations have been carried out in this house by various methods, and several scientific papers have been published so far [14–16].

From the group of residential buildings for collective housing, we chose high-rise building in New Belgrade. It was built in the 1960s as block type. The soliter has a basement, while on the ground floor there are outlets and business premises. The apartments are located in the first floor upward. The soliter has 16 floors. One of the important parameters in the selection of building in municipality New Belgrade is the fact that this municipality is the most populated in Serbia.

The long-term radon measurements were performed with passive device Radtrak² Radonova based on CR-39 track detector. The detectors were exposed for three months from March to June. In the high-rise building, passive radon detectors were deployed at some of the floors in one or several apartments. Time series of measured radon concentrations in the studied residential buildings were obtained using two active devices: SN1029 with the following characteristics declared by the manufacturer – the measurement ranging from 1 Bq·m⁻³ to 99.99 kBq·m⁻³, accuracy equal to ±25%, sensitivity of 0.16 counts/h/Bq·m⁻³ and SN1030 with the following characteristics – the measurement ranging from 1 Bq·m⁻³ to 99.99 kBq·m⁻³, accuracy equal to ±20%, sensitivity of 0.4 counts/h/Bq·m⁻³. SN1029 device were calibrated at the accredited metrological Lab (SUJCHBO Kamenna, Czech Republic) in 2015 and model SN1030 were calibrated by the manufacturer in 2017. The both instruments participated in 2018 NRPI Intercomparisons of radon gas continuous monitors and also, SN1029 device participated in 2015 NRPI Intercomparisons of radon gas measurement devices at SURO v.v.i. Institute, Prague, Czech Republic within the IAEA Technical Cooperation Projects RER 9153 and RER 9127, with excellent results. These are measuring devices of simple construction and practical application. It is a counter with the addition of a sensor for measuring meteorological parameters. The operator can adjust the time sequences from 0.5 h to 24 h. One measurement cycle can take 1000 h or a total of 720 time sequences (the number of successive measurements, i.e. points in a time series). The devices were set to operate in a 2-h time sequence. One was fixed in the downstairs living room and the other was fixed in repositioning floors in apartment buildings. Each measurement cycle on a given floor lasted seven days.

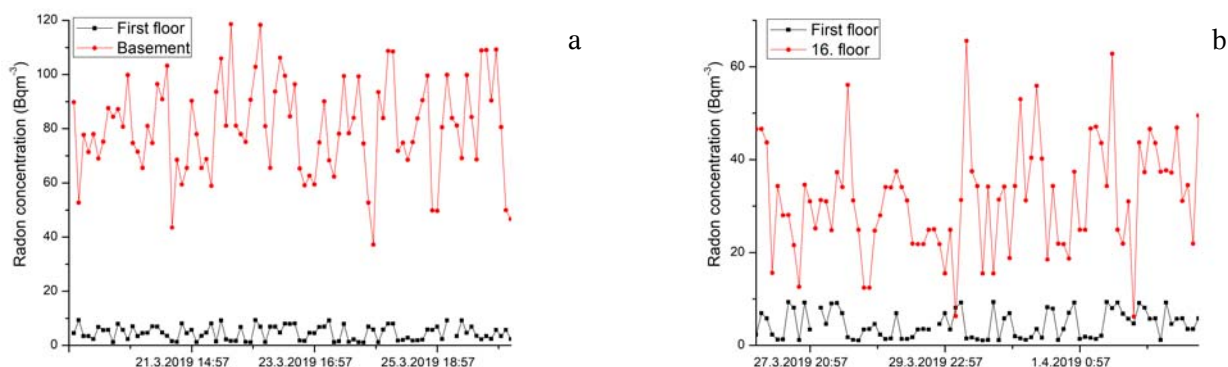


Fig. 1. The time series of the radon concentrations at the first floor vs. basement (a) and 16th floor (b) in the big residential building.

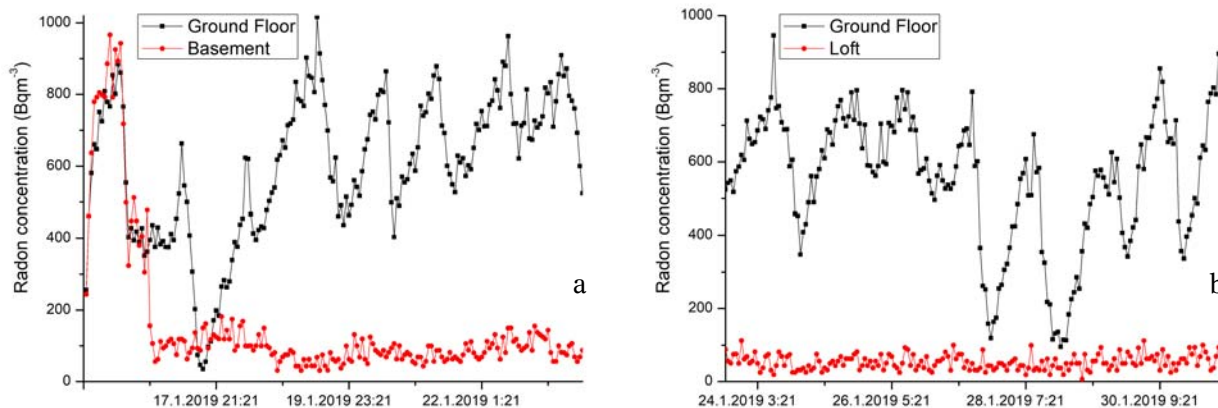


Fig. 2. The time series of the radon concentrations at the first floor vs. basement (a) and loft (b) in the single-family house.

Table 1. Results of indoor radon measurements in the high-rise residential building using passive (Radtrak² Radonova) and active radon devices

Floor level	Radon concentration/ Passive device (Radtrak ²) [Bq·m ⁻³]	Average radon concentration per floor level (Radtrak ²) [Bq·m ⁻³]	Arithmetic mean (standard deviation) radon concentration over measuring cycle [Bq·m ⁻³]
Basement	52 ± 10	53.5	81(17)
	69 ± 12		
	38 ± 10		
	55 ± 10		
1	<10	14	5(3)
	14 ± 8		
2	17 ± 8	17	24(9)
3			25(10)
4	21 ± 8	20.5	26(11)
	20 ± 8		
5	11 ± 8	19	
	27 ± 10		
6	22 ± 8	17	
	12 ± 8		
7	17 ± 8	23	25(10)
	23 ± 8		
8	22 ± 8	22	
9	15 ± 8	17.7	24(10)
	16 ± 8		
10	22 ± 8	17.5	
	15 ± 8		
11	20 ± 8	16	
	16 ± 8		
12	<10	<10	
14	20 ± 8	18.5	29(9)
	17 ± 8		
15	15 ± 8	15.5	
	16 ± 8		
16	31 ± 8	31	32(12)
Overall mean	24	21.6	30

Results and discussions

Figure 1 shows the illustrative examples that show radon time series from high-rise building, and Fig. 2 originates from the observed single-family house.

The arithmetic mean radon concentrations obtained from long- and short-term measurements are shown in Tables 1 and 2 for high-rise building and single-family house with loft, respectively.

In the family house, it is possible to notice marked variations in radon concentration with 1-day periodicity. Also interesting is the ratio of radon concentration on the ground floor to the basement of the house, which is the opposite of the usual situation in houses with a basement. This inverse behaviour can be explained by the fact that the basement does not cover the whole ground floor but a smaller part of it. The rest of the ground floor is covered by a concrete slab as a substrate, but cracks and poor joint with the walls are potential sources of elevated radon. Also, the differences in the results between two methods, passive and active devices, are due to the fact that presented radon values are measured in different seasons. With high-rise residential building, the situation is the opposite and it can be considered from the first floor that the dominant source of radon is the building material. There may even be a slight increase in the mean radon concentration on the higher floors. Also, the results show very low radon level on the first floor (well below the outdoor values) in the apartment. In such sense, we performed test intercomparison radon measurements for two active devices SN1029 and SN1030 in well-defined and controlled radon atmosphere (radon concentration below 30 Bq·m⁻³) in the Underground Low-background Laboratory in the Institute of Physics Belgrade [17, 18]. Additional testing includes the same place and time of the measurements but different sampling time set to 1, 2, 4, 8 and 12 h. The results are shown in Table 3.

In the above performed measurements, both devices show significant differences in the low-level radon range, which may originate from individual instruments characteristics presented in the “Materials and methods” section.

Table 2. Results of indoor radon measurements in the single-family house with loft using passive (Radtrak² Radonova) and active radon devices

Floor level	Radon concentration/Passive device (Radtrak ²) [Bq·m ⁻³]	Arithmetic mean (standard deviation) radon concentration over measuring cycle [Bq·m ⁻³]
Basement		160(202)
Ground level	330 ± 50	579(194)
Loft	18 ± 8	53(21)

Table 3. Test intercomparison indoor radon measurements with active radon devices SN1029 and SN1030

	Arithmetic mean (standard deviation) radon concentration over measuring cycle [Bq·m ⁻³]				
Sampling time [h]	1	2	4	8	12
SN1029	28(12)	28(11)	27(7)	23(6)	32(14)
SN1030	12(6)	14(7)	10(3)	12(5)	14(6)

Conclusions

The results show that the radon behaviour in two different residential buildings is diametrically opposite. In the single-family house with loft we registered intense difference between radon concentration in the ground level and loft, while in the high-rise residential building the radon level was almost the same at all floors and hence we may conclude that radon originated mainly from building materials. However, the results from the high-rise building can be predicted on the basis of work of a group of authors who have determined the internal exposure from construction material used in Serbia which originates from the exhalation of radon and thoron [19] and the study presented in this article [10]. We can expect similar results in any other multistorey buildings in Serbia. In the future work, we will focus on the additional radon measurements in the typical residential buildings from other types of houses.

Acknowledgments. The authors acknowledge funding provided by the Institute of Physics Belgrade through the grant by the Ministry of Education, Science and Technological Development of the Republic of Serbia.

ORCID

V. Udovicic  <http://orcid.org/0000-0002-7839-1537>

References

- Bochicchio, F., Campos-Venuti, G., Piermattei, S., Nucetelli, C., Risica, S., Tommasino, L., Torri, G., Magnoni, M., Agnesod, G., Sgorbati, G., Bonomi, M., Minach, L., Trotti, F., Malisan, M. R., Maggiolo, S., Gaidolfi, L., Giannardi, C., Rongoni, A., Lombardi, M., Cherubini, G., D'Ostilio, S., Cristofaro, C., Pugliese, M., Martucci, V., Crispino, A., Cuzzocrea, P., Sansone Santamaria, A., & Cappai, M. (2005). Annual average and seasonal variations of residential radon concentration for all the Italian Regions. *Radiat. Meas.*, *40*, 686–694.
- Friedmann, H. (2005). Final results of the Austrian Radon Project. *Health Phys.*, *89*(4), 339–348.
- Du, L., Prasauskas, T., Leivo, V., Turunen, M., Pekkonen, M., Kiviste, M., Aaltonen, A., Martuzevicius, D., & Haverinen-Shaughnessy, U. (2015). Assessment of indoor environmental quality in existing multi-family buildings in North-East Europe. *Environ. Int.*, *79*, 74–84.
- Cucoş (Dinu), A., Cosma, C., Dicu, T., Begy, R., Moldovan, M., Papp, B., Niță, D., Burgehele, B., & Sainz, C. (2012). Thorough investigations on indoor radon in Băița radon-prone area (Romania). *Sci. Total Environ.*, *431*, 78–83.
- Yarmoshenko, I., Vasilyev, A., Malinovsky, G., Bossew, P., Žunić, Z. S., Onischenko, A., & Zhukovsky, M. (2016). Variance of indoor radon concentration: Major influencing factors. *Sci. Total Environ.*, *541*, 155–160.
- Kropat, G., Bochud, F., Jaboyedoff, M., Laedermann, J. P., Murith, C., Palacios, M., & Baechler, S. (2014). Major influencing factors of indoor radon concentrations in Switzerland. *J. Environ. Radioact.*, *129*, 7–22.
- Borgoni, R., De Francesco, D., De Bartolo, D., & Tzavidis, N. (2014). Hierarchical modeling of indoor radon concentration: how much do geology and building factors matter? *J. Environ. Radioact.*, *138*, 227–237.
- Xie, D., Liao, M., & Kearfott, K. J. (2015). Influence of environmental factors on indoor radon concentration levels in the basement and ground floor of a building – A case study. *Radiat. Meas.*, *82*, 52–58.
- Man, C. K., & Yeung, H. S. (1999). Modeling and measuring the indoor radon concentrations in high-rise buildings in Hong Kong. *Appl. Radiat. Isot.*, *50*, 1131–1135.
- Vukotić, P., Zekić, R., Antović, N. M., & Andjelić, T. (2019). Radon concentrations in multi-story buildings in Montenegro. *Nucl. Technol. Radiat. Prot.*, *34*, 165–174.
- Lorenzo-González, M., Ruano-Ravina, A., Peón, J., Piñeiro, M., & Barros-Dios, J. M. (2017). Residential radon in Galicia: a cross-sectional study in a radon-prone area. *J. Radiol. Prot.*, *37*(3), 728–741.
- Elío, J., Cinelli, G., Bossew, P., Gutiérrez-Villanueva, J. L., Tollefsen, T., De Cort, M., Nogarotto, A., & Braga, R. (2019). The first version of the Pan-European Indoor Radon Map. *Nat. Hazards Earth Syst. Sci.*, *19*, 2451–2464.
- Jovanović Popović, M., Ignjatović, D., Radivojević, A., Rajčić, A., Čuković Ignjatović, N., Đukanović, Lj., & Nedić, M. (2013). *National typology of residential*

- buildings in Serbia*. Belgrade: Faculty of Architecture University of Belgrade.
14. Udovičić, V., Maletić, D., Banjanac, R., Joković, D., Dragić, A., Veselinović, N., Živanović, J., Savić, M., & Forkapić, S. (2018). Multiyear indoor radon variability in a family house—A case study in Serbia. *Nucl. Technol. Radiat. Prot.*, 33(2), 174–179.
 15. Maletić, D., Udovičić, V., Banjanac, R., Joković, D., Dragić, A., Veselinović, N., & Filipović, J. (2014). Comparison of multivariate classification and regression methods for indoor radon measurements. *Nucl. Technol. Radiat. Prot.*, 29, 17–23.
 16. Filipović, J., Maletić, D., Udovičić, V., Banjanac, R., Joković, D., Savić, M., & Veselinović, N. (2016). The use of multivariate analysis of the radon variability in the underground laboratory and indoor environment. *Nukleonika*, 61(3), 357–360. DOI: 10.1515/nuka-2016-0059.
 17. Udovičić, V., Aničin, I., Joković, D., Dragić, A., Banjanac, R., Grabež, B., & Veselinović, N. (2011). Radon time-series analysis in the Underground Low-level Laboratory in Belgrade, Serbia. *Radiat. Prot. Dosim.*, 145(2/3), 155–158.
 18. Udovičić, V., Filipović, J., Dragić, A., Banjanac, R., Joković, D., Maletić, D., Grabež, B., & Veselinović, N. (2014). Daily and seasonal radon variability in the underground low-background laboratory in Belgrade, Serbia. *Radiat. Prot. Dosim.*, 160(1/3), 62–64.
 19. Ujić, P., Čeliković, I., Kandić, A., Vukanac, I., Đurašević, M., Dragosavac, D., & Žunić, Z. S. (2010). Internal exposure from building materials exhaling ^{222}Rn and ^{220}Rn as compared to external exposure due to their natural radioactivity content. *Appl. Radiat. Isot.*, 68, 201–206.

See discussions, stats, and author profiles for this publication at: <https://www.researchgate.net/publication/354089202>

Performance of the MICE diagnostic system

Article · August 2021

CITATION

1

READS

47

137 authors, including:



Mariyan Bogomilov

Sofia University "St. Kliment Ohridski"

174 PUBLICATIONS 3,828 CITATIONS

[SEE PROFILE](#)



Galina Vankova-Kirilova

Sofia University "St. Kliment Ohridski"

74 PUBLICATIONS 1,282 CITATIONS

[SEE PROFILE](#)



Maurizio Bonesini

INFN - Istituto Nazionale di Fisica Nucleare

1,681 PUBLICATIONS 27,241 CITATIONS

[SEE PROFILE](#)



Rafael Severio Mazza

University of São Paulo

80 PUBLICATIONS 9,737 CITATIONS

[SEE PROFILE](#)



This is a repository copy of *Performance of the MICE diagnostic system*.

White Rose Research Online URL for this paper:
<https://eprints.whiterose.ac.uk/177329/>

Version: Published Version

Article:

Bogomilov, M, Tsenov, R, Vankova-Kirilova, G et al. (134 more authors) (2021)
Performance of the MICE diagnostic system. *Journal of Instrumentation*, 16 (8). P08046.

<https://doi.org/10.1088/1748-0221/16/08/p08046>

Reuse

This article is distributed under the terms of the Creative Commons Attribution (CC BY) licence. This licence allows you to distribute, remix, tweak, and build upon the work, even commercially, as long as you credit the authors for the original work. More information and the full terms of the licence here:
<https://creativecommons.org/licenses/>

Takedown

If you consider content in White Rose Research Online to be in breach of UK law, please notify us by emailing eprints@whiterose.ac.uk including the URL of the record and the reason for the withdrawal request.



eprints@whiterose.ac.uk
<https://eprints.whiterose.ac.uk/>

PAPER • OPEN ACCESS

Performance of the MICE diagnostic system

To cite this article: The MICE collaboration *et al* 2021 *JINST* **16** P08046

View the [article online](#) for updates and enhancements.



ECS The Electrochemical Society
Advancing solid state & electrochemical science & technology
2021 Virtual Education

Intensive Short Courses

Sun, Oct 10 & Mon, Oct 11

Providing students and professionals with in-depth education on a wide range of topics

Early registration deadline: Sep 13, 2021

Register early and save!

The advertisement features a woman with curly hair wearing a headset and smiling while working on a laptop in a modern office setting. The background includes a corkboard with various notes and a potted plant on the desk.

MUON ACCELERATORS FOR PARTICLE PHYSICS — MUON

Performance of the MICE diagnostic system

The MICE collaboration

M. Bogomilov,^a R. Tsenov,^a G. Vankova-Kirilova,^a Y.P. Song,^b J.Y. Tang,^b Z.H. Li,^c
R. Bertoni,^d M. Bonesini,^d F. Chignoli,^d R. Mazza,^d V. Palladino,^e A. de Bari,^f D. Orestano,^g
L. Tortora,^g Y. Kuno,^h H. Sakamoto,^{h,1} A. Sato,^h S. Ishimoto,ⁱ M. Chung,^j C.K. Sung,^j
F. Filthaut,^{k,2} M. Fedorov,^l D. Jokovic,^m D. Maletic,^m M. Savic,^m N. Jovancevic,ⁿ J. Nikolov,ⁿ
M. Vretenar,^o S. Ramberger,^o R. Asfandiyarov,^p A. Blondel,^p F. Drielsma,^{p,3} Y. Karadzhov,^p
G. Charnley,^q N. Collomb,^q K. Dumbell,^q A. Gallagher,^q A. Grant,^q S. Griffiths,^q T. Hartnett,^q
B. Martlew,^q A. Moss,^q A. Muir,^q I. Mullacrane,^q A. Oates,^q P. Owens,^q G. Stokes,^q
P. Warburton,^q C. White,^q D. Adams,^r V. Bayliss,^r J. Boehm,^r T.W. Bradshaw,^r C. Brown,^{r,4}
M. Courthold,^r J. Govans,^r M. Hills,^r J.-B. Lagrange,^r C. Macwaters,^r A. Nichols,^r
R. Preece,^r S. Ricciardi,^r C. Rogers,^r T. Stanley,^r J. Tarrant,^r M. Tucker,^r S. Watson,^{r,5}
A. Wilson,^r R. Bayes,^{s,6} J.C. Nugent,^s F.J.P. Soler,^s R. Gamet,^t P. Cooke,^t V.J. Blackmore,^u
D. Colling,^u A. Dobbs,^{u,7} P. Dornan,^u P. Franchini,^{u,*} C. Hunt,^{u,8} P.B. Jurj,^u A. Kurup,^u
K. Long,^u J. Martyniak,^u S. Middleton,^{u,9} J. Pasternak,^u M.A. Uchida,^{u,10} J.H. Cobb,^v
C.N. Booth,^w P. Hodgson,^w J. Langlands,^w E. Overton,^{w,11} V. Pec,^w P.J. Smith,^w
S. Wilbur,^w G.T. Chatzitheodoridis,^{x,12,13} A.J. Dick,^{x,13} K. Ronald,^{x,13} C.G. Whyte,^{x,13}
A.R. Young,^{x,13} S. Boyd,^y J.R. Greis,^{y,14} T. Lord,^y C. Pidcott,^{y,15} I. Taylor,^{y,16} M. Ellis,^{z,17}

¹Current address: RIKEN 2-1 Hirosawa, Wako, Saitama, Japan.

²Also at Radboud University, Houtlaan 4, Nijmegen, Netherlands.

³Current address: SLAC National Accelerator Laboratory, 2575 Sand Hill Road, Menlo Park, CA, U.S.A.

⁴Also at College of Engineering, Design and Physical Sciences, Brunel University, Kingston Lane, Uxbridge, U.K.

⁵Current address: ATC, Royal Observatory Edinburgh, Blackford Hill, Edinburgh, U.K.

⁶Current address: Laurentian University, 935 Ramsey Lake Road, Sudbury, ON, Canada.

⁷Current address: OPERA Simulation Software, Network House, Langford Locks, Kidlington, U.K.

⁸Current address: CERN, Esplanade des Particules 1, Geneva, Switzerland.

⁹Current address: School of Physics and Astronomy, University of Manchester, Oxford Road, Manchester, U.K.

¹⁰Current address: Rutherford Building, Cavendish Laboratory, JJ Thomson Avenue, Cambridge, U.K.

¹¹Current address: Arm, City Gate, 8 St Mary's Gate, Sheffield, U.K.

¹²Also at School of Physics and Astronomy, Kelvin Building, University of Glasgow, Glasgow, U.K.

¹³Also at Cockcroft Institute, Daresbury Laboratory, Sci-Tech Daresbury, Keckwick Ln, Daresbury, Warrington, U.K.

¹⁴Current address: TNG Technology Consulting, Beta-Strasse 13A, Unterföhring, Germany.

¹⁵Current address: Department of Physics and Astronomy, University of Sheffield, Hounsfield Rd, Sheffield, U.K.

¹⁶Current address: Defence Science and Technology Laboratory, Porton Down, Salisbury, U.K.

¹⁷Current address: Macquarie Group, 50 Martin Place, Sydney, Australia.

**R.B.S. Gardener,^{z,18} P. Kyberd,^z J.J. Nebrensky,^z M. Palmer,^{aa} H. Witte,^{aa} D. Adey,^{ab,19}
**A.D. Bross,^{ab} D. Bowring,^{ab} P. Hanlet,^{ab} A. Liu,^{ab,20} D. Neuffer,^{ab} M. Popovic,^{ab}
**P. Rubinov,^{ab} A. DeMello,^{ac} S. Gourlay,^{ac} A. Lambert,^{ac} D. Li,^{ac} T. Luo,^{ac} S. Prestemon,^{ac}
**S. Virostek,^{ac} B. Freemire,^{ad,20} D.M. Kaplan,^{ad} T.A. Mohayai,^{ad,21} D. Rajaram,^{ad,22}
**P. Snopok,^{ad} Y. Torun,^{ad} L.M. Cremaldi,^{ae} D.A. Sanders,^{ae} D.J. Summers,^{ae,23}
L.R. Coney,^{af,24} G.G. Hanson^{af} and C. Heidt^{af,25}**********

^a*Department of Atomic Physics, St. Kliment Ohridski University of Sofia,
 5 James Bourchier Blvd, Sofia, Bulgaria*

^b*Institute of High Energy Physics, Chinese Academy of Sciences,
 19 Yuquan Rd, Shijingshan District, Beijing, China*

^c*Sichuan University, 252 Shuncheng St, Chengdu, China*

^d*Sezione INFN Milano Bicocca and Dipartimento di Fisica G. Occhialini,
 Piazza della Scienza 3, Milano, Italy*

^e*Sezione INFN Napoli and Dipartimento di Fisica, Università Federico II,
 Complesso Universitario di Monte S. Angelo, Via Cintia, Napoli, Italy*

^f*Sezione INFN Pavia and Dipartimento di Fisica, Università di Pavia, Via Agostino Bassi 6, Pavia, Italy*

^g*Sezione INFN Roma Tre and Dipartimento di Matematica e Fisica, Università Roma Tre,
 Via della Vasca Navale 84, Roma, Italy*

^h*Osaka University, Graduate School of Science, Department of Physics,
 1-1 Machikaneyamacho, Toyonaka, Osaka, Japan*

ⁱ*High Energy Accelerator Research Organization (KEK), Institute of Particle and Nuclear Studies,
 Tsukuba, Ibaraki, Japan*

^j*Department of Physics, UNIST, 50 UNIST-gil, Ulsan, South Korea*

^k*Nikhef, Science Park 105, Amsterdam, Netherlands*

^l*Radboud University, Houtlaan 4, Nijmegen, Netherlands*

^m*Institute of Physics, University of Belgrade, Pregrevica 118, Belgrade, Serbia*

ⁿ*Faculty of Sciences, University of Novi Sad, Trg Dositeja Obradovića 3, Novi Sad, Serbia*

^o*CERN, Esplanade des Particules 1, Geneva, Switzerland*

^p*DPNC, Section de Physique, Université de Genève, 24 Quai Ernest-Ansermet, Geneva, Switzerland*

^q*STFC Daresbury Laboratory, Keckwick Ln, Daresbury, Cheshire, U.K.*

^r*STFC Rutherford Appleton Laboratory, Harwell Campus, Didcot, U.K.*

^s*School of Physics and Astronomy, Kelvin Building, University of Glasgow, Glasgow, U.K.*

^t*Department of Physics, University of Liverpool, Oxford St, Liverpool, U.K.*

^u*Department of Physics, Blackett Laboratory, Imperial College London, Exhibition Road, London, U.K.*

^v*Department of Physics, University of Oxford, Denys Wilkinson Building, Keble Rd, Oxford, U.K.*

^w*Department of Physics and Astronomy, University of Sheffield, Hounsfield Rd, Sheffield, U.K.*

¹⁸Current address: Inawisdom, Columba House, Adastral park, Martlesham, Ipswich, U.K.

¹⁹Current address: Institute of High Energy Physics, Chinese Academy of Sciences, 19 Yuquan Rd, Shijingshan District, Beijing, China.

²⁰Current address: Euclid Techlabs, 367 Remington Blvd, Bolingbrook, IL, U.S.A.

²¹Current address: Fermilab, Kirk Rd and Pine St, Batavia, IL, U.S.A.

²²Current address: KLA, 2350 Green Rd, Ann Arbor, MI, U.S.A.

²³Deceased.

²⁴Current address: European Spallation Source ERIC, Partikelgatan 2, Lund, Sweden.

²⁵Current address: Swish Analytics, Oakland, CA, U.S.A.

*Corresponding author.

^x*SUPA and the Department of Physics, University of Strathclyde, 107 Rottenrow, Glasgow, U.K.*

^y*Department of Physics, University of Warwick, Gibbet Hill Road, Coventry, U.K.*

^z*College of Engineering, Design and Physical Sciences, Brunel University, Kingston Lane, Uxbridge, U.K.*

^{aa}*Brookhaven National Laboratory, 98 Rochester St, Upton, NY, U.S.A.*

^{ab}*Fermilab, Kirk Rd and Pine St, Batavia, IL, U.S.A.*

^{ac}*Lawrence Berkeley National Laboratory, 1 Cyclotron Rd, Berkeley, CA, U.S.A.*

^{ad}*Illinois Institute of Technology, 10 West 35th St, Chicago, IL, U.S.A.*

^{ae}*University of Mississippi, University Ave, Oxford, MS, U.S.A.*

^{af}*University of California, 900 University Ave, Riverside, CA, U.S.A.*

E-mail: p.franchini@imperial.ac.uk

ABSTRACT: Muon beams of low emittance provide the basis for the intense, well-characterised neutrino beams of a neutrino factory and for multi-TeV lepton-antilepton collisions at a muon collider. The international Muon Ionization Cooling Experiment (MICE) has demonstrated the principle of ionization cooling, the technique by which it is proposed to reduce the phase-space volume occupied by the muon beam at such facilities. This paper documents the performance of the detectors used in MICE to measure the muon-beam parameters, and the physical properties of the liquid hydrogen energy absorber during running.

KEYWORDS: Accelerator Applications; Accelerator modelling and simulations (multi-particle dynamics, single-particle dynamics); Accelerator Subsystems and Technologies; Beam-line instrumentation (beam position and profile monitors, beam-intensity monitors, bunch length monitors)

ARXIV EPRINT: [2106.05813](https://arxiv.org/abs/2106.05813)

Contents

1	Introduction	1
2	Time-of-flight detectors	3
3	Cherenkov detectors	5
4	KLOE-light calorimeter	7
5	Electron muon ranger	9
6	Tracking	11
6.1	Trackers	11
6.2	Beam-based detector alignment	14
7	Liquid hydrogen absorber	17
8	Summary and conclusions	21

1 Introduction

Stored muon beams have been proposed as the basis of a facility capable of delivering lepton-antilepton collisions at very high energy [1, 2] and as the source of uniquely well-characterised neutrino beams [3–5]. In the majority of designs for such facilities the muons are produced from the decay of pions created when an intense proton beam strikes a target. The phase-space volume occupied by the tertiary muon beam must be reduced (cooled) before the beam is accelerated and subsequently injected into a storage ring. The times taken to cool the beam using techniques that are presently in use at particle accelerators (synchrotron-radiation cooling [6], laser cooling [7–9], stochastic cooling [10], electron cooling [11] and frictional cooling [12]) are long when compared with the lifetime of the muon. Ionization cooling [13, 14], in which a muon beam is passed through a material (the absorber) where it loses energy, and is then re-accelerated, occurs on a timescale short compared with the muon lifetime. Ionization cooling is therefore the only technique available to cool the muon beam at a neutrino factory or muon collider. The international Muon Ionization Cooling Experiment (MICE) provided the proof-of-principle demonstration of the ionization-cooling technique [15].

MICE operated at the ISIS Neutron and Muon Source at the STFC Rutherford Appleton Laboratory. The ISIS synchrotron accelerates pulses of protons to a kinetic energy of 800 MeV at 50 Hz. For MICE operation, a titanium target was dipped into the halo of the proton beam at 0.78 Hz. Pions created in the interaction of the beam and target were captured in a quadrupole triplet (see figure 1). A beam line composed of dipole, solenoid, and quadrupole magnets captured muons produced through pion decay and transported the resulting muon beam to the MICE apparatus. The

momentum of the muon beam was determined by the settings of the two dipole magnets D1 and D2. Beams having muon central momenta between $140 \text{ MeV}/c$ and $240 \text{ MeV}/c$ were used for ionisation cooling studies. The emittance of the beam injected into the experiment was tuned using a set of adjustable diffusers, some made of tungsten and some of brass. The cooling cell was composed of a liquid hydrogen or lithium hydride absorber placed inside a focus coil (FC) module, sandwiched between two scintillating-fibre trackers (TKU, TKD) placed in superconducting solenoids (SSU, SSD). Together, SSU, FC, and SSD formed the magnetic channel. The MICE coordinate system is such that the z -axis is coincident with the beam direction, the y -axis points vertically upwards, and the x -axis completes a right-handed coordinate system.

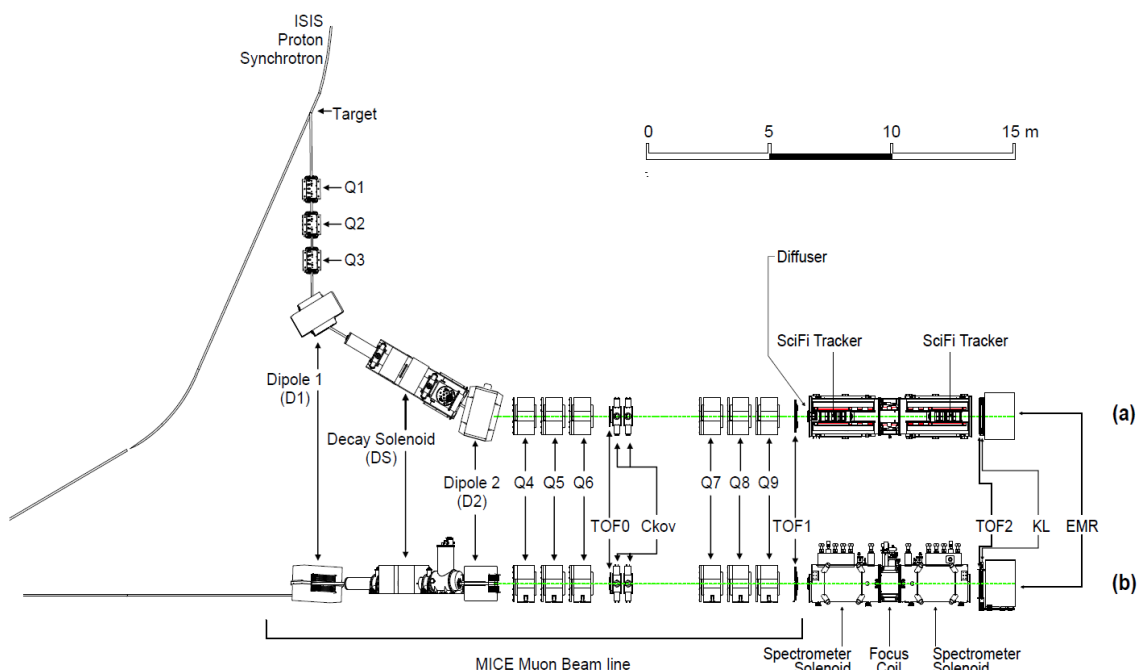


Figure 1. MICE, top (a) and side (b) views, showing the full beam line starting from the target position on the proton synchrotron with the quadrupoles and dipoles (Q1 to Q9, D1, D2), the Decay Solenoid, and instrumented magnetic channel elements (including the trackers upstream, TKU, and downstream, TKD, of the cooling channel, placed inside superconducting solenoids, respectively SSU and SSD) with all the other PID detectors (three TOF stations, two Ckov detectors, KL and the EMR). The cooling cell, defined to be the liquid hydrogen absorber vessel inside the focus coil (FC), is shown in figure 17.

MICE measured the passage of single particles through the apparatus which were aggregated into a beam offline. This paper documents the performance, during 2015-2017, of the instrumentation which was used to fully characterise the beam and its evolution along the magnetic channel, and quantifies the physical properties of the liquid hydrogen absorber. The beam instrumentation consisted of three time-of-flight detectors (TOF0, TOF1, TOF2) discussed in section 2, two threshold Cherenkov counters (CkovA, CkovB) discussed in section 3, a sampling calorimeter (KL) discussed in section 4, a tracking calorimeter (EMR) discussed in section 5, and the scintillating-fibre trackers discussed in section 6. The properties of the liquid hydrogen absorber are described in section 7.

2 Time-of-flight detectors

Three scintillator hodoscopes were used: to measure the time of flight (TOF) of the particles that made up the beam; to measure the transverse position at which the particle crossed each of the detectors; and to provide the trigger for the experiment. TOF0 and TOF1 [16–18] were placed upstream of the magnetic channel, while TOF2 [19] was located downstream of the channel, mounted in front of the KL pre-shower detector (see figure 1). At 240 MeV/ c , the difference in the TOF for a muon and a pion between TOF0 and TOF1 was about 1.3 ns. The system was therefore designed to measure the TOF with a precision of 100 ps. This allowed the TOF between the first pair of TOF stations to be used to discriminate between pions, muons, and electrons, contained within the beam, with near 100% efficiency [20]. In addition, by assuming a mass hypothesis for each particle, the TOF measurement was used to infer the particle momentum. The TOF detectors, which operated smoothly during the running periods, were essential for all the measurements that were performed [15, 20–24].

Each TOF station was made of two planes of 1 inch thick scintillator bars oriented along the x and y directions. The bars of TOF0 (TOF1, TOF2) were made of Bricon BC-404 (BC-420) plastic scintillators. A simple fishtail light-guide was used to attach each end of each bar to Hamamatsu R4998 fast photomultiplier tubes (PMTs). Each PMT was enclosed in an assembly that included the voltage divider chain and a 1 mm thick μ -metal shield. For TOF1 and TOF2 an additional soft iron (ARMCO) local shield was also used [25, 26]. The shield was required to reduce the stray magnetic field within the PMT to a negligible level [18]. To increase the count-rate stability, active dividers were used. One TOF detector is illustrated in figure 2.

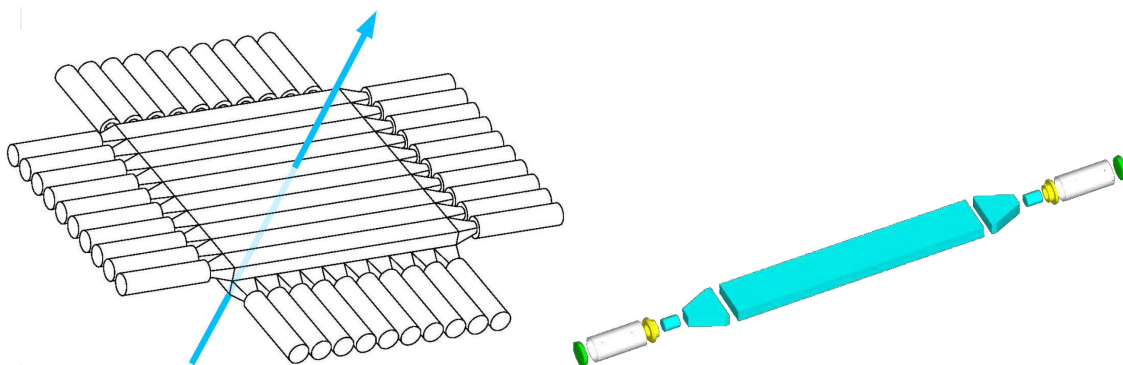


Figure 2. The structure of the time-of-flight detectors [16, 18] showing the horizontal and vertical layers of slabs (left) and an exploded view of each slab (right). The components of each slab are the central scintillator bar, two fishtail, clear plastic light-guides coupled to clear plastic matching pieces, and two PMTs. The beam direction is represented by the blue arrow perpendicular to the slabs.

The active areas of the three hodoscopes were $40 \times 40 \text{ cm}^2$ (TOF0), $42 \times 42 \text{ cm}^2$ (TOF1), and $60 \times 60 \text{ cm}^2$ (TOF2). Each of the planes in TOF0 and TOF2 had 10 slabs while those in TOF1 had 7. A passive splitter was used to take the signal from each of the PMTs to a LeCroy 4115 leading-edge discriminator followed by a CAEN V1290 TDC for time measurement and to a CAEN V1724 FADC for pulse-height measurement. A local readout trigger was issued if the signals from each of the two PMTs on a single slab crossed a specific threshold and overlapped. TOF1 was used to trigger the readout of the experiment for most of the data taking.

Calibration. The intensity of the scintillation light produced when a particle crossed the plastic scintillator rose rapidly before decaying with a characteristic time of 1.8 ns. The scintillation light travelled from the particle-crossing point to each end of the scintillator slab. The light’s travel time depended on the distance of the particle crossing from the PMT. The propagation speed of the light pulse along the slabs was determined to be 13.5 cm/ns.

The local readout-trigger signal was distributed to all TDC boards and was used as the reference time. The time between a particle hit in a TOF slab and the time when the trigger was generated varied with the position of the hit along the slab. As a consequence, the reference time had an offset dependent on the crossing position, an effect referred to as the readout-trigger signal delay. To compensate for this, the final time measurement in each station was an average of the times recorded for each channel above threshold.

Further delay was introduced by the signal-transit time of each PMT and of the cable that led the signal to the readout electronics. These signal-transit times were unique for each individual readout channel and were determined by dedicated measurements. The use of a linear, leading-edge discriminator led to a correlation between the total charge in the pulse and the time at which the discriminator fired. This correlation, referred to as the time-walk, introduced a systematic offset in the time recorded by the TDC that was dependent on the pulse height.

Precise determination of the TOF required a calibration procedure that allowed channel-by-channel variations in the response of the system to be accounted for. The calibration procedure described in [27] accounted for each of the effects identified above.

Reconstruction. A particle crossing a TOF station passed through two orthogonal slabs. Signals from each PMT were corrected for time-walk, readout-trigger signal delay, and the channel-specific delays. The slab-crossing time was taken to be the average of the corrected PMT times. Two slab signals were taken to have been produced by the passage of a particle if their slab-crossing times were within a 4 ns window. These two *matched* slabs were used to define a pixel of area given by the width of the slabs. The particle-crossing time was then determined as the average of the slab-crossing times and the approximate position of the particle crossing was refined using the PMT signals in the two orthogonal slabs.

Performance. The difference, Δt , between the slab-crossing times for *matched* slabs was used to determine the intrinsic time resolution, σ_t of the TOF system. The Δt resolution, $\sigma_{\Delta t}$, is given by $\sigma_{\Delta t} = 2\sigma_t$, assuming that the intrinsic resolution is the same in each of the planes that make up a particular TOF station. Figure 3 shows the distributions of Δt for TOF0, TOF1, and TOF2 for a representative set of data taken in 2017. The RMS width of the distributions are 114 ps, 126 ps, and 108 ps for TOF0, TOF1, and TOF2 respectively. The distributions are similar, and the RMS of each distribution is consistent with the measured intrinsic resolution of approximately 60 ps [18].

Figure 4 shows an example distribution of the measured TOF between TOF0 and TOF1. The TOF peaks characteristic of electrons, muons, and pions are clearly separated. The width of the electron peak is approximately 0.10 ns, consistent with the spread calculated from a naive quadrature addition of the timing resolution of the individual TOF stations.

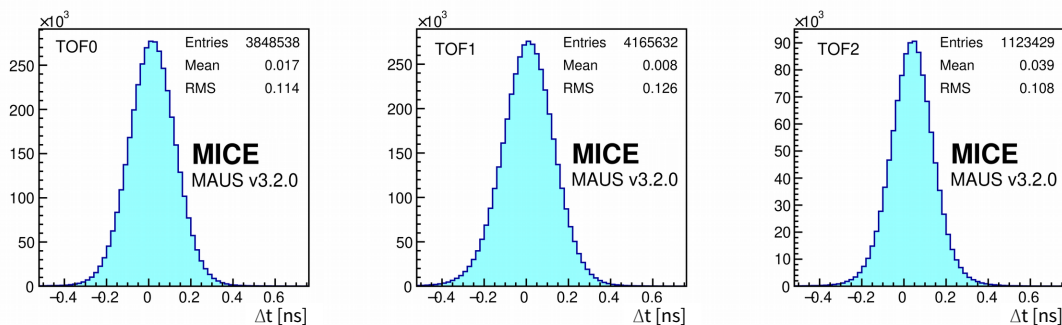


Figure 3. Slab Δt distributions. Total width of the distribution is due to the resolution of the individual channels and due to the offsets in their Δt distributions.

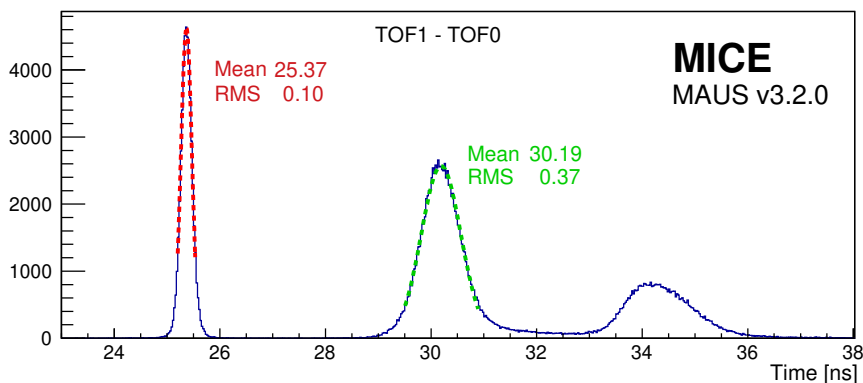


Figure 4. Time of flight between TOF0 and TOF1 after all corrections have been applied. The electron (left-most peak, shown in red), the muon (central peak, shown in green), and the pion (right-most peak, shown in blue) peaks are clearly separated.

3 Cherenkov detectors

The threshold Cherenkov counters were designed to distinguish muons from pions at particle momenta $\gtrsim 200 \text{ MeV}/c$, where the precision of the time-of-flight measurement was not sufficient for conclusive identification. Two high-density silica aerogel Cherenkov detectors with refractive indices $n=1.07$ (CkovA) and $n=1.12$ (CkovB) were used [28]. The structure of the detectors is shown in figure 5. Light was collected in each counter by four eight-inch, UV-enhanced PMTs and recorded using CAEN V1731 FADCs [29]. The two detectors were placed directly one after the other in the beamline and located just after TOF0.

The refractive indices of CkovA and CkovB result in detection thresholds for muons of approximately $280 \text{ MeV}/c$ and $210 \text{ MeV}/c$ respectively. For pions, the thresholds are approximately $367 \text{ MeV}/c$ (CkovA) and $276 \text{ MeV}/c$ (CkovB). MICE was designed to operate using beams with a central momentum between $140 \text{ MeV}/c$ and $240 \text{ MeV}/c$. The Cherenkov counters' thresholds were chosen to provide muon identification for beams of $210 \text{ MeV}/c$ and above, while the TOFs provide muon identification for beam below $210 \text{ MeV}/c$. Unambiguous identification of particle species using the Cherenkovs exploited the momentum measurement provided by the trackers.

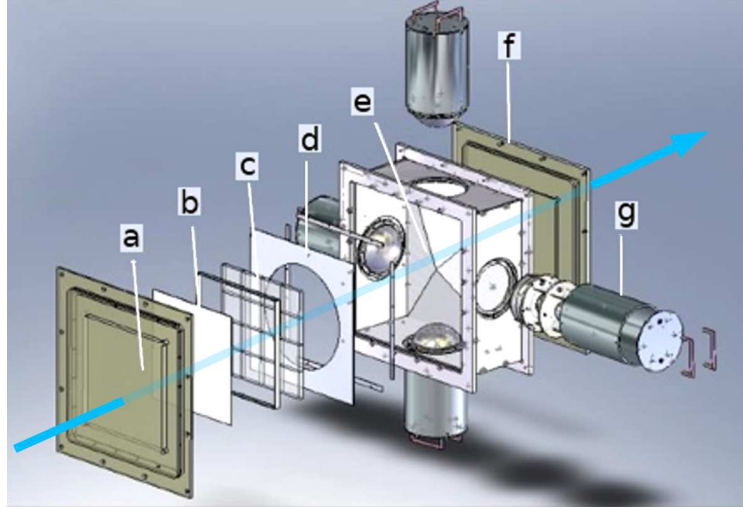


Figure 5. MICE aerogel Cherenkov counter: a) entrance window, b) mirror, c) aerogel mosaic, d) acetate window, e) GORE DRP reflector panel, f) exit window and g) eight-inch PMT in iron shield. The beam direction is represented by the blue arrow traversing the detector.

Performance. The performance of the detectors was determined using beams for which the momentum range was broad enough to observe the turn-on points and to allow the asymptotic light yields (as the particle velocity divided by the speed of light, β , approaches 1) to be obtained from fits to the data. The normalised photo-electron yields observed in CkovA and CkovB are plotted as a function of $\beta\gamma$ (where $\gamma = (1 - \beta^2)^{-\frac{1}{2}}$) in figure 6. The pedestal in the photo-tube response arising from background photons has been subtracted. The approximate turn-on points for CkovA and CkovB were found at $\beta\gamma \approx 2.6$ and ≈ 2.1 respectively, corresponding to refractive indices of $n \approx 1.07$ and ≈ 1.11 which are in broad agreement with the properties of the aerogel radiators.

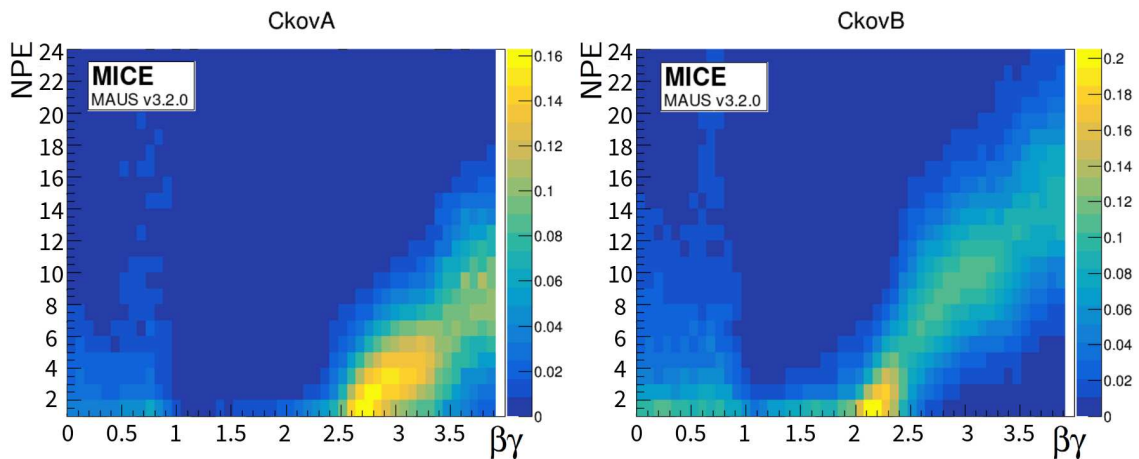


Figure 6. Photoelectron yields versus $\beta\gamma$ in CkovA and CkovB, where βc is the particle velocity and $\gamma = (1 - \beta^2)^{-\frac{1}{2}}$.

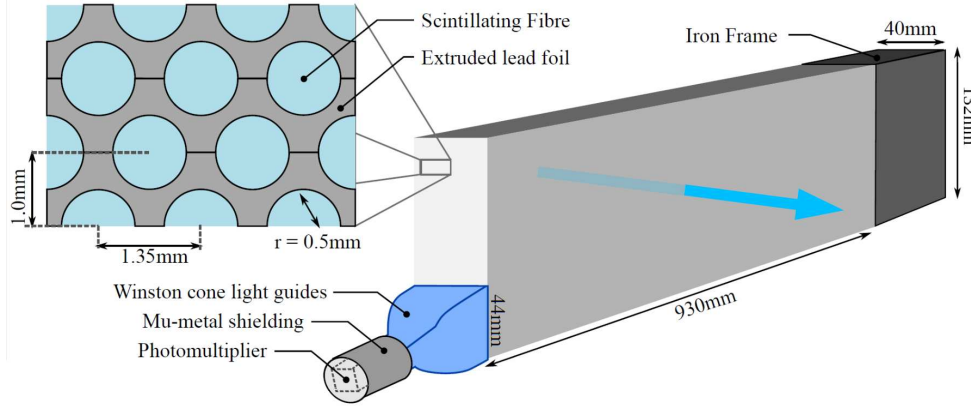


Figure 7. Single slab design of MICE KLOE-Light Calorimeter [31]; only one of the six PMT assemblies is shown. The beam direction is represented by the blue arrow traversing the slab.

4 KLOE-light calorimeter

The KLOE-Light (KL) pre-shower sampling calorimeter was composed of extruded lead foils in which scintillating fibres were placed. At normal incidence the thickness of the detector was 2.5 radiation lengths. The detector provided energy deposition and timing information and was used to distinguish muons from decay electrons [20]. The KL consisted of a series of layers of 1 mm diameter BICRON BCF-12 scintillating fibres embedded in an appropriately shaped lead sheets (see figure 7). Each fibre was separated by 1.35 mm from its neighbours within a layer and the distance between the centres of the fibres in adjacent layers was 0.98 mm. One layer was shifted by half the fibre pitch with respect to the next. The volume ratio of scintillator to lead was approximately 2:1, “lighter” than the ratio of 1:1 used in the similar calorimeter of the KLOE experiment [30]. Lead/scintillator layers were stacked into slabs, 132 mm in depth. A total of 7 slabs formed the whole detector, which had an active volume of 93 cm×93 cm×4 cm. Scintillation light was guided from each slab into a total of six PMTs (three at each end). Iron shields were fitted to each photomultiplier to mitigate the effect of stray magnetic fields. The signal from each PMT was sent to a shaping amplifier module that stretched the signal in time to match the sampling rate of the CAEN 1724 FADCs.

Performance. To study the response of the KL, the particle momentum was determined from the measured time-of-flight between TOF0 and TOF1. To compensate for the effect of attenuation the performance was evaluated in terms of the “ADC product” given by:

$$\text{ADC}_{\text{prod}} = \frac{2 \times \text{ADC}_{\text{left}} \times \text{ADC}_{\text{right}}}{(\text{ADC}_{\text{left}} + \text{ADC}_{\text{right}})}; \quad (4.1)$$

where ADC_{left} and $\text{ADC}_{\text{right}}$ are the signals from the two ends of a slab and the factor of 2 is present for normalisation. Data was taken with no field in the spectrometer solenoids or the focus coil at beam-momentum settings chosen to span the range of momenta used during MICE running. The resulting momentum distributions were centred at 140, 170, 200, 240, and 300 MeV/c. The response of the KL to muons and pions was observed to increase with beam momentum.

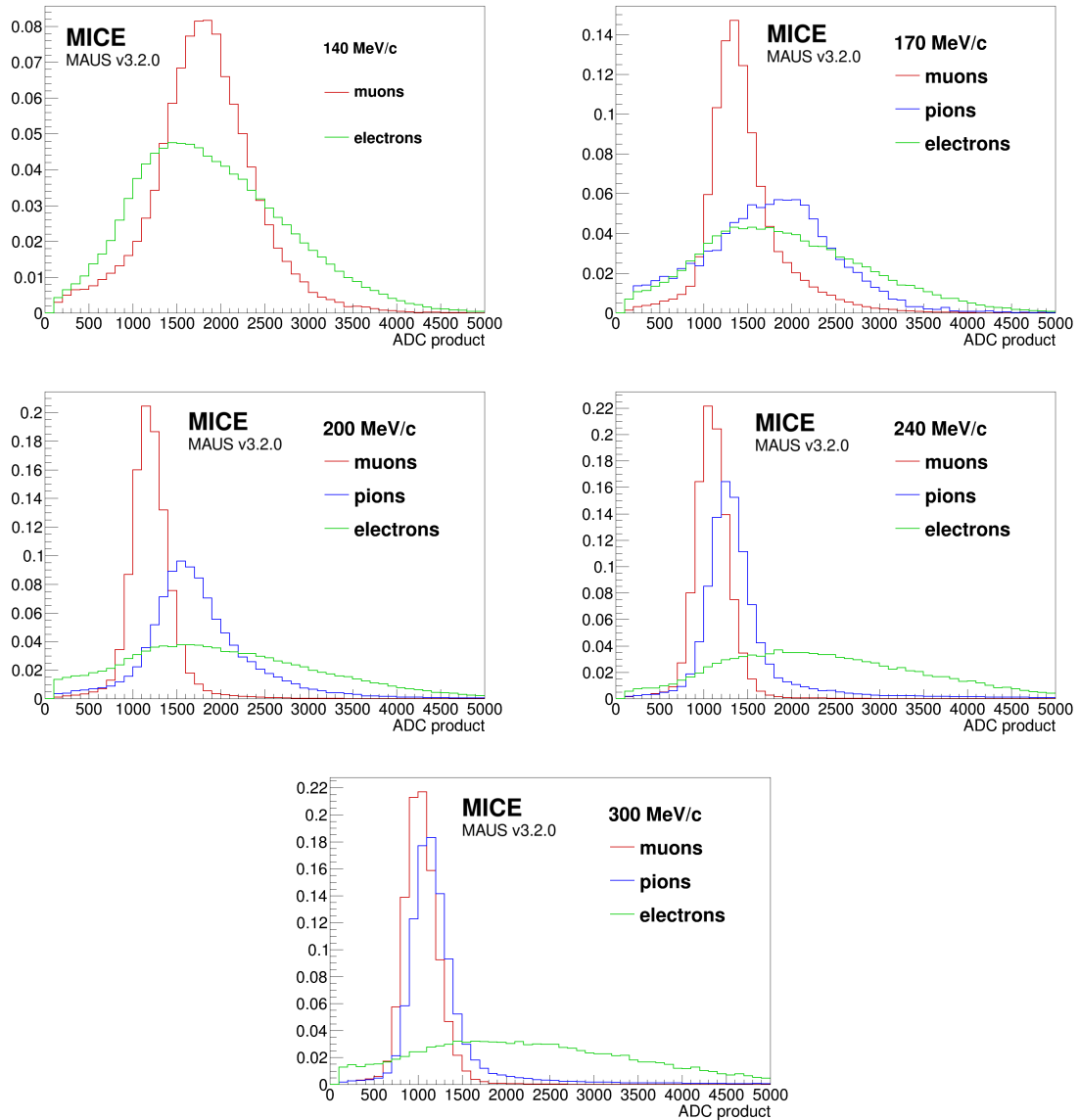


Figure 8. Comparison of ADC products of muons (red), pions (blue) and electrons (green) traversing the KL, at 140 MeV/ c (top left), 170 MeV/ c (top right), 200 MeV/ c (middle left), 240 MeV/ c (middle right) and 300 MeV/ c (bottom).

Figure 8 presents a comparison of the response to muons, pions and electrons for various beam momentum settings. At high momentum, for example 300 MeV/ c , the ADC product distributions for muons and pions are similar. At lower momentum the distributions become increasingly dissimilar, the pions having a broader distribution arising from hadronic interactions. The difference between the detector’s response to pions and muons has been exploited to determine the pion contamination in the muon beams used for the MICE cooling measurements [20].

The ADC product distribution measured using a 300 MeV/ c beam is compared to the MAUS [32] simulation of the detector response in figure 9. The simulation takes into account

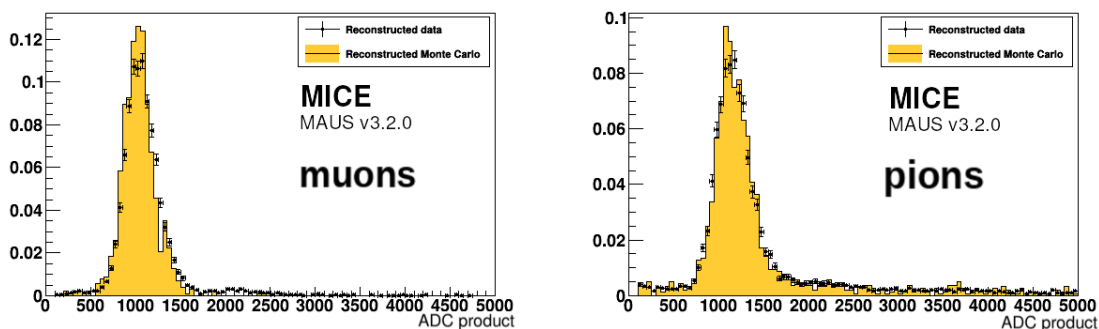


Figure 9. Comparison between data and Monte Carlo simulation of KL response to muons (left) and pions (right) at $300 \text{ MeV}/c$.

the light production distribution of the scintillating fibres, and the response of the PMTs for which the gain was approximately 2×10^6 . The data is well described by the simulation.

5 Electron muon ranger

The EMR was a fully-active scintillator detector [33] with a granularity that allowed track reconstruction. The EMR consisted of extruded triangular scintillator bars arranged in planes. Each plane contained 59 bars and covered an area of 1.27 m^2 . Figure 10 shows the bar cross section and the arrangement of the bars in a plane. Triangular bars were chosen so that tracks moving parallel to the detector axis could not travel along the gaps between bars. Successive planes were mounted perpendicularly, so that hits in neighbouring planes defined a position. A single “X-Y module” was a pair of orthogonal planes. The scintillation light was collected using a wavelength shifting (WLS) fibre glued inside each bar. At each end, the WLS fibre was coupled to clear fibres that transported the light to a PMT. All the WLS fibres from one edge of a plane were read out using one single-anode PMT (SAPMT) so that an integrated charge measurement could be used to determine the energy deposited in the plane. The signals from the fibres emerging from the other edge of the plane were recorded individually using multi-anode PMTs (MAPMTs). The full detector was made up of 24 X-Y modules giving a total active volume of approximately 1 m^3 .

Measurements of the performance of the completed detector demonstrated an efficiency per plane of $99.73 \pm 0.02\%$ [33, 34]. The level of crosstalk was within acceptable values for the type of MAPMT used, with an average of $0.20 \pm 0.03\%$ between adjacent channels and a mean amplitude equivalent to $4.5 \pm 0.1\%$ of the primary signal. Only four dead bars were present.

The primary purpose of the EMR was to distinguish between a muon that crossed the entire magnetic channel and those which decayed in flight producing an electron. Muons and electrons exhibited distinct behaviours in the detector. A muon produced a single straight track before either stopping or exiting the scintillating volume. Electrons showered in the lead of the KL and created a broad cascade of secondary particles. Two main geometric variables, the “plane density” and the “shower spread”, were used to differentiate them. The detector was capable of identifying electrons with an efficiency of 98.6% , providing a purity for the MICE beam that exceeds 99.8% .

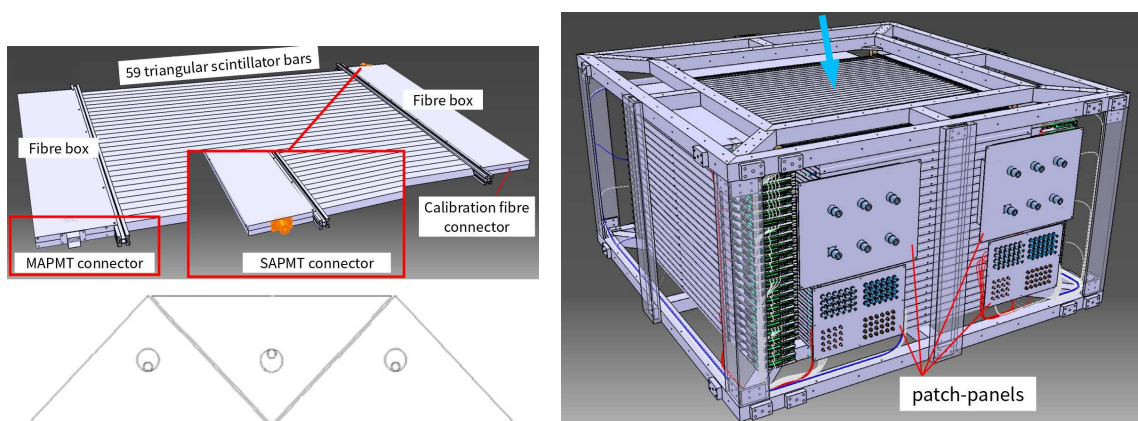


Figure 10. Drawing of one EMR plane (top left), cross section of the arrangement of 3 bars and their wavelength shifting fibres (bottom left) and drawing of the full detector and its supporting structure from a top perspective (right). The beam direction is represented by the blue arrow perpendicular to the detector.

The EMR also proved to be a powerful tool for the reconstruction of muon momenta in the range 100–280 MeV/ c [23].

Performance. A full description of the detector and the reconstruction algorithms used may be found in reference [23]. Here the performance of the EMR detector over the course of the experiment is summarised.

To measure the performance of the EMR the MICE beamline was set to deliver a nominal momentum of 400 MeV/ c . This maximised the muon transmission to the EMR and its range in the detector. In this configuration the beamline produced pions and muons in comparable quantities, as well as a smaller number of electrons. Time-of-flight between TOF1 and TOF2 was used to identify particle species and only particles compatible with the muon hypothesis were included in the analysis. Particles entering the muon sample had a momentum larger than 350 MeV/ c at the upstream surface of TOF2 and were expected to cross both TOF2 and the KL and penetrate the EMR. $99.62 \pm 0.03\%$ of the particles entering TOF2 were observed to produce hits in the EMR. The small inefficiency may be attributed to pions in the muon sample that experienced hadronic interactions in the KL. If hits were produced in the detector, an (x, y) pair, defining a space point, was reconstructed $98.56 \pm 0.06\%$ of the time.

To evaluate the efficiency of the scintillator planes, only the muons that traversed the entire detector were used. Muons were selected which produced a hit in the most downstream plane. For these events a hit was expected in at least one bar in each plane on its path. The mode of the hit-multiplicity distribution per plane was one, in $3.26 \pm 0.02\%$ of cases a plane traversed by a muon did not produce a signal in the MAPMT, and the probability that the track was not observed in the SAPMT was $1.88 \pm 0.01\%$.

Electron rejection. A broad range of beamline momentum settings was used to characterise the electron-rejection efficiency. Particle species were characterised upstream of the EMR using the time-of-flight between TOF1 and TOF2. For each momentum setting, a fit was carried out to determine the position of the muon and electron time-of-flight peaks and events were selected

accordingly to form muon and electron-template samples. Particles with a time-of-flight larger than the upper limit of the muon sample were either pions or slow muons and were rejected.

To distinguish the muon tracks from the electron-induced showers, two particle-identification variables were defined based on the distinct characteristics of the two particle species. The first is the plane density, ρ_p :

$$\rho_p = \frac{N_p}{Z_p + 1}, \quad (5.1)$$

where N_p is the number of planes hit and Z_p the number of the most downstream plane [23]. A muon deposits energy in every plane it crosses until it stops, producing a plane density close to one. An electron shower contains photons that may produce hits deep inside the fiducial volume without leaving a trace on their path, reducing the plane density. The second variable is the normalised $\hat{\chi}^2$ of the fitted straight track given by

$$\hat{\chi}^2 = \frac{1}{N - 4} \sum_{i=1}^N \frac{\text{res}_{x,i}^2 + \text{res}_{y,i}^2}{\sigma_x^2 + \sigma_y^2}, \quad (5.2)$$

where N is the number of space points (one per bar hit), $\text{res}_{q,i}$ the residual of the space point with respect to the track in the qz projection and σ_q the uncertainty on the space point in the qz projection, $q = x, y$ [35]. This quantity represents the transverse spread of the hits produced by the particle in the EMR. A muon produced a single track giving $\hat{\chi}^2$ close to one, while an electron shower produced a larger value. The two discriminating variables can be combined to form a statistical test on the particle hypothesis. Dense and narrow events will be tagged as muons while non-continuous and wide showers will not. The quality of this statistical test was characterised in terms of the fraction of the muon sample that is rejected, α , and the fraction of the electron sample that is selected, β .

The momentum of the particles was measured by the downstream tracker and this information used to determine the momentum dependence of the contamination and loss in the range 100–300 MeV/ c . Figure 11 shows the loss, α , and the contamination, β , as a function of the momentum measured in TKD. α increases towards low muon momentum. This is due both to an increase in the decay probability between TOF2 and the EMR and a decrease in the number of muons that cross the KL to reach the EMR.

6 Tracking

The MICE instrumentation allowed individual particles to be tracked from TOF0 to the EMR, a distance of more than 15 m. High-resolution particle tracking was provided by two scintillating-fibre trackers (section 6.1). The precise relative alignment of the time-of-flight hodoscopes and the trackers was obtained by combining the measurements of both detector systems (section 6.2).

6.1 Trackers

The two high-precision scintillating-fibre trackers each had a sensitive volume that was 110 cm in length and 30 cm in diameter [36]. Each tracker was composed of five stations (labelled 1 to 5, with station 1 being closest to the cooling cell) held in position using a carbon-fibre space-frame. Adjacent stations were separated by different distances ranging from 20 cm to 35 cm. The

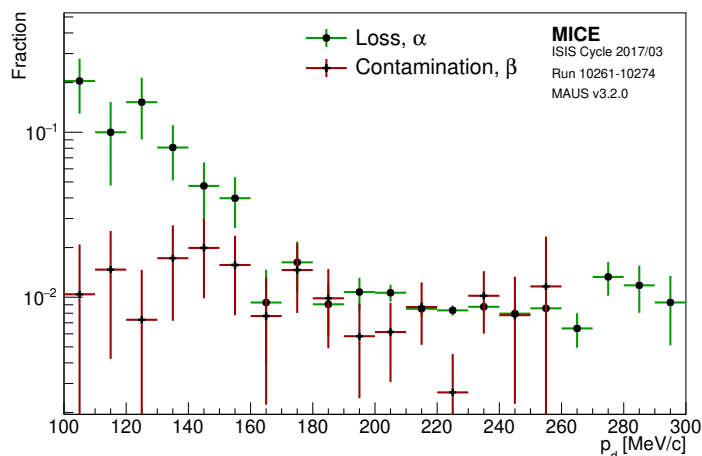


Figure 11. Percentage of electron contamination, β , and muon loss, α , for different ranges of momentum measured in the downstream tracker, p_d . The error bars are based on the statistical uncertainty in a bin, and the bin width set by the resolution of the measurement.

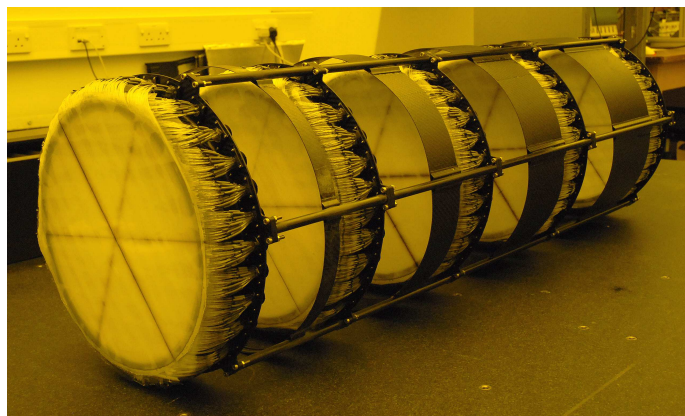


Figure 12. Photograph, with UV-filtered light, of one of the MICE trackers, showing the five stations. Each station has three doublet planes of scintillating fibres, each plane at 120° to the next (the central fibres of each plane can be seen as darker lines traversing the station).

separations were chosen to ensure that the azimuthal rotation of track position did not repeat from one station to the next. This property was exploited in the ambiguity-resolution phase of the pattern recognition. Each tracker was instrumented with an internal LED calibration system and four 3-axis Hall probes to monitor the field. A photograph of one of the trackers on the bed of the coordinate measuring machine used to verify the mechanical alignment of the stations is shown in figure 12.

Each tracker station consisted of three doublet layers of $350\ \mu\text{m}$ scintillating fibres; these layers were arranged such that each was set at an angle of 120° with respect to the next. This arrangement ensured that there were no inactive regions between adjacent fibres. Fibres were grouped into one bundle of seven for each readout channel, to match the resolution to that imposed by multiple scattering and reduce the overall number of readout channels. This resulted in a spatial resolution per doublet layer of $470\ \mu\text{m}$ and a measured light yield of approximately 10 photo-electrons [36].

The light from the seven scintillating fibres was coupled into a single clear fibre which took it to a visible light photon counter (VLPC) [37]. The signals from the VLPCs were digitised using electronics developed by the D0 collaboration [38].

Reconstruction. The reconstruction software for the trackers is described in [39]. Each of the 15 doublet layers provided 214 readout channels. Calibration data taken without beam was used to determine the pedestal and the gain of each channel. These calibrations were used to correct the number of photoelectrons (NPE) corresponding to the signal recorded by the tracker electronics. The first step in the reconstruction was to record the unique channel number associated with each NPE value in a “digit”. Digit profiles were used to identify hot or dead channels which were masked from the reconstruction to reduce the rate of ambiguities that had to be resolved in the pattern recognition and to ensure the accuracy of the calibration. The reconstruction proceeded to create “spacepoints” from the intersection of digits in adjacent doublet layers. Spacepoints were constructed from clusters from all three planes (a triplet spacepoint) or from any two out of the three planes (a doublet spacepoint). The pattern-recognition algorithm searched for spacepoints from neighbouring stations that were consistent with the helical trajectory of a charged particle in the solenoidal field. In the final stage of the tracker reconstruction the track parameters were estimated using a Kalman filter.

Noise. Digits above a certain NPE threshold were admitted to the spacepoint-finding algorithm. Noise in the electronics arising from, for example, the thermal emission of electrons, could give rise to digits passing the threshold. Any digit not caused by the passage of a charged particle was classified as noise. To isolate noise from signal during beam-on data collection, events containing a track which included a spacepoint in each of the five tracker stations were selected. All digits corresponding to the track were removed from the total set of digits and the remainder were considered to be noise. The average noise rate per channel per event was then calculated as the total number of digits above the NPE threshold divided by the number of active channels and the number of events in the sample. The result of this calculation was that, for an NPE threshold of 2, the fraction of digits arising from noise was 0.18% in the upstream tracker and 0.06% in the downstream tracker.

Track-finding efficiency. The track-finding efficiency was determined using a sample of events for which the time-of-flight determined from hits in TOF1 and TOF2 was consistent with passage of a muon. This requirement ensured that the particle had been transmitted successfully through the magnetic channel, crossing both trackers. The track-finding efficiency was defined to be the number of events in which a track was successfully reconstructed divided by the total number of events in the sample. The results of the efficiency analysis are tabulated in table 1 for a range of nominal beam momentum and emittance settings. The track-finding efficiency obtained in this way averaged over beam conditions was 98.70% for the upstream tracker and 98.93% for the downstream tracker. The spacepoint-finding efficiency, defined as the number of spacepoints found divided by the number of space points expected, was also determined. The spacepoint-finding efficiency is summarised for a range of beam conditions in table 2.

The efficiency of the trackers over the data taking period was evaluated by selecting events with a measured time-of-flight between TOF1 and TOF2 consistent with the passage of a muon. Events were required to contain at least one hit within the fiducial volume of the tracker. An event was added to the numerator of the efficiency calculation if it contained a single space point in each of

Table 1. The track finding efficiency for the upstream and downstream trackers for 140 MeV/ c and 200 MeV/ c beams, and for 3, 6 and 10 mm nominal emittances.

Momentum	Emittance	Upstream tracks found	Downstream tracks found
200 MeV/ c	3 mm	98.38%	99.19%
200 MeV/ c	6 mm	99.42%	96.07%
140 MeV/ c	6 mm	98.37%	99.16%
140 MeV/ c	10 mm	98.47%	98.93%
Average		98.70%	98.21%

Table 2. The spacepoint-finding efficiency, in the presence of a track, for the upstream and downstream trackers for 140 MeV/ c and 200 MeV/ c beams, and for 3, 6 and 10 mm nominal emittances.

Momentum	Emittance	Upstream spacepoints found	Downstream spacepoints found
200 MeV/ c	3 mm	98.04%	97.41%
200 MeV/ c	6 mm	99.41%	94.63%
140 MeV/ c	6 mm	97.99%	99.16%
140 MeV/ c	10 mm	98.07%	97.44%
Average		98.44%	97.01%

the five tracker stations. The evolution of the tracking efficiency in the upstream and downstream trackers is shown in figure 13. The efficiency is shown separately for data taken in the presence of a magnetic field (“helical”) and with the solenoids turned off (“straight”). The data shows that the efficiency was generally greater than 99.0%. Water vapour ingress to the cold end of the VLPC cassettes caused the loss of channels and contributed to a reduction in the tracking efficiency. This was recovered by warming and drying the VLPCs.

Track-fit performance. Monte Carlo simulation with realistic field, beam conditions and detector geometry was used to estimate the performance of the track fit. A beam centred at 140 MeV/ c with 10 mm nominal emittance, representing a typical data set, was used for the study. Results are presented in figure 14 for the upstream tracker and figure 15 for the downstream tracker. The resolution in the total momentum and transverse momentum is observed to be ~ 1.1 MeV/ c independent of momentum in the range 120 MeV/ c to 160 MeV/ c . The small bias in the transverse and the total momentum did not give rise to significant effects in the analysis and was considered in systematic error studies.

6.2 Beam-based detector alignment

A beam-based alignment algorithm was developed to improve the resolution on the position of the scintillating-fibre trackers relative to the time-of-flight hodoscopes. The starting point for the beam-based alignment was the geometrical survey of the detectors in the MICE Hall which was performed using laser geodesy. Survey monuments on the TOF frames were surveyed with respect

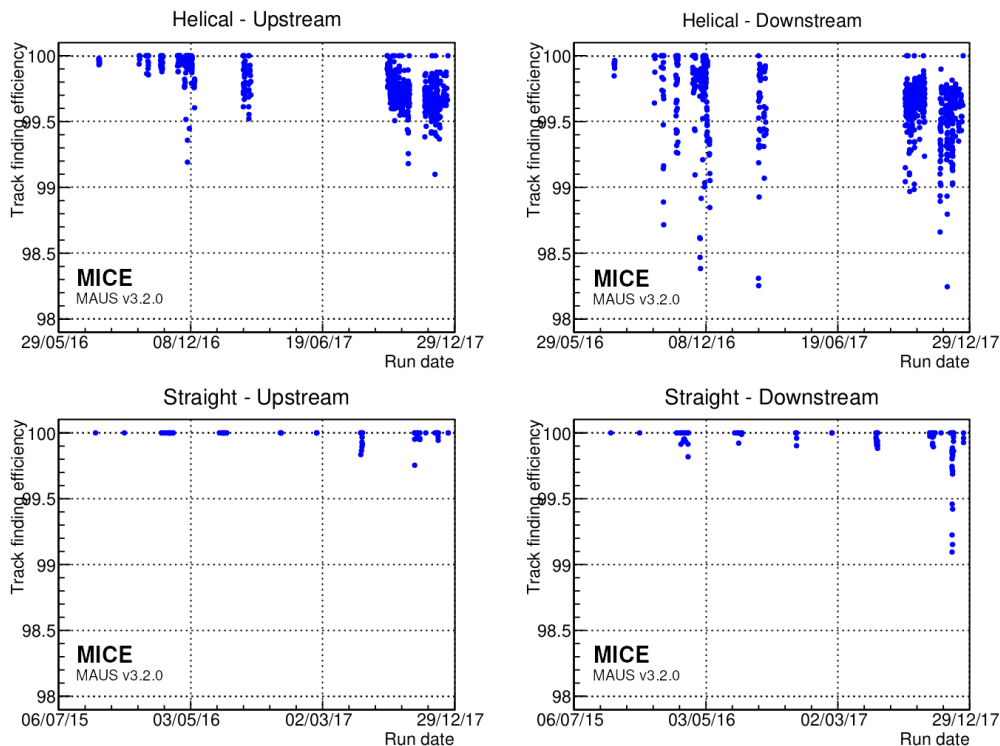


Figure 13. Evolution of the straight and helical track finding efficiencies over time for: the upstream (left); and downstream (right) trackers during the key periods of data taking since 2015. Each dot represents a single data taking run between 10 minutes and 3 hours long.

to the MICE Hall survey network. The trackers had been dowelled in position in the bores of the spectrometer solenoids. The dowels were used to locate each tracker precisely with respect to the axis of the warm bore of its solenoid. The position of the trackers along the beam line was inferred from the measurement of survey monuments mounted on the spectrometer-solenoid cryostats outer jackets. The beam-based alignment was used to determine the azimuthal orientation of the trackers with a resolution of $6 \text{ mrad}/\sqrt{N}$ and their position transverse to the beamline with a resolution of $20 \text{ mm}/\sqrt{N}$, where N is the number of tracks used in the analysis [40].

Analysis method. The position of each tracker in the MICE Hall coordinate system was described using the location of its centre and a set of three angles corresponding to rotation about the x axis (α), the y axis (β) and the z axis (ϕ). The rotation of the tracker about the z axis has a negligible effect on the alignment since ϕ was determined precisely at installation. An initial estimate for the position of each tracker along the beamline had been inferred from the survey. The surveyed location of the TOFs was used as the reference for the tracker alignment. The line that joins the centre of TOF1 with the centre of TOF2 was chosen as the reference axis. A deviation from this axis was considered to be due to misalignment of the trackers. The alignment could not be determined on a single-particle basis due to multiple Coulomb scattering in the absorber and other material present on the beamline. Therefore, the mean residuals in position (x and y) and angle (α and β) of the trackers with respect to the TOF1-TOF2 axis were evaluated to determine the alignment constants.

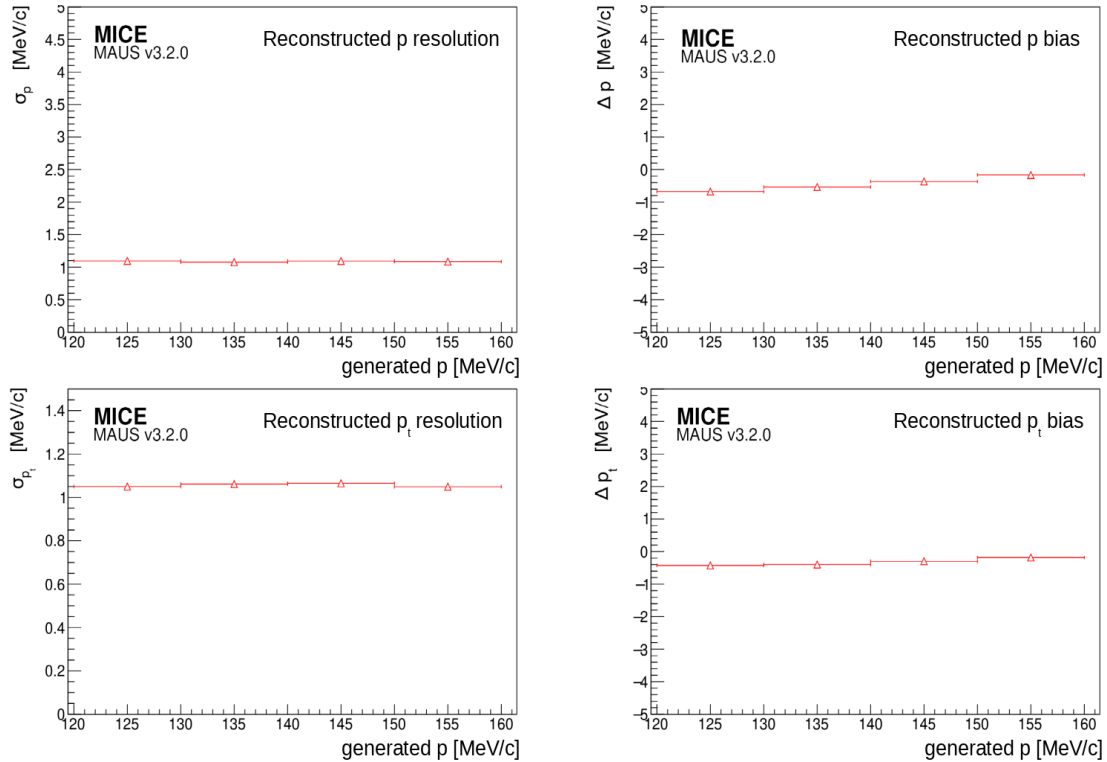


Figure 14. Momentum reconstruction resolution (left) and bias (right) for the total momentum (top) and transverse momentum component (bottom) in the upstream tracker.

Each TOF provided a single spacepoint in the Hall coordinate system. In Hall coordinates, on average, the track reconstructed between TOF1 and TOF2 should agree with the track reconstructed in each tracker, i.e. the mean residuals in x , y , α , and β should be zero. Applying this reasoning to the unknown offset and angles leads to a system of equations for the four unknown constants [40]. The measurement of four residual distributions per tracker yields the alignment constants. The main source of bias was the scattering in the material between TOF1 and TOF2. If the beam was not perfectly centred, particles preferentially scraped out on one side of the magnet bore, anisotropically truncating the tail of the residual distribution. A fiducial cut was applied to the upstream sample in order to remove this effect.

Data were recorded with the superconducting magnets turned off. High momentum beams were used to reduce the RMS scattering angle and to maximise transmission. Each data set was processed independently. Figure 16 shows the alignment parameters determined for each run during a specific data taking period. The measurements are in good agreement with one another and show no significant discrepancy: an agreement between the independent fits guaranteed an unbiased measurement of the alignment constants. The constant-fit χ^2/ndf was close to unity for each fit, indicating that there were no additional sources of significant uncertainty. The optimal parameters are summarised in table 3.

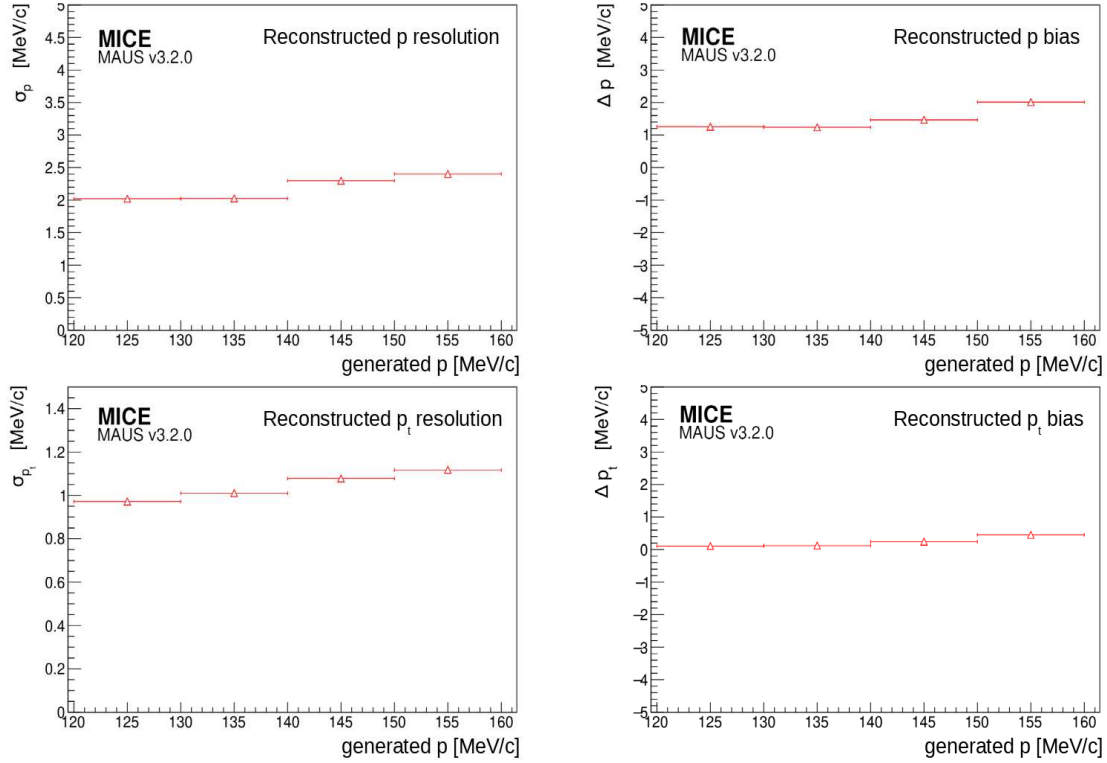


Figure 15. Momentum reconstruction resolution (left) and bias (right) for the total momentum (top) and transverse momentum component (bottom) in the downstream tracker.

Table 3. Optimal alignment constants measured in the high-momentum straight-track data acquired during May 2017 (summarised from figure 16).

	x [mm]	y [mm]	α [mrad]	β [mrad]
TKU	-0.032 ± 0.094	-1.538 ± 0.095	3.382 ± 0.030	0.412 ± 0.029
TKD	-2.958 ± 0.095	2.921 ± 0.096	-0.036 ± 0.030	1.333 ± 0.030

7 Liquid hydrogen absorber

The accurate characterisation of the properties of the liquid hydrogen absorber was a critically-important contribution to the study of ionisation cooling. The instrumentation used for this purpose and its performance are presented in this section.

The absorber vessel consisted of a cylindrical aluminium body sealed with two thin aluminium end windows, as shown in figure 17. The absorber vessel contained 22 l of liquid. The body of the absorber had an inner diameter of 300 mm and the end flanges were separated by a distance of 230 mm. The vessel was surrounded by a second pair of safety windows. The length along the central axis, between the two domes of the end windows, was 350 mm [41].

Variation of the density of liquid hydrogen due to varying temperature and pressure. The energy lost by a muon travelling through the liquid hydrogen absorber depends on the path length and

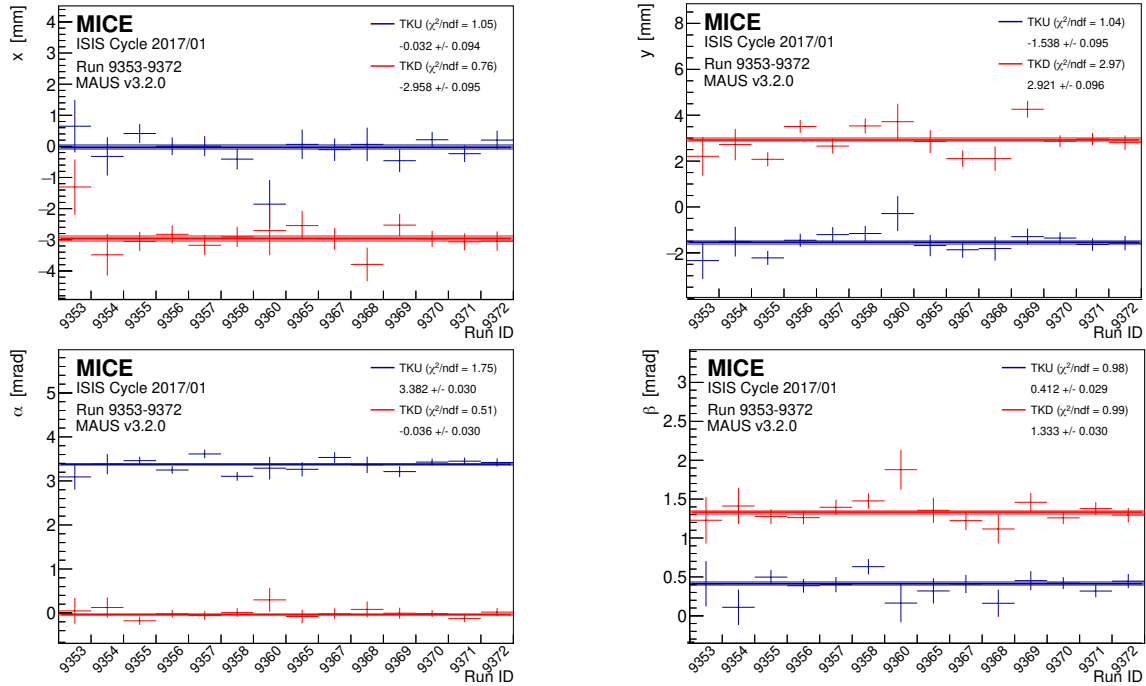


Figure 16. Consistency of the alignment algorithm results for upstream (blue) and downstream (red) trackers across runs acquired during the 2017/01 ISIS user cycle. The quantities x , y , α , and β are defined in the text.

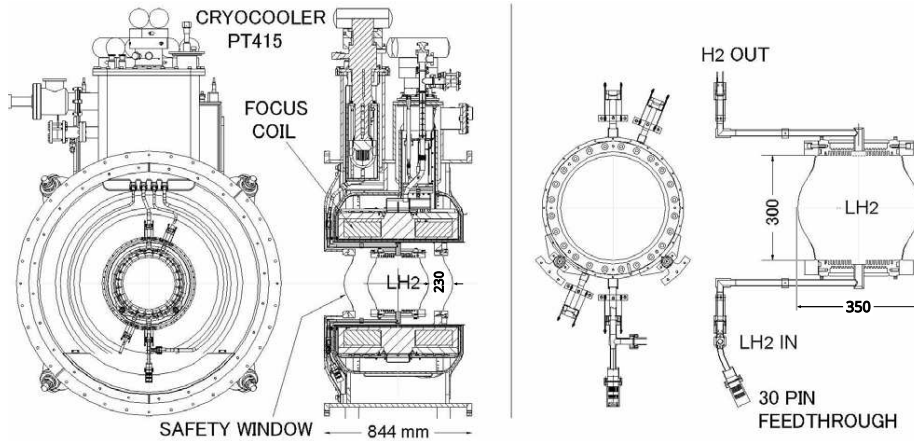


Figure 17. Left panel: drawing of the focus coil (FC) module showing the principal components. Right panel: detail of the liquid hydrogen absorber vessel [41].

on the density of the liquid hydrogen. The density of liquid hydrogen is a function of temperature and pressure. The temperature of the vessel was measured by eight LakeShore Cernox 1050 SD sensors, but with the values truncated for storage at a granularity of 0.1 K. Four of the sensors were used solely as temperature sensors, while the other four were also used as level sensors to ensure the liquid hydrogen reached the top of the vessel. The sensors were arranged in pairs, with two mechanically clamped at the top of the vessel, two at a polar angle of 45° to vertical from the top of the vessel, two at a polar angle of 45° to the bottom of the vessel, and a final two at the bottom of the vessel.

Cooldown and liquefaction were completed slowly over eight days at a pressure of 1105 mbar after which the vessel's pressure was lowered to 1085 mbar [41]. The vessel then remained in this steady state during the 21 day period of data taking, after which the vessel was vented. For the venting process, the cryocooler used to liquefy hydrogen was switched off and heaters were switched on to deliver a nominal power of 50 W to the absorber vessel. This resulted in an increase in pressure to 1505 mbar until the temperature stabilised at the boiling point. A rapid increase in temperature was observed once all the liquid hydrogen had boiled off.

The temperature sensors had a typical accuracy of ± 9 mK and a long-term stability of ± 12 mK at 20 K. The magnetic-field dependent temperature error, $\Delta T/T$, at 2.5 T is 0.04%, equivalent to ± 8 mK at 20 K [42]. These uncertainties were quoted by the manufacturer of the sensors. Magnetic fields caused reversible calibration shifts on the temperature measurements. To reduce the uncertainty in the liquid hydrogen density a calibration procedure was devised that used the boiling point, as observed during the venting process. A correction to the observed temperature reading was obtained by applying a cut-off correction, a correction for the effect of the magnetic field based on the current in the focus coil and its polarity, a correction for the non-linearity of the sensors, and a boiling point scaling factor [43].

The boiling point of hydrogen at 1085 mbar is 20.511 K. The sensors had a total uncertainty of 17 mK (9 mK accuracy, 12 mK stability, 8 mK magnetic). The deviation from the non-linearity of the sensors [42] added, on average, 0.03 K to the uncertainty. The temperature scaling and magnet-current correction factors also had an associated uncertainty as they were derived based on the 0.1 K resolution of the retrieved, truncated, values. For example, a calibrated sensor at boiling temperature and 1505 mbar should read 21.692 K, but we can only retrieve a value of 21.65 K (21.6 K truncated plus 0.05 K cut-off correction [43]) i.e. off by 0.042 K. The pressure sensors had an uncertainty of ± 5 mbar which equated to ± 0.016 K during steady state. The pressure uncertainty (± 5 mbar) added another uncertainty to the temperature calibration constants of ± 0.014 K. Collectively, all these uncertainties summed in quadrature to 0.2 K for each sensor.

While in the steady state condition the liquid hydrogen was close to the boiling temperature of liquid parahydrogen [43] (density of 70.53 kg/m^3): the average temperature of the eight sensors was (20.51 ± 0.07) K at 1085 mbar (figure 18) allowing us to determine the uncertainty in the density over this period as 0.08 kg/m^3 .

Contraction of the absorber vessel due to cooling. The absorber was cooled from room temperature to the operating temperature of the experiment (20.51 K), contracting the vessel. The linear contraction of Al-6061 as it is cooled from 293 K is given by:

$$\alpha = -4.1277 \times 10^{-3}T - 3.0389 \times 10^{-6}T^2 + 8.7696 \times 10^{-8}T^3 - 9.9821 \times 10^{-11}T^4 \quad (7.1)$$

where T is the operating temperature [44]. The equation is the result of a fit to data collated by the National Institute of Standards and Technology (NIST) and has an associated curve fit error of 4%. At the MICE operating temperature, this corresponds to a linear contraction of the vessel along each plane of 0.415%. As a result the length of the bore contracted by (1.45 ± 0.05) mm. The vessel was suspended within the warm bore of the focus coil and was therefore free to contract in each plane without restriction.

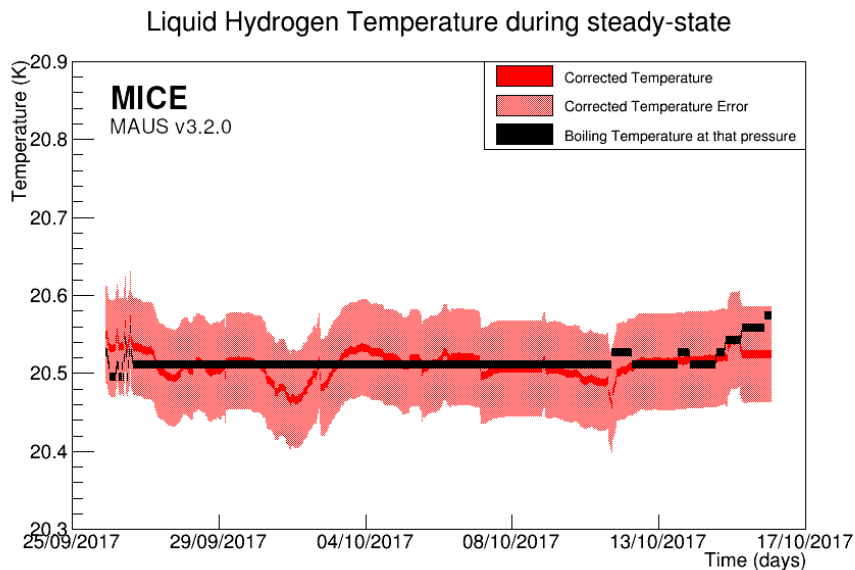


Figure 18. Average liquid hydrogen temperature recorded by the sensors during the steady state period. After applying all the correction factors the temperature remains at or close to the boiling point temperature.

Deflection of absorber vessel windows due to internal pressure. To minimise energy loss and Coulomb scattering by the absorber vessel, the window thickness was minimised. The liquid hydrogen circuit was pressurised above atmospheric pressure to prevent air ingress [41, 45]. The vessel was designed to withstand at least 2500 mbar internally. The internal pressure was limited by the 1.5 bar relief valve to atmosphere, whilst the vessel was surrounded by vacuum.

The pressure at which the absorber operated resulted in deflection of the absorber windows. These deflections were modelled using ANSYS [46], and the uncertainty in the window deflection derived from this model was 20%. The model showed a linear dependence of the window deflection on pressure up to 2 Bar when the windows begin to yield. The pressure sensors were accurate to ± 5 mbar (0.25% of 2 Bar). At (1085 ± 5) mbar, the typical MICE operating pressure, this corresponded to a deflection of (0.5374 ± 0.1076) mm (model uncertainty) ± 0.0022 mm (sensor uncertainty) at the centre of the absorber window.

Variation of the absorber vessel window thicknesses. On its passage through the absorber a muon would lose energy in the aluminium of the pair of hydrogen-containment windows, the two aluminium safety windows, and the liquid hydrogen itself. At the centre of the absorber, the total amount of aluminium the muon beam passed through was (785 ± 13) μm , producing a variance of 1.68%. However, as the windows were thin, the effects on energy loss were negligible. A 200 MeV/c muon passing along the central axis of an empty absorber lost 0.345 MeV, introducing a 0.006 MeV uncertainty on energy loss.

Total systematic uncertainty on energy loss. The principal contributions to the systematic uncertainty on energy loss in the liquid hydrogen absorber are: the uncertainty in the contraction of the absorber vessel, the uncertainty in the deflection of the hydrogen-containment windows due to internal pressure, and the uncertainty in the variation of the window thickness. The impact of the

contraction of vessel and the deflection of the windows resulted in a reduction of the length of the vessel on axis of (0.4 ± 0.2) mm. The change in the combined thicknesses of the absorber windows on axis is $13 \mu\text{m}$. The average temperature during the steady state period of the experiment when the pressure remained constant at (1085 ± 5) mbar is (20.51 ± 0.07) K corresponding to a liquid hydrogen density of (70.53 ± 0.08) kg/m^3 .

During the MICE data taking, muon beams with nominal momenta of 140, 170, 200 and 240 MeV/c were used. The energy loss and its uncertainty were calculated. The calculation used a central bore length of (349.6 ± 0.2) mm, a total window thickness of (0.785 ± 0.013) mm and a liquid hydrogen density of (70.53 ± 0.08) kg/m^3 . For a 140 MeV/c muon this corresponds to an energy loss of (10.88 ± 0.02) MeV, while for a 200 MeV/c muon particle this corresponds to an energy loss of (10.44 ± 0.02) MeV. For a muon travelling along the centre axis of the absorber the systematic uncertainty in the energy loss is 0.2%.

8 Summary and conclusions

A complete set of particle detectors has permitted the full characterisation and study of the evolution of the phase space of a muon beam through a section of a cooling channel in the presence of liquid hydrogen and lithium hydride absorbers, leading to the first measurement of ionization cooling. The PID performance of the detectors is summarised in table 4 and table 5 and is fully compatible with the specification of the apparatus [47].

Table 4. Summary of the performance of the MICE PID detectors.

Detector	Characteristic	Performance
Time-of-Flight	time resolution	0.10 ns
KLOE-Light	muon PID efficiency	99%
Electron Muon Ranger	electron PID efficiency	98.6%

Table 5. Summary of the MICE PID detector performance for different beam settings.

Momentum	KL efficiency			EMR efficiency		Track finding efficiency					
	electrons	muons	pions	electrons	muons	3 mm		6 mm		10 mm	
						US	DS	US	DS	US	DS
140 MeV/c	95%	97%	n.a.	98%	35%			98%	99%	98%	99%
170 MeV/c	95%	99%	89%	99%	99%						
200 MeV/c	94%	99%	95%	100%	99%	99%	96%	99%	96%		
240 MeV/c	96%	99%	97%	99%	99%						
300 MeV/c	95%	99%	98%	n.a.	99%						

All the different elements of the MICE instrumentation have been used to characterise the beam and the measurement of the cooling performance for a different variety of beam momenta, emittance, and absorbers. The measurement of the physical properties of the liquid hydrogen

absorber have been fully described here. The experiment has thus demonstrated a technique critical for a muon collider and a neutrino factory and brings those facilities one step closer.

Acknowledgments

The work described here was made possible by grants from the Department of Energy and National Science Foundation (U.S.A.), the Istituto Nazionale di Fisica Nucleare (Italy), the Science and Technology Facilities Council (U.K.), the European Community under the European Commission Framework Programme 7, the Japan Society for the Promotion of Science and the Swiss National Science Foundation, in the framework of the SCOPES programme. We gratefully acknowledge all sources of support. We acknowledge the use of Grid computing resources deployed and operated by GridPP in the U.K. [48]. We are also grateful to the staff of ISIS for the reliable operation of ISIS.

The MAUS software used to reconstruct and analyse the MICE data is available at [49].

References

- [1] D.V. Neuffer and R.B. Palmer, *A high-energy high-luminosity $\mu^+\mu^-$ collider*, *Conf. Proc. C* **940627** (1995) 52.
- [2] R.B. Palmer, *Muon colliders*, *Rev. Accel. Sci. Tech.* **7** (2014) 137.
- [3] S. Geer, *Neutrino beams from muon storage rings: characteristics and physics potential*, *Phys. Rev. D* **57** (1998) 6989 [Erratum *ibid.* **59** (1999) 039903] [[hep-ph/9712290](#)].
- [4] ISS PHYSICS WORKING GROUP collaboration, *Physics at a future neutrino factory and super-beam facility*, *Rept. Prog. Phys.* **72** (2009) 106201 [[arXiv:0710.4947](#)].
- [5] M. Apollonio et al., *Oscillation physics with a neutrino factory*, [hep-ph/0210192](#).
- [6] S.Y. Lee, *Accelerator physics*, third edition, **World Scientific**, Singapore (2012).
- [7] S. Schröder et al., *First laser cooling of relativistic ions in a storage ring*, *Phys. Rev. Lett.* **64** (1990) 2901.
- [8] J.S. Hangst, M. Kristensen, J.S. Nielsen, O. Poulsen, J.P. Schiffer and P. Shi, *Laser cooling of a stored ion beam to 1 mK*, *Phys. Rev. Lett.* **67** (1991) 1238.
- [9] P.J. Channell, *Laser cooling of heavy-ion beams*, *J. Appl. Phys.* **52** (1981) 3791.
- [10] J. Marriner, *Stochastic cooling overview*, *Nucl. Instrum. Meth. A* **532** (2004) 11 [[physics/0308044](#)].
- [11] V.V. Parkhomchuk and A.N. Skrinsky, *Electron cooling: 35 years of development*, *Phys. Usp.* **43** (2000) 433 [*Usp. Fiz. Nauk* **170** (2000) 473].
- [12] A. Antognini et al., *Demonstration of muon-beam transverse phase-space compression*, *Phys. Rev. Lett.* **125** (2020) 164802 [[arXiv:2003.11986](#)].
- [13] A.N. Skrinsky and V.V. Parkhomchuk, *Cooling methods for beams of charged particles* (in Russian), *Sov. J. Part. Nucl.* **12** (1981) 223 [*Fiz. Elem. Chast. Atom. Yadra* **12** (1981) 557].
- [14] D. Neuffer, *Principles and applications of muon cooling*, *Part. Accel.* **14** (1983) 75.
- [15] MICE collaboration, *Demonstration of cooling by the Muon Ionization Cooling Experiment*, *Nature* **578** (2020) 53 [[arXiv:1907.08562](#)].
- [16] M. Bonesini, *The design of MICE TOF0 detector*, **MICE note 145**, (2006), accessed 14 May 2021.

- [17] R. Bertoni et al., *The construction and laboratory tests for MICE TOF0/1 detectors*, [MICE note 241](#), (2008), accessed 14 May 2021.
- [18] MICE collaboration, *The design and commissioning of the MICE upstream time-of-flight system*, [Nucl. Instrum. Meth. A](#) **615** (2010) 14 [[arXiv:1001.4426](#)].
- [19] R. Bertoni et al., *The construction of the MICE TOF2 detector*, [MICE note 286](#), (2010), accessed 14 May 2021.
- [20] MICE collaboration, *Pion contamination in the MICE muon beam*, [2016 JINST](#) **11** P03001 [[arXiv:1511.00556](#)].
- [21] MICE collaboration, *The MICE muon beam on ISIS and the beam-line instrumentation of the Muon Ionization Cooling Experiment*, [2012 JINST](#) **7** P05009 [[arXiv:1203.4089](#)].
- [22] MICE collaboration, *Characterisation of the muon beams for the Muon Ionisation Cooling Experiment*, [Eur. Phys. J. C](#) **73** (2013) 2582 [[arXiv:1306.1509](#)].
- [23] MICE collaboration, *Electron-muon ranger: performance in the MICE muon beam*, [2015 JINST](#) **10** P12012 [[arXiv:1510.08306](#)].
- [24] MICE collaboration, *First particle-by-particle measurement of emittance in the Muon Ionization Cooling Experiment*, [Eur. Phys. J. C](#) **79** (2019) 257 [[arXiv:1810.13224](#)].
- [25] M. Bonesini, R. Bertoni, A. de Bari and M. Rossella, *Behaviour in magnetic fields of fast conventional and fine-mesh photomultipliers*, [Nucl. Instrum. Meth. A](#) **693** (2012) 130 [[arXiv:1207.4909](#)].
- [26] M. Bonesini et al., *The TOF1 local shielding*, [MICE note 455](#), (2015), accessed 14 May 2021.
- [27] Y. Karadzhov et al., *TOF detectors time calibration*, [MICE note 251](#), (2009), accessed 14 May 2021.
- [28] L. Cremaldi, D.A. Sanders, P. Sonnek, D.J. Summers and J. Reidy Jr, *A Cherenkov radiation detector with high density aerogels*, [IEEE Trans. Nucl. Sci.](#) **56** (2009) 1475 [[arXiv:0905.3411](#)].
- [29] L. Cremaldi et al., *Progress on Cherenkov reconstruction in MICE*, [MICE note 473](#), (2015), accessed 14 May 2021.
- [30] F. Ambrosino et al., *Calibration and performances of the KLOE calorimeter*, [Nucl. Instrum. Meth. A](#) **598** (2009) 239.
- [31] E. Overton, *Studies and developments within the Muon Ionisation Cooling Experiment*, Ph.D. thesis, [Sheffield U.](#), Sheffield, U.K. (2014).
- [32] R. Asfandiyarov et al., *MAUS: the MICE Analysis User Software*, [2019 JINST](#) **14** T04005 [[arXiv:1812.02674](#)].
- [33] R. Asfandiyarov et al., *The design and construction of the MICE electron-muon ranger*, [2016 JINST](#) **11** T10007 [[arXiv:1607.04955](#)].
- [34] F. Drielsma, *Electron-muon ranger: hardware characterization*, master's thesis, Geneva U., Geneva, Switzerland (2014) [[arXiv:1710.06946](#)].
- [35] F. Drielsma, *Measurement of the increase in phase space density of a muon beam through ionization cooling*, Ph.D. thesis, [Geneva U.](#), Geneva, Switzerland (2018)
- [36] M. Ellis et al., *The design, construction and performance of the MICE scintillating fibre trackers*, [Nucl. Instrum. Meth. A](#) **659** (2011) 136 [[arXiv:1005.3491](#)].
- [37] M. Petroff and M. Stapelbroek, *Photon-counting solid-state photomultiplier*, [IEEE Trans. Nucl. Sci.](#) **36** (1989) 158.

- [38] D0 collaboration, *The upgraded D0 detector*, *Nucl. Instrum. Meth. A* **565** (2006) 463 [[physics/0507191](#)].
- [39] A. Dobbs et al., *The reconstruction software for the MICE scintillating fibre trackers*, *2016 JINST* **11** T12001 [[arXiv:1610.05161](#)].
- [40] F. Drielsma, *Beam-based detector alignment in the MICE muon beam line*, [arXiv:1805.06623](#).
- [41] MICE collaboration, *The liquid-hydrogen absorber for MICE*, *2018 JINST* **13** T09008 [[arXiv:1807.03019](#)].
- [42] *Temperature measurement and control catalog*, https://www.lakeshore.com/docs/default-source/product-downloads/lakeshoretc_1.pdf, accessed 2 October 2018.
- [43] C. Brown et al., *Systematic uncertainties in the liquid hydrogen absorber*, *MICE note 524*, (2018), accessed 14 May 2021.
- [44] G. Hardin, *Aluminum 6061-T6 (UNS AA96061)*, <https://www.nist.gov/mml/acmd/aluminum-6061-t6-uns-aa96061>, accessed 3 October 2018.
- [45] S. Ishimoto, S. Suzuki, M. Yoshida, M.A. Green, Y. Kuno and W. Lau, *Liquid hydrogen absorber for MICE*, *Conf. Proc. C* **100523** (2010) 421.
- [46] M. Green et al., *Does one know the properties of a MICE solid or liquid absorber to better than 0.3 percent?*, *MICE note 155*, (2006), accessed 14 May 2021.
- [47] MICE collaboration, *Proposal to the Rutherford Appleton Lab: an international Muon Ionization Cooling Experiment (MICE)*, *MICE note 21*, (2003), accessed 14 May 2021.
- [48] D. Britton et al., *GridPP: the U.K. grid for particle physics*, *Phil. Trans. Roy. Soc. A* **367** (2009) 2447.
- [49] MICE collaboration, *Source code of MAUS — the MICE Analysis User Software*, [10.17633/rd.brunel.8337542.v2](https://doi.org/10.17633/rd.brunel.8337542.v2), (2019).



Correlation analysis of solar energetic particles and secondary cosmic ray flux

Nikola Veselinović^a, Mihailo Savić, Aleksandar Dragić, Dimitrije Maletić, Radomir Banjanac, Dejan Joković, David Knežević, and Vladimir Udovičić

Institute of Physics Belgrade, University of Belgrade, Pregrevica 118, Belgrade 11080, Serbia

Received 31 January 2021 / Accepted 5 May 2021 / Published online 8 June 2021
© The Author(s), under exclusive licence to EDP Sciences, SIF and Springer-Verlag GmbH Germany, part of Springer Nature 2021

Abstract. Galactic cosmic rays entering heliosphere are modulated by interplanetary magnetic field which is carried away from the Sun by the solar wind. Cosmic rays are additionally modulated by coronal mass ejections and shock waves, which can produce Forbush decrease, a transient decrease in the observed galactic cosmic ray intensity. Measurements of magnetic field and plasma parameters in near-Earth space detect regularly coronal mass ejections, so it is important to understand the correlation between near-Earth particles fluxes associated with these coronal mass ejections and Forbush decreases. By combining in situ measurements of solar energetic particles with ground-based observations by the Belgrade muon detector, we analysed the dynamics of the variation of galactic cosmic rays. Correlation between variations of the flux of the cosmic rays and average in situ particle fluxes was investigated during Forbush decreases. Correlation exhibited dependence on the energy of solar wind particles, but also on cut-off rigidities of cosmic rays detected on the ground. The goal of cross-correlation analysis is to help in better understanding of how coronal mass ejections affect space weather as well as the effects they have on primary cosmic ray variations as detected by ground-based cosmic ray detectors.

1 Introduction

Space weather has been widely used as a term to define impact of the Sun, heliosphere and geomagnetic field on our biosphere and our technological systems. Understanding space weather is a matter of both scientific interest and practical importance as its impact could potentially be hazardous to our civilisation. Cosmic ray (CR) observations can also be used to study space weather. Primary (or galactic) CRs are high-energy nuclei (mainly protons) that originate from outside of our solar system. Their flux and energy range is covering several tens of orders of magnitude (flux from 10^{-28} up to 10^4 ($\text{m}^2 \text{sr sec eV/nucleon}$)⁻¹ and energy range up to 10^{21} eV [10]). As charged particles, CRs are sensitive to magnetic field, so often it is more convenient to use geomagnetic rigidity instead of energy to characterise primary CRs. Geomagnetic rigidity is defined as $R = B\rho = pq$, where B is the magnetic field, ρ is the gyroradius of the particle due to this field, p is the particle momentum and q is its charge [14]. As they traverse interplanetary space, galactic CRs interact with helio-

spheric magnetic field. The heliosphere is the region of space around the Sun dominated by the solar wind and the interplanetary magnetic field (IMF). The solar wind is a stream of supersonic plasma blowing outward from the Sun. IMF represents solar magnetic field carried by highly conducting solar wind plasma. Interaction of CRs with this large-scale field modulates CRs flux intensity measured on Earth, which is nested deep inside the heliosphere. Interaction with the heliosphere causes gradient and curvature drift motion of CRs and scattering by the magnetic irregularities embedded in the solar wind [19]. Variations in the solar magnetic field directly affect the heliosphere, most prominent being the solar cycle variation with a period of about 11 years. Solar cycle affects activity of the Sun which is visible in varying number of sunspots, solar flares (SFs) and coronal mass ejections (CMEs). Coronal mass ejection is an extreme solar activity event, followed by significant release of charged particles and accompanying magnetic field from solar corona. Intensity of measured CRs flux anticorrelates with the activity of the Sun, with lower intensity during maximum of the solar cycle and higher intensity during minimum of solar activity.

One of the transient phenomena of this interaction is the Forbush decrease (FD), which represents a rapid depression in CR flux. It is usually characterised by a sudden decrease reaching minimum within one day, followed by a subsequent gradual recovery phase, which

Supplementary information The online version of this article (<https://doi.org/10.1140/epjd/s10053-021-00172-x>) contains supplementary information, which is available to authorized users.

^a e-mail: veselinovic@ipb.ac.rs (corresponding author)

can last for several days. Typical causes of FD are transient interplanetary events related to interplanetary coronal mass ejections (ICMEs). If the speed of the ICME is greater than fast magnetosonic wave speed in the solar wind reference frame, ambient solar wind plasma will be compressed. The shock can be formed, which is driven ahead of ICME and can cause enhancement of IMF. FD can also be formed due to corotating interaction regions between different solar wind streams with different speed [2]. In this paper, we will only focus on ICME induced FDs, of which we will study four cases.

Correlation between parameters characterising FDs (like magnitude of the decrease, duration, one-step or two-step FDs, etc.) and solar wind parameters has been studied for some time. There is reasonable evidence for correlation between FD magnitude and amplitude of magnetic field enhancement B , velocity of CME, maximum solar wind velocities and other parameters as shown in [7, 22]. Also, profile of FDs is modelled and compared with CME magnetic structure, starting from the simple force-free flux rope with circular cross section, but it can deviate from this ideal concept. FD magnitude is explained with cumulative effect of diffusion of CRs through the turbulent sheath region [3, 11]. FD is also energy dependent, where amplitude of decrease is typically around several percent. Higher-rigidity CRs only weakly interact with magnetic disturbances, so no significant change of the flux can be expected for CRs with rigidity of several dozen GV [9]. In order to detect FD at any location, larger statistics are needed for CRs of lower energy. CRs also interact with geomagnetic field which imposes the minimal rigidity CRs must have in order to reach Earth's surface. This geomagnetic cut-off rigidity depends on geomagnetic latitude. It is smaller at the poles and increases with latitude, with some exceptions due to deviation of Earth's magnetic field from the magnetic dipole model (i.e., South Atlantic anomaly [4]).

Primary CRs arriving at Earth interact with atoms and molecules in Earth's atmosphere. CRs with energy above 300–400 MeV/nucleon generate showers of secondary particles. These secondary CRs consist of electrons and photons (electromagnetic component) and harder, in terms of energy, nuclear component of the cascade. Nuclear component, at the bottom of the atmosphere, is composed mainly of muons, protons, neutrons and neutrinos. Secondary CRs can be observed with detectors in the atmosphere (balloon probes), on the ground or even underground. High-energy muons can penetrate deep underground and can be an important component of the background in experiments requiring high sensitivity (dark matter search, proton decay, etc.).

There is a well-known correlation between parameters of solar wind plasma and CR flux, and the goal of this paper is to extend the study of FDs, specifically its magnitude and time evolution, to wider range of parameters of the heliosphere measured routinely with satellites. We concentrate our study on previously scarcely used parameters of the solar wind, particularly flux of

charged particles of different energies. These particles are the source of inhomogeneity in the IMF, so the goal is to try and find distinguishing characteristics of FDs, like magnitude of decrease and FD profile that can be related to the satellite proton flux data, and examine their potential correlation with other space weather parameters. This additional information can be useful in finding explicit connection between parameters of solar wind and CR flux and can lead to better understanding of these complex processes.

2 CR data

In order to provide higher count rate, detector on Earth has to be omnidirectional and to detect integral flux over different range of energies. For the last seventy years secondary CRs are measured using standard ground-based neutron monitors (NMs) [6]. There is a worldwide network of NMs (<http://www01.nmdb.eu/>) that measures flux of secondary CRs originated from primary CRs with rigidity range approximately between 1 GV and 20 GV. Every node of the worldwide network of ground stations has its unique cut-off rigidity depending on its geomagnetic coordinates and height. The other type of widely used ground-based CR detectors are muon monitors. Muon monitors are sensitive to primary CRs of higher rigidity and complement NMs measurements [26]. Worldwide network of these muon stations is still rudimentary, but it can provide insight into flux variation of primary CRs with energies higher than CRs detected by NMs. Since both NMs and muon detectors are energy-integrating detectors and use entire atmosphere above it as a moderator, it is not trivial to relate count rate of these detectors to the flux or energy spectrum of primary CRs at the top of the atmosphere. One needs to know the response of a detector to a unit flux of CRs with the given energy, the so-called detector yield function. Yield functions can be calculated either theoretically, using a numerical simulation of the nucleonic cascade caused by energetic cosmic rays in the Earth's atmosphere, e.g., [8], or semi-empirically, for example based on a latitudinal survey [16].

As flux of secondary cosmic rays is also sensitive to varying properties of the atmosphere through which these CRs propagate, it is necessary to conduct flux correction of the measured flux for atmospheric parameters, where atmospheric pressure correction is the most important. In addition to atmospheric pressure, CR muons are sensitive to temperature variations in the atmosphere, starting from the top of the atmosphere all the way to the ground level. There are several procedures for corrections of these effects which are regularly used. Most commonly used are the integral method and the method of effective level of generation, but some novel techniques have also been introduced in recent years [25]. Correction for these atmospheric parameters is necessary in order to increase detector sensitivity to

Table 1 Properties of primary CR flux related to muons detected at Belgrade CR station

Detector	Muon flux 1/(m ² s)	$E_{0.05}$ (GeV)	E_{med} (GeV)	$E_{0.95}$ (GeV)	Cut-off rigidity (GV)
GLL	137(6)	11	59(2)	915	5.3
UL	45(2)	31	137(5)	1811	12

variations of primary CRs flux and more precisely study the influence of solar modulation on galactic CRs.

Belgrade CR station started collecting data with the current experimental set-up in 2009. The station consists of two separate detector units: one placed on ground level (GLL) and the other in shallow underground (UL), both utilising the same experimental set-up. Such configuration provides opportunity to monitor muon fluxes in two different energy ranges with all other external parameters (such as atmospheric parameters, geomagnetic location and experimental set-up) being the same. Underground part of the station detects muons originated from primary CRs with higher energy because of the layer of soil overburden (13 m of loess) which absorbs lower-energy muons. Details of the detector systems at the Belgrade CRs station as well as calculated response functions are presented in [29]. The station is situated at the Laboratory for Nuclear Physics at the Institute of Physics Belgrade, Serbia. The altitude of the station is 78 m above sea level. Its geographic coordinates are: 44°51' N and 20°23' E, with geomagnetic latitude of 39°32' N. Sensitivity of Belgrade CR detectors to galactic CRs is given in Table 1, where primary CRs with the energy below $E_{0.05}$ (and above $E_{0.95}$) contribute with 5% to the count rate of the corresponding detector, and E_{med} is median energy based on simulation. In preparation for the analysis, detected muon count rates are corrected for efficiency, as well as for barometric and atmospheric temperature effects. Temperature effect correction is done using integral method [24].

3 Satellite data

In recent years, satellites provide new direct measurements of primary CRs flux in the heliosphere and the geomagnetic field. Also, detectors mounted on spacecraft allow us to probe even further, as Voyager recently crossed heliospheric boundary and for the first time galactic CRs flux was measured outside the heliosphere. The problem with such measurements is limitation to the size of the detectors, due to constraints of the construction of the satellites. In order to have valid statistics and good resolution, only low-energy particle flux can be measured. These low-energy particles are sensitive to geomagnetic field, which can introduce additional perturbation. Also, measurements of low-energy CRs can be masked by the increased flux of low-energy solar energetic particles (SEPs) in the MeV energy range. FDs detected by ground-based detectors are measured in energy range several orders of

magnitude higher than the energy range available to satellites measurements. (NMs detect flux that originate from ~ 10 GeV, single muon detectors higher than that up to ~ 100 GeV, while solar weather satellite measurements range up to several 100 MeV.) SEP occurrence is sporadic and depends on which part of the solar cycle we are in, so long-term studies with stable data quality are necessary if we are to study solar modulation of CRs. Such long-term measurements have been performed with various spacecrafts during the last four decades. Data measured on different interplanetary locations are then used for modelling of the heliosphere, which is important for understanding and forecasting space weather. This is a relatively new and dynamic field that is still expanding. More in situ measurements that can be catalogued [17] and compared with data from ground based stations will improve our understanding of near space environment.

In this paper, we use proton data from ERNE (Energetic and Relativistic Nuclei and Electron experiment) detector at the SOHO (Solar and Heliospheric Observatory) (https://omniweb.gsfc.nasa.gov/ftpbrowser/flux_spectr_m.html), which has been performing measurements in Lagrangian point L1 for the last quarter of a century described in [13] and references therein. Experiments that collect in situ particles data are ERNE and COSTEP (Comprehensive SupraThermal and Energetic Particle analyser), where data are combined to meet requirements of the mission. ERNE detector provides proton flux data in relatively large energy range (1.6 to 131 MeV) separated in several energy channels (1.3–1.6, 1.6–2.0, 2.0–2.5, 2.5–3.2, 3.2–4.0, 4.0–5.0, 5.0–6.4, 6.4–8.0, 8.0–10, 10–13, 13–16, 16–20, 20–25, 25–32, 32–40, 40–50, 50–64, 64–80, 80–100, 100–130 MeV). Measurements are taken with two different detectors: LED (low-energy detector) covers lower-energy and HED (high-energy detector) which covers higher-energy channels [28]. Satellites, including SOHO, also measure in situ parameters of the space environment and gather data about magnetic field, solar wind and concentration and flux of various types of particles on the location. Satellite data relevant to heliospheric studies are, among other places, available at GSFC/Space Physics Data Facility, in the form of low- and high-resolution OMNI data (https://spdf.gsfc.nasa.gov/pub/data/omni/low_res_omni/). In this study, we used the low-resolution OMNI data that contain hourly data for the solar wind magnetic field and plasma parameters, energetic proton fluxes, and geomagnetic and solar activity indices for different regions in proximity to Earth [12].

4 Four prominent FD events during rising phase of solar cycle 24

Previous (24th) solar cycle started in December 2008 and ended in November 2019 (as available from Sunspot Index and Long-term Solar Observations database <http://www.sidc.be/silso/node/167>). It had an unusually weak maximum, with smoothed maximum international sunspot number of 116. For comparison, in cycles 22 and 23 this number was 214 and 180, respectively (as available from Sunspot Index and Long-term Solar Observations database <http://sidc.be/silso/home>). Same period was also characterised by smaller number of FDs, especially ones with larger amplitudes.

There were fifteen strong FDs (with magnitude of decrease larger than 5% for particles with 10 GV rigidity) recorded in the rising phase of solar cycle 24, however in this study we will limit our analysis to four events detected by the Belgrade Cosmic Ray Station (<http://www.cosmic.ipb.ac.rs/>). Other prominent FDs that occurred in this period have not being detected by either GLL or UL detector due to discontinuity of operation, so they have been omitted from this study. All four events followed ejections from an active region on the Sun, accompanied by a solar flare with interplanetary shock wave and sudden storm commencing (SSC), and disturbance in the geomagnetic field. All of these FDs were seen by the NM detector network as well.

First significant FD of solar cycle 24 was recorded on 18 February 2011 and has been caused by a CME heading directly towards Earth [20]. It has been detected by most ground stations around the world. Its morphology is influenced by the interaction of two CMEs, first slower and the second faster (with respective speeds of 390 km/s and 1020 km/s), that occurred a day apart [27]. Geomagnetic activity has been relatively weak due to orientation of the magnetic field of the ejecta [21].

Second event was observed on 7 March 2012. It included an X-class flare (X5.4), that occurred in NOAA AR 11429 with an intense halo CME, followed by several smaller flares and another partial CME. It caused one of the strongest FDs of the last solar cycle. Observed solar activity was also related to the intense geomagnetic storm that followed [15].

A strong SF (X1.6) was detected by several spacecrafts during 10 September 2014, originating from active region NOAA AR 2158. Based on the SOHO coronagraph images, this flare was associated with a CME that was aimed towards Earth, where it arrived on September 12. This activity resulted in a major geomagnetic storm, one of the strongest in 2014.

In the second half of June 2015, solar activity was very intense, since a number of CMEs and flares were produced from the powerful AR 12371, which dominated solar activity during that period [23]. The impact of these CMEs on the Earth's magnetosphere resulted in a moderate to severe G4-class geomagnetic storm that occurred on the summer solstice. The result was a very interesting and unusual modulation galactic CRs flux, which appeared as a series of FDs.

For the study of FD events and their relationship with IMF and geomagnetic disturbances, researchers from IZMIRAN (Pushkov Institute of Terrestrial Magnetism, Ionosphere and Radio Wave Propagation, Russian Academy of Sciences) created an FD database (<http://spaceweather.izmiran.ru/eng/dbs.html>) which contains various FD parameters, as well as their relationship with heliospheric and geomagnetic parameters covering several solar cycles [1]. Properties of the four selected FDs, taken from the IZMIRAN database, are given in Table 2.

5 Data analysis

In order to establish the usability of SOHO SEP flux data in the study of CR variations, we will first analyse how muon count rate time series compare with some of the IMF parameters more commonly used in the analysis of solar activity-induced CR variations. To this end, we compare hourly muon count rates (measured by Belgrade muon station and corrected for atmospheric effects) with time series for selected parameters from OMNI database. To give more weight to this qualitative analysis, we concentrate only on periods of extreme solar activity, in particular periods of the occurrence of four FD events described in Sect. 4. We then examine the relationship between measured muon count rates and the SOHO/ERNE SEP flux data and analyse any discerning features in comparison with the ones observed in OMNI data time series. The period selected for this analysis is approximately one solar rotation of 27 days. All probes at L1 are about an hour upstream of the magnetosphere so all their data are interspersed with data from spacecraft close to Earth (e.g., IMP 8). In order to compute hourly averages “at Earth” this time shift has to be taken into account (https://omniweb.gsfc.nasa.gov/html/ow_data.html).

Next, we investigate the short-term correlation between SEP flux and muon count rate data during time periods of four selected FDs. Muon time series for this procedure were selected for times where average muon flux was significantly lower than the background level. Background level was determined from moving averages for hourly count rates 10 days before the event. We then perform correlative analysis between SOHO SEP flux data and muon count rates for a period of one year (from 01.06.2010 to 31.05.2011), in order to establish the long-term relationship. For further insight, we also look into the correlation between these variables during the periods of reduced geomagnetic activity (International Quiet Days) and increased geomagnetic activity (International Disturbed Days).

Finally, we look in greater detail into SOHO SEP flux time series. In order to perform more quantitative analysis, time-integrated flux is calculated for SEP data for different SOHO energy bins and for the duration of selected FD events. In order to provide a parameter for characterisation for different FD events, calculated integral flux is plotted as a function of proton energy and

Table 2 Selected FD and interplanetary disturbance parameters (taken from IZMIRAN database)

Parameter	FD 1	FD 2	FD 3	FD 4	Parameter comment
Date of FD	18.2.2011.	8.3.2012.	12.9.2014.	22.6.2015.	
Date of parent solar event	15.2.2011.	7.3.2012.	10.9.2014.	21.6.2015.	
AR number	1158	11429	2158	12371	NOAA active region
V_{meanC}	584	1198	906	1040	The average ICME velocity between the Sun and the Earth, calculated using the time of the beginning of the associated CME observations (in km/s)
V_{max}	691	737	730	742	Maximal hourly solar wind speed in the event (in km/s)
B_{max}	31	23.1	31.7	37.7	Maximal hourly IMF strength in the event (in nT)
B_{zmin}	- 5.5	- 16.1	- 9.5	- 26.3	Minimal hourly Bz component of the IMF in the event (in nT)
R_{bulk}	72.25	146.2	131.35	171.25	An estimate of the maximum proton rigidity (in GV) that can be reflected by the total magnetic field, integrated from the event onset to the FD minimum
Magn	5.2	11.7	8.5	8.4	FD magnitude for particles with 10 GV rigidity, calculated as maximal range CRs density variations in the event, obtained by GSM from NM network data (in %)
MagnM	4.7	13.1	6.9	10.4	FD magnitude for particles with 10 GV rigidity, corrected on magnetospheric effect with Dst-index (in %)
TminM	7	20	9	11	Time from the FD onset to minimum, calculated from the data corrected for magnetospheric effect
Kp_{max}	5	8	6.33	8.33	Maximal Kp-index in the event
Ap_{max}	48	207	94	236	Maximal 3-hour Ap-index in the event
Dst_{min}	- 30	- 143	- 75	- 204	Minimal Dst-index in the event (in nT)
Flare class	X2.2	X5.4	X1.6	M2.6	Associated X-ray flare data
SSN	85	97	126	56	Number of sunspot at the FD onset day

fitted with a power function. Dependence of magnitude for selected FDs on the exponents obtained from fitted distributions is then analysed.

6 Results and discussion

Comparison between time series of selected IMF parameters from OMNI database and muon count rate time

series during the periods of four selected FD events is shown in Fig. 1. Observed anticorrelation between muon count rates and proton flux and temperature, as well as with the overall IMF magnetic field and detected plasma speed, is in agreement with previously stated evidence in the literature [30].

Similar comparison between muon count rate time series and selected channels of SOHO/ERNE proton flux data for the same time intervals is shown in Fig.

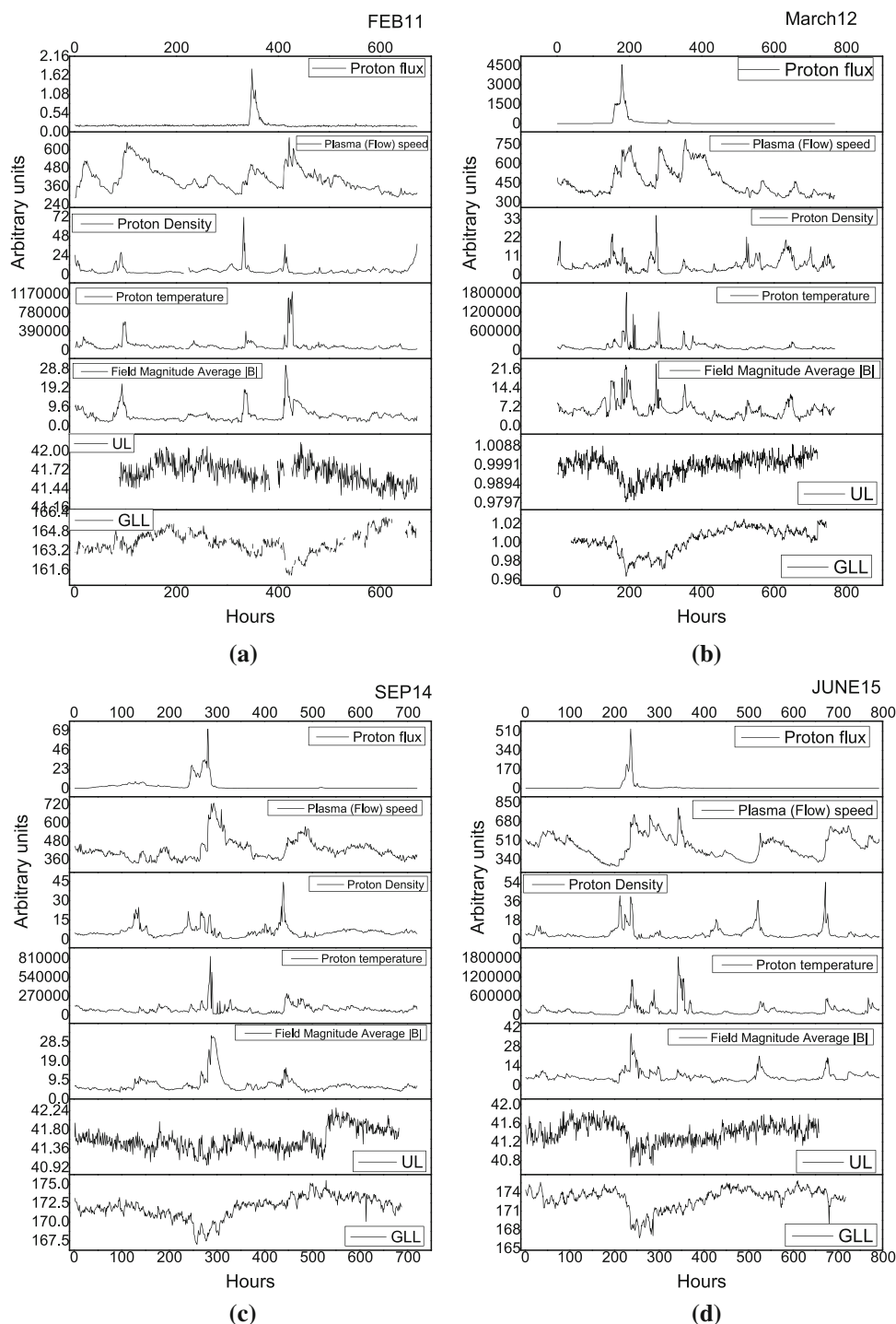


Fig. 1 Time series for particle and plasma parameters (taken from OMNI database) in the time interval of approximately one month around the occurrence of four selected FD events: **a** February 2011 (start of time interval on 1 February), **b** March 2012 (start of time interval on 1 March), **c** September 2014 (start of time interval on 1 September) and **d** June 2015 (start of time interval on 13 June)

2. For the sake of clarity, we chose three energy channels (1.6–2 MeV, 16–20 MeV, 100–130 MeV), approximately one order of magnitude apart, where first channel is measured with LED and the other two with HED detector on SOHO/ERNE instrument. In case of the

February 2011 event, there is an observable time lag (≈ 55 h) between the increase of measured proton flux at low-energy channels (1.6–2 MeV and 16–20 MeV energy channels) and the beginning of FD recorded at ground station. This time lag is also present between

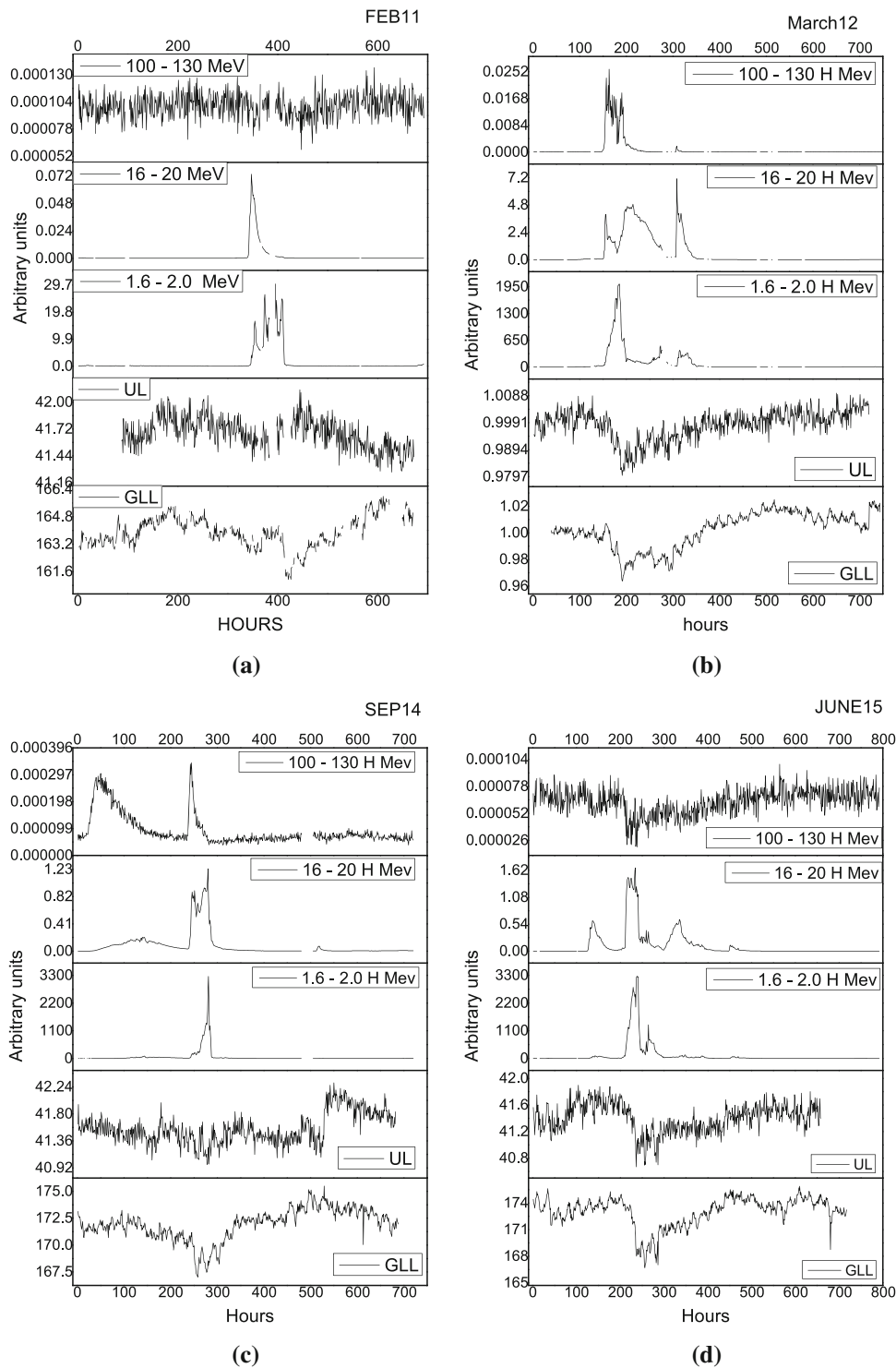


Fig. 2 Hourly time series for different proton channels from SOHO/ERNE and two muon detectors at Belgrade CR station, in the time interval of approximately one month around the occurrence of four selected FD events: **a)**February (start of time interval on 1 February) 2011, **b** March 2012 (start of time interval on 1 March), **c** September 2014 (start of time interval on 1 September) and **d** June 2015 (start of time interval on 13 June)

OMNI proton flux data and ground station measurements for this FD alone. FD is a complex modulation of CR flux that depends on a lot of parameters, like magnitude of magnetic field and its components,

speed of solar wind and CMEs (with CME average speed ≈ 490 km/s), most of which are listed in Table 2. Parameter values for all four ICMEs are mostly comparable, but one difference that stands out is the discrep-

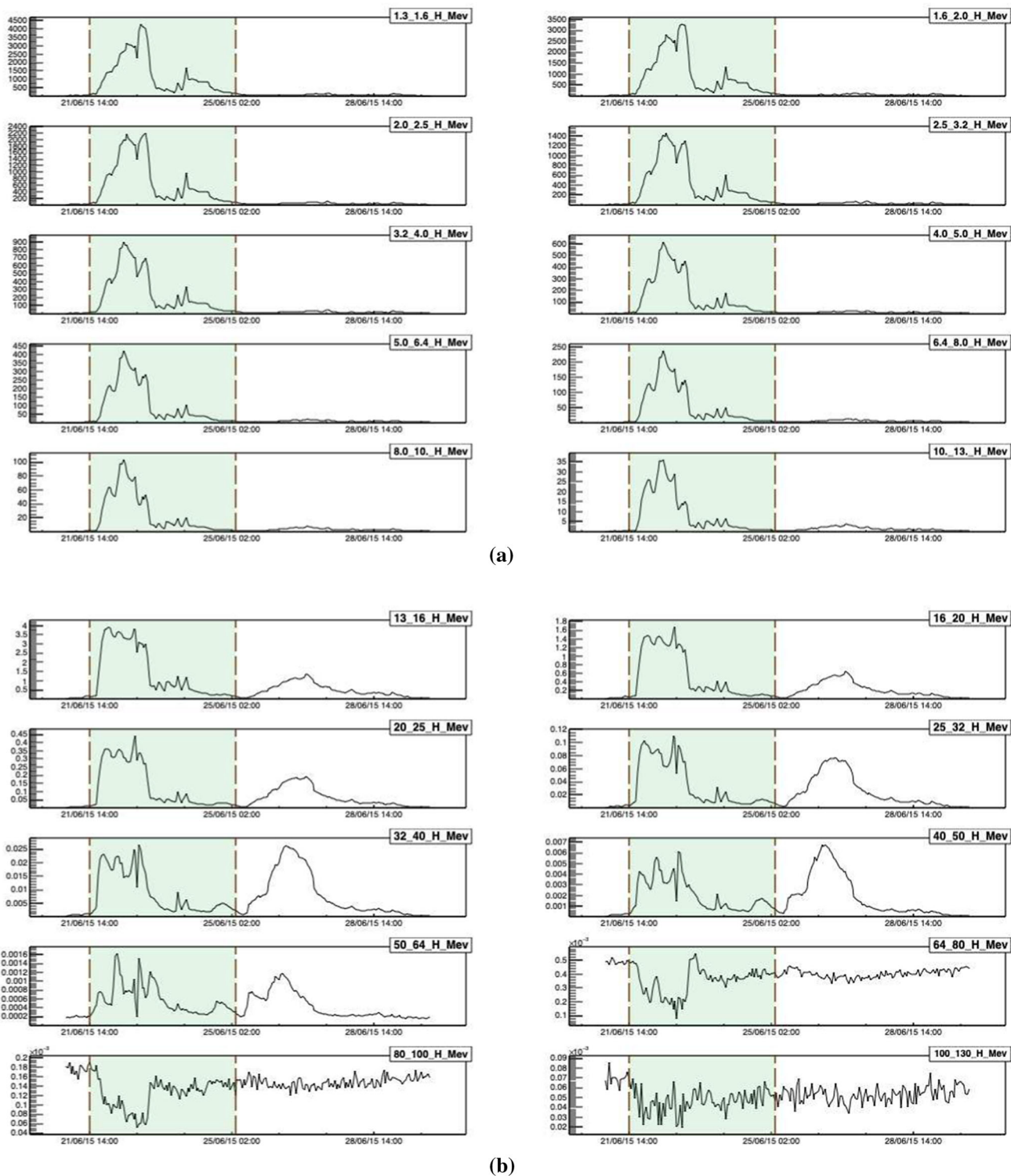


Fig. 3 Differential SEP fluxes during extreme solar event in June 2015, measured by SOHO/ERNE proton channels. Vertical dashed lines indicate the time for the start and the end of interval used to calculate the integral flux

ancy in average CME velocity (584 km/s from Table 2.) for the FD of February 2011, which can possibly explain the observed time lag for this particular FD.

Based on the observed time lag and other coincident features, we can establish good agreement between

SOHO low-energy channel data and OMNI data time series. As for high-energy channels, SEP time series in 100–130 MeV energy range for February 2011 and June 2015 events appear to correlate with muon count rate measurements on the ground. One possible explanation

Table 3 Statistical correlation between Belgrade CR station and SOHO/ERNE measurements during the periods of four selected FD events

FD	Energy range (MeV)	GLL		UL	
		Pearson coefficient	<i>P</i> value	Pearson coefficient	<i>P</i> value
FEB 11	1.6–2.0 H	– 0.10877	0.01	– 0.05285	0.2
	16–20 H	– 0.18384	2×10^{-5}	– 0.10732	0.01
	100–130 H	0.24204	$< 10^{-6}$	– 0.13212	0.02
MAR 12	1.6–2.0 H	– 0.48477	$< 10^{-6}$	– 0.43994	$< 10^{-6}$
	16–20 H	– 0.72033	$< 10^{-6}$	– 0.68221	$< 10^{-6}$
	100–130 H	– 0.29172	$< 10^{-6}$	– 0.27822	$< 10^{-6}$
SEP 14	1.6–2.0 H	– 0.2839	$< 10^{-6}$	– 0.48052	$< 10^{-6}$
	16–20 H	– 0.37814	$< 10^{-6}$	– 0.63735	$< 10^{-6}$
	100–130 H	– 0.04951	0.007	– 0.10466	0.2
JUN 15	1.6–2.0 H	– 0.3921	$< 10^{-6}$	– 0.27531	$< 10^{-6}$
	16–20 H	– 0.31229	$< 10^{-6}$	– 0.17113	$< 10^{-6}$
	100–130 H	0.48588	$< 10^{-6}$	0.39296	$< 10^{-6}$

could be that in addition to SEP these energy channels are also populated by very low-energy CRs.

We can further investigate this assumption by looking more closely into SOHO SEP flux time series for one of the two weaker FD events. We have selected June 2015 event, as time series for higher-energy channels appear to be slightly more informative. Figure 3 shows proton flux series for all energy channels measured by SOHO/ERNE detector. From these plots, it is apparent that proton fluxes for energies larger than 64 MeV exhibit different dynamic relative to fluxes of lower energies, and seem to be in anticorrelation with them. This indeed supports the assumption these channels are populated by low-energy CR.

Another way we can illustrate this observation more quantitatively is by performing relative analysis. Firstly, we will look into short-term correlations between proton flux and muon count rate time series during four selected FD events. Correlation between respective time series was found using Pearson correlation coefficient. For significance two-tailed test is used. Correlation coefficient and its significance level between ground station and in situ measurement from SOHO/ERNE instrument is given in Table 3.

Due to higher energy of the primary CRs detected in UL, the correlation between SEPs and measured flux in UL is smaller than correlation between SEPs and flux measured in GLL. The greatest anticorrelation (i.e., between GLL and UL data and 16–20 MeV protons ≈ -0.7) is observed for the strongest ICME (and corresponding FD) of March 2012, and this anticorrelation is observed in all energy channels. However, for lower-intensity events of June 2015 and February 2011, correlations between detected CR flux in GLL and highest energy channel (100–130 MeV) are mostly positive. These observations further confirm the assumption about high-energy channels being populated by low-energy CR, which is especially evident in case of low-intensity FD events.

Table 4 Pearson correlation coefficient for the correlation between CR flux detected at Belgrade CR station (GLL detector) and flux of protons of different energies detected with SOHO/ERNE detector, for the period of one year (from June 2010 May 2011)

	GLL	
	Pearson coefficient	<i>P</i> value
H 1.3–1.6 MeV	– 0.02	0.13
H 1.6–2.0 MeV	– 0.02	0.16
H 2.0–2.5 MeV	– 0.02	0.20
H 2.5–3.2 MeV	– 0.01	0.27
H 3.2–4.0 MeV	– 0.01	0.36
H 4.0–5.0 MeV	– 0.01	0.57
H 5.0–6.4 MeV	< 0.01	0.75
H 6.4–8.0 MeV	< 0.01	1.00
H 8.0–10 MeV	< 0.01	0.78
H 10–13 MeV	0.01	0.57
H 13–16 MeV	0.01	0.41
H 16–20 MeV	0.01	0.31
H 20–25 MeV	0.01	0.26
H 25–32 MeV	0.01	0.24
H 32–40 MeV	0.01	0.27
H 40–50 MeV	0.01	0.46
H 50–64 MeV	< 0.01	0.80
H 64–80 MeV	0.05	< 0.01
H 80–100 MeV	0.12	< 0.01
H 100–130 MeV	0.07	< 0.01

Similar results, with even greater correlation between the entire time profile for flux measured with NMs and solar wind speed and magnetic field during ICME, are reported for stronger FDs during solar cycle 23 [5].

Next, we will analyse long-term correlations between SOHO proton flux and measured muon count rates. Pearson coefficients for this correlation over a period of one year (from June 2010 May 2011), when activity of the Sun was low at the commencement of the 11-years cycle, are presented in Table 4. Here we see very

Table 5 Pearson correlation coefficient for the correlation between CR flux detected at Belgrade CR station (GLL detector) and flux of protons of different energies detected with SOHO/ERNE detector, during international geomagnetically quiet and disturbed days for the period of one year (from June 2010 May 2011)

	GLL Quiet days		GLL Disturbed days	
	Pearson coefficient	<i>P</i> value	Pearson coefficient	<i>P</i> value
H 1.3–1.6 MeV	0.01	0.61	– 0.05	0.13
H 1.6–2.0 MeV	0.01	0.80	– 0.05	0.14
H 2.0–2.5 MeV	0.02	0.30	– 0.05	0.13
H 2.5–3.2 MeV	0.03	0.11	– 0.05	0.12
H 3.2–4.0 MeV	0.04	0.04	– 0.05	0.10
H 4.0–5.0 MeV	0.05	0.02	– 0.06	0.08
H 5.0–6.4 MeV	0.05	0.01	– 0.06	0.07
H 6.4–8.0 MeV	0.06	0.01	– 0.06	0.06
H 8.0–10 MeV	0.06	0.01	– 0.06	0.06
H 10–13 MeV	0.06	0.01	– 0.06	0.07
H 13–16 MeV	0.06	< 0.01	– 0.06	0.08
H 16–20 MeV	0.06	< 0.01	– 0.05	0.10
H 20–25 MeV	0.06	< 0.01	– 0.05	0.12
H 25–32 MeV	0.06	< 0.01	– 0.05	0.15
H 32–40 MeV	0.06	< 0.01	– 0.04	0.20
H 40–50 MeV	0.06	< 0.01	– 0.02	0.57
H 50–64 MeV	0.07	< 0.01	0.07	0.03
H 64–80 MeV	0.25	< 0.01	0.08	0.02
H 80–100 MeV	0.38	< 0.01	0.11	< 0.01
H 100–130 MeV	0.15	< 0.01	0.09	0.01

little correlation between CR and proton fluxes in all but the highest energy channels (above 64 MeV).

Table 5 shows the same correlation analysis if only data for 10 geomagnetically quietest or 5 geomagnetically most disturbed days of each month (http://isgi.unistra.fr/events_qdays.php) are used. The fact that we observe a significant increase of positive correlation coefficients in the case of geomagnetically quiet days, further corroborates the assumption about the mixed nature of particles that populate higher-energy channels. Consequentially, care should be taken how data from these channels are treated in analysis.

To provide further quantitative support for the use of SOHO SEP flux measurements in the analysis of FD events, we will calculate integral proton flux in all energy channels for the four selected FDs. Integration intervals are selected to include the period of increased proton flux that corresponds to a particular FD, but not to extend the interval to include potential follow-up structures that cannot be associated with the event. One such selection for all energy channels, for June 2015 event, is indicated by dashed lines in Fig. 3. In Fig. 4, we show thusly calculated integral flux as a function of particle energy (where lower boundary values from SOHO SEP energy bins are taken), using both linear and log scale for clarity.

One feature that can be noticed from plots in Fig. 4 is that integral flux drops off is more steeply in February 2011 than for others studied FDs, where a change in the trend between high-energy and low-energy range can be observed. FD that occurred in March 2012 was the longest and the most intensive of the four. Steepness of

the integral flux for this FD shows relatively more populated proton channels with higher energies compared to weaker FD. This is in agreement with strongest modulation of CRs flux during this FD. There is a discontinuity in the integral flux between proton energy channel 13–16 MeV and 16–20 MeV due to different acquisition method from different instruments, and possibly because of degradation of the detectors on board the spacecraft [13] and saturation of the instrument due to high intensity of solar protons [18].

One simple way to characterise relative abundance of SEP particles of different energies for a given event would be to fit described integral flux distribution with a power function, where (in a simple approximation) larger exponent would indicate greater relative abundance of lower-energy particles, while smaller exponent would point to greater relative abundance of higher-energy particles. Distributions were fitted with a power function given by the formula $I(E) = a * E^b$ (where I is the integral flux and E is particle energy), resulting fits represented by red lines in Fig. 4, while values for the exponents of power function fits are represented in Table 6.

If SOHO protons flux measurements are to be proved useful in the analysis of FD events, SEP flux characteristics should correlate with some of the FD and interplanetary disturbance parameters. To test this, we have analysed dependence of different FD parameters on the exponent of the integral proton flux power distribution (labelled b in the formula in previous paragraph). We have found some correlation for most tested parameters, most striking being one between the magnitude

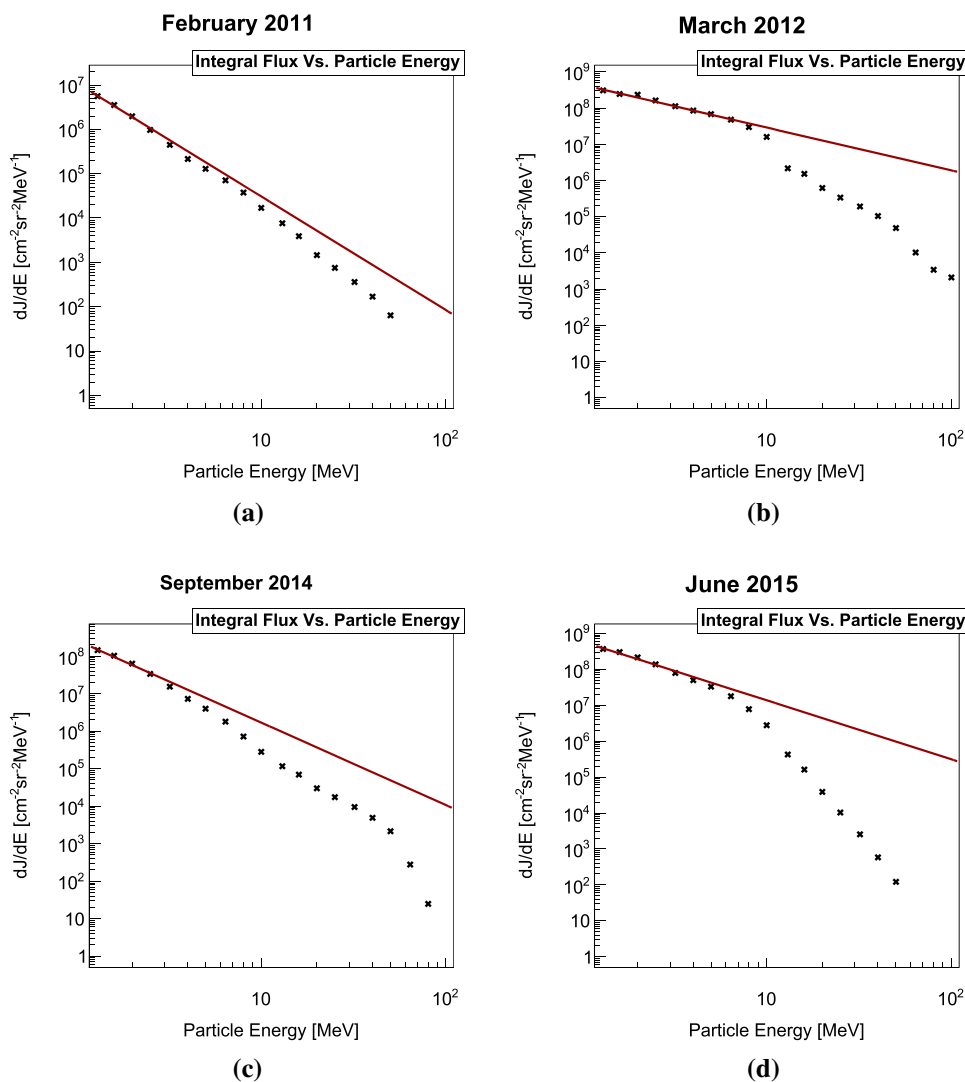


Fig. 4 Time-integrated flux of differential SEP fluxes during the four selected FD events: **a** February 2011, **b** March 2012, **c** September 2014 and **d** June 2015, in linear and logarithmic scale. Power function fits are represented by red lines

Table 6 Exponent values of power function fits of integral proton flux distributions

FD	Power function exponent values
FEB 2011	- 2.56
MAR 2012	- 1.18
SEP 2014	- 2.20
JUN 2015	- 1.64

of FD for particles with 10 GV rigidity (corrected for magnetospheric effect) and the exponent of the integral flux. This dependence (strictly for illustrative purposes fitted with linear fit) is shown in Fig. 5.

Observed strong dependence is potentially a very good indicator that SOHO SEP flux measurements can be a valid source of data to be used in the analysis of

interplanetary disturbances and their interaction with cosmic rays.

7 Conclusions

Analysing strong aperiodic variations of cosmic ray flux, such as Forbush decreases, allows us to study violent processes that occur on the Sun, and corresponding perturbations in the heliosphere, using Earth-based detectors. In addition to cosmic ray flux and magnetic field data commonly used to study such events, we have extended analysis to include proton flux measurements, obtained using spacecraft mounted detectors. Based on the analysis of four selected Forbush decrease events, we have found SOHO/ERNE proton flux measurements to be consistent with solar plasma parameters, as well as with observations by the ground-based muon detectors.

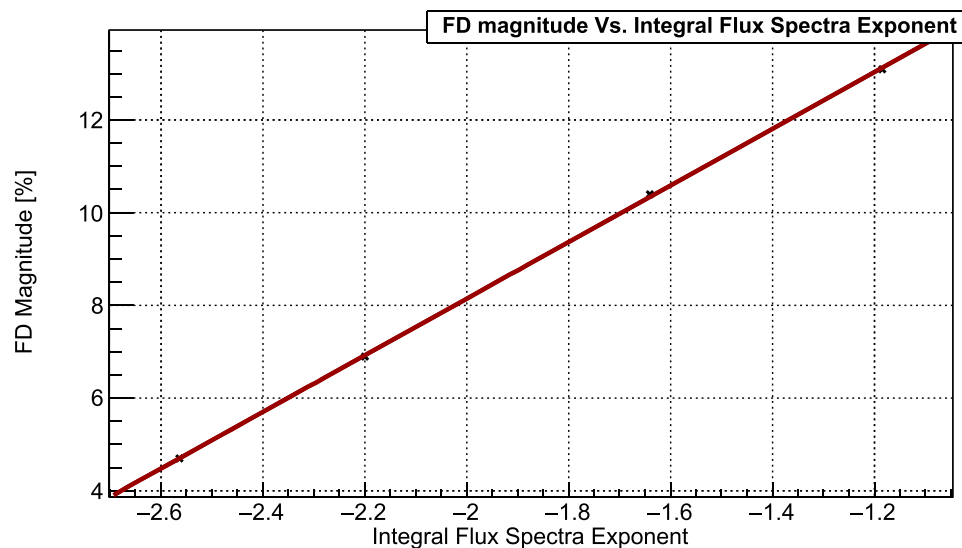


Fig. 5 Dependence of FD magnitude, corrected for magnetospheric effect with Dst-index for particles with 10 GV rigidity, on the power exponent of the integral SEP flux, four selected FD events: **a** February 2011, **b** March 2012, **c** September 2014 and **d** June 2015. Linear fit (for illustrative purposes) is indicated by the red line

We have concluded that during Forbush decrease events lower-proton-energy channels are dominated by SEP particles, while in higher-energy channels there is a contribution of low-energy cosmic rays, especially apparent during less intense events. We have found a clear correlation between Forbush decrease magnitude (corrected for magnetospheric effect with Dst-index for particles with 10 GV rigidity) and power exponent of the integral flux of SOHO/ERNE measurements. This result gives grounds to further pursue the analysis of heliospheric proton flux data, as it may yield additional valuable information. Such information can potentially help us to classify and study in greater detail the dynamics of interaction of cosmic rays in the heliosphere.

Acknowledgements The authors acknowledge funding provided by the Institute of Physics Belgrade, through the grant by the Ministry of Education, Science and Technological Development of the Republic of Serbia. We also acknowledge use of NASA/GSFC's Space Physics Data Facility's OMNIWeb (or CDAWeb or ftp) service and OMNI data as well as team behind SOHO, which is a project of international collaboration between ESA and NASA. We would also like to thank the referees for constructive and useful advice.

Data Availability Statement "This manuscript has data included as electronic supplementary material".

References

1. A.A. Abunin, M.A. Abunina, A.V. Belov, S.P. Gaidash, E.A. Eroshenko, I.I. Pryamushkina, L.A. Trefilova, E.I. Gamza, *J. Phys. Conf. Ser.* **1181**, 012062 (2019). <https://doi.org/10.1088/1742-6596/1181/1/012062>
2. K.P. Arunbabu, H.M. Antia, S.R. Dugad, S.K. Gupta, Y. Hayashi, S. Kawakami, P.K. Mohanty, T. Nonaka, A. Oshima, P. Subramanian, *A and A* **555**, A139 (2013). <https://doi.org/10.1051/0004-6361/201220830>
3. K.P. Arunbabu, H.M. Antia, S.R. Dugad, S.K. Gupta, Y. Hayashi, S. Kawakami, P.K. Mohanty, A. Oshima, P. Subramanian, *A and A* **580**, A41 (2015). <https://doi.org/10.1051/0004-6361/201425115>
4. C.R.A. Augusto, V. Kopenkin, C.E. Navia, K.H. Tsui, H. Shigueoka, A.C. Fauth, E. Kemp, E.J.T. Manganote, M.A. Leigui de Oliveira, P. Miranda, R. Ticona, A. Velarde, *ApJ* **759**, 143 (2012). <https://doi.org/10.1088/0004-637X/759/2/143>
5. A. Bhaskar, G. Vichare, K.P. Arunbabu et al., *Astrophys. Space Sci.* **361**, 242 (2016). <https://doi.org/10.1007/s10509-016-2827-8>
6. V. Belov, *SpaceSci. Rev.* **93**(1), 79–105 (2000). <https://doi.org/10.1023/A:1026584109817>
7. H.V. Cane, *Space Sci. Rev.* **93**, 55–77 (2000). <https://doi.org/10.1023/A:1026532125747>
8. J.M. Clem, L.I. Dorman, *Space Sci. Rev.* **93**, 335–359 (2000). <https://doi.org/10.1023/A:1026508915269>
9. E.S. Comedi, A.S. Elias, B.S. Zossi, S. Bruno, *JASTP* **211**, 105475 (2020). <https://doi.org/10.1016/j.jastp.2020.105475>
10. M. Duldig, *Science* **314**(5798), 429–430 (2006). <https://doi.org/10.1126/science.1134046>
11. M. Dumbović, B. Vršnak, J. Guo et al., *Sol. Phys.* **295**, 104 (2020). <https://doi.org/10.1007/s11207-020-01671-7>
12. J.H. King, N.E. Papitashvili, *J. Geophys. Res.* **110**, A02104 (2005). <https://doi.org/10.1029/2004JA010649>
13. P. Kühl, B. Heber, R. Gómez-Herrero, O. Malandraki, A. Posner, H. Sierks, *J. Space Weather Space Clim.* (2020). <https://doi.org/10.1051/swsc/2020056>
14. S.Y. Lee, *Accelerator Physics*, 2nd edn. (World Scientific, Singapore, 2004)

15. M. Livada, H. Mavromichalaki, C. Plainaki, *Astrophys. Space Sci.* **363**, 8 (2018). <https://doi.org/10.1007/s10509-017-3230-9>
16. R.A. Caballero-Lopez, H. Moraal, *JGR Space Phys.* **117**, A12 (2012). <https://doi.org/10.1029/2012JA017794>
17. R. Miteva, S.W. Samwel, M.V. Costa-Duarte, *JASTP* (2018). <https://doi.org/10.1016/j.jastp.2017.05.003>
18. R. Miteva, D. Danov, in *Proceedings of the tenth Workshop 'Solar Influences on the Magnetosphere, Ionosphere and Atmosphere', Primorsko, Bulgaria*, ed. by K. Georgieva, B. Kirov, D. Danov, 2018. <https://doi.org/10.31401/WS.2018.proc>
19. H. Moraal, *Space Sci. Rev.* **176**, 299–319 (2013). <https://doi.org/10.1007/s11214-011-9819-3>
20. S.Y. Oh, Y. Yi, *A Sol. Phys.* **280**, 197–204 (2012). <https://doi.org/10.1007/s11207-012-0053-2>
21. A. Papaioannou, A. Belov, H. Mavromichalaki et al., *J. Phys. Conf. Ser.* **409**, 012202 (2013). <https://doi.org/10.1088/1742-6596/409/1/012202>
22. A. Papaioannou, M. Belov, E. Abunina, A. Eroshenko, A. Abunin, S. Anastasiadis, Patsourakos, H. Mavromichalaki, *ApJ* **890**, 101 (2020). <https://doi.org/10.3847/1538-4357/ab6bd1>
23. E. Samara, A. Smponias, I. Lytrosyngounis et al., *Sol. Phys.* **293**, 67 (2018). <https://doi.org/10.1007/s11207-018-1290-9>
24. M. Savić, A. Dragić, N. Veselinović et al., *XXV ECRS 2016 Proceedings—eConf C16-09-04.3*, e-Print: 1701.00164 [physics.ins-det], [arXiv:1701.00164v1](https://arxiv.org/abs/1701.00164)
25. M. Savić, A. Dragić, D. Maletić et al., *Astropart. Phys.* (2019). <https://doi.org/10.1016/j.astropartphys.2019.01.006>
26. M. Savić, N. Veselinović, A. Dragić et al., *ASR* **63**, 4 (2019). <https://doi.org/10.1016/j.asr.2018.09.034>. ISSN 0273-1177
27. M. Temmer, A.M. Veronig, V. Peinhardt, B. Vršnak, *ApJ* **785**, 85 (2014). <https://doi.org/10.1088/0004-637X/785/2/85>
28. J. Torsti, E. Valtonen, M. Lumme et al., *Sol. Phys.* **162**, 505–531 (1995). <https://doi.org/10.1007/BF00733438>
29. N. Veselinović, A. Dragić, M. Savić, D. Maletić, D. Joković, R. Banjanac, V. Udovičić, *NIM A* **875**, 1 (2017). <https://doi.org/10.1016/j.nima.2017.09.008>. ISSN 0168-9002
30. L.-L. Zhao, H. Zhang, *ApJ* **827**, 13 (2016). <https://doi.org/10.3847/0004-637X>

MULTIVARIATE ANALYSIS OF TWO-YEAR RADON CONTINUOUS MONITORING IN GROUND LEVEL LABORATORY IN THE INSTITUTE OF PHYSICS BELGRADE

by

Dimitrije M. MALETIĆ¹, Radomir M. BANJANAC¹, Dejan R. JOKOVIĆ¹, Aleksandar L. DRAGIĆ¹, Nikola B. VESELINOVIĆ¹, Mihailo R. SAVIĆ¹, Zoran R. MIJIĆ¹, Vladimir I. UDOVIČIĆ^{1*}, Svetlana D. ŽIVKOVIĆ-RADETA², and Jelena V. UDOVIČIĆ²

¹ Institute of Physics Belgrade, National Institute of the Republic of Serbia,
University of Belgrade, Belgrade, Serbia

² Faculty of Applied Ecology Futura, Belgrade Metropolitan University, Belgrade, Serbia

Scientific paper

<https://doi.org/10.2298/NTRP2304273M>

Multivariate classification and regression analysis of multiple meteorological variables and indoor radon activity concentration in Ground Level Laboratory in the Institute of Physics Belgrade, was performed and discussed. Meteorological variables used in this analysis were from radon active device, nearby meteorological station and finally from Global Data Assimilation System. Single variate analysis has identified variables with greatest value of Pearson's correlation coefficient with radon activity concentration and also, variables with greatest separation of events with increased radon activity concentration of over 200 Bqm⁻³ and of events with radon level below this value. This initial analysis is showing the expected behavior of radon concentration with meteorological variables, with emphasis on data periods with or without air conditioning and with emphasis on indoor water vapor pressure, which was, in our previous research, identified as important variable in analysis of radon variability. This single variate analysis, including all data, proved that Global Data Assimilation System data could be used as a good enough approximate replacement for meteorological data from nearby meteorological station for multivariate analysis. Variable importance of Boosted Decision Trees with Gradient boosting multivariate analysis method are shown for all three periods and most important variables were discussed. Multivariate regression analysis gave good results, and can be useful to better tune the multivariate analysis methods.

Key words: continuous radon monitoring, multivariate analysis, Global Data Assimilation System, meteorological station

INTRODUCTION

Primarily, radon problem presents a health hazard [1]. The research of the dynamics of radon in various environments, living or working places, is of great importance in terms of protection against ionizing radiation and in designing of measures for its reduction. In the Low-Background Laboratory for Nuclear Physics extensive research on various radon fields has been done in the past, especially radon monitoring in the special designed low-background underground and ground level laboratory, with the aim of investigating the rare nuclear processes [2]. Besides radon monitoring in the laboratory, we work on several research topics regarding radon: using multivariate classification and regression methods, as developed for data analysis

in high-energy physics [3], to study connection of climate variables and variations of radon concentrations, modelling of the indoor radon behaviour and national indoor radon mapping [4], taking interest in similar indoor radon mapping analysis in Montenegro [5], or by research of radon variability in a single dwelling [6], using advanced analysis tools, or performing continuous measurements in multi-store building [7] or laboratory space [8]. Indoor radon variability depends on many variables. Soil content, and building characteristics are very important. In case of researching of indoor radon variability, meteorological effects become the most important ones. With recent experiences with lowering the limits of indoor radon level, both in dwellings and working places, and the demand for decrease of public radon exposure, the need for more detailed knowledge on radon variability is increasing. Besides a possibility for improvement of mitigation

* Corresponding author, e-mail: udovicic@ipb.ac.rs

techniques, we could look into creating online warning pages, like we already have, for example, for UV radiation. These online warning pages, with information on radon concentration variations, could be interesting to people living in dwellings or working spaces with previously known radon problem, or dwellings with radon activity concentration close to 200 Bqm⁻³ limit. These online warnings, could indicate a call for some temporary measures like starting of increased ventilation or reducing exposure. Local radon warning pages could be based on local meteorological station, but for larger regions, meteorological modeled data like Global Data Assimilation System (GDAS) could be used. In this paper we were looking into the possibility of using GDAS data in prediction of indoor radon variability, by jointly looking into GDAS and nearby meteorological station, and compare the results.

DATA PREPARATION AND SELECTION

The radon continuous monitoring in ground level laboratory was performed with active device RadonEye Plus2 with time sampling of one hour. The device recorded variables: Rn-activity, indoor temperature and indoor humidity. The radon the measurement was done from November 2020 to November 2022. After looking into indoor temperature data, we decided to do three analysis, one with using all the data samples (whole period of measurement's), second using only data when air conditioning (AC) was operating, and third sample used for analysis was for periods when air conditioning was OFF (noAC).

Meteorological station located in Institute of Physics Belgrade yard, and maintained by Environmental Physics Laboratory [8], has being recording variables at 5 minute interval, and hourly values are used for this analysis. Variables are named by adding prefix outside; outside-cloudbase, outside-dew point, outside-humidity, outside-temp, outside-pressure and outside-rain.

The US National Centers for Environmental Prediction (NCEP) runs a series of computer analyses and forecasts operationally. One of the operational systems is the GDAS. At National Oceanic and Atmospheric Administration's (NOAA) Air Resources Laboratory (ARL), NCEP model output is used for air quality transport and dispersion modeling. The ARL archives GDAS output which contains basic fields, such as the temperature, pressure and humidity. Those GDAS data are very interesting since they are widely used by weather forecast groups worldwide, and our idea is that if we could use this freely accessed and frequently updated database, we could improve forecasting of some kind of *relative* indoor radon concentrations, and indicate by result of automatic online MVA regression analysis when to expect increased indoor radon concentrations based on meteorological variables.

Because MVA methods are rather robust, and we wanted to see which, if any of GDAS variables are suited for our purpose, we included most of variables in our analysis. The GDAS1 data is available for integer values of latitude and longitude, so, for all variables', each data point was firstly 2-D linearly interpolated using variables' values on four integer latitudes and longitudes, surrounding latitude and longitude of our laboratory. The GDAS1 data is available for every three hours, so linear interpolation of each variable's data point was made in order that we can use hourly data. The GDAS1 variables used in our analysis can be identified as ones with prefix GDAS1; GDAS1-CAPE (convective available potential energy), GDAS1-CINH (convective inhibition), GDAS1-CPP6 (accumulated convective precipitation), GDAS1-CRAI (categorical rain), GDAS1-DSWF (downward short wave radiation flux), GDAS1-HCLD (high cloud cover), GDAS1-LCLD (low cloud cover), GDAS1-LHTF (latent heat net flux at surface), GDAS1-LIB4 (best 4-layer lifted index), GDAS1-LISD (standard lifted index), GDAS1-MCLD (middle cloud cover), GDAS1-PBLH (planetary boundary layer height), GDAS1-PRSS (pressure at surface), GDAS1-RH2M (relative humidity at 2m AGL), GDAS1-SHGT (geopotential height), GDAS1-SHTF (sensible heat net flux at surface), GDAS1-SOLM (volumetric soil moisture content), GDAS1-T02M (temperature at 2m AGL), GDAS1-TCLD (total cloud cover), GDAS1-TMPS (temperature at surface), GDAS1-TPP6 (accumulated precipitation), GDAS1-mofi-e (momentum flux intensity), GDAS1-mofd-e (momentum flux direction). In this analysis using GDAS data, we also could indicate if variables measured by local meteorological station do not differ too much from GDAS modeled and interpolated ones, that GDAS variables could be used in this kind of MVA analysis.

We included previously found interesting variable in radon research [6] and that is water vapor pressure in outdoor and indoor air, as well as the difference of the two. In order to calculate the water vapor pressure in air, we need to calculate the value of the saturation water vapor pressure

$$es(T) = 0.6108 \cdot e^{\frac{17.27 \cdot T}{T + 237.3}} \quad (1)$$

In addition, the slope of the relationship between the saturation water vapor pressure (es [kPa]) and the air temperature T [°C], is given in [9, 10], so including the slope, we get new formula for the saturation water vapor pressure

$$es(T) = \frac{4098 \cdot \left(0.6108 \cdot e^{\frac{17.27 \cdot T}{T + 237.3}} \right)}{(T + 237.3)^2} \quad (2)$$

and since the formula used to calculate the relative humidity is

Figure 1. The Rn activity indoor (a) and vapor pressure difference of outdoor and indoor (b). Note that with much greater outdoor water vapor pressure than indoor, comes influx of radon-free water vapor, and that results in significant decrease of indoor Rn activity

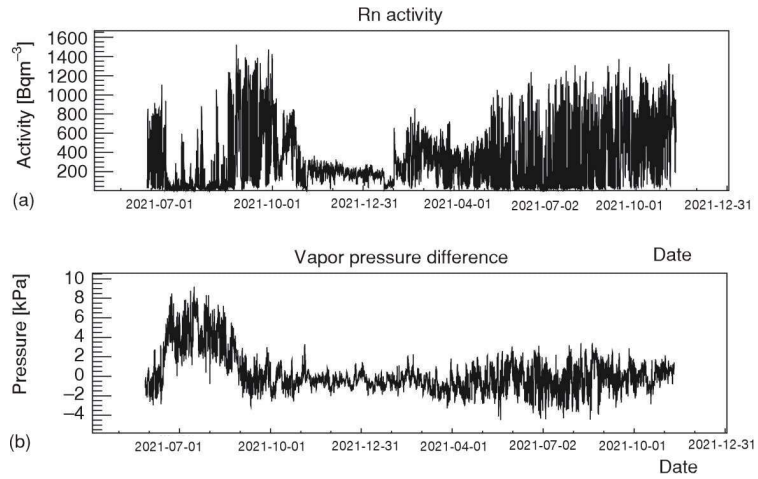
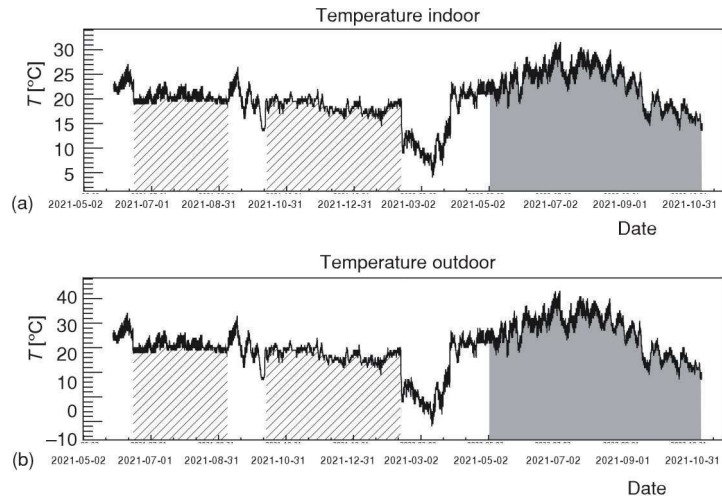


Figure 2. Indoor temperature (a) and outdoor temperature (b) is shown. Indoor temperature which was used for analysis when air conditioning (AC) was on, is indicated in two line pattern areas, while gray shaded interval indicates period when air conditioning was off (noAC)



$$RH = \frac{\text{vapor pressure}}{es(T)} \quad (3)$$

we get the formula to calculate the vapor pressure in air

$$\text{vapor pressure}(T, RH) = RH \cdot \frac{4098 \cdot \left(0.6108 \cdot e^{\frac{17.27 \cdot T}{T+237.3}} \right)}{(T + 237.3)^2} \quad (4)$$

Using this formula, we calculate four variables: indoor-vapor-press (vapor pressure from indoor-temperature and indoor-humidity data), outside-vapor-press (vapor pressure from outdoor outside-humidity, outside-temp data), diff-vapor-press (vapor pressure difference of outdoor and indoor) and gdas1-vapor-press (vapor pressure from GDAS1-T02M, GDAS1-RH2M data). On the bottom of fig. 1 the vapor pressure difference is shown, and it can be clearly seen that if the outer vapor pressure is much higher than the indoor vapor pressure, the indoor radon activity is lower fig. 1(a).

Out of two years of data taking, after merging all the data together to form a single hourly event with all the variables measured at that time, the number of useful hourly events was 12654. Table 1 shows the num-

Table 1. Summary table of number of hourly events used for specific part of analysis

	noAC	AC	All period
Signal training	1343	912	3428
Signal testing	1343	912	3428
Signal training and testing	2686	1824	6856
Background training	942	1531	2899
Background testing	942	1531	2899
Background training and testing	1884	3062	5798

ber of hourly events used for each of the three periods of analysis, which were split, firstly into signal and background events, where signal events are those for which Rn activity is more than 200 Bqm⁻³, and background is less than that value, and then each set was split once more, into training and testing sample to be used in MVA analysis. Table 1 also shows the number of events used, and split, in periods with air condition operation on (AC), line pattern area on fig. 2(a), and air conditioning off (noAC) gray on fig. 2(a).

Before performing the multivariate (MVA) analysis, we have looked into single variable analysis, and the best way to see if variables could be useful for analysis is if they have, firstly, the greatest correlation with radon activity (concentration), and, secondly, which variable profiles for

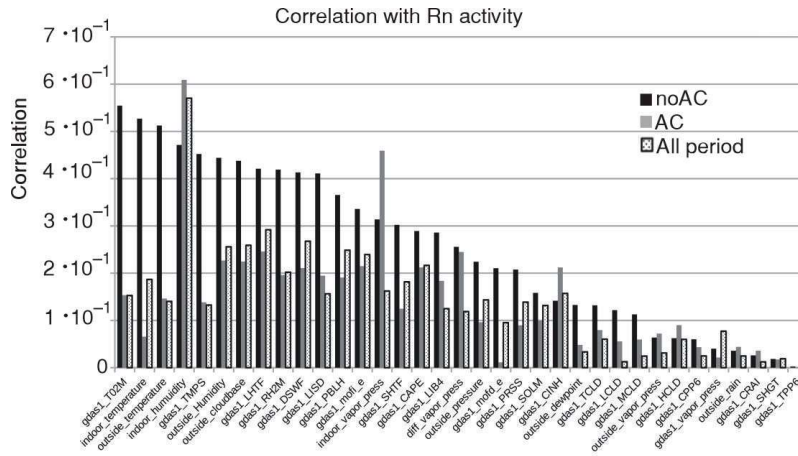


Figure 3. The modulus of Pearson's correlation coefficients of radon activity with each of variables used in the analysis is shown. Note the decreasing of correlation with temperature variables, and increasing with humidity variables, when air conditioning (AC) was turned on

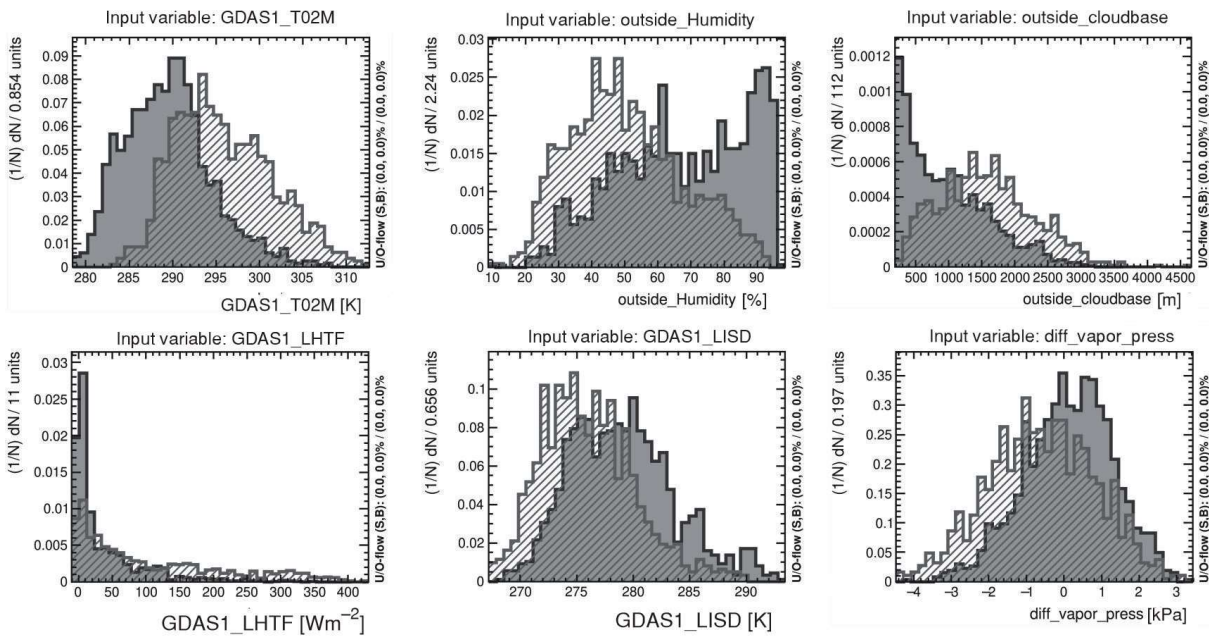


Figure 4. For some variables there is a significant separation of distributions of variables' values for events with low and events with high radon activity. Variables shown are: temperature at height of 2 m above the ground (GDAS1-T02M), outside relative air humidity, measure of lowest visible part of the cloud (cloudbase), latent heat net flux at the surface (LHTF), standard lifted index (LISD) and the difference of water vapor pressure from indoor and outdoor

high Rn activity (signal) and low (background) data samples, have smallest overlap, meaning that they have greatest separation of high and low Rn activity samples. So, firstly, we are looking into modulus of Pearson's correlation coefficients for each of the variables used in this analysis with radon activity, fig. 3. Since the greatest variation of radon activity should give the best insight into correlation with variables, we are firstly looking into data with air condition off (noAC). To the variables with greatest modulus of Pearson's correlation coefficients with Rn activity (noAC) are temperature variables from all three sources of data GDAS, radonometar and meteorological station (GDAS1-T02M, indoor-temperature, outside-temperature, GDAS1-TMPS), than humidity (indoor-humidity, outside-humidity), outside-cloudbase, followed with GDAS variables: GDAS1-LHTF (latent heat net flux on surface) and GDAS1-DSWF (downward short wave radiation flux) and GDAS1-RH2M (relative humidity at height of 2 m), followed by indoor-vapor-pressure. When air conditioning

is turned on, there is a change in correlation, where temperature variables correlations are decreasing, and there is an increase in correlation of humidity variables like indoor-humidity and indoor-vapor-pressure. We observe this change since temperature is now holding at approximately the same level by air conditioning, and any variation of radon activity we see does not come from approximately constant temperature. We noticed the similarity in modulus of Pearson's correlation coefficients of outside-T02M and outside-temperature with Rn activity of 55.4 % and 51.2 %, respectively, for noAC data, and 15.3 % and 14.6 %, respectively, for AC data. Also, outside-humidity and gdas1-RH2M with 44.4 % and 41.9 %, respectively, for noAC and 22.7 % and 19.6 % for AC data. When looking into pressure data, outside-pressure and GDAS1-PRSS have modulus of Pearson's correlation coefficients of 22.4 % and 20.8 %, respectively, for noAC data and 9.6 % and 9.0 % for AC data.

When looking into separation of variables for signal and background samples, fig. 4 shows selected

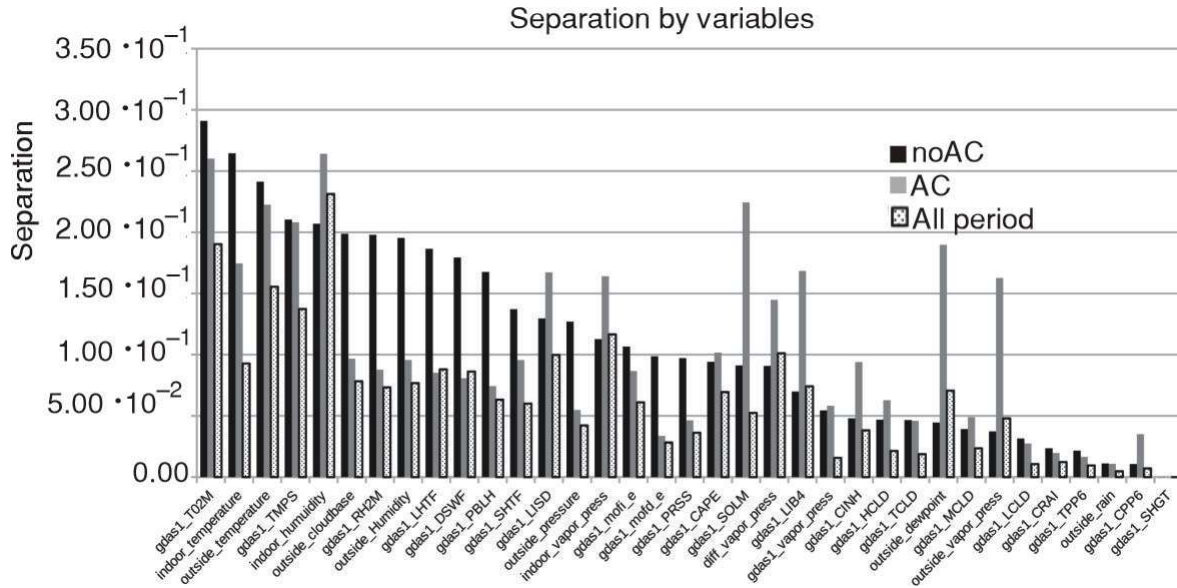


Figure 5. Separation of events with low and high Rn activity by each variable

variables, where separation can be seen with naked eye, and also, separations of high and low Rn activity for different variables can be roughly compared. But, we want to have more precise insight into separation, and for all three samples AC, noAC and samples of whole measurement period. This is shown in fig. 5 where we can see that for noAC, temperature variables have most significant separation values, as was the case with modulus of Pearson's correlation coefficients with Rn activity on fig. 3. With air conditioning turned on, the variables of humidity and vapor pressure gain in separation value, while indoor temperature is decreasing its separation value. Notice that the change is not so pronounced as was the case with correlation variables. Again, we noticed the similarity separation values of outside-T02M and outside-temperature 29.1 % and 24.1 %, respectively, for noAC data, and 26.0 % and 20.8 %, respectively, for AC data. Also, outside-humidity and GDAS1-RH2M with 19.8 % and 19.5 %, respectively, for noAC and 8.8 % and 9.6 % for AC data. When looking into pressure data, outside-pressure and GDAS1-PRSS have separation values of 12.7 % and 9.7 %, respectively, for noAC data and 5.5 % and 4.6 % for AC data.

MULTIVARIATE CLASSIFICATION ANALYSIS

Toolkit for multivariate analysis (TMVA) [11] implemented in ROOT [12] framework for data analysis, has many of multivariate methods and tools implemented, which are frequently used for data analysis, as in High energy physics, also by data scientists in general. We will not get into details of wide spread of multivariate methods available, which can be found in

TMVA manual [11]. The usage of those multivariate methods in TMVA is rather standardized. What is advantageous in using TMVA is that we could compare many of multivariate methods using the same training and testing sample. Also, the TMVA was used in many analyses, and is constantly under development, with many new methods implemented. The TMVA offers comparison of methods developed for other frameworks, like methods developed in programming languages Python, or R, or modern methods like Deep and Convolutional Neural Networks, which is best to be run in multi-thread mode or on CPU or on GPU (graphical cards).

In MVA analysis, the data sample consists of events. Event is composed of data measured/recorded at the same time for each input variable. We can run MVA as Classification, Classification with category, and Regression. The MVA Classification is done when sample is divided into two samples (classes); signal and background. The MVA methods are trained to make the same classification using events they have not seen before, and their performance in classification is measured. Second MVA analysis is done as regression analysis. It is similar to classification, in the sense that the number of classes into which initial sample is divided is much bigger, and the value of classifier is not only 1 (signal) and 0 (background) but has much more values in between. Classification with category was not used, as the maximum performance of Classification is obtained when no other categorical values besides 1 (signal) and 0 (background) are used. Future performance tests could include categories like; very high, high, medium, low and very low radon concentrations.

When a sample is prepared, MVA classification needs some time to complete the training process for

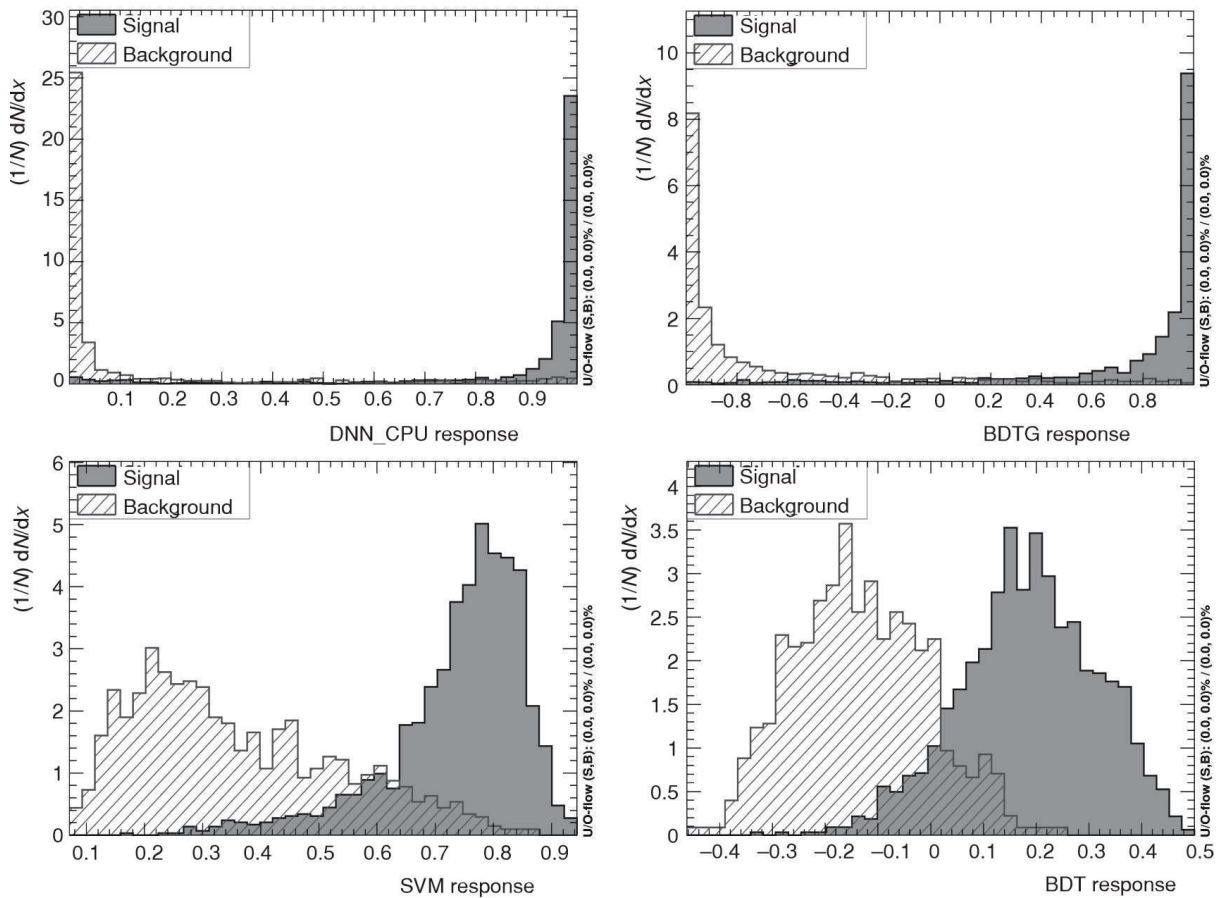


Figure 6. Response of MVA methods to events with low and high Rn activity

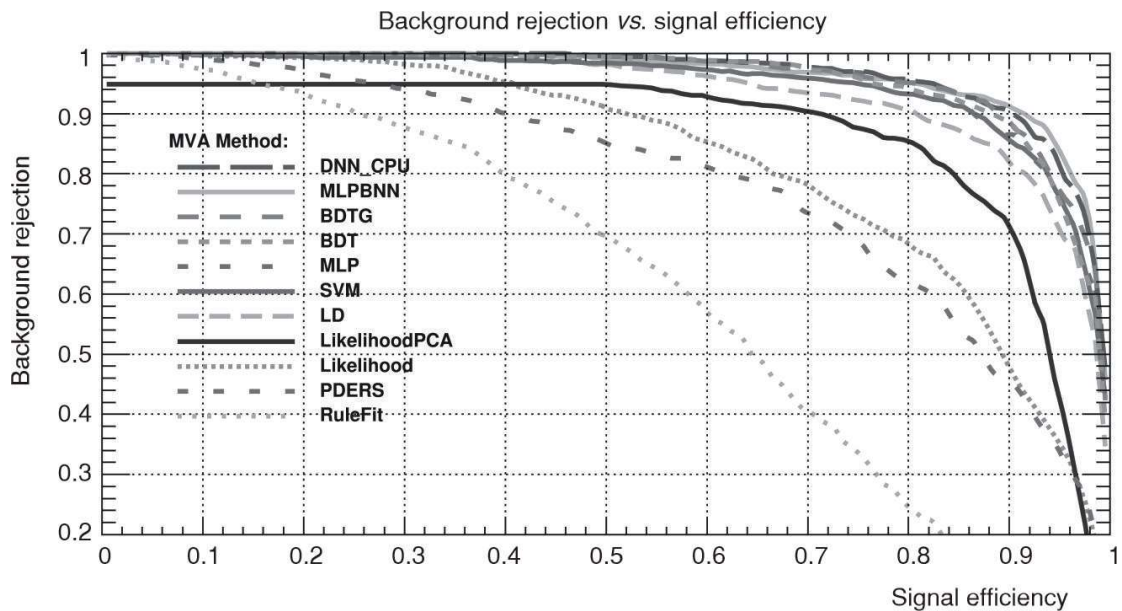
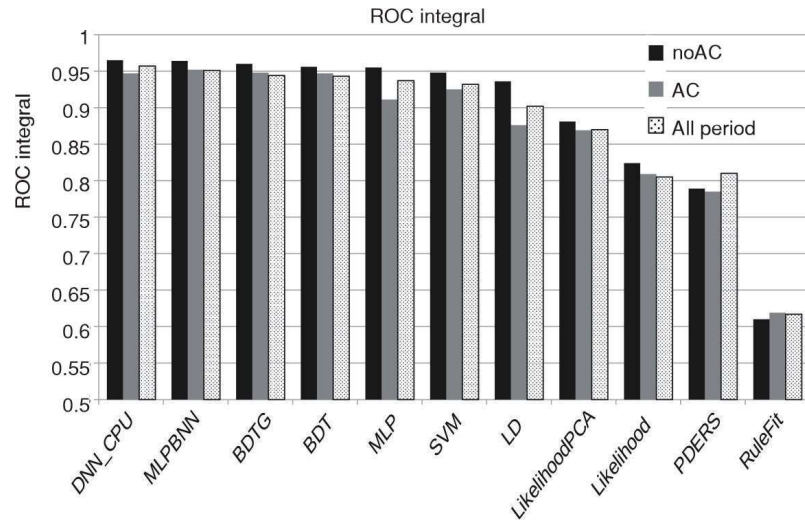


Figure 7. The ROC curve for MVA methods for the time interval where air conditioning was off (noAC)

each of MVA methods selected for comparison. Besides training, the sample of same number of events is used for evaluation, or testing, where MVA method is tested on samples not seen before (not used for training). The performance of some MVA method is expressed only using testing/evaluation sample.

The fig. 6 shows the response of best performing MVA methods, in analysis of noAC data, to events with low and high Rn activity, or signal and background. We can see, in fig. 7, that by looking into Receiver Operating Characteristic (ROC) curve comparison of all selected multivariate methods, that several

Figure 8. Value of the ROC integral for MVA methods for the selected time intervals, AC and noAC, and for whole time interval



methods have very good performances and also, very close performances. It is very good to have several methodologically very different multivariate methods performing in similar way, since this gives us confidence that classification is applicable. To illustrate this point, we can say that, very generally speaking, ANN are based on convolution of selected function to the resulting multivariate functional dependence, while Boosted Decision Trees are based on multidimensional space (cube) cuts, for approximation of multivariate functional dependence, and it is very good that both have very good performances in MVA classification.

The comparison of ROC curve integrals for best performing methods, for MVA classification analysis for all three intervals; noAC, AC and all-period analysis is shown at fig. 8. For five best performing methods, DNN-CPU (Deep Neural Network), MLPBNN (Multi-Layer Perceptron Bayesian regulator Neural Network), BDTG (Boosted Decision Trees with Gradient boosting), BDT (Boosted Decision Trees), and MLP (Multi-Layer Perceptron – an ANN), results are very similar, and also for all the three intervals, which is very important in sense that while variables' correlation with Rn activity vary greatly, this is easily overcome in MVA methods, adding very important property of robustness in variable selection. We should note that all the mentioned methods are ANN or DBT based multivariate methods.

The resulting trained multivariate methods are now ready to be included into some web applications, or used in variables' analysis. In web applications, Radon alarm could be constructed, when based on input variables, there is a great probability of increased indoor radon activity. For example, some places where it is known from previous measurements, like from participation in large indoor radon survey, that dwelling or working space has a problem with increased indoor radon concentration, some measures like increased ventilation or longer brakes from work, could be made. In variables' analysis, the simplification of MVA approximation of

underlying multivariable function dependence could be made, not only with classification, but more effectively with regression methods.

The MVA methods which are trained and tested using full set of variables and all available data are ready to be used in some application. But, we can continue our work and try to modify something in our analysis chain to see if we can get better performance or method which uses lower number of input variables, without big loss in performance. We can make different selection of training data sets, like truncation of outlier data, we can change the number of input variables, or change parameters specific for each MVA method. For this purpose, it could be very useful to look into variable importance for specific MVA method, for example for BDTG in fig. 9, in order to look into the influence of variables on MVA decision. To show why this is useful we pay attention on Pearson's correlation coefficients of input variables and radon concentrations and notice that there could be several variables with high correlation coefficient with radon concentration, but highly inter-correlated with each other, which results in no gain in MVA method performance if we add several variables which are inter-correlated. So, we can exclude variables if their exclusion does not lower the MVA method performance. We choose to look into importance of variables on BDTG classification, for all time intervals. Again, we start with noAC intervals, where indoor radon activity was highest, and indoor temperature was not regulated. We start with two GDAS variables, GDAS1-SHTF (sensible heat net flux at surface) and GDAS1-SOLM (volumetric soil moisture content), followed by indoor-humidity and diff-vapor-pressure, and GDAS1-T02M at position 6, with some other variables similarly important as gdas momentum flux direction and gdas cloud cover variables.

When comparing data from meteorological station and gdas data, we cannot compare them in, for example, multivariate importance, since if one variable is chosen to be used in MVA training, similar variable in, for example Pearson's correlation coefficients or

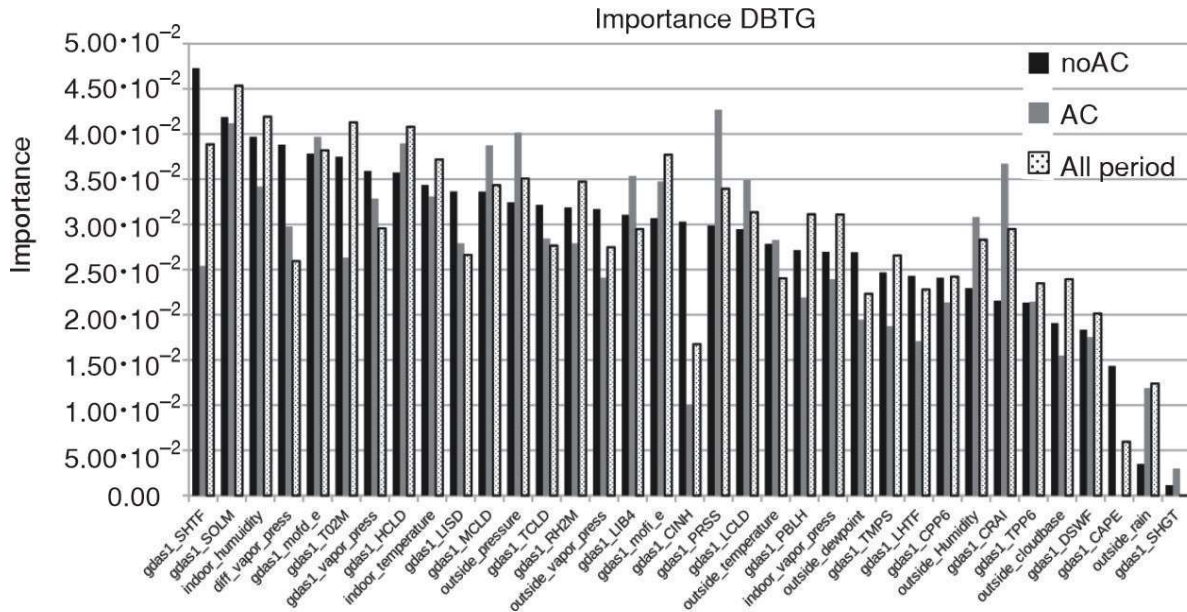


Figure 9. Variable importance for MVA method BDTG for time intervals, AC and noAC, and for the whole time interval

separation of variable for increased and for low Rn activity value, do not have power to make discrimination. Comparison can only be used when each variable is observed separately in a single variable analysis. Also, similar situation can happen with preparation of variables, where resulting variables are, de-correlated, and first variable is significant for further analysis but other, very similar variable before de-correlation, remains with negligible significance for further analysis.

THE MVA REGRESSION

Regression analysis often fails if there is not a strong dependence of target variable, in our case Rn activity, on input variables. Reasoning is the following: Classification analysis has only two outputs, either it is signal (1) or background (0), but in case of regression,

there are many more values between 0 and 1, and much more dependence, or events is needed to get positive results here. We ran MVA regression for three time intervals, noAC, AC and all-period. The BDTG and DNN-CPU show good prediction results after MVA regression training procedure, as a result of RMS of deviations of true and evaluated value of Rn activity are satisfyingly small, as is shown in fig. 10. The fig. 11 shows this in more detail for BDTG in noAC regression analysis, where the distribution of deviations is shown for each event in the testing sample.

CONCLUSIONS

Single variate analysis of correlations of each of meteorological variable with indoor radon activity and Multivariate classification and regression analysis of all meteorological variables and radon activity was per-

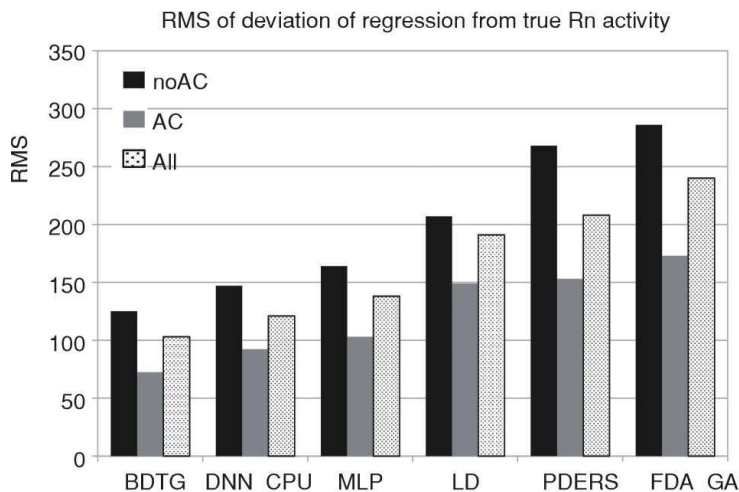


Figure 10. The RMS of deviations of regressions from true value for selected time intervals, AC and noAC, and for the whole time interval, for several MVA regression methods

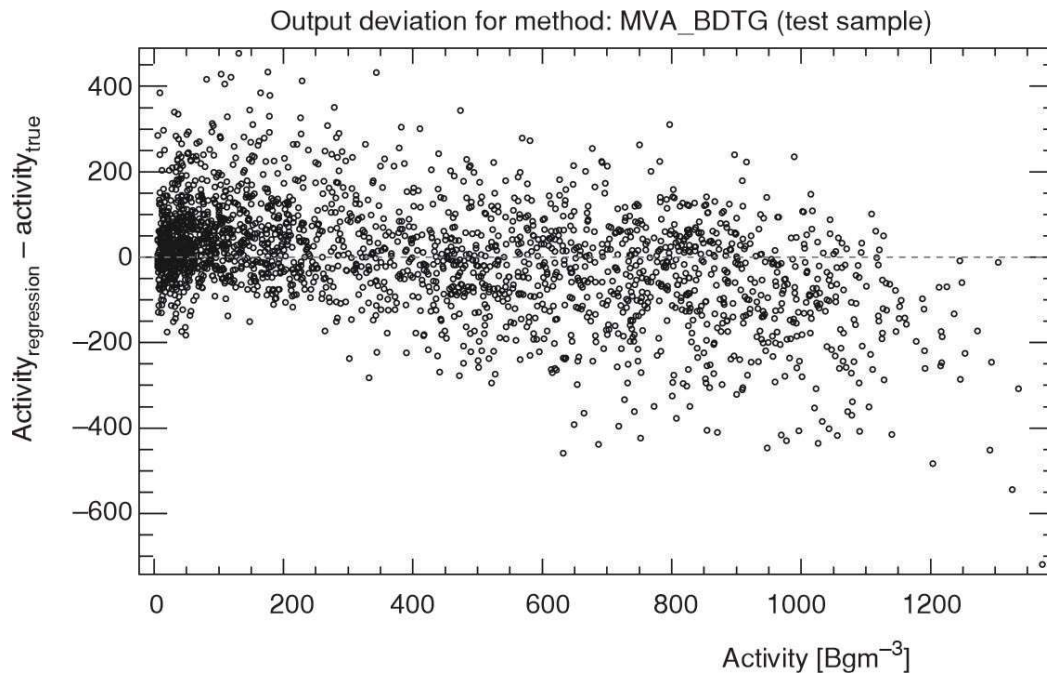


Figure 11. Deviation of regression from true value for noAC period and BDTG MVA method

formed and discussed. Meteorological variables used in this analysis were from radonometar device, then from a nearby meteorological station and finally from GDAS data. Single variate analysis has identified variables with greatest value of modulus of Pearson's correlation coefficient with Rn activity, and also variables with greatest separation of events with increased Rn activity of over 200 Bqm^{-3} and of events with Rn activity below this value. This initial analysis and looking into variables were showing the expected behavior of Rn concentration with meteorological variables, with emphasis on data periods with or without air conditioning, and also with emphasis on previously found variable of indoor water vapor pressure. This single variate analysis and observing all the data proved also useful for conclusion that GDAS data could be used as a good enough approximate replacement for meteorological data from the nearby meteorological station for MVA analysis. The MVA classification analysis found several very well performing MVA methods which can be used in web application or for further detailed analysis of specific input variables. Variable importance of BDTG MVA method was shown for all three periods, and most important variables were discussed. Finally, MVA regression analysis gave also good results, and more quality measurements in this rarely accessed ground level laboratory would be useful to better tune the MVA methods, and do more detailed analysis.

ACKNOWLEDGMENT

Authors thank the NOAA Air Resources Laboratory (<https://www.arl.noaa.gov/>) for GDAS data.

(<https://www.ready.noaa.gov/gdas1.php>). Authors thank the Environmental Physics Laboratory (<http://www.envpl.ipb.ac.rs/>) for meteorological station data. The authors acknowledge funding provided by the Institute of Physics Belgrade, through grant by Ministry of Education, Science and Technological Development of the Republic of Serbia.

AUTHORS' CONTRIBUTIONS

The original idea and draft were carried out by D. M. Maletić. The data provided by R. M. Banjanac, V. I. Udovičić and Z. Mijić. Statistical analysis was done by D. M. Maletić, D. R. Joković and A. L. Dragić. N. B. Veselinović, M. R. Savić, S. Živković-Radeta and J. V. Udovičić worked on data preparation and selection. All the authors analyzed and discussed the results and reviewed the manuscript.

REFERENCES

- [1] ***, WHO Handbook on Indoor Radon: A Public Health Perspective, World Health Organization, Switzerland, 94, 2009
- [2] Dragić, A., et al., The New Set-Up in the Belgrade Low-Level and Cosmic-Ray Laboratory, *Nucl Technol Radiat*, 26 (2011), 3, pp. 181-192
- [3] Maletić, D., et al., Comparison of Multivariate Classification and Regression Methods for the Indoor Radon Measurements, *Nucl Technol Radiat*, 29 (2014), 1, pp. 17-23
- [4] Eremić-Savković, M., et al., Results of the First National Indoor Radon Survey Performed in Serbia, *Journal of Radiological Protection*, 40 (2020), 2, pp. N22-N30

- [5] Vukotić, P., et al., Influence of Climate, Building, and Residential Factors on Radon Levels in Ground-Floor Dwellings in Montenegro, *Nucl Technol Radiat*, 36 (2021), 1, pp. 74-84
- [6] Udovičić, V., et al., Multiyear Indoor Radon Variability in a Family House – a Case Study in Serbia, *Nucl Technol Radiat*, 33 (2018), 2, pp. 174-179
- [7] Udovičić, V., et al., Radon Variability Due to Floor Level in Two Typical Residential Buildings in Serbia, *Nukleonika*, 65 (2020), 2, pp. 121-125
- [8] Maletić, D., et al., Correlative and Multivariate Analysis of Increased Radon Concentration in Underground Laboratory, *Radiation Protection Dosimetry*, 162 (2014), 1-2, pp. 148-151
- [9] Tetens, O., About Some Meteorological Terms (original: Über Einige Meteorologische Begriffe.) *Z. Geophys*, 6 (1930) pp. 297-309
- [10] Murray, W., On the Computation of Saturation Vapor Pressure, *J. Applied Meteorology*, 6 (1967), pp. 203-204
- [11] Hoecker, A., et al, TMVA – Toolkit for Multivariate Data Analysis. *PoS ACAT*, 40 (2009), p. 12
- [12] Brun, R., Rademakers, F., ROOT – An Object Oriented Data Analysis Framework, *Nucl. Inst. & Meth. in Phys. Res. A*, 389 (1997), pp. 81-86

Received on December 18, 2023

Accepted on February 12, 2024

**Димитрије М. МАЛЕТИЋ, Радомир М. БАЊАНАЦ, Дејан Р. ЈОКОВИЋ,
Александар Ј. ДРАГИЋ, Никола Б. ВЕСЕЛИНОВИЋ, Михаило Р. САВИЋ, Зоран Р. МИЈИЋ,
Владимир И. УДОВИЧИЋ Светлана Д. ЖИВКОВИЋ-РАДЕТА, Јелена В. УДОВИЧИЋ**

**МУЛТИВАРИЈАНТНА АНАЛИЗА ДВОГОДИШЊЕГ КОНТИНУАЛНОГ
МОНИТОРИНГА РАДОНА У НАДЗЕМНОЈ ЛАБОРАТОРИЈИ У
ИНСТИТУТУ ЗА ФИЗИКУ У БЕОГРАДУ**

Приказана је мултиваријантна класификациона и регресиона анализа односа метеоролошких варијабли и концентрације радона у затвореној и ретко приступачној приземној лабораторији Института за физику Београд. Податке о метеоролошким варијаблама и концентрацији радона, коришћене у овој анализи, добијамо из активног уређаја за краткорочна мерења концентрације радона у затвореном простору, оближње метеоролошке станице и из података Глобалног система асимилације података. Једно-варијантном анализом идентификоване су варијабле са највећом вредношћу модула Пирсоновог коефицијента корелације са концентрацијом радона, као и варијабле са највећом моћи раздвајања догађаја са повећаном концентрацијом радона више од (200 Bq m^{-3}) и догађаја са нижом концентрацијом од ове вредности. Ова почетна анализа и сагледавање варијабли показују очекивану везу концентрације радона и метеоролошких варијабли, са нагласком на анализу података из различитих временских интервала, када је у лабораторији радила и када није радила климатизација, као и са нагласком на варијаблу разлика унутрашњег и спољњег притиска водене паре. Ова једно-варијантна анализа доводи до закључка да се подаци Глобалног система асимилације података могу користити као довољно добра приближна замена за метеоролошке податке из оближње метеоролошке станице за мултиваријантну анализу. Мултиваријантном класификационом анализом пронађено је неколико веома добрих мултиваријантних метода које се могу користити у некој веб апликацији или за даљу детаљну анализу специфичних улазних варијабли. Приказана је важност варијабли за мултиваријантни метод стабла одлучивања за сва три периода мерења, а разматране су и најважније варијабле. Коначно, мултиваријантна регресиона анализа је такође дала добре резултате, што може да буде корисно при оптимизацији класификационих мултиваријантних метода.

Кључне речи: континуирани радон мониторинг, мултиваријантна анализа, Глобални систем асимилације података, метеоролошка станица

Analyzing solar activity with Belgrade muon station: case study of 2021 November 4th Forbush decrease

N.B. Veselinović^{ORCID}, M.B. Savić, D.M. Maletić, A.L. Dragić,
R.M. Banjanac, D.R. Joković, D. Knežević, M. Travar and
V.I. Udovičić

*Institute of Physics Belgrade, University of Belgrade, Pregrevica 118,
11080 Belgrade, Serbia, (E-mail: veselinovic@ipb.ac.rs)*

Received: September 19, 2023; Accepted: October 16, 2023

Abstract. The first significant Forbush decrease of the solar cycle 25 was recorded on November 4th, 2021. The Forbush decrease was observed with numerous ground based cosmic rays stations including Belgrade cosmic rays muons' station. Series of coronal mass ejections during October 28–November 4 2021. produce conditions for this Forbush decrease. We discuss here the variation of cosmic rays' flux detected with ground-based detectors and connection with conditions, measured in-situ, in interplanetary space around Earth, flux of solar wind protons measured with SOHO probe to assess implication for solar-terrestrial coupling processes.

Key words: Cosmic rays – Forbush decrease – Space weather – muon detector

1. Introduction

One of the methods of researching solar-terrestrial coupling processes is observing the response of the flux of cosmic rays (CR) to various types of disturbances (or drivers) in the heliosphere. Transient phenomena detected in CR flux due to modulation in the heliosphere is the Forbush decrease: a sudden drop in CR flux followed by a gradual return to the previous level. It occurs as CR interact with irregularities in the interplanetary magnetic field (IMF), usually connected with the emission of coronal plasma known as a coronal mass ejection (CME) and its interplanetary counterpart (ICME) (Yermolaev et al., 2021). In recent decades, space probes have measured IMF parameters in-situ as well as particle flux. The detected particles can be fast-moving particles, known as solar energetic particles (SEPs), related to violent eruptions from the Sun that can cause a sudden increase in measured CR flux at the surface - a ground level enhancement (GLE). The other particles detected with probes, aside from solar wind particles and SEPs, are energetic storm particles (ESP) accelerated locally by shocks driven by fast ICMEs (Desai & Giacalone, 2016) and low-energy CR

(Veselinović et al., 2021). It has been shown (Koldobskiy et al., 2019; Savić et al., 2023; Kolarski et al., 2023) that parameters measured in-situ correlate with the magnitude and time evolution of FD. The end of October and the beginning of November 2021 marked extreme activity with a strong X-class solar flare (CIT), accompanied by the first Ground Level Enhancement (GLE) event in this cycle on October 28th, measured by several ground stations (Papaioannou, A. et al., 2022). There were several typical CMEs during this period. Most pronounced were two halo CMEs on October 28th and November 2nd. The second halo CME, due to its speed, caught up with previous ICMEs and produced a CME-CME interaction (Li et al., 2022). These disturbances created additional modulation of CR, producing the first strong FD in the present solar cycle, detected by multiple ground stations around the globe (Chilingarian et al., 2022).

The present case-study combines in-situ measurements of solar wind parameters and proton flux in near-Earth space with measurements on the ground to analyze how these parameters affect parameters of the FD detected on November 4th, 2021.

2. Ground level cosmic ray observations

The most widely method of detecting CR use detectors that are part of the worldwide network of Neutron Monitors (NM) (<https://www.nmdb.eu/nest/>). One of the other species of these secondary CR that can be detected and used for monitoring primary CR are muons.

2.1. Belgrade muon detector

The ground level Belgrade muon station (GLL) is a part of the Low-Background Laboratory for Nuclear Physics at the Institute of Physics, Belgrade, Serbia. The energy range of the observed primary CR extends and complements the energy ranges detected by the NM network, but is still sensitive to CR modulation of the heliosphere. Details of the experimental setup, as well as the calculated response function of the detectors, are presented in (Veselinović et al., 2017).

2.2. Ground level data analysis

Both NM and muon detectors measure integral flux over different energy ranges, so the median energy of the detected primary CR is used in the analysis of the measured data. Another property of the detector system is Cut-off rigidity, the minimal magnetic rigidity that the CR must have in order to penetrate the IMF and geomagnetic field. To determine the amplitude of the FD for each station, which differs in median energy and asymptotic direction, a baseline was established using the average hourly count rate during mid-October 2021 when solar activity was low. For this study, we utilized 1-hour time series of CR flux detected at 17 NM stations and GLL data (Table 1).

Table 1. Cut-off rigidity (R_c) and median energy (E_m) of primary CR for several stations.

Stations	R_c (GV)	E_m (GeV)	Stations	R_c (GV)	E_m (GeV)
Belgrade	5.3	63	Kerguelen	1.14	10.4
Athens	8.53	17.8	Oulu	0.8	10.3
Guadalajara	6.95	15.4	Apatity	0.65	10.3
Baksan	5.6	13.7	Norilsk	0.63	10.3
Jungfraujoch	4.5	12.6	Tixie Bay	0.5	10.2
Lomnický štít	3.84	12	Fort Smith	0.3	10.2
Dourbes	3.18	11.5	Inuvik	0.3	10.2
Kiel	2.36	11	S. Pole bare	0.1	10.1
Yakutsk	1.65	10.6	S. Pole	0.1	10.1

Median energy for NM was found using formula given in [Li et al. \(2023\)](#) and median energy for GLL was found using Monte Carlo method of CR transport. Dependence of FD amplitude on CR median energy is given by power law ([Cane, 2000](#))

$$\frac{\Delta N}{N} = E^{-a} \quad (1)$$

Here N is CR flux, E is median energy and a is power exponent that depends on heliospheric conditions.

A scatter plot of the selected event is given ([Figure 1](#)) plotted in log-log scale and it shows clear median rigidity dependence of the amplitude of FD.

Steeper spectrum during this event shows greater modulation of primary CR. If GLL data is included in the plot, the power exponent is not so large so that can be interpreted as stronger modulation of the lower energy CR due to CME-CME interaction. Linear regression is performed to find power indices correspond to November 2021 event. Power index for NM only is 1.23 ± 0.22 and for NM and GLL power index is 0.62 ± 0.10 . This is, in general, in good agreement with some previous studies ([Lingri et al. \(2016\)](#) and references within).

3. Relation to in-situ measured data

In this study we used measured in-situ parameters relevant for heliospheric studies which are available at GSFC/Space Physics Data Facility, in the form of 1-hour resolution OMNI data (<https://spdf.gsfc.nasa.gov/pub/data/omni/lowresomni/>). Also we used proton flux data gathered by SOHO probe with two detectors, ERNE and EPHIN, onboard SOHO probe ([Torsti et al., 2000](#); [Kühl & Heber, 2019](#)) at Lagrange point 1 in vicinity of Earth. Comparison between 1-hour time series of selected parameters of IMF from OMNI data and

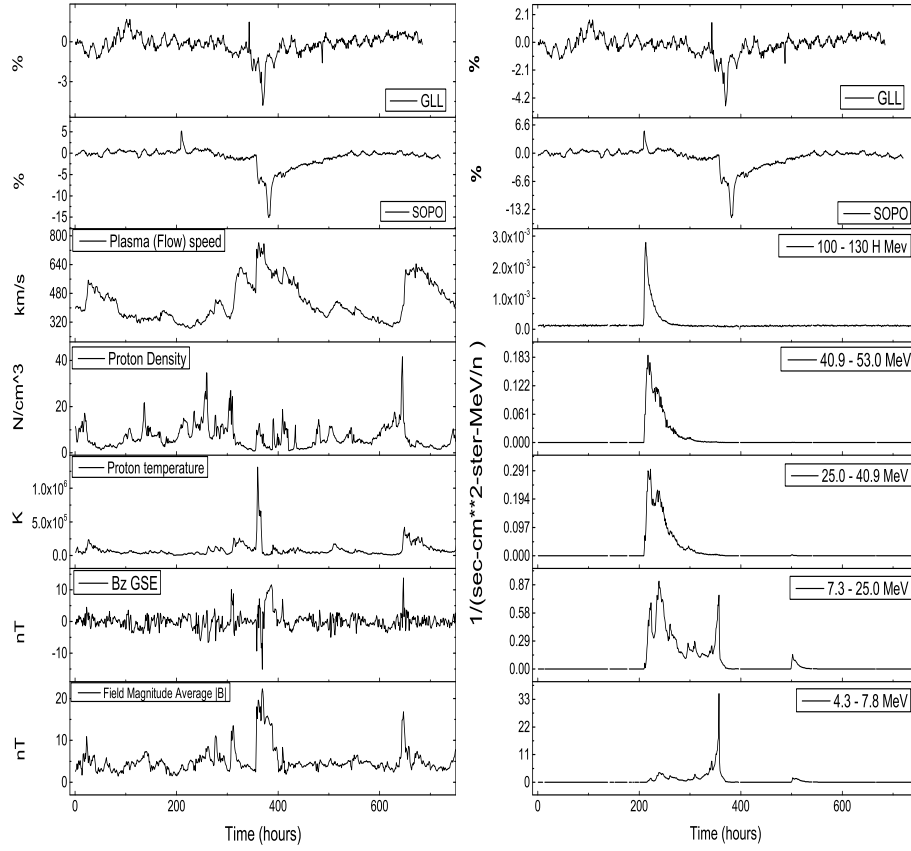


Figure 2. Left: Time series for plasma parameters (taken from OMNI database) and cosmic ray flux (measured at South Pole NM and GLL) from October 20th until November 20th, 2021. Right: Hourly time series for different proton energy channels from SOHO/ERNE and SOHO/EPHIN and two CR detectors time series for the same period.

this complicated shock-associated ICME disturbance where multiple shocks and transient flows merged is challenging and other studies (Zhao & Zhang, 2016; Werner et al., 2019) showed similar complex dependence of CR flux on different parameters of the IMF condition.

4. Summary

In this work we studied the FD occurred in November 4th, 2021, using data from Belgrade muon station and other multiple sources. Increased solar activity at the beginning of the November 2021 had a measurable effect on CR, observed as a

Table 2. Pearson correlation coefficients for the correlation between CR flux detected at Belgrade CR station (GLL), at South pole (SOPO), flux of protons of different energies from SOHO/ERNE and SOHO/EPHIN and plasma parameters (from OMNI database) for the period from October 20th until November 20th, 2021.

	SOPO		GLL	
	Pearson Corr.	p-value	Pearson Corr.	p-value
SOPO	1		0.52	$<10^{-5}$
GLL	0.52	$<10^{-5}$	1	
B Average	-0.55	$<10^{-5}$	-0.48	$<10^{-5}$
Bz	-0.4	$<10^{-5}$	-0.15	$<10^{-4}$
Proton temperature	-0.18	$<10^{-5}$	-0.23	$<10^{-5}$
Proton Density	0.23	$<10^{-5}$	0.14	$<10^{-4}$
Plasma (Flow) speed	-0.61	$<10^{-5}$	-0.53	$<10^{-5}$
7.3-25.0 MeV p	0.17	$<10^{-5}$	-0.12	0.002
4.3-7.8 MeV p	0.01	0.67	-0.29	$<10^{-5}$
25.0-40.9 MeV p	0.21	$<10^{-5}$	0.02	0.5
40.9-53.0 MeV p	0.21	$<10^{-5}$	0.03	0.45
80-100 H Mev p	0.22	$<10^{-5}$	0.03	0.37

decrease in measured flux by all relevant CR stations. Energy range of affected primary CR was wide enough so effect was detected by neutron monitors but also muon detectors. Rapid decrease was detected with CR detectors around the world and it was one of the consequence, along with the strong G3-class geomagnetic storm, auroras and GLE event, of series of overlapping CMEs. We showed that based on measured amplitude of FD of the range of ground station that higher energy CR was less affected with heliospheric disturbance. Cross correlations between time series of CR flux and IMF and solar wind characteristics during these strongly disturbed heliospheric conditions were presented. Lack of strong correlation is also apparent for higher energy CR flux time series and time series of the heliospheric parameters and proton flux of certain energy ranges. This proves that, in order to better understand solar-terrestrial coupling processes, particularly its effect for higher energy particles requires more data from various sources and various probes and this analysis can be done in the future.

Acknowledgements. The authors acknowledge funding provided by the Institute of Physics Belgrade, through the grant by the Ministry of Science, Technological Development and Innovations of the Republic of Serbia. We also acknowledge use of NASA/GSFC's Space Physics Data Facility's OMNIWeb (or CDAWeb or ftp) service, and OMNI data as well as team behind SOHO, which is a project of international collaboration between ESA and NASA. We acknowledge the NMDB database, founded under the European Union's FP7 program (contract no.213007) for providing data.

References

- Cane, H. V., Coronal Mass Ejections and Forbush Decreases. 2000, *Space Science Reviews*, **93**, 55, DOI: 10.1023/A:1026532125747
- Chilingarian, A., Hovsepyan, G., Martoyan, H., et al. 2022, Forbush decrease observed by SEVAN particle detector network on November 4, 2021
- Desai, M. & Giacalone, J., Large gradual solar energetic particle events. 2016, *Living Reviews in Solar Physics*, **13**, 3, DOI: 10.1007/s41116-016-0002-5
- Kühl, P. & Heber, B., Revising More Than 20 Years of EPHIN Ion Flux Data-A New Data Product for Space Weather Applications. 2019, *Space Weather*, **17**, 84, DOI: <https://doi.org/10.1029/2018SW002114>
- Kolarski, A., Veselinović, N., Srećković, V. A., et al., Impacts of Extreme Space Weather Events on September 6th, 2017 on Ionosphere and Primary Cosmic Rays. 2023, *Remote Sensing*, **15**, DOI: 10.3390/rs15051403
- Koldobskiy, S. A., Bindi, V., Corti, C., Kovaltsov, G. A., & Usoskin, I. G., Validation of the Neutron Monitor Yield Function Using Data From AMS-02 Experiment, 2011-2017. 2019, *Journal of Geophysical Research: Space Physics*, **124**, 2367, DOI: <https://doi.org/10.1029/2018JA026340>
- Li, W.-h. et al., A study of Forbush Decreases effects with DAMPE experiment. 2023, *PoS, ICRC2023*, 1311, DOI: 10.22323/1.444.1311
- Li, X., Wang, Y., Guo, J., & Lyu, S., Solar Energetic Particles Produced during Two Fast Coronal Mass Ejections. 2022, *The Astrophysical Journal Letters*, **928**, L6, DOI: 10.3847/2041-8213/ac5b72
- Lingri, D., Mavromichalaki, H., Belov, A., et al., Solar Activity Parameters and Associated Forbush Decreases During the Minimum Between Cycles 23 and 24 and the Ascending Phase of Cycle 24. 2016, *Solar Physics*, **291**, 1025, DOI: 10.1007/s11207-016-0863-8
- Papaioannou, A., Kouloumvakos, A., Mishev, A., et al., The first ground-level enhancement of solar cycle 25 on 28 October 2021. 2022, *A&A*, **660**, L5, DOI: 10.1051/0004-6361/202142855
- Savić, M., Veselinović, N., Dragić, A., et al., New insights from cross-correlation studies between solar activity indices and cosmic-ray flux during Forbush decrease events. 2023, *Advances in Space Research*, **71**, 2006, DOI: <https://doi.org/10.1016/j.asr.2022.09.057>, recent progress in the physics of the Sun and heliosphere
- Torsti, J., Mäkelä, P., Teittinen, M., & Laivola, J., SOHO/Energetic and Relativistic Nucleon and Electron Experiment Measurements of Energetic H, He, O, and Fe Fluxes during the 1997 November 6 Solar Event. 2000, *The Astrophysical Journal*, **544**, 1169, DOI: 10.1086/317219
- Veselinović, N., Dragić, A., Savić, M., et al., An underground laboratory as a facility for studies of cosmic-ray solar modulation. 2017, *Nuclear Instruments and Methods in Physics Research Section A: Accelerators, Spectrometers, Detectors and Associated Equipment*, **875**, 10, DOI: <https://doi.org/10.1016/j.nima.2017.09.008>

- Veselinović, N., Savić, M., Dragić, A., et al., Correlation analysis of solar energetic particles and secondary cosmic ray flux. 2021, *The European Physical Journal D*, **75**, 173, DOI: 10.1140/epjd/s10053-021-00172-x
- Werner, A. L. E., Yordanova, E., Dimmock, A. P., & Temmer, M., Modeling the Multiple CME Interaction Event on 6–9 September 2017 with WSA-ENLIL+Cone. 2019, *Space Weather*, **17**, 357, DOI: <https://doi.org/10.1029/2018SW001993>
- Yermolaev, Y. I., Lodkina, I. G., Dremukhina, L. A., Yermolaev, M. Y., & Khokhlachev, A. A., What Solar-Terrestrial Link Researchers Should Know about Interplanetary Drivers. 2021, *Universe*, **7**, DOI: 10.3390/universe7050138
- Zhao, L.-L. & Zhang, H., Transient galactic cosmic-ray modulation during solar cycle 24: A comparative study of two prominent Forbush decrease events. 2016, *The Astrophysical Journal*, **827**, 13, DOI: 10.3847/0004-637X/827/1/13

Forbush decrease events associated with coronal mass ejections: Classification using machine learning

M.R. Savić[✉], N.B. Veselinović, A.L. Dragić, D.M. Maletić,
R.M. Banjanac, D.R. Joković, D.Knežević, M.Travar and
V.I. Udovičić

*Institute of Physics Belgrade, University of Belgrade, Pregrevica 118,
11080 Belgrade, Serbia (E-mail: msavic@ipb.ac.rs)*

Received: September 27, 2023; Accepted: October 22, 2023

Abstract. In presented work we further explore previously indicated possibility of the existence of two classes of Forbush decrease events, established by the prior analysis of the correlation between the shape of energetic proton fluence spectra and Forbush decrease properties. In an attempt to increase statistical robustness of the analysis and potentially reduce the uncertainties, we have developed an alternative classification procedure that employs machine learning and utilizes space weather parameters as input variables. Based on the overall performance, efficiency and flexibility of different machine learning methods we selected the best performing algorithm and established the optimal boundary value of Forbush decrease intensity to be used for class separation. A subset of good input variables was selected based on their predictive power.

Key words: cosmic rays – Forbush decrease – coronal mass ejection – solar energetic particles

1. Introduction

The dynamic activity of the Sun's coronal magnetic field can give rise to complex space weather events. These events may include solar flares (SFs), coronal mass ejections (CMEs), their interplanetary counterparts known as interplanetary coronal mass ejections (ICMEs), the emission of solar energetic particles (SEPs), and similar phenomena (Kahler, 1992; Yashiro & Gopalswamy, 2008; Gopalswamy, 2022).

One such complex event can produce a number of effects in the heliosphere, one of which is the acceleration of solar wind particles. There is a distinction between particles accelerated by a SF in the lower Sun's atmosphere and those accelerated locally by the CME shock. The later are often referred to as energetic storm particles (ESPs) (Desai & Giacalone, 2016).

Additionally, the passage of a CME can affect the primary cosmic rays (CRs) potentially resulting in a sudden drop in the observed CR flux, followed by a

recovery phase that takes place over the several following days. This effect is known as a Forbush decrease (FD) and can be observed by Earth-based CR detectors.

A previous study of the relationship between transient modulations in the fluxes of energetic protons and cosmic rays (measured near and at Earth respectively) indicated an existence of two classes of FD events (Savić et al., 2023). The main objective of this work is to expand this analysis and investigate whether a specific set of space weather (SW) parameters can be successfully used as input parameters for classification. The proposed procedure would aim to separate FD events into classes as indicated by the aforementioned analysis, while increasing the statistical significance and potentially the reliability of the analysis. Additional positive outcome of a successful classification would be the selection of a subset of SW parameters that prove to be good input variables. These variables could then be further used for the prediction of FD magnitudes utilizing some regression algorithm.

2. Motivation

As simultaneous ESP and FD events are very likely a consequence of the passage of an ICME, a relationship between them was assumed. To establish this possible connection, correlation of characteristics of proton fluence spectra and FD parameters was investigated (as described in more detail in Savić et al. (2023)).

The proton fluence spectra were calculated from in situ measurements at L1 by SOHO/ERNE instrument (Torsti et al., 1995), and fitted by a double-power law, as shown for one selected event on Figure 1.

Exponents obtained from these fits were used to parameterize the spectra shape, and some degree of correlation between these exponents and FD magnitudes was established. However, this analysis also indicated a possible existence of two classes of FD events, as illustrated in Figure 2. The plot shows the dependence of the FD magnitude corrected for the magnetospheric effect on one of the proton fluence spectra exponents. The green oval indicates a supposed class of events that exhibit a stronger correlation between these two variables, while the red oval indicates a class of events where this correlation is apparently weaker. One possible way to define the boundary between these two classes could be by introducing a cut on the intensity of the event.

Due to relatively low statistics of events where proton fluence can be reliably determined, one idea for extending this analysis is to try and utilize other space weather parameters in order to increase statistics and more strongly establish the assumed existence of two classes of FD events.

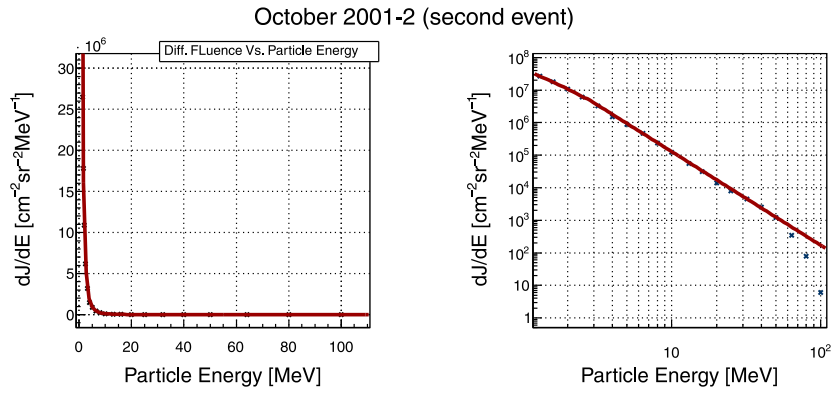


Figure 1. Proton fluence spectra at L1 for one event during October 2001, in linear (left) and logarithmic scale (right).

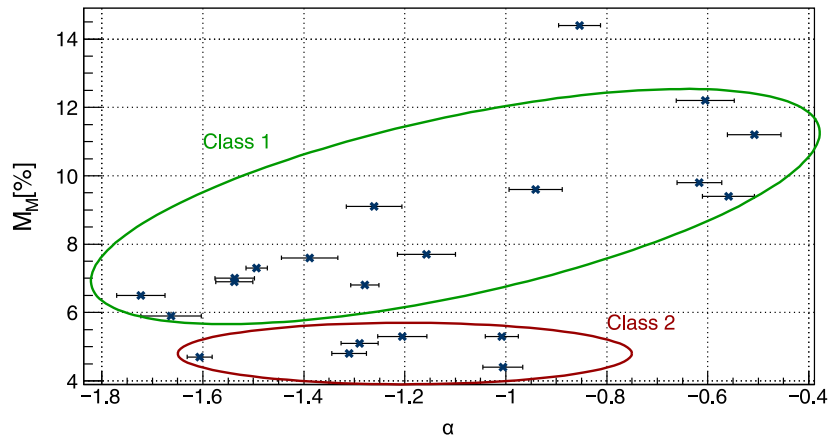


Figure 2. The dependence of the FD magnitude corrected for the magnetospheric effect (M_M) on one of the exponents used to parameterize the proton fluence spectra (α). Two assumed classes of FD events are indicated by the green and red ovals.

3. Methods and Results

IZMIRAN catalogue of Forbush effects (IZMIRAN, 2016) was used as the source of SW related data, as it contains an extensive list of FD events and associated SW parameters. The parameters selected from the IZMIRAN catalogue to be used in the analysis presented here fall into several categories: parameters describing the source (Otype, Stype) or the characteristics of the CME (Vmean, CMEwidth); solar wind parameters (Vmax, KTmax, KTmin); parameters describing interplanetary or geomagnetic field (Bzmin, Kpmax, Apmag, Dstmin); and parameters related to the associated solar flare (Xmagn, Sdur, SSN).

Several machine-learning-based classification methods implemented in the TMVA analysis network (Hoecker et al., 2007) were employed in order to establish the optimal FD magnitude for the separation of two classes (boundary criteria mentioned in Section 2), as well as to determine the optimal classification algorithm. Comparing the efficiency of various methods available in the TMVA (shown of Figure 3), it was found that the optimal separation between two classes is achieved with FD magnitude cut set to 6%, as separation efficiency seems to drop-off beyond that for most methods. Support vector machine (SVM) (Cortes & Vapnik, 1995) was identified as the overall best-performing algorithm.

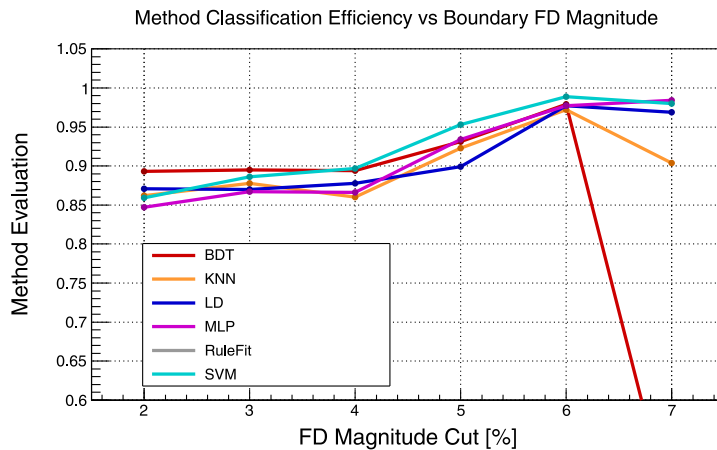


Figure 3. Comparison of the classification efficiency of various TMVA methods dependence on the FD magnitude cut used for class separation.

SVM implementation in the scikit-learn package (Pedregosa et al., 2011) was utilized to identify which of the SW parameters could reliably classify FD events. Third-degree polynomial kernel was found to have the most flexible and efficient performance.

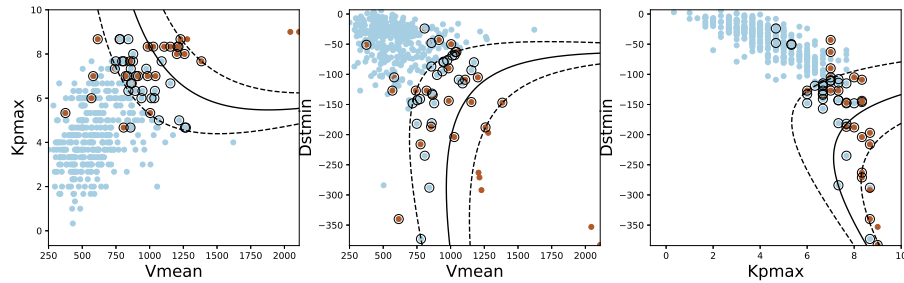


Figure 4. Example of SVM classification using some of SW parameters (mean CME velocity, maximum Kp index and minimal Dst index over the event's duration) that proved to be good input variables for FD classification.

Obtained results appear to confirm the assumption regarding the existence of two classes of FD events. Furthermore, a subset of SW parameters that provide a more reliable classification of FD events was determined. These include mean CME velocity (V_{mean}) and geomagnetic indices (K_{pmax} , A_{pmax} , D_{stmin}), with a possible inclusion of the solar wind speed (V_{max}) and minimal hourly component of the interplanetary magnetic field (B_{zmin}). Decision boundaries between some pairs of mentioned good input variables are showed on Figure 4. Other SW variables proved to be less well suited for classification (as illustrated in Figure 5, for K_{Tmin} and K_{Tmax}).

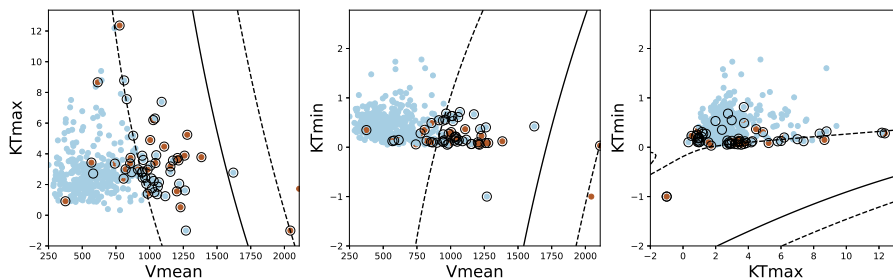


Figure 5. Example of SVM classification using some of SW parameters (K_{Tmax} , K_{Tmin}) that proved to be less well suited input variables for FD classification.

The identified good variables could prove useful in a potential future extension of the analysis. More specifically, they could serve as an input for a regression procedure that would potentially allow the prediction of FD magnitudes.

This prediction would provide either estimates of FD magnitude as measured by Earth-based detectors or, more importantly, estimates of FD magnitudes corrected for the magnetospheric effect.

4. Conclusions

The potential existence of two classes of FD events was investigated. To increase statistical robustness and reduce uncertainties, the analysis was expanded to include a wider set of various space weather parameters. Machine learning techniques were employed in an attempt to separate FD events into two assumed classes, using a number of selected SW parameters as input variables. We compared the efficiency of different machine learning algorithms, and established the optimal boundary value of FD intensity to be used for class separation. The SVM algorithm was selected for the analysis based on its overall performance, efficiency and flexibility, and used to select a subset of space weather variables to be used for reliable classification of FD events. This subset of good variables could prove useful for a future extension of the analysis, where they would provide an input for a regression procedure used to predict FD magnitudes.

Acknowledgements. This work was funded by the Institute of Physics Belgrade, University of Belgrade, through a grant by the Ministry of Science, Technological Development and Innovations of the Republic of Serbia.

We kindly acknowledge the usage of data from the SOHO experiment, as well as data from the catalogue of Forbush effects and interplanetary disturbances provided by the IZMIRAN Space Weather Prediction Center.

References

- Cortes, C. & Vapnik, V., Support Vector Networks. 1995, *Machine Learning*, **20**, 273
- Desai, M. & Giacalone, J., Large gradual solar energetic particle events. 2016, *Living Reviews in Solar Physics*, **13**, 3, DOI: 10.1007/s41116-016-0002-5
- Gopalswamy, N., The Sun and Space Weather. 2022, *Atmosphere*, **13**, DOI: 10.3390/atmos13111781
- Hoecker, A., Speckmayer, P., Stelzer, J., et al., TMVA - Toolkit for Multivariate Data Analysis. 2007, *arXiv e-prints*, physics/0703039, DOI: 10.48550/arXiv.physics/0703039
- IZMIRAN. 2016, Space weather prediction center (IZMIRAN), <http://spaceweather.izmiran.ru/eng/index.html>
- Kahler, S. W., Solar flares and coronal mass ejections. 1992, *Annual Review of Astronomy and Astrophysics*, **30**, 113, DOI: 10.1146/annurev.aa.30.090192.000553
- Pedregosa, F., Varoquaux, G., Gramfort, A., et al., Scikit-learn: Machine Learning in Python. 2011, *Journal of Machine Learning Research*, **12**, 2825

- Savić, M., Veselinović, N., Dragić, A., et al., New insights from cross-correlation studies between solar activity indices and cosmic-ray flux during Forbush decrease events. 2023, *Advances in Space Research*, **71**, 2006, DOI: 10.1016/j.asr.2022.09.057
- Torsti, J., Valtonen, E., Lumme, M., et al., Energetic Particle Experiment ERNE. 1995, *Solar Physics*, **162**, 505, DOI: 10.1007/BF00733438
- Yashiro, S. & Gopalswamy, N., Statistical relationship between solar flares and coronal mass ejections. 2008, *Proceedings of the International Astronomical Union*, **4**, DOI: 10.1017/S1743921309029342

The study of atmospheric effects on cosmic ray muons in the Low Background Laboratory for Nuclear Physics at the Institute of Physics Belgrade

**Mihailo Savić, Nikola Veselinović, Aleksandar Dragić, Dimitrije Maletić,
Dejan Joković, Vladimir Udovičić, Radomir Banjanac and David Knežević**

*Institute of Physics Belgrade, University of Belgrade, Pregrevica 118, 11080
Belgrade, Serbia
Email: msavic@ipb.ac.rs*

Galactic cosmic rays are being modulated in the heliosphere by different processes on the Sun. Upon arriving at Earth, they interact with nuclei in the atmosphere and produce secondary cosmic rays. Changing conditions in the atmosphere affect the propagation of secondary cosmic rays, especially the muon component. To increase the effectiveness of ground-based muon detectors these atmospheric effects need to be decoupled from non-atmospheric ones, and corrected for. To this end, in the Low Background Laboratory for Nuclear Physics at the Institute of Physics Belgrade, we are using several existing techniques but have also developed two new empirical methods for modeling and correction of barometric and temperature effects on cosmic ray muons. Newly developed methods proved to be equally or more effective than the most widely used ones. Such results allow for more precise study of solar modulation and more reliable long term monitoring of galactic cosmic ray flux, and could provide further insight into the relationship between atmospheric parameters and propagation of secondary cosmic rays in the atmosphere.

Cosmic Rays and Their Connection to Space Weather and Earth's Climate

Mihailo Savić^{1*}, Nikola Veselinović¹, Aleksandar Dragić¹,
Dimitrije Maletić¹, Dejan Joković¹, Radomir Banjanac¹,
Vladimir Udovičić¹, David Knežević¹ and Miloš Travar¹

¹Institute of Physics Belgrade, Pregrevica 118, Belgrade, Serbia

*Correspondence: Mihailo Savić, msavic@ipb.ac.rs

Abstract: Cosmic rays have been studied for over a century. In addition to investigating their fundamental properties, such as origin, composition, and acceleration mechanisms, some of the most important studies in the field involve the interaction of cosmic rays within the heliosphere, near-Earth space, and the immediate Earth's environment. These areas have been of particular interest in recent years.

One such type of study focuses on the modulation of cosmic rays by the solar magnetic field and the geomagnetic field in the heliosphere and Earth's magnetosphere, respectively. Among other things, the study of these modulations allows for the indirect observation of solar events, which produce characteristic signatures in the interplanetary magnetic field.

Another interesting aspect of cosmic ray physics involves the interactions of secondary cosmic rays, primarily the muon component, within Earth's atmosphere. Precise models of these interactions allow for corrections for atmospheric effects to be made to the muon flux, increasing the sensitivity of Earth-based detectors. Additionally, these models can enable inverse

diagnostics of the atmosphere, potentially providing an additional technique for atmospheric sounding.

Thus, precise monitoring of cosmic ray variations can serve as a proxy for measuring solar activity and variations in Earth's atmosphere. This can be invaluable in situations where direct measurements are not available and can provide significant contributions to the study of space weather and Earth's climate.

Keywords: cosmic rays, solar physics, atmospheric effects, space weather, Earth climate

New empirical methods for correction of meteorological effects on cosmic ray muons

M. Savić,^{a,*} A. Dragić,^a D. Maletić,^a N. Veselinović,^a D. Joković,^a R. Banjanac,^a V. Udovičić^a and D. Knežević^a

^a*Institute of Physics Belgrade,
Pregrevica 118, 11080 Belgrade, Serbia
E-mail: msavic@ipb.ac.rs*

Flux of muon component of secondary cosmic rays is affected by varying conditions in the atmosphere. Dominant effects are barometric and temperature effect, which reflect variations of atmospheric pressure and atmospheric temperature respectively. Precise modelling and correction for these meteorological effects significantly increases sensitivity of Earth-based muon detectors to variations of primary cosmic ray flux. We are presenting two recently developed empirical methods for correction of meteorological effects on cosmic ray muons. First method is based on principal component analysis, while second employs multivariate analysis using machine learning techniques. Both methods are applied for correction of barometric and temperature effects, but can easily be generalised to take more atmospheric parameters into account. We apply these corrections to muon count rates measured by Belgrade cosmic ray station and study their effect on sensitivity of detection of periodic and aperiodic flux variations of primary cosmic rays. Comparison with the most widely used method for correction of meteorological effects – integral method, as well as with neutron monitor data, demonstrates very high effectiveness of presented methods.

*37th International Cosmic Ray Conference (ICRC 2021)
July 12th – 23rd, 2021
Online – Berlin, Germany*

*Presenter

1. Introduction

Cosmic ray muons (hard component of secondary cosmic rays) are affected by variations of atmospheric parameters as they propagate toward Earth. There are a number of meteorological effects that affect cosmic ray muon flux, most prominent being the *barometric (pressure) effect* and the *temperature effect*, which depend on atmospheric pressure and atmospheric temperature respectively. Apart from fundamental, precise modelling of these effects also has practical importance, as it allows for correction that significantly increases the sensitivity of ground based muon monitors to variations of primary cosmic rays.

A number of methods for correction of barometric and temperature effect have been developed over the years. Some (i.e. method of effective level of generation [1]) are empirical in nature, while others (most notably integral method) rely on the theory of meteorological effects, developed by Dorman [2] among others. All these methods are at least in some part approximative, but for all intents and purposes we have decided to use the integral method as a reference in our analysis, as it gives the most complete treatment of the problem.

The idea behind the work presented here is to try and develop a new, easy to use empirical method, less approximative in nature, compare it to the reference integral method, and investigate whether a more precise model of meteorological effects can be constructed, and possibly some additional information extracted. In order to most completely treat the meteorological effects, both atmospheric pressure and full atmospheric temperature profile need to be taken into account. For analysis that involves that many potentially highly correlated input variables, we have decided to employ modern techniques used for decorrelation and dimensionality reduction, and introduce two new methods for modelling and correction of meteorological effects - *PCA method* based on principal component analysis (PCA), and *MVA method* based on multivariate analysis (MVA) via use of machine learning. Though these two are somewhat similar in nature, a more "hands on" approach of the PCA method can offer a somewhat different insight than the more "blackbox" machine learning approach.

2. Data

2.1 CR data

Muon count rates used in this analysis were measured in the Ground Level Laboratory (GLL) of the Low Background Laboratory for Nuclear Physics, at the Institute of Physics Belgrade [3]. More detailed description of the laboratory and current detector system can be found in some of our previous work [4]. Muon count rates can have arbitrary time resolution but five-minute and hour sums were used in the analysis. For quality and consistency of data reasons, and to remove potential biases due to annual variation, data for a period of one year (from 01.06.2010 to 31.05.2011) were selected.

2.2 Meteo data

This analysis requires information about both atmospheric pressure and vertical atmospheric temperature profile. Data about atmospheric pressure is readily available from the Republic Hydro-meteorological Servis of Serbia. As for the vertical temperature profile data, temperatures for 24

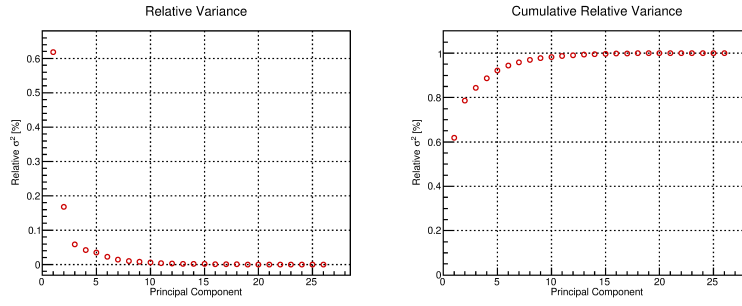


Figure 1: Relative variance (left) and cumulative relative variance (right) for all 26 principal components.

isobaric levels modelled by the Global Forecast System (GFS) [5] were used, starting from the top layer of the atmosphere (10 mb), to the level just above ground level (975 mb). For the above ground layer, locally measured temperature was used as the model was performing poorly there. More details about the preparation of meteorological data is available elsewhere [7].

3. Methodology

3.1 PCA method

Principal component analysis is a well established technique for dimensionality reduction of complex problems that involve large number of correlated variables, and as such very well suited for application to our problem. Using principal component decomposition we have transformed the initial set of correlated meteorological variables (locally measured atmospheric pressure, 24 modelled temperatures, and locally measured ground temperature) to a set of 26 uncorrelated principal components.

Using a series of tests typically used in such analysis (cumulative percentage rule, modified Kaiser's rule, mean eigenvalue rule, ...), we have determined that the first six components (responsible for close to 95% of total variance, as seen on Figure 1) are significant. Composition of the these components is shown on Figure 2, where variables on the x-axis are atmospheric pressure followed by atmospheric temperatures, starting from the top layer of the atmosphere.

Correlative analysis of muon count rate and significant principal components showed practically no correlation between measured muon count rate and the second principal component, further reducing the set of principal components to five. This is an interesting results as this component, mainly composed of lower stratosphere and upper troposphere temperatures, is responsible for close to 17% of total variation of meteorological variables.

Finally, we have determined the muon count rate corrected for meteorological effects according to formula:

$$N_{\mu}^{(corr)} = N_{\mu} - \langle N_{\mu} \rangle \sum_i k_i PC_i, \quad i = 1, 3, 4, 5, 6 \quad (1)$$

where $N_{\mu}^{(corr)}$ is corrected, N_{μ} measured and $\langle N_{\mu} \rangle$ mean muon count rate, while k_i , that correspond to principal components PC_i , are coefficients determined by linear regression, as shown on Figure 3. Full analysis and results are presented in more detail in our other work [8].

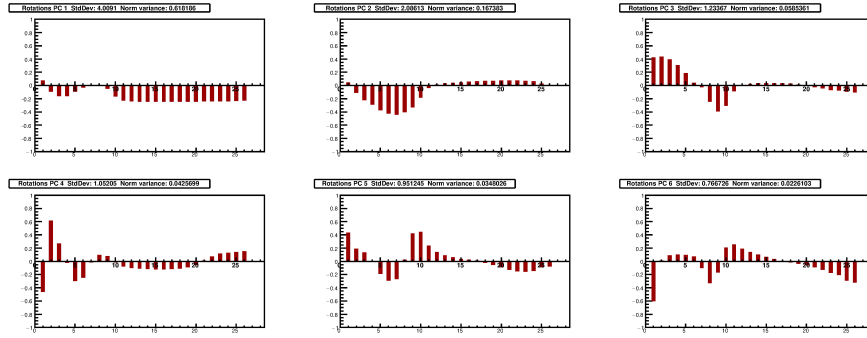


Figure 2: Composition for six most significant principal components. Meteorological variables are on the x-axis, first one being atmospheric pressure, followed by atmospheric temperatures (starting with the top layer of the atmosphere and ending with the ground level).

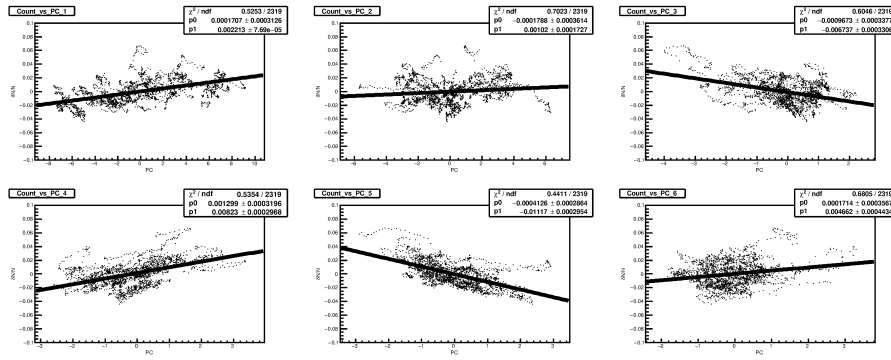


Figure 3: Muon count rate dependence on principal components for six most significant components, distributions fitted with linear function.

3.2 MVA method

Multivariate analysis utilising machine learning techniques can be a powerful tool for modelling of highly correlated systems. We have tested a number of algorithms implemented in Toolkit for Multivariate Data Analysis (TMVA), which has been successfully used for classification and regression problems in particle physics. For us, regression application is of greater interest, as the idea is to train and test multivariate algorithms on a subset of data (for geomagnetically quiet days), where most of the variation can be attributed to atmospheric effects, using meteorological variables as input and muon count rate as the target value. Trained algorithms can be then used on a full data set to predict the muon count rate (which would ideally depend only on meteorological parameters), and corrected muon count rate can be calculated using the formula:

$$N_{\mu}^{(corr)} = \Delta N_{\mu} + \langle N_{\mu} \rangle, \quad \Delta N_{\mu} = N_{\mu}^{(mod)} - N_{\mu}, \quad (2)$$

where $N_{\mu}^{(corr)}$ is corrected, N_{μ} measured, $N_{\mu}^{(mod)}$ modelled, and $\langle N_{\mu} \rangle$ is mean muon count rate.

Minimal average quadratic deviation of modelled from measured value was the only criterion used for optimisation of algorithm parameters in the training phase, so a series of tests have been

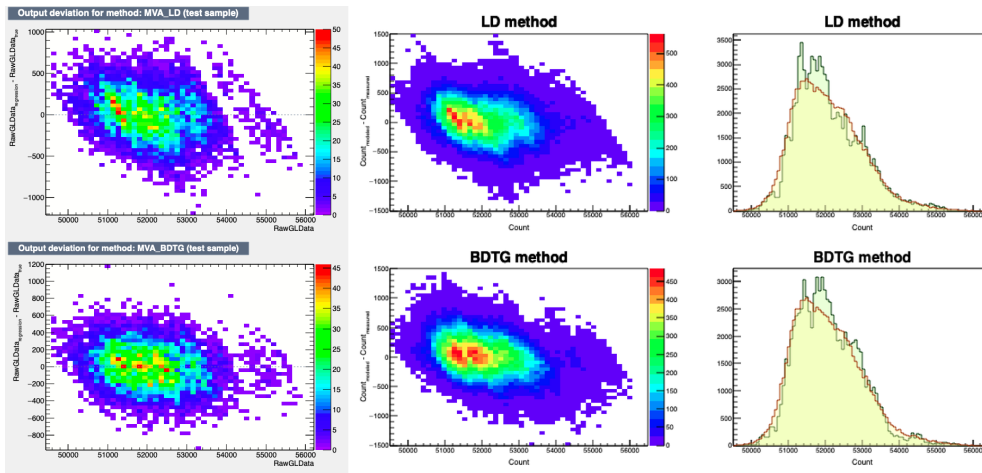


Figure 4: Modelled count rate and its deviation from measured count rate as a function of measured count rate for LD (top) and BDTG (bottom) algorithms. Deviation distributions for test data set are on left, for the full data set are in the middle, while distributions of modelled count rate (compared with the measured one) are on the right.

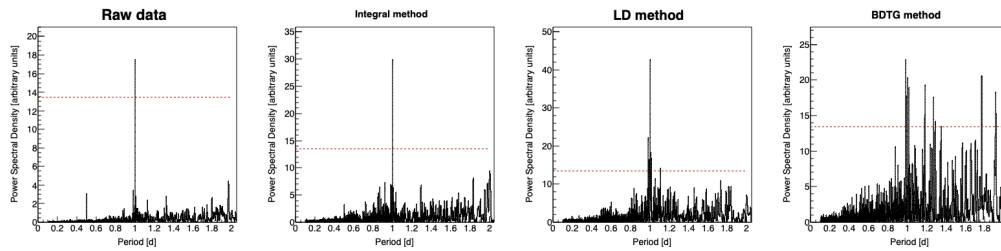


Figure 5: Power spectra for periods in the interval $[0, 2]$ days, for measured data (far left), and data corrected using integral (central left), LD (central right) and BDTG (far right) methods.

devised in order to investigate the consistency of application of trained algorithms and minimise the possibility of artificial features being introduced.

Some of the tests included comparison of distributions of residual deviation of modelled from measured data for the test and full data set, or looking for anomalous features in distributions of modelled count in comparison with measured count distribution (both types of distributions for selected algorithms shown in Figure 4).

Based on these tests, the best performing algorithm proved to be LD (Linear Discriminant method), which is closely related to PCA approach. The second best potential candidate was BDTG (Gradient Boosted Decision Tree method), but there are probably some limits to its applicability, as indicated by spectral analysis (Figure 5). From the remaining tested methods, algorithms based on probability density techniques performed more poorly, which was not that surprising as the problem analysed here involves highly linear dependencies, but poor performance of methods based on neural networks was not expected, and possibly some improvement can be made there.

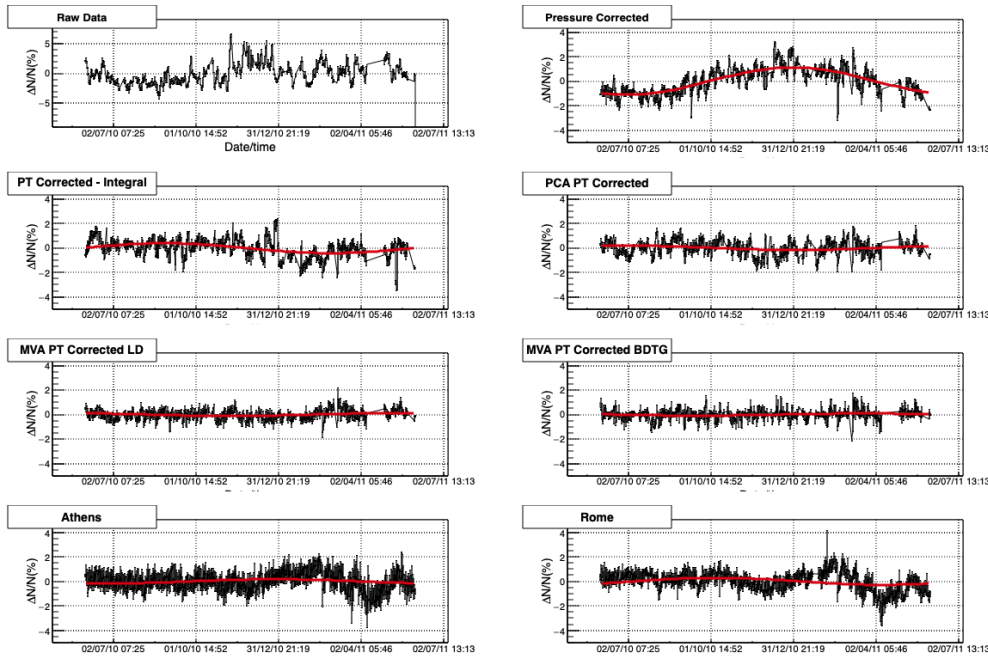


Figure 6: Muon count rate time series and reference neutron monitor data for the period of one year (01.06.2010-31.05.2011), fitted with sine function with a period of one year.

4. Results

4.1 Effect of corrections on periodic CR variations

One way to assess the performance of different methods for correction of meteorological effects could be to compare the efficiency with which they remove the annual variation due to temperature variation. In order to determine this variation, we have fitted pressure corrected data with a sine function, with a period of one year. Amplitude determined from such fit is then used as an estimate of magnitude of the annual variation. The same procedure was used to determine the residual annual variation after the correction via use of different methods (Figure 6). As neutron monitor count rates are usually considered to negligibly depend on atmospheric temperature (at least in the first approximation), we can treat their time series the same way in order to estimate the expected annual variation magnitude.

Table 1 shows amplitudes for the annual variation calculated based on plots in Figure 6, as well as reduction in annual variation relative to pressure corrected data. As can be seen, values for PCA and LD methods are closer to the estimates based on the neutron monitor data than the integral method value, while for BDTG method the value is somewhat smaller.

4.2 Effect of corrections on aperiodic CR variations

To study the effect of corrections on aperiodic variations we have selected the most intense Forbush decrease event in the one year period used for the analysis. For the event that occurred on 18.02.2011, we determined the amplitude of decrease for data corrected via different methods and reference neutron monitors, using procedure suggested by Barbashina et al. [9] (as shown on

Method/ Neutron monitor	P corr.	Integral	PCA	LD	BDTG	Athens	Rome
Annual amplitude [%]	1.11(9)	0.40(3)	0.18(5)	0.11(3)	0.086(9)	0.17(5)	0.29(1)
Relative reduction [% of P corrected]	-	64(10)	84(28)	90(30)	92(30)	-	-

Table 1: Amplitude and reduction of the amplitude of annual variation relative to pressure corrected data (P corr.) for pressure and temperature corrected data (using integral and selected multivariate methods). Athens and Rome neutron monitor data also included for reference

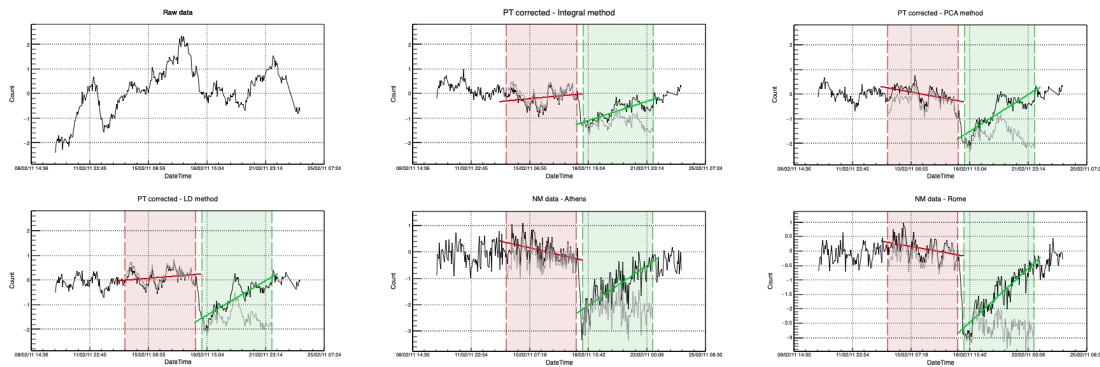


Figure 7: Muon count rate time series and reference neutron monitor data for the period around the Forbush decrease event of 18.02.2011. Highlighted intervals are used for detrending and calculation of decrease amplitude.

Method/ Neutron monitor	Integral	PCA	LD	BDTG	Athens	Rome
FD amplitude [%]	1.38(14)	1.52(21)	1.96(18)	1.10(13)	1.97(15)	2.68(15)
Relative FD amplitude	4.31(44)	4.90(66)	7.09(65)	4.78(56)	5.30(40)	8.65(48)

Table 2: Amplitudes and relative amplitudes for the Forbush decrease event of 18.02.2011 for pressure and temperature corrected muon data and reference neutron monitors

Figure 7). Additionally, as a measure of sensitivity to such events, we have introduced amplitude calculated relative to standard deviation of count rates leading up to the event.

Values for thusly calculated amplitudes and relative amplitudes are shown in Table 2. LD algorithm has values comparable to neutron monitor values, but that is at least in part due to somewhat larger calculated amplitude. This is most likely a feature pertaining to the specific event, as preliminary results for other events outside the interval used in this work show values closer to expected.

5. Conclusions

Two new methods for correction of meteorological effects on cosmic ray muons are introduced. Both are fully empirical, require knowledge about the atmospheric pressure and atmospheric temperature profile and can be applied to any muon monitor. The effect on reduction of the annual variation of CR data, as well as the effect on sensitivity of FD event detection was compared to the integral method and reference neutron monitor data. Their effectiveness was comparable or possibly better than for the integral method, allowing for the possibility that a part of meteorological effects is not taken into account by theory.

References

- [1] A Duperier, "The Meson Intensity at the Surface of the Earth and the Temperature at the Production Level", in Proceedings of the Physical Society. Section A, volume 62, number 11, pages 684, year 1949, doi: 10.1088/0370-1298/62/11/302
- [2] Dorman, L. I., "On the temperature effect of the hard component of cosmic rays", in Reports of Academy of Sciences of USSR (DAN SSSR), volume 95, issue 1, pages 49 - 52, year 1954b
- [3] Low Background Laboratory for Nuclear Physics, url: <http://www.cosmic.ipb.ac.rs/>
- [4] Dragic Aleksandar, Udovicic Vladimir, Banjanac Radomir, Jokovic Dejan, Maletic Dimitrije, Veselinovic Nikola, Savic Mihailo, Puzovic Jovan, Anicin Ivan, "The New Set-Up in the Belgrade Low-Level and Cosmic-Ray Laboratory", in NUCLEAR TECHNOLOGY AND RADIATION PROTECTION, volume 26, number 3, pages 181-192, year 2011, doi: 10.2298/NTRP1103181D
- [5] GFS, url: <https://www.ncdc.noaa.gov/data-access/model-data/model-datasets/global-forecast-system-gfs>
- [6] Berkova M., Belov A., Eroshenko E., Yanke Victor, "Temperature effect of muon component and practical questions of how to take into account in real time", in Astrophysics and Space Sciences Transactions, year 2012, pages 41-44, volume 8, doi: 10.5194/astra-8-41-2012
- [7] Savic Mihailo, Dragic Aleksandar, Veselinovic Nikola, Udovicic Vladimir, Banjanac Radomir, Jokovic Dejan, Maletic Dimitrije, "Effect of pressure and temperature corrections on muon flux variability at ground level and underground", in "25th European Cosmic Ray Symposium", Torino, Italy, eprint: 1701.00164, year 2016
- [8] Savic Mihailo, Dragic Aleksandar, Maletic Dimitrije, Veselinovic Nikola, Banjanac Radomir, Jokovic Dejan, Udovicic Vladimir, "A novel method for atmospheric correction of cosmic-ray data based on principal component analysis", in ASTROPARTICLE PHYSICS, volume 109, pages 1-11, year 2019, doi: 10.1016/j.astropartphys.2019.01.006
- [9] Barbashina N., Dmitrieva Anna, Kompaniets K., Petrukhin A., Timashkov D., Shutenko V., Yakovleva Elena, Yashin, Igor, "Specific features of studying Forbush decreases in the muon flux", in Bulletin of The Russian Academy of Sciences: Physics, year 2009, pages 343-346, volume 73, doi: 10.3103/S1062873809030198

RADON VARIABILITY DUE TO FLOOR LEVEL IN THE TWO TYPICAL RESIDENTIAL BUILDINGS IN SERBIA

Vladimir Udovičić¹, Nikola Veselinovic¹, Dimitrije Maletic¹, Radomir Banjanac¹, Aleksandar Dragic¹, Dejan Jokovic¹, Mihailo Savic¹, David Knezevic¹, Maja Eremic Savkovic²

¹*Institute of Physics Belgrade, University of Belgrade, Belgrade, Serbia*

²*Serbian Radiation and Nuclear Safety and Security Directorate, Belgrade, Serbia*

E-mail: udovicic@ipb.ac.rs

It is well known that one of the factors that influences the indoor radon variability is the floor level of the buildings. Considering the fact that the main source of indoor radon is radon in soil gas, it is expected that the radon concentration decreases at higher floors. Thus, at higher floors the dominant source of radon is originating from building materials and in some cases there may be deviations from the generally established regularity. On the other hand, the radon variability due to floor level, especially in big cities with a much higher number of high-rise buildings and population density compared with rural environments, may have an impact on the assessments of collective dose from radon.

According to the national typology [1], there are six types of residential buildings in Serbia; two for family housing: Freestanding single-family house and single-family house in a row, and four for multi-family housing: Freestanding residential building, residential building - lamella (apartment block with repeated multiple – lamellar – cores and separate entrances), residential building in a row and high-rise residential building. Distribution of buildings by type at national level shows that 97.23% of all residential buildings are family housing. Also, for all defined types of buildings number of floors ranges from one to eight above the ground level. Freestanding family houses are mostly ground floor (37%) or ground floor with loft in use (26%), while there is a very low representation of houses that have more than two floors (5%), with average height of family buildings of 1.4. In that sense, we chose one freestanding single-family house with loft with well-known radon characteristics [2] and one sixteenth floor high-rise residential building for this study.

The indoor radon measurements are performed with two active devices. One was fixed in the living room at the ground level and the second one was moved through the floors of the residential building. Every measuring cycle at the specified floor lasted seven days with the sampling time of the two hours. In this work, the analysis of the obtained results is shown in details.

Ref.

- [1] Jovanović Popović M., Ignjatović D., Radivojević A., Rajčić A., Čuković Ignjatović N., Đukanović Lj. & Nedić M. (2013), National Typology of Residential Buildings in Serbia, Faculty of Architecture University of Belgrade, Belgrade (2013), ISBN 978-86-7924-102-3.
- [2] Udovičić V., Maletic D., Banjanac R., Joković D., Dragic A., Veselinović N., Živanović J., Savić M., Forkapić S. Multiyear Indoor Radon Variability in a Family House – a Case Study in Serbia, Nuclear Technology and Radiation Protection Vol. XXXIII, No. 2 (2018), pp. 174-179.

Cosmic ray flux measurements at Belgrade cosmic rays station during Solar cycle 24

N. VESELINOVIĆ¹, M. SAVIĆ¹, A. DRAGIĆ¹, D. MALETIĆ¹, D. JOKOVIĆ¹, V. UDOVIČIĆ¹, R. BANJANAC¹, D. KNEŽEVIĆ¹

¹ *Institute of physics, University of Belgrade, Pregrevica 118, Belgrade, Serbia*

E-mail: veselinovic@ipb.ac.rs

It has been well known for more than half a century that solar activity is responsible for modulation of galactic cosmic ray reaching Earth (Potgieter 2013). Low-background Laboratory for Nuclear Physics at the Institute of Physics, Belgrade is dedicated to low-background spectroscopy and cosmic rays measurement. Measurements are performed at interconnected spaces: at the surface level (78m a.s.l.) and in the underground laboratory at the depth of 25 m.w.e. with identical sets of detectors and analyzing electronics thus creating opportunity to monitor simultaneously muon flux at different energies. The cosmic-ray muon count rate and energy loss spectra in plastic scintillator detectors are recorded and from experimental data and with the use of GEANT4 computer simulation the flux and vertical intensities have been determined (Veselinović *et al.* 2017). The aim of the present work is to present study of energy dependent solar modulation process during Solar cycle 24 utilizing a shallow underground laboratory with detector configuration sensitive to primaries in the energy region exceeding sensitivity of neutron monitors (Savić *et al.* 2019).

References

- Potgieter, M.S.:2013, *Living Rev. Sol. Phys.* **10**, 3
Savić M. et al.: 2019, *Advances in Space Research*, **63**,4
Veselinović N. et al. :2017, *Nuclear Instruments and Methods in Phy. Res. A* , **875**

CORRELATION ANALYSIS OF SOLAR WIND PARAMETERS AND SECONDARY COSMIC RAYS FLUX

NIKOLA VESELINović, MIHAILO SAVIĆ, ALEKSANDAR DRAGIĆ,
DIMITRIJE MALETIĆ, DEJAN JOKOVIĆ, RADOMIR BANJANAC,
VLADIMIR UDOVIČIĆ and DAVID KNEŽEVIĆ

*Institute of Physics Belgrade
Pregrevica 118, Belgrade, Serbia
E-mail veselinovic@ipb.ac.rs*

Abstract. Galactic cosmic rays (GCRs) entering the heliosphere are disturbed by solar wind and Sun's magnetic field, see Potgieter 2013 Coronal mass ejections (CMEs) structure and shockwave can additionally modulate GCRs, which could result in a transient decrease followed by a gradual recovery in the observed galactic cosmic ray intensity, known as Forbush decrease (FD) see Maričić et al.2014. CMEs are regularly observed via in-situ measurements of plasma and magnetic field in near-Earth space so it is important to understand the relationship between the FDs and near-Earth particles flux associated with these CMEs.

During last 24th Solar cycle, unprecedented extent of heliospheric observations has been achieved thanks to the several new satellites in orbit and CMEs can be observed throughout the heliosphere from the Sun to the Earth, allowing us to relate ground observations to remote sensing data, for Mars see Freiherr von Forstner et al. 2019. We analyzed the dynamics of the variation of galactic cosmic rays (GCR) combining in situ measurement of the particles species present in solar wind with ground observations (worldwide neutron monitor (NM) network and Belgrade's muon detector). This dynamics compared for several CMEs induced FD events. Variations in interplanetary plasma and field parameters during, before, and after the Forbush decreases were examined. Correlation between the 1-hour variations of GCR and several different one-hour averaged particle fluxes was found during FDs and it depends on energy of the particles of the solar wind as well as cut-off rigidities of secondary cosmic rays detectors on ground. These correlations were compared with correlation between same parameters during quiet period of the solar activity. This cross-correlation analysis can help in better understanding of Earth-affecting CMEs and space weather but also to predict GCR flux during extreme solar events.

References

- Freiherr von Forstner, J. L. et al. : 2019, *Space Weather*, **17**, 586– 598.
Maričić, D., Vršnak, B., Dumbović, M. et al. : 2014, *Sol Phys* **289**, 351–368.
Potgieter, M. S.: 2013, *Living Rev. Sol. Phys.* **10**, 3 (2013).

New insights from cross-correlation studies between solar activity indices and cosmic-ray fluxes during Forbush decreases

Nikola Veselinović, Mihailo Savić, Aleksandar Dragić, Dimitrije Maletić, Radomir Banjanac, Dejan Joković, David Knežević and Vladimir Udovičić

*Institute of Physics Belgrade, University of Belgrade, Pregrevica 118,
11080 Belgrade, Serbia*

Observed galactic cosmic rays intensity can be subjected to transient decrease, called Forbush decreases, which can be driven by solar activity and shockwaves in Heliosphere with solar origin, in terms of flares and coronal mass ejections (Miteva et al., 2018 [1]). By combining in-situ measurements, using space borne instruments, of solar energetic particles with ground-based observations we investigate the relationship between solar activity indices, as well as event-integrated spectra of solar energetic particles (Belov et al, 2021 [2]) with intensity measurements of cosmic rays during these strong transient decreases. We present cross-correlation studies (Veselinović et al, 2021 [3]) using data from the SOHO/ERNE measurements at 19 energy thresholds between 1.6 and 90 MeV/n, neutron monitors and solar observatories collected during strongest Forbush decreases over last two solar cycles.

References

- [1] Miteva, R., Samwel, S.W. & Costa-Duarte, M.V. The *Wind*/EPACT Proton Event Catalog (1996 – 2016). *Sol Phys* **293**, 27 (2018).
<https://doi.org/10.1007/s11207-018-1241-5>
- [2] Belov A. *et al* 2021 *ApJ* **908** 5. <https://doi.org/10.3847/1538-4357/abd724>
- [3] Veselinović, N., Savić, M., Dragić, A. *et al*. Correlation analysis of solar energetic particles and secondary cosmic ray flux. *Eur. Phys. J. D* **75**, 173 (2021). <https://doi.org/10.1140/epjd/s10053-021-00172-x>

Simulation of production of the cosmogenic radionuclides in loess

Development of a Geant4 application which models propagation and interaction of cosmic rays with the soil - loess, including the simulation of creation of cosmogenic radionuclides in soil is reported. CORSIKA is used to simulate the propagation of cosmic rays through atmosphere to the ground. The distribution of concentration of produced radionuclides by depth from simulation is presented thus allowing alternative method of study loess geomorfology but also to study cosmic ray flux modulated by the sun activity on long-term scale. The possibility of detection using laboratory equipment of these cosmogenic radionuclides created in soil is discussed.

Length of presentation requested

Oral presentation: 8 min + 2 min questions (Poster-type talk)

Please select between one and three keywords related to your abstract

Cosmic Rays

2nd keyword (optional)

Nuclear physics - experimental

3rd keyword (optional)

Primary authors: VESELINOVIC, Nikola; MALETIC, Dimitrije; SAVIC, Mihailo (Institute of Physics Belgrade); Dr DRAGIĆ, Aleksandar (Institute of Physics Belgrade); JOKOVIC, Dejan (Institute of Physics, University of Belgrade); Dr BANJANAC, Radomir (Institute of physics Belgrade); Dr KNEŽEVIĆ, David (Institute of physics Belgrade); Dr UDOVIČIĆ, Vladimir (Institute of Physics Belgrade)

Presenter: VESELINOVIC, Nikola

Nucleosynthesis

80

The radiogenic heating of planets and the ^{40}K question

Author: Georgios Perdikakis

¹ *Central Michigan University*

Corresponding Author:perdi1g@cmich.edu

The quantity of radioactive isotopes in a planet's mantle and the evolution of its heating due to the isotopes' radioactive decay determines the capability of that planet to develop geological features associated with a habitable environment, such as surface crust and plate tectonics. The solar system was formed from a large quantities of Potassium (K), a major element available in the interstellar medium at the time it subsequently deposited inside our planet's mantle and Potassium's long-lived radioactive isotope ^{40}K is still present in large quantities inside the planet. The beta particles that it emits heat up earth's mantle for the last several billions of years and largely contribute to the habitable nature of Earth. Predicting the amount of ^{40}K enrichment in the solar system of a given exoplanet would be fundamental for a reliable calculation of the planet's heating evolution and would allow us to make estimates on the likely existence of a habitable environment. Potassium, however, has a complex production and (destruction) mechanism in the r-process nucleosynthesis point of view, the uncertainty in the abundance of ^{40}K is associated with the reactions that create and destroy ^{40}K in stellar nucleosynthesis processes and the corresponding reaction rates. In my talk, I will discuss the importance of potassium in the context of exoplanet-related research, the origin of potassium in stars, the nuclear physics aspects that affect the existence of ^{40}K and current experimental efforts to constrain the relevant reaction rates.

Length of presentation requested:

Oral presentation: 25 min + 5 min questions (Review-type talk)

Please select between one and three keywords related to your abstract:

Nuclear physics - experimental

2nd keyword (optional):

Nucleosynthesis

3rd keyword (optional):

Habitability, Exoplanets

81

Simulation of production of the cosmogenic radionuclides in loess

Authors: Nikola Veselinović¹, Dimitrije Maletić², Mihailo Savić³, Aleksandar Dragić⁴, Dejan Joković¹, Radomir Banjanač¹, David Knežević¹, Vladimir Udovičić¹¹ *Institute of Physics Belgrade*² *Institute of Physics, University of Belgrade*³ *Institute of physics Belgrade*⁴ *Institute of physics Belgrade*

⁵ *Institute of Physics Belgrade*

Corresponding Authors: veselinovic@ipb.ac.rs, maletic@ipb.ac.rs, yokovic@ipb.ac.rs, banjanac@ipb.ac.rs, davidk@ipb.ac.rs, udovicic@ipb.ac.rs, dragic@ipb.ac.rs, msavic@ipb.ac.rs

Development of a Geant4 application which models propagation and interaction of cosmic rays with the soil - loess, including the simulation of creation of cosmogenic radionuclides in soil is reported. CORSIKA is used to simulate the propagation of cosmic rays through atmosphere to the ground. The distribution of concentration of produced radionuclides by depth from simulation is presented thus allowing alternative method of study loess geomorfology but also to study cosmic ray flux modulated by the sun activity on long-term scale. The possibility of detection using laboratory equipment of these cosmogenic radionuclides created in soil is discussed.

Length of presentation requested:

Oral presentation: 8 min + 2 min questions (Poster-type talk)

Please select between one and three keywords related to your abstract:

Cosmic Rays

2nd keyword (optional):

Nuclear physics - experimental

3rd keyword (optional):

82

Spectroscopy of ^{48}Cr by the $^{50}\text{Cr}(p, t)^{48}\text{Cr}$ reaction

Authors: Philip Adsley¹, Sifundo Binda²

¹ *Texas A&M University*

² *WITS/ITL*

Corresponding Authors: padsley@tamu.edu, 1395463@students.wits.ac.za

The radioactive nucleus ^{44}Ti is thought to be produced in Core-Collapse Supernovae (CCSNe) with the amount produced being sensitive to internal dynamics of the explosion. ^{44}Ti is a potential diagnostic tool for understanding the behaviour of these stellar explosions.

The amount of ^{44}Ti produced depends not only on the production reactions but also on the destruction reactions, most notably the $^{44}\text{Ti}(\alpha, p)^{47}\text{V}$ reaction which proceeds through states in the compound nucleus ^{48}Cr . This reaction is usually treated through statistical models (see, for example, the recent study by Chipps and collaborators [PhysC 102,035806](#)) but it is not clear that this is valid given the limitations of the levels which can be populated in ^{44}Ti fusion (natural parity, isoscalar) and the influence of α -particle clustering behaviour on other α -particle induced reactions.

Spectroscopy in the Gamow Window of the $^{44}\text{Ti}(\alpha, p)^{47}\text{V}$ reaction has been performed using the $^{50}\text{Cr}(p, t)^{48}\text{Cr}$ reaction with the K600 magnetic spectrometer at iThemba LABS in South Africa. A number of excited states have been observed, many for the first time, giving insights into the validity of statistical models for the $^{44}\text{Ti}(\alpha, p)^{47}\text{V}$ reaction.

Length of presentation requested:

Oral presentation: 8 min + 2 min questions (Poster-type talk)

Please select between one and three keywords related to your abstract:

Nuclear physics - experimental

CORRELATION OF SOLAR WIND PARAMETERS WITH COSMIC RAYS OBSERVED WITH GROUND STATION

Nikola Veselinović¹, Mihailo Savić¹, Aleksandar Dragič¹, Dimitrije Maletić¹, Dejan Joković¹, Radomir Banjanač¹, Vladimir Udovičić¹, David Knežević¹

¹Institute of Physics, University of Belgrade, Pregrevica 118, 11080 Belgrade, Serbia;
e-mail: nikola.veselinovic@ipb.ac.rs, mihailo.savic@ipb.ac.rs, aleksandar.dragic@ipb.ac.rs,
dimitrije.maletic@ipb.ac.rs, dejan.jokovic@ipb.ac.rs, radomir.banjanac@ipb.ac.rs, vladimir.udovicic@ipb.ac.rs,
david.knezevic@ipb.ac.rs

Solar activity and conditions in heliosphere can be a critical driver of human impact space weather as they can damage electronics and threaten the lives of astronauts as well as increase radiation hazards to high-altitude, high-latitude aviation. It has been well known for more than half a century that solar activity has a strong influence of cosmic ray flux reaching to the Earth (anti-correlation). Solar wind, by both particle drift patterns and structures is responsible for galactic cosmic ray flux modulation, hence the flux of observed galactic cosmic rays varies (GCR) with the solar wind reflecting the solar activity so one could use cosmic ray flux measured at the surface of the earth and in space to monitor the space weather and solar activity. Drops of a few percent in near-Earth GCR flux (Forbush decreases) are well known to be associated with the near-Earth passage of solar wind structures resulting from corotating interaction regions (CIRs) and transient coronal mass ejections (CMEs). We investigated how FDs vary with the properties of the driving solar wind structure. In this context, we study correlations between galactic cosmic rays (GCR) and particles of different species and energies of the solar wind based on the analyses of observational data from our muon detector, worldwide network of neutron detectors and satellites. We perform comparative analysis of Forbush events during Solar cycle 24, which happens during *STEREO* era, enabling in situ and remote observations of solar wind particles' flux from three well-separated heliospheric locations.

Heliospheric and atmospheric parameters affecting cosmic rays flux measured at Belgrade muon station

Nikola VESELINOVIĆ, Mihailo Savić, Aleksandar Dragić, Dimitrije Maletić, Dejan Joković, Radomir Banjanac, David Knežević, Vladimir Udovičić

*The Low-background Laboratory for Nuclear Physics, Institute of Physics, University of Belgrade
veselinovic@ipb.ac.rs*

Belgrade Muon station monitor secondary cosmic ray flux for two decades. It is a part of The Low-background Laboratory for Nuclear Physics (LBLNP) at the Institute of Physics, Belgrade, Serbia. Measurements are done simultaneously at ground level and at shallow-underground level which is suitable for studies of energy dependence of cosmic-ray variations. Overview of laboratory's activity and research is given. Progress in several different research topics studied, ranging from correction of secondary cosmic rays flux on atmospheric parameters using multivariate analysis, upgrade of instrumental setup and determining concentration of in situ cosmogenic radionuclides based on simulation, to studying correlation between solar wind parameters and measured muon flux during transient or quasi-periodic cosmic-ray variations like Forbush decreases. Also a planned future collaboration is discussed with goal of developing and using worldwide network of novel, low-cost and portable detectors for cosmic ray muon and neutron flux measurements and its application in studying heliospheric and environmental parameters.

KEYWORDS: cosmic rays, measured flux, ground and underground station

MULTI-INSTRUMENTAL INVESTIGATION OF THE POWERFUL SOLAR FLARES IMPACT ON THE IONOSPHERE: CASE STUDY

**A. Kolarski¹, N. Veselinović¹, V. A. Srećković¹, Z. Mijić¹,
M. Savić¹ and A. Dragić¹**

¹Institute of Physics Belgrade, UB, Pregrevica 118, 11080 Belgrade, Serbia

*E-mail : aleksandra.kolarski@ipb.ac.rs, nikola.veselinovic@ipb.ac.rs,
vlada@ipb.ac.rs, zoran.mijic@ipb.ac.rs, mihailo.savic@ipb.ac.rs,
aleksandar.dragic@ipb.ac.rs*

Case study of energetic solar events which included strongest solar flare of the previous solar cycle, X9.3 from 6 September 2017 and accompanying Coronal Mass Ejections (CMEs) directed towards Earth is presented through ionospheric and primary cosmic rays implications. Conducted analysis and numerical simulations were done both on data from ground-based Belgrade Very Low Frequency (VLF) and Cosmic Ray (CR) stations and space-borne satellite platforms of GOES and SOHO missions. Some of the main findings regarding related disturbances of ionospheric parameters and on primary cosmic rays are presented in this work.

Study on 2021 November 4 Forbush decrease with Belgrade muon station

**Dimitrije M. Maletić, Nikola B. Veselinović, Mihailo R. Savić,
Aleksandar L. Dragić, Radomir M. Banjanac, Dejan R. Joković,
David Knezević, Miloš Travar and Vladimir I. Udovičić**

*Institute of Physics Belgrade, Pregrevica 118, 11080 Belgrade, Serbia
E-mail: maletic@ipb.ac.rs*

The first significant Forbush decrease of rising phase of the solar cycle 25 was recorded on November 4, 2021. It was detected with numerous ground based cosmic rays stations around the world (Chilingarian et al. 2022). including Belgrade cosmic rays muons' station. Belgrade cosmic rays' muon station is located at the Institute of Physics Belgrade and it constantly measures muon flux during cycle 24 (and 25) originated from primary cosmic rays with higher median energy than neutron monitors (Veselinović et al. 2017). This rapid decrease in the observed galactic cosmic ray intensity was the result of a series of coronal mass ejections during October 28–November 2. (Li et al. 2022), and their interplanetary counterparts (ICME) that led to strong G3-class geomagnetic storm, auroras and even first Ground Level Enhancement of the cycle 25 (Papaioannou et al. 2022). We discuss here the variation of cosmic rays' flux detected with ground-based detectors with different median rigidity during this recent event. Also, we compare conditions, measured in-situ, in interplanetary space around Earth, flux of solar wind protons measured with SOHO/ERNE probe, at Lagrange Point 1 and properties of detected Forbush decrease in order to asses implication for solar-terrestrial coupling processes.

References

- Chilingarian, A., Hovsepyan, G., Martoyan, H., Karapetyan, T., et al., 2022
<https://arxiv.org/abs/2212.13514>
Li, X., Wang, Y., Guo, J., Lyu, S., 2022 *ApJL* 928 L6
Papaioannou, A., Kouloumvakos, A., Mishev, A., Vainio R., et al., 2022, *A&A*, 660 L5
Veselinović, N., Dragić, A., Savić, M., Maletić, D., et al. 2017, *NiM A*, 875

Multi-instrumental investigation of extreme space weather events in September 2017: Data and modeling

**Nikola B. Veselinović, Aleksandra Kolarski, Vladimir A. Srećković,
Zoran R. Mijić, Mihailo R. Savić and Aleksandar L. Dragić**

*Institute of Physics Belgrade, Pregrevica 118, 11080 Belgrade, Serbia
E-mail: veselinovic@ipb.ac.rs*

Strong Solar activity during September 2017, despite being in the declining phase of cycle 24, produced several solar flares, accompanied by a series of coronal mass ejections that led to complex and geoeffective plasma structures in the heliosphere (Luhmann et al., 2020). These events, involving interactions between plasma structures (Albert et al., 2020), as well as their influence on Earth's environment are very difficult to forecast.

A number of studies used different approaches to analyze influence of Solar activity on particular phenomena either in heliosphere (Kozev et al., 2022, Savić et al., 2023) or ionosphere responses (Kolarski et al., 2022, Srećković et al., 2021). Recently, several investigations based on multi-instrumental measurements and numerical simulations show more comprehensive insight into the ionospheric responses and change of primary cosmic rays' flux due to the extreme Solar activity (Kolarski et al., 2023, Barta et al., 2022).

The focus of this research is to investigate the phenomena induced by the extreme event in near-Earth space and Earth's atmosphere during September 2017, with an emphasis on studying and modeling the variations in cosmic ray flux and disturbances in the lower ionosphere in correlation with Solar activity. The investigation is based on ground-based measurements such as from neutron monitors, very low-frequency (VLF) radio wave stations, and cosmic ray detectors, as well as in situ measurements from different space probes.

The results of this study show that the ionospheric atomic and molecular data like sharpness and effective reflection height and electron density obtained from Belgrade VLF data measurements, are in correlation with incident X-ray flux while time series of cosmic rays' flux measured at Belgrade muon station correspond to disturbance of near-Earth heliospheric conditions.

The multi-instrumental approach accompanied with numerical modeling of specific space weather events additionally contribute to better understanding of solar-terrestrial coupling processes.

References

- Albert, D., Antony, B., Ba, Y. A., Babikov, Y. L., et al., 2020, *Atoms*, 8, 76
- Barta, V., Natras, R., Srećković, V., Koroncay, D., et al., 2022, *Front. Environ. Sci.* 10:904335.
- Kolarski, A., Veselinović, N., Srećković, V. A., Mijić, Z., et al., 2023, *Remote Sens.* 15, 1403
- Kolarski, A., Srećković, V. A., Mijić, Z. R., 2022, *Appl. Sci.* 12, 582
- Kozarev, K., Nedal, M., Miteva, R., Dechev, M. and Zucca, P., 2022, *Front. Astron. Space Sci.* 9:801429.
- Luhmann, J. G., Gopalswamy, N., Jian, L. K. et al., 2022, *Sol Phys* 295, 61
- Savić, M., Veselinović, N., Dragić, A., et al., 2023, *Adv. Sp. Research*, 71,4
- Srećković, V. A., Šulić, D. M., Vujčić, V., Mijić, Z. R., et al., *Appl. Sci.* 2021, 11, 11574

Classification of Forbush decrease events utilizing machine learning

**Mihailo R. Savić, Nikola B. Veselinović, Aleksandar L. Dragić,
Dimitrije M. Maletić, Radomir M. Banjanac, Dejan R. Joković,
David Knežević, Miloš Travar and Vladimir I. Udovičić**

*Institute of Physics Belgrade, Pregrevica 118, 11080 Belgrade, Serbia
E-mail: msavic@ipb.ac.rs*

The potential existence of two classes of Forbush Decrease (FD) events has already been suggested by the analysis of energetic proton fluence spectra measured at L1 (Savić et al. 2023). We further explore this assumption in the work presented herein.

The most powerful coronal mass ejections, which can lead to Forbush Decreases, often occur during periods of increased solar activity. Coincidentally, such intense phenomena can also result in complex interactions in the heliosphere, where accurate determination of energetic proton fluence may become more difficult. Therefore, in order to increase statistical robustness and reduce uncertainties, we try to expand the classification procedure to include a wider set of various space weather parameters, that are more reliably determined.

The IZMIRAN database of Forbush decreases (IZMIRAN 2021) serves as an online repository, and contains an extensive list of FD events, along with a large number of associated space weather parameters. The idea for the presented analysis is to employ machine learning techniques in an attempt to separate FD events into two assumed classes, using a number of selected parameters from the IZMIRAN database as input variables. We compared the efficiency of different machine learning algorithms using the TMVA package integrated in the ROOT analysis framework (Hocker 2007), and tried to establish the optimal boundary value of FD intensity to be used for separation. The Support Vector machine algorithm (SVM, Cortes 1995) was selected for the analysis based on its overall performance, efficiency and flexibility. Finally, a subset of space weather variables to be used for classification was selected based on their predictive power.

References

- Cortes, C., Vapnik, V., 1995, Mach Learn, 20, 273–297.
Hocker, Andreas; 2007, CERN-OPEN-2007-007.
IZMIRAN Space Weather Prediction Center, 2021
Savić, Mihailo; Veselinović, Nikola; Dragić, Aleksandar, Maletić, Dimitrije; Joković, Dejan; Udovičić, Vladimir; Banjanac, Radomir; Knežević, David; 2023, ASR, 71, 4, 2006-2016.

Serbian space weather research activities

*Nikola VESELINOVIĆ
Institute of Physics Belgrade
veselinović@ipb.ac.rs*

Strong variation of solar activity and accompanied space weather phenomena can affect Earth's environment and our civilization. Cosmic rays, originated from outside of the Solar system are also sensitive to properties of interplanetary medium and violent energetic events originated from the Sun that can additionally modulate cosmic rays. Here, a correlation between various space weather indices and energetic particles flux measured in-situ at L1 and measured ground-level cosmic ray muon flux is investigated. Found connection between proton flux fluence spectra and selected parameters of associated Interplanetary coronal mass ejections and variation of primary cosmic rays can improve analysis of how violent energetic events, with irregular sporadic occurrence, affect space weather and induce primary cosmic ray variations but also affect Earth's magnetosphere and upper atmosphere. These events can produce Forbush decreases, a transient decrease in the observed galactic cosmic ray intensity that can be detected by ground-based cosmic ray detectors. Ground-based muon detectors are sensitive to higher energies of primary cosmic rays than the network of standard devices like neutron monitors and can expand the range of energy of monitored cosmic rays. Plans for a worldwide network of ground muon detectors are discussed as well as plans and goals of space weather related Serbian CUBESAT project. The goal of CUBESAT project, still in the initial phase, is to study solar activity from LEO and to correlate acquired data with VLF measurements of the ionosphere and CR measurements conducted at the Institute of Physics. These projects will have strong educational and outreach components because of the necessity to develop research capacity in study of the integrated Sun-Earth system.

KEYWORDS: solar energetic particles; secondary cosmic ray muon flux; ground-based and satellite observations

SIMULACIJA PRODUKCIJE NEUTRONA MIONIMA IZ KOSMIČKOG ZRAČENJA U OLOVNOJ ZAŠTITI GERMANIJUMSKOG DETEKTORA

**Dejan JOKOVIĆ, Dimitrije MALETIĆ, Vladimir UDOVIČIĆ,
Radomir BANJANAC, Aleksandar DRAGIĆ, Mihailo SAVIĆ,
Nikola VESELINOVIĆ i David KNEŽEVIĆ**

*Institut za fiziku u Beogradu, Univerzitet u Beogradu, Beograd, Srbija,
yokovic@ipb.ac.rs, maletic@ipb.ac.rs, udovicic@ipb.ac.rs, banjanac@ipb.ac.rs,
dragic@ipb.ac.rs, msavic@ipb.ac.rs, veselinovic@ipb.ac.rs, davidk@ipb.ac.rs*

SADRŽAJ

Zbog svojih osobina, olovo se uobičajeno koristi kao materijal za zaštitu germanijumskih detektora. Mioni iz kosmičkog zračenja u interakcijama sa olovom proizvode sekundarno zračenje, koje doprinosi ukupnom fonu detektora. Značajan deo ove komponente fona čine neutroni proizvedeni u interakcijama miona u olovnoj zaštiti. Neutroni mogu biti poseban problem u eksperimentima u dubokim podzemnim laboratorijama. U podzemnoj laboratoriji u Institutu za fiziku u Beogradu, germanijumski detektor, koji se nalazi u olovnoj zaštiti, može raditi u koincidenciji sa mionskim detektorom. U ovom režimu rada mogu se proučavati različiti efekti u germanijumskom detektoru izazvani mionima, posebno efekti koji potiču od neutrona proizvedenih mionima. Ovde su predstavljeni rezultati Geant4 simulacija produkcije neutrona u olovu mionima iz kosmičkog zračenja. Rezultat ovih simulacija je procena prinosa neutrona – broja proizvedenih neutrona u olovu po jedinici dužine puta – u interakcijama miona. Pored toga, određena je raspodela multipliciteta neutrona, kao broja proizvedenih neutrona u jednoj interakciji.

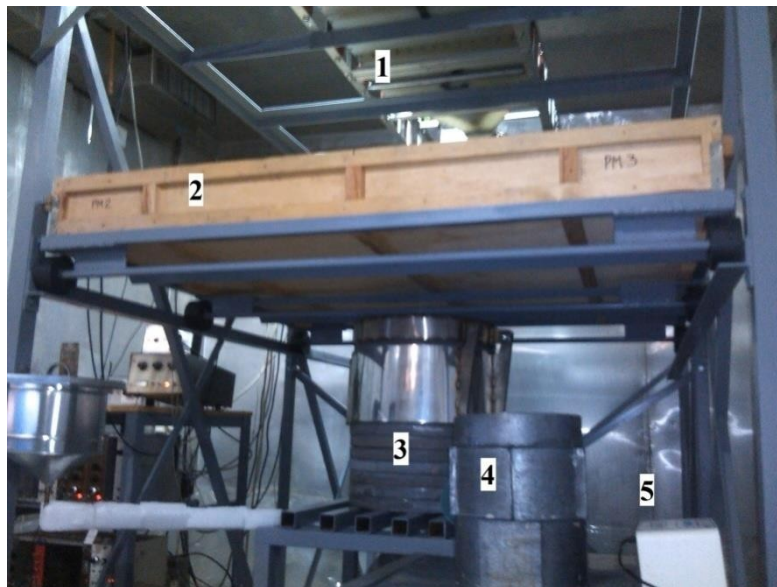
1. Uvod

U eksperimentima u kojima se traže retki događaji glavni problem je redukcija fonskog zračenja. Zato se ovi eksperimenti vrše u podzemnim laboratorijama, gde je fon u odnosu na površinu Zemlje znatno niži. Međutim, mioni iz kosmičkog zračenja su veoma prodorne čestice, prisutne i u dubokim podzemnim laboratorijama, i zato čine važan izvor fonskog zračenja u ovakvim osetljivim eksperimentima. Poseban problem je mionima indukovano sekundarno zračenje u detektorima i njihovoj okolini (detektorskoj zaštiti, zidovima, itd). Značajan doprinos fonu potiče od neutrona proizvedenih u interakcijama miona sa materijalom u okolini detektora [1].

U Niskofonskoj laboratoriji Instituta za fiziku u Beogradu intenzitet kosmičkog zračenja kontinuirano se meri od 2002. godine [2,3]. Geografski položaj laboratorije je takav da se kosmičko zračenje koje se detektuje u osnovi sastoji od mionske tvrde komponente, uz izvestan procenat meke elektromagnetne komponente. Laboratorija se sastoji od nadzemnog i plitko ukopanog podzemnog dela na dubini od 12 m ispod površine. Zemljište (les) iznad podzemne laboratorije ima gustinu približno $2,0 \text{ g/cm}^3$ – efektivni apsorpcioni sloj iznosi približno 25 hg/cm^3 (25 m.w.e.). Na toj dubini prisutna je praktično samo mionska komponenta kosmičkog zračenja. Zbog svojih niskofonskih karakteristika, laboratorija je osposobljena za izučavanje različitih pojava generisanih kosmičkim zračenjem, pre svega događaja indukovanih mionima iz kosmičkog zračenja u germanijumskim detektorima, kao i u pasivnoj zaštiti detektora.

U podzemnoj laboratoriji nalazi se HPGe detektor deklarisan aktivne zapremine 149 cm^3 i relativne efikasnosti 35 %. Podzemna pozicija detektora, zajedno sa olovnom

zaštitom debljine 12 cm, daje značajno smanjenje fonskog zračenja. Pored pasivne zaštite, za aktivnu veto zaštitu germanijumskog detektora mogu se koristiti postojeći scintilacioni detektori kosmičkog zračenja. Plastični scintilacioni detektor nalazi se neposredno iznad olovne zaštite; dimenzije detektora su 100 cm × 100 cm × 5 cm. Oba detektora – HPGe i scintilacioni – vezani su za analogno-digitalni konvertor, koji omogućava snimanje i čuvanje svih detektovanih događaja. Svi događaji analiziraju se *off-line*. Uz odgovarajuće selekzione kriterijume mogu se izdvojiti svi koincidentni i/ili antikoincidentni događaji u scintilacionom i HPGe detektoru [4,5].



Slika 1. Ekperimentalna konfiguracija u podzemnoj laboratoriji: scintilacioni detektori (1,2) i germanijumski detektor u olovnoj zaštiti (3).

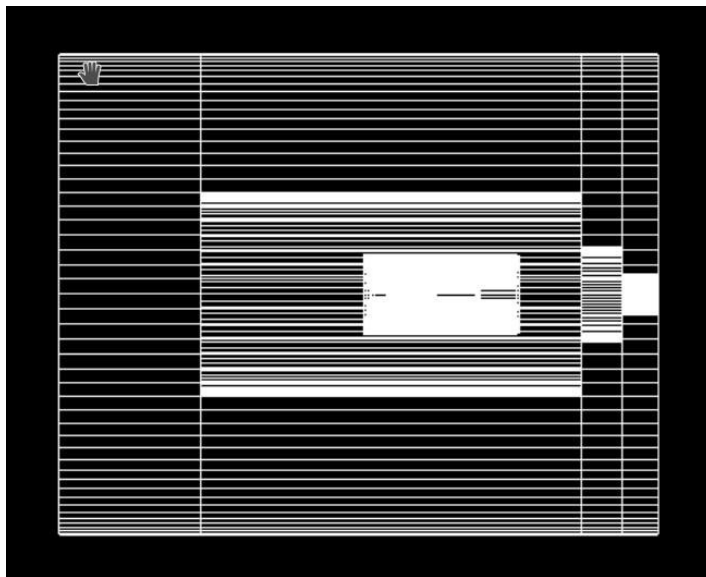
Prvi rezultati merenja produkcije neutrona mionima iz kosmičkog zračenja u olovnoj zaštiti HPGe detektora objavljeni su 2013. godine. Podaci su snimani tokom više od 400 dana merenja, u koincidentnom režimu rada scintilator-HPGe detektor. Analizom ovih podataka dobijen je rezultat za fluks neutrona proizvedenih mionima, na dubini naše podzemne laboratorije [6]. Merenja su kontinuirano nastavljena, sa većom statistikom snimljenih događaja; analiza ovih podataka je u toku. Pored eksperimentalnih merenja, uporedo su urađene Monte Carlo simulacije produkcije neutrona u olovnoj zaštiti, bazirane na Geant4 *framework*-u. Ovde su predstavljeni prvi rezultati simulacija: procena prinosa neutrona (broj neutrona po jedinici dužine) u interakcijama miona, kao i raspodela multipliciteta proizvedenih neutrona.

2. Metod

Geant4 je softverski paket za Monte Carlo simulacije transporta i interakcija čestica sa materijom [7]. On sadrži kompletan alat za modelovanje geometrije detektora, fizičkih procesa, primarnih i sekundarnih događaja, kao i odziva detektora. Na osnovi Geant4 platforme razvijena je posebna aplikacija za simulacije odziva germanijumskog i scintilacionih detektora u laboratoriji. Aplikacija je fleksibilna i omogućuje simulacije pojedinačnih i koincidentnih režima rada detektora. Prethodno je korišćena u različitim

slučajevima koji su zahtevali precizne simulacije scintilacionih i germanijumskih detektora [2,4,8,9].

Olovna zaštita je geometrije šupljeg cilindra, unutar kojeg se nalazi germanijumski detektor. Visina cilindra je 51 cm, prečnik osnove 41 cm, a debljina olovnog zida je 12 cm. Detektor je konstruisan prema specifikaciji proizvođača. Skica detektora i olovnog cilindra prikazana je na slici 2.



Slika 2. Skica olovne zaštite germanijumskog detektora.

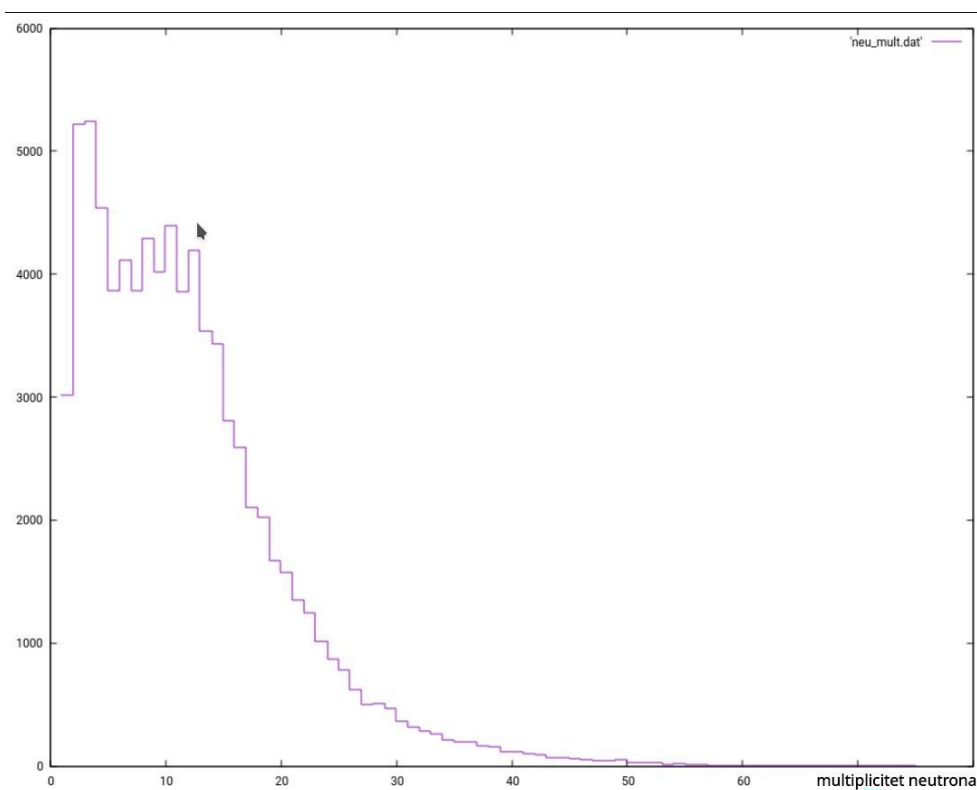
Primarni događaji generisani su definisanjem incidentne čestice, njene pozicije, pravca kretanja i energije. Incidentne čestice su pozitivni i negativni mioni; odnos broja pozitivnih i broja negativnih miona je 1,3. Početne pozicije miona na površini olovnog cilindra određene su na sledeći način: prvo se odabere gornja horizontalna strana ili vertikalna strana cilindra, prema verovatnoći da kosmički mion pogodi horizontalnu ili vertikalnu stranu, a zatim se odabere pozicija na datoj površini iz uniformne raspodele. Pravac kretanja miona sempliran je iz raspodele miona po pravcima, u funkciji od zenitnog ugla θ , koja je proporcionalna $\cos^{1,55}\theta$. Energija miona određena je iz energijske raspodele miona na površini Zemlje, pri čemu se uzimaju oni mioni koji uspeju da prođu kroz 12 m zemljišta. Detaljnija procedura generisanja primarnih događaja i izvođenje raspodele miona po pravcima i energijama može se videti u [4]. Fizički procesi u kojima učestvuju mioni – elektromagnetni i nuklearni – uključeni su u simulaciju kroz predefinisane Geant4 klasu QGSP_BERT_HP; ova klasa omogućava simulacije interakcija čestica sa velikom preciznošću.

3. Rezultati i diskusija

Prvi cilj simulacije bio je da se odredi broj proizvedenih neutrona u interakcijama miona sa jezgrima olova, po jedinici dužine puta, pri njihovom prolasku kroz olovnu zaštitu germanijumskog detektora. Generisanih primarnih događaja bilo je 10^8 ; ovaj broj može biti povezan sa vremenom eksperimentalnih merenja, uzimajući u obzir fluks miona u podzemnoj laboratoriji.

Ukupan broj proizvedenih neutrona bio je 934 000. Odavde je određen prinos neutrona, kao odnos broja neutrona i proizvoda gustine olova i srednje dužine puta miona kroz

olovo. Srednja dužina puta miona je 26,6 cm, a proizvod gustine olova i srednje dužine puta iznosi 302 g/cm^3 . Dobijena vrednost za prinos neutrona je $3,1 \times 10^{-5} \text{ neut./(gcm}^{-2}\text{)}$. Pored prinosa neutrona, određena je raspodela multipliciteta neutrona – broja neutrona proizvedenih u interakciji jednog miona sa olovom. Mion može proizvesti više od jednog neutrona na svom putu kroz olovo, što za rezultat ima više neutronske fonske događaja u detektoru koji potiču od jednog miona. Događaji su vremenski razdvojeni, odnosno detektuju se sa vremenskim razmakom, u zavisnosti od trenutka i mesta produkcije neutrona. Ovi događaji registruju se u detektoru kao signali sa vremenskim kašnjenjem, unutar definisanog vremenskog prozora mionskog događaja. To može poslužiti za selekciju fonskih događaja koji potiču od neutrona indukovanih mionima. Raspodela multipliciteta neutrona prikazana je na slici 3. Najveći broj miona proizvede manje od 10 neutrona u kaskadi, dok srednji multiplicitet neutrona iznosi 11,5. Dobijena raspodela slaže se sa rezultatima ranijih sličnih simulacija [10].



Slika 3. Raspodela multipliciteta neutrona proizvedenih mionima iz kosmičkog zračenja u olovnoj zaštiti HPGE detektora.

Rezultati simulacije pokazali su da ovaj metod može biti koristan za procenu produkcije neutrona mionima iz kosmičkog zračenja. On može dati detaljniji uvid u mehanizam produkcije neutrona. Osim toga, rezultati simulacije mogu pomoći u analizi podataka eksperimentalnih merenja, njihovom boljem razumevanju i evaluaciji.

4. Zahvalnica

Ovaj rad finansiran je od Instituta za fiziku u Beogradu kroz projekat Ministarstva prosvete, nauke i tehnološkog razvoja Republike Srbije.

5. Literatura

- [1] D. Mei, A. Hime. Muon-induced background study for underground laboratories. *Phys. Rev. D* 73, 2006, 053004.
- [2] A. Dragić, D. Joković, R. Banjanac, V. Udovičić, B. Panić, J. Puzović, I. Aničin. Measurement of cosmic ray muon flux in the Belgrade ground level and underground laboratories. *Nucl. Instr. Meth. A* 591, 2008, 470-475.
- [3] M. Savić, A. Dragić, D. Maletić, N. Veselinović, R. Banjanac, D. Joković, V. Udovičić. A novel method for atmospheric correction of cosmic-ray data based on principal component analysis. *Astropart. Phys.* 109, 2019, 1-11.
- [4] D. Joković, A. Dragić, V. Udovičić, R. Banjanac, J. Puzović, I. Aničin. Monte Carlo simulations of the response of a plastic scintillator and an HPGe spectrometer in coincidence. *Appl. Radiat. Isot.* 67, 2009, 719-722.
- [5] A. Dragić, V. Udovičić, R. Banjanac, D. Joković, D. Maletić, N. Veselinović, M. Savić, J. Puzović, I. Aničin. The new set-up in the Belgrade low-level and cosmic-ray laboratory. *Nucl. Techn. Radiat. Prot.* 26, 2011, 181-192.
- [6] A. Dragić, I. Aničin, R. Banjanac, V. Udovičić, D. Joković, D. Maletić, M. Savić, N. Veselinović, J. Puzović. Neutrons produced by muons at 25 mwe. *J. Phys.: Conf. Ser.* 409, 2013 012054.
- [7] S. Agostinelli et al. Geant4 – a simulation toolkit. *Nucl. Instr. Meth. A* 506, 2003, 250-303.
- [8] M. Krmar, J. Hansman, N. Jovančević, N. Lalović, J. Slivka, D. Joković, D. Maletić. A method to estimate a contribution of Ge(n,n') reaction to the low-energy part of gamma spectra of HPGe detectors. *Nucl. Instr. Meth. A* 709, 2013, 8-11.
- [9] J. Nikolić, T. Vidmar, D. Joković, M. Rajačić, D. Todorović. Calculation of HPGe efficiency for environmental samples: comparison of EFFTRAN and GEANT4. *Nucl. Instr. Meth. A* 763, 2014, 347-353.
- [10] L. Reichhart et al. Measurement and simulation of the muon-induced neutron yield in lead. *Astropart. Phys.* 47, 2017, 67-76.

MONTE CARLO SIMULATION OF THE COSMIC RAY MUON INDUCED NEUTRON PRODUCTION IN THE LEAD SHIELD OF THE GERMANIUM DETECTOR

**Dejan JOKOVIĆ, Dimitrije MALETIĆ, Vladimir UDOVIČIĆ,
Radomir BANJANAC, Aleksandar DRAGIĆ, Mihailo SAVIĆ,
Nikola VESELINOVIĆ and David KNEŽEVIĆ**

*Institute of Physics Belgrade, University of Belgrade, Belgrade, Serbia,
yokovic@ipb.ac.rs, maletic@ipb.ac.rs, udovicic@ipb.ac.rs, banjanac@ipb.ac.rs,
dragic@ipb.ac.rs, msavic@ipb.ac.rs, veselinovic@ipb.ac.rs, davidk@ipb.ac.rs*

ABSTRACT

Lead is usually used as a common shielding material for germanium detectors. Cosmic ray muons produce secondary particles in their interactions with lead nuclei, which contribute to overall background radiation detected by germanium detectors. Neutrons produced in muon interactions in lead shield make a significant part of this background component. Cosmic ray induced neutrons are a particular problem in experiments carried out in deep underground laboratories.

In the low-level underground laboratory at Institute of Physics Belgrade, a germanium detector and a muon detector operate in coincidence. This provides studying of different effects in the germanium detector induced by cosmic rays, especially effects originated from the cosmic ray induced neutrons.

Here, the results of Geant4 simulations of the cosmic ray muon induced neutron production in the lead shield of the germanium detector are presented. Estimate of the neutron yield – number of neutrons produced per unit path length – in muon interactions is obtained. The result is 3.1×10^{-5} neutrons/(gcm⁻²). Also, the neutron multiplicity distribution is determined, as a distribution of number of neutrons produced per muon interaction. The average multiplicity is 11.5.

DISTRIBUCIJA KONCENTRACIJE RADONA PO SPRATNOSTI STAMBENIH ZGRADA

Vladimir UDOVIĆIĆ¹, Dimitrije MALETIĆ¹, Aleksandar DRAGIĆ¹,
Radomir BANJANAC¹, Dejan JOKOVIĆ¹, Nikola VESELINOVIĆ¹,
Mihailo SAVIĆ¹, David KNEŢEVIĆ¹ i Maja EREMIĆ-SAVKOVIĆ²

- 1) Institut za fiziku u Beogradu, Institut od nacionalnog znaĉaja za Republiku Srbiju, Beograd, Srbija, udovic@ipb.ac.rs, maletic@ipb.ac.rs, dragic@ipb.ac.rs, banjanac@ipb.ac.rs, yokovic@ipb.ac.rs, veselinovic@ipb.ac.rs, msavic@ipb.ac.rs, davidk@ipb.ac.rs
- 2) Direktorat za radijacionu i nuklearnu sigurnost i bezbednost Srbije, Beograd, Srbija, eremic.savkovic@srbatom.gov.rs

SADRŢAJ

Dobro je poznato da je jedan od faktora koji utiĉe na varijabilnost radona u zatvorenom prostoru spratnost stambenih zgrada. Imajući u vidu ĉinjenicu da glavni izvor radona u zatvorenim prostorijama potiĉe iz zemljišta, oĉekuje se smanjenje koncentracije radona na višim spratovima. Na višim spratovima dominantan izvor radona potiĉe od graĐevinskog materijala, a u nekim sluĉajevima moĐe doći do odstupanja od ove opšte utvrĐene pravilnosti. S druge strane, varijabilnost radona zbog spratnosti, posebno u velikim gradovima, sa mnogo većim brojem visokih zgrada i gustom naseljenosti u poreĐenju sa ruralnim sredinama, moĐe uticati na procenu kolektivne doze koja potiĉe od radona. U tom smislu, a u svrhu naših istraĐivanja, izabrali smo jednu tipiĉnu porodiĉnu kuću sa potkrovljem i jedan šesnaestospratni soliter. Merenje koncentracije radona u odabranim stambenim objektima izvršeno je sa dva aktivna ureĐaja. Jedan je bio fiksiran u dnevnoj sobi u prizemlju, a drugi je menjao poziciju po spratovima u stambenim zgradama. Svaki merni ciklus na datom spratu trajao je sedam dana uz vreme uzorkovanja od dva sata. U ovom radu detaljno je uraĐena analiza dobijenih rezultata.

1. Uvod

Izvori radona u stambenim i poslovnim zgradama su, pre svega iz zemljišta, graĐevinskog materijala i vode. S obzirom na prirodu nastanka i svih pomenutih izvora, koncentracija radona je veša u prizemnim prostorijama u odnosu na stanove na višim spratovima stambenih objekata. U literaturi se moĐe pronaći dosta radova koji se bave uticajem raznih faktora na nivo i varijabilnost radona u zatvorenim prostorijama, pa izmeĐu ostalih i uticajem spratnosti [1-4]. U sluĉaju velikih stambenih objekata sa vešim brojem spratova, moĐe se uoĉiti odstupanje od opšte pravilnosti, jer je na višim spratovima dominantan izvor radona graĐevinski materijal, te se mogu uoĉiti povešane koncentracije radona u odnosu na situaciju na nišim spratovima. U tom smislu, uraĐena su merenja radona u dva tipična stambena objekta. Izbor zgrada je baziran na rezultatima iz monografije „Nacionalna tipologija stambenih zgrada Srbije— grupe autora sa Arhitektonskog fakulteta [5]. S obzirom na specifiĉnosti gradnje u Srbiji, broj

tipova zgrada je tako sveden na šest kategorija, dve za porodično stanovanje i četiri kategorije za kolektivno stanovanje; porodično stanovanje: 1. slobodnostoješa kuša, 2. kuša u nizu i kolektivno stanovanje: 3. slobodnostoješa zgrada, 4. zgrada u nizu, 5. zgrada u nizu tipa lamele (ponavlja se više zgrada rađениh по istom projektu, zgrada sa više ulaza...) i 6. soliter (slobodnostoješa zgrada velike spratnosti). Pokazuje se da više od 97% svih stambenih zgrada tине samostojеše porodične kuše. Takođe, za sve definisane tipove zgrada broj spratova se kreše od jednog do osam, pri tјemu su samostojеše porodične kuše uglavnom prizemne (37%) ili prizemne sa potkrovljem (26%), dok je veoma niska zastupljenost kuša koje imaju više od dva sprata (5%), sa prosečnom visinom porodičnih zgrada od 1,4 [5].

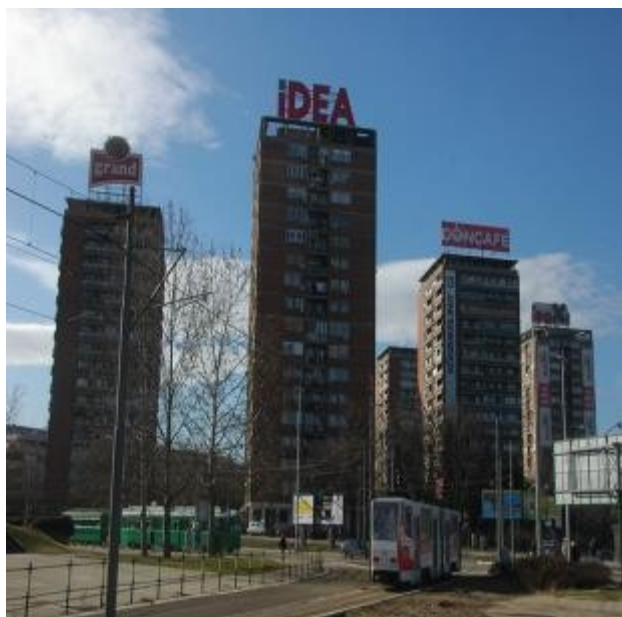
2. Eksperimentalna postavka

Izabrana su dva stambena objekta, jedan iz grupe za porodično stanovanje i jedan soliter iz grupe za kolektivno stanovanje. Porodična kuća (slika 1) ima karakterističan stil gradnje u kome se kuća gradi više godina uz konstantno dograđivanje i nadogradnju, što potencijalno može biti izvor ulaska radona u takve kuće. Kuća ima podrum i izgrađena je od standardnih materijala (cigla-blok, beton, malter). Na kraju je u rađena i izolacija korišćenjem stiropora debljine 5 cm. U kući su već vršena višegodišnja merenja koncentracije radona različitim metodama, o čemu je do sada publikovano nekoliko naučnih radova [6-8].



Slika 1. Tipična porodična kuća u Beogradu.

Iz grupe stambenih zgrada za kolektivno stanovanje izabran je soliter na Novom Beogradu (slika 2). Izgrađen je šezdesetih godina prošlog veka, blokovskog tipa. Soliter ima podrum, dok se u prizemlju nalaze lokali i poslovne prostorije. Stanovi se nalaze od prvog sprata pa naviše. Soliter ima 16. spratova.



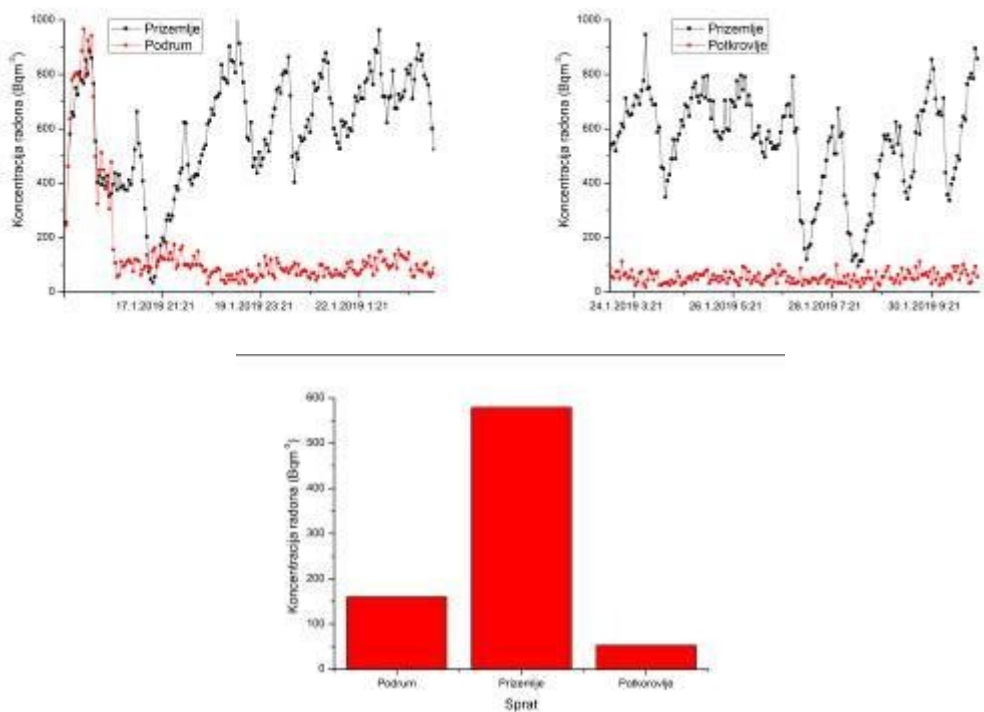
Slika 2. Soliter na Novom Beogradu.

Vremenske serije merenih koncentracija radona u ispitivanim stambenim objektima dobijene su pomoću dva aktivna uređaja SN1029 i SN1030 (proizvođača Sun Nuclear Corporation). To su merni uređaji jednostavne konstrukcije i primene u praksi. U suštini, radi se o brojaču sa dodatkom senzora za merenje meteoroloških parametara. Nedostatak uređaja je nemogućnost merenja koncentracije radona u zemljištu i vodi. Operater može podesiti vremenske sekvence od 0,5 do 24 sati. Jedan ciklus merenja može trajati 1000 sati ili ukupno 720 vremenskih sekvenci (broj sukcesivnih merenja, odnosno tačaka u vremenskoj seriji). Uređaji su bili podešeni da rade u vremenskoj sekvenci od 2 sata. Jedan je bio fiksiran u dnevnoj sobi u prizemlju, a drugi je menjao poziciju po spratovima u stambenim zgradama. Svaki merni ciklus na datom spratu trajao je sedam dana.

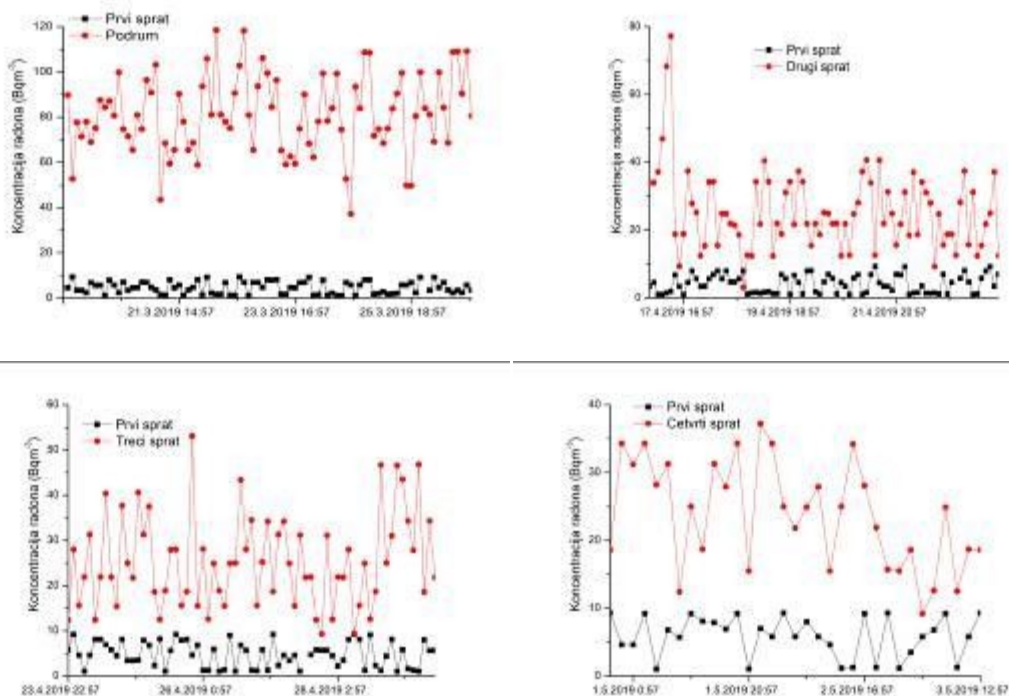
3. Rezultati i diskusija

Na slikama 3 i 4 su prikazani dobijeni rezultati merenja, kako vremenske serije tako i usrednjene koncentracije radona u ispitivanim stambenim objektima za zadati ciklus merenja od sedam dana.

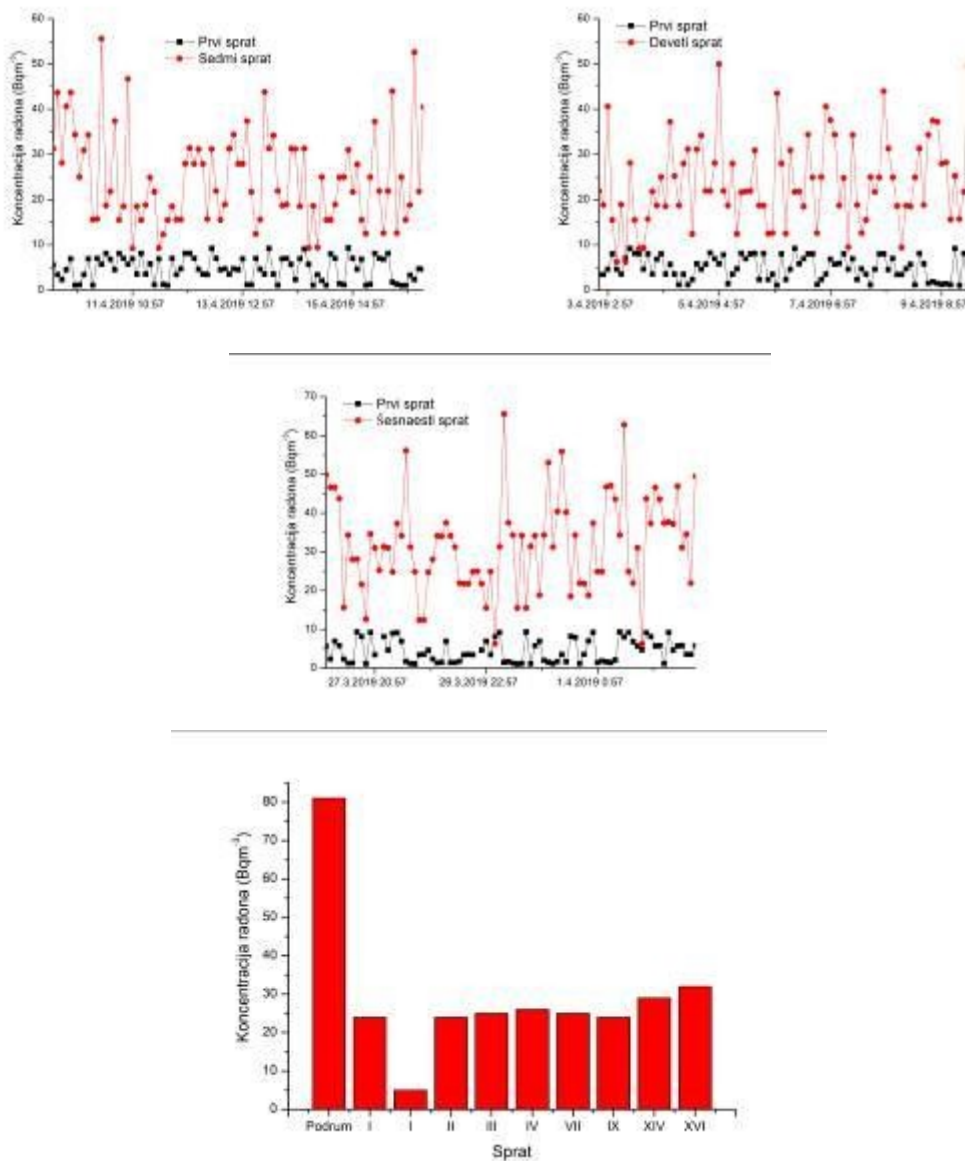
S obzirom da je detektor koji je sve vreme stajao u prizemlju solitera pokazao neobično niske vrednosti za koncentraciju radona, uradili smo uporedno merenje sa drugim detektorom u susednom, kao i u stanu u kome se nalazio fiksirani detektor. Dobijeni rezultati pokazuju izvesnu razliku, ali s obzirom da se radi o domenu izrazito niskih nivoa radona, pretpostavka je da su i merne nesigurnosti velike.



Slika 3. Vremenske serije i srednja koncentracija radona po spratovima u porodičnoj kući.



Slika 4. Vremenske serije i srednja koncentracija radona po spratovima u soliteru.



Slika 4. Nastavak.

4. Zaključak

Dobijeni rezultati pokazuju da je ponašanje radona u dva različita stambena objekta dijametralno suprotno. U porodičnoj kuši je moguše uoiti izrazite varijacije koncentracije radona uz jednodnevnu periodiku. Takođe, interesantan je odnos koncentracije radona u prizemlju, u odnosu na podrum kuše, koji je suprotan od uobičajene situacije kod kuša sa podrumom. Ovo inverzno ponašanje moe se protumaiti činjenicom da podrum ne prekriva celo prizemlje već njegov manji deo. Ostali deo prizemlja je pokriven betonskom ploom kao podlogom, ali sa pukotinama i lošim spojem sa zidovima predstavlja potencijalni izvor povišenog radona. Kod solitera je situacija suprotna i moe se smatrati da već od prvog sprata dominantan izvor radona je graevinski materijal. Tak se moe uoiti blagi rast srednje koncentracije radona na

вишим спратовима. No, добјени резултати у солитеру се могу предвидети, а на основу рада групе аутора који су одредили интерно излагање из грађевинског материјала, који се користи у Србији, а које потиже од ешалације радона и торона [9].

5. Zahvalnica

Ovaj rad je realizovan uz podršku Ministarstva prosvete, nauke i tehnološkog razvoja Republike Srbije u okviru projekta pod brojem III43002.

6. Literatura

- [1] F. Bochicchio, G. Campos-Venuti, S. Piermattei, C. Nuccetelli, S. Risica, L. Tommasino, G. Torri, M. Magnoni, G. Agnesod, G. Sgorbati, M. Bonomi, L. Minach, F. Trotti, M.R. Malisan, S. Maggiolo, L. Gaidolfi, C. Giannardi, A. Rongoni, M. Lombardi, G. Cherubini, S. D'Ostilio, C. Cristofaro, M. Pugliese, V. Martucci, A. Crispino, P. Cuzzocrea, A. Sansone Santamaria, M. Cappai. Annual average and seasonal variations of residential radon concentration for all the Italian Regions. *Radiat. Meas.* 40, 2005, 686-694.
- [2] H. Friedmann. Final Results of the Austrian Radon Project. *Health Phys.* 89(4), 2005, 339-348.
- [3] R. Borgoni, D. De Francesco, D. De Bartolo, N. Tzavidis. Hierarchical modeling of indoor radon concentration: how much do geology and building factors matter? *J. Environ. Radioact.* 138, 2014, 227-237.
- [4] M. Lorenzo-González, A. Ruano-Ravina, J. Peón, M. Piñeiro, J. Miguel Barros-Dios. Residential radon in Galicia: a cross-sectional study in a radon-prone area. *J. Radiol. Prot.* 37(3), 2017, 728-741.
- [5] M. Jovanović Popović, D. Ignjatović, A. Radivojević, A. Rajtić, N. Šuković Ignjatović, Lj. Đukanović, M. Nedić. National Typology of Residential Buildings in Serbia, Faculty of Architecture University of Belgrade, Belgrade, 2013, ISBN 978-86-7924-102-3.
- [6] V. Udovičić, D. Maletić, R. Banjanac, D. Joković, A. Dragić, N. Veselinović, J. Tivanović, M. Savić, S. Forkapić. Multiyear Indoor Radon Variability in a Family House – a Case Study in Serbia. *Nucl. Tech. Radiat. Protect.* XXXIII (2), 2018, 174-179.
- [7] D. Maletić, V. Udovičić, R. Banjanac, D. Joković, A. Dragić, N. Veselinović, J. Filipović. Comparison of multivariate classification and regression methods for indoor radon measurements. *Nucl. Tech. Radiat. Protect.* 29, 2014, 17-23.
- [8] J. Filipović, D. Maletić, V. Udovičić, R. Banjanac, D. Joković, M. Savić, N. Veselinović. The use of multivariate analysis of the radon variability in the underground laboratory and indoor environment. *Nukleonika* 61(3), 2016, 357-360.
- [9] P. Ujić, I. Telić, A. Kandić, I. Vukanac, M. Đurašević, D. Dragosavac, Z. S. Tunić. Internal exposure from building materials exhaling ^{222}Rn and ^{220}Rn as compared to external exposure due to their natural radioactivity content. *Appl. Radiat. Isot.* 68, 2010, 201–206.

INDOOR RADON DISTRIBUTION DUE TO FLOOR LEVEL IN THE RESIDENTIAL BUILDINGS

**Vladimir UDOVICIC¹, Nikola VESELINOVIC¹, Dimitrije MALETIC¹,
Radomir BANJANAC¹, Aleksandar DRAGIC¹, Dejan JOKOVIC¹,
Mihailo SAVIC¹, David KNEZEVIC¹ and Maja EREMIC-SAVKOVIC²**

1) *Institute of Physics Belgrade, University of Belgrade, Belgrade, Serbia,
udovicic@ipb.ac.rs, maletic@ipb.ac.rs, dragic@ipb.ac.rs, banjanac@ipb.ac.rs,
yokovic@ipb.ac.rs, veselinovic@ipb.ac.rs, msavic@ipb.ac.rs, davidk@ipb.ac.rs*

2) *Serbian Radiation and Nuclear Safety and Security Directorate, Belgrade,
Serbia, eremic.savkovic@srbatom.gov.rs*

ABSTRACT

It is well known that one of the factors influencing indoor radon variability is the floor level of residential buildings. Bearing in mind the fact that the main source of indoor radon is from radon in soil gas, a radon concentration on upper floors is expected to decrease. On the upper floors, the dominant source of radon originates from building materials, and in some cases there may be deviations from this generally established regularity. On the other hand, radon variability due to floor level, especially in large cities, with a much larger number of high buildings and density of population compared to rural areas, can affect the estimation of the collective dose derived from radon. In this sense, and for the purpose of our research, we chose a typical family house with a loft and sixteen high-rise building. Indoor radon measurements in selected residential buildings were done with two active devices. One was fixed in the living room on the ground floor, while the other was changing the position on the floors in residential buildings. Each measuring cycle on the floor lasted for seven days with a sampling time of two hours. In this paper, an analysis of the obtained results has been done in detail.

PROCENA TEMPERATURSKOG PROFILA ATMOSFERE NA OSNOVU DETEKTOVANOG FLUKSA KOSMIČKIH MIONA

Mihailo SAVIĆ, Vladimir UDOVIČIĆ, Dimitrije MALETIĆ, Aleksandar DRAGIĆ, Radomir BANJANAC, Dejan JOKOVIĆ, Nikola VESELINOVIĆ i David KNEŽEVIĆ

Institut za fiziku u Beogradu, Institut od nacionalnog značaja za Republiku Srbiju, Beograd, Srbija, msavic@ipb.ac.rs

SADRŽAJ

Uticaj atmosferskih parametara na intenzitet mionske komponente sekundarnog kosmičkog zračenja dobro je poznat. Dominantan doprinos varijaciji fluksa kosmičkih miona usled atmosferskih parametara daju dva meteorološka efekta - barometarski (usled varijacije atmosferskog pritiska) i temperaturski (usled varijacije temperature atmosfere). Postoji više teorijskih i empirijskih modela koji dobro opisuju ove zavisnosti. Obično se na osnovu ovih modela vrši korekcija kako bi se eliminisala varijacija fluksa kosmičkih miona atmosferskog porekla.

Obrnuto, osetljivost mionskih detektora na varijacije atmosferskih parametara može se iskoristiti da se na osnovu poznatih parametara modela i poznatog odbroja kosmičkih miona odredi temperatura različitih nivoa atmosfere. U ovom radu ćemo demonstrirati ovaj pristup na osnovu podataka merenih mionskim monitorima Niskofonske laboratorije za nuklearnu fiziku Instituta za fiziku u Beogradu i primenom empirijskog modela meteoroloških efekata, zasnovanog na tehnici dekompozicije na osnovne komponente.

1. Uvod

Intenzitet pljuskova sekundarnog kosmičkog zračenja zavisi od atmosferskih meteoroloških parametara. To se naročito odnosi na mionsku komponentu sekundarnog kosmičkog zračenja. Dva efekta dominantno utiču na fluks sekundarnih miona: barometarski koji opisuje antikorelaciju fluksa kosmičkih miona sa atmosferskim pritiskom [1] i temperaturski koji se odnosi na uticaj varijacije atmosferske temperature na detektovani intenzitet miona [2].

Osim fundamentalnog, detaljno poznavanje meteoroloških efekata ima značaj u proceduri korekcije na date efekte, čime se povećava osetljivost zemaljskih detektora kosmičkog zračenja na varijacije neatmosferskog porekla. Alternativno, dobar model meteoroloških efekata bi u principu omogućio predviđanje atmosferskih parametara na osnovu merenja fluksa miona. Ovo je potencijalno značajno za određivanje temperatura pojedinih slojeva atmosfere u slučaju da su druge metode nedostupne.

Postoji više predloženih metoda za predikciju atmosferskih meteoroloških parametara na osnovu merenja intenziteta kosmičkog zračenja zemaljskim detektorima. Mogu se bazirati na merenju različitih komponenti fluksa kosmičkih miona [3, 4], simultanom merenju neutronske i mionske komponente [5] ili upotrebi mionskog teleskopa sposobnim da meri ugaonu distribuciju intenziteta [6]. Sve pomenute metode karakteriše relativna kompleksnost eksperimentalne postavke i analize. Takođe, zajedničko svim pomenutim metodama je da se u proceduri određivanja atmosferskih temperatura oslanjaju na teorijski izračunate koeficijente za opisivanje zavisnosti intenziteta miona od temperaturskog profila atmosfere. Ovaj pristup ima određenih ograničenja usled nužno aproksimativnog karaktera i neprilagođenosti konkretnom

detektorskom sistemu.

U ovom radu, mi ćemo demonstrirati upotrebljivost jednostavnije eksperimentalne postavke i primenu empirijskog modela meteoroloških efekata na određivanje temperaturskog profila atmosfere.

2. Eksperimentalni podaci i obrada

U Niskofonskoj laboratoriji za nuklearnu fiziku Instituta za fiziku u Beogradu mionski fluks se meri kontinualno od 2009. godine, na nivou zemlje i na dubini od 25 m.w.e. Eksperimentalna postavka se sastoji od scintilacionog detektora i sistema za akviziciju. Detektor je plastični scintilator dimenzija 100cm×100cm×5cm sa četiri fotomultiplikatora postavljena na ćoškovce. U srcu sistema za akviziciju nalazi se brzi analogno-digitalni konverter sposoban da u realnom vremenu precizno određuje vreme detekcije i amplitudu signala [7]. U ovoj analizi korišćeni su podaci snimljeni detektorom na nivou zemlje u periodu od 01.06.2010. do 31.05.2011. godine.

Za opisivanje meteoroloških efekata na kosmičke mione, u okviru Niskofonske laboratorije razvijen je empirijski model baziran na tehnici dekompozicije na osnovne komponente (Principal Component Analysis - PCA) [8]. Metod se zasniva na ideji da se u analizi meteoroloških efekata sa skupa visoko korelisanih meteoroloških parametara pređe na skup linearno nezavisnih promenljivih, kao i potencijalno smanji dimenzionalnost problema zadržavanjem samo statistički značajnih osnovnih komponenti u analizi. Koeficijenti zavisnosti detektovanog odbroja miona od tako određenih osnovnih komponenti su pouzdaniji, jer su manje podložni statističkim fluktuacijama. Ovde ćemo primeniti ovaj model kako bismo na osnovu odbroja miona merenog u nadzemnoj laboratoriji odredili temperature različitih nivoa atmosfere.

Neka je C_X matrica tipa $n \times m$ koja predstavlja m merenja n različitih meteoroloških parametara. Dekompozicijom na osnovne komponente se sa skupa n meteoroloških varijabli prelazi na skup n osnovnih komponenti, čije vrednosti su reprezentovane matricom C_Y , takođe tipa $n \times m$. Ova relacije se može predstaviti jednačinom:

$$C_Y = PC_X, \quad (1)$$

gde je P matrica transformacije čiji redovi predstavljaju kompoziciju osnovnih komponenti.

Na slici 1 prikazana je kompozicija prvih 9 osnovnih komponenti. Na x-osi su meteorološke promenljive: pritisak, temperature 24 izobarna nivoa (10, 20, 30, 50, 70, 100, 150, 200, 250, 300, 350, 400, 450, 500, 550, 600, 650, 700, 750, 800, 850, 900, 925 i 975 mb) i temperatura na nivou tla. Na y-osi su prikazane vrednosti kosinusa uglova rotacije pri prelasku sa skupa meteoroloških varijabli na skup osnovnih komponenti.

Na osnovu statističke i korelacione analize zaključeno je da su za meteorološke efekte od značaja samo pet osnovnih komponenti, i to komponente 1, 3, 4, 5 i 6 [8].

Zavisnost varijacije detektovanog odbroja miona od ovih komponenti, usled meteoroloških efekata, data je jednačinom:

$$\delta N_{PC} = \sum_i k_i PC_i, \quad i = 1, 3, 4, 5, 6 \quad (2)$$

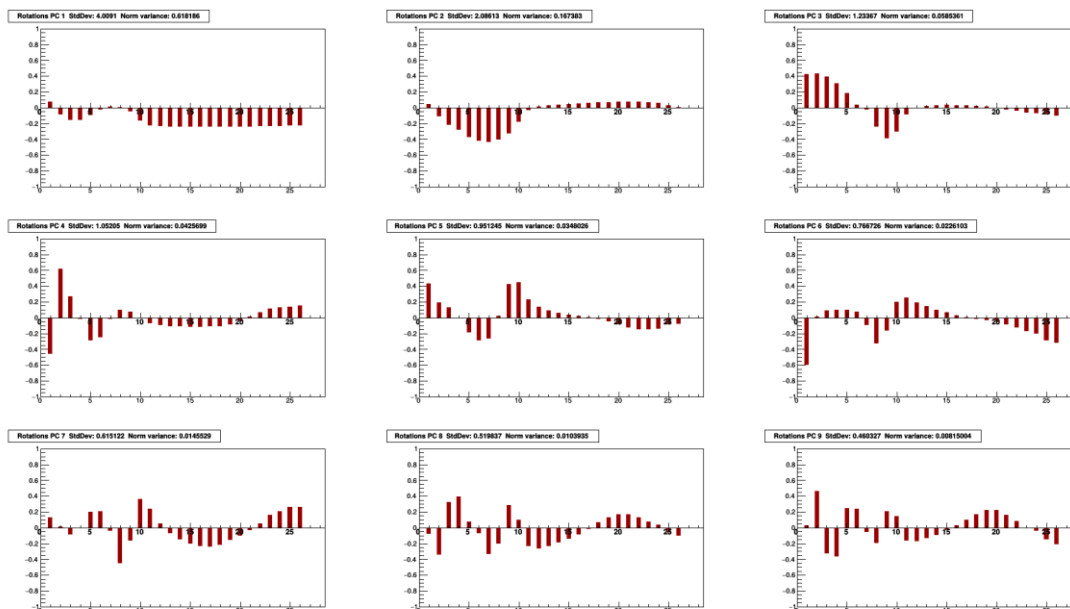
gde su PC_i osnovne komponente a k_i odgovarajući koeficijenti.

Pomoću ove relacije u principu je moguće proceniti vrednosti osnovnih komponenti na osnovu poznatog odbroja.

Dalje, transformišući jednačinu 1 kao:

$$C_X = P^{-1} C_Y = P^T C_Y \quad (3)$$

na osnovu procenjenih vrednosti osnovnih komponenti sada je moguće odrediti procenjene vrednosti meteoroloških parametara.



Slika 1. Kompozicija prvih devet osnovnih komponenti. Na x-osi su meteorološke promenljive: pritisak, temperature 24 izobarna nivoa (10, 20, 30, 50, 70, 100, 150, 200, 250, 300, 350, 400, 450, 500, 550, 600, 650, 700, 750, 800, 850, 900, 925 i 975 mb) i temperatura na nivou tla. Na y-osi su prikazane vrednosti uglova rotacije.

3. Rezultati i diskusija

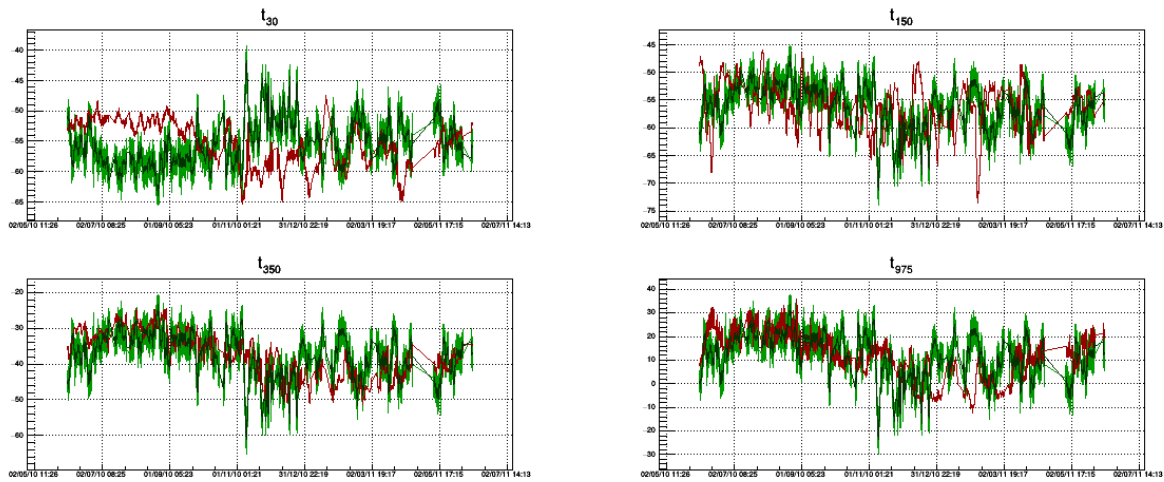
Za pomenuti referentni period određeni su koeficijenti u jednačini 2, uzimajući u obzir samo geomagnetno mirne dane [8]. Pomoću ovako određenih koeficijenata i merenog odbroja određene su procenjene vrednosti za pet signifikantnih osnovnih komponenti za ceo referentni period. Zatim su na osnovu jednačine 3 određene procenjene vrednosti meteoroloških parametara. Na slici 2 prikazane su vremenske serije merenih i procenjenih vrednosti meteoroloških parametara za izabrane izobarne nivoe.

Zbog preglednosti, prikazani su grafici za četiri različita nivoe. Kao referentni izabrani su nivoi od 30 mb (stratosfera), 150 mb (tropopauza/gornja troposfera), 350 mb (troposfera) i 975 mb (u blizini zemlje). Na plotovima crvenom linijom prikazane su merene vrednosti a svetlo zelenom vrednosti procenjene na osnovu merenog odbroja miona. Takođe, kako bi se dala jasnija slika i smanjio efekat fluktuacija merenog odbroja, vremenska serija predviđenih vrednosti je smutovana (*smoothing*) i prikazana na graficima tamno zelenom bojom.

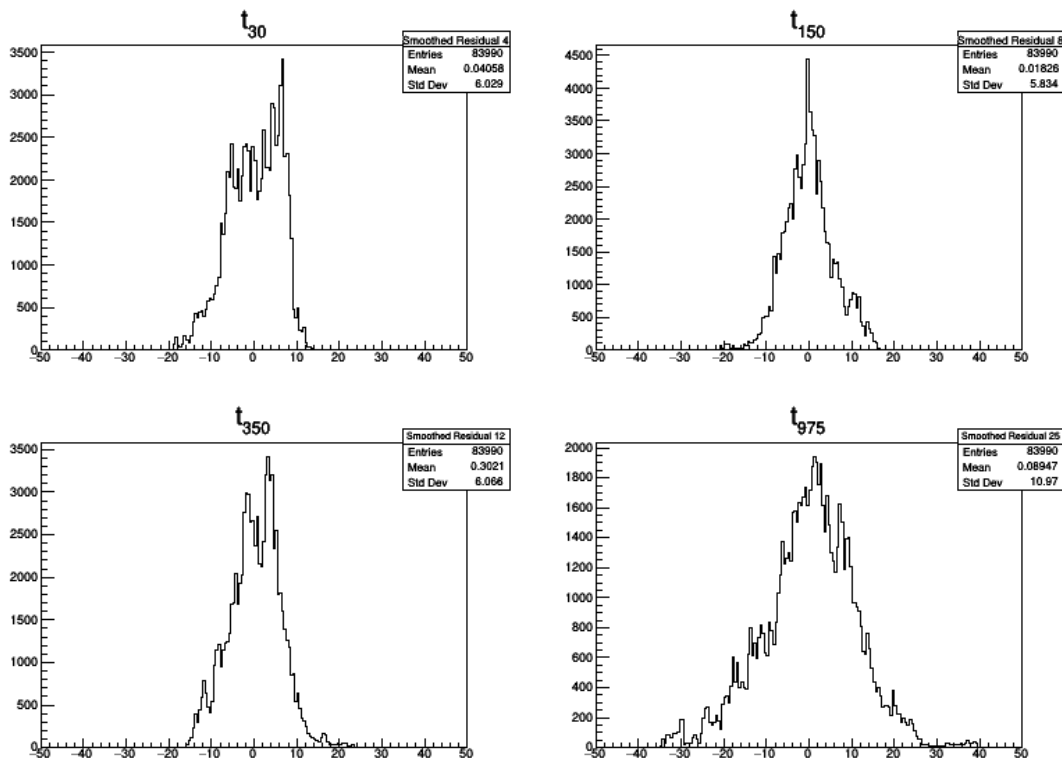
Na slici 3 prikazana je raspodela razlika merenih i procenjenih vrednosti meteoroloških parametara.

Osim analize vremenskih serija, još jedan kriterijum za određivanje efikasnosti predviđanja temperature pojedinih nivoe mogao bi biti na osnovu širine prikazanih raspodela. Međutim, varijacija temperatura različitih nivoe nije ista tako da ovo može dati nepotpunu sliku. Stoga su u tabeli 1 prikazane vrednosti standardnih devijacija ovih raspodela, standardnih devijacija merenih vrednosti, kao i relativan odnos ove dve

veliĉine koji daje bolji uvid u efikasnost predikcije temperatura pojedinih nivoa atmosfere.



Slika 2. Vremenske serije merenih i procenjenih vrednosti meteoroloških parametara za izobrne nivoe od 30, 150, 350 i 975 mb. Merene vrednosti - crvena linija, procenjene - svetlo zelena linija i smutovane procenjene - tamno zelena linija.



Slika 3. Raspodela razlika merenih i procenjenih vrednosti meteoroloških parametara za izobarne nivoe od 30, 150, 350 i 975 mb.

Tabela 1. Standardna devijacija raspodela razlika merenih i procenjenih vrednosti (σ_r), raspodele vrednosti merenih temperatura (σ_t) i relativan odnos ove dve vrednosti (σ_r/σ_t).

	t ₁₀	t ₂₀	t ₃₀	t ₅₀	t ₇₀	t ₁₀₀	t ₁₅₀	t ₂₀₀	t ₂₅₀	t ₃₀₀	t ₃₅₀	t ₄₀₀
σ_r	9.314	5.246	6.029	3.645	3.940	4.032	5.834	7.455	5.761	5.679	6.066	6.297
σ_t	7.154	4.844	3.669	3.320	2.862	3.055	4.012	5.754	5.111	5.658	6.237	6.460
σ_r/σ_t	1.302	1.083	1.643	1.098	1.377	1.320	1.454	1.296	1.127	1.004	0.973	0.975

t ₄₅₀	t ₅₀₀	t ₅₅₀	t ₆₀₀	t ₆₅₀	t ₇₀₀	t ₇₅₀	t ₈₀₀	t ₈₅₀	t ₉₀₀	t ₉₂₅	t ₉₇₅	t _{ground}
6.386	6.415	6.389	6.387	6.504	6.863	7.340	8.085	8.985	9.956	10.40	10.97	11.20
6.518	6.510	6.466	6.415	6.428	6.616	6.841	7.253	7.793	8.456	8.810	9.444	9.523
0.980	0.985	0.988	0.996	1.012	1.037	1.073	1.115	1.153	1.177	1.181	1.161	1.176

Na osnovu predstavljenih grafika i tabela možemo videti da se najbolje slaganje dobija za sloj atmosfere od 300 do 600 mb. Nešto slabije slaganje dobija se za nivoe u blizini tla, što je u skladu sa kompleksnijom dinamikom temperatura u ovih slojevima, kao i za slojeve od 100 do 200 mb, u kojima dominantno dolazi do produkcije miona. Ovaj drugi podatak je moguća posledica činjenice da je za mione detektovane na površini zemlje značajniji negativni temperaturski efekat, asociran sa jonizacionim gubicima i verovatnoćom raspada miona u nižim slojevima atmosfere, dok pozitivni temperaturski efekat u vezi sa verovatnoćom nastanka miona u sloju između 100 i 200 mb ima manji doprinos. Najslabije slaganje dobija se za neke od nivoe u stratosferi i tropopauzi, što se može videti na primeru temperature nivoea od 30 mb koji je u značajnom delu godine antikorelisan sa procenjenom temperaturom. Ovo je možda uslovljeno manjim varijacijama temperature na ovim nivoima kao i činjenicom da postoji značajna varijacija temperature ovih nivoea koja nije korelisana sa intenzitetom kosmičkih miona, sadržana u osnovnoj komponenti 2 (slika 1).

4. Zaključak

Preliminarna analiza je pokazala da postoji dosta dobro slaganje merenih i procenjenih atmosferskih temperatura za veći broj nivoea. Procenjene temperature imaju uglavnom konzistentne vremenske serije i dobro opisuju godišnju varijaciju. Najbolje slaganje sa merenim vrednostima dobija se u višim slojevima troposfere. Stoga, prikazani rezultati predstavljaju dobru polaznu osnovu za dalju analizu.

5. Zahvalnica

Ovaj rad je realizovan uz podršku Ministarstva prosvete, nauke i tehnološkog razvoja Republike Srbije u okviru projekta pod brojem OI 171002.

Literatura

- [1] L. Myssowsky and L. Tuwim. "Unregelmäßige Intensitätsschwankungen der Höhenstrahlung in geringer Seehöhe". *Zeitschrift für Physik* 39.2-3 (1926).
- [2] A Duperier. "The Temperature Effect on Cosmic-Ray Intensity and the Height of

- Meson Formation". *Proceedings of the Physical Society* 61.1 (1948), ñ. 34.
- [3] Miyazaki Y. and M. Wada. "Simulation of cosmic ray variation due to temperature effect", *Acta phys. Acad. Sci. hung.*, 29, Suppl. 2, 591-595 (1970).
- [4] Kohno, T., Imai, K., Inue, A., Kodama, M., & Wada, M. "Estimation of the Vertical Profile of Atmospheric Temperature from Cosmic-Ray Components". *Proceedings of the 17th International Cosmic Ray Conference, held in Paris, France*. Volume 10., p.289
- [5] L.I.Dorman, *Cosmic Rays in the Earth's Atmosphere and Underground*, Springer 2004.
- [6] V.V. Borog, O.V. Belonosova, A.S. Davydov, G.M. Kruchenitskii, S.P. Perov and V.G.Yanke. "Study of Atmospheric Temperature at Different Altitudes using Muon Angular Distribution at Sea Level". *29th International Cosmic Ray Conference Pune (2005)* 2, 381-384
- [7] Aleksandar Dragic, Vladimir Udovicic, Radomir Banjanac, Dejan Jokovic, Dimitrije Maletic, Nikola Veselinovic, Mihailo Savic, Jovan Puzovic. "The New Setup in the Belgrade Low-Level and Cosmic-Ray Laboratory". *Nuclear Technology & Radiation Protection: Year 2011*, Vol. 26, No. 3, pp.181-192
- [8] M Savic at al. "A novel method for atmospheric correction of cosmic-ray data based on principal component analysis". *Astroparticle Physics* **109 (2019)**.

ATMOSPHERIC TEMPERATURE PROFILE ESTIMATION BASED ON MEASURED COSMIC RAY MUON FLUX

Mihailo SAVIĆ, Vladimir UDOVIČIĆ, Dimitrije MALETIĆ, Aleksandar DRAGIĆ, Radomir BANJANAC, Dejan JOKOVIĆ, Nikola VESELINOVIĆ i David KNEŽEVIĆ










*Institute of Physics Belgrade, University of Belgrade, Belgrade, Serbia,
msavic@ipb.ac.rs*

ABSTRACT

The effect of atmospheric parameters in secondary cosmic ray muon component is well known. This is mainly through two dominant meteorological effects - barometric (due to atmospheric pressure variation) and temperature (due to atmospheric temperature variation). There are several theoretical and empirical models that describe these effects well. Usually this knowledge is used to correct for secondary cosmic ray variations due to atmospheric effects.

Alternatively, once model parameters are established, sensitivity of cosmic ray muon detectors to variations of atmospheric origin can be used to estimate temperatures for different layers of the atmosphere. In this work we will demonstrate this procedure using cosmic ray data measured in Low Background Laboratory for Nuclear Physics at Institute of Physics Belgrade, combined with parameters of empirical model for meteorological effects based on principal component analysis.

Implications of the Temperature Effect Analysis Using Simulated Secondary Cosmic Muon Data

Savić, M.R.,¹  Veselinović, N.B.,¹  Dragić, A.L.,¹  Maletić, D.M.,¹ 
Joković, D.R.,¹  Banjanac, R.M.,¹  Knežević, D.,¹  Travar, M.¹  and
Udovičić, V.I.¹ 

¹*Institute of Physics Belgrade, Pregrevica 118, 11080 Belgrade, Serbia*
E-mail: msavic@ipb.ac.rs

As it propagates through the atmosphere, the muon component of secondary cosmic rays is influenced by variations in atmospheric parameters. The two most significant atmospheric effects affecting the muon flux detected at ground level are the barometric effect, due to changes in atmospheric pressure, and the temperature effect, caused by fluctuations in atmospheric temperature.

To enhance the sensitivity of ground-based muon detectors to cosmic ray variations of non-atmospheric origin, these effects must be corrected, with the temperature effect being more complex to model. The most well-established method for correcting the temperature effect is the integral method, based on the theory of atmospheric effects (Dorman 2004). However, as it is not so straightforward to implement, several empirical methods have been developed over the years, including the effective level of generation method (Duperier 1949), the mass-averaged temperature method (Dvornikov et al. 1976), as well as more recent approaches based on principal component analysis (Savić et al. 2019) and machine learning applications (Savić et al. 2021).

Each theoretical and empirical approach has its advantages and limitations, and directly comparing the effectiveness of these methods with real measured data is not necessarily simple. One way to address this is to test model performance on simulated data, where atmospheric variation is the only source of flux change. Preliminary results from data simulated with the CORSIKA package (Heck et al. 1998) provide a clearer picture of the strengths and limitations of these methods. Specifically, the results suggest that the integral method may lead to overcorrections if applied too directly, an issue that hadn't been that obvious before.

References

Dorman, L., Cosmic Rays in the Earth's Atmosphere and Underground. 10.1007/978-1-4020-2113-8. (2004).

- Duperier A., The meson intensity at the surface of the earth and the temperature at the production level, Proceedings of the Physical Society. Section A 62 (11) (1949) 684.
- V. Dvornikov, Y. Y. Krest'yannikov, A. Sergeev, Determination of the variation of average-mass temperature of the atmosphere by data of cosmic ray intensity., Geomagnetism and aeronomy 16 (1976) 923–925.
- M. Savić, A. Dragić, D. Maletić, N. Veselinović, R. Banjanac et al., A novel method for atmospheric correction of cosmic-ray data based on principal component analysis, Astropart.Phys. 109 (2019), 1-11.
- Savić, M., Maletić, D., Dragić, A., Veselinović, N., Joković, D., Banjanac, R., et al. (2021). Modeling meteorological effects on cosmic ray muons utilizing multivariate analysis. Space Weather, 19, e2020SW002712.
- Heck, D.; Knapp, J.; Capdevielle, J. N.; Schatz, G.; Thouw, T., CORSIKA: a Monte Carlo code to simulate extensive air showers. Forschungszentrum Karlsruhe GmbH, Karlsruhe (Germany)., Feb 1998, V + 90 p., TIB Hannover, D-30167 Hannover (Germany).